

SOLID MECHANICS AND ITS APPLICATIONS

J.M. Huyghe, Peter A. C. Raats and
Stephen C. Cowin (Eds.)

IUTAM Symposium on
**Physicochemical and
Electromechanical
Interactions in
Porous Media**

IUTAM

 Springer

IUTAM Symposium on Physicochemical and Electromechanical
Interactions in Porous Media

SOLID MECHANICS AND ITS APPLICATIONS

Volume 125

Series Editor: G.M.L. GLADWELL
Department of Civil Engineering
University of Waterloo
Waterloo, Ontario, Canada N2L 3G1

Aims and Scope of the Series

The fundamental questions arising in mechanics are: *Why?*, *How?*, and *How much?*
The aim of this series is to provide lucid accounts written by authoritative researchers giving vision and insight in answering these questions on the subject of mechanics as it relates to solids.

The scope of the series covers the entire spectrum of solid mechanics. Thus it includes the foundation of mechanics; variational formulations; computational mechanics; statics, kinematics and dynamics of rigid and elastic bodies; vibrations of solids and structures; dynamical systems and chaos; the theories of elasticity, plasticity and viscoelasticity; composite materials; rods, beams, shells and membranes; structural control and stability; soils, rocks and geomechanics; fracture; tribology; experimental mechanics; biomechanics and machine design.

The median level of presentation is the first year graduate student. Some texts are monographs defining the current state of the field; others are accessible to final year undergraduates; but essentially the emphasis is on readability and clarity.

For a list of related mechanics titles, see final pages.

IUTAM Symposium on Physicochemical and Electromechanical Interactions in Porous Media

Edited by

J.M. Huyghe

*Department of Biomedical Engineering,
Eindhoven University of Technology,
Eindhoven, The Netherlands*

Peter A.C. Raats

*formerly of Wageningen University and Research Centre,
Wageningen, The Netherlands*

and

Stephen C. Cowin

*New York Center for Biomedical Engineering,
School of Engineering, The City College,
New York, NY, U.S.A.*

A C.I.P. Catalogue record for this book is available from the Library of Congress.

ISBN-10 1-4020-3864-X (HB)
ISBN-13 978-1-4020-3864-8 (HB)
ISBN-10 1-4020-3865-8 (e-book)
ISBN-13 978-1-4020-3865-5 (e-book)

Published by Springer,
P.O. Box 17, 3300 AA Dordrecht, The Netherlands.

www.springeronline.com

Printed on acid-free paper

All Rights Reserved

© 2005 Springer

No part of this work may be reproduced, stored in a retrieval system, or transmitted in any form or by any means, electronic, mechanical, photocopying, microfilming, recording or otherwise, without written permission from the Publisher, with the exception of any material supplied specifically for the purpose of being entered and executed on a computer system, for exclusive use by the purchaser of the work.

Printed in the Netherlands.

Contents

Foreword	ix
Acknowledgments	xi
List of Participants	xiii
Part I MICROMECHANICS	
Bones Have Ears: An Application of Bone Poroelasticity <i>Stephen C. Cowin</i>	3
Representative Microstructure Finite Elements for Collagen Gels <i>Preethi L. Chandran and Victor H. Barocas</i>	37
Part II COUPLING AND WAVES	
Viscous Effects in Particulates <i>J. Carlos Santamarina, Julio R. Valdes, Angelica M. Palomino and Jose Alvarelllos</i>	45
Pore Roughness Effects on High-Frequency Permeability <i>David Smeulders, Andrea Cortis, Jean Luc Guermond and Denis Lafarge</i>	53
Influence of High-Frequency Acoustic Waves on the Flow of a Liquid through Porous Material: Experimental and Theoretical Investigation <i>Pietro Poesio and Gijs Ooms</i>	61
Part III NUMERICAL SIMULATION	
Large Strain Analysis of 3-D Viscoelastic Swelling of Charged Tissues and Gels <i>Wolfgang Ehlers, Bernd Markert and Ayhan Acartürk</i>	69
Theoretical and Finite Element Models for Coupled Electro-Mechano- Chemical Transport in Soft Tissues <i>Bruce R. Simon, Gregg A. Radtke, Zun P. Liu, Paul H. Rigby and Stuart K. Williams</i>	75

Porous Effects in the Description of the Dynamics of Granular Avalanches <i>Shiva P. Pudasaini, Yongqi Wang and Kolumban Hutter</i>	81
A Multiphase Approach for the Analysis of Hygro-Thermo-Chemo-Mechanical Interactions in Concrete at Early Ages and at High Temperature <i>Dariusz Gawin, Francesco Pesavento and Bernard A. Schrefler</i>	91
Study of Drying Shrinkage Cracking by Lattice Gas Automaton and Environmental Scanning Electron Microscope <i>Dragana Jankovic</i>	99
Part IV ELECTROMECHANICS AND SWELLING	
Osmotic Transport through Clays and Capsules <i>John D. Sherwood and Frédéric Risso</i>	111
Electrokinetics in Random Deformable Porous Media <i>Józef Joachim Telega and Ryszard Wojnar</i>	117
Chemoporoelastic Parameter Identification of a Reactive Shale <i>Emmanuel Detournay, Joel Sarout, Chee Tan and Jean Caurel</i>	125
Measurements of Deformations and Electrical Potentials in a Charged Porous Medium <i>Arjan J.H. Frijns, Jacques M. Huyghe and Marcel W. Wijlaars</i>	133
Incorporating Chemical Effects in a Porothermoelastic Formulation and Application to Inclined Boreholes <i>Shailesh Ekbote and Younane Abousleiman</i>	141
Part V MAGNETIC RESONANCE	
Ion Transport and Crystallization in Porous Materials as Studied by Magnetic Resonance Imaging <i>Leo Pel, Henk P. Huinink and Klaas Kopinga</i>	149
Numerical and Experimental Studies of the Water and Ionic Mobilities within Suspensions of Charged Anisotropic Colloids <i>Alfred Delville and Patrice Porion</i>	159
Part VI TWO POROSITIES	
A Chemo-Mechanical Model for Articular Cartilage <i>Fernando M.F. Simões and Benjamin Loret</i>	167
A Dual Porosity Model for Contaminant Transport in Expansive Clays <i>Márcio A. Murad and Christian Moyne</i>	173

<i>Contents</i>	vii
Part VII DIFFUSION, DISPERSION AND ADSORPTION	
On Adsorption and Diffusion in Microstructured Porous Media <i>Pasquale Giovine</i>	183
Effect of Water Volume Fraction on Electrical Conductivity and Ion Diffusivity in Agarose Gels <i>Wei Yong Gu, Hai Yao and Adriana L. Vega</i>	193
Hydrodynamic Dispersion and Chemical Reaction in Porous Media: The Use of Space Like Coordinates <i>David E. Smiles</i>	201
Development of a Finite Element Approach to Mechanics, Transport and Biosynthesis in Tissue Engineering <i>Bram G. Sengers, Rolf A.A. Pullens, Cees W.J. Oomens and Frank P.T. Baaijens</i>	207
Transport Across Single and Series Arrays of Membranes <i>Peter Raats</i>	213
Part VIII MICROSTRUCTURE	
A Second Gradient Model for Deformable Porous Matrices Filled with an Inviscid Fluid <i>Francesco dell'Isola, Giulio Sciarra and Romesh C. Batra</i>	221
Relationship between Pore Structure and Fluid Transport in Argillaceous Rocks <i>Alexander Hildenbrand, Bernhard M. Krooss and Janos L. Urai</i>	231
Part IX ELECTROMAGNETIC WAVES	
Towards a Better Understanding of the Electromagnetic Properties of Soils <i>Katherine Klein and Yu-Hsing Wang</i>	241
Porous Media Evaluation Using Frequency-Dependent Electrokinetics <i>Philip M. Reppert and Taufiqar R. Khan</i>	251
Part X CHEMO- AND ELECTRO-OSMOSIS	
Charge Neutrality – Does It Exist? <i>Lynn S. Bennethum</i>	259
Shrinking and Cracking of Swelling Porous Media <i>Pieter H. Groenevelt</i>	267

Modelling of Chemical Osmosis in Clay <i>Sam Bader and Ruud J. Schotting</i>	275
Coupling between Chemical and Electrical Osmosis in Clays <i>J.P. Gustav Loch, Katja Richter and Thomas J.S. Keijzer</i>	283
Theoretical Analysis of the Influence of a diffuse Double-Layer on Darcy's Law <i>David Smith and Peter Pivonka</i>	289
Fluid Flow in the Self-Optimised Structure of Compact Bone <i>Theo H. Smit and Jacques M. Huyghe</i>	299
Interaction between Aqueous Solution Transport and Stress/Strain in a Deformable Porous Medium <i>Jean-Claude Bénet, Jérôme Boscus and Vincent Richefeu</i>	307
Part XI PHASE TRANSITION AND CAPILLARITY	
About the Proper Choice of Variables to Describe Flow-Induced Crystallization in Polymer Melts <i>Jan van Meerveld and Markus Hütter</i>	315
A Micromechanics Approach to the Mechanically-Induced Dissolution in Porous Media <i>Eric Lemarchand, Luc Dormieux and Franz-Josef Ulm</i>	321
Modeling of Ice Formation in Porous Media <i>Joachim Bluhm, Max J. Setzer and Jens Kruschwitz</i>	329
Thermomechanical Modelling for Freezing of Solute Saturated Soil <i>Juha Hartikainen and Martti Mikkola</i>	335
A Microscopic Description of Crystal Dissolution and Precipitation <i>C.J. van Duijn and I. Sorin Pop</i>	343
Theoretical Modeling and Experimental Monitoring of Material Destruction during Drying <i>Stefan Jan Kowalski</i>	349
Two Phase Flow in Capillary Porous Thermo-Elastic Materials <i>Tim Ricken and Reint de Boer</i>	359
Author Index	365

Foreword

The application of porous media mechanics which traditionally was mostly focussed upon geomechanics, has spread to a vast area of science. This area includes polymer science, biomechanics, biomaterials, ceramics. Many of these areas of application require the integration of many physical phenomena into one single porous media model. Electrochemistry, statistical physics, fluid mechanics, molecular biology and electromagnetism are just a few examples of these.

Particularly biomedical applications are engulfing the scientific literature. The scientific community is realising more and more that all tissues of the human body are porous media in which quantification of the dynamic relations between fluid flow, solute diffusion-convection, stresses and strains are of paramount importance in medical applications. Increasing evidence shows that living cells are very sensitive to mechanical stress, and that they shape the tissue that surrounds them according to the stimuli to which they are subjected. Bone cells and endothelial cells respond to fluid flow. Even the functioning cell itself is understood today as a versatile porous medium in which water and ions play an important role in the translation of the genetic code encrypted into the DNA-molecule. Now that the genetic code has been uncovered, the focus of science shifts towards the unraveling of the mechanisms by which this code manifests itself into a living cell, organs and bodies. Continuum mechanics and poromechanics in particular may play a mayor role in this undertaking.

The chair of the symposium concluded the opening address of this symposium by claiming that (1) poromechanics has transformed the geotechnical sciences in the 20th century and (2) the applications of poromechanics in the biomedical sciences in the 21st century may well supersede by far the applications of poromechanics in the field of geomechanics. This IUTAM symposium focussed upon bringing together people who deal with the mechanics of interactions in deforming porous media. These interactions include physico-chemical (solvation forces, adsorption), electrochemical (streaming potentials, electro-osmosis, electrophoresis), thermal and biological events. Generally the visitors were experts from the fields of biomechanics, geomechanics or poly-

mer science. The communication between these fields has been fostered by the organization of this symposium.

The topics chosen for the sessions were typically chosen so as to represent problems common to all three fields of application. For example, Micromechanics of Porous Media, Electromechanical Interactions, Chemical and Electro-osmosis, Nuclear Magnetic Resonance in Porous Media, Dual Porosity. The symposium included 49 oral presentations and a dozen poster presentations. The meeting attracted 60 participants from 15 countries: Australia, Belgium, Brazil, Canada, Finland, France, Germany, Italy, The Netherlands, Poland, Portugal, Sweden, Switzerland, United Kingdom, United States.

Jacques Huyghe
Associate Professor
Eindhoven University of Technology
Department of Biomedical Engineering
Eindhoven, The Netherlands
September 2004

Acknowledgments

The symposium was sponsored by the following organizations:

- International Union of Theoretical and Applied Mechanics.
- Department of Biomedical Engineering, Eindhoven University of Technology, The Netherlands
- Kluwer Academic Publishers, Dordrecht, The Netherlands.

We are grateful for the support of our sponsors.

International Scientific Committee

Dick H. van Campen (Netherlands, Representative IUTAM)
Olivier Coussy (France)
Stephen C. Cowin (USA, Cochair)
Wolfgang Ehlers (Germany)
Jacques M. Huyghe (Netherlands, Chair)
Yoram Lanir (Israel)
Marcio A. Murad (Brazil)
Peter A.C. Raats (Netherlands)
J. Carlos Santamarina (USA)

Local Organising Committee

Yvonne M.J. Biemans
Corrinus C. van Donkelaar
Jacques M. Huyghe (Chair)
Peter A.C. Raats
Marleen H.W. Rieken
Reinder W. Roos
Aat C. Stuurman
Marcel W. Wijlaars

List of Participants

- Y. Abousleiman
University of Oklahoma, Sarkeys Energy Center
Suite P119, 100 E. Boyd Street
Norman, OK 73019-1014
USA
yabousle@ou.edu
+1-405-3252900
+1-405-3257491

- S. Bader
TU Delft
Postbus 5048 K.4.93
2600 GA Delft
The Netherlands
s.bader@citg.tudelft.nl
+31-15-2788155
+31-15-2785915

- V. Barocas
University of Minnesota
312 Church St. Se
Minneapolis, MN 55455
USA
baroc001@umn.edu
+1-612-6265572
+1-612-6266583

- J-C.B. Benet
LMGC-UMR CNRS 5508
Cc 048 Université Montpellier II Place E. Bataillo
34095 Montpellier
France
benet@lmgc.univ-montp2.fr
+33-467-143755
+33-467-144555

- L. Bennethum
University of Colorado at Denver
PO Box 173364 Campusbox 170 Suite 638
Denver, CO 80202
USA
Lynn.Bennethum@cudenver.edu

+1-303-5564810

+1-303-5568550

- Y.M.J. Biemans
Eindhoven University of Technology
PO Box 513
5600 MB Eindhoven
The Netherlands
y.m.j.biemans@tue.nl
+31-40-2472279
+31-40-2447355

- J. Bluhm
University Essen, FB10
Universitätsstr. 15
45141 Essen
Germany
joachim.bluhm@uni-essen.de
+49-201-1832660
+49-201-1832680

- C.V.C. Bouten
Eindhoven University of Technology
PO Box 513, Whoog 4.123
5600 MB Eindhoven
The Netherlands
c.v.c.bouten@tue.nl
+31-40-2473006
+31-40-2447355

- D.H. van Campen
Eindhoven University of Technology
PO Box 513
5600 MB Eindhoven
The Netherlands
d.h.v.campen@tue.nl
+31-40-2472710
+31-40-2437175

- J. Carmeliet
KU Leuven, Dept. of Civil Eng.
Kasteelpark Arenberg 51
B-3001 Heverlee
Belgium

jan.carmeliet@bwk.kuleuven.ac.be
+32-16-321343
+32-16-321980

- O. Coussy
LCPC
58 Bld. Lefebvre
75015 Paris
France
olivier.coussy@enpc.fr
+33-164153622
+33-164153741

- S.C. Cowin
City University of New York
2166 Broadway, Apt. 12D
New York, NY 10024-6671
USA
scccc@cunyvm.cuny.edu
+1-212-7997970
+1-212-7997970

- A.D. Delville
CNRS
CRMD, 1B rue de la Ferrollerie
45071 Orleans
France
delville@cnrs-orleans.fr
+33-238155369
+33-238255376

- E. Detournay
University of Minnesota, Dept. of Civil Eng.
500 Pillsbury Drive SE
Minneapolis, MN 55455
USA
detou001@umn.edu
+1-612-6253043
+1-612-6267750

- C.C. van Donkelaar
Eindhoven University of Technology
PO Box 513
5600 MB Eindhoven

The Netherlands
c.c.v.donkelaar@tue.nl
+31-40-2474837
+31-40-2447355

- L. Dormieux
LMSGC/ENPC/CNRS
ENPC, 6 et 8, Avenue Blaise Pascal
77455 Marne-la-Vallée
France
dormieux@lmsgc.enpc.fr
+33-164-153660
+33-164-153748
- N.J.B. Driessen
Eindhoven University of Technology
PO Box 513
5600 MB Eindhoven
The Netherlands
n.j.b.driessen@tue.nl
+31-40-2473048
+31-40-2447355
- H. van Duijn
Eindhoven University of Technology
PO Box 513
5600 MB Eindhoven
The Netherlands
c.j.v.duijn@tue.nl
+31-40-2472855
- W. Ehlers
University of Stuttgart, Inst. of Applied Mechanics
Pfaffenwaldring 7
70569 Stuttgart
Germany
ehlers@mechbau.uni-stuttgart.de
+49-711-6856346
+49-711-6856347
- A.J.H. Frijns
Eindhoven University of Technology
PO Box 513 Whoog 3.126
5600 MB Eindhoven

The Netherlands
a.j.h.frijns@tue.nl
+31-40-2474825
+31-40-2433445

- D.J. Gawin
Techn. Univ. of Lodz, Dept. Building Phys. and Build. Mat.
Al. Politechniki 6
93-590 Lodz
Poland
gawindar@p.lodz.pl
+48-42-6313560
+48-42-6313556
- P.G. Giovine
University of Reggio Calabria, Mech. and Mater.
Via Graziella, 1 Localita Feo di Vito
I-89060 Reggio Calabria
Italy
giovine@unirc.it
+39-965-331280
+39-965-310084
- P.H. Groenevelt
University of Guelph
Dept. of Land Resource Science
Guelph, Ontario N1G 2W1
Canada
pgroenev@lrs.uoguelph.ca
+1-519-8244120
+1-519-8245730
- W. Gu
University of Miami
1251 Memorial Drive, MCA 219A
Coral Gables, FL 33146
USA
wgu@miami.edu
+1-305-2845434
+1-305-2846494
- J. Hartikainen
Helsinki University of Technology
PO Box 1100

02015 HUT Espoo
Finland
juha.hartikainen@csc.fi
+358-9-4513078
+358-9-4513070

- A. Hildenbrand
RWTH-Aachen, LEK
Lochnerstr. 4-20
52062 Aachen
Germany
alexandra.hildenbrand@vito.be
+49-241-8098296
+49-241-8092152
- H. Huinink
Eindhoven University of Technology
PO Box 513
5600 MB Eindhoven
The Netherlands
h.p.huinink@tue.nl
+31-40-2475375
+31-40-2432598
- K. Hütter
Darmstadt University of Technology, Dept. of Mechan.
Hochschulstr. 1
64289 Darmstadt
Germany
hutter@mechanik.tu-darmstadt.de
+49-6151-162991
+49-6151-164120
- J.M. Huyghe
Eindhoven University of Technology
PO Box 513
5600 MB Eindhoven
The Netherlands
j.m.r.huyghe@tue.nl
+31-40-2473137
+31-40-2447355
- F. dell'Isola
University of Rome "La Sapienza"

Via Eudossiana, 18
I-00184 Rome
Italy
francesco.dellisola@uniroma1.it
+39-644-585297

- D. Jankovic
TU Delft, Civil Engineering
Stevinweg 1
2628 CN Delft
The Netherlands
dj32826@yahoo.com
+31-15-2783752
+31-15-2786383
- K. Klein
University of Toronto
35 St. George Street
Toronto, Ontario M5S 1A4
Canada
klein@civ.utoronto.ca
+416-946-5712
+416-978-5054
- S.J.K. Kowalski
Poznań University of Technology
pl. Marii Skłodowskiej-Curie 2
60-965 Poznań
Poland
kowal@rose.man.poznan.pl
+61-6653622
+61-6653649
- J. Kruschwitz
University Essen
Universitätsstr. 15 FB10 IBPM
45141 Essen
Germany
jens.kruschwitz@uni-essen.de
+49-201-1834595
+49-201-1833968
- Y. Lanir
Dept. Biomedical Eng. Technion

Technion City
32000 Haifa
Israel
yoram@biomed.technion.ac.il
+972-4-8376440
+972-4-8234131

- R. Larsson
Chalmers University of Technology
Department of Applied Mechanics
S-412 96 Göteborg
Sweden
ragnar.larsson@me.chalmers.se
+46-31-7725267
+46-31-7721303
- E. Lemarchand
CNRS-LML
Boulevard Langevin, Cité Scientifique
59655 Villeneuve d'Ascq
France
lemarchand@lmsgc.enpc.fr
+33-320-337182
+33-320-337153
- G. Loch
Utrecht University, Faculty of Earth Sciences
Budapestlaan 4
3584 CD Utrecht
The Netherlands
jpgl@geo.uu.nl
+31-30-2535042
+31-30-2535302
- K. Malakpoor
Eindhoven University of Technology
Dept. Mathematics Science, PO Box 513
5600 MB Eindhoven
The Netherlands
k.malakpoor@tue.nl
+31-40-247 42 90
+31-40-244 24 89
- B. Markert
University of Stuttgart, Inst. of Applied Mechanics

Pfaffenwaldring 7
70569 Stuttgart
Germany
markert@mechbau.uni-stuttgart.de
+49-711-6856341
+49-711-6856347

- R.L. Mauck
Columbia University, Dept. of Biomed. Eng.
351 Engineering Terrace, MC 8904, 1210 Amsterdam Avenue
New York, NY 10027
USA
rm159@columbia.edu
+1-212-8546731
+1-212-8548725
- J. van Meerveld
Institute of Polymers, ETH Zürich
Sonneggstrasse 3
CH-8092 Zürich
Switzerland
meerveld@mat.ethz.ch
+41-1-6324545
+41-1-6321076
- J.G.M. van Mier
Swiss Federal Institute of Technology
Institute for Building Materials
8093 Zürich
Switzerland
vanmier@ibwk.baug.ethz.ch
+41-1-6332709
+31-1-6331087
- M.J. Mikkola
Helsinki University of Technology
Otakaari 1.M.
02150 Espoo
Finland
martti.mikkola@hut.fi
+358-9-4513067
+358-9-4513070
- C. Moyne
CNRS-CEMTA

2 Avenue de la Forêt de Haye BP 160
54504 Vandoeuvre
France
cmoyne@ensem.inpl-nancy.fr
+3-83-595607
+3-83-595531

- M.A. Murad
Nat. Lab of Scientific Computing
Av. Getulio Vargas 333
25651-070 Petropolis
Brazil
murad@lncc.br
+55-24-22336149
+55-24-22336165

- C. Oddou
Université de Paris 12
61, Avenue du Generale-de gaulle
94010 Creteil
France
oddou@univ-paris12.fr

- C.W.J. Oomens
Eindhoven University of Technology
PO Box 513
5600 MB Eindhoven
The Netherlands
c.w.j.oomens@tue.nl
+31-40-247 2818
+31-40-244 7355

- L. Pel
Eindhoven University of Technology
PO Box 513
5600 MB Eindhoven
The Netherlands
l.pel@tue.nl
+31-40-2473406
+31-40-2432598

- M.A. Peletier
Centrum voor Wiskunde en Informatica
Kruislaan 413

1098 SJ Amsterdam
The Netherlands
peletier@cwui.nl
+31-20-5924226
+31-20-5924199

- F. Plouraboué
CNRS UMR 5502
GEMP/IMFT Allées du Pr. C. Soula
31400 Toulouse
France
plourab@imft.fr
+33-561-285880
+33-561-285899
- P. Poesio
Delft University of Technology
Leeghwaterstraat 21
2628 CB Delft
The Netherlands
pietro.poesio@shell.com
+31-70-4476055
+31-70-4473366
- S.R. Pride
University of Rennes 1
Campus Beaulieu, Batiment 15
35042 Rennes cedex
France
spride@univ-rennes1.fr
+33-223-236737
+33-223-236090
- S.P. Pudasaini
Darmstadt University of Technology, Dept. of Mechan.
Hochschulstr. 1
64289 Darmstadt
Germany
pudasain@mechanik.tu-darmstadt.de
+49-6151-165370
+49-6151-164120
- P.A.C. Raats
Wageningen University and Research Centre

Paaskamp 16
9301 KL Roden
The Netherlands
pac.raats@home.nl
+31-50-5018735

- P. Reppert
School of the Environment, Clemson University
338 Brackett Hall
Clemson, SC 29634
USA
reppert@clemson.edu
+1-864-6565019
+1-864-6561041
- K. Richter
Utrecht University, Dept. Earth Sciences
PO Box 80021
3508 TA Utrecht
The Netherlands
richter@geo.uu.nl
+31-30-2535016
+31-30-2535302
- T. Ricken
Universität Essen, Institut für Mechanik
45117
Essen
Germany
tim.ricken@uni-essen.de
+49-201-1832679
+49-201-1832680
- M.H.W. Rieken
Eindhoven University of Technology
PO Box 513
5600 MB Eindhoven
The Netherlands
m.h.w.rieken@tue.nl
+31-40-2472851
+31-40-2447355
- R.W. Roos
Eindhoven University of Technology

PO Box 513
5600 MB Eindhoven
The Netherlands
r.w.roos@tue.nl
+31-40-2475398
+31-40-244 7355

- J.C. Santamarina
Georgia Institute of Technology
Civil Engineering
Atlanta, GA 30332
USA
carlos.santamarina@ce.gatech.edu
+1-404-8947605
+1-404-8942282
- R.J. Schotting
TU Delft
Postbus 5048 K.4.92.1
2600 GA Delft
The Netherlands
r.j.schotting@citg.tudelft.nl
+31-15-2784844
+31-15-2785915
- G. Sciarra
University of Rome “La Sapienza”, Dept. Chemical Eng.
Via Eudossiana, 18
I-00184 Rome
Italy
giulio.sciarra@uniroma1.it
+39-644-4585230
- B.G. Sengers
Eindhoven University of Technology
PO Box 513 Room WH 4.103
5600 MB Eindhoven
The Netherlands
b.g.sengers@tue.nl
+31-40-2473075
+31-40-2447355
- J.D. Sherwood
Schlumberger Cambridge Research

High Cross, Madingley Rd
Cambridge CB3 0EL
UK
sherwood@cambridge.oilfield.slb.com
+44-1223-325363
+44-1223-327019

- F. Simoes
Instituto Superior Técnico
Av. Rovisco Pais, Decivil
1049-001 Lisboa
Portugal
fsimoes@civil.ist.utl.pt
+351-218418409
+351-218497650
- B. Simon
The University of Arizona
Aero and Mech. Engr. PO 210119
Tucson, AZ 85721-0119
USA
simon@ame.arizona.edu
+1-520-6214451
+1-520-6218191
- D.M.J. Smeulders
Delft University of Technology
PO Box 5028
2600 GA Delft
The Netherlands
d.m.j.smeulders@ta.tudelft.nl
+31-15-2787599
+31-15-2784891
- D.E. Smiles
CSIRO
PO Box 1666
Canberra 2601
Australia
david.smiles@csiro.au
+61-2-62465966
+61-2-62465965
- T.H. Smit
Vrije Universiteit Medisch Centrum

Postbus 7057
1007 MB Amsterdam
The Netherlands
th.smit@vumc.nl
+31-20-4441245
+31-20-4444147

- D. Smith
The University of Newcastle
Discipline of Civil, Surveying, Environmental Engn
Callaghan 2308
Australia
cedws@cc.newcastle.edu.au
+61-2-49216057
+61-2-49216991
- A. Stuurman
Eindhoven University of Technology
PO Box 513
5600 MB Eindhoven
The Netherlands
d.h.v.campen@tue.nl
+31-40-2472710
+31-40-2437175
- F. Suh
Tulane University
Lindy Boggs 500
New Orleans, LA 70118
USA
fsuh@tulane.edu
+1-504-8655852
+1-504-8628779
- J.J. Telega
Polish Academy of Sciences, Inst. of Fundamental Techn.
ul. Swietokrzyska 21
00-049 Warsaw
Poland
jtelega@ippt.gov.pl
+48-22-8265129
+48-22-8269815
- M.W. Wijlaars
Eindhoven University of Technology

PO Box 513
5600 MB Eindhoven
The Netherlands
m.w.wijlaars@tue.nl
+31-40-2474813
+31-40-2447355

- L.H.G. Wouters
Eindhoven University of Technology
PO Box 513
5600 MB Eindhoven
The Netherlands
l.h.g.wouters@tue.nl
+31-40-2474088
+31-40-2447355

I

MICROMECHANICS.

Chairman: Y. Abousleiman

BONES HAVE EARS:

An Application of Bone Poroelasticity

Stephen C. Cowin

*The New York Center for Biomedical Engineering
Departments of Biomedical and Mechanical Engineering
The School of Engineering of The City College and
The Graduate School of The City University of New York
New York, NY 10031, U.S.A.*

Abstract The mechanosensory mechanisms in bone include (i) the cell system that is stimulated by external mechanical loading applied to the bone; (ii) the system that transduces that mechanical loading to a communicable signal; and (iii) the systems that transmit that signal to the effector cells for the maintenance of bone homeostasis and for strain adaptation of the bone structure. The effector cells are the osteoblasts and the osteoclasts. These systems and the mechanisms that they employ have not yet been unambiguously identified. A summary is presented of the current theoretical and experimental evidence suggesting that osteocytes are the principal mechanosensory cells of bone, that they are activated by the effects of fluid flowing through the osteocyte canaliculi, and that the electrically coupled three-dimensional network of osteocytes and lining cells is a communications system for the control of bone homeostasis and structural strain adaptation. A bone poroelastic (BP) model is employed to model the fluid flow behavior caused by the mechanical loading of bone. The similarities of the mechanotransduction system in bone with the mechanotransduction system used by the cells of the hearing system will be described. Both cell systems sense mechanical vibrations in a fluid domain.

Keywords: mechanosensation, bone, hearing, cell systems

Introduction

It has long been known that living adult mammalian bone tissue adapts its material properties, and that whole bones adapt their shape, in response to altered mechanical loading [204–206, 57, 58, 191, 92, 110]. Progress is being made in understanding the cellular mechanisms that accomplish the absorption and deposition of bone tissue. The physiological mechanism by which the mechanical loading applied to bone is sensed by the tissue, and the mechanism by which the sensed signal is transmitted to the cells which accomplish the

Jacques M. Huyghe et al. (eds), IUTAM Proceedings on Physicochemical and Electromechanical Interactions in Porous Media, 3–36.

© 2005 Springer. Printed in the Netherlands.

surface deposition, removal and maintenance, have not been identified. The purpose of this contribution is to review some of the background research on these mechanosensory mechanisms and to outline candidates for the mechanosensory system. See [35] for an earlier review of similar literature.

Mechanoreception is the term used to describe the process that transmits the informational content of an extracellular mechanical stimulus to a receptor cell. Mechanotransduction is the term used to describe the process that transforms the mechanical stimulus' content into an intra-cellular signal. The term mechanosensory is employed to mean both mechanoreception and mechanotransduction. Additional processes of inter-cellular transmission of transduced signals are required at tissue, organ and organismal structural levels. The mechanosensing process(es) of a cell enables it to sense the presence of, and to respond to, extrinsic physical loadings. This property is widespread in uni- and multicellular animals [54, 101, 53, 74, 73, 36]; plants [201, 65] and bacteria [152]. Tissue sensibility is a property of a connected set of cells and it is accomplished by the intracellular processes of mechanoreception and mechanotransduction.

The Connected Cellular Network (CCN)

The bone cells that lie on all bony surfaces are osteoblasts, either active or inactive. Inactive osteoblasts are called bone-lining cells; they have the potential of becoming active osteoblasts (Figure 1). The bone cells that are buried in the extracellular bone matrix are the osteocytes. Each osteocyte, enclosed within its mineralized lacuna, has many (perhaps as many as 80) cytoplasmic processes (Figure 1, Figure 2). These processes are approximately 15 mm long and are arrayed three-dimensionally in a manner that permits them to interconnect with similar processes of up to as many as 12 neighboring cells. These processes lie within mineralized bone matrix channels called canaliculi (Figure 2, Figure 3). The small space between the cell process plasma membrane and the canalicular wall is filled with bone fluid and macromolecular complexes of unknown composition. All bone cells except osteoclasts are extensively interconnected by the cell process of the osteocytes forming a connected cellular network (CCN) [152]. The interconnectivity of the CCN is graphically illustrated by Figure 4 which is a scanning electron micrograph showing the replicas of lacunae and canaliculi in situ in mandibular bone from a young subject aged 22 years. The inset of Figure 4 shows enlarged lacunae identified by a rectangle.

The touching cell processes of two neighboring bone cells contain gap junctions [8, 46, 47, 95, 182, 96, 67, 25]. A gap junction is a channel connecting two cells. The location of the gap junction is indicated by the arrowheads in Figure 2. The walls of the channel consist of matching rings of proteins pier-



Figure 1. Diagram of a thin bone trabecula (5) showing the four types of bone cells. Osteoblasts (8) and their precursors (7) are shown on the upper surface over a layer of uncalcified osteoid matrix (9), osteocytes (6) are shown in their lacunae, an osteoclast (1) and a bone lining cell (3) are shown on the lower surface. Capillaries (4), containing red blood cells in their lumina, and a fibroblast (2) are shown near the trabecula. Adapted from Krstic (1978).

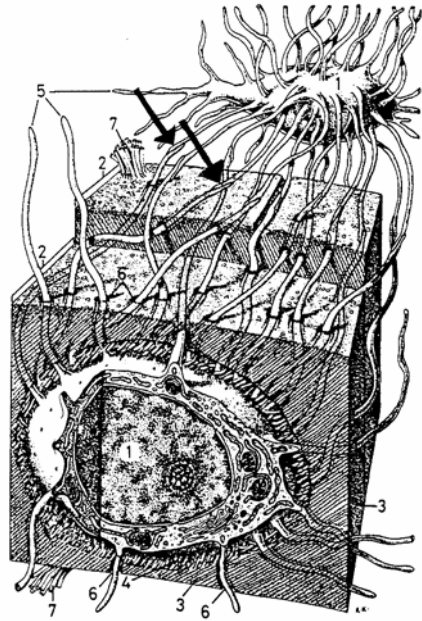


Figure 2. Diagram of two osteocytes (1) in the lamellar bone of calcified bone matrix (3). Two neighboring lamellae (2) with different collagen fiber orientations (7) are visible. The osteocytic cell bodies are located in lacunae and are surrounded by a thin layer of uncalcified matrix (4). Their cell processes (5) are housed in canaliculi (6). Some of the gap junctions between the cell processes are indicated (arrows). Modified from Krstic (1978).

cing the membrane of each cell, and when the rings associated with two cells connect with each other, the cell-to-cell junction is formed. This junction allows ions and compounds of low molecular weight to pass between the two cells without passing into the extracellular space. The proteins making up a gap junction are called connexins; in bone the protein is either connexin 43 or 45, with 43 predominating (the number refers to the size of the proteins calculated in kilodaltons) [130, 131, 113]. A ring of connexins in one cell membrane is generally called a connexon or hemichannel. Both mechanical strain and fluid shear stress cause increased expression of the connexin 43 in vascular tissues [28]. In cardiac tissue the turnover rate of connexin 43 is very rapid [7]. The rapid dynamics of gap junction turnover and the plasticity of gap

junction expression in response to various stimuli offer the possibility for remodeling of the intercellular circuits both within and between communication compartments in the cardiovascular system [187]. In bone, gap junctions connect superficial osteocytes to periosteal and endosteal osteoblasts. All osteoblasts are similarly interconnected laterally on a bony surface; perpendicular to the bony surface, gap junctions connect periosteal osteoblasts with preosteoblastic cells, and these, in turn, are similarly interconnected. Effectively, each CCN is a true syncytium [47, 182, 165, 96]. Gap junctions are found where the plasma membranes of a pair of markedly lapping canalicular processes meet [165]. In compact bone, canaliculi cross the cement lines that form the outer boundary of osteons. Thus extensive communication exists between osteons and interstitial regions [38].

Bone cells are electrically active [10, 11, 24, 121, 170]. In addition to permitting the intercellular transmission of ions and small molecules, gap junctions exhibit both electrical and fluorescent dye transmission [93, 183, 187, 133]. Gap junctions are electrical synapses, in contradistinction to interneuronal, chemical synapses; and, significantly, they permit bi-directional signal traffic (e.g., biochemical, ionic, electrical etc.). In a physical sense, the CCN represents the hard wiring [30, 140, 141, 150] of bone tissue.

Mechanosensation in Bone: Stimuli

The stimulus for bone remodeling is defined as that particular aspect of the bone's stress or strain history that is employed by the bone to sense its mechanical load environment and to signal for the deposition, maintenance or resorption of bone tissue. The bone tissue domain or region over which the stimulus is felt is called the sensor domain. When an appropriate stimulus parameter exceeds threshold values, loaded tissues respond by the triad of bone adaptation processes: deposition, resorption and maintenance. The CCN is the site of intracellular stimulus reception, signal transduction and intercellular signal transmission. It is thought that stimulus reception occurs in the osteocyte [30], and that the CCN transduces and transmits the signal to the surface lining or osteoblast. The osteoblasts alone directly regulate bone deposition and maintenance, and indirectly regulate osteoclastic resorption [119]. The possible role of the osteoblast as a stimulus receptor has not yet been thoroughly investigated [156]. Although it is reasonably presumed that initial mechanosensory events occur at the plasma membrane of the osteocytic soma and/or canalicular processes, the initial receptive, and subsequent transductive, processes are not well understood.

It follows that the true biological stimulus, although much discussed, is not precisely known. A variety of mechanical loading stimuli associated with ambulation (at a frequency of one to two Hz) have been considered for bone re-

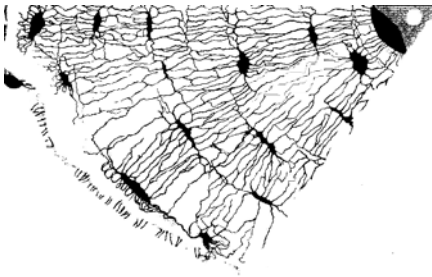


Figure 3. A pie-shaped section of an osteon. The osteonal canal is on the upper right, the cement line to the left. The osteonal canal is part of the vascular porosity (PV), the lacunae and the canaliculi are part of the lacunar-canalicular porosity (PLC) and the material in the space that is neither PV or PLC contains the collagen-apatite porosity (PCA). The three interfaces, the cement line, the cellular interface (IC) and the lacunar-canalicular interface are each indicated. The radius of an osteon is usually about 100 mm, and the long axis of a lacuna is about 15 mm. Using this information it should be possible to establish the approximate scale of the printed version of this illustration. Previously published in Cowin (1999).

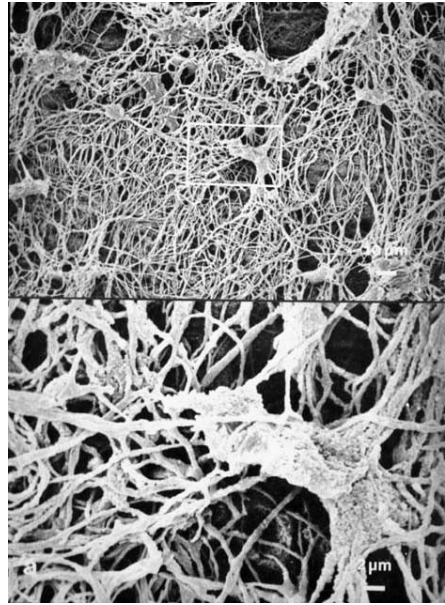


Figure 4. A scanning electron micrograph showing the replicas of lacunae and canaliculi in situ in mandibular bone from a young subject aged 22 years. The inset shows enlarged lacunae identified by a rectangle. This micrograph illustrates the interconnectivity of the connected cellular network (CCN). Copied from Atkinson and Hallsworth (1983).

modeling. The majority has followed Wolff [205, 206] in suggesting that some aspect of the mechanical loading of bone is the stimulus. The mechanical stimuli suggested include strain [29], stress [205, 206], strain energy [60, 86], strain rate [80–82, 151, 111, 66, 55], and fatigue microdamage [20, 118]. In some cases the time-averaged values of these quantities are suggested as the mechanical stimulus, and in others the amplitudes of the oscillatory components and/or

peak values of these quantities are the candidates for the mechanical stimulus. Two-dozen possible stimuli were compared in a combined experimental and analytical approach [14]. The data supported strain energy density, longitudinal shear stress and tensile principal stress or strain as stimuli; no stimulus that could be described as rate dependent was among the two dozen possible stimuli considered in the study. For a consideration of the stimulus in microgravity see Cowin [32].

The case for strain rate as a remodeling stimulus has been building over the last quarter century. The animal studies of Hert and his coworkers [80–82] suggested the importance of strain rate. Experiments [111, 66, 55] have quantified the importance of strain rate over strain as a remodeling stimulus. In order to gain an understanding the cellular mechanism for bone remodeling Weinbaum et al. [198, 199] suggested that the prime mover is the bone strain rate driven motion of the bone fluid whose signal is transduced by osteocytes. The bone poroelastic (BP) model was developed by Weinbaum et al. [198, 199] and Cowin et al. [31] to explain the connection between the mechanical loading on the whole bone and the signal transduced by osteocytes. In the (BP) model the shear stress from the bone fluid flow over the osteocytic processes in the canaliculi is a cellular mechanism-based model suggesting strain rate as a stimulus. A later study by You et al. [209] showed that it was not shear stress applied directly to the cell membrane, but rather the force created by fluid drag on the fibers of the glycocalyx of the cell transmitted to the cell membrane. This study will be described in greater detail in the section on strain amplification. Recent studies [70, 128] that showed bone deposition to be related to strain gradients actually demonstrate a dependence upon strain rate if the BP model developed in Weinbaum et al. [198, 199] and Cowin et al. [31] is realistic.

In experiments with cultured cells it has been shown that osteocytes, but not periosteal fibroblasts, are extremely sensitive to fluid flow, resulting in increased prostaglandin as well as nitric oxide production [104, 105]. Three different cell populations, namely osteocytes, osteoblasts, and periosteal fibroblasts, were subjected to two stress regimes, pulsatile fluid flow and intermittent hydrostatic compression [104]. Intermittent hydrostatic compression was applied at 0.3 Hz with a 13-kPa peak pressure. The pulsatile fluid flow was a fluid flow with a mean shear stress of 0.5 Pa with cyclic variations of 0.02 Pa at 5 Hz. The maximal hydrostatic pressure rate was 130 kPa/sec and the maximal fluid shear stress rate was 12 Pa/sec. Under both stress regimes, osteocytes appeared more sensitive than osteoblasts, and osteoblasts more sensitive than periosteal fibroblasts. However, despite the large difference in peak stress and peak stress rate, pulsatile fluid flow was more effective than intermittent hydrostatic compression. Osteocytes, but not the other cell types, responded to 1 hour pulsatile fluid flow treatment with a sustained prostaglandin E2 upregula-

tion lasting at least one hour after pulsatile fluid flow was terminated. By comparison, IHC needed 6 hours of treatment before a response was found. These results suggested that osteocytes are more sensitive to mechanical stress than osteoblasts, which are again more sensitive than periosteal fibroblasts. Furthermore, osteocytes appeared particularly sensitive to fluid shear stress, more so than to hydrostatic stress. These conclusions are in agreement with the theory that osteocytes are the main mechanosensory cells of bone, and that they detect mechanical loading events by the canalicular flow of interstitial fluid which results from that loading event. The BP model developed in Weinbaum et al. [198, 199] and Cowin et al. [31] used Biot's porous media theory to relate loads applied to a whole bone to the flow of canalicular interstitial fluid past the osteocytic processes. These calculations predicted fluid induced shear stresses of 0.8-3 Pa, as a result of peak physiological loading regimes. The findings that bone cells in vitro actually respond to fluid shear stress of 0.2-6 Pa [163, 202, 87, 104, 105] lend experimental support to the BP model [198, 199, 31].

Osteocytes also rapidly release nitric oxide in response to stress [160, 105] and this NO response seems to be required for the stress-related prostaglandin release [105]. Therefore, the behavior of osteocytes compares to that of endothelial cells which regulate the flow of blood through the vascular system, and also respond to fluid flow of 0.5 Pa with increased prostaglandin and nitric oxide production [79]. The response of endothelial cells to shear stress is likely related to their role in mediating an adaptive remodeling of the vasculature, so as to maintain constant endothelial fluid shear stress throughout the arterial site of the circulation [99].

Skeletal muscle contraction is a typical bone-loading event and has been suggested [137-139] as a stimulus. Frequency is one of the critical parameters of the muscle stimulus and it serves to differentiate this stimulus from the direct mechanical loads of ambulation which occur at a frequency of one to two Hz. The frequency of contracting muscle in tetanus is from 15 Hz to a maximum of 50 - 60 Hz in mammalian muscle [126]. It has been observed [123, 166] that these higher order frequencies, significantly related to bone adaptational responses, are [169] "... present within the (muscle contraction) strain energy spectra regardless of animal or activity and implicate the dynamics of muscle contraction as the source of this energy band." The close similarity of muscle stimulus frequencies to bone tissue response frequencies is noted below.

Strain Amplification

There is a fundamental paradox in the physiology of bone mechanosensation. The paradox (Figure 5) is that the strains applied to whole bone (i.e., tissue level strains) are much smaller (0.04 % to 0.3 %) than the strains (1 %

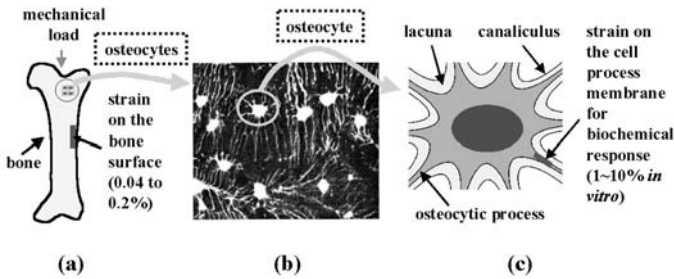


Figure 5. This figure illustrates the paradox addressed in mechanosensation. (a) An illustration of the small strains that the whole bone experiences, strains that are in the range 0.04 to 0.3 percent and seldom exceed 0.1 percent. The last two panels, (b) Photomicrograph of osteocytes encased in bone matrix (c) Osteocyte in lacuna, illustrate that large strains (1 to 10 percent) on cell membrane are needed to induce biochemical intracellular response *in vitro*. The paradox in the bone mechanosensing system is that the strains that activate the bone cells are two orders of magnitude larger than the strains to which the whole bone organ is subjected. Previously published in You et al. (2001).

to 10 %) that are necessary to cause bone signaling in deformed cell cultures [55, 167]. Osteocytes (Figure 2) are believed to be the critical mechanical sensor cells [30, 18], although the mechanism by which osteocytes perceive mechanical load is not known. One widely held idea is that cell membrane stretch occurs as a direct result of surrounding tissue deformation. If this is the case, then strain on osteocyte membranes should be comparable to the bone tissue strain. However, *in vitro* studies show that in order to induce any cellular response by direct mechanical deformation of bone cells, deformations need to be one to two orders of magnitude larger than the bone tissue strains normally experienced by the whole bone *in vivo* [209, 17]. Similar cell strain magnitudes are needed to activate fibroblasts and chondrocytes (15 %) [4] suggesting that in their sensitivity to mechanical strain, osteocytes may not be different from other connective tissue cells. However, in bone the larger strains needed to stimulate osteocytes cannot be derived directly from matrix deformations, as they would cause bone fracture. Thus, in bone there is an inherent contradiction between material and biological stimulation requirements. A hypothesis and model to deal with this contradiction is given in You et al. [209].

The flow of bone fluid due to mechanical loading through the lacuno-canalicular system is an important aspect of the BP model considerations presented in You et al. [209]. Between the osteocyte cell process membrane and canaliculus wall is the pericellular space through which the bone fluid flows (Figure 2, Figure 3). A pericellular organic matrix appears to fill the space [3, 174]. This matrix is supported by transverse fibrils [185] that appear to anchor and center the cell process in its canaliculus. When a whole bone is

deformed, the BP model shows that the deformation-induced pressure gradient will cause bone fluid to flow in the pericellular space of the lacunar-canalicular system [198, 199, 31, 209, 70, 128] and induce a drag force on the matrix fibers.

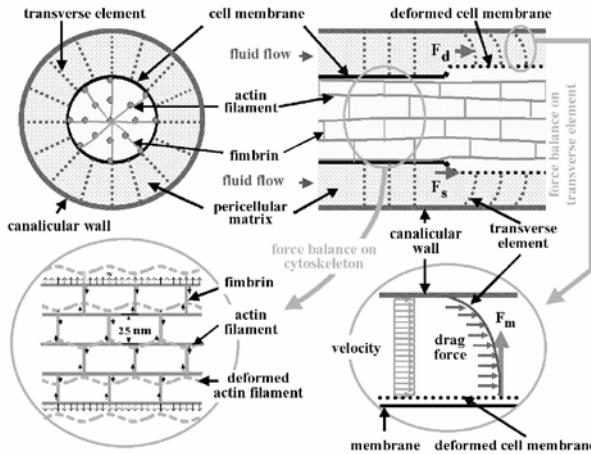


Figure 6. Schematic model showing the structure of the PM, the intracellular actin cytoskeleton inside the process and the connection between the PM and the IAC. (a) transverse cross-section of canalculus showing the fluid annular shape of the region and transverse (radial) pericellular fibers. (b) longitudinal cross-section before and after the transverse elements are deformed by the flow. (c) schematic of the cell process cytoskeletal structure in longitudinal axial section used to estimate the Young's modulus in the radial (vertical) direction. Since the length of the cell process is 300 times its radius, it is considered infinite in the longitudinal (horizontal) direction. The axial actin filaments shown are modeled as continuous infinite beams with two types of loadings depending on whether the actin filaments are peripheral or interior. The small vertical arrows indicate the direction of the loading. The (fimbrin) links between these infinitely long beams are considered to be rigid. (d) Force balance on a transverse element. Previously published in You et al. (2001).

The effect of fluid drag forces on the pericellular matrix and its coupling to the intracellular actin cytoskeleton and the strain amplification that results from this coupling, was examined in You et al. [209]. The fluid drag on an attached pericellular matrix causes a circumferential (hoop) strain in the membrane-cytoskeleton of the cell process. The BP model considerations in You et al. [209] show that, for the loading range 1 to 20 MPa and frequency range 1-20 Hz, it is, indeed, possible to produce cellular level strains in bone that are up to 100 fold greater than normal tissue level strains (0.04% to 0.3 %). Thus, the strain in the cell process membrane due to the loading can be of the same order as the *in vitro* strains measured in cell culture studies where intracellular biochemical responses are observed for cells on stretched elastic substrates.

An idealized model for an individual canaliculus with its central cell process is a tube containing a centrally positioned osteocyte process and its surrounding fluid annulus filled with a mesh-like pericellular matrix is shown in Figure 6. For the pericellular component, only two structural elements are critical for this mechanical model: 1) a space-filling pericellular matrix with a fiber spacing D that is sufficiently small, and 2) transverse fibrils which tether the cell process to the canalicular wall. From a mechanics point of view, any matrix, which has these two characteristics, should function equivalently, although the degree of strain amplification will change with the fiber spacing D . There is growing evidence to support this basic structure. First, a space-filling pericellular matrix surrounding osteocytes is well-established [174, 3, 185–1]. Second, transverse tethering elements were first clearly identified in Fig.3 [185]. The pericellular space surrounding the osteocyte process varies from 14 nm to 100 nm [27, 200, 104], depending on species, age, age of osteocyte, histological bone type, skeletal location etc. EM studies by You et al.[210] on adult mice indicate a pericellular space of 30-50 nm. You et al.[210] also observed that the cell process is invariably located at the center of the canalicular cross-section suggesting that the transverse fibrils are tension elements that anchor and position the cell process within the canaliculus.

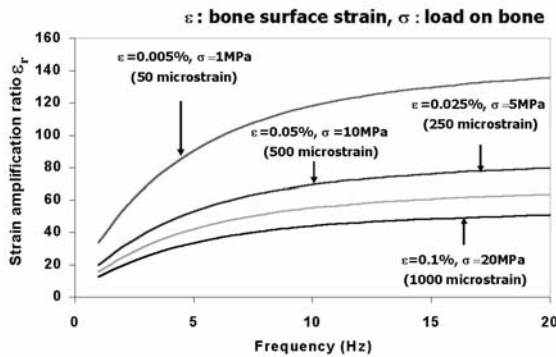


Figure 7. Strain amplification: A plot of the strain amplification ratio ϵ_r as a function of the load frequency for different load magnitudes. Strain amplification ratio is defined as the ratio of the hoop strain in the cell process membrane to the bone surface strain at the osteonal lumen. ϵ is the strain on the whole bone; σ is the load on the whole bone. Previously published in You et al. (2001).

Both albumin and proteoglycan exist in the pericellular space [174, 155]. The effective diameter of albumin is approximately 7nm, similar to the spacing of glycosaminoglycans (GAG) side chains along a proteoglycan monomer [16]. The BP model [198, 199, 31] suggested that the value of pore size leads to shear stresses of 0.5 to 3.0 Pa for mechanical loads in the physiological range

and good agreement with the experimental data for the relaxation time of stress generated potentials (SGP) in bone under four point bending [177, 178, 180]. A pericellular matrix with a most likely pore size of 7nm was assumed for the BP model considerations in You et al. [209].

Finally, the matrix must be attached to the cell process and the canalicular wall in order for the drag force to be transmitted to the membrane and its underlying intracellular actin cytoskeleton. If such linker molecules are present, drag forces exerted on the matrix fibers will produce a tensile stress on these linker molecules that, in turn, will produce radial (hoop) strain in the intracellular actin cytoskeleton as schematically shown in Figure 6. Possible candidates for these attachment molecules are CD44, laminin, and various integrins. [64, 149].

Osteocyte processes contain a space-filling actin bundle [103, 189], whose actin filaments are cross-linked at regular intervals along the axis of the process by a linker molecule recently identified as fimbrin [189] as shown in Figure 6c. The axial actin filaments are six nm in diameter. Fimbrin is also found in intestinal microvilli [63] as well as non-intestinal cell microvilli [12]. The typical spacing of fimbrin cross-linked actin filaments in microvilli is approximately 25 nm [23]. This spacing is consistent with the EM observation in [103, 189] for an osteocyte process.

The strain amplification ratio e_r is defined as the ratio of the hoop strain in the cell process membrane to the bone surface strain at the osteonal lumen. The effect of frequency on the strain amplification ratio at different loading magnitudes is shown in Figure 7, where the strain amplification ratio is plotted against the loading frequency from 1 to 20 Hz. The hoop strain is calculated at the position of maximum flow or pressure gradient, which is located at the surface of the Haversian canal. Thus, the strain amplification ratio shown in Figure 7 can be considered as an upper bound. The curves show a monotonic increase in the amplification ratio as a function of frequency for a prescribed loading. One observes that the amplification ratio varies from 19 to 122 and depends significantly on the magnitude of the loading. When the loading magnitude is one MPa, corresponding to 50 mstrain at the osteonal lumen, the strain amplification ratio e_r is 122 at 20 Hz. For this loading the cell process strain is 0.68 percent. For a 20 MPa load at 20 Hz, $e_r = 44$ and the cell process strain is 4.9 percent. The corresponding values of e_r at 1 Hz for a 1 and 20 MPa load are 51 and 19 and the corresponding strains are 0.29 and 2.1 percent, respectively. Strains of the order of 0.3 percent or greater fall in the range where cellular level biochemical responses have been observed in vitro in four point bending [160].

Mechanosensation in bone: Reception and transduction

The osteocyte has been suggested as the stimulus sensor, the receptor of the stimulus signal [30]; histologic and physiologic data are consistent with this suggestion [3–1, 112]. The placement and distribution of osteocytes in the CCN three-dimensional array is architecturally well suited to sense deformation of the mineralized tissue encasing them [112]. Since only a population of cells, and not an individual receptor [50], can code unambiguously, the osteocytes in the CCN are potential mechanoreceptors by virtue of their network organization. Osteocytic mechanotransduction may involve a number of different processes or cellular systems. These processes include stretch- and voltage-activated ion channels, cyto-matrix sensation-transduction processes, cyto-sensation by fluid shear stresses, cyto-sensation by streaming potentials and exogenous electric field strength. Each of these processes or cellular systems is discussed below.

Stretch- and voltage-activated ion channels

The osteocytic plasma membrane contains stretch-activated ion channels [18, 72, 48, 102, 75], vbR133, vbR61 that are also found in many other cell types [171, 173]. When activated in strained osteocytes, they permit passage of certain ions [171–173], including K^+ , Ca^{2+} , Na^+ and Cs^+ . Such ionic flow may, in turn, initiate cellular electrical events ; e.g., bone cell stretch-activated channels may modulate membrane potential as well as Ca^{2+} ion flux [18, 77]. Rough estimates of osteocytic mechanoreceptor strain sensitivity have been made [30], and the calculated values cover the morphogenetically significant strain range of 0.1 % to 0.3 % in the literature [111, 167, 168]. This appears to be too low a strain to open a stretch-activated ion channel.

As in most cells, the osteocytic plasma membrane contains voltage-activated ion channels, and transmembrane ion flow may be a significant osseous mechanotransductive process [24, 162, 51, 90]. It is also possible that such ionic flow generates osteocytic action potentials, capable of transmission through gap junctions [183].

Cyto-matrix sensation-transduction processes

The mineralized matrix of bone tissue is strained when loaded. Macromolecular mechanical connections between the extracellular matrix and the osteocytic cell membrane exist and these connections may be capable of transmitting information from the strained extracellular matrix to the bone cell nuclear membrane. The basis of this mechanism is the physical continuity of the transmembrane integrin molecule, which is connected extracellularly with the macromolecular collagen of the organic matrix and intracellularly with the

cytoskeletal actin. The latter, in turn, is connected to the nuclear membrane [185, 85, 197, 68, 164, 26, 52, 45, 186, 176, 127, 22, 88, 91]. It is suggested that such a cytoskeletal lever chain, connecting to the nuclear membrane, can provide a physical stimulus able to activate the osteocytic genome [95], possibly by first stimulating the activity of such components as the c-fos genes [95, 197, 176, 192, 175, 208, 194, 78, 158, 115, 94].

Cyto-sensation by fluid shear stresses

An hypothesis concerning the mechanism by which the osteocytes housed in the lacunae of mechanically loaded bone sense the load applied to the bone by the detection of dynamic strains was suggested in [198, 199, 31]. It was proposed that the osteocytes are stimulated by relatively small fluid shear stresses acting on the membranes of their osteocytic processes. A hierarchical model of bone tissue structure that related the cyclic mechanical loading applied to the whole bone to the fluid shear stress at the surface of the osteocytic cell process was presented in [198, 199, 31]. In this model the sensitivity of strain detection is a function of frequency; in the physiological frequency range (1-20 Hz), associated with either locomotion (1-2 Hz) or the maintenance of posture (15-30 Hz), the fluid shear stress is nearly proportional to the product of frequency and strain. Thus if bone cells respond to strains on the order of 0.1 % at frequencies of one or two Hz, they will also respond to strains on the order of 0.01 % at frequencies of 20 Hz. The fluid shear stresses would also strain the macromolecular mechanical connections between the cell and the extracellular bone matrix mentioned in the section above; thus fluid shear stress is also potentially capable of transmitting information from the strained matrix to the bone cell nuclear membrane, where it can effectively regulate its genomic functions.

Several investigators [159, 115, 108] have examined other aspects of the lacunar-canalicular porosity using simple circular pore models and have attempted to analyze its possible physiological importance. These studies have primarily emphasized the importance of the convective flow in the canaliculi between the lacunae as a way of enhancing the supply of nutrients between neighboring osteocytes. Previous studies on the relaxation of the excess pore pressure have been closely tied to the strain generated potentials (SGPs) associated with bone fluid motion. The SGP studies are briefly reviewed below.

The cyto-sensation is actually caused by fluid drag rather than fluid shear

The model of You et al. discussed in the previous section was used to make a second interesting prediction. It demonstrated that in any cellular system where

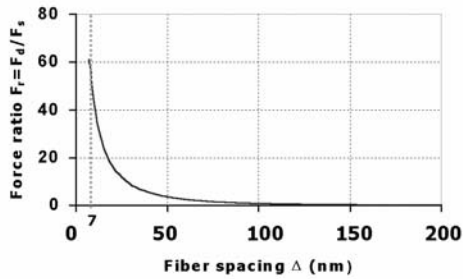


Figure 8. The relationship between force ratio and average fiber spacing Δ . Note the force ratio at $\Delta = 7$ nm is 19.6. $\Delta = 7$ nm is typical of the average spacing of GAG side chains along a core protein and the effective diameter of the albumin molecule which is known to be sieved by an equivalent matrix in capillary endothelium. This varies between 5 and 12 nm. The force ratio is defined as the ratio of the drag force on the fibers to the shear force on the cell process membrane per unit length of cell process. Previously published in You et al. (2001).

cells are subject to fluid flow and tethered to more rigid supporting structures, the tensile forces on the cell due to the drag forces on the tethering fibers may be many times greater than the fluid shear force on the cell membrane. As proposed in the BP model [198, 199, 31] the fluid flow will also induce shear stress on the cell process membrane. These stresses have been shown to mechanically stimulate bone cells [163, 202]. In the case of the extension [209] of the BP model for fluid flow in the canaliculus, the drag force on the matrix is larger than the fluid shear force. The matrix must be attached to the cell process and the canalicular wall in order for the drag force to be transmitted to the membrane and its underlying intracellular actin cytoskeleton.

The force ratio F_r is defined as the ratio of the drag force on the fibers to the shear force on the cell process membrane per unit length of cell process. The relationship between the force ratio F_r and the average fiber spacing D is plotted in Figure 8. Note the force ratio at $D = 7$ nm is 19.6. $D = 7$ nm is typical of the average spacing of GAG side chains along a core protein and the effective diameter of the albumin molecule that is known to be sieved by an equivalent matrix in capillary endothelium. This varies between 5 and 12 nm.

Cyto-sensation by streaming potentials

The fact that the extracellular bone matrix is negatively charged due to its proteins means that a fluid electrolyte bounded by the extracellular matrix will have a diffuse double layer of positive charges. When the fluid moves, the excess positive charge is convected, thereby developing streaming currents and streaming potentials (Figure 9). The cause of the fluid motion is the deformation of the extracellular matrix due to whole bone mechanical loading.

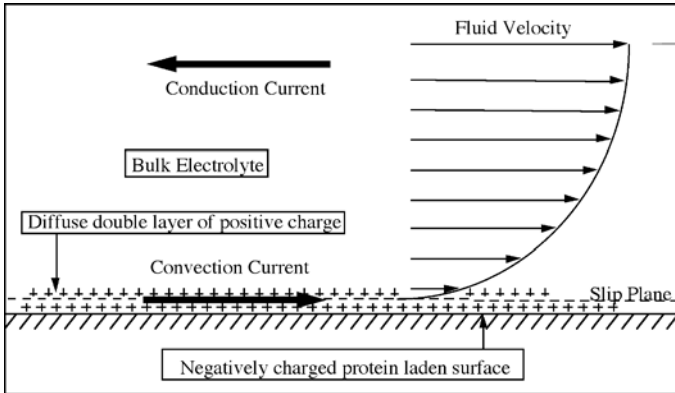


Figure 9. Strain-generated potentials (SGP's) in bone fluid channels. The source of SGP's stems from the fact that the extracellular bone matrix is negatively charged due to negative fixed charges on carbohydrates and proteins; thus a fluid electrolyte bounded by the extracellular matrix will have a diffuse double layer of positive charges. When the fluid moves, the excess positive charge is convected, thereby developing streaming currents and streaming potentials. A conduction current is thought to balance the convection current. The bulk electrolyte is neutral with respect to charge. The fluid motion is caused by the pore fluid pressure gradients induced by the deformation of the extracellular matrix due to whole bone mechanical loading.

Pollack and coworkers [177, 178, 161] have laid an important foundation for explaining the origin of strain-generated potentials (SGPs). However the anatomical site in bone tissue that is the source of the experimentally observed SGPs is not agreed upon. It was concluded in [178] that this site was the collagen-hydroxyapatite porosity of the bone mineral, because small pores of approximately 16 nm radius were consistent with their experimental data if a poroelastic-electrokinetic model with unobstructed and connected circular pores was assumed [177]. However in [31] it was shown that the data presented in [178, 180, 153] are also consistent with the larger pore space (100 nm) of the lacunar-canalicular porosity being the anatomical source site of the SGPs if the hydraulic drag and electrokinetic contribution associated with the passage of bone fluid through the surface matrix (glycocalyx) of the osteocytic process are accounted for. The mathematical model presented in [177] and the BP model [198, 199, 31, 209] are similar in that they combine poroelastic and electrokinetic theory to describe the phase and magnitude of the SGP. The two theories differ in the description of the interstitial fluid flow and streaming currents at the microstructural level and in the anatomical structures that determine the flow. In the BP model this resistance resides in the fluid annulus that surrounds the osteocytic processes, i.e. the cell membrane of the osteocytic process, the walls of the canaliculi and the glycocalyx (also called the surface matrix or capsule) that exists in this annular region. In [31] the pres-

ence of the glycocalyx increases the SGPs and the hydraulic resistance to the strain-driven flow. The increased SGP matches the phase and amplitude of the measured SGPs. In the [177] model this fluid resistance and SGP are achieved by assuming that an open, continuous small pore structure (= 16 nm radius) exists in the mineralized matrix. The BP model has been developed further [212–215, 193] and a review of the related poroelastic literature has appeared [34].

Experimental evidence indicating that the collagen-hydroxyapatite porosity of the bone mineral is unlikely to serve as the primary source of the SGP is obtained from several sources, including the estimates of the pore size in the collagen-hydroxyapatite porosity and permeability studies with different size labeled tracers in both mineralized and unmineralized bone. Such permeability studies clearly show time-dependent changes in the interstitial pathways as bone matures. At the earliest times, the unmineralized collagen-proteoglycan bone matrix is porous to large solutes. The studies with ferritin (10 nm in diameter) in two-day old chick embryo [44] show a continuous halo around primary osteons five minutes after the injection of this tracer. The halo passes right through the lacunar-canalicular system suggesting that, before mineralization, pores of the size predicted in [178] (radii = 16 nm) can exist throughout the bone matrix. In contrast, a report of an experiment [132] using this same tracer in adult dogs also found a fluorescent halo surrounding the Haversian canals; however this halo was not continuous but formed by discrete lines suggesting that the pathways were limited to discrete pores whose spacing was similar to that observed for canaliculi. This conclusion is supported by the studies [190] in the alveolar bone of five-day-old rats using the much smaller tracer, microperoxidase (MP) (2 nm). These studies clearly showed that the MP only penetrated the unmineralized matrix surrounding the lacunae and the borders of the canaliculi (see Fig. 13 of this study) and was absent from the mineralized matrix. Using more mature rats, the study of [6] confirmed the failure of the small (2 nm) MP tracer to penetrate the mineralized matrix tissue from the bone fluid compartments.

Exogenous electric field strength

Bone responds to exogenous electrical fields [154]. While the extrinsic electrical parameters are unclear, field strength may play an important role [154, 13]. A significant parallelism exists between the parameters of exogenous electrical fields and the endogenous fields produced by muscle activity. Bone responds to exogenous fields in an effective range of 1-10 mV/cm, strengths that are on the order of those endogenously produced in bone tissue during normal (muscle) activity [124].

Mechanosensation in bone: Signal Transmission

From a communications viewpoint the CCN is multiply noded (each osteocyte is a node) and multiply connected (Figure 4). Each osteocytic process is a connection between two osteocytes, and each osteocyte is multiply connected to a number of osteocytes that are near neighbors. Cell-to-cell communication is considered first below, then some speculative considerations of the ability of the CCN to compute as well as signal are described. It is useful to note the possibility that bone cells, like neurons, may communicate intercellular information by volume transmission, a process that does not require direct cytological contact, but rather utilizes charges in the environment [59, 117, 181].

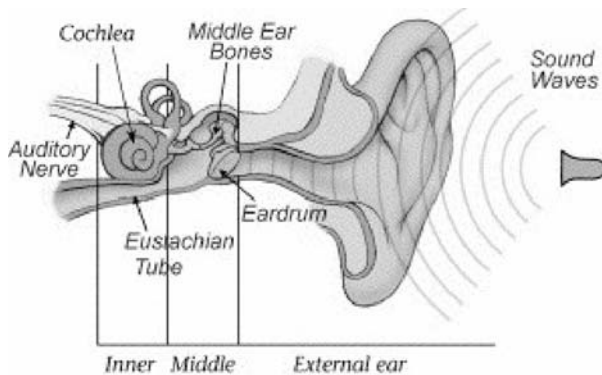


Figure 10. Anatomy of the ear. This figure is adapted from one on the website <http://www.bcm.tmc.edu/oto/research/cochlea/Hearing/index.html> associated with John S. Oghalai, M.D. in Otolaryngology at the Baylor College of Medicine.

Cell-to-cell communication

In order to transmit a signal over the CCN one osteocyte must be able to signal a neighboring osteocyte that will then pass the signal on until it reaches an osteoblast on the bone surface. There are varieties of chemical and electrical cell-to-cell communication methods [42]. The passage of chemical signals, such as Ca^{2+} , from cell to cell appears to occur at a rate that would be too slow to respond to the approximately 30 Hz signal associated with muscle firing. The focus here is on electrical cell-to-cell communication. A cable model for cell-to-cell communication in an osteon has been formulated [212, 213]. The spatial distribution of intracellular electric potential and current from the cement line to the lumen of an osteon was estimated as the frequency of the loading and conductance of the gap junction were altered. In this model the intracellular potential and current are driven by the mechan-

ically induced strain generated streaming potentials (SGPs) produced by the cyclic mechanical loading of bone. The model differs from earlier studies [76] in that it pursues a more physiological approach in which the micro-anatomical dimensions of the connexon pores, osteocytic processes and the distribution of cellular membrane area and capacitance are used to quantitatively estimate the leakage of current through the osteoblast membrane, the time delay in signal transmission along the cable and the relative resistance of the osteocytic processes and the connexons in their open and closed states. The model predicts that the cable demonstrates a strong resonant response when the cable coupling length approaches the osteonal radius. The theory also predicts that the pore pressure relaxation time for the draining of the bone fluid into the osteonal canal is of the same order as the characteristic diffusion time for the spread of current along the membrane of the osteocytic processes. This coincidence of characteristic times produced a spectral resonance in the cable at 30 Hz. These two resonances led to a large amplification of the intracellular potential and current in the surface osteoblasts, which could serve as the initiating signal for osteoblasts to conduct remodeling.

Signal processing and integration

When a physical representation of a CCN, such as Figure 1, is viewed by someone familiar with communications there is often an intuitive response that the CCN may function as a neural network for processing the mechanical loading stimulus signals being felt over the network. That idea is explored here with no justification other than shared intuition. A CCN is operationally analogous to an artificial neural network in which massively parallel, or parallel distributed, signal processing occurs [50, 43, 120].

A CCN consists of a number of relatively simple, densely interconnected, processing elements (bone cells), with many more interconnections than cells. Operationally these cells are organized into layers: an initial input, a final output and one or more intermediate or hidden layers. However such networks need not be numerically complex to be operationally complex [109].

The operational processes are identical, in principle, for all bone cells in all layers. Each cell in any layer may simultaneously receive several weighted (i.e., some quantitative measure) inputs. In the initial layer these are the loading stimuli (mechanoreception). Within each cell independently, "... all the weighted inputs are then summed ..." [196]. This net sum is then compared, within the cell, against some threshold value. If this liminal value is exceeded, a signal is generated (mechanotransduction in input layer cells) that is then transmitted identically to all the hidden layer cells (adjacent osteocytes) to which each initial layer cell is connected. Similar processes of weighted signal summation, comparison and transmission occur in these layers until final

layer cells (osteoblasts) are reached. The outputs of these surface situated cells regulate the specific adaptation process of each group of osteoblasts [157]. All neighboring osteoblasts that carry out an identical bone adaptational process form a communication compartment, a cohort of structurally and operationally similar cells, since all these cells are interconnected by open, functional gap junctions. At the boundary between such compartments that are carrying out different adaptational processes, the intervening gap junctions are closed and are incapable of transmitting information. These boundaries are probably changing continuously as some of the cells have some down time [188, 93].

Information is not stored discretely in a CCN, as is the case in conventional computers. Rather it is distributed across all or part of the network, and several types of information may be stored simultaneously. The instantaneous state of a CCN is a property of all of its cells and of their connections. Accordingly its informational representation is redundant, assuring that the network is fault, or error, tolerant; i.e., one or several inoperative cells causes little or no noticeable loss in network operations [196].



Figure 11. An exposed cross-section of the cochlea illustrating its three chambers. Adapted from an illustration on the website <http://www.finchcms.edu/anatomy/histohome/lectures/ear/sld001.htm>.

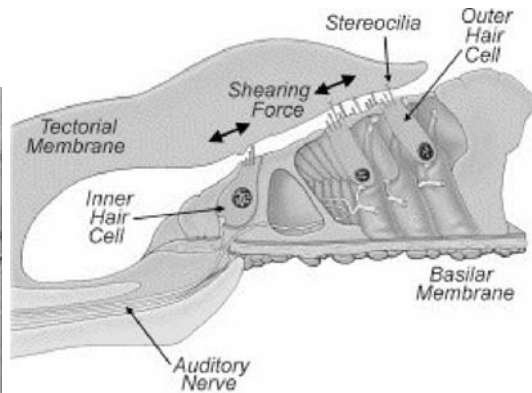


Figure 12. The organ of Corti. The organ of Corti is the structure that partitions the chambers of the cochlea illustrated in Figure 11. This figure is adapted from one on the website <http://www.bcm.tmc.edu/oto/research/cochlea/Hearing/index.html> associated with John S. Oghalai, M.D. in Otolaryngology at the Baylor College of Medicine.

CCNs exhibit oscillation; i.e., iterative reciprocal (feedback) signaling between layers enables them to adjustively self-organize. This is related to the fact that CCNs are not preprogrammed, rather they learn by unsupervised training [56], a process involving the adaptation of the CCNs to the responses of the cytoskeleton to physical activity [41]. In this way the CCN adjusts to the customary mechanical loading of the whole bone [111]. In a CCN, structurally more complex attributes and behavior gradually self-organize and emerge during operation. These are not reducible; they are neither apparent nor predictable from a prior knowledge of the behavior of individual cells.

As noted above, gap junctions as electrical synapses permit bi-directional flow of information. This is the cytological basis for the oscillatory behavior of a CCN. The presence of sharp discontinuities between groups of phenotypically different osteoblasts is related also to an associated property of gap junctions, i.e., their ability to close and so prevent the flow of information [98, 106]. Significantly, informational networks can also transmit inhibitory signals, a matter beyond our present scope [116].

It is suggested that a CCN displays the following attributes: Developmentally it is self-organized and self-adapting and, in the sense that it is epigenetically regulated, it is untrained. Operationally it is a stable, dynamic system, whose oscillatory behavior permits feedback; in this regard, it is noted that a CCN operates in a noisy, non-stationary environment, and that it also employs useful and necessary inhibitory inputs.

The CCN permits a triad of histological responses to a (seemingly) unitary loading event. Although in this chapter, as in almost all the related literature, the organization of bone cells is treated as if it existed only in two dimensions, and as if bone tissue loadings occurred only at certain discrete loci, and that without consideration of loading gradients, the biological situation is otherwise. Given such a loading event, a three-dimensional bone volume, gradients of deformation must exist, and each osteocyte may sense correspondingly different strain properties. Moreover, it is probable that each osteocyte potentially is able to transmit three different signals in three different directions, some stimulatory and some inhibitory: such states have not yet been modeled [142, 143].

A tentative mechanotransduction synthesis

The molecular lever mechanisms that permit muscle function to directly regulate the genomic activity of strained bone cells, including their phenotypic expression, when combined together with electric field effects and contraction frequency energetics, provides a biophysical basis for an earlier hypothesis of epigenetic regulation of skeletal tissue adaptation [135, 136, 146, 147].

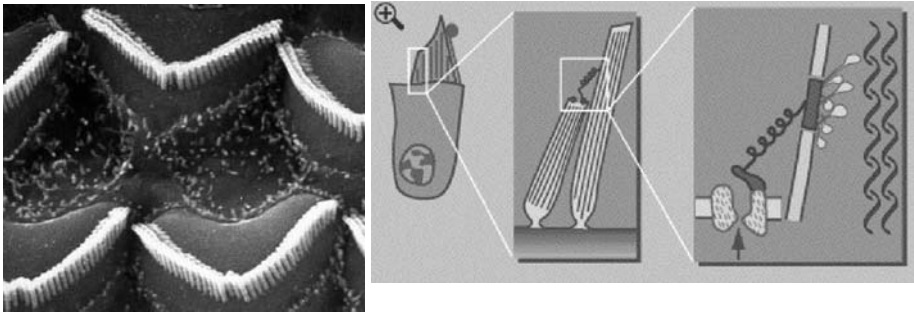


Figure 13. Left : An array of hair cells. Right :The movement of a hair cell's cilia bundle (left panel) opens ion channels at the tips of the cilia. When the bundle tilts to the right (middle panel), tip links from the higher cilia pull up the gates of the ion channels on adjoining, shorter cilia. This (still middle panel) close-up shows how a tip link between two cilia opens an ion channel on the shorter cilium. Even more highly magnified in the right panel, the open channel allows ions into the cell. This illustration is by Jennifer Jordan, RCW Communications, Inc. (adapted from a sketch by James Hudspeth, HHMI, University of Texas Southwestern Medical Center at Dallas).

It is probable [144, 145] that electrical and mechanical transductive processes are neither exhaustive nor mutually exclusive. While utilizing differing intermediate membrane mechanisms and/or processes, they share a common final pathway [185]; i.e., both mechanical and electrical transductions result in transplasma membrane ionic flow(s), creating a signal(s) capable of intercellular transmission to neighboring bone cells via gap junctions [198, 199, 31, 212, 213, 211]. These signals are inputs to a CCN, whose outputs regulate the bone adaptational processes.

The primacy of electrical signals is suggested here, since while bone cell transduction may also produce small biochemical molecules that can pass through gap junctions, the time-course of mechanosensory processes is believed to be too rapid for the involvement of secondary messengers [18, 201, 21]. As noted above, the passage of chemical signals, such as Ca^{2+} , from cell to cell appears to occur at a rate that would be too slow to respond to the approximately 30 Hz signal associated with muscle firing.

Mechanosensation in the auditory system

Hearing works by the ear detecting sound waves, converting them into neural signals and then sending the signals to the brain.* The ear has three divisions: the external ear, the middle ear, and the inner ear (Figure 10). The external ear collects sound waves and funnels them down the ear canal, where they vibrate the eardrum. Within the middle ear, the eardrum is connected to

the middle ear bones. These are the smallest bones in the body, and they mechanically carry the sound waves to the inner ear. The eustachian tube connects the middle ear to the upper part of the throat, equalizing the air pressure within the middle ear to that of the surrounding environment. The inner ear contains the cochlea. This organ converts sound waves into neural signals. These signals are passed to the brain via the auditory nerve.

Mechanosensation occurs in the cochlea (Figure 10). A section through the cochlea is shown in Figure 11. Coiling around the inside of the cochlea, the organ of Corti (Figure 12) contains the cells responsible for hearing, the hair cells (Figure 13, left). There are two types of hair cells: inner hair cells and outer hair cells. These cells have stereocilia or “hairs” that stick out. The bottom of these cells is attached to the basilar membrane, and the stereocilia are in contact with the tectorial membrane. Inside the cochlea, sound waves cause the basilar membrane to vibrate up and down. This creates a shearing force (Figure 12) between the basilar membrane and the tectorial membrane, causing the hair cell stereocilia to bend back and forth (Figure 14). The movement of a hair cell’s cilia bundle opens ion channels at the tips of the cilia (Figure 13, right). When the bundle tilts to the right (middle panel of righthandside of Figure 13), tip links from the higher cilia pull up the gates of the ion channels on adjoining, shorter cilia. A close-up shows how a tip link between two cilia opens an ion channel on the shorter cilium. Even more highly magnified at the right of Figure 13, the open channel allows ions into the cell. This leads to internal changes within the hair cells that create electrical signals. Auditory nerve fibers rest below the hair cells and pass these signals on to the brain. Therefore, the bending of the stereocilia is how hair cells sense sounds.

Outer hair cells have a special function within the cochlea. They are shaped cylindrically, like a can, and have stereocilia at the top of the cell (Figure 13), and a nucleus at the bottom. When the stereocilia are bent in response to a sound wave, an electromotile response occurs. This means the cell changes in length. Therefore, with every sound wave, the cell shortens and then elongates. This pushes against the tectorial membrane, selectively amplifying the vibration of the basilar membrane. This allows us to hear very quiet sounds.

The similarities between the cytoplasmic processes of bones cells and the stereocilia of hair cells are that they both (1) measure mechanical deformations (vibrations of a fluid domain), (2) communicate their measurement to a network, (3) do this with dendritic structures, (4) the dendrites of both cells are constructed of similar materials (e.g., actin and fimbrin) and (5) the initial signaling in both cases consists of opening ion channels. While the hair cells communicate their information to a network that feeds to the brain, the bones cells connect to a lower level network (CCN) with (potentially) local decision-making software.

References

- [1] Aarden, E. M., Burger, E. H., and Nijweide, P. J. (1994) Function of osteocytes in bone. *Journal of Cell Biochemistry* **55**, 287-299
- [2] Aarden, E.M. (1996) The third cell- a study of the role of the osteocyte in bone. *Thesis, Leiden*
- [3] Aarden, E.M., Wassenaar, A.M., Alblas, M.J. and Nijweide, P.J. (1996) Immunocytochemical demonstration of extracellular matrix proteins in isolated osteocytes. *Histochemical Cell Biology* **106** 495-501
- [4] Almekinders, L.C., Banes, A.J. and Ballenger, C.A. (1993) Effects of repetitive motion on human fibroblasts. *Medical Science of Sports Exercise* **25** 603-607
- [5] Atkinson, P.J. and Hallsworth, A.S. (1983) The changing structure of aging human mandibular bone. *Gerodontology* **2** 57-66
- [6] Ayasaka, N., Kondo ,T., Goto, T., et al. (1992) Differences in the transport systems between cementocytes and osteocytes in rats using microperoxidase as a tracer. *Archives of Oral Biology* **37** 363-368
- [7] Beardslee, M.A., Laing, J.G., Beyer, E.C. et al. (1998) Rapid turnover of connexin 43 in the adult rat heart. *Circulation Research* **83** 629-635
- [8] Bennett, M.V.L., Goodenough, D.A. (1978) Gap junctions. Electronic coupling and intercellular communication. *Neuroscience Research Progress Bulletin* **16** 373-485
- [9] Bhalla, U.S. and Iyengar, R. (1999) Emergent properties of networks of biological signaling pathways. *Science* **283** 381-383
- [10] Bingmann, D., Tetsch, D. and Fritsch, J. (1988a) Membraneigenschaften von zellen aus knochenexplantaten. *Zeitschrift Zahnartzl Implantologie* **IV** 277-281
- [11] Bingmann, D., Tetsch, D. and Fritsch, J. (1988b) Membrane properties of bone cells derived from calvaria of newborn rats (tissue culture). *Pfluger's Architecture* **S412** R14-15
- [12] Bretscher, A. and Weber, K. (1980) Fimbrin, a new microfilament-associated protein present in microvilli and other cell surface structures. *Journal of Cell Biology* **86** 335-340
- [13] Brighton, C.T., Okerehe, E., Pollack, S., et al. (1992) In vitro bone-cell response to a capacitively coupled electrical field. Role of field strength, pulse pattern and duty cycle. *Clinical Orthopedics and Related Research* **285** 255-262
- [14] Brown, T.D., Pedersen, D.R., Gray, M.L., et al. (1990) Toward an identification of mechanical parameters initiating periosteal remodeling: a combined experimental and analytic approach. *Journal of Biomechanics* **23** 893-905
- [15] Brown, T.D., Bottlang, M., Pederson, D.R. et al. (1998) Loading paradigms-intentional and unintentional- for cell culture mechanostimulus. *American Journal of Medical Science* **316** 162-168
- [16] Buckwalter, J.A. and Rosenberg, L.C. (1982) Electron microscopic studies of cartilage proteoglycans. Direct evidence for the variable length of the chondroitin sulfate-rich region of proteoglycan subunit core protein. *Journal of Biological Chemistry* **257(16)** 9830-9839
- [17] Burger, E.H. and Veldhuijzen, J.P. (1993) Influence of mechanical factors on bone formation, resorption, and growth in vitro. *Bone, Editor B. L/Hall* **7** 37-56. CRC Press, Boca Raton, Florida

- [18] Burger, E.H., Klein Nulend, J. and Cowin, S.C. (1998) Mechanotransduction in bone. *Advances in Organ Biology*, Editor M. Zaidi **5a** 107-118. JAI Press Inc, London
- [19] Cammarota, Jr., J.P. and Onaral, B. (1998) State transitions in physiologic systems: A complexity model for loss of consciousness. *IEEE Transactions on Biomedical Engineering* **45** 1017-23
- [20] Carter, D.R. and Hayes, W.C. (1976) Bone compressive strength: the influence of density and strain rate. *Science* **194** 174-1175
- [21] Carvalho, R.S., Scott, J.E., Suga, D.M., et al. (1994) Stimulation of signal; transduction pathways in osteoblasts by mechanical strain potentiated by parathyroid hormone. *Journal of Bone and Mineral Research* **9** 999-1011
- [22] Carvalho, R.S., Schaffer, J.L. and Gerstenfeld, L.C. (1998) Osteoblasts induce osteopontin expression in response to attachment on fibronectin: demonstration of a common role for integrin receptors in the signal transduction processes of cell attachment and mechanical stimulation. *Journal of Cellular Biochemistry* **70** 376-390
- [23] Chailley, B. Nicolas, G. and Laine, M. C. (1989) Organization of actin microfilaments in the apical border of oviduct ciliated cells. *Biology of the Cell* **67** 81-90
- [24] Chesnoy-Marchais, D. and Fritsch, J. (1988) Voltage-gated sodium and calcium currents in rat osteoblasts. *Journal of Physiology* **398** 291-311
- [25] Civitelli, R. (1995) Cell-cell communication in bone *Calcified Tissue International* **56** (Suppl. 1) S29-S31
- [26] Clark, E.A. and Brugge, J. S. (1995) Integrins and signal transduction pathways: the road taken. *Science* **268** 233-239
- [27] Cooper, R.R., Milgram, J.W., Robinson, R.A. and Maryland, B. (1966) Morphology of the osteon. *Journal of Bone and Joint Surgery* **48-A(7)** 1239-1271
- [28] Cowan, D.B., Lye, S.J. and Langille, B. L. (1998) Regulation of vascular connexin 43 gene expression by mechanical loads. *Circulation Research* **82** 786-93
- [29] Cowin, S.C. and Hegedus, D.M. (1976) Bone remodeling I: a theory of adaptive elasticity. *Journal of Elasticity* **6** 313-325
- [30] Cowin, S.C., Moss-Salentijn, L. and Moss, M. L. (1991) Candidates for the mechanosensory system in bone. *Journal of Biomechanical Engineering* **113** 191-197
- [31] Cowin, S.C., Weinbaum, S. and Zeng, Yu (1995) A case for bone canaliculi as the anatomical site of strain generated potentials. *Journal of Biomechanics* **28** 1281-1296
- [32] Cowin, S.C. (1998) On mechanosensation in bone under microgravity. *Bone* **22** 119S-125S
- [33] Cowin, S.C. and Weinbaum, S. (1998) Strain amplification in the bone mechanosensory system. *American Journal of Medical Science* **316** 184-188
- [34] Cowin, S.C. (1999) Bone poroelasticity. *Journal of Biomechanics* **32** 218-238
- [35] Cowin, S.C. and Moss, M. L. (2000) Mechanosensory mechanisms in bone. *Textbook of Tissue Engineering, 2nd edition*, Editors: R. Lanza, R. Langer, and W. Chick 723-738, Academic Press, San Diego, California
- [36] Cui, C., Smith, D.O. and Adler, J. (1995) Characterization of mechanosensitive channels in *Escherichia coli* cytoplasmic cell membrane by whole-cell patch clamp recording. *Journal of Membrane Biology* **144** 31-42
- [37] Culshaw, P. (1996) *Smart Structures and Materials* Boston, Artech House

- [38] Curtis, T.A., Ashrafi, S.H. and Weber, D. F. (1985) Canalicular communication in the cortices of human long bones. *Anatomical Record* **212** 336-344
- [39] Davidson, R.M., Tatakis, D.W. and Auerbach, A.L. (1990) Multiple forms of mechanosensitive ion channels in osteoblast-like cells. *European Journal of Physiology* **416** 646-51
- [40] Dayhoff, J. (1990) *Neural Network Architecture* van Nostrand Reinhold, New York
- [41] Dayhoff, J.E., Hameroff, S.R., Lahoz-Beltra, R., et al. (1992) Intracellular mechanisms in neuronal learning: adaptive models. *International Joint Conference on Neural Networks* 173-178
- [42] De Mello, W.C. (1987) The ways cells communicate. *Cell-to-cell Communication* 1-20, Plenum Press, New York
- [43] Denning, P.J. (1990) Neural networks. *American Scientist* **80** 426-429
- [44] Dillaman, R.M. (1984) Movement of ferritin in the 2 day-old chick femur. *Anatomical Record* **209** 445-453
- [45] Dolce, C., Kinniburgh, A.J. and Dziak, R. (1996) Immediate early-gene induction in rat osteoblastic cells after mechanical deformation. *Archives of Oral Biology* **41** 1101-1108
- [46] Doty, S.B. (1981) Morphological evidence of gap junctions between bone cells. *Calcified Tissue International* **33** 509-512
- [47] Doty, S.B. (1989) Cell-to-cell communication in bone tissue. *The Biological Mechanism of Tooth Eruption and Root Resorption*. Editor, Z. Davidovitch 61-69. EBSCO Media, Birmingham, Alabama
- [48] Duncan, R. and Misler, S. (1989) Voltage-activated and stretch activated Ba²⁺ conducting channels in an osteoblast-like cell line (URM 106). *Federation of European Biochemical Societies* **251** 17-21
- [49] Duncan, R.L. and Turner, C. H. (1995) Mechanotransduction and the functional response of bone to mechanical strain. *Calcified Tissue International* **57** 344-358
- [50] Edin, B.B. and Trulsson, M. (1992) Neural network analysis of the information content in population responses from human periodontal receptors. *Science of Neural Networks SPIE* **1710** 257-266
- [51] Ferrier, J., Crygorczyk, C., Grygorczyk, R., et al. (1991) Ba²⁺-induced action potentials in osteoblastic cells. *Journal of Membrane Biology* **123** 255-259
- [52] Forgacs, G. (1995) Biological specificity and measurable physical properties of cell surface receptors and their possible role in signal transduction through the cytoskeleton. *Biochemical Cell Biology* **73** 317-326
- [53] Fraser, D.J. and Macdonald, A.G. (1994) Crab hydrostatic pressure sensors. *Nature* **371** 383-384
- [54] French, A.S. (1992) Mechanotransduction. *Annual Review of Physiology* **54** 135-152
- [55] Fritton, S.P., McLeod, K.J. and Rubin, C.T. (2000) Quantifying the strain history of bone: spatial uniformity and self-similarity of low magnitude strains. *Journal of Biomechanics* **33** 317-325
- [56] Fritzke, B. (1994) Growing cell structures-a self-organizing network for unsupervised and supervised learning. *Neural Networks* **7** 1441-1460
- [57] Frost, H.M. (1964) *The Laws of Bone Structure* Charles C. Thomas, Springfield, IL
- [58] Frost, H.M. (1969) Tetracycline based histological analysis of bone remodeling. *Calcified Tissue Research* **3** 211-237

- [59] (1991). *Volume Transmission in the Brain*. Editors J. Fuxe and L.F. Agnati Raven Press, New York
- [60] Fyhrie, D.P. and Carter, D. R. (1986) A unifying principle relating stress to trabecular bone morphology. *Journal of Orthopedic Research* **4** 304-317
- [61] Ghazi, A., Berrier, C., et.al. (1998) Mechanosensitive ion channels and their mode of activation. *Biochimie* **80** 357-62
- [62] Gilbertson, T.A. (1998) Peripheral mechanisms of taste. *The Scientific Basis of Eating*. Editor R.W.A. Linden **9** 1-28. Karger, Basel
- [63] Glenney, Jr., J.R., Kaulfus, P. Matsudaira, P. and Weber, K. (1981) F-actin binding and bundling properties of fimbrin, a major cytoskeletal protein of microvillus core filaments. *Journal of Biological Chemistry* **256** 9283-9288
- [64] Gohel, A.R., Hand, A.R. and Gronowicz, G. A. (1995) Immunogold localization of beta 1-integrin in bone: effect of glucocorticoids and insulin-like growth factor I on integrins and osteocyte formation. *Journal of Histochemistry and Cytochemistry* **43** 1085-96
- [65] Goldsmith, P. (1994) Plant stems: A possible model system for the transduction of mechanical information in bone modeling. *Bone* **15** 249-250
- [66] Goldstein, S.A., Matthews, L.S., Kuhn, J.L., et al. (1991) Trabecular bone remodeling: an experimental model. *Journal of Biomechanics* **24 (Suppl. 1)** 135-150
- [67] Gourdie, R. and Green, C. (1993) The incidence and size of gap junctions between bone cells in rat calvarial. *Anatomical Embryology* **187** 343-352
- [68] Green, P. B. (1994) Connecting gene and hormone action to form, pattern and organogenesis: biophysical transductions. *Journal of Experimental Botany* **45 (Special Issue)** 1775-1788
- [69] Green, S. S. and Triffitt, T. (1997) The animal brain as a quantal computer. *Journal of Theoretical Biology* **184** 385-403
- [70] Gross, T.S., Edwards, J.L., et.al. (1997) Strain gradients correlate with sites of periosteal bone formation. *Journal of Bone and Mineral Research* **12** 982-8
- [71] Grossberg, S. (1988) *Neural Networks and Artificial Intelligence* MIT Press, Cambridge, MA
- [72] Guggino, S.E., LaJeunesse, D., Wagner, J.A., et al. (1989) Bone remodeling signaled by a dihydropyridine- and phenylalkylamine-sensitive calcium channel. *Proceedings of the National Academy of Science* **8** 2957-2960
- [73] Hackney, C.M. and Furness, D.N. (1995) Mechanotransduction in vertebrate hair cells: structure and function of the stereociliary bundle. *American Journal of Physiology* **268 (Cell Physiol.37)** C1-C13
- [74] Hamill, O.P. and McBride, Jr., D.W. (1995) Mechanoreceptive membrane channels. *American Scientist* **83** 30-37
- [75] Hamill, O.P. and McBride, Jr., D.W. (1996) The pharmacology of mechanogated membrane ion channels. *Pharmacological Reviews* **48** 231-248
- [76] Harrigan, T.P. and Hamilton, J.J. (1993) Bone strain sensation via transmembrane potential changes in surface osteoblasts: loading rate and microstructural implications. *Journal of Biomechanics* **26** 183-200
- [77] Harter, L.V., Hruska, K.A. and Duncan, R.L. (1995) Human osteoblast-like cells respond to mechanical strain with increased bone matrix protein production independent of hormonal regulation. *Endocrinology* **136** 528-535

- [78] Haskin, C. and Cameron, I. (1993) Physiological levels of hydrostatic pressure alter morphology and organization of cytoskeletal and adhesion proteins in MG-63 osteosarcoma cells. *Biochemical Cell Biology* **71** 27-35
- [79] Hecker, M., Mülsch, A., Bassenge, E., and Busse, R. (1993) Vasoconstriction and increased flow: two principal mechanisms of shear stress-dependent endothelial autocoid release. *American Journal of Physiology* **265** (*Heart Cir. Physiol.* **34**) H828-H833
- [80] Hert, J., Liskova, M. and Landgrot, B. (1969) Influence of the long-term continuous bending on the bone. An experimental study on the tibia of the rabbit. *Folia Morphologia* **17** 389-399
- [81] Hert, J., Liskova, M. and Landa, J. (1971) Reaction of bone to mechanical stimuli. Part I. Continuous and intermittent loading of tibia in rabbit. *Folia Morphologia* **19** 290-300
- [82] Hert, J., Pribylova, E. and Liskova, M. (1972) Reaction of bone to mechanical stimuli. Part 3. Microstructure of compact bone of rabbit tibia after intermittent loading. *Acta anatomica* **82** 218-230
- [83] Heylighen, F. (1997) Publications on complex, evolving systems: A citation based survey. *Complexity* **2** 31-36
- [84] Hinton, G.E. and Anderson, J.A. (1989) *Parallel Models of Associative Memory* Lawrence Erlbaum Assoc Publ, Hillsdale, N.J
- [85] Hughes, D.E., Salter, D.M., Dedhar, S., et al. (1993) Integrin expression in human bone. *Journal of Bone and Mineral Research* **8** 527-533
- [86] Huiskes, R., Weinans, H.J., Grootenboer, H.J., et al. (1987) Adaptive bone remodeling theory applied to prosthetic-design analysis. *Journal of Biomechanics* **20** 1135-1150
- [87] Hung, C.T., Pollack, S.R., Reilly, T.M., and Brighton, C.T. (1995) Real-time calcium response of cultured bone cells to fluid flow. *Clinical Orthopedics and Related Research* **313** 256-269
- [88] Ingber, D.E. (1998) Cellular basis of mechanotransduction. *Biology Bulletin* **194** 323-327
- [89] Jacobs, R., Ed. (1998) *Osseoperception* Catholic University, Leuven
- [90] Jan, L.Y. and Jan, Y.N. (1992) Tracing the roots of ion channels. *Cell* **69** 715-718
- [91] Janmey, P.A. (1998) The cytoskeleton and cell signaling: component localization and mechanical coupling. *Physiological Review* **78** 763-774
- [92] Jaworski, Z.F.G., Liskova Kiar, M. and Uhthoff, H.K. (1980) Effect of long term immobilization on the pattern of bone loss in older dogs. *Journal of Bone and Joint Surgery* **62B** 104-110
- [93] Jeansonne, B.G., Feagin, F.F., et al. (1979) Cell-to-cell communication of osteoblasts. *Journal of Dental Research* **58** 1415-1423
- [94] Johnson, M.W., Chakkalakal ,D.A., Harper, R.A., et al.(1982) Fluid flow in bone. *Journal of Biomechanics* **11** 881-885
- [95] Jones, D.B. and Bingmann, D. (1991) How do osteoblasts respond to mechanical stimulation? *Cells and Materials* **1** 329-340
- [96] Jones, S.J., Gray, C., Sakamaki, H., et al.(1993) The incidence and size of gap junctions between bone cells in rat calvaria. *Anatomical Embryology* **187** 343-352
- [97] Junge, D. (1998) *Oral Sensorimotor Function* Medico Dental Media, International, Inc., Pacific, MO

- [98] Kam, E. and Hodgins, M. B. (1992) Communication compartments in hair follicles and their implication in differentiative control. *Development* **114** 389-393
- [99] Kamiya, A., Bukhari, R., and Togawa, T. (1984) Adaptive regulation of wall shear stress optimizing vascular tree function. *Bulletin of Mathematical Biology* **46** 127-137
- [100] Kashimori, Y., Funakubo, H. and Kambara, T. (1998) Effect of syncytium structure of receptor systems on stochastic resonance by chaotic potential fluctuation. *Biophysical Journal* **75** 1700-1711
- [101] Kernan, M., Cowan, D., Zuker, C. (1994) Genetic dissection of mechanoreception-defective mutations. *Drosophila Neuron* **12** 1195-1206
- [102] Keynes, R.D. (1994) The kinetics of voltage-gated ion channels. *Quarterly Review of Biophysics* **27** 339-434
- [103] King, G.J. and Holtrop, M.E. (1975) Actin-like filaments in bone cells of cultured mouse calvaria as demonstrated by binding to heavy meromyosin. *Journal of Cell Biology* **66** 445-451
- [104] Klein-Nulend, J., Van der Plas, A., Semeins, C.M., Ajubi, N.E., Frangos, J.A., Nijweide, P.J., and Burger, E.H. (1995a) Sensitivity of osteocytes to biomechanical stress in vitro. *FASEB Journal* **9** 441-445
- [105] Klein-Nulend, J., Semeins, C.M., Ajubi, N.E., Nijweide, P.J., and Burger, E.H. (1995b) Pulsating fluid flow increases nitric oxide (NO) synthesis by osteocytes but not periosteal fibroblasts - correlation with prostaglandin upregulation. *Biochemican and Biophysics Research Communication* **217** 640-648
- [106] Kodoma, R. and Eguchi, G. (1994) The loss of gap junctional cell-to-cell communication is coupled with dedifferentiation of retinal pigmented epithelial cells in the course of transdifferentiation into the lens. *International Journal of Developmental Biology* **38** 357-364
- [107] Krstic, R.V (1978) *Die Gewebe des Menschen und der Saugetiere* Springer Verlag, Berlin
- [108] Kufahl, R.H. and Saha, S. (1990) A theoretical model for stress-generated fluid flow in the canaliculi-lacunae network in bone tissue. *Journal of Biomechanics* **23** 171-180
- [109] Kupfermann, I. (1992) Neural networks: they do not have to be complex to be complex. *Behavioral Brain Science* **15** 767-768
- [110] Lanyon, L.E., Goodship, A.E., Pye, C.J., MacFie, J.H. (1982) Mechanically adaptive bone remodeling. *Journal of Biomechanics* **15** 147-154
- [111] Lanyon, L.E. (1984) Functional strain as a determinant for bone remodeling. *Calcified Tissue International* **36** S56-S61
- [112] Lanyon, L.E. (1993) Osteocytes, strain detection, bone modeling and remodeling. *Calcified Tissue International* **53** (Suppl 1) S102-S106
- [113] Lecanda, F., Towler, D.A., et.al. (1998) Gap junctional communication modulates gene expression in osteoblastic cells. *Molecular Biology of the Cell* **9** 2249-58
- [114] Lee, D.H., Freaan, S.P., Lees, P. et al. (1998) Dynamic mechanical compression influences nitric oxide by articular chondrocytes. *Biochemical and Biophysics Research Communication* **251** 580-585
- [115] Machwate, M., Jullienne, A., Moukhtar, M., et al. (1995) Temporal variation of c-fos protot-ocogene expression during osteoblasts differentiation and osteogenesis in developing rat bone. *Journal of Cell Biochemistry* **57** 62-70

- [116] Marotti, G., Ferretti, M., Muglia, M. A., et al. (1992) A quantitative evaluation of osteoblast-osteocyte relationships on growing endosteal surface of rabbit tibiae. *Bone* **13** 363-368
- [117] Marotti, G. (1996) The structure of bone tissues and the cellular control of their deposition. *Italian Journal of Anatomical Embryology* **101** 25-7
- [118] Martin, R.B. and Burr, D.B. (1982) A hypothetical mechanism for the stimulation of osteonal remodeling by fatigue damage. *Journal of Biomechanics* **15** 137-139
- [119] Martin, T.J. and Ng, K.W. (1994) Mechanisms by which cells of the osteoblastic lineage control osteoclast formation and activity. *Journal of Cellular Biochemistry* **56** 357-366
- [120] Martino, R.L., Johnson, C.A., Suh, E.B., et al. (1994) Parallel computing in biomedical research. *Science* **265** 902-907
- [121] Massass, R., Bingmann, D., Korenstein, R., et al. (1990) Membrane potential of rat calvaria bone cells: dependence on temperature. *Journal of Cell Physiology* **144** 1-11
- [122] McClelland, J.L. and Rumelhart, D.E. (1987) *Parallel Distributed Processing. Psychological and Biological Models. Vol. 2* M.I.T. Press, Cambridge, MA
- [123] McLeod, K.J. and Rubin, C.T. (1992) The effect of low-frequency electrical fields on osteogenesis. *Journal of Bone and Joint Surgery* **74A** 920-929
- [124] McLeod, K.J., Donahue, H.J., et al. (1993) Electric fields modulate bone cell function in a density-dependent manner. *Journal of Bone and Mineral Research* **8** 977-984
- [125] McLeod, K.J., Rubin, C.T., et al. (1998) Skeletal cell stresses and bone adaptation. *American Journal of Medical Science* **316** 176-183
- [126] McMahon, T.A. (1984) *Muscles, Reflexes, and Locomotion* Princeton University Press, Princeton, New Jersey
- [127] Meazzini, M.C., Toma, C.D., et al. (1998) Osteoblast cytoskeletal modulation in response to mechanical strain in vitro. *Journal of Bone and Joint Surgery* **16** 170-180
- [128] Mi, L.Y., Basu, M., Fritton, S.P., Cowin, S.C. (2004a) Analysis of avian bone response to mechanical loading: Part One: Distribution of bone fluid shear stress induced by bending and axial loading, in preparation.
- [129] Mi, L.Y., Basu, M., Fritton, S.P., Cowin, S.C. (2004b) Analysis of avian bone response to mechanical loading: Part Two:, in preparation.
- [130] Minkoff, R., Rundus, V.R., Parker, S.B., et al. (1994) Gap junction proteins exhibit early and specific expression during intramembranous bone formation in the developing chick mandible. *Anatomical Embryology* **190** 231-241
- [131] Minkoff, R., Bales, E.S., et al. (1999) Antisense oligonucleotide blockade of connexin expression during embryonic bone formation: Evidence of functional compensation within a multigene family. *Developmental Genetics* **24** 43-56
- [132] Montgomery, R.J., Sutker, B.D., et al. (1988) Interstitial fluid flow in cortical bone. *Microvascular Research* **23** 188-200
- [133] Moreno, A.P., Rook, M.B., et al. (1994) Gap junction channels: distinct voltage-sensitive and -insensitive conductance states. *Biophysics Journal* **67** 113-119
- [134] Morris, C.E. (1990) Mechanosensitive ion channels. *Journal of Membrane Biology* **113** 93-107
- [135] Moss, M.L., Young, R. (1960) A functional approach to craniology. *American Journal of Physical Anthropology* **18** 81-92

- [136] Moss, M.L. (1962) The Functional Matrix. *Vistas in Orthodontics*. Editors B. Kraus and R. Reidel 85-98, Lea and Febiger, Phila
- [137] Moss, M.L. (1968) The primacy of functional matrices in orofacial growth. *Transactions of the British Society for the Study of Orthodontal Dental Practice* **19** 65-73
- [138] Moss, M.L. (1969) A theoretical analysis of the functional matrix. *Acta Biotheoretica* **18** 195-202
- [139] Moss, M.L. (1978) *The Muscle-bone Interface: An Analysis of a Morphological Boundary* Center for Human Growth and Development, Ann Arbor, Michigan
- [140] Moss, M.L. (1991a) Bone as a connected cellular network: modeling and testing. *Topics in Biomedical Engineering*. Editor G. Ross 117-119. Pergamon Press, New York
- [141] Moss, M.L. (1991b) Alternate mechanisms of bone remodeling: their representation in a connected cellular network model. *Annals of Biomedical Engineering* **19** 636
- [142] Moss, M.L. (1997a) The functional matrix hypothesis revisited. 1. The role of mechano-transduction. *American Journal of Orthodontal and Dentofacial Orthopedics* **112** 8-11
- [143] Moss, M.L. (1997b) The functional matrix hypothesis revisited. 2. The role of an osseous connected cellular network. *American Journal of Orthodontal and Dentofacial Orthopedics* **112** 221-6
- [144] Moss, M.L. (1997c) The functional matrix hypothesis revisited. 3. The genomic thesis. *American Journal of Orthodontal and Dentofacial Orthopedics* **112** 338-42
- [145] Moss, M.L. (1997d) The functional matrix hypothesis revisited. 4. The epigenetic anti-thesis and the resolving synthesis. *American Journal of Orthodontal and Dentofacial Orthopedics* **112** 410-7
- [146] Moss, M.L. and Salentijn, L. (1969a) The primary role of the functional matrices in facial growth. *American Journal of Orthodontics* **55** 566-577
- [147] Moss, M.L., Salentijn, L. (1969b) The capsular matrix. *American Journal of Orthodontics* **56** 474-490
- [148] Moss-Salentijn, L. (1992) The Human Tactile System. em Advanced Tactile Sensing for Robotics. Editor H.R.Nicholls **Chapter4** World Scientific Publishing, Singapore
- [149] Nakamura, H. (1995) Localization of CD44, the hyaluronate receptor, on the plasma membrane of osteocytes and osteoclasts in rat tibiae. *Cell Tissue Research* **280** 225-233
- [150] Nowak, R. (1992) Cells that fire together, wire together. *Journal of NIH Research* **4** 60-64
- [151] O'Connor, J. A., Lanyon, L.E. and MacFie, H. (1982) The influence of strain rate on adaptive bone remodeling. *Journal of Biomechanics* **15** 767-781
- [152] Olsson, S. and Hanson, B.S. (1995) Action potential-like activity found in fungal mycelia is sensitive to stimulation. *Naturwissch.* **82** 30-31
- [153] Otter, M.W., Palmieri, V.R., Wu, D.D., et al. (1992) A comparative analysis of streaming potentials In Vivo and In Vitro. *Journal of Orthopaedic Research* **10** 710-719
- [154] Otter, M.W., McLeod, K.J., Rubin, C.T. (1998) Effects of electromagnetic fields in experimental fracture repair. *Clinical Orthopedic Related Research* **355S** S90-S104
- [155] Owan, M. and Triffitt, J.T. (1976) Extravascular albumin in bone tissue. *Journal of Physiology* **257** 293-307
- [156] Owan, I., Burr, D.B., et.al. (1997) Mechanotransduction in bone:osteoblasts are more responsive to fluid forces than mechanical strain. *American Physiological Society* **273** C810-15

- [157] Parfitt, A.M. (1994) Osteonal and hemi-osteonal remodeling: the spatial and temporal framework for signal traffic in adult human bone. *Journal of Cell Biochemistry* **55** 273-286
- [158] Petrov, A.G. and Usherwood, P.N. (1994) Mechanosensitivity of cell membranes. Ion channels, lipid matrix and cytoskeleton. *European Biophysics* **23** 1-19
- [159] Piekarski, K. and Munro, M. (1977) Transport mechanism operating between blood supply and osteocytes in long bones. *Nature* **269 (5623)** 80-82
- [160] Pitsillides, A.A., Rawlinson, S.C.F., et.al. (1995) Mechanical strain-induced NO production by bone cells: a possible role in adaptive bone (re)modeling? *FASEB Journal* **9** 1614-22
- [161] Pollack, S.R., Petrov, N., et al. (1984) An anatomical model for streaming potentials in osteons. *Journal of Biomechanics* **17** 627-636
- [162] Ravelsloot, J.H., van Houten, R.J., Ypey, D.L., et al. (1991) High-conductance anion channels in embryonic chick osteogenic cells. *Journal of Bone and Mineral Research* **6** 355-363
- [163] Reich, K.M., Gay, C.V., Frangos, J.A. (1990) Fluid shear stress as a mediator of osteoblast cyclic adenosine monophosphate production. *Journal of Cellular Physiology* **143**, 100-104
- [164] Richardson, A. and Parsons, J.T. (1995) Signal transduction through integrins: A central role for focal adhesion. *Bioessays* **17** 229-236
- [165] Rodan, G. (1992) Introduction to bone biology. *Bone* **13** S3-S6
- [166] Rodriquez, A.A., Agre, J.C., et al.(1993) Acoustic myography compared to electromyography during isometric fatigue and recovery. *Muscle and Nerve* **16** 188-192
- [167] Rubin, C.T. and Lanyon, L.E. (1984) Regulation of bone formation by applied dynamic loads. *Journal of Bone and Joint Surgery* **66A** 397-415
- [168] Rubin, C. T. and Lanyon, L.E. (1987) Osteoregulatory nature of mechanical stimuli: function as a determinant for adaptive bone remodeling. *Journal of Orthopedic Research* **5** 300-310
- [169] Rubin, C.T., Donahue ,H.J., et al. (1993) Optimization of electric field parameters for the control of bone remodeling: exploitation of an indigenous mechanism for the prevention of osteopenia. *Journal of Bone and Mineral Research* **8 (Suppl.2)** S573-S581
- [170] Rubinacci, A., Villa, I., et al. (1998) Osteocyte-bone lining cell system at the origin of steady ionic current in damaged amphibian bone. *Calcified Tissue International* **63** 331-339
- [171] Sachs, F. (1986) Biophysics of mechanoreception. *Membrane Biochemistry* **6** 173-195
- [172] Sachs, F. (1988) Mechanical transduction in biological systems. *CRC Review of Biomedical Engineering* **16** 141-169
- [173] Sackin, H. (1995) Mechanosensitive channels. *Annual Review of Physiology* **57** 333-353
- [174] Sauren, Y.M.H.F., Mieremet, R.H.P., Groot, C.G. and Scherft, J.P. (1992) An electron microscopic study on the presence of proteoglycans on the mineralized matrix of rat and human compact lamellar bone. *The Anatomical Record* **232** 36-44
- [175] Sadoshima, J., Takahashi, T., et al. (1992) Roles of mechano-sensitive ion channels, cytoskeleton and contractile activity in stretch-induced immediate-early gene expression and hypertrophy of cardiac myocytes. *Proceedings of the National Academy of Science* **89** 9905-9909

- [176] Salter, D.M., Robb, J.E. and Wright, M.O. (1997) Electrophysiological responses of human bone cells to mechanical stimulation: evidence for specific integrin function in mechanotransduction. *Journal of Bone and Mineral Research* **12** 1133-1141
- [177] Salzstein, R.A., Pollack, S.R., et al. (1987) Electromechanical potentials in cortical bone-I. A continuum approach. *Journal of Biomechanics* **20** 261-270
- [178] Salzstein, R.A. and Pollack, S.R. (1987) Electromechanical potentials in cortical bone-II. Experimental analysis. *Journal of Biomechanics* **20** 271-280
- [179] Sasaki, N. and Odajima, S. (1996) Elongation mechanism of collagen fibrils and force-strain relations of tendon at each level of structural hierarchy. *Journal of Biomechanics* **29** 1131-1136
- [180] Scott, G.C. and Korostoff, E. (1990) Oscillatory and step response electromechanical phenomena in human and bovine bone. *Journal of Biomechanics* **23** 127-143
- [181] Schaul, N. (1998) The fundamental neural mechanisms of electroencephalography. *Electroencephalography and clinical neurophysiology* **106** 101-107
- [182] Schirmmacher, K., Schmitz, I., et al. (1992) Characterization of gap junctions between osteoblast-like cells in culture. *Calcified Tissue International* **51** 285-290
- [183] Schirmmacher, K., Brummer, F., et al. (1993) Dye and electric coupling between osteoblasts-like cells in culture. *Calcified Tissue International* **53** 53-60
- [184] Shafik, A. (1998) Electro-oophorogram: a preliminary study of the electrical activity of the ovary. *Gyneol Obstet Invest* **46** 105-110
- [185] Shapiro, F., Cahill, C., et al. (1995) Transmission electron microscopic demonstration of vimentin in rat osteoblast and osteocytic cell bodies and processes using the immunogold technique. *Anatomical Record* **241** 39-48
- [186] Shyy, J.Y. and Chien, S. (1997) Role of integrins in cellular responses to mechanical stress and adhesion. *Current Opinion in Cell Biology* **9** 707-713
- [187] Spray, D.C. (1994) Physiological and pharmacological regulation of gap junction channels. *Molecular Mechanisms of Epithelial Cell Junctions: From Development to Disease*. Editor S. Chi 195-215. RG Landes, Austin
- [188] Spray, D.C. (1998) Gap junction proteins; where do they live and how do they die? *Circulation Research* **83** 679-681
- [189] Tanaka-Kamioka, K. Kamioka, H. Ris, H. and Lim, S.S. (1998) Osteocyte shape is dependent on actin filaments and osteocyte processes are unique actin-rich projections. *Journal of Bone and Mineral Research* **13(10)** 1555-1568
- [190] Tanaka, T. and Sakano, A. (1985) Differences in permeability of microperoxidase and horseradish peroxidase into alveolar bone of developing rats. *Journal of Dental Research* **64** 870-876
- [191] Uthoff, H.K. and Jaworski, Z.F.G. (1978) Bone loss in response to long term immobilization. *Journal of Bone and Joint Surgery* **60B** 420-429
- [192] Uitto, V.J. (1991) Extracellular matrix molecules and their receptors: an overview with special emphasis on periodontal tissues. *Crit Review of Oral Biological Medicine* **2** 323-354
- [193] Wang, L., Fritton, S.P., et al. (1999) Fluid pressure relaxation depends upon osteonal microstructure: modeling of an oscillatory bending experiment. *Journal of Biomechanics* **32** 663-672

- [194] Wang, N., Butler, J.P., Ingber, D.E. (1993) Mechanotransduction across the cell surface and through the cytoskeleton. *Science* **260** 1124-1127
- [195] Wang, Z.L. and Kang, Z.C. (1998) *Functional and Smart Materials* Plenum Press, New York
- [196] Wasserman, P.D. (1989) *Neural Computation. Theory and Practice* van Nostrand Reinhold, New York
- [197] Watanabe, H., Miake, K., Sasaki, J. (1993) Immunohistochemical study of the cytoskeleton of osteoblasts in the rat calvaria. *Acta anatomica* **147** 14-23
- [198] Weinbaum, S., Cowin, S.C., Zeng, Y. (1991) A model for the fluid shear stress excitation of membrane ion channels in osteocytic processes due to bone strain. *Advances in Bioengineering. Editor R. Vanderby, Jr.* 317-320. American Society of Mechanical Engineers, New York
- [199] Weinbaum, S., Cowin, S.C., Zeng, Y. (1994) Excitation of osteocytes by mechanical loading-induced bone fluid shear stresses. *Journal of Biomechanics* **27** 339-360
- [200] Weinger, J.M. and Holtrop, M.E. (1974) An Ultrastructural study of bone cells: the occurrence of microtubules, microfilaments and tight junctions. *Calcified Tissue Research* **14** 15-29
- [201] Wildron, D.C., Thain, J.F., et al. (1992) Electrical signaling and systematic proteinase inhibitor induction in the wounded plant. *Nature* **360** 62-65
- [202] Williams, J.L., Iannotti, J.P., Ham, A., Bleuit, J., and Chen, J.H. (1994) Effects of fluid shear stress on bone cells. *Biorheology* **31** 163-170
- [203] Wilson, D.A., Sullivan, R.M. (1998) Peripheral mechanisms of smell *The Scientific Basis of Eating. Editor R.W.A. Linden* **9** 29-39. Karger, Basel
- [204] Wolff, J. (1870) Uber der innere Architektur der Knochen und ihre Bedeutung fur die Frage vom Knochenwachstum. em Arch. path. Anat. Physio. Med., Virchovs Arch **50** 389-453
- [205] Wolff, J. (1892) em Das Gesetz der Transformation der Knochen Hirschwald, Berlin
- [206] Wolff, J. (1986) *The Law of Bone Remodelling* Springer, Berlin
- [207] Wriggers, W., Milligan, R.A., Schuller, K. et al. (1998) Self-organized neural networks bridge the biomolecular gap. *Journal of Molecular Biology* **284** 1247-54
- [208] Yanagishita, M. (1993) Function of proteoglycans in the extracellular matrix. em Acta Path Jap **4** 283-293
- [209] You, L., Cowin, S.C., Schaffler, M. and Weinbaum, S. (2001) A model for strain amplification in the actin cytoskeleton of osteocytes due to fluid drag on pericellular matrix. em Journal of Biomechanics **34** 1375-1386
- [210] You, L., Weinbaum, S., Cowin, S.C., and Schaffler, M.B. (2004) Ultrastructure of the osteocyte process. *Anal. Rec.* in preparation
- [211] Zeng, Y., Cowin, S.C., Weinbaum, S. (1994) A fiber matrix model for fluid flow and streaming potentials in the canaliculi of an osteon. *Annals of Biomedical Engineering* **22** 280-292
- [212] Zhang, D., Cowin, S.C., and Weinbaum, S. (1997) Electrical signal transmission and gap junction regulation in bone cell network: a cable model for an osteon. *Annals of Biomedical Engineering* **25** 357-374
- [213] Zhang, D., Cowin, S.C., and Weinbaum, S. (1998a) Electrical signal transmission in a bone cell network: The influence of a discrete gap junction. *Annals of Biomedical Engineering* . **26** 644-659

- [214] Zhang, D., Weinbaum, S and Cowin, S.C. (1998b) On the Calculation of Bone Pore Water Pressure due to Mechanical Loading. *International Journal of Solids and Structures* **35** 4981-4997
- [215] Zhang, D., Weinbaum, S and Cowin, S.C. (1998c) Estimates of the peak pressures in the bone pore water. em *Journal of Biomechanical Engineering* **120** 697-703
- [216] Zorntzer, S.F., Davis, J., Lau, C. (1990) em *An Introduction to Neural and Electronic Networks* Academic Press, San Diego
- [217] Zuker, C.S., Ranganathan, R. (1999) The path to specificity. *Science* **283** 650-651

REPRESENTATIVE MICROSTRUCTURE FINITE ELEMENTS FOR COLLAGEN GELS

Preethi L. Chandran

*Department of Biomedical Engineering
University of Minnesota, Twin Cities, Minnesota, USA*

Victor H. Barocas

*Department of Biomedical Engineering
University of Minnesota, Twin Cities, Minnesota, USA*

baroc001@umn.edu

Abstract We present a method for simulation of collagen gels and more generally for materials comprised of a fibrillar network. The method solves a representative microstructural problem on each finite element in lieu of a constitutive equation. The method captures key features of microstructural rearrangement while maintaining the ability to perform simulations on the (large) functional length scale.

Keywords: Fiber, Network, Multi-scale Model

Introduction

Hierarchical materials - those that function on the macroscopic scale but contain a microscopic substructure - present particular modeling challenges because of the large difference between the functional and structural length scales. Macroscopic models are necessary to predict function, but purely macroscopic models cannot fully account for structural-level behavior. Models that account explicitly for the structural level rapidly become intractable on the functional scale because of the large number of components. Hierarchical materials are well studied, leading to poroelasticity theory, mixture theory, and volume averaging theory. All of the treatments consider phase variation in a smoothed way, with the fraction and phase properties of each phase treated as continuous on the functional scale even though the phases are discrete on the structural scale. The resulting equations, in terms of stresses or free energies,

Jacques M. Huyghe et al. (eds), IUTAM Proceedings on Physicochemical and Electromechanical Interactions in Porous Media, 37–42.

© 2005 Springer. Printed in the Netherlands.

require constitutive relations for each phase and for interphase coupling. Homogenization theory is an important technique to convert from the microscopic to macroscopic scale. In homogenization theory, a representative piece (the "repeat unit") of the microstructure is subjected to test strains. By rigorously solving for the force/stress in the repeat unit, a constitutive law is developed for the macroscopic level. Homogenization theory has been used for many biomedical problems, and it has proven to be an invaluable tool. Homogenization formulations exist for cases in which the primary mechanism of load transfer is between fiber and continuum (as in fiber-reinforced composites), or when the microstructure is relatively unchanged by the deformations of interest (as in bone). When the dominant interaction is fiber-fiber and the fiber matrix rearranges as the material deforms, however, there is no repeat unit or explicit equation for the stress response, rendering the homogenization formulation, in current form, insufficient.

Collagen fibers form the structural basis of many tissues, including skin, artery, and articular cartilage. Also important are tissue equivalents (TEs), first produced by trapping fibroblasts in a type I collagen lattice [1]. TEs are used to provide an *in vitro* model of the *in vivo* environment. Recently, TEs have emerged as precursors for artificial tissues [2]. TEs are biocompatible and highly cellularized, but their use as tissue replacements is limited by strength considerations.

Early investigators (e.g., [3]) devised continuum constitutive equations describing fibrillar tissues, providing the foundation for later research. Most theoretical treatments of articular cartilage (e.g., [4]) account for many important features such as interstitial flow, nonlinear elasticity, and osmotic pressure. The behavior of the underlying collagen network is lumped by a macroscopic constitutive law. This approach restricted the applicability to the range of deformations studied experimentally. There is no good mechanism to relate network properties (collagen fibril density and orientation) with macroscopic tissue behavior or to incorporate collagen fibril damage.

Some researchers have used approximate microscopic descriptions to develop more rigorous macroscopic constitutive laws. A microstructural model of AC [5] linked the directionality of mechanical stiffness of cartilage to the orientation of its microstructure. The biphasic composite model of [6] uses an isotropic fiber network described by a simple linear-elastic equation. A homogenization method based on a unit cell containing a single fiber and a surrounding matrix was used to predict the variations in AC properties with fiber orientation and fiber-matrix adhesion. A recent model of heart valve mechanics [8] accounts for fiber orientation and predicts a wide range of behavior but does not account for fiber-fiber interactions.

Representative Microstructure Finite Elements

Our approach [9], which we refer to as Representative Microstructure Finite Elements (RMFE), probes both the structural and the functional length scales of the material. The method is a variant on standard finite elements in that the constitutive equation is replaced with a representative microstructural problem based on the local microstructure within each element (cf. [10]). In the following paragraphs, we summarize the major features and recent improvements in our method and then demonstrate it on a test problem.

We consider a macroscopic model of a two-dimensional, hyperelastic network, incorporating the microstructural details in a systematic manner. The model equations at equilibrium reduce to stress continuity,

$$\nabla \cdot \boldsymbol{\sigma} = 0 \quad (1)$$

where the stress $\boldsymbol{\sigma}$ is a function only of the displacement \mathbf{u} . To obtain the weak formulation of Eq. 1 we multiply it by a test function \mathbf{w} and integrate the equation by parts over the domain Ω .

$$\int_{\Omega} \mathbf{w} \cdot (\nabla \cdot \boldsymbol{\sigma}) dV = \int_{\delta\Omega} \mathbf{w} \cdot (\mathbf{n} \cdot \boldsymbol{\sigma}) dA - \int_{\Omega} (\nabla \mathbf{w} : \boldsymbol{\sigma}) dV = 0 \quad (2)$$

where \mathbf{n} is the outward normal to the boundary $\delta\Omega$. At this point, the finite element method is implemented by restricting \mathbf{w} to a finite-dimensional subspace of the vector function space. Boundary conditions are introduced in the standard finite-element manner.

The Microscopic-Scale Problem

A representative microscopic network is introduced within each finite element allowing macroscopic strain to be transferred to the network boundaries. The representative network is designed to capture the essential features of the collagen mesh in a tissue equivalent - interconnectivity and fiber nonlinearity. The network within each finite element is chosen so as to be the smallest representative unit of the microstructure within the material space of the element. The fibers in each element are assumed to be independent of those in other elements. The macroscopic spatial variations are captured by the element-to-element variations in the network. The representative network is generated randomly and has these features:

- Each intersection of collagen fiber segments is assumed to be a crosslink.
- Each segment of a collagen fiber between nodes is free to move independently of other segments but may not move through crosslinks.
- All segments have the same diameter and material properties.

- Fiber segments are nonlinear, exhibiting an exponential constitutive equation that makes them much stiffer in tension than in compression.

Having constructed the microscopic mesh, we specify the microscopic problem based on the macroscopic nodal displacements. The displacements of the elemental boundaries are given by the macroscopic solution (although the internal microscopic scale displacements are not necessarily affine). The microscopic problem is to find node positions and segment lengths such that the boundary nodes are as specified by the macroscopic displacements and the internal nodes experience no net force. The boundary nodes have displacement specified and are subjected to a non-zero net force. The next step in the solution process is to convert those forces into the macroscopic stress tensor.

Stress Averaging

In our current model, the stress is assumed to be constant over the element (i.e., the stress is treated as piecewise constant on the macroscopic scale). We therefore assign the macroscopic stress a value equal to the spatial average of the microscopic stress:

$$\sigma = \frac{1}{A} \int_A \sigma^* dA, \quad (3)$$

where σ is the macroscopic stress, A is the area of the representative microstructural network, and σ^* is the stress in the microstructural network. The micro-scale stress σ^* is difficult to work with explicitly because it is zero in non-fiber regions and is different on each fiber segment. We therefore introduce a factor of ∇x (which is trivially equal to the identity because it is the gradient of a vector with respect to itself), integrate by parts, and apply the divergence theorem (cf. [11]):

$$\int_A \sigma^* \cdot (\nabla \mathbf{x}) dA = \int_A \nabla \cdot (\sigma^* \mathbf{x}) dA - \int_A \mathbf{x} (\nabla \cdot \sigma^*) dA \quad (4)$$

$$= \int_{\delta A} \mathbf{n} \cdot (\sigma^* \mathbf{x}) ds - \int_A \mathbf{x} (\nabla \cdot \sigma^*) dA \quad (5)$$

where \mathbf{n} is the unit normal to the boundary δA . The second term on the RHS is zero because the microscale network is at mechanical equilibrium, so

$$\sigma = \frac{1}{A} \int_{\delta A} \mathbf{n} \cdot (\sigma^* \mathbf{x}) ds = \frac{1}{A} \sum_{\delta A} \mathbf{f} \mathbf{x}, \quad (7)$$

where \mathbf{f} is the force exerted on the boundary by a fiber segment attached thereto at position \mathbf{x} . Summing over the entire boundary and dividing by the area gives the macroscopic stress from the force and position data.

Test Problem

To explore the effect of structural changes on mechanical function, we simulated a sample (Figure 1, crudely representing a damaged or scarred tissue) that was homogeneously aligned horizontally except for the central five elements, which were isotropic. Figure 1 also shows the calculated deformation of the sample for 25% stretch. Although the isotropic region contains the same collagen density (by total segment length), it undergoes a 5% greater area change than the surrounding tissue. In addition, the total force required for 25% stretch was approximately 5% lower for the case for the "damaged" than for an "undamaged" sample in which the internal elements were aligned.

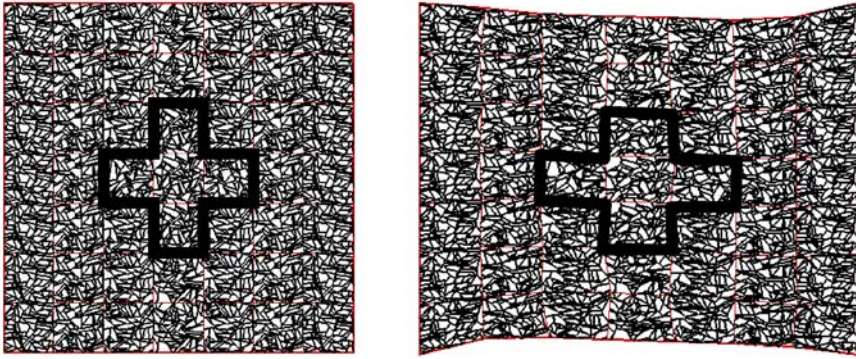


Figure 1. Uniaxial Extension of a Non-Homogeneous Sample. The figure shows simulation results for uniaxial extension of an initially (a) square sample whose orientation is primarily left-to-right, except for the central cross-shaped region, which is isotropic. After 25% stretching (b), the cross-shaped region is deformed more than the surrounding tissue, with roughly a 5% greater increase in area.

Discussion

We have presented a multi-scale method to simulate a fibrillar structure such as a collagen tissue equivalent. The method is able to predict macroscopic behavior based on microscopic properties, and it also demonstrates the microscopic restructuring that can occur during deformation. Although the method is computationally demanding, the potential for parallelization is high, and three-dimensional problems should not be out of reach.

An important issue, particularly in light of the symposium goals, is that of interstitial flow. The RMFE framework should be compatible with a biphasic

or mixture-theory approach, in which interstitial flow could be accounted for by the addition of a Darcy-like term. The question of whether the effect is best incorporated at the microscopic scale (drag on individual fibrils) or the macroscopic level (an extra term in the stress balance) is still open.

Acknowledgments

This work was supported primarily by the MRSEC Program of the National Science Foundation under Award Number DMR-0212302. A supercomputing resource grant from the University of Minnesota Supercomputing Institute for Digital Simulation and Advanced Computation is gratefully acknowledged.

References

- [1] Bell, E., Ivarsson, B. and Merrill, C. (1979) Production of a tissue-like structure by contraction of collagen lattices by human fibroblasts of different proliferative potential in vivo. *Proceedings of the National Academy of Sciences of the USA* **76**, 1274-1278
- [2] Lopez Valle, C.A., Auger, F.A., Rompre, P.A., Bouvard, V. and Germain L. (1992) Peripheral anchorage of dermal equivalents. *British Journal of Dermatology* **127**, 365-371
- [3] Lanir, Y.(1982) Constitutive equations for fibrous connective tissues. *Journal of Biomechanics* **18**, 1-12
- [4] Lai, W.M., Hou, J.S. and Mow, V.C. (1991) A triphasic theory for the swelling and deformation behaviors of articular cartilage. *Journal of Biomechanical Engineering* **113**, 245-258
- [5] Farquhar, T., Dawson, P.R. and Torzilli, P.A. (1990) A microstructural model for the anisotropic drained stiffness of articular cartilage. *Journal of Biomechanical Engineering* **112**, 414-425
- [6] Soulhat, J., Buschmann, M.D. and Shirazi-Adl, A. (1999) A fibril-network-reinforced model biphasic model of cartilage in unconfined compression. *Journal of Biomechanical Engineering* **121**, 340-347
- [7] Schwartz, M.H., Leo, P.H. and Lewis J.L. (1994) A microstructural model for the elastic response of articular cartilage. *Journal of Biomechanics* **27**, 865-873
- [8] Billiar, K.L., and Sacks, M.S. (2000) Biaxial mechanical properties of native and glutaraldehyde-treated aortic valve cusp: Part II - A structural constitutive model. *Journal of Biomechanical Engineering* **122**, 327-335
- [9] Agoram, B., and Barocas, V.H. (2001) Coupled macroscopic and microscopic scale modeling of fibrillar tissues and tissue equivalents. *Journal of Biomechanical Engineering* **123**, 362-369
- [10] Bruels, R.G.M., Sengers, B.G., Oomens, C.W.J., Bouten, C.V.C. and Baaijens, F.P.T. (2002) Predicting local cell deformations in engineered tissue constructs: a multilevel finite element approach. *Journal of Biomechanical Engineering* **124**, 198-206
- [11] Nemet-Nasser, S., and Hori, M. (1993) *Micromechanics: Overall Properties of Heterogeneous Materials*, Elsevier

II

COUPLING AND WAVES.

Chairman: C. Klein

VISCOUS EFFECTS IN PARTICULATES

J. Carlos Santamarina

Georgia Institute of Technology

Julio R. Valdes

San Diego State University

Angelica M. Palomino

Georgia Institute of Technology

Jose Alvarellos

Georgia Institute of Technology, and INTEVEP

carlos.santamarina@ce.gatech.edu

Abstract Particulate materials are inherently multiphase. The solid phase includes the load-carrying granular skeleton and mobile particles. The fluid that fills the pores may be polar or non-polar, Newtonian or Maxwellian, and either single-phase or the mixture of non-miscible fluids. Fluids and viscous drag forces lead to unique phenomena in particulate materials, including the displacement of mobile particles and formation clogging, particle migration in asymmetric AC-electric fields, non unique contact angles, and the relative motion of non-miscible permeating fluids.

Keywords: clogging, contact angle, particle drift, fluid drift

Introduction: Phenomena

Particulate materials are inherently porous, pervious, non-linear and non-elastic. Interparticle forces determine the mechanical properties of the granular skeleton, including its strength, stiffness and volume change. The pore space is filled with a single fluid or mixed fluids. The presence of fluids alters interparticle forces, sustains various energy coupling mechanisms, changes all forms of conduction and diffusion properties, and gives rise to various linear and non-linear phenomena. Table 1 lists some of these processes.

Jacques M. Huyghe et al. (eds), IUTAM Proceedings on Physicochemical and Electromechanical Interactions in Porous Media, 45–51.

© 2005 Springer. Printed in the Netherlands.

Table 1. Some fluid-related effects in particulate media

Hydrostatic (single-phase fluid)	Archimedes buoyancy. Effective stress - established at the boundary. Alters interparticle electrical forces (repulsion, van der Waals attraction, hydration).
Constant hydraulic gradient (single-phase fluid)	Hagen-Poiseuille leading to Kozeny-Carman fluid flow. Effective stress gradient due to viscous drag: volume and strength changes. Coupled gradients: chemical, thermal, electrical. Particle alignment. Fines migration. Relates to clogging, non-linear flow, sand production.
AC hydraulic gradient (single-phase fluid)	Particle alignment (relaxation) and fabric formation control. Seismoelectric. In electrolytes: relative size and charge of cations and anions in pore fluid. In porous medium (even if water is de-ionized): particle size, surface charge, counterions size and charge. Pressure diffusion. Liquefaction - fluidization. Terzaghi-Biot effects including slow P-wave. Frequency dependency of viscous forces. Resonance and relaxation. Dispersion-attenuation. Even at small strains, the presence of fluids increases attenuation more than 10 times, both in single and mixed fluid phase.(Kramers-Kroning). Strain-rate effects on strength and stiffness.
Asymmetric AC (DC=0) Non-linear	Fluid displacement (single and multiphase). Preventing fingering and percolation in multiphase flow. Mixed Fluid-phase. Young's contact angle. Fluid pressure: Laplace and Kelvin. Capillary interparticle forces affect strength, stiffness and volume change (shrinkage). Changes in conduction and diffusion - Percolation and scaling. Residual saturation. Mixed fluids exhibit Maxwellian behavior. Viscous effects triggered by other gradients - Energy coupling.
DC:electro-osmosis. AC:electro-seismic.	Particle alignment. Asymmetric AC-field and particle drift. Chemo-osmosis. Thermal consolidation - Desiccation shrinkage. DC: electro-osmosis. AC: electro-seismic.

The purpose of this paper is to report on three fluid-related phenomena in particulate materials: fines migration and formation clogging, particle drift in AC-electric fields, and mixed fluid conditions. Processes are analyzed at the microscale.

Table 2. Important relations related to fluid flow in granular media

$Re = \frac{\rho_a dV}{\eta}$	Reynold's number. Ratio between inertial and viscous forces
$F_{drag} = 3\pi d\eta V$	Stoke's viscous drag on spherical particle (diameter d , fluid velocity V). Applies to $Re < 1$
$F_{drag} = 8\pi L\eta V$	Poiseuille's drag against cylindrical tube (diameter d , fluid velocity V , Turbulence $Re > 2000$)
$u = \frac{\epsilon_0 \epsilon_r \zeta}{\eta} B$	Smoluchowski's electrophoretic particle velocity u in an electric field E as a function of the zeta potential.
$\Delta.U = Tc\left(\frac{1}{r_1} + \frac{1}{r_2}\right)$ $= -\frac{\rho_a RT}{M} \ln \frac{P}{P_0}$	Laplace-Kelvin equation. Difference in fluid pressure $\Delta.U$ across two-fluid interface. Related to surface tension Tc and the curvature radii r_1 and r_2
$\cos\theta = \frac{h_c \rho_a E}{4T_c} c$	Contact angle related to capillary rise h_c

Parameters and Equations

Salient mathematical expressions related to fluid flow are summarized in Table 2. The terminal sedimentation velocity is reached when the buoyant weight balances Stokes' viscous drag. Likewise, the Kozeny-Carman expression for flow rate in a pervious medium reflects the balance between the driving force and Poiseuille's drag. Viscous drag converts a hydraulic gradient into an effective stress gradient in the granular skeleton.

The fluid phase that fills the voids between particles can be multiphase, such as oil-and-water or water-and-air. Molecules at the interface between the two fluids experience asymmetric time-average van der Waals forces. This results in a curved interface that tends to decrease in surface area of the interface. The pressure difference between the two fluids $\Delta\mu = u_1 - u_2$ depends on the curvature of the interface characterized by radii r_1 and r_2 , and the surface tension, T_S (Table 2). In fluid-air interfaces, the vapor pressure is affected by the curvature of the air-water interface as expressed in Kelvin's equation. Curvature affects solubility in liquid-liquid interfaces. Unique force equilibrium conditions also develop near the tripartite point where the interface between the two fluids approaches the solid surface of a particle. The resulting contact angle θ captures this interaction.

Flow and Fines Migration – Clogging

The transport of mobile particles within the porous network is called fines migration and is governed by particle-level forces and geometrical constraints. In some cases, migrating fines are retained at pore throats, clog the porous network and produce a severe decrease in permeability. Fines migration and clogging are relevant in multiple fields ranging from biological filters to pet-

roleum recovery. Fines mobilization, retardation, and bridging cause radial clogging. Each of these mechanisms are briefly discussed next. For more details see Valdes [3].

Mobilization. Fluid drag can yield particle detachment and mobilization. Mobilization depends on the balance among participating particle-level forces (gravitational and electrical), the magnitudes of which are controlled by particle size, and electrochemical fluid characteristics.

Retardation. A mobilized particle inherently falls behind the moving fluid since the drag force experienced by the particle is proportional to the relative velocity. Hydrodynamic conditions around the tortuous geometry of the pore space, gravity, inertial effects, high flow velocity and collisions enhance retardation. Retardation increases the local concentration of particles near pore throats.

Bridging. Migratory particles can be retained at pore throats that are larger than the diameter of a single particle by forming bridges. However, bridge formation requires the simultaneous arrival of a sufficient number of particles. Therefore, retardation is required for bridging.

Radial Clogging. Radial flow towards a well (Figure 1), implies a radial velocity field that permits gravity retardation in the far field (particles tend to sediment), and causes inertial retardation in the near field (particles collide with pore walls). The interplay between these retardation mechanisms renders a non-homogeneous ring-like clogging pattern at a characteristic distance that depends on the interplay between the participating phenomena described above and the hydrodynamic regime.

Drift in Asymmetric AC-electric Field

Electrophoresis is the motion of charged particles relative to the electrolyte in response to an applied DC-electric field: the field causes a shift in the particle counterion cloud, the counterion-diminished end of the particle attracts other counterions from the bulk fluid, counterions from the displaced cloud diffuse out into the bulk fluid, and the particle migrates. The particle velocity is predicted by the Smoluchowski equation.

When a low frequency AC electric field is imposed, the particle oscillates around its mean position and platy particles may become optimally aligned with the field. At high frequencies, neither particle shift nor alignment takes place. However, translational movement of dispersed particles can be attained in an asymmetric AC field (without a DC component). The observed drift is attributed to the velocity-dependent viscous drag force in relation to double layer polarization as sketched in Figure 2; for reference, bacteria swim at 0.02-1 mm/s. For more details see Palomino [2]. The field frequency ω must be low enough such that ionic concentrations and hydrodynamic fields may adjust to

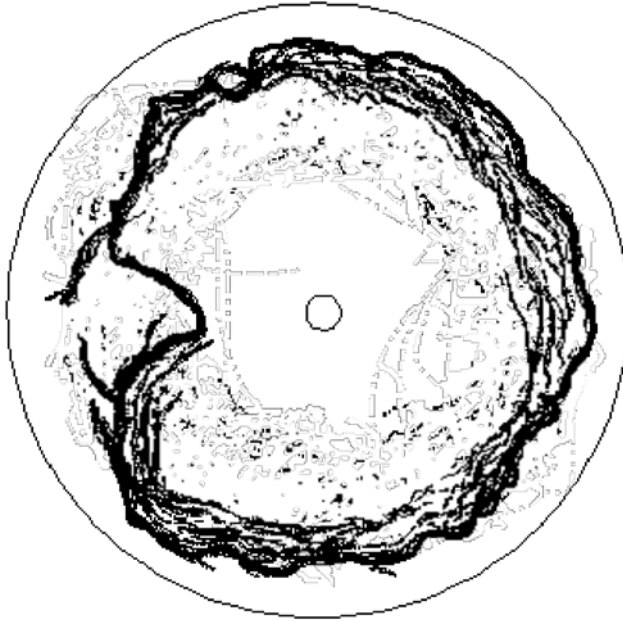


Figure 1. Clogging ring formation in experimental radial flow system

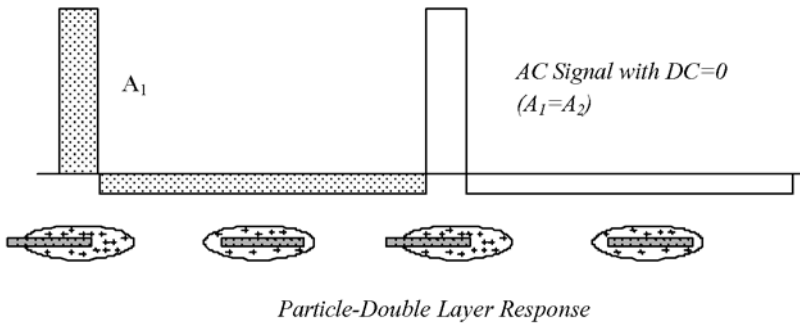


Figure 2. Particle drift in asymmetric AC field

changes in the electric field E . A beat function made of two superimposed harmonics with a phase shift may be conveniently used for these tests.

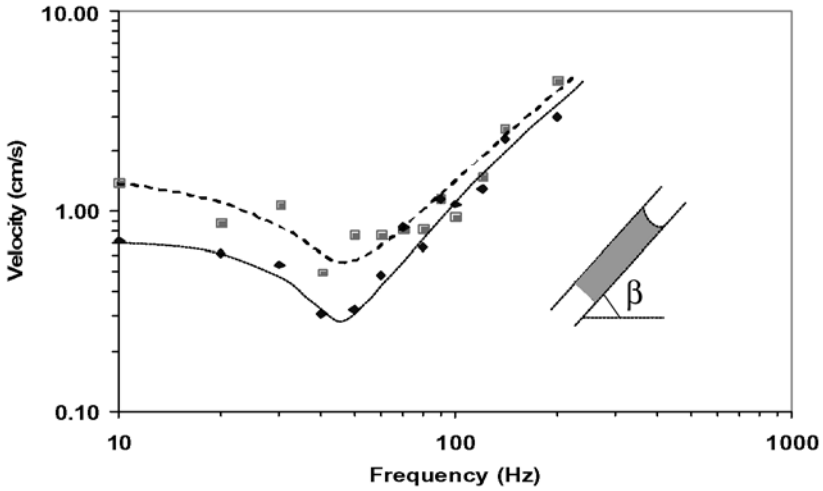


Figure 3. Liquid stability in a tilted capillary tube

Mixed Fluid Phase

Most fluids in engineering are Newtonian. However, fluids such as petroleum and blood are Maxwellian, that is, the stress tensor is not only a function of the strain rate but also a function of strain itself. The Maxwellian relaxation is the ratio between the fluid viscosity and stiffness.

Capillary forces in mixed fluid phase conditions are inversely proportional to the curvature of the interface. Therefore, menisci introduce elasticity to the mixed fluid, and mixtures of two Newtonian fluids exhibit global Maxwellian response. For more details see Alvarelos [1]. his behavior is experimentally demonstrated with a capillary tube partially filled with a water droplet. The tube is tilted at an angle β smaller than the critical angle that causes unstable displacement. Then, a harmonic excitation is applied to the tube in the axial direction. For each frequency, the amplitude of the vibration is increased until the water droplet becomes unstable and flows in the capillary. Data in Figure 3 show a minimum required tube velocity between 40 and 50 Hz. This behavior indicates resonance of the visco-elastic system. The ratio of the relaxation time and characteristic time for pure viscous effect is larger than 11.64.

Acknowledgments

NSF, Petro. Venezuela, Goizueta Foundation.

References

- [1] Alvarellos, J. (2003) Fundamental Study of Capillary Phenomena in Porous Media. Ph.D. Dissertation, Georgia Tech, Atlanta, Georgia
- [2] Palomino, A.M. (2004) Electrokinetics and Particle Drift. Internal Report, Georgia Tech, Atlanta, Georgia
- [3] Valdes, J.R. (2002) Fines Migration and Formation Damage - Microscale Studies Ph.D. Dissertation, Georgia Tech, Atlanta, Georgia

PORE ROUGHNESS EFFECTS ON HIGH-FREQUENCY PERMEABILITY

David Smeulders and Andrea Cortis

Delft University of Technology, PO Box 5028, 2600 GA, Delft, The Netherlands

d.m.j.smeulders@ta.tudelft.nl

Jean Luc Guermond

LIMSI, UPR 3251 (CNRS), BP 133, 91403 Orsay, France

Denis Lafarge

LAUM, UMR 6613, Av. O. Messiaen, 72017, Le Mans, France

Abstract The high-frequency behaviour of the dynamic permeability is studied. In the case that the solid-fluid interface appears locally flat, we give a new derivation for the characteristic length Λ . In the case of wedge-shaped intrusions, the classical approach is modified by an additional higher-order term, which is depending on the apex angle of the wedge. Precise numerical simulations confirmed this dependency.

Keywords: Dynamic permeability, pore roughness, numerical simulations

Introduction

By definition, the dynamic permeability $k(\omega)$ describes the (linear) response of a simple incompressible fluid in a porous medium subjected to a harmonic pressure drop across the sample. This response has been widely studied before [2, 6, 10], and is involved in many problems and applications. As an example, the dynamic permeability is the fundamental ingredient to describe sound propagation in a fluid-saturated rigid-framed porous medium as long as the wavelength is large compared to the characteristic sizes of pores and grains in the medium. Relaxing the assumption of a rigid frame, the concept may be incorporated in the Biot theory.

Under the assumption that the fluid-solid interface appears locally flat if the viscous skin depth δ is small enough, Johnson et al. [6] obtained the high-

frequency result

$$k(\omega) = \frac{\varepsilon^2 \phi}{\alpha_\infty} (1 - C\varepsilon + \dots). \quad (1)$$

Here, $\varepsilon = \sqrt{\nu/i\omega} = (1 - i)\delta/2$ is the complex viscous skin depth parameter, and ϕ , α_∞ , and C are purely geometrical parameters, respectively the porosity, tortuosity, and $C = 2/\Lambda$, where Λ is a pore size parameter characterizing transport properties of the porous material [6].

We will first clarify the existing discrepancies between the result (1) and the expression by Sheng & Zhou [9]. Next, we will consider a rugged geometry in the form of two-dimensional pore channels with wedge-shaped intrusions (see Fig. 1), and we will show that the high-frequency result becomes

$$k(\omega) = \frac{\varepsilon^2 \phi}{\alpha_\infty} (1 - C\varepsilon - C_w \varepsilon^w + \dots), \quad (2)$$

where the exponent w ($1 < w < 2$) is related to the apex angle γ ($0 < \gamma < \pi$) of the wedges:

$$w = \frac{2\pi}{2\pi - \gamma}. \quad (3)$$

We found that (3) is different from an expression proposed by Achou & Avel-

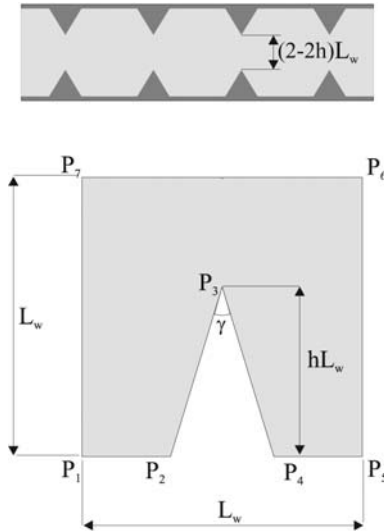


Figure 1. Geometry of the two-dimensional channel with intrusive wedges (top picture). The dimensions of the wedges are drawn at the bottom picture.

laneda [1]. A theoretical study and numerical simulations will show that (3) is the correct expression.

Conceptual Model

We define the scaled velocity field $\tilde{\mathbf{v}}$, which solves the following oscillating Stokes flow problem:

$$\varepsilon^{-2}\tilde{\mathbf{v}} = -\nabla\tilde{p} + \Delta\tilde{\mathbf{v}} + \mathbf{e}, \quad \nabla \cdot \tilde{\mathbf{v}} = 0, \quad (4)$$

where \mathbf{e} is the unit macroscopic pressure gradient. Moreover, we assume that $\tilde{\mathbf{v}} = 0$ on the pore surface S_p , and that \tilde{p} is compact, which means that the field has a constant pore averaged value, i.e., on the average it does not increase or decrease in the direction of \mathbf{e} . The dynamic permeability is, by definition, the direct pore volume average

$$k(\omega) = \frac{\phi}{V_p} \int_{V_p} \tilde{\mathbf{v}} \cdot \mathbf{e} dV. \quad (5)$$

Similarly, we define the scaled potential field \mathbf{E} which solves the potential problem

$$\mathbf{E} = -\nabla\Phi + \mathbf{e}, \quad \nabla \cdot \mathbf{E} = 0. \quad (6)$$

Here, $\mathbf{E} \cdot \mathbf{n} = 0$ on S_p (Neumann type boundary condition), where \mathbf{n} is the unit outward normal from the pore region, and Φ is compact. \mathbf{E} can be interpreted as the microscopic electric field induced in the pore space when a unit macroscopic field \mathbf{e} is applied, assuming insulating solid phase and uniform conductivity in the pore fluid. Its pore volume average is directly related to the tortuosity α_∞ :

$$\frac{1}{\alpha_\infty} = \frac{1}{V_p} \int_{V_p} \mathbf{E} \cdot \mathbf{e} dV. \quad (7)$$

Using integration by parts it is easily verified that for any compact field Φ there is the orthogonality relation

$$\int_{V_p} \mathbf{w} \cdot \nabla\Phi dV = 0, \quad (8)$$

for any divergence-free field \mathbf{w} having zero normal component on the pore surface. Thus, the dynamic permeability and tortuosity may be written in equivalent form:

$$k(\omega) = \frac{\phi}{V_p} \int_{V_p} \tilde{\mathbf{v}} \cdot \mathbf{E} dV, \quad (9)$$

$$\frac{1}{\alpha_\infty} = \frac{1}{V_p} \int_{V_p} E^2 dV. \quad (10)$$

We now consider the high-frequency limit $\varepsilon/L_w \rightarrow 0$ of the scaled field $\tilde{\mathbf{v}}$, where L_w is a characteristic pore size. As argued by [6], the fluid motion

is given by potential flow except for a boundary layer of thickness δ near the pore walls. To leading order, we have $\varepsilon^{-2}\tilde{\mathbf{v}} \rightarrow \mathbf{E}$ and $\tilde{p} \rightarrow \Phi$ in the bulk potential flow region. A more exact replacement would be $\varepsilon^{-2}\tilde{\mathbf{v}} \rightarrow \mathbf{E} - \nabla\Pi$ and $\tilde{p} \rightarrow \Phi + \Pi$, with Π being a small, $\mathcal{O}(\varepsilon)$, compact perturbation induced by the presence of the boundary layer. Assuming that the boundary layer is small enough so that the walls of the pores appear locally flat, the perturbation term may be determined by introducing in the analogous electric conductivity problem a layer of variable conductivity near the pore walls. The variable conductivity is chosen to generate for the current the known variations of the tangential components of the velocity field in the boundary layer. When the pore walls have a non-trivial shape, the divergence-free nature of the current naturally implies the existence of normal components near the pore walls that act as a source for the perturbed potential in the bulk. Following the assumption of locally plane pore walls, the tangential components of the velocity in the boundary layer may be written to leading order [7]

$$\varepsilon^{-2}\tilde{\mathbf{v}} = (1 - e^{-\beta/\varepsilon})\mathbf{E}, \quad (11)$$

where β is a local co-ordinate measured from the pore walls into the bulk of the pore. We thus consider the perturbed potential problem ($\nabla \cdot \tilde{\mathbf{v}} = 0$)

$$\varepsilon^{-2}\tilde{\mathbf{v}} = \sigma(\mathbf{r})(\mathbf{E} - \nabla\Pi). \quad (12)$$

The field $\varepsilon^{-2}\tilde{\mathbf{v}}$ is the current induced when a unit electric field is applied for a medium having insulating solid phase and conductivity $\sigma(\mathbf{r}) = 1 - \exp(-\beta/\varepsilon)$ in the pore region. Current conservation yields:

$$\nabla \cdot (\sigma\nabla\Pi) = \mathbf{E} \cdot \nabla\sigma. \quad (13)$$

In the limit $\varepsilon/L_w \rightarrow 0$, only derivatives normal to the pore walls need to be considered. Straightforward integration yields the following velocity pattern in the boundary layer:

$$\varepsilon^{-2}\tilde{\mathbf{v}} = (1 - e^{-\beta/\varepsilon})\mathbf{E} + \varepsilon\mathbf{n}[1 - (1 + \beta/\varepsilon)e^{-\beta/\varepsilon}] \left(\frac{\partial E_\beta}{\partial \beta} \right)_{\beta=0}. \quad (14)$$

Setting $\beta/\delta \rightarrow \infty$ in (14) and (12), we derive the boundary condition $\partial\Pi/\partial\beta = \varepsilon(\partial E_\beta/\partial\beta)_{\beta=0}$. The velocity field hence determined in the bulk is (Cortis et al. 2003):

$$\varepsilon^{-2}\tilde{\mathbf{v}} = \mathbf{E} + \varepsilon\mathbf{N}, \quad (15)$$

where the perturbation field \mathbf{N} is a purely geometrical vector field, accounting for the presence tangential components in the boundary layer. Now evaluating the integral (5), the first term $\varepsilon^2\phi/\alpha_\infty$ in (1) stems from the leading bulk term

\mathbf{E} in (15) and the constant boundary layer tangential term \mathbf{E} in (14). The second term $(\varepsilon^2\phi/\alpha_\infty)C\varepsilon$ stems from two contributions leading to the new result:

$$\frac{2}{\Lambda} = \frac{\int_{S_p} \mathbf{E} \cdot \mathbf{e} dS}{\int_{V_p} E^2 dV} - \frac{\int_{S_p} \Phi(\partial E_\beta/\partial\beta) dS}{\int_{V_p} E^2 dV}. \quad (16)$$

The first is a boundary layer contribution related to the tangential components $-\exp(-\beta/\varepsilon)\mathbf{E}$ in (14). The second stems from the perturbation field $\varepsilon\mathbf{N}$ [4]. Sheng & Zhou [9] erroneously identified $2/\Lambda$ to be the first term on the right-hand-side of (16), because they used the incomplete replacement $\varepsilon^{-2}\tilde{\mathbf{v}} \rightarrow \mathbf{E}$. Note that in straight pore channels ($\mathbf{E} = \mathbf{e}$) the second contribution vanishes while the first reduces to the pore surface-to-volume ratio S_p/V_p . In general, both contributions are of the same order of magnitude. It can also be shown [4] that (16) can be rewritten as

$$\frac{2}{\Lambda} = \frac{\int_{S_p} E^2 dS}{\int_{V_p} E^2 dV}, \quad (17)$$

which is the classical relation obtained by [6]. A more compact way to derive (16), is to use (9) instead of (5). No bulk contribution arises because of the orthogonality (8) between \mathbf{E} and \mathbf{N} .

Corrugated Pore Channels

As argued by Achdou & Avellaneda [1], a two-dimensional reasoning is sufficient to study the singularity. The periodic geometry is depicted in Fig. 1. The wedge is defined by its apex angle γ . Introducing polar co-ordinates r, θ , we set the origin $r = 0$ on the tip of the wedge and count the angle θ from one side of the wedge. The singular potential field $\mathbf{E}(r, \theta)$ may be written [7]

$$E_r = Anr^{n-1} \cos n\theta \quad E_\theta = -Anr^{n-1} \sin n\theta, \quad (18)$$

where A is an amplitude factor and $\frac{1}{2} < n = \pi/(2\pi - \gamma) < 1$. The contribution of the wedges to the integral (9) may be evaluated noting that the velocity field $\tilde{\mathbf{v}}$ matches to leading order the value $\varepsilon^2\mathbf{E}$ on the bounding surface of the potential flow region. Thus, according to (18), the external potential fields \mathbf{E} and $\tilde{\mathbf{v}}$ must vary like ε^{n-1} and ε^{n+1} , respectively, when integrating in the boundary layer around the tip of a wedge. Simultaneously, the spatial extend of this boundary layer around the tip shrinks like ε^2 . It thus follows that the wedge contribution to (9) will be $\mathcal{O}(\varepsilon^2\varepsilon^{n+1}\varepsilon^{n-1}) = \mathcal{O}(\varepsilon^{2+2n})$, which yields the result (2), (3). Achdou & Avellaneda [1] used (5), which is perfectly justified as long as the integration is performed over the entire pore volume consisting of boundary layer and perturbed bulk flow. The former contribution is $\mathcal{O}(\varepsilon^2\varepsilon^{n+1}) = \mathcal{O}(\varepsilon^{n+3})$, and they obtain the relation $w = 1 + \pi/(2\pi - \gamma)$

between the exponent w in (2) and the apex angle γ . The perturbed bulk potential flow should also be taken into account, however, and it happens that it is now a dominant contribution.

Numerical Computations

Numerical computations of the fields $\tilde{\mathbf{v}}$ and \mathbf{E} were performed for the periodic geometry depicted in Fig. 1. The values for the apex angle γ and the wedge height h were varied. The Stokes problem was solved using the variational formulation of the problem and a N_1 Finite-Element code based on a Uzawa decomposition method. To ensure accuracy, we have used an iterative automatic method, i.e., the solution is computed on the N_1 mesh, next an a-posteriori estimate of the error is computed, and finally the mesh is locally refined accordingly by means of a Delaunay technique developed by Rebay [8]. Successful use of this refinement method on sharp-edged wedges was reported by Firdaouss et al. [5]. Once the flow field is known, the dynamic permeability is computed using (1). Coherent computations of the potential field \mathbf{E} and the parameters (7), (17) were obtained using either the Schwartz-Christoffel transformation technique [3], or the method by [5]. From (2) it follows that the real part of the dynamic permeability should satisfy in the high-frequency limit, $\text{Re}\{k(\omega)\}/\delta^3 = A + B_w\delta^{w-1}$, where the constant A is related to the formation factor α_∞/ϕ and inverse length C , and the constant B_w is related to w , C_w , and the formation factor. The values of A , B_w , and w can be obtained by comparison between the high-frequency numerical data for $\text{Re}\{k(\omega)\}/\delta^3$ and the above theoretical form.

As an example, we show in Fig. 2 the results obtained for the exponent w when the wedge angle γ varies between 0 and $\pi/2$. The wedge height h is set 0.5. In the singular limit of knife-edge intrusions ($\gamma = 0$), the value $w = 1$ indicates the merging of the different terms. For flat surfaces $\gamma = \pi$, the value $w = 2$ will be obtained. The computed data are relatively close to the theory, the Achdou & Avellaneda predictions being plotted for comparison. As compared to the situation in smooth pore channels, the effect of sharp wedges is to produce a much slower convergence of the high-frequency dynamic permeability with respect to the Johnson et al. [6] development (1). In these situations, the development (2) does a much better job.

Summary

Analyzing in detail the fluid velocity patterns in oscillating tube flow, we have provided a new derivation of the Johnson et al. high-frequency development [6] and a new expression of the characteristic length Λ . Two different contributions to the dynamic permeability are now apparent. One stems from the boundary layer; another stems from a perturbation potential flow in the

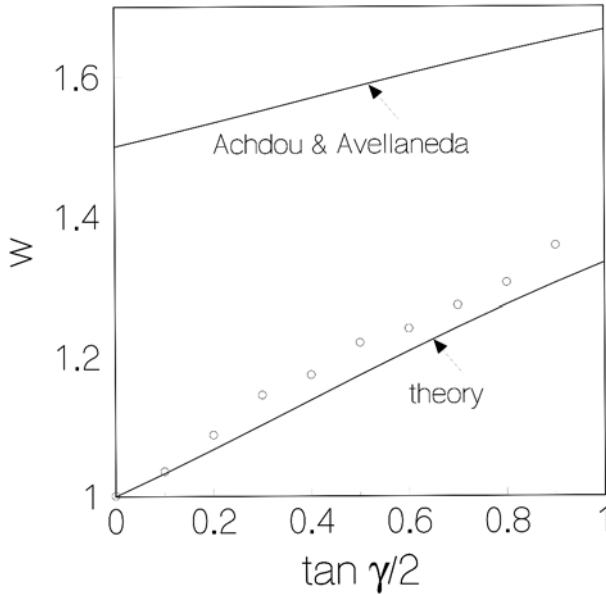


Figure 2. Dependence of the exponent w on the wedge apex angle γ for $h = 0.5$. The circles represent the numerical computations.

bulk, induced by the presence of the boundary layer. This understanding was applied to derive the correct form of the leading higher-order terms for sharp-edged geometries. Numerical computations substantiated this derivation.

References

- [1] Achdou, Y. and Avellaneda, M. (1992) Influence of pore roughness and poresize dispersion in estimating the permeability of a porous medium from electrical measurements, *Phys Fluids* **4** (12), 2561
- [2] Auriault, J.-L., Borne, L. and Chambon, R. (1985) Dynamics of porous saturated media, checking of the generalized law of Darcy, *J. Acous. Soc. Am.* **77**, 1641
- [3] Cortis, A. and Smeulders, D.M.J. (2001) On the viscous length scale of wedged shaped porous media, *Int. J. Engng Sci.* **235**, 307
- [4] Cortis, A., Smeulders, D.M.J., Guermont, J.-L. and Lafarge, D. (2003) Influence of pore roughness on high-frequency permeability, *Phys. Fluids* **15**, In press
- [5] Firdaouss, M., Guermont, J.-L. and Lafarge, D. (1998) Some remarks on the acoustic parameters of sharp edged porous media, *Int. J. Engng Sci.* **36**, 1035
- [6] Johnson, D.L., Koplik, J. and Dashen, R. (1987) Theory of dynamic permeability and tortuosity in fluidsaturated porous media, *J. Fluid Mech.* **176**, 379
- [7] Landau, L.D. and Lifschitz, E.M. (1959) *Fluid Mechanics*
- [8] Rebay, S. (1993) Efficient unstructured mesh generation by means of Delaunay triangulation and Bowyer-Watson algorithm, *J. Comp. Phys.* **106** (1), 125

- [9] Sheng, P. and Zhou, M. (1988) Dynamic permeability in porous media, *Phys. Rev. Lett.* **61** (14), 1591
- [10] Smeulders, D.M.J., Eggels, R.L.G.M and Van Dongen, M.E.H. (1992) Dynamic permeability: reformulation of theory and new experimental data, *J. Fluid Mech.* **245**, 211

INFLUENCE OF HIGH-FREQUENCY ACOUSTIC WAVES ON THE FLOW OF A LIQUID THROUGH POROUS MATERIAL: EXPERIMENTAL AND THEORETICAL INVESTIGATION

Pietro Poesio and Gijs Ooms

J. M. Burgers Center, Delft University of Technology, Laboratory for Aero- and Hydrodynamics, Leeghwaterstraat 21, 2628 CB Delft, The Netherlands

pietro.poesio@shell.com and g.ooms@wbmt.tudelft.nl

Abstract In this paper the effect of ultrasound on flow through porous media has been investigated both experimentally and theoretically. Ultrasounds (20 and 40 kHz) have been proved to increase the flow rate through porous media. Two effects have been found of relevance. Decrease in viscosity due to dissipation of acoustic waves and acoustic streaming. The two effects have been modeled and those models compared with experimental data.

Keywords: Ultrasounds, temperature effect, acoustic streaming.

Introduction

Fouling of the near wellbore region of an oil reservoir can lead to a dramatic decrease in oil productivity. Different techniques, such as acid treatment and fracturing of the reservoir, have been developed to remove the fouling particles and restore the initial permeability. These techniques have negative side effects: they are expensive, dangerous, and environment unfriendly. Therefore a new technique has been proposed and investigated: the irradiation with high-frequency acoustic waves of the near wellbore region. However the results of the new technique are rather variable: in some cases an increase in productivity is recorded while in other cases no effect is measured. A more fundamental investigation of the ultrasonic cleaning technique is needed. However the effect of ultrasonic waves on fluid flow through porous material is still not fully understood and needs attention before considering the effect of acoustic waves on the removal of fouling particles. Therefore, in this paper we present the results of a study of the influence of high-frequency acoustic waves on the

Jacques M. Huyghe et al. (eds), IUTAM Proceedings on Physicochemical and Electromechanical Interactions in Porous Media, 61–66.

© 2005 Springer. Printed in the Netherlands.

flow of a liquid through a porous material without fouling particles. In the review article by [2] several mechanisms have been proposed for the influence of acoustic waves on the flow through a porous material. They mention, for instance, the reduction in adherence between pore wall and liquid, acoustic streaming, acoustic cavitation, in-pore turbulence, viscosity decrease due to energy dissipation, etc. [1] have developed a model based on peristaltic liquid transport caused by deformation of the pore walls due to the traveling acoustic waves. However no certainty exists as to which mechanism is the correct one.

In this paper we report on a detailed experimental and theoretical investigation of the influence of acoustic waves on laminar liquid flow through the Berea sandstone. We focus our investigation on Berea sandstone, which is representative for the sandstone of an oil reservoir, with permeability 100 to 300 mD and on acoustic frequencies below the critical frequency [3].

Description of the Experiments

The experiments were carried out in the set-up shown in Fig. 1. The cores that were used for the experiments were cylindrically shaped Berea sandstone samples. The length of the cores was 20 cm and the diameter 7.62 cm. The porosity was about 0.25. The initial permeability was 100-300 mD for all samples. During an experiment a core was placed in a rubber sleeve to keep it fixed during the experiment. It was then placed in a steel vessel in which down-hole reservoir conditions of up to 150 bars and 100°C were simulated. An acoustic horn was placed at one end of the core (see Fig. 1). The high pressure in the vessel made it possible to avoid cavitation. For pressures lower than 100 bars the influence of cavitation becomes noticeable. The space between the vessel and sleeve, which was filled with water, was pressurized to 180 bars to make the rubber sleeve completely seal off.

There were four pressure measurements, two along the core, at 2.54 cm and 10.70 cm, and two at both ends of the core (see Fig. 1). dP_1 is the pressure drop over the first part of the core sample, dP_2 the pressure drop over the middle part and dP_c the total pressure drop over the core. The pressure drop over the third part dP_3 can be calculated in the following way $dP_3 = dP_c - (dP_1 + dP_2)$. To measure the temperatures T1 and T2 at two locations in the core we installed two thermocouples at the sidewall of the porous medium, through the rubber sleeve (see Fig. 1). Also the temperatures at the front and back sides of the core were measured. The data were sent to a digital data recorder and processed on a computer. In front of the core an acoustic horn of 20 or 40 kHz was placed. A microphone was placed at the end side of the core. It was used to measure the amplitude of the acoustic signal after passage through the core. In this way the damping of the signal was determined during the experiments.

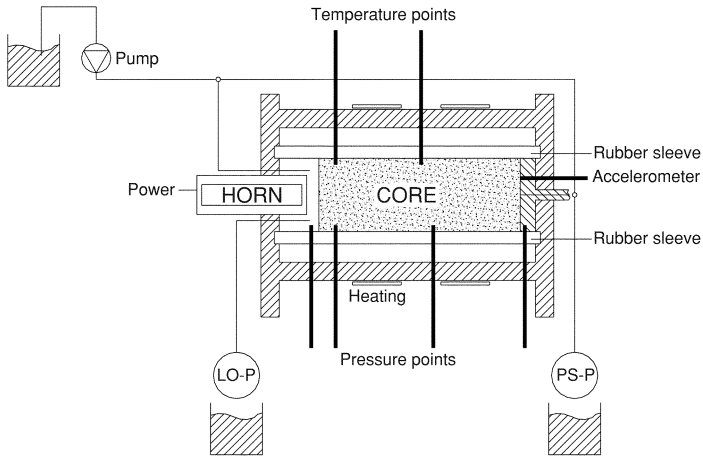


Figure 1. Experimental set-up.

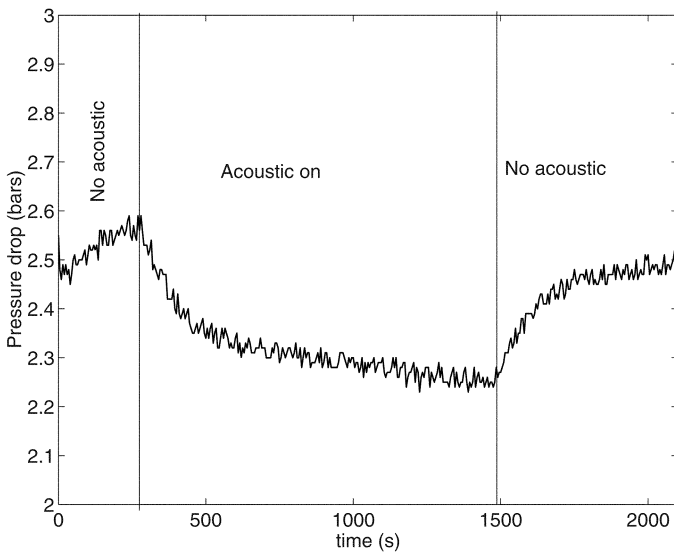


Figure 2. Pressure drop evolution for the middle part of the core (dP_2 , in Fig. 1) during acoustic irradiation. The acoustic power is 25% of the maximum power (2 kW).

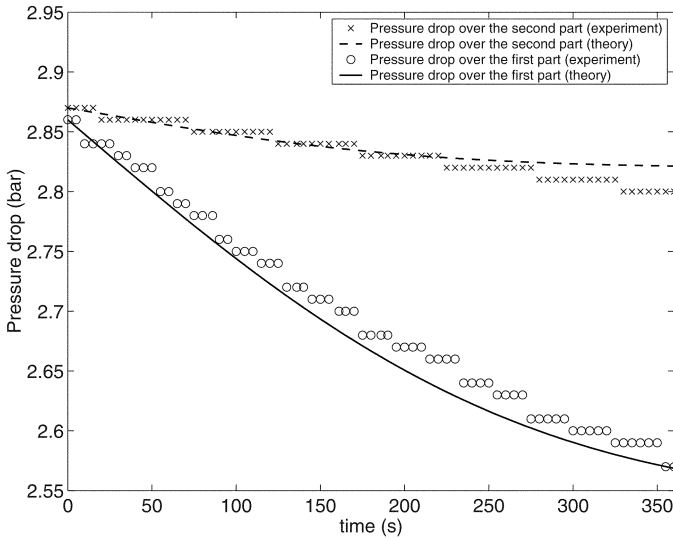


Figure 3. Pressure drop evolution with time across the first and the second part of the core (dP_1 and dP_2 , in Fig. 1): comparison between the experimental measurements and the theoretical predictions.

In order to investigate the effect of high-frequency acoustic waves on the flow of a brine through the sandstone the following procedure was followed: 1) we impose a certain flow rate of the liquid by means of a pump and measure the pressures and temperatures inside the core, 2) the acoustic irradiation is applied by switching on the acoustic horn, and 3) the pressures and temperatures in the core are again measured and compared with the initial ones. In Fig.2 an example is given of the measured pressure drop over the middle part of the core as function of time during such an experiment. The pressure drop decreases about 20% during acoustic irradiation. When the acoustic horn is switched off, the effect disappears again. So the acoustic waves decrease the pressure drop in case of an applied flow rate, or the acoustic waves increase the liquid flow rate in case of an applied pressure gradient. In the next section we will study this interesting phenomenon theoretically in order to find an explanation.

Theoretical Explanation

The velocity, pressure and temperature of the liquid inside the core can be calculated from the following set of equations:

$$\frac{\partial v}{\partial x} = 0, \quad (1)$$

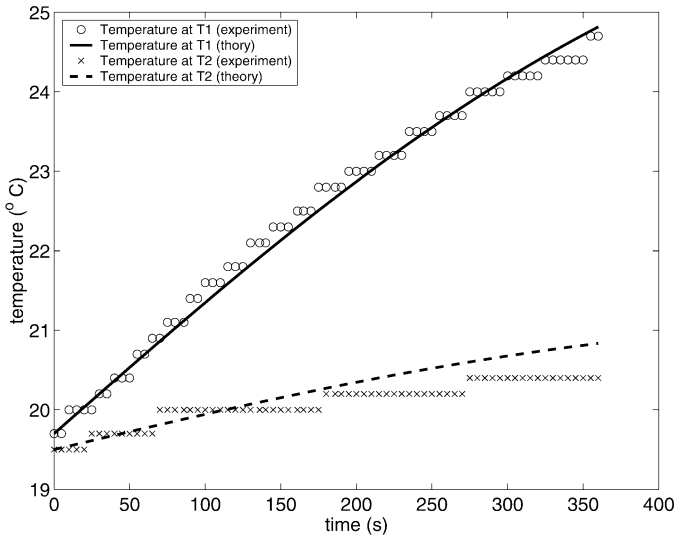


Figure 4. Temperature evolution with time at two distances from the front part of the core as indicated in Fig. 1: comparison between experimental measurements (continuous lines) and theoretical predictions (broken lines).

$$\frac{\rho_f}{\phi} \frac{\partial v}{\partial t} = -\frac{\partial p}{\partial x} - \frac{\mu(T)}{K} v + S_{mom}, \quad (2)$$

$$(\phi \rho_f c_f + (1 - \phi) \rho_p c_p) \frac{\partial T}{\partial t} + \rho_f c_f v \frac{\partial T}{\partial x} = \lambda \frac{\partial^2 T}{\partial x^2} + S_{therm}, \quad (3)$$

where

$$S_{therm} = \frac{\partial I}{\partial x} \quad S_{mom} = c_{fast,slow} \frac{\partial M}{\partial x}, \quad (4)$$

$$I = I_{fast,0}(1 - e^{-2\alpha_{fast}x}) + I_{slow,0}(1 - e^{-2\alpha_{slow}x}), \quad (5)$$

$$M = \frac{I}{c_{fast,slow}^2}. \quad (6)$$

Moreover, v is the fluid velocity, ρ_f and μ are the density and the viscosity of the fluid, respectively; ϕ and K are porosity and permeability of the core; $c_{f,s}$ are specific heat of the fluid and of the solid respectively; $c_{fast,slow}$ are the sound propagation speed of the fast and slow waves; $I_{fast,slow}$ are the intensities of the fast and slow waves, while $\alpha_{fast,slow}$ are their damping coefficients. We use an effective medium approach for the liquid, describing the effect of the acoustic waves as source terms. There are two source terms. First there is the heat source term S_{therm} , which is caused by the quick damping of the acoustic waves in the porous material. However, a traveling acoustic wave has not only energy but also momentum. So when the wave dissipates its energy, it

will also lose its momentum which is transferred to the liquid S_{mom} . Eq. (1) is the continuity equation; the liquid is considered as incompressible. Eq. (2) is the momentum equation for the fluid; it is an extension of the Darcy equation. Eq. (3) is the temperature equation. The source terms are given by Eqs.(4), (5) and (6).

These equations have been used to calculate the effect of the high-frequency acoustic waves on the pressures and temperatures of the liquid inside the core. A typical example of a comparison between experimental measurements and theoretical predictions for pressures and temperatures are shown in Figs. 3 and 4 respectively. The agreement is rather good.

Discussion

During the evaluation of our calculations we noticed, that the dissipation of the acoustic waves has an important influence on the temperature of the liquid. The dissipation caused an increase of the liquid temperature, which in its turn caused a decrease of the liquid viscosity and, as a result, the pressure gradient over the core decreased at constant liquid flow rate. This phenomenon is completely responsible for the pressure drop effect. It is a measurable effect and has to be taken into account when studying acoustic irradiation of porous materials. From the evaluation of the calculations we could also conclude, that the momentum transfer of the acoustic waves to the liquid, i.e. acoustic streaming, has a negligible effect on pressures and temperatures of the liquid, although the effect is measurable.

References

- [1] Aarts A.C.T. and Ooms G. (1998) Net flow of compressible viscous liquids induced by traveling waves in porous media. *Journal of Engineering Mathematics* **34**, 435-450
- [2] Beresnev I. A. and Johnson P. A.(1994) Elastic wave stimulation of oil production: A review of methods and results. *Geophysics* **59**(6), 1000-1017
- [3] Biot M. A. (1956) Theory of propagation of elastic waves in a fluid-saturated porous medium. Low frequency range. *Journal of Acoustical Society of America* **28**, 168-191
- [4] Poesio P., Ooms G., Barake S., and Bas v.d. (2002) An investigation of the influence of acoustic waves on the liquid flow through a porous material, *Journal of Acoustical Society of America* **111**(5), 2019-2025
- [5] Poesio P., Ooms G., Schraven A., and Bas v.d. (2002) Theoretical and experimental investigation of acoustic streaming in a porous material *Physics Reviews E* **66**, 016309

III

NUMERICAL SIMULATION.

Chairmen: C.W.J. Oomens, W. Ehlers

LARGE STRAIN ANALYSIS OF 3-D VISCOELASTIC SWELLING OF CHARGED TISSUES AND GELS

Wolfgang Ehlers, Bernd Markert and Ayhan Acartürk

University of Stuttgart

Institute of Applied Mechanics (CE), Chair II

Pfaffenwaldring 7

70569 Stuttgart

Germany

{ehlers, markert, acar}@mechbau.uni-stuttgart.de

Abstract Materials like soft biological tissues undergo large viscoelastic deformations during the swelling process. Following this, it is the goal of this contribution to merge the advances of finite viscoelasticity laws and the state of the art in electrochemical swelling theories within a well-founded multiphasic concept. The numerical treatment is carried out fully 3-d in the framework of the FEM.

Keywords: TPM, swelling, viscoelasticity, finite deformations, FEM

Multiphasic Formulation

The Theory of Porous Media (TPM) is a macroscopic continuum theory which is based on the theory of mixtures and the concept of volume fractions. For more details see [1] and citations therein.

Constituents, volume fractions and densities

Proceeding from a binary mixture consisting of solid and fluid constituents φ^α denoted by $\alpha = \{S, F\}$, the solid phase is extended by incorporating the volume free fixed charges φ^{fc} . Furthermore, the interstitial fluid φ^F is assumed to be composed of three components φ^β , namely the liquid solvent, the cations and the anions, in the following indicated by $\beta = \{L, +, -\}$. By introducing the volume fractions $n^\alpha = dv^\alpha/dv$, the saturation constraint yields

$$\sum_{\alpha} n^{\alpha} = n^S + \underbrace{n^L + n^+ + n^-}_{n^F} = 1. \quad (1)$$

Jacques M. Huyghe et al. (eds), IUTAM Proceedings on Physicochemical and Electromechanical Interactions in Porous Media, 69–74.

© 2005 Springer. Printed in the Netherlands.

The introduction of the volume fractions motivates the definition of two density functions, the effective density $\rho^{\alpha R} = dm^\alpha/dv^\alpha$ and the partial density $\rho^\alpha = dm^\alpha/dv$, which relate the mass m^α of φ^α to its volume v^α and to the bulk volume v . The density functions are coupled by $\rho^\alpha = n^\alpha \rho^{\alpha R}$. Furthermore, $\rho^\beta = n^F c_m^\beta M_m^\beta$ denotes the partial density of φ^β [5]. Herein, the concentration $c_m^\beta = dn_m^\beta/dv^F$ relates the moles n_m^β to the volume v^F , and the molar mass $M_m^\beta = dm^\beta/dn_m^\beta$ relates the mass m^β to the moles.

Kinematics

Following the idea of superimposed continua, each constituent follows its individual motion $\chi_\alpha(\mathbf{X}_\alpha, t)$ and has its own velocity field with respect to different reference positions \mathbf{X}_α :

$$\mathbf{x} = \chi(\mathbf{X}_\alpha, t), \quad \dot{\mathbf{x}}_\alpha = \frac{d_\alpha \chi_\alpha(\mathbf{X}_\alpha, t)}{dt}. \quad (2)$$

Therein, $(\cdot)'_\alpha$ denotes the material time derivative with respect to φ^α .

The model under consideration incorporates seven independent fields, namely the solid displacement $\mathbf{u}_S = \mathbf{x} - \mathbf{X}_S$, the seepage velocity $\mathbf{w}_F = \dot{\mathbf{x}}_F - \dot{\mathbf{x}}_S$, the relative ion velocities $\mathbf{w}_\gamma = \dot{\mathbf{x}}_\gamma - \dot{\mathbf{x}}_S$, the entire fluid pressure p and the ion concentrations c_m^γ . Herein, $\gamma = \{+, -\}$ only indicates the mobile ions. For the liquid solvent, it is assumed that $\dot{\mathbf{x}}_L \approx \dot{\mathbf{x}}_F$, i. e., $\mathbf{w}_L \approx \mathbf{w}_F$.

Balance relations

Proceeding from materially incompressible constituents without any mass exchanges due to chemical reactions, volume balances for the constituents φ^α and concentration balances for the components φ^β are introduced:

$$(n^\alpha)'_\alpha + n^\alpha \operatorname{div} \dot{\mathbf{x}}_\alpha = 0, \quad (n^F c_m^\beta)'_\beta + n^F c_m^\beta \operatorname{div} \dot{\mathbf{x}}_\beta = 0. \quad (3)$$

The volume balance of the charged solid and of the fixed charges can be integrated analytically leading to [4]

$$n^S = n_{0S}^S \det \mathbf{F}_S^{-1}, \quad c_m^{fc} = c_{m0S}^{fc} \frac{n_{0S}^F}{n^F} \det \mathbf{F}_S^{-1}, \quad (4)$$

where $n_{0S}^S, n_{0S}^F = 1 - n_{0S}^S$ and c_{m0S}^{fc} are initial values and \mathbf{F}_S is the material deformation gradient. Following *Truesdell's* metaphysical principles, the mixture volume balance can be obtained as the sum of the partial volume balances:

$$(n^S + n^F)'_S = \operatorname{div} [(\mathbf{u}_S)'_S + n^F \mathbf{w}_F] = 0. \quad (5)$$

For the numerical implementation, the component concentration balances are rewritten in terms of the solid motion leading to

$$n^F (c_m^\beta)'_S + c_m^\beta \operatorname{div} (\mathbf{u}_S)'_S + \operatorname{div} (n^F c_m^\beta \mathbf{w}_\beta) = 0. \quad (6)$$

Note that under the assumptions $c_m^L = \text{const.}$ and $\{n^+, n^-\} \ll n^L$, the volume balance of the liquid component φ^L is equivalent to that of the entire fluid.

Moreover, the quasi static momentum balances are given by

$$\mathbf{0} = \text{div } \mathbf{T}^\alpha + \rho^\alpha \mathbf{b} + \hat{\mathbf{p}}^\alpha. \quad (7)$$

Therein, $\mathbf{T}^\alpha = (\mathbf{T}^\alpha)^T$ are the symmetric partial *Cauchy* stress tensors, $\rho^\alpha \mathbf{b}$ represent the body forces and $\hat{\mathbf{p}}^\alpha$ are the momentum productions, where $\hat{\mathbf{p}}^S + \hat{\mathbf{p}}^F = \mathbf{0}$ must hold due the overall conservation of momentum.

Constitutive equations

To close the set of governing equations, additional constitutive relations must be introduced. Following the general effective stress principle, one finds

$$\mathbf{T}^\alpha = -n^\alpha \mathcal{P} \mathbf{I} + \mathbf{T}_E^\alpha, \quad \hat{\mathbf{p}}^F = \mathcal{P} \text{grad } n^F + \hat{\mathbf{p}}_E^F, \quad (8)$$

where the *Lagrangean* multiplier \mathcal{P} maintains the incompressibility condition. For the so-called extra quantities $(\cdot)_E$, some further constitutive assumptions are needed. From thermodynamical considerations, it follows that

$$\mathbf{T}_E^\alpha = -n^\alpha \sum_{\beta} \mu_F^\beta \mathbf{I} + \mathbf{T}_{E\text{mech.}}^\alpha, \quad \hat{\mathbf{p}}_E^F = \sum_{\beta} \mu_F^\beta \text{grad } n^F - \frac{(n^F)^2 \gamma^{FR}}{k^F} \mathbf{w}_F, \quad (9)$$

where μ_F^β are the electrochemical potentials of φ^β per fluid volume [J/m^3] and $\mathbf{T}_{E\text{mech.}}^\alpha$ is the purely mechanical part of \mathbf{T}_E^α , where, *a priori*, $\mathbf{T}_{E\text{mech.}}^F \approx \mathbf{0}$. Moreover, γ^{FR} is the effective fluid weight and k^F denotes the *Darcy* permeability which may depend on the deformation state [2]. Following this, one can introduce the entire (hydraulic and osmotic) fluid pressure as $p = \mathcal{P} + \pi$, where $\pi := \sum_{\beta} \mu_F^\beta$ is the osmotic pressure.

In finite viscoelasticity, it is convenient to proceed from a multiplicative split of the solid deformation gradient $\mathbf{F}_S = \mathbf{F}_{Se} \mathbf{F}_{Si}$ into elastic and inelastic parts. Furthermore, from rheological considerations, one obtains the ansatz of a decomposed solid extra *Kirchhoff* stress $\boldsymbol{\tau}_{E\text{mech.}}^S(\mathbf{F}_S, \mathbf{F}_{Se}) = \boldsymbol{\tau}_{EQ}^S(\mathbf{F}_S) + \boldsymbol{\tau}_{NEQ}^S(\mathbf{F}_{Se})$ into equilibrium parts (Index *EQ*) describing the basic elasticity and non-equilibrium parts (Index *NEQ*) vanishing in the thermodynamic equilibrium, where $\boldsymbol{\tau}_{E\text{mech.}}^S = J_S \mathbf{T}_{E\text{mech.}}^S$, where $J_S = \det \mathbf{F}_S$.

Proceeding from an *Ogden*-type material formulation, which is extended towards an inelastic porous media application, volumetric extension terms are developed which describe the finite volume change including the concept of a volumetric compaction point. Thus, the equilibrium part of the mechanical

solid extra stress can be obtained by

$$\begin{aligned} \boldsymbol{\tau}_{EQ}^S = & \mu_0^S \sum_{j=1}^3 \sum_{k=1}^3 \mu_{k0}^* (\lambda_j^{\alpha_{k0}/2} - 1) \mathbf{N}_j + \\ & + \frac{\Lambda_0^S}{\gamma_0 - 1 + \frac{\gamma_0 + 1}{(1 - n_{0S}^S)^2}} \left(J_S^{\gamma_0} - \frac{J_S (1 - n_{0S}^S)^{\gamma_0}}{(J_S - n_{0S}^S)^{\gamma_0 + 1}} + \frac{J_S n_{0S}^S}{1 - n_{0S}^S} \right) \mathbf{I}, \end{aligned} \quad (10)$$

whereas the non-equilibrium part is computed from

$$\begin{aligned} \boldsymbol{\tau}_{NEQ}^S = & \mu^S \sum_{j=1}^3 \sum_{k=1}^3 (\mu_k^*) \left[\lambda_{ej}^{\alpha_k/2} - 1 \right] \mathbf{N}_{ej} + \\ & + \frac{\Lambda^S}{\gamma - 1 + \frac{\gamma + 1}{(1 - n_i^S)^2}} \left[(J_{Se})^\gamma - \frac{J_{Se} (1 - n_i^S)^\gamma}{(J_{Se} - n_i^S)^{\gamma + 1}} + \frac{J_{Se} n_i^S}{1 - n_i^S} \right] \mathbf{I}. \end{aligned} \quad (11)$$

In (10) and (11), λ_j are the eigenvalues of the *Cauchy-Green* deformation tensors $\mathbf{C}_S = \mathbf{F}_S^T \mathbf{F}_S$ or $\mathbf{B}_S = \mathbf{F}_S \mathbf{F}_S^T$, λ_{ej} are the eigenvalues of the elastic *Cauchy-Green* deformation tensors $\mathbf{C}_{Se} = \mathbf{F}_{Se}^T \mathbf{F}_{Se}$ or $\mathbf{B}_{Se} = \mathbf{F}_{Se} \mathbf{F}_{Se}^T$ and $\mathbf{N}_j = \partial \lambda_j / \partial \mathbf{B}_S$ and $\mathbf{N}_{ej} = \partial \lambda_{ej} / \partial \mathbf{B}_{Se}$ denote the eigentensors corresponding to the eigenvalues λ_j and λ_{ej} . Furthermore, μ_0^S and μ^S are the first macroscopic *Lamé* constants and μ_{k0}^* , α_{k0} and μ_k^* , α_k are the dimensionless *Ogden* parameters. Moreover, in the volumetric extension terms, Λ_0^S and Λ^S are the second *Lamé* constants, γ_0 and γ are parameters that influence the volumetric non-linearity, $J_{Se} = \det \mathbf{F}_{Se}$ is the determinant of the elastic part of the deformation gradient, and $n_i^S = n_{0S}^S \det \mathbf{F}_{Si}^{-1}$ is the inelastic solidity with respect to the intermediate configuration [2].

The inelastic strain as an internal state variable is obtained from a linear evolution equation formulated with respect to the intermediate configuration:

$$\hat{\mathbf{D}}_{Si} = \hat{\mathbf{D}}^{-1} \hat{\boldsymbol{\tau}}_{NEQ}^S, \quad \hat{\mathbf{D}}^{-1} = \frac{1}{2\eta^S} (\mathbf{I} \otimes \mathbf{I})^{\frac{23}{2}} - \frac{\zeta^S}{2\eta^S (2\eta^S + 3\zeta^S)} (\mathbf{I} \otimes \mathbf{I}). \quad (12)$$

Therein, $\hat{\mathbf{D}}^{-1}$ is the positive definite, isotropic, fourth order viscous compliance, where η^S and ζ^S are the macroscopic viscosity parameters, $\hat{\mathbf{D}}_{Si}$ is the inelastic solid deformation rate and $\hat{\boldsymbol{\tau}}_{NEQ}^S = \mathbf{F}_{Se}^{-1} \boldsymbol{\tau}_{NEQ}^S \mathbf{F}_{Se}^{T-1}$ is the corresponding non-equilibrium stress tensor. Furthermore, the superscript ($\hat{\cdot}$) indicates the belonging to the intermediate configuration.

To solve equations (9), the molar electrochemical potentials [J/mol] of the fluid components are needed which are given by

$$\mu_m^L = \mu_{m0}^L + R\theta \ln \frac{c_m^L}{\sum_{\beta} c_m^{\beta}}, \quad \mu_m^\gamma = \mu_{m0}^\gamma + R\theta \ln c_m^\gamma + z^\gamma F\xi. \quad (13)$$

These terms are related to μ_F^β via $\mu_m^\beta = \mu_F^\beta / c_m^\beta$. Moreover, μ_{m0}^β are the initial chemical potentials of the components, R is the universal gas constant, θ is the

absolute *Kelvin's* temperature, z^γ are the valences of the ions, F is the *Faraday* constant and ξ is the electrical potential.

Interstitial fluid flow, ion diffusion and osmotic pressure

The interstitial fluid flow is described by an extended *Darcy* filter law via

$$n^F \mathbf{w}_F = -\frac{k^F}{\gamma^{FR}} \left(\text{grad } p - \rho^{FR} \mathbf{b} + \sum_{\beta} \text{grad } \mu_F^{\beta} \right), \quad (14)$$

whereas the ion diffusion is governed by an extended *Nernst-Planck* equation

$$c_m^\gamma \mathbf{w}_\gamma = -D^\gamma \left[\text{grad } c_m^\gamma + z^\gamma c_m^\gamma \frac{F}{R\theta} \text{grad } \xi \right] + c_m^\gamma \mathbf{w}_F. \quad (15)$$

Therein, $n^F \mathbf{w}_F$ is the so-called filter velocity. Note that $c_m^\gamma \mathbf{w}_F$ is added to the ion velocities to get the velocities relative to the solid motion.

To describe macromolecular solutions, the *Donnan* theory is used in form of the *Donnan* equation

$$c_m^+ c_m^- = \bar{c}_m^+ \bar{c}_m^-. \quad (16)$$

Therein, the quantities \bar{c}_m^+ and \bar{c}_m^- indicate the ion concentrations of the external solution. The osmotic pressure π is computed from the osmolarity difference of the internal and the external solution:

$$\pi = R\theta [(c_m^+ + c_m^-) - (\bar{c}_m^+ + \bar{c}_m^-)]. \quad (17)$$

Reduction to monovalent solutions

For simplicity, the model equations are reduced for the description of monovalent salt solutions. In particular, the model is verified for a Na^+Cl^- solution. Thus, with the valences $z^+ = 1$, $z^- = -1$ and $z^{fc} = -1$, an external concentration \bar{c}_m and an internal concentration c_m are defined via the electroneutrality condition of the external and the internal solutions, respectively:

$$\begin{aligned} z^+ \bar{c}_m^+ + z^- \bar{c}_m^- &= 0 & \longrightarrow & \bar{c}_m^+ = \bar{c}_m^- =: \bar{c}_m, \\ z^+ c_m^+ + z^- c_m^- + z^{fc} c_m^{fc} &= 0 & \longrightarrow & c_m := c_m^-, \quad c_m^+ = c_m + c_m^{fc}. \end{aligned} \quad (18)$$

Following this, c_m^+ is no more an independent field and, thus, the governing equations can be transformed into a displacement-pressure-concentration formulation allowing for an efficient numerical treatment within the FEM.

Moreover, with the electroneutrality condition (18)₂, the equations (16) and (17) can be used to compute the equilibrium concentration and the osmotic pressure of the internal solution [3]:

$$c_m = \sqrt{\bar{c}_m^2 + \left(\frac{c_m^{fc}}{2} \right)^2} - \frac{c_m^{fc}}{2}, \quad \pi = R\theta (2c_m + c_m^{fc} - 2\bar{c}_m). \quad (19)$$

Finally, by use of the ion diffusion equation (15), the assumption that there is no electrical current

$$\mathbf{I} = FA(c_m^+ \mathbf{w}_+ - c_m^- \mathbf{w}_-) = \mathbf{0}, \quad (20)$$

yields a conditional equation for the gradient of the electrical potential which is needed in (14) and (15).

Numerical Example

To demonstrate the capability of the presented model, a free swelling experiment on hydrogel is simulated by the FE tool PANDAS. Therefore, a 3-dimensional block is discretized with hexagonal extended *Taylor-Hood* elements with a quadratic approximation of \mathbf{u}_S and linear approximations of p and c_m . To initiate swelling, the concentration of the external solution is decreased from 0.15 mol/l to 0.125 mol/l within 10 sec.

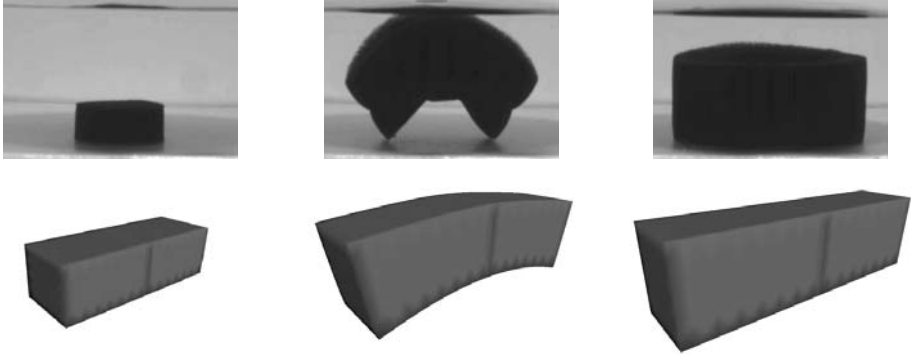


Figure 1. Qualitative comparison of a free swelling experiment on a soot-coloured hydrogel disc (experiment by J. M. Huyghe, 1999) with the 3-d FEM simulation via PANDAS

References

- [1] Ehlers, W. (2002). Foundations of multiphasic and porous materials. In Ehlers, W. and Bluhm, J., editors, *Porous Media: Theory, Experiments and Numerical Applications*, pages 3–86. Springer-Verlag, Berlin.
- [2] Ehlers, W. and Markert, B. (2003). A macroscopic finite strain model for cellular polymers. *International Journal of Plasticity*, 19:961–976.
- [3] Huyghe, J. M. and Janssen, J. D. (1997). Quadriphasic mechanics of swelling incompressible porous media. *International Journal of Engineering Science*, 35:793–802.
- [4] Lai, W. M., Hou, J. S., and Mow, V. C. (1991). A triphasic theory for the swelling and deformation behaviours of articular cartilage. *ASME Journal of Biomechanical Engineering*, 113:245–258.
- [5] Mow, V. C., Ateshian, G. A., Lai, W. M., and Gu, W. Y. (1998). Effects of fixed charges on the stress-relaxation behavior of hydrated soft tissues in a confined compression problem. *International Journal of Solids Structures*, 35:4945–4962.

THEORETICAL AND FINITE ELEMENT MODELS FOR COUPLED ELECTRO-MECHANOCHEMICAL TRANSPORT IN SOFT TISSUES

Bruce R. Simon, Gregg A. Radtke, Zun P. Liu

Aerospace and Mechanical Engineering

The University of Arizona

Tucson, Arizona, USA 85721-0119

simon@ame.arizona.edu

Paul H. Rigby and Stuart K. Williams

Biomedical Engineering IDP

The University of Arizona

Tucson, Arizona, USA

Abstract A general theoretical and finite element model (FEM) for soft tissue structures is described including arbitrary constitutive laws based upon a continuum view of the material as a mixture or porous medium saturated by an incompressible fluid and containing charged mobile species. Example problems demonstrate coupled electro-mechano-chemical transport and deformations in FEMs of layered materials subjected to mechanical, electrical and chemical “loading” while undergoing small or large strains.

Keywords: Finite element models; coupled electrical, mechanical, chemical transport; large strain; soft tissues

Introduction

The development of biomechanical models derived from continuum formulations for transport of water and charged species in porous media has been carried out for various soft tissues [1-3] and implemented using finite element models (FEMs) [4-8]. Such models provide quantitative views of the response of these complex structures that is especially useful in the study of orthopedic, vascular, ocular, and soft tissue substitutes developed by tissue engineering. In this paper a formulation and FEM are described that incorporate and extend these works in a very general model that identifies physical material properties and allows transient analyses of both natural and artificial soft tissue structures.

Jacques M. Huyghe et al. (eds), IUTAM Proceedings on Physicochemical and Electromechanical Interactions in Porous Media, 75–80.

© 2005 Springer. Printed in the Netherlands.

Theory

Soft biological structures exhibit finite strains and nonlinear anisotropic material response. The hydrated tissue can be viewed as a fluid-saturated porous medium or a continuum mixture of incompressible solid (s), mobile incompressible fluid (f), and three (or an arbitrary number) mobile charged species ($\alpha, \beta = p, m, b$). A mixed Electro-Mechano-Chemical-Porous-Media-Transport or “EMCPMT” theory (previously denoted as the “LMPHETS” theory) is presented with (a) primary fields (continuous at material interfaces): displacements, u_i and generalized potentials, $\tilde{v}^{\xi*}$ ($\xi, \eta = f, e, m, b$) and (b) secondary fields (discontinuous): pore fluid pressure, p^f ; electrical potential, $\tilde{\mu}^e$; and species concentration (molarity), $c^\alpha = dn^\alpha/dV^f$ or apparent concentration, $\hat{c}^\alpha = nc^\alpha$ and $\tilde{c}^\alpha = Jnc^\alpha = dn^\alpha/dV_0$. The porosity, $n = 1 - J^{-1}(1 - n_0)$ and $n_0 = n_0(X_i) = dV_0^f/dV_0$ for a fluid-saturated solid. Fixed charge density (FCD) in the solid is defined as $c^F = dn^F/dV^f$, $\hat{c}^F = nc^F$, and $\tilde{c}_0^F = \tilde{c}_0^F(X_i) = Jnc^F = dn^F/dV_0$.

Lagrangian field equations

The field equations given in Lagrangian form are (a) the conservation of momentum (quasi-static, no body forces) and mass equations

$$T_{ji,j} = 0, \quad \tilde{J}_{k,k}^{\xi r} + \tilde{Q}^\xi = 0 \quad (1)$$

with $\tilde{Q}^f = J$, $\tilde{Q}^e = 0$, $\tilde{Q}^{\bar{\alpha}} = \tilde{c}^{\bar{\alpha}}$, ($\bar{\alpha} = m, b$) and relative fluxes, $\tilde{j}_i^{\xi r} : \tilde{j}_i^{fr} = \tilde{v}_i^{fr}, \tilde{j}_i^{er} = \tilde{v}_i^{er} = \Sigma_\alpha z^\alpha \tilde{j}_i^{\alpha r}, \tilde{j}_i^{\bar{\alpha} r} = c^{\bar{\alpha}} \tilde{v}_i^{\bar{\alpha} r}$; (b) the kinematic equations defining engineering strain, Green’s strain, and gradients in potentials as

$$e_{ij} = (u_{i,j} + u_{j,i})/2 \quad E_{ij} = (F_{ki}F_{kj} - \delta_{ij})/2 \quad \tilde{e}_i^{\xi r} = \tilde{v}_i^{\xi r} \quad (2)$$

with $J = \det F_{ij}$, $F_{ij} = x_{i,j}$, and $H_{ij} = F_{ik}^{-1}F_{jk}^{-1}$; and (c) the constitutive equations including an “effective stress principle” and a generalized Darcy law

$$\sigma_{ij} = \sigma_{ij}^{eff} - p^f \delta_{ij}, \quad \tilde{j}_i^{\xi r} = - \sum_\eta \tilde{L}_{ij}^{\xi\eta} \tilde{e}_j^{\eta*} \quad (3)$$

where $S_{ij} = S_{ij}^{eff} - J H_{ij} p^f$ and $S_{ij}^{eff} = J F_{ik}^{-1} \sigma_{km}^{eff} F_{jm}^{-1}$. If a porohyperelastic theory is used, then $S_{ij}^{eff} = \partial U^{eff} / \partial E_{ij}$ and e.g. a “Fung form” (associated with an LMPHETS model [5] defines $\varphi = \varphi(E_{kl}, J, n, \tilde{v}^{\xi*}, \theta)$ so that $U^{eff} = U^{eff}(\varphi)$ and $\tilde{L}_{ij}^{\xi\eta} = \tilde{L}_{ij}^{\xi\eta}(\varphi)$. For the isotropic, “exponential Fung” constitutive model, $U^{eff} = (1/2)C_0[\exp(\varphi) - 1]$ and $\varphi = \varphi(I'_1, I'_2, J, n, \tilde{v}^{\xi*}, \theta)$. The invariants are defined as $I'_1 = J^{-2/3}I_1$, $I_1 = 3 + 2E_{kk}$, $I'_2 = J^{-4/3}I_2$, and $I_2 = 3 + 4E_{kk} + 2[E_{kk}]^2 - 2E_{ij}E_{ij}$. The

generalized Darcy law can be written (using the PHETS formulation [4]) in the form $\tilde{v}_i^{fr} = -\tilde{k}_{ij}^{ff} \{p_{,j}^f + \Sigma_\alpha [\Sigma_\beta \tilde{b}_{jk}^{f\beta} c^\beta (\partial \tilde{\mu}^\beta / \partial c^\alpha) + \delta_{jk} (\partial p^0 / \partial c^\alpha) c_{,k}^\alpha + \tilde{b}_{jk}^{f\alpha} c^\alpha F_c z^\alpha \tilde{\mu}_{,k}^e]\}$ and Fick's law $\tilde{j}_i^{\alpha r} = -\Sigma_\beta \tilde{d}_{ij}^{\alpha\beta} c_{,j}^\beta - \tilde{d}_{ij}^{\alpha e} \tilde{\mu}_{,j}^e + \tilde{b}_{ij}^{\alpha f} c^\alpha \tilde{v}_j^{fr}$ (using the "PHETS" model) where the permeability, \tilde{k}_{ij}^{ff} ; diffusivities, $\tilde{d}_{ij}^{\alpha\beta}$ and $\tilde{d}_{ij}^{\alpha e}$; and convection coefficients, $\tilde{b}_{ij}^{\alpha f}$ are directly related to $\tilde{L}_{ij}^{\xi\eta}$; e.g., $\tilde{L}_{ij}^{ff} = \tilde{k}_{ij}^{ff}$, $\tilde{L}_{ij}^{f\alpha} = c^\alpha \tilde{k}_{ik}^{ff} \tilde{b}_{kj}^{f\alpha} = \tilde{L}_{ji}^{\alpha f}$, etc. The electro-neutrality (constraint) is $\Sigma_\alpha (z^\alpha \tilde{c}^\alpha) + \tilde{c}_0^F = 0$ and the generalized potentials, $\tilde{v}^{\xi*}$ are $\tilde{v}^{f*} = \tilde{\mu}^{f*}$, $\tilde{v}^{e*} = (F_c z^p)^{-1} \tilde{\mu}^{p*}$, and $\tilde{v}^{\alpha*} = -(z^\alpha / z^p) \tilde{\mu}^{p*} + \tilde{\mu}^{\alpha*}$. Total fluid pressure is $\tilde{\mu}^{f*} = p^f + p^o$, the osmotic pressure, $p^o = p_0^o - R\theta \Sigma \phi^\alpha c^\alpha$, and electro-chemical potentials $\tilde{\mu}^{\alpha*} = F_c z^\alpha \tilde{\mu}^e + \tilde{\mu}^\alpha$ with $\tilde{\mu}^{\alpha*} = F_c z^\alpha \tilde{\mu}^e + \tilde{\mu}^\alpha$. The required material properties for the Fung effective stress principle are $U^{eff}(\varphi)$, $\tilde{L}_{ij}^{\xi\eta}(\varphi)$, $\varphi = \varphi(E_{kl}, J, \tilde{v}^{\xi*}, \theta)$, as well as $R, F_c, \phi^\alpha, \gamma^\alpha$, and z^α ; and the initial porosity, $n_0(X_i)$; FCD, $\tilde{c}_0^F(X_i)$; and (uniform) temperature, θ .

Lagrangian finite element model

The field equations form an initial boundary value problem that can be solved (subject to constraints and the initial-boundary conditions) using a FEM. Interpolations in each finite element are $\mathbf{u} = \mathbf{N}_u \bar{\mathbf{u}}$; $\mathbf{e} = \mathbf{B}_u \bar{\mathbf{u}}$, $\mathbf{E} = \mathbf{e} + \mathbf{e}^{NL} = [\mathbf{B}_u + (\mathbf{B}_u^{NL})/2] \bar{\mathbf{u}}$, $\dot{\mathbf{E}} = \dot{\mathbf{e}} + \dot{\mathbf{e}}^{NL} = \bar{\mathbf{B}}_u \dot{\bar{\mathbf{u}}}$, $\dot{J} = \hat{\mathbf{B}}_u \dot{\bar{\mathbf{u}}}$ with $\mathbf{N}_u = \mathbf{N}_u(\mathbf{X})$, $\mathbf{B}_u = \mathbf{L}_X \mathbf{N}_u$, $\bar{\mathbf{B}}_u = (\mathbf{B}_u + \mathbf{B}_u^{NL})$, $\hat{\mathbf{B}}_u = J \mathbf{H}^T \bar{\mathbf{B}}_u$, $\mathbf{B}_u^{NL} = \mathbf{A}_\theta \mathbf{G}$; and $\tilde{\mathbf{v}}^{\xi*} = \mathbf{N}_\xi \tilde{\mathbf{v}}^\xi$ and $\tilde{\mathbf{e}}^\xi = \mathbf{B}_\xi \tilde{\mathbf{v}}^\xi$. The spatial gradients \mathbf{L}_X and ∇_X and matrices $\mathbf{E}, \mathbf{e}, \mathbf{e}^{NL}, \mathbf{B}_u^{NL}, \mathbf{A}_\theta$, and \mathbf{G} ; etc. are given in vector-matrix notation [9]. Elemental residuals are $\boldsymbol{\psi}_u = \int \bar{\mathbf{B}}_u^T \mathbf{S} dV_0 - \int \mathbf{N}_u^T \mathbf{t}^{(\sigma)} dA = \mathbf{0}$ and $\boldsymbol{\psi}_\xi = -\int \mathbf{N}_\xi^T Q^\xi dV_0 - \int \mathbf{B}_\xi^T \tilde{\mathbf{j}}^{\xi*} dV_0 - \int \mathbf{N}_\xi^T \mathbf{t}^{(\xi)} dA = \mathbf{0}$ where $\mathbf{t}^{(\sigma)} = [\sigma_{ji} \hat{n}_j]$ and $\mathbf{t}^{(\xi)} = [j_k^{\xi r} \hat{n}_k]$. Incremental residuals are $\Delta \boldsymbol{\psi} = [\hat{\mathbf{c}}(\mathbf{p})] \Delta \dot{\mathbf{p}} + [\hat{\mathbf{k}}(\mathbf{p})] \Delta \mathbf{p} - \Delta \hat{\mathbf{P}}^{ext} = \mathbf{0}$ where $\boldsymbol{\psi}^T = \langle \boldsymbol{\psi}_u^T \boldsymbol{\psi}_\xi^T \rangle$ and $\mathbf{p}^T = \langle \bar{\mathbf{u}}^T \tilde{\mathbf{v}}^{\xi T} \rangle$. A time integrator is applied yielding $[\mathbf{k}^*] = (\hat{\theta} \Delta t)^{-1} [\hat{\mathbf{c}}] + [\hat{\mathbf{k}}]$ that is assembled to the global form, $[\mathbf{K}^*] \Delta \mathbf{r} = -\boldsymbol{\Psi}$; and solved using an iterative predictor-corrector algorithm.

Representative Results

EMCPMT models will be described that can simulate transient electro-mechano-chemo diffusion, convection, and osmosis in one-dimensional FEMs composed of one and/or multiple layers of porous material with prescribed $n_0(X_i)$ and FCD, $\tilde{c}_0^F(X_i)$ in the solid. The left (L) and right (R) interfaces are water baths containing prescribed concentrations of up to three charged species (p, m, b). Mechanical force (stress) or displacement; fluid pressure, and electrical potential will also be prescribed on these interfaces. The first example is

classical diffusion and convection of a single neutral species with small strains in a single layer of deformable porous media. The Eulerian properties (k^{ff} , b^{fc} , etc.) are constant. The initial-boundary conditions are: $\sigma_{\mathbf{L}} = -p_{\mathbf{L}}^f = \text{ramp}$ to $-P_{\mathbf{L}}$, $c_{\mathbf{L}}^b = c_{\mathbf{L}}$; and $u_{\mathbf{R}} = 0$, $p_{\mathbf{R}}^f = 0$, $c_{\mathbf{R}}^b = c_{\mathbf{R}} < c_{\mathbf{L}}$. Figure 1 illustrates the time history of the concentration, $c^b(X, t)$ with the expected diffusion from high to low concentration and convection species transport due to the gradient in p^f . For this relatively low level of applied load/pressure the strains are small and there are associated small changes in porosity as time increases. Although the strains are relatively small, there is a slight change in

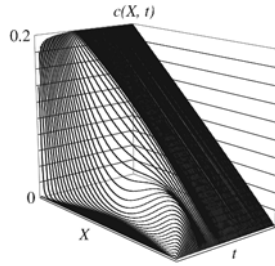


Figure 1. Concentration, $c^b(X, t)$, for small strain.

porosity during the response that affects the concentrations and other fields. Figure 2 shows the porosity for the same problem in which the applied stress is increased to produce finite straining in the material. Figure 3 illustrates

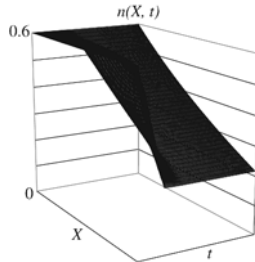


Figure 2. Porosity, $n(X, t)$, for finite strain.

the marked effects on concentration associated with a significant reduction in porosity (due to material compression). The last representative FEM simulates diffusion and convection of three charged species ($z^p = +1$, $z^m = -1$, $z^b = -1$) with small strains in two layers of deformable porous media. There are two baths (L, R) and the FCD = +1 in left material and FCD = -1 in right material. The initial-boundary conditions are the same as the first example. However, $c_{\mathbf{L}}^p > c_{\mathbf{R}}^p$, $c_{\mathbf{L}}^m < c_{\mathbf{R}}^m$, and $\tilde{\mu}_{\mathbf{L}}^e > \tilde{\mu}_{\mathbf{R}}^e = 0$. Figure 4 illustrates the time history of the concentration and shows the diffusion with convection of

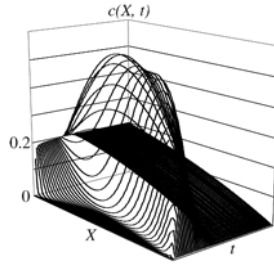


Figure 3. Concentration, $c^b(X, t)$, for finite strain.

the mobile charged species transport from high to low concentrations coupled with electrical diffusion due to charge interactions and convection associated with relative pore fluid motion in the material. The expected discontinuities in concentration are evident at the material interface as well as at the left and right interfaces with the bath solutions. Other complex FEMs have been developed

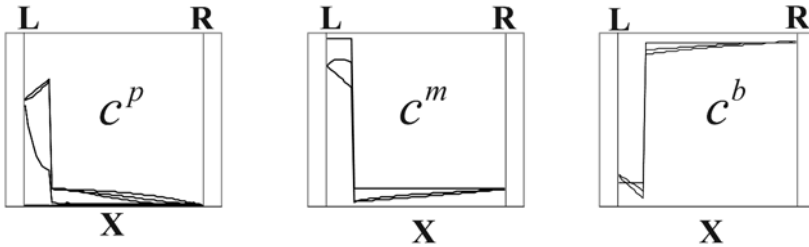


Figure 4. Transient small strain diffusion-convection in two materials.

to demonstrate the versatility of this EMCPMT formulation. These include more complicated finite strain problems with electrical, chemical, and mechanical coupling effects (including osmosis) for various known initial porosity (tissue fluid) and FCD distributions.

Conclusions

The methods and FEMs described have application to biomechanics and tissue engineering research in cardiovascular, orthopedic, and local drug delivery systems. Two- and three-dimensional FEMs can be generated for various biological structures once experimental data is available for the necessary anisotropic material properties as well as the appropriate structural geometry/anatomy and initial/boundary conditions. Current applications include study of large arteries and arterial grafts where coupled transport is of interest for normal and pathological conditions and tissue engineered graft designs.

These procedures are also applicable for the analysis of nonlinear, coupled electro-mechano-chemical transport phenomena in soils and geomechanics.

Acknowledgements

Support from NSF Grant BES-9810098, the University of Arizona Foundation, and a University of Arizona Foreign Travel Grant is gratefully acknowledged.

References

- [1] Lai, W. M., Hou, J.S., and Mow, V.C. (1991) A triphasic theory for the swelling and deformation behaviors of articular cartilage. *Journal of Biomechanical Engineering* **113**, 245-258
- [2] Gu, W.Y., Lai, W.M, and Mow, V.C. (1998) A mixture theory for charged-hydrated soft tissues containing multi-electrolytes: passive transport and swelling behaviors. *Journal of Biomechanical Engineering* **120**, 169-180
- [3] Levenston, M.E., Frank, E.H., and Grodzinsky, A.J. (1999) Electrokinetic and poroelastic coupling during finite deformations of charged porous media. *Journal of Applied Mechanics* **66**, 323-333
- [4] Simon, B.R., Radtke, G.A., Rigby, Williams, S. K. and Liu, Z.P. (2002) Extended 'LMPH-ETS' finite element models for coupled mechano-electro-chemical transport in soft tissues. ASME BED IMECE 2002-32604, Scott, E., editor
- [5] Simon, B.R., Kaufmann, M.V., Liu, J., and Baldwin, A.L. (1998) Porohyperelastic-transport-swelling theory, material properties, and finite element models for large arteries. *International Journal of Solids and Structures* **35**, 5021-5031
- [6] Sun, D.N., Gu, W.Y., Guo, X.E., Lai, W.M., and Mow, V.C. (1999) A mixed finite element formulation of triphasic mechano-electrochemical theory for charged, hydrated biological soft tissues. *International Journal for Numerical Methods in Engineering* **45**, 1375-1402
- [7] Simon, B.R. and Kaufmann, M.V. (1990) Finite element models for arterial wall mechanics and transport. *Biofluid Methods in Vascular and Pulmonary Systems, Biomechanical Systems Techniques and Applications*, Leondes, C. T. editor, IV, CRC Press, New York, 5.1-5.32
- [8] Snijders, H., Huyghe, J.M., and Janssen, J.D. (1995) Triphasic finite element model for swelling porous media. *International Journal for Numerical Methods* **20**, 1039-1046
- [9] Zienkiewicz, O.C. (1979) *The Finite Element Method*. McGraw-Hill, New York

POROUS EFFECTS IN THE DESCRIPTION OF THE DYNAMICS OF GRANULAR AVALANCHES

Shiva P. Pudasaini, Yongqi Wang and Kolumban Hutter

*Department of Mechanics, Darmstadt University of Technology,
Hochschulstrasse 1, D-64289 Darmstadt, Germany*

{pudasaini,wang,hutter}@mechanik.tu-darmstadt.de

Abstract Granular mixtures are porous media of immense importance in geophysical and industrial applications. Snow avalanches, debris- and mud-flows, landslides and rockslides are examples of rapid flows of geomaterials whereas flows of fine granular materials in silos, hoppers, rotating drums and heap formations are examples from process engineering. In order to understand these phenomena properly, one needs physical–mathematical descriptions including appropriate constitutive relations and suitable numerical simulations. We present recently developed model equations by *Pudasaini & Hutter* for free gravity-driven flows of a single phase dry granular material down complicated real mountain terrains generated by arbitrary space curves with slowly varying curvature and torsion. These are very important extensions to the successful *Savage-Hutter* (SH) theory. Because of the density preserving assumption the effect of the porosity can only be accounted for in the closure statements. This is done here and its consequences are illustrated. Shock-capturing numerical schemes are used to integrate the model hyperbolic conservation system of equations in order to control spurious jumps in the mapping of the descending masses. The physical significance of the numerical simulations is discussed.

Introduction

Avalanches, debris-, mud-flows and landslides are common natural phenomena to mountain inhabitants. Accidents involving damage of property and life and devastating singular incidences have regularly occurred in the past. These are the major reasons why the study of avalanches is a topic of public concern. The *physics of the formation* of the rapid motion of a large mass of soil, gravel or snow and the *dynamics of the motion* must be understood, if the danger due to the release of a certain mass of gravel or snow should be avoided or the impact of a moving mass on the avalanche track or on obstructing build-

Jacques M. Huyghe et al. (eds), IUTAM Proceedings on Physicochemical and Electromechanical Interactions in Porous Media, 81–89.

© 2005 Springer. Printed in the Netherlands.

ings be estimated. The last few years have witnessed increased efforts devoted to the physical understanding of the avalanche formation and motion in complex topography. We present here an extended Savage-Hutter theory [10] by Pudasaini and Hutter [9] to rapid shear flows of dry granular masses in a *non-uniformly curved and twisted channel* having both *curvature and torsion*. This makes the extended model amenable to realistic snow and debris motions down arbitrary guiding topographies ([6, 9]). One prerequisite of this model is the assumption of the density preserving of the underlying continuum equations, and so the effects of the pore space are formally not accounted for. However, the constitutive equations may in an indirect way account for porous effects, and here in this paper we shall propose such an indirect dependence for the basal friction law. The equations as derived by Pudasaini and Hutter [9] remain formally the same, only the basal bed friction angle is no longer constant but now experiences a pressure dependence. We present results of numerical integrations for a particular case of the extended theory, namely for the cylindrical channel which is curved in the down-hill direction. To account for the shock phenomena a shock-capturing numerical scheme is used. The results disclose fundamental features of the dynamics of avalanches when porous effects are significant.

Model Equations

In this paper, (x, y) form a curved reference surface, where x is the coordinate along the talweg of a mountain valley, while y is the circular arc length in a cross-sectional plane perpendicular to the talweg whose value is determined by the relation $y = \varepsilon\theta z_T$, where ε is the aspect ratio between the avalanche height and the extent, θ is the azimuthal angle and z_T is the radial distance between the master curve and the talweg. The channel topography and the geometry of the avalanche in the lateral and longitudinal directions are illustrated in Figs. 1a) and 1b), respectively. As in the previous models of the *SH*-theory, Pudasaini & Hutter [9] recently formulated the balance laws of mass and momentum for curved and twisted channels in these slope fitted coordinates. The final thickness averaged non-dimensional balance laws of mass and momentum in the down-slope and cross-slope directions take the form

$$\frac{\partial h}{\partial t} + \frac{\partial}{\partial x}(hu) + \frac{\partial}{\partial y}(hv) = 0, \quad (1)$$

$$\frac{\partial}{\partial t}(hu) + \frac{\partial}{\partial x}(hu^2) + \frac{\partial}{\partial y}(huv) = hs_x - \frac{\partial}{\partial x}\left(\frac{\beta_x h^2}{2}\right), \quad (2)$$

$$\frac{\partial}{\partial t}(hv) + \frac{\partial}{\partial x}(huv) + \frac{\partial}{\partial y}(hv^2) = hs_y - \frac{\partial}{\partial y}\left(\frac{\beta_y h^2}{2}\right), \quad (3)$$

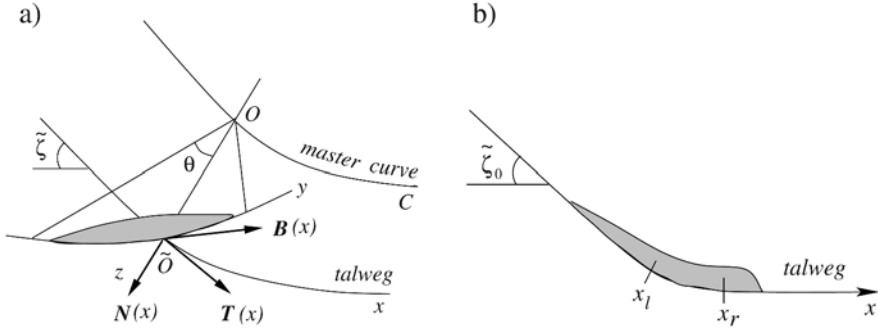


Figure 1. a) For a given value of the arc length, the avalanche domain in the lateral direction occupies a region in a circular section of a plane perpendicular to the talweg of the valley and θ is the azimuthal angle in this plane. The depth of the avalanche in this section is represented by a height function (of the avalanche) which at different positions are not parallel but radial. $O\tilde{O} = z_T$ is the radial distance between the master curve and the talweg. The lateral coordinate, y , is determined by the transformation $y = \varepsilon\theta z_T$, where ε is the aspect ratio between the avalanche height and the extent. $\{\mathbf{T}, \mathbf{N}, \mathbf{B}\}$ is the moving orthonormal unit triad following the talweg (equivalently the master curve). $\tilde{\zeta}$ is the slope angle of the talweg with the horizontal. b) Avalanche passing from the downslope region into the run-out zone in a vertical plane containing the talweg of the valley. In this picture, x_l and x_r are the left and right end points of the continuous transition between the straight inclined upper part with inclination angle $\tilde{\zeta}_0$ and horizontal run-out in the valley. For simplicity, torsion effects are not shown.

where h is the depth of the avalanche measured along the normal direction of the reference surface and the factors β_x and β_y are defined, respectively, as $\beta_x = -\varepsilon g_z K_x$, $\beta_y = -\varepsilon g_z K_y$. Net driving accelerations, s_x and s_y in the down-slope and cross-slope directions, respectively, and are given by

$$s_x = g_x - \frac{u}{|\mathbf{u}|} \tan \delta (-g_z + \lambda \kappa \eta u^2) + \varepsilon g_z \frac{\partial b}{\partial x}, \quad (4)$$

$$s_y = g_y - \frac{v}{|\mathbf{u}|} \tan \delta (-g_z + \lambda \kappa \eta u^2) + \varepsilon g_z \frac{\partial b}{\partial y}; \quad (5)$$

with $|\mathbf{u}| = \sqrt{u^2 + v^2}$. g_x , g_y and g_z are the components of the gravity acceleration along the down-slope, cross-slope and normal directions, respectively,

$$\begin{aligned} g_x &= [b_1 n_2 - b_2 n_1] / \Delta, \\ g_y &= [t_2 (n_1 \eta + b_1 \zeta) - t_1 (n_2 \eta + b_2 \zeta)] / \Delta, \\ g_z &= [t_1 (b_2 \eta - n_2 \zeta) - t_2 (b_1 \eta - n_1 \zeta)] / \Delta, \\ \Delta &= t_1 (n_2 b_3 - b_2 n_3) + t_2 (b_1 n_3 - n_1 b_3) + t_3 (n_1 b_2 - b_1 n_2), \\ \eta &= \cos(\theta + \varphi(x) + \varphi_0), \quad \zeta = \sin(\theta + \varphi(x) + \varphi_0), \quad \varphi(x) = - \int_{x_0}^x \tau(x') dx', \end{aligned} \quad (6)$$

where φ_0 is an arbitrary constant and $\varphi(x)$ accounts for the accumulation of the torsion. Also, $b = b(x, y)$ is the basal topography and the aspect ratio

ε , and the measure of curvature λ relative to the typical avalanche length, are both small numbers. (t_i) , (n_i) and (b_i) , $1 \leq i \leq 3$, are the components of \mathbf{T} , \mathbf{N} and \mathbf{B} , respectively, of the talweg with respect to the standard Cartesian basis. The first terms on the right-hand side of (4) and (5) are due to the gravity accelerations in the down- and cross-slope directions, respectively. The second terms emerge from the dry Coulomb friction and the third terms are the projections of the topographic variations along the normal direction. K_x and K_y are called the *earth pressure coefficients*. These values can be determined as functions of the internal (ϕ) and basal (δ) angles of friction [2],

$$\begin{aligned} K_{x_{act/pass}} &= 2 \sec^2 \phi \left(1 \mp \sqrt{1 - \cos^2 \phi \sec^2 \delta} \right) - 1, \\ K_{y_{act/pass}} &= \frac{1}{2} \left(K_x + 1 \mp \sqrt{(K_x - 1)^2 + 4 \tan^2 \delta} \right), \end{aligned} \quad (7)$$

where K_x , K_y are *active* during dilatational motion (upper sign) and *passive* during compressional motion (lower sign). Equations (1)–(3) constitute a *two-dimensional conservative system of equations*. These extended model equations can reproduce all previous model equations of the *SH*-theory [1, 2, 8, 11].

Given the material parameters δ and ϕ and the elevation of the basal topography, b , above the curved reference surface, equations (1)–(3) allow h , u and v to be computed as functions of space and time once appropriate initial and boundary conditions are prescribed, where h is the avalanche depth, and (u, v) are the depth-averaged velocity profiles parallel to the flow path.

Pressure Dependence of the Friction Angles

A pressure dependence of the internal angle of friction is known to represent the quantification of the pore space dependence of internal friction [3]. Such a dependence has also been observed in wall friction experiments for the bed friction angle [5, 13] of soil. So, we must assume $\delta = \delta(p)$ and $\phi = \phi(p)$, where p is the pressure. However, since the *SH*-theory has only manifested a weak dependence of the avalanche geometry on the values of ϕ , we shall ignore a pressure dependence of ϕ , so $\phi = \text{const}$. Experiments indicate a decrease of the bed friction angle with pressure [3, 5, 13], the simplest parameterisation is linear and we choose

$$\delta = \delta_0 - \frac{\delta_0 - \delta_1}{p_1} p, \quad (8)$$

in which δ_0 is the pressure independent bed friction angle and δ_1 is its value at $p = p_1$. Scaling p and p_1 according to $p = \varrho g[H]\bar{p}$, $p_1 = \varrho g[H_1]$, equation (8) takes the form

$$\delta = \delta_0 \left\{ 1 - \frac{[H]}{[H_1]} \frac{\delta_0 - \delta_1}{\delta_0} \bar{p} \right\}, \quad (9)$$

in which \bar{p} at the base is given by $\bar{p} = (-g_z + \lambda\kappa\eta u^2) h$ is the dimensionless pressure. Formula (9) is remarkable in the following respect: the pressure dependent term is not scale invariant because it involves the factor $[H]/[H_1]$. We shall choose the following notation and study its influence upon the avalanche motion

$$\Pi = \frac{[H]}{[H_1]} \frac{\delta_0 - \delta_1}{\delta_0}. \quad (10)$$

Numerical Integration

Due to the hyperbolicity and nonlinearity of the model equations, associated with possible shocks in granular flows over non-trivial topography, numerical solutions with the traditional high-order accuracy methods are often accompanied with numerical oscillations of the depth profile and velocity field. This usually leads to numerical instabilities unless these are properly counteracted by a sufficient amount of artificial numerical diffusion. Here, a non-oscillatory central (NOC) difference scheme with a *total variation diminishing* (TVD) limiter for the cell reconstruction is employed, see e.g. [4], [12]; we obtain numerical solutions without spurious oscillations. In order to test the model equations, we consider an ideal mountain subregion in which the talweg is defined by the slope function

$$\tilde{\zeta}(x) = \begin{cases} \tilde{\zeta}_0, & 0 \leq x \leq x_l, \\ \tilde{\zeta}_0 \left(\frac{x_r - x}{x_r - x_l} \right), & x_l \leq x \leq x_r, \\ 0, & x \geq x_r, \end{cases} \quad (11)$$

where $\tilde{\zeta}_0 = 50^\circ$ is the straight upper part of the talweg which merges into a horizontal run-out as shown in Fig. 1b), and $x_l = 13$ and $x_r = 17$ are the initial and the final points of the continuous transition. The azimuthal angle $\theta \in [-17.9^\circ, 17.9^\circ]$, which accounts for a (shallow) circular variation of the bed topography in the lateral direction, and the non-dimensional distance $z_T = 16$ corresponding to $y \in [-5, 5]$, Fig. 1a). A hemi-spherical cap with radius $R_0 = 1.85$ holding the granular material in it is placed at $(x_0, y_0) = (5.0, 0.0)$ of the chute and suddenly released. The phenomenological parameters are chosen as $\delta_0 = 26.5^\circ$ and $\phi = 37^\circ$ which correspond to *Vestolen*, a sort of plastic particles of lens-like shape and 4 mm diameter on *drawing paper*. The values of ε and λ are taken to be unity. For more detail, see [8].

Discussion

Results for $\Pi = 0$

Figure 2a) depicts the evolution of the avalanching body at 10 non-dimensional time steps in a vertical plane containing the talweg of the valley. The first four panels clearly show that once the cap is opened, the avalanche accelerates and spreads rapidly in the downslope direction due to the channelling effect in the cross-slope direction, the gravity and dilatation. Although the front is descending rapidly, the tail moves a bit upward (second panel) because of the fluidisation of the mass and the support of the material from the down-hill (front) side. At $t = 4$ the front reaches the transition zone and the tail also starts to move downward. At $t = 6$, the front part of the body has fully reached the transition zone. Therefore the mass at the front is contracting due to the effect of the passive earth pressure coefficient, but the mass in the tail is still extending. At $t = 7$, the deposition of the mass starts in the vicinity of the lower part of the transition zone. Owing to the effect of the curvature, the flowing body starts contracting. For $t > 8$, a steep surface (height) gradient starts to develop on the tail side of the avalanche. Although the front of the body is almost in stillstand the mass from the tail is still continuously flowing down and deposited on the tail side of the body. This leads to the shock front moving upstream. The physical explanation for this is that from the front there is a strong resistive force from the bed which prevents the body from further advecting. So, whatever comes from the upper part of the channel, it must be deposited at the back side of the body. Consequently, the mass body must extend upward. The last four panels show the continuous development of the upcoming shock, while there is no simultaneous motion at the front.

Scale effects due to the pressure dependence of δ

As an example, the value of the parameter Π is taken to be 0.4 which corresponds to the reference values $\delta_1 = 20^\circ$ and $H/H_1 = 1.6$. Figure 2b) represents a series of numerical results for the same data as in Fig. 2a) but with the pressure dependent bed friction angle as given by (9). The granular body is more fluidised since this angle decreases. Consequently, the run-out distance is larger and the height of the deposit is shallower compared with the constant bed friction angle. The last panels indicate that the front of the avalanche for variable bed friction angle is about 20% farther away than for a constant bed friction angle. Similarly, the maximum pile height of the final deposit for variable bed friction angle is about 25% less than in the previous case. These conclusions are more or less applicable right after the release of the mass, but the comparison is more pronounced as time elapses. Due to the excess fluidity, the formation of the shock is weaker in the last four panels.

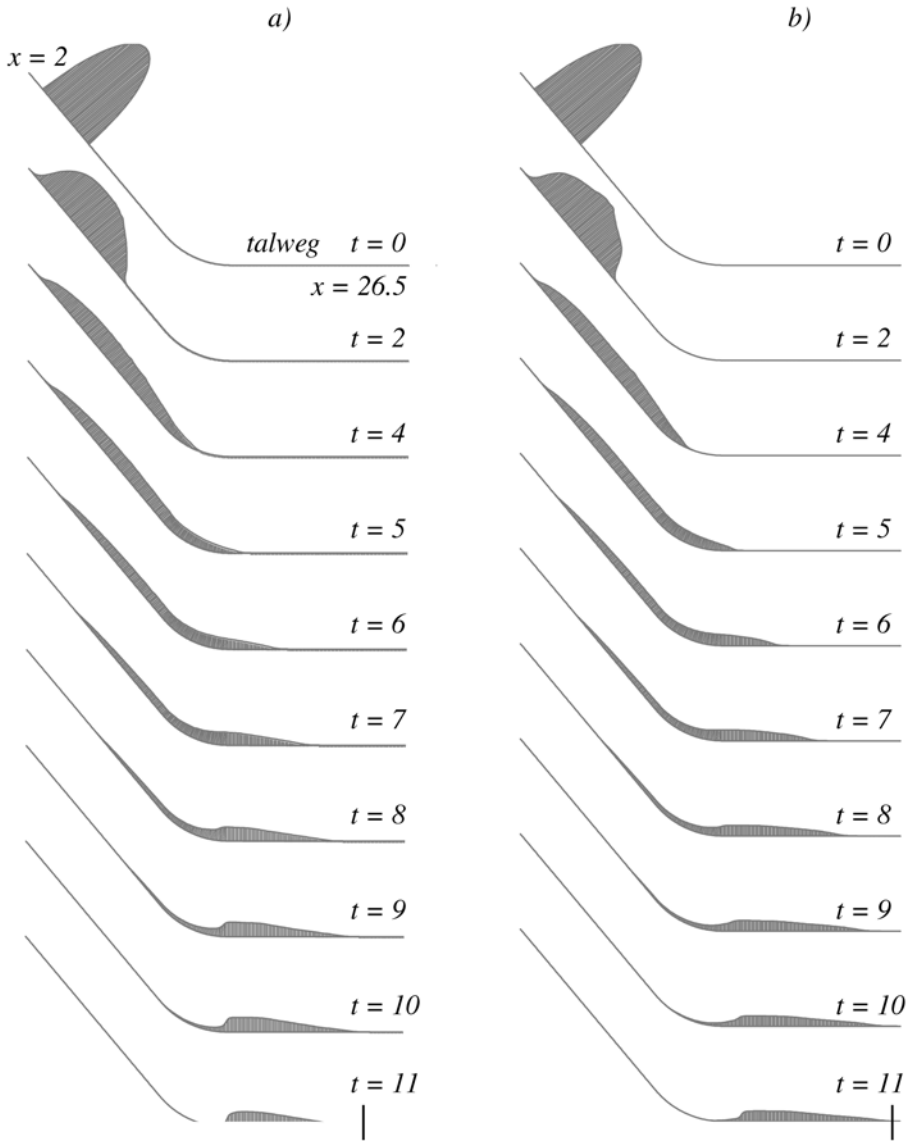


Figure 2. a) A series of numerical simulations of avalanche motion with internal and basal friction angles $\phi = 37^\circ$ and $\delta = 26.5^\circ$, for different time points. The avalanche thickness is plotted using curvilinear coordinate x which runs from left to right along the talweg of length 26.5. We do not explicitly see here the volume preserving of the material since we have plotted only the central section of the avalanche in the vertical plane that contains the talweg. The remaining mass goes in the sidewise direction. b) Same as in a) but with the variable bed friction angle. In this case the avalanche body is more fluidised, the travel distance (indicated by $|$ in the last panels) increases and the height of the deposit decreases considerably.

Conclusion

We have considered the extended Savage-Hutter theory by Pudasaini and Hutter [9] and its simulations using the NOC difference scheme with TVD limiter which gives high resolution of shock solutions without any spurious oscillations near the discontinuities. The simulations presented here demonstrate the fact that the inclusion of the pore pressure via the bed friction angle considerably influences the dynamics of avalanches. The increase in pressure decreases the bed friction which leads to the effective fluidisation of the descending mass resulting to a remarkably larger run-out zone. Further tasks may be the verification of these results by field or laboratory events of avalanches and debris.

Acknowledgments

We thank W. Fellin from the Institute for Geotechnique and Tunnel Engineering, University of Innsbruck, Austria for the discussions concerning the pressure dependences of the internal and bed friction angles, ϕ and δ , respectively. Financial support was provided by the Deutsche Forschungsgemeinschaft through the project - *Hu 412/33-1: "Avalanche Dynamics in Complex Topography"*

References

- [1] Gray, J.M.N.T., Wieland, M. and Hutter, K. (1999) Gravity-driven free surface flow of granular avalanches over complex basal topography. *A Proceedings of Royal Society London* **455**, 1841-1874
- [2] Hutter, K., Siegel, M., Savage, S.B. and Nohguchi, Y. (1993) Two-dimensional spreading of a granular avalanche down an inclined plane. I. Theory. *Acta Mech.* **100**, 37-68
- [3] Lambe, T.W. and Whitman, R.V. (1979) *Soil Mechanics*, John Wiley and Sons
- [4] LeVeque, R.J. (1992) *Numerical Methods for Conservation Laws*. Second edition, Birkhäuser: Basel/Boston/Berlin.
- [5] Potyondy, J.G. (1961) Skin friction between soils and construction materials. *Geotechnique* **11**, 339-353
- [6] Pudasaini, S.P., Wang, Y. and Hutter, K. (2004) Dynamics of Avalanches Along General Mountain Slopes. *Annals of Glaciology*. **38**, in press
- [7] Pudasaini, S.P. and Hutter, K. (2003) Granular Avalanche Model in Arbitrarily Curved and Twisted Mountain Terrain: A Basis for Extension to Debris Flow. In: Dieter Rickenmann and Cheng-lung Chen (Eds.) *Debris-Flow Hazards Mitigation: Mechanics, Prediction and Assessment*, **1**, 491-502, Millpress.
- [8] Pudasaini, S.P. (2003) Dynamics of Flow Avalanches Over Curved and Twisted Channels: Theory, Numerics and Experimental Validation. Ph.D. thesis, Department of Applied Mechanics, Darmstadt University of Technology, Germany
- [9] Pudasaini, S.P. and Hutter, K. (2003) Rapid Shear Flows of Dry Granular Masses Down Curved and Twisted Channels. *J. Fluid Mech.* **495**, 193-208

- [10] Savage, S.B. and Hutter, K. (1989) The motion of a finite mass of granular material down a rough incline. *J. Fluid Mech.* **199**, 177-215
- [11] Savage, S.B. and Hutter, K. (1991) Dynamics of avalanches of granular materials from initiation to runout. Part I: Analysis. *Acta Mech.* **86**, 201-223
- [12] Tai, Y.-C. (2000) Dynamics of Granular Avalanches and their Simulations with Shock-Capturing and Front-Tracking Numerical Schemes. Ph.D. thesis, Department of Applied Mechanics, Darmstadt University of Technology, Germany
- [13] Tejchman, J. and Wu, W. (1995) Experimental and numerical study of sand-steel interfaces. *International Journal for Num. Math. in Geomechanics* **19**, 513-536

A MULTIPHASE APPROACH FOR THE ANALYSIS OF HYGRO-THERMO- CHEMO-MECHANICAL INTERACTIONS IN CONCRETE AT EARLY AGES AND AT HIGH TEMPERATURE

Dariusz Gawin,¹ Francesco Pesavento² and Bernard A. Schrefler³

¹*Department of Building Physics and Building Materials
Technical University of Lodz, Poland*

gawindar@ck-sg.p.lodz.pl

²*Department of Structural and Transportation Engineering
University of Padova, Italy*

pesa@caronte.dic.unipd.it

³*Department of Structural and Transportation Engineering
University of Padova, Italy*

bas@caronte.dic.unipd.it

Abstract A fully coupled model of hygro-thermo-chemo-mechanical phenomena in concrete is presented. A mechanistic approach has been used to obtain the governing equations, by means of the hybrid mixture theory. The final equations are written in terms of the chosen primary and internal variables. The model takes into account coupling between hygral, thermal, chemical phenomena (hydration or dehydration), and material deformations, as well as changes of concrete properties, caused by these processes, e.g. porosity, permeability, stress-strain relation, etc.

Keywords: heat and mass transport, concrete deformations, high temperature, hydration.

Introduction

Hygro-themo-chemo-mechanical behaviour of concrete is of great practical importance in many fields of civil engineering. Modelling these phenomena, especially in fresh concrete structures or concrete elements exposed to fire, is a complex problem. Several non-linear phenomena, like heat and mass sources associated with hydration or dehydration processes, phase changes, hysteresis of sorption isotherms, material properties dependent on moisture content, tem-

perature and gas pressure, and some inherent couplings between chemical, hygro-thermal and material deformation processes should be taken into account. Usually a phenomenological approach is used in modelling of concrete, e.g. [1, 2], often omitting its multiphase nature. In this paper we present a general, mechanistic model which allows for numerical analysis of concrete, both at early ages and at high temperature, considering hygro-thermal and chemical processes, and material deformations, as well as interactions between them and several non-linearities of the material properties.

Mathematical Model

Concrete is modeled as a multi-phase material, which is assumed to be in thermodynamic equilibrium state locally. The voids of the skeleton are filled partly with liquid water and partly with a gas phase (mixture of dry air and vapour). The liquid phase consists of bound water, which is present in the whole range of moisture content, and capillary water, which appears when water content exceeds the upper limit of the hygroscopic region, S_{ssp} . Moisture content is described here by the degree of saturation with water, S_w . The gas phase is a mixture of dry air and water vapor (condensable constituent), and is assumed to be an ideal gas. The chosen primary variables of the model are: gas pressure p^g , capillary pressure $p^c = p^g - p^w$, (p^w denotes water pressure) temperature T , displacement vector of the solid matrix \mathbf{u} . The internal variables are degree of cement hydration Γ_{hydr} , mechanical and thermo-chemical damage parameters, d and V respectively. Physical explanation of our model, including energy and mass transport mechanisms considered, can be found in [3]-[10].

The mathematical model consists of four balance equations. These equations have been obtained in [3] by use of Volume Averaging Theory also called hybrid mixture theory, [11]-[13]. The mass balance of the dry air includes both diffusive and advective components of the mass fluxes,

$$\begin{aligned} -n \frac{\partial S_w}{\partial t} - \beta_s (1 - n) S_g \frac{\partial T}{\partial t} + S_g \text{div} \mathbf{v}^s + \frac{S_g n}{\rho^a} \frac{\partial \rho^a}{\partial t} + \frac{1}{\rho^a} \text{div} \mathbf{J}_g^a + \\ + \frac{1}{\rho^a} \text{div} (n S_g \rho^a \mathbf{v}^{gs}) + \frac{(1 - n) S_g}{\rho^s} \frac{\partial \rho^s}{\partial \Gamma_{hydr}} \frac{\partial \Gamma_{hydr}}{\partial t} = \frac{\dot{m}_{hydr}}{\rho^s} S_g \end{aligned} \quad (1)$$

and has been summed with the solid skeleton mass balance equation in order to eliminate the time derivative of porosity. Because of this, some terms related to thermal dilatation and mechanical deformation of the skeleton (the second and third terms on L.H.S.), as well as the mass source (sink) resulting from chemical reactions of the skeleton (hydration or dehydration) appear in (1). Symbol t denotes time, \dot{m}_{hydr} mass source (or sink) related to the hydration (or dehydration) process, β_s cubic thermal expansion coefficient of the solid skeleton, \mathbf{v}_{gs} gas velocity relative to the solid skeleton, \mathbf{J}_g^a - diffusive flux of the

dry air; the subscripts and superscripts: s , w , a , v and g are related to solid, liquid water, dry air, water vapor and gas phase, respectively.

The mass balances of liquid water and of vapor, summed together to eliminate the source term related to phase changes (evaporation-condensation or adsorption-desorption), form the mass balance equation of water species, [3],

$$\begin{aligned}
& n(\rho^w - \rho^v) \frac{\partial S_w}{\partial t} - \beta_{swg} \frac{\partial T}{\partial t} + (\rho^v S_g + \rho^w S_w) \operatorname{div} \mathbf{v}^s + S_g n \frac{\partial \rho^v}{\partial t} + \\
& \quad + \operatorname{div} \mathbf{J}_g^v + \operatorname{div} (n S_g \rho^v \mathbf{v}^{gs}) + \operatorname{div} (n S_w \rho^w \mathbf{v}^{ws}) + \quad (2) \\
& + \frac{(1-n)(S_g \rho^v + \rho^w S_w)}{\rho^s} \frac{\partial \rho^s}{\partial \Gamma_{hydr}} \frac{\partial \Gamma_{hydr}}{\partial t} = \frac{\rho^v S_g + \rho^w S_w - \rho^s}{\rho^s} \dot{m}_{hydr}
\end{aligned}$$

where $\beta_{swg} = \beta_s(1-n)(S_g \rho^v + S_w \rho^w) + n\beta_w S_w \rho^w$, \mathbf{v}^{ws} denotes water velocity relative to the solid skeleton. As before, also these balance equations are summed up with the solid phase mass conservation equation in order to eliminate the time derivative of porosity.

The enthalpy conservation equation of the multiphase medium, obtained from the sum of the appropriate balance equations of the constituents includes the heat effects due to phase changes and hydration (dehydration) process, as well as the convectonal and latent heat transfer,

$$\begin{aligned}
(\rho C_p)_{ef} \frac{\partial T}{\partial t} + (\rho_w C_p^w \mathbf{v}^{ws} + \rho_g C_p^g \mathbf{v}^{gs}) \cdot \operatorname{grad} T - \operatorname{div} (\lambda_{ef} \operatorname{grad} T) = \quad (3) \\
= -\dot{m}_{vap} \Delta H_{vap} + \dot{m}_{hydr} \Delta H_{hydr},
\end{aligned}$$

where $(\rho C_p)_{ef}$ is effective thermal capacity, C_p isobaric specific heat, λ_{ef} effective thermal conductivity, ΔH_{vap} and ΔH_{hydr} specific enthalpies of the phase change and the hydration (dehydration) process, \dot{m}_{vap} mass source or sink of vapor related to the evaporation (desorption) or condensation (adsorption) process. In the hygroscopic moisture range, S_{ssp} , the terms in equations (2) and (3), which describe the liquid phase, concern the bound water, thus ΔH_{vap} should be substituted by ΔH_{ads} , i.e. enthalpy of adsorption. In equation (3) the phase change term has been substituted using the liquid water mass balance equation.

Introducing Bishop's stress tensor $\boldsymbol{\sigma}''$, called also effective stress tensor, [3], responsible for all the deformations of a concrete, the linear momentum conservation equation of the whole medium is given by, [8, 14],

$$\operatorname{div} (\boldsymbol{\sigma}'' - \alpha \mathbf{I} p^s) + [(1-n)\rho^s + n S_w \rho^w + n(1-S_w)\rho^g] \mathbf{g} = 0 \quad (4)$$

where \mathbf{I} is unit, second order tensor, α Biot's coefficient, \mathbf{g} acceleration of gravity. Pressure in the solid phase p^s is given by the following formula [14],

$$p^s = p^g - \chi_s^{ws} p^c \quad (5)$$

where χ_s^{ws} means the solid surface fraction in contact with the wetting film, depending on saturation degree, S_w , of the pores.

The evolution equation for the degree of cement hydration Γ_{hydr} , appearing in (2), has the following form [10, 15],

$$\frac{\partial \Gamma_{hydr}}{\partial t} = \tilde{A}_\Gamma(\Gamma_{hydr}) \cdot \beta_\varphi(\varphi, \Gamma_{hydr}) \cdot \exp\left(-\frac{E_a}{RT}\right) \quad (6)$$

where \tilde{A}_Γ is hydration degree-related, normalized affinity, β_φ an experimental coefficient describing effect of relative humidity on the hydration rate, E_a activation energy of hydration, and R universal gas constant.

When the dehydration process at high temperature is analyzed, because of its irreversible nature, one can assume, [7], that,

$$\Gamma_{hydr} = \Gamma_{hydr}(T_{max}) \quad (7)$$

where $T_{max}(t)$ is the highest temperature reached by the concrete till time instant t .

At elevated temperature a joint action of thermo-chemical concrete degradation, V , accounting for high temperature related micro-cracking and dehydration, and external load-related cracking, d , is described by the total damage parameter, D , given by [7],

$$D = 1 - \frac{E(T)}{E_0(T)} \frac{E_0(T)}{E_0(T_o)} = 1 - (1 - d) \cdot (1 - V) \quad (8)$$

where E and E_0 are values of Young's modulus of the mechanically damaged and undamaged concrete, T and T_o mean the actual and initial values of temperature.

The evolution equation for thermo-chemical damage, $V(t)$, which should be experimentally determined, has the following form,

$$V = V(T_{max}) \quad (9)$$

The evolution equation for mechanical damage, d , (both for concrete at early ages and at high temperature) is assumed according to the non-local, isotropic damage theory by Mazars and Pijaudier-Cabot [16],

$$d = d(\tilde{\epsilon}) \quad (10)$$

where $\tilde{\epsilon}$ is equivalent strain.

The governing equations (1) - (10) are completed by an appropriate set of state and thermodynamic equations as well as boundary conditions and constitutive relationships. The latter ones express some inherent couplings between chemical and hygro-thermal phenomena and medium deformations.

For sake of brevity, only general forms of the most important relations are given below.

For concrete at early ages the most important is the effect of chemical processes on its transport and strength properties, e.g. porosity $n=f(\Gamma_{hydr})$, intrinsic permeability $k=f(\Gamma_{hydr},d)$, and mass source related to the hydration $\dot{m}_{hydr} = f(\dot{\Gamma}_{hydr})$. Creep of concrete is modeled by means of the solidification theory [17], where the degree of cement hydration Γ_{hydr} is used as the volume fraction of the load-bearing portion of hydrated cement.

For concrete at high temperature the most important is the effect of cracking and dehydration process on the material properties, e.g. porosity $n=f(\Gamma_{hydr})$, intrinsic permeability $k=f(\Gamma_{hydr},D,T)$, and its deformations. Irreversible part of strains and so called thermal creep are expressed as functions of thermochemical damage parameter V , [8].

The governing equations of the model are discretized in space by means of the finite element method [3, 18], and in time through a fully implicit finite difference scheme (backward difference) [18], resulting in the nonlinear equation set of the following form, [4, 7],

$$\mathbf{C}(\mathbf{x}_{n+1}) \frac{\mathbf{x}_{n+1} - \mathbf{x}_n}{\Delta t} + \mathbf{K}(\mathbf{x}_{n+1}) \mathbf{x}_{n+1} - \mathbf{f}(\mathbf{x}_{n+1}) = \mathbf{0} \quad (11)$$

where $\mathbf{x}^T = \{\bar{\mathbf{p}}^g, \bar{\mathbf{p}}^c, \bar{\mathbf{T}}, \bar{\mathbf{u}}\}$, n is the time step number and Δt the time step length, and the nonlinear (matrix) coefficients $\mathbf{C}(\mathbf{x})$, $\mathbf{K}(\mathbf{x})$ and $\mathbf{f}(\mathbf{x})$ are given in detail in [7].

The presented model has been successfully applied for solution of several 1-D and 2-D problems, concerning performance of concrete structures at high temperature, e.g. [4]-[8], and at early ages [9, 10].

Conclusions

A finite element model of concrete based on a mechanistic approach has been presented. Concrete is considered as multiphase porous visco-elastic material in which phase changes, different fluid flows and non-linearities with respect to temperature, moisture content and hydration degree have been taken into account. The particular approach permits to consider the different coupled phenomena, which take place in concrete during maturing and when it is exposed to high temperature. Further research on introducing a direct coupling between hydration degree and material creep described by the solidification theory is in progress, as well as the development of fully coupled thermal creep model.

Acknowledgements

This work was carried out in the framework of the UE project MÆCENAS (Modelling of Ageing in Concrete Nuclear Power Plant Structures), No. FIKS-CT-2001-00186.

References

- [1] Bazant, Z.P. (ed.) (1988) *Mathematical Modeling of Creep and Shrinkage of Concrete*, Wiley, Chichester
- [2] Bazant, Z.P. and Kaplan, M.F. (1996) *Concrete at High Temperatures: Material Properties and Mathematical Models*, Longman, Harlow
- [3] Lewis, R.W. and Schrefler, B.A. (1998) *The Finite Element Method in the Static and Dynamic Deformation and Consolidation of Porous Media*, 2nd ed., Wiley, Chichester
- [4] Gawin, D., Majorana, C.E. and Schrefler, B.A. (1999) Numerical analysis of hygro-thermic behaviour and damage of concrete at high temperature. *Mech. Cohes.-Frict. Mat.* **4**, 37-74
- [5] Gawin, D., Pesavento, F. and Schrefler, B.A. (2002) Simulation of damage – permeability coupling in hygro-thermo-mechanical analysis of concrete at high temperature, *Comm. Num. Meth. Engrg.* **18**, 113-119
- [6] Gawin, D., Pesavento, F. and Schrefler B.A. (2002) Modelling of hygro-thermal behaviour and damage of concrete at temperature above critical point of water. *Int. J. Numer. Anal. Meth. Geomech.* **26**, 537-562
- [7] Gawin, D., Pesavento, F. and Schrefler, B.A. (2003) Modelling of hygro-thermal behaviour of concrete at high temperature with thermo-chemical and mechanical material degradation. *Comput. Methods Appl. Mech. Engrg.* **192**, 1731-1771
- [8] Gawin, D., Pesavento, F. and Schrefler, B.A. Modelling of deformations of high strength concrete at elevated temperatures, submitted for publication
- [9] Gawin, D., Pesavento, F. and Schrefler, B.A. (2002) A multiphase approach in the analysis of behavior of concrete as porous-viscous material, H.A. Mang, F.G. Rammerstorfer, J. Eberhardsteiner (eds), <http://wccm.tuwien.ac.at> Proc. of WCCM V, Vienna
- [10] Gawin, D., Pesavento, F. and Schrefler, B.A. Hygro-thermo-chemo-mechanical modelling of concrete at early ages, in preparation
- [11] Hassanizadeh, S.M. and Gray, W.G. (1979) General conservation equations for multiphase systems: 1. Averaging procedure. *Adv. Water Resources* **2**, 131-144.
- [12] Hassanizadeh, S.M. and Gray, W.G. (1979) General conservation equations for multiphase systems: 2. Mass, momenta, energy and entropy equations. *Adv. Water Resources* **2**, 191-203
- [13] Hassanizadeh, S.M. and Gray, W.G. (1980) General conservation equations for multiphase systems: 3. Constitutive theory for porous media flow, *Adv. Water Resources* **3**, 25-40
- [14] Gray, W.G. and Schrefler, B.A. (2001) Thermodynamic approach to effective stress in partially saturated porous media, *Eur. J. Mech. A/Solids* **20**, 521-538
- [15] Ulm, F.-J. and Coussy, O. (1995) Modeling of thermo-chemo-mechanical couplings of concrete at early ages. *J. Eng. Mech. ASCE* **121**(7), 785-794

- [16] Mazars, J. and Pijaudier-Cabot, J. (1989) Continuum damage theory – Application to concrete. *J. of Eng. Mechanics ASCE* **115**(2), 345-365
- [17] Bazant, Z.P. and Prasanna, S. (1989) Solidification theory for concrete creep. I: Formulation, II: Verification and Application, *J. Eng. Mech. ASCE* **115**(8), 1691-1725
- [18] Zienkiewicz, O.C. and Taylor, R.L. (1989) *The Finite Element Method*, Vol. 1, 4th edn., Mc Graw Hill, London

STUDY OF DRYING SHRINKAGE CRACKING BY LATTICE GAS AUTOMATON AND ENVIRONMENTAL SCANNING ELECTRON MICROSCOPE

Dragana Jankovic

Delft University of Technology, Delft, The Netherlands

D.Jankovic@ct.tudelft.nl

Abstract Numerical modelling of moisture flow, drying shrinkage and crack phenomena in cement microstructure, by coupling a Lattice Gas Automaton and a Lattice Fracture Model, highlighted the importance of a shrinkage coefficient (α_{sh}) as the most significant parameter for achieving realistic numerical results. Therefore, experiments on drying of cement paste samples were conducted in an Environmental Scanning Electron Microscope to find the shrinkage coefficient relating shrinkage deformations and moisture contents. Illustration of moisture flow in the heterogeneous sample by the Lattice Gas Automaton analysis is also presented.

Keywords: Lattice Gas Automaton, Lattice Fracture Model, Environmental Scanning Electron Microscope

Introduction

The focus of our current research is on understanding of the drying shrinkage and cracking phenomenon in porous cement-based composites through modelling and experimentation. The goal is to find the causes of early age cracks in order to improve the material microstructure. Moisture flow modelling is done using a modified Lattice Gas Automaton (LGA), whereas cracking is simulated using the Lattice Fracture Model (LFM) [1]. The modelling is supported by recent experimental observations of drying shrinkage cracking in model concrete, using an Environmental Scanning Electron Microscope (ESEM) [2],[3] fluorescent microscopy and Acoustic Emission (AE) monitoring [4], and measurements of moisture profiles during drying by Nuclear Magnetic Resonance (NMR) [3],[5]. Drying tests conducted in the ESEM were used to get a better understanding of the shrinkage process. The ESEM test results were analyzed by means of the digital image correlation [2] in the

Jacques M. Huyghe et al. (eds), IUTAM Proceedings on Physicochemical and Electromechanical Interactions in Porous Media, 99–107.

© 2005 Springer. Printed in the Netherlands.

program Vic-2D, to find differential displacements and strains due to relative humidity variations. These measurements should lead to the determination of a moisture dependent shrinkage coefficient, which is the key-parameter in the numerical model.

Link between Drying Experiment in the ESEM and Numerical Simulation

Moisture flow due to evaporation from young, porous cement paste causes early volume changes in the complex, yet not completely known, process of drying shrinkage. Non-uniform shrinkage in the heterogeneous early age cement microstructure may induce stresses that result in microcracks. We believe that, although re-wetting is usually applied, as early age curing in concrete structures, microcracks remain open [3]. They become the weakest spots in the cement microstructure, influencing together with eigenstresses, the mechanical properties of concrete and long term durability of the structures in the presence of mechanical load [6]. This especially concerns the porous, bond zone between aggregate and cement paste, intensively researched in 1960s [7], [8]. In the formulation of the shrinkage law [9] (Eq. 1), the differential shrinkage deformations $\Delta\epsilon_{sh}$ are assumed to depend on the shrinkage coefficient α_{sh} and moisture content as follows:

$$\Delta\epsilon_{sh} = \alpha_{sh}\Delta h = \alpha_{sh}(E_l - E_L), \quad (1)$$

where E_l is evaporated water and E_L is total free water, and $\Delta\epsilon_{sh}$ represents the difference in the deformations between the two subsequent steps. The value of α_{sh} is found to be constant, provided the equilibrium relative humidity (RH) is reached in the cement paste and is in the range of 40% and 100% [9]. However, the relation between shrinkage deformations and moisture content below 40% RH is not known. In order to find this relation, a drying procedure, including casting, polishing and curing of thin cement paste samples (size 10 x 10 x 1 mm³), was developed [2] and drying to low relative humidity (20%) was performed in the ESEM.

ESEM Tests

The moisture content of samples, in equilibrium, in the ESEM is varied at constant temperature (10°C), while lowering the pressure in the ESEM chamber from 9 torr to 2 torr. At the same time, relative humidity varies from 100% to 20%. The created chamber climate induces evaporation of the unbound (free) water in the cement paste (CP) samples without or with an embedded aggregate (to model simple concrete). It has been observed that curing conditions, sample age, water/cement (w/c) ratio, the presence of an aggregate, as well as the value of the RH, gives rise to different drying behaviour of the

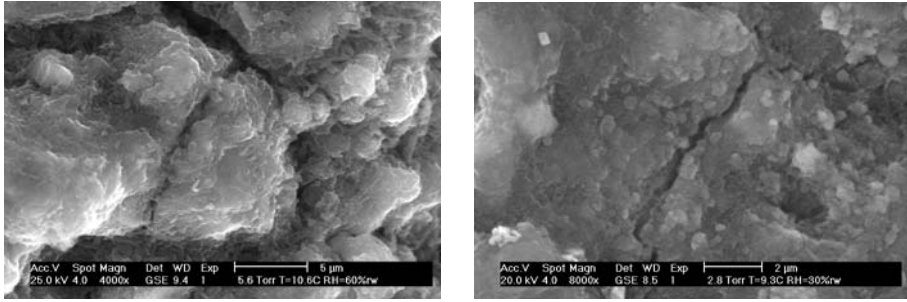


Figure 1. Microcracks in pure cement paste (CP) samples at 7 days (left); crack noticed after re-wetting to 60% RH and at 51 days (right); crack noticed after re-wetting to 30% RH.

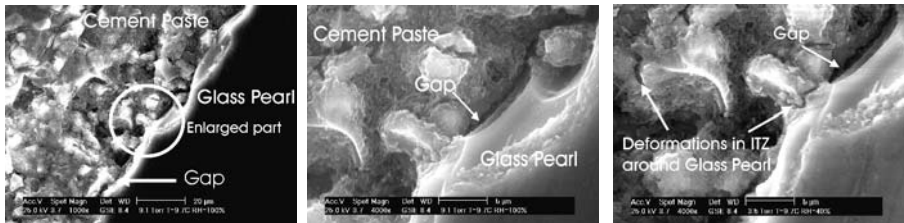


Figure 2. Drying shrinkage images of 32-days old CP with aggregate (glass pearl). Images are taken with GSE detector: a gap is observed near the obstacle at (a) 100% RH (left). Owing to the non-uniform shrinkage, deformations in the bond zone (ITZ) are clearly visible at high magnification, in the matrix during drying from (b) 100% (middle) to (c) 40% RH (right).

samples. The weight loss due to water evaporation was measured on unpolished samples at three stages: at the fresh state (after 5 min of mixing), after 1 day, and after 7 days. The total weight loss was 11% after 7 days. This is in a good agreement with the 12% moisture loss reported by L'Hermite [9], where however different drying methods and sizes of samples had been used. Observations of a single sample spot in the ESEM have shown that, under these drying conditions, the CP samples deformed. The deformations were more significant in wet cured samples than in dry cured ones. Larger deformations as well as microcracks developed in the wet cured cement paste samples of ages ranging from a minimum of 4 days, to a maximum of 51 days, both in samples with or without an aggregate (Fig. 1).

In the cement paste samples with an embedded aggregate, circumferential gaps, approximately $1 \mu\text{m}$ wide, sometimes emerged between aggregate (glass pearl) and CP prior to the drying tests. These gaps are enlarged due to drying in Fig. 2.

The existing gap could result from the sample preparation, but testing of the samples at different ages proved the age influence. We can assume that, at the start of hydration, CP and aggregate stick together. They are practically

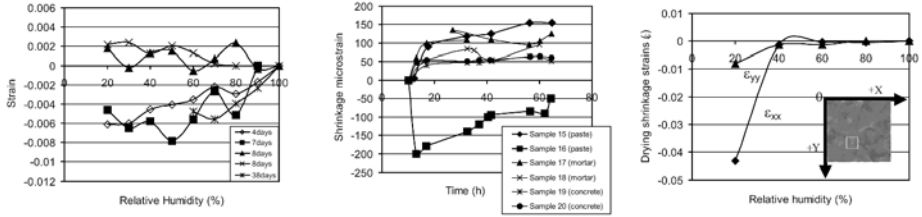


Figure 3. (left) Drying shrinkage strains in wet cured cement paste samples after drying at different RH, (middle) drying shrinkage in time (unpublished results from the tests at DTU, Denmark), (right) drying shrinkage strains (ϵ_{xx} and ϵ_{yy}) of 32 days old cement paste sample with a glass pearl inclusion.

“glued” by the water film on the aggregate surface, which is formed in the mixing process and still present at early age. There is no gap in the 4-5 days old CP sample. As the aging of the samples continues (32 days), the process of hydration slows down. Shrinkage deformation that develops at the sample edges, is probably a product of the inner desiccation, caused by hydration. When the early shrinkage begins the smoothness of the obstacle surface and consequent low adhesion may only contribute to the gap formation around the obstacle (Fig. 2). Since in the ESEM the whole $10 \times 10 \text{ mm}^2$ surface of a specimen cannot be observed at the same time during drying, it is not possible to draw conclusions about the exact RH value that is critical for crack growth.

To calculate the shrinkage coefficient (α_{sh}), digital image correlation analysis is used to infer the drying deformations (strains) due to the changes in relative humidity from the ESEM tests [2],[10]. It has been observed that the relation between plane deformations (swelling or shrinkage) and variations in RH, depends on the age of the cement paste. In very young CP samples, swelling occurred (Fig. 3a), while samples mostly older than 28 days demonstrated shrinkage, independently of the presence of a single aggregate.

Besides the mentioned tests, calculation of the shrinkage coefficient following Equation 1 demands additional ESEM tests to be performed. The procedure would be to save several digital images (not just one as was done in the previous experiments) during the equilibrium time at every relative humidity (chamber relative humidity equals relative humidity of CP sample), in a number of sequential steps, in order to relate deformations and drying time.

The moisture dependent shrinkage coefficients resulting from Eq. 1, are used as input in the coupled model for drying and cracking of virtual CP samples [1]. Cracking is caused by the “moisture load”, applied in the finite element Lattice Fracture Model (LFM), as an axial “eigen” force F as follows:

$$F_{sh} = \Delta\sigma_{sh}A = \Delta\epsilon_{sh}EA = \alpha_{sh}\Delta hEA, \quad (2)$$

where Δh is a moisture content, E is Young's modulus of concrete, assumed a constant throughout the analysis and A is a cross sectional area of a beam element in the LFM.

The moisture content Δh is obtained from numerical simulations with the Lattice Gas Automaton (LGA). A two dimensional isotropic lattice gas, i.e. a modified FHP (Frisch-Hasslacher-Pomeau) model suggested in the 80s [11] is used for mimicking moisture flow. Due to the relatively simple input and allowance of complex boundary conditions in porous concrete, the LGA turned out to be very suitable in comparison with other numerical models.

To simulate sample drying, the LGA model removes particles in the course of time [1]. The density, i.e. the number of particles per node, changes since particles move from one node to another and accordingly change relative humidity of the sample

Lattice Gas Automaton, FHP Model

The LGA is a variant of a cellular automaton, introduced as an alternative numerical approximation to the partial differential equation of Navier-Stokes and the continuity equations, whose analytical solution leads to the macroscopic approach of fluid dynamics. The microscopic behavior of the LGA has been shown to be very close to the Navier-Stokes (N-S) equations for incompressible fluids at the macroscopic level.

In order to bridge the gap between the discretized micro- and macro-worlds, averaging of the variables is necessary. Macroscopic variables in the N-S equation, are the density ρ and the momentum \mathbf{I} , which are functions of the lattice space vector \mathbf{r} and time t . The local density ρ is the summation of the average number of particles travelling along each of six (hexagonal) directions, with velocity \mathbf{c}_i . Multiplication of the density ρ by the velocity vector \mathbf{u} equals linear momentum ($\mathbf{I} = \rho\mathbf{u}$). Boolean algebra is applied for the expressions of the discretized variables density and momentum, respectively, as follows:

$$\rho(\mathbf{r}, t) = \sum_i N_i(\mathbf{r}, t) \quad (3)$$

$$\mathbf{I} = \rho(\mathbf{r}, t)\mathbf{u}(\mathbf{r}, t) = \sum_i \mathbf{c}_i N_i(\mathbf{r}, t) \quad (4)$$

where $\rho(\mathbf{r}, t)$ is the density per node, \mathbf{u} is the mean velocity, ($\mathbf{I} = \rho\mathbf{u}$) is the momentum, \mathbf{c}_i is the velocity of a single particle in any of six directions ($i = 0, \dots, 5$) and $N_i(\mathbf{r}, t)$ is the average particle population of the cell expressed as the Fermi-Dirac distribution. Further derivations and theoretical explanations of the LGA and FHP models can be found in the literature [12].

In the LGA model for moisture flow and drying of porous media (Fig. 4), a maximum of seven fluid particles is present at each node of a regular, triangular

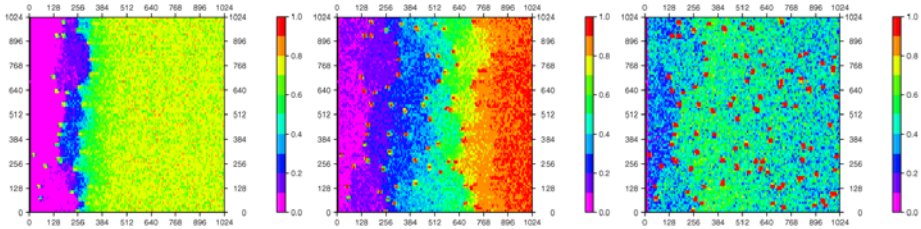


Figure 4. Lattice Gas Automaton (lattice 1024x1024): drying in a heterogeneous sample with small sized obstacles (20 x 20 lattice sites) after (left) 500, (middle) 1500 and (right) 3500 LGA steps ($r = 0$).

lattice [12]. Six fluid particles can move freely in any of six (hexagonal) lattice directions, at each time step, from one lattice node to the other, with a unit velocity c_i . The seventh particle stays at rest, having zero velocity.

Inputting solid particles at fixed positions, of different sizes simulates a solid phase in the fluid lattice (Fig. 4). The number of fluid particles per node and their interaction law (collisions) affect the physical properties of real fluid such as viscosity. Particle movements are divided into the so called propagation step (spatial shift) and collisions. Not all particles take part in the collisions. It strongly depends on their current positions on the lattice in a certain LGA time step. In order to avoid an additional spurious conservation law [13], a minimum of two- and three-body collisions (FHP1 rule) is necessary to conserve mass and momentum along each lattice line. Collision rules FHP2 (22 collisions) and FHP5 (12 collisions) have been used for most of the previous analyses [1],[2],[14], since the reproduction of moisture flow in capillaries, in comparison to the results from NMR tests [3], is then the most realistic.

Example: LGA simulation of heterogeneous media

The LGA models can reproduce flow in homogenous and heterogeneous media [3] with different-sized solid particles. An example is presented in Figure 5. Drying of the LGA sample is initiated from the left side by an input of low density particles. Boundary conditions are periodic in the vertical direction, while on the left side a solid wall is placed. Collision among fluid particles is defined by the FHP2 collision rule, while the no slip (bounce-back) condition is assumed between the solid wall and the fluid particles. To determine the influence of boundary conditions on the speed of drying and moisture gradient, both specular-reflection ($r = 1$), and bounce-back ($r = 0$) rules are used to represent the interaction between the solid and fluid particles (Fig. 5). Drying is always faster in the samples where specular-reflection rule is applied, while the moisture gradient is slightly higher with the application of bounce-back reflection rule, including an increase in noise.

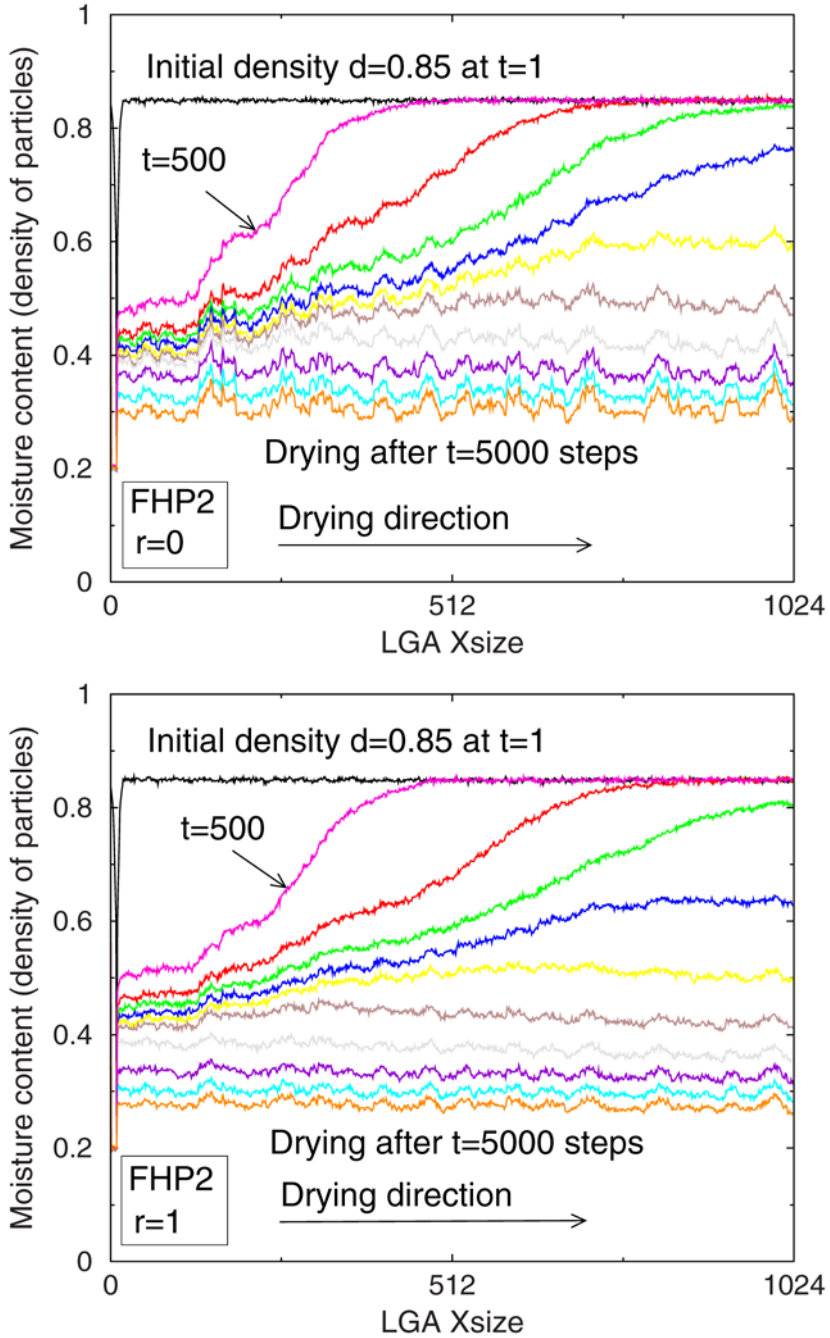


Figure 5. Moisture flow distribution for samples with added solid clusters (20 x 20 lattice sites) with (top) bounce-back rule ($r = 0$) and (bottom) specular-reflection rule ($r = 1$).

Observations and Discussion

Modelling of moisture flow in porous media can be successfully done by applying cellular automata methods, such as the simple 2-D LGA. Generally, there is good qualitative agreement between the numerical results and NMR data [3]. In both LGA and NMR, time and space are variables. Matching LGA and NMR results requires matching their Re numbers. This will couple LGA steps to a real time scale and facilitates quantitatively fitting the parameters to experimental observations like the NMR data [3]. The good agreement between LGA flow and real flow ensures that the moisture content Δh is realistic enough for the input in Eq. 2 in order to create drying cracks in the coupling analysis. In that respect, the Reynolds number ($Re = lu/n$) must be kept low ($Re \ll 1$), while kinematic viscosity ($n = m/r$) must increase (two-, three- to five-body collision, must be kept low).

The current experimental research, in comparison to the tests from the literature [9],[10],[15], shows that moisture flow and subsequent drying deformations could be successfully tested on thin cement paste samples ($d = 1$ mm). In order to get a better understanding of the deformation processes and influential parameters, observations must be performed at different ages of the cement paste. Although still in a developing phase, ESEM as a tool shows advantages for measuring moisture dependent deformations in drying samples.

Both experimental and numerical work is currently in progress. Coupling of the drying, deformation and fracture processes is a complex problem, where, for the sake of simplicity, possible coupling between flow in cracks in the solid has not been considered

Acknowledgments

The present study is supported by the Dutch Technology Foundation (STW) and the Priority Program Materials Research (PPM) which is gratefully acknowledged.

References

- [1] Jankovic, D., Küntz, M. and Van Mier, J.G.M. (2001) Numerical Analysis of Moisture Flow and Concrete Cracking by means of Lattice Type Models. *Proceedings of FraMCoS-4, Cachan, France* **1**, 231–238.
- [2] Jankovic, D. and Van Mier, J.G.M. (2002) Preliminary Investigation of Drying Shrinkage Cement Paste Specimens. *Proceedings of International Conference on New Challenges in Mesomechanics, Aalborg University, Denmark* **1**, 265–271.
- [3] Jankovic, D. and Van Mier, J.G.M. (2003) Drying of Porous Media: Numerical and Experimental Approach. *Proceedings of EURO-C 2003, Computational Modeling of Concrete Structures, St. Johann im Pongau, Austria*, 453–461.
- [4] Shiotani, T., Bisschop, J. and Van Mier, J.G.M. (2003) Temporal and Spatial Development of Drying Shrinkage in Cement-based Materials. *Engineering Fracture Mechanics*

- 70, 1509–1525.
- [5] Bisschop, J., Pel, L. and Van Mier, J.G.M. (2003) Mechanisms of Drying Shrinkage Microcracking in Concrete. *to appear in Cement and Concrete Research*.
 - [6] Van Vliet, M.R.A. and Van Mier, J.G.M. (2000) Experimental Investigation on Size Effect in Concrete and Sandstone under Uniaxial Tension. *Engineering Fracture Mechanics* **65**, 165–188.
 - [7] Hsu, T.T.C. (1963) Mathematical Analysis of Shrinkage Stresses in a Model of Hardened Concrete. *ACI Journal, Proceedings* **60**, **3**, 371–390.
 - [8] Hsu, T.T.C. and Slate, F.O. (1963) Tensile Bond Strength between Aggregate and Cement Paste or Mortar. *ACI Journal, Proceedings* **60**, **4**, 465–485.
 - [9] L’Hermite, R.G. (1965) Volume change of concrete. *Proceedings of International Conference on the Structure of Concrete and its Behaviour Under Load*, 131–145.
 - [10] Neubauer, C.M. (1997) On the Chemistry, Microstructure, and Deformation Properties of Cement Pastes: Towards a New Strategy for Controlling Drying Shrinkage. *Ph.D. Thesis, Northwestern University*.
 - [11] Frisch, U., Hasslacher, B. and Pomeau, Y. (1986) Lattice-Gas Automata for the Navier-Stokes Equation. *Physical Review Letters* **56**, **14**, 1505–1508.
 - [12] Frisch, U., d’Humières, D., Hasslacher, B., Lallemand, P., Pomeau, Y. and Rivet, J-P. (1987) Lattice Gas Hydrodynamics in Two and Three Dimensions. *Complex Systems* **1**, 648–670.
 - [13] Wolfram, S. (1986) Cellular Automaton Fluids 1: Basic Theory. *Journal of Statistical Physics* **45**, 471–526.
 - [14] Jankovic, D. and Van Mier, J.G.M. (2001) Crack Development in Concrete due to Moisture Flow. *HERON, Special edition* **46**, **3**, 169–180.
 - [15] Pihlajavaara, S.E. (1965) On the Main Features and Methods of Investigation of Drying and Related Phenomena in Concrete. *Ph.D. Thesis. University of Helsinki, Finland, Julkaisu 100 Publication, Helsinki*.

IV

ELECTROMECHANICS AND
SWELLING.

Chairmen: O. Coussy, B. Simon

OSMOTIC TRANSPORT THROUGH CLAYS AND CAPSULES

John D. Sherwood¹ and Frédéric Risso²

¹*Schlumberger Cambridge Research, High Cross, Madingley Road, Cambridge CB3 0EL, U.K.*

²*Institut de Mécanique des Fluides de Toulouse, Allée du Professeur Camille Soula, 31400 Toulouse, France*

Abstract Osmosis through a clay membrane, and osmotic swelling of a capsule formed from an HSA-alginate membrane, are compared. Compacted clay acts as an imperfect semipermeable membrane. When the clay membrane separates two salt solutions of different concentrations, osmotic effects are observed, and two relaxation processes control the rate at which the salt solutions come into equilibrium. Capsules, created with an HSA-alginate membrane, exhibit osmotic swelling when the salt concentration of the surrounding fluid is changed. Their return to a new equilibrium exhibits only a single relaxation rate. Analysis explains why two relaxation rates are observed in one case and not in the other.

Introduction

Transport of water and ions between two solutions separated by a clay membrane was studied in [1], using linear transport relations valid when chemical potential differences across the membrane are small [2]. Two relaxation processes were found to control the rate at which the solutions came into equilibrium with each other, and both relaxation rates were observed in experiments. Transport was characterised by three independent coefficients, all of which could be estimated from the experimental results.

Transport of salt and water into a capsule was considered in [3]. Osmotic swelling of the capsule was assumed to be due to Donnan equilibrium between the salt solution outside the capsule and the interior solution which also contained polyelectrolyte molecules. The polyelectrolyte was unable to pass through the membrane which formed the wall of the capsule, but salt could pass freely. A model similar to that used for the clay membrane predicts two relaxation rates, only one of which was observed in experiments in which the salt concentration was varied in the external reservoir [4].

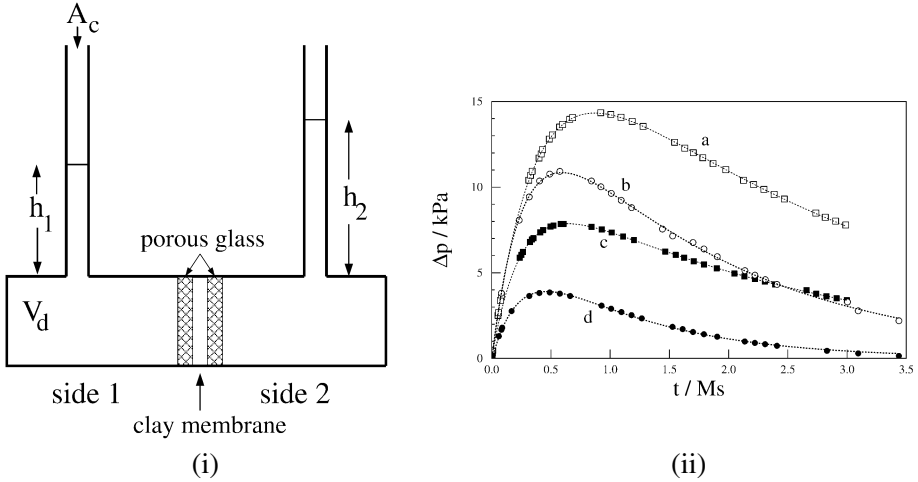


Figure 1. (i) The clay membrane cell. (ii) Differential pressure Δp as a function of time t . (a) SWy-2, CaCl_2 , 3 M & 0.5 M; (b) STx-1, CaCl_2 , 3 M & 0.5 M; (c) SWy-2, NaCl , 3 M & 0.5 M; (d) STx-1, NaCl , 3 M & 0.5 M.

Transport of Salt and Water Through a Clay Membrane

We consider first transport of water and salt across a clay membrane. The salt dissociates into ν_+ cations of valence z_+ and ν_- anions of valence z_- . We assume that all solutions are ideal, so that the the chemical contributions to the electrochemical potentials within the solution on side i of the membrane are $\mu_{i\text{w}} = p_i V_{\text{w}} + RT \ln x_{i\text{w}} \approx p_i V_{\text{w}} - RT(x_{i+} + x_{i-})$ and $\mu_{i\pm} = p_i V_{\pm} + RT \ln x_{i\pm}$, where the subscripts (w, \pm) indicate water and ions, R is the gas constant, T the absolute temperature, p the pressure, x_{w}, x_{\pm} are mole fractions and V_{w}, V_{\pm} are partial molar volumes. There will be an additional electrical contribution $Fz_{\pm}\phi$, where ϕ is the electrical potential and F is the Faraday. Transport through the membrane depends upon the difference in electrochemical potentials across the membrane. If these differences are small, there will be linear transport relations of the form [2]

$$f_{\text{w}} = \lambda_{11}\Delta\mu_{\text{w}} + \lambda_{12}(\Delta\mu_{+} + z_{+}F\Delta\phi) + \lambda_{13}(\Delta\mu_{-} + z_{-}F\Delta\phi) \quad (1a)$$

$$f_{+} = \lambda_{21}\Delta\mu_{\text{w}} + \lambda_{22}(\Delta\mu_{+} + z_{+}F\Delta\phi) + \lambda_{23}(\Delta\mu_{-} + z_{-}F\Delta\phi) \quad (1b)$$

$$f_{-} = \lambda_{31}\Delta\mu_{\text{w}} + \lambda_{32}(\Delta\mu_{+} + z_{+}F\Delta\phi) + \lambda_{33}(\Delta\mu_{-} + z_{-}F\Delta\phi) \quad (1c)$$

where (f_{w}, f_{\pm}) are the flux of water and ions, measured in moles, from side 1 to side 2, and Δ indicates a difference, e.g. $\Delta p = p_1 - p_2$. By Onsager's principle we expect $\lambda_{ij} = \lambda_{ji}$.

The experimental cell, depicted in figure 1(i), is built of insulating materials. A jump in potential $\Delta\phi$ will quickly be established across the membrane so that electroneutrality is maintained and no current flows. We can therefore consider

the flux of salt $f_s = f_-/\nu_- = f_+/\nu_+$ rather than the fluxes of the individual ionic species. We define a chemical potential $\mu_s = \nu_+\mu_+ + \nu_-\mu_-$ for salt. Zero current implies $z_+f_+ + z_-f_- = 0$, which enables us to eliminate $\Delta\phi$ from (1) and obtain transport relations

$$f_w = \lambda_{ww}\Delta\mu_w + \lambda_{ws}\Delta\mu_s \quad (2a)$$

$$f_s = \lambda_{sw}\Delta\mu_w + \lambda_{ss}\Delta\mu_s \quad (2b)$$

where $\lambda_{sw} = \lambda_{ws}$. Thus there are three independent transport coefficients.

In practice we measure changes in pressure and salt concentration, rather than chemical potential, and it can be helpful to think of transport coefficients in terms of Darcy flow and diffusion. We define $x_s = n_s/(n_w + n_s)$, where n_w, n_s are the number of moles of water and salt, and write the change in chemical potential of salt across the membrane as

$$\Delta\mu_s = (\nu_+V_+ + \nu_-V_-)\Delta p + RT[\nu_+\Delta(\ln x_+) + \nu_-\Delta(\ln x_-)] \quad (3a)$$

$$\approx V_s\Delta p + (\nu_+ + \nu_-)RT(\Delta x_s)/x_s. \quad (3b)$$

The transport relations (2) can then be re-written in terms of Δp and Δx_s . Sherwood & Craster [1] chose to write these transport relations in the form

$$f_w = (1 - x_s)k\Delta p - V_w^{-1}[(1 - \lambda)(\nu_+ + \nu_-)RTk + \lambda V_s D]\Delta x_s \quad (4a)$$

$$f_s = \lambda x_s k\Delta p + \lambda D\Delta x_s, \quad (4b)$$

where k is a Darcy transmission coefficient, D a diffusivity, and λ is a transmission coefficient such that $\lambda = 1$ corresponds to unimpeded flow of salt and $\lambda = 0$ corresponds to a perfect ion-exclusion membrane. Thus $1 - \lambda$ is a reflection coefficient. If the liquid viscosity is μ , then $k = k_d/(V_w\mu h)$, where k_d is the standard Darcy permeability of the clay membrane.

If a volume δV of fluid moves across the membrane the level of liquid in each capillary (of cross-sectional area A_c) will change by an amount $\delta h = \delta V/A_c$. Changes in the liquid density ρ_0 are negligible, and hence the rate of change of pressure with time t is

$$\frac{d(\Delta p)}{dt} = -2S\rho_0g(V_w f_w + V_s f_s)/A_c = A\Delta p + B\Delta x_s, \quad (5)$$

where g is the acceleration due to gravity and

$$A = -2Sg\rho_0kV_w/A_c, \quad B = 2Sg\rho_0(1 - \lambda)(\nu^+ + \nu^-)RTk/A_c. \quad (6)$$

The rate of change of salt concentration is

$$\frac{d(\Delta x_s)}{dt} = -\frac{2S}{n_w^0}(f_s - x_s f_w) = C\Delta p + E\Delta x_s, \quad (7)$$

where

$$C = 2Skx_s^0(1 - \lambda)/n_w^0 \quad (8)$$

$$E = -\frac{2S}{n_w^0} \left\{ \lambda D + \frac{x_s^0(1 - \lambda)(\nu^+ + \nu^-)RTk}{V_w} \right\}, \quad (9)$$

and n_w^0 is number of moles of water in each reservoir at equilibrium. Equations (5) and (7) have solution

$$\Delta p = \Delta p_0 \frac{(\lambda_2 e^{-k_1 t} - \lambda_1 e^{-k_2 t})}{\lambda_2 - \lambda_1} + \lambda_1 \lambda_2 \Delta x_s^0 \frac{(e^{-k_1 t} - e^{-k_2 t})}{\lambda_2 - \lambda_1} \quad (10a)$$

$$\Delta x_s = \Delta p_0 \frac{(e^{-k_1 t} - e^{-k_2 t})}{\lambda_1 - \lambda_2} + \Delta x_s^0 \frac{(\lambda_1 e^{-k_1 t} - \lambda_2 e^{-k_2 t})}{\lambda_1 - \lambda_2}, \quad (10b)$$

where $\Delta p_0, \Delta x_s^0$ are the initial values of $\Delta p, \Delta x_s$ at $t = 0$, the λ_i are given in [1], $k_1 \simeq -E$ corresponds to a diffusion rate and $k_2 \simeq -A$ to the rate of Darcy flow.

Figure 1(ii) shows experimental results obtained when a membrane of compacted clay separates salt solutions initially at 3 M and 0.5 M. The salt reflection coefficient $1 - \lambda \ll 1$, so that $\Delta p \ll RT/V_w$ and both Δp and Δx_s are eventually zero. However, before this equilibrium is attained transient pressures are observed: the curves in fig. 1(ii) are best fits to the form (10a). From the two rate constants and magnitude of the pressure we may estimate the three transport coefficients in (4).

Donnan Equilibrium

We now consider a capsule which consists of liquid surrounded by a closed semi-permeable membrane (figure 2); details are provided in [3, 4]. Water and salt can pass through the membrane from side 1 (inside the capsule) to side 2 (outside), and vice versa, but large polymer molecules cannot. Trapped inside the capsule are n_{1p} polyelectrolyte molecules of valence z_p and partial molar volume V_{1p} . The resulting Donnan equilibrium is reviewed in [5, 6]. Inside the capsule, electroneutrality requires $z_p n_{1p} + z_+ n_{1+} + z_- n_{1-} = 0$. We now assume the salt to be monovalent. At equilibrium there is a jump in electrical potential across the membrane; inside the capsule $x_{1+} x_{1-} \approx x_{2+} x_{2-} \approx x_{2s}^2$ with $x_{1\pm} = \frac{1}{2}(Q \mp z_p x_{1p})$ where

$$Q = x_{1+} + x_{1-} = (4x_{1+}x_{1-} + z_p^2 x_{1p}^2)^{1/2}. \quad (11)$$

The jump in pressure across the membrane is

$$V_w \Delta p = RT \ln \frac{x_{2w}}{x_{1w}} \approx RT(Q + x_{1p} - 2x_{2s}). \quad (12)$$

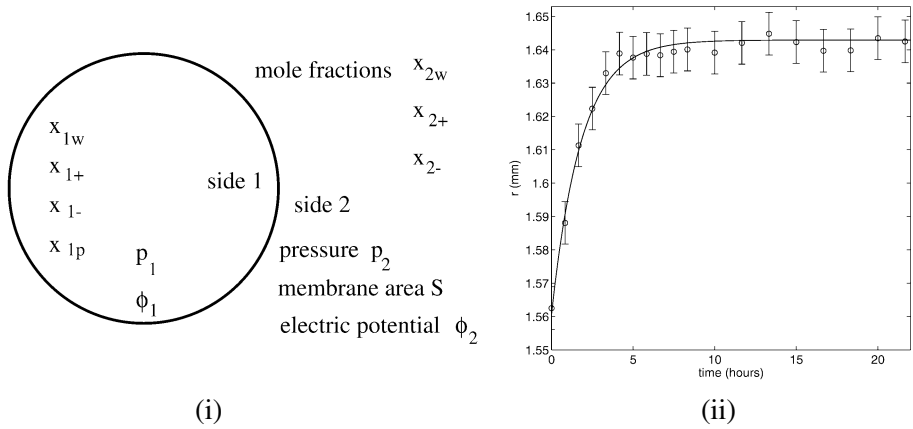


Figure 2. (i) The swelling capsule. (ii) The radius $r(t)$ of a capsule as a function of time t after removal at $t = 0$ from a solution of NaCl at 11 g/l and immersion in a solution at 3.5 g/l. Experiment \circ ; predicted response assuming $D = 4.5 \text{ mmol m}^{-2} \text{ s}^{-1}$.

The total volume of solution within the capsule is $V_1 = V_w n_{1w} + V_+ n_{1+} + V_- n_{1-} + V_p n_{1p}$. When the pressure within the capsule varies, the surrounding membrane deforms by an amount that depends upon its mechanical properties. If the change in capsule volume is small, we may assume a linear relation

$$\Delta p = G(V_1 - V_0) = G(V_w n_{1w} + V_+ n_{1+} + V_- n_{1-} + V_p n_{1p} - V_0), \quad (13)$$

where V_0 is some reference volume and G is related to the elastic properties (and thickness) of the membrane. The volume change is assumed small i.e. $|V - V_0| \ll V_0$ and hence $G \gg \Delta p/V$.

When we consider transport into the capsule, we must be wary of using (2). At equilibrium the electrochemical potentials of water and ions are equal on the two sides of the membrane, but the chemical potentials are not. We assume that transport through a membrane separating two reservoirs at fixed chemical potentials has been characterised and can be represented by (2). We then assume that (2) can be used to estimate transport into and out of the capsule when the jumps in chemical potential are replaced by small departures from the equilibrium jumps. The analysis follows closely that of §3, and predicts two relaxation rates for the salt concentration, pressure and capsule volume, as in (10). However, a change in x_{2s} outside the capsule excites only the diffusive eigensolution: the amplitude of the Darcy transport eigensolution is much smaller. Since the volume change of the capsule is small, the new equilibrium salt concentration within the capsule can be achieved only by exchange of salt and water, and the process is controlled by diffusion. As the salt concentration inside the capsule changes, so does the osmotic pressure, and the consequent changes in volume can be accommodated by the more rapid Darcy flow.

Experiments were performed using capsules with membranes made of covalently linked human serum albumin (HSA) and alginate [7, 8]. Details are given in [4]. Figure 2 shows the evolution of a capsule after removal at time $t = 0$ from a solution of NaCl at 11 g/l and immersion in a solution at 3.5 g/l. The experimental results fit well to a single exponential, leading to an estimate for D [3].

Pressure applied to the external solution would also increase the pressure inside the capsule, and in the absence of fluid compressibility there would be no change in the capsule volume. Without access to the inside of the capsule we cannot apply a pressure difference to investigate Darcy flow through the membrane. One possibility, yet to be tested experimentally, is to add to the external solution an uncharged polymer which cannot pass through the membrane. The external chemical potential of water is thereby reduced [9], and the resulting flow out of the capsule can be shown to depend upon the permeability k of the membrane.

Acknowledgments

We thank B. Craster (SCR) and F. Collé-Paillot (IMFT) for providing the experimental data shown in figures 1 and 2, and F. Edwards-Lévy & M.-C. Lévy (Faculté de Pharmacie, Reims) for the capsules discussed in §3.

References

- [1] Sherwood, J.D. and Craster, B. (2000) Transport of water and ions through a clay membrane. *J. Colloid Interface Sci.* **230**, 349–358
- [2] Staverman, A.J. and Smit, J.A.M. (1975) Physical Chemistry: Enriching topics from colloid and surface science, H. van Olphen and K.J. Mysels, Eds. Theorex, La Jolla, California
- [3] Sherwood, J.D., Risso, F., Collé-Paillot, F., Edwards-Lévy, F., and Lévy, M.C. (2003) Rates of transport through a capsule membrane to attain Donnan equilibrium. *J. Colloid Interface Sci.* **263**, 202–212.
- [4] Collé-Paillot, F. (2002) Mouvement et déformation d'une capsule bioartificielle au sein d'un écoulement en petit tube. Ph.D thesis, Université Paul Sabatier, Toulouse
- [5] Overbeek, J.Th.G. (1956) The Donnan Equilibrium. *Prog. Biophys.* **6**, 57–84
- [6] Sherwood, J.D. (1993) Biot poroelasticity of a chemically active shale. *Proc. R. Soc. Lond. A* **440**, 365–377
- [7] Lévy, M.-C. and Edwards-Lévy, F. (1996) Coating alginate beads with cross-linked biopolymers: a novel method based on a transacylation reaction. *J. Microencapsulation* **13**, 169–183
- [8] Edwards-Lévy, F. and Lévy, M.-C. (1999) Serum albumin-alginate coated beads: mechanical properties and stability. *Biomaterials* **20**, 2069–2084
- [9] Parsegian, V.A., Rand, R.P., Fuller, N.L., and Rau, D.C. (1986) Osmotic Stress for the Direct Measurement of Intermolecular Forces. *Methods in Enzymology* **127**, (Packer, L., ed.), Academic Press, New York, 400–416

ELECTROKINETICS IN RANDOM DEFORMABLE POROUS MEDIA*

Józef Joachim Telega and Ryszard Wojnar

*Polish Academy of Sciences, Institute of Fundamental Technological Research,
Świętokrzyska 21, 00-049 Warszawa, Poland, e-mail: jtelega@ippt.gov.pl*

Abstract The aim of this contribution is to derive macroscopic equations describing flow of two-ionic species electrolytes through porous piezoelectric media with random, not necessarily ergodic, distribution of pores. Under assumption of ergodicity the macroscopic equations simplify and are obtained by using the Birkhoff ergodic theorem.

Introduction

In modelling and analysis of flows through porous media one can distinguish deterministic and stochastic approaches. Many porous media, both natural ones as well as man-made reveal random distribution of pores. The synthetic article [13] provides an account of effective models of flows through random rigid porous media (transport problem). Electrokinetics in such media was studied by [2].

In this paper the problem of stationary flow of two-ionic species electrolyte through random piezoelectric porous media is studied, thus extending our earlier paper [14], where periodicity was assumed. To derive the macroscopic equations we use the method of stochastic two-scale convergence in the mean developed by [4]. Solid phase was assumed to be piezoelectric since according to [9] wet bone reveals piezoelectric properties, cf. also [15]. We recall that a strong conviction prevails that for electric effects in bone only streaming potentials are responsible.

Macroscopic equations are given in Sect. 4 without the assumption of ergodicity. In Sect. 5 we provide comments on the case where ergodicity applies.

*The authors were supported by EC through the project MIAB, No QLK6-CT-1999 - 02024 and SPUB (KBN, Poland).

Description of Random Porous Media and the Method of Stochastic Two-scale Convergence in the Mean

Natural and man-made porous media usually possess formidably complex microstructure, often hierarchical. In this paper we shall not discuss hierarchical microstructures revealed, for instance by fractured porous media and biological tissues like bone and soft tissue. However, recently developed stochastic reiterated homogenisation enables one to determine macroscopic properties of random porous media with hierarchical architecture, cf. [11].

Let $(\Omega, \mathcal{F}, \mu)$ denote a probability space where \mathcal{F} is a complete σ -algebra and μ is the probabilistic measure. Assume that Ω is acted on by an n -dimensional dynamical system $T(\mathbf{x}) : \Omega \rightarrow \Omega$, such that for each $\mathbf{x} \in \mathbb{R}^n$, both $T(\mathbf{x})$ and $T(\mathbf{x})^{-1}$ are measurable, and such that the following conditions are satisfied: (a) $T(\mathbf{0})$ is the identity map on Ω and for $\mathbf{x}_1, \mathbf{x}_2 \in \mathbb{R}^n$, $T(\mathbf{x}_1 + \mathbf{x}_2) = T(\mathbf{x}_1)T(\mathbf{x}_2)$; (b) for each $\mathbf{x} \in \mathbb{R}^n$ and measurable set $F \in \mathcal{F}$, $\mu(T(\mathbf{x})^{-1}F) = \mu(F)$, i.e. μ is an invariant measure for T ; (c) for each $F \in \mathcal{F}$, the set $\{(\mathbf{x}, \omega) \in \mathbb{R}^n \times \Omega | T(\mathbf{x})\omega \in F\}$ is a $d\mathbf{x} \times d\mu$ measurable subset of $\mathbb{R}^n \times \Omega$, where $d\mathbf{x}$ stands for the Lebesgue measure on \mathbb{R}^n , cf. [4].

We observe that $T(\mathbf{x})^{-1} = T(-\mathbf{x})$. The dynamical system satisfying (a)-(c) is also called a *measure preserving flow*. We can now introduce random homogeneous fields, starting from the random variable f :

$$f \in L^1(\Omega), \quad \tilde{f}(\mathbf{x}, \omega) \equiv f(T(\mathbf{x})\omega). \quad (1)$$

We observe that \tilde{f} is also called the statistically homogeneous (i.e. stationary) random process. Statistical homogeneity means that two geometric points of the space are statistically undistinguishable, or the statistical properties of the medium are invariant under the action of translation. Then we have a group $\{U_{\mathbf{x}} | \mathbf{x} \in \mathbb{R}^n\}$ of isometries on $L^2(\Omega) = L^2(\Omega, \mathcal{F}, \mu)$ defined by

$$(U(\mathbf{x})f)(\omega) = f(T(\mathbf{x})\omega), \quad \mathbf{x} \in \mathbb{R}^n, \omega \in \Omega, f \in L^2(\Omega).$$

A dynamical system is said to be *ergodic*, if every invariant function, i.e. satisfying $f(T(\mathbf{x})\omega) = f(\omega)$ is *constant* almost everywhere in Ω .

Examples of statistically homogeneous media are provided in [11], also (2002a, 2003).

Let $g \in L^1_{\text{loc}}(\mathbb{R}^n)$, i.e. g is integrable on every measurable bounded set $K \subset \mathbb{R}^n$. A number $M\{g\}$ is called the mean value of g if

$$\lim_{\varepsilon \rightarrow 0} \int_K g(\varepsilon^{-1}\mathbf{x})d\mathbf{x} = |K| M\{g\}. \quad (2)$$

Here $|K|$ denotes the Lebesgue measure of K . Of crucial importance is the *Birkhoff ergodic theorem* which states that for $f \in L^\alpha(\Omega)$, $\alpha \geq 1$,

$$f(T(\frac{\mathbf{x}}{\varepsilon})\omega) \rightharpoonup M\{f(T(\mathbf{x})\omega)\} \quad \text{weakly in } L^\alpha_{\text{loc}} \quad (3)$$

and $M\{f(T(\mathbf{x})\omega)\}$, considered as a function of $\omega \in \Omega$, is invariant. Moreover, we have

$$\langle f \rangle \stackrel{\text{df}}{=} \int_{\Omega} f(\omega) d\mu = \int_{\Omega} M\{f(T(\mathbf{x})\omega)\} d\mu. \quad (4)$$

In particular, if the system $T(\mathbf{x})$ is ergodic, then

$$M\{f(T(\mathbf{x})\omega)\} = \langle f \rangle \quad \text{for almost all } \omega \in \Omega.$$

Let Q be a given, deterministic, bounded domain in \mathbb{R}^n and let $G \in \mathcal{F}$. We set

$$G(\omega) = \{\mathbf{x} \in \mathbb{R}^n | T(\mathbf{x})\omega \in G\}, \quad (5)$$

$$Q_{\varepsilon}(\omega) = Q \setminus \mathcal{G}_{\varepsilon}(\omega), \quad \text{where } \mathcal{G}_{\varepsilon}(\omega) = \{\mathbf{x} \in \mathbb{R}^n | \varepsilon^{-1}\mathbf{x} \in G(\omega)\}. \quad (6)$$

Such a definition of random domain $Q_{\varepsilon}(\omega)$ is suitable for theoretical considerations. In practice, the random sets $G(\omega)$ or $\mathcal{G}_{\varepsilon}(\omega)$ have to be described more precisely, cf. [1, 11, 13] and the references therein.

To carry out stochastic homogenisation, elements of local stochastic calculus are needed. For more details, the reader is referred to [4, 11, 13].

Anyway, one can define the stochastic gradient $\nabla_{\omega} f$, stochastic divergence $\text{div}_{\omega} \mathbf{v}$, etc.

In the periodic case ω is to be identified with local variable $\mathbf{y} \in Y$, where Y is the so-called *basic cell*.

The set of all functions $f \in L^2(\Omega)$ invariant for T (i.e. $f(T(\mathbf{x})) = f, \mu - \text{a.e. on } \Omega$, for all $\mathbf{x} \in \mathbb{R}^n$) is a closed subset of $L^2(\Omega)$ and denoted by $I^2(\Omega)$. We set $M^2(\Omega) = [I^2(\Omega)]^{\perp}$. We introduce a projection $E : L^2(\Omega) \rightarrow L^2(\Omega)$ determined by

$$(Ef)(\omega) = \lim_{\lambda \rightarrow \infty} \frac{1}{(2\lambda)^n} \int_{[-\lambda, \lambda]^n} f(T(\mathbf{x})\omega) d\mathbf{x}, \quad \mu - \text{a.e. } \omega \in \Omega. \quad (7)$$

We have $M^2(\Omega) = \ker E$; moreover: (i) if $f \in L^2(\Omega)$ then $f \in I^2(\Omega)$ if and only if $\nabla_{\omega} f = 0$, (ii) for any multi-index $\alpha = (\alpha_1, \dots, \alpha_n)$,

$$\partial^{\alpha} \varphi(T(\mathbf{x})\omega) = (D^{\alpha} \varphi)(T(\mathbf{x})\omega), \quad \varphi \in \mathcal{D}^{\infty}(\Omega)$$

where $\partial^{\alpha} = \partial^{|\alpha|} / \partial x_1^{\alpha_1} \dots \partial x_n^{\alpha_n}$, (iii) let $\mathbf{u} \in L^2(\Omega)^n, \mathbf{v} \in L^2(\Omega)^n, \text{curl}_{\omega} \mathbf{u} = \mathbf{0}, \text{div}_{\omega} \mathbf{v} = 0$, then

$$\int_{\Omega} \mathbf{u} \cdot \mathbf{v} d\mu = \int_{\Omega} E(\mathbf{u}) \cdot E(\mathbf{v}) d\mu. \quad (8)$$

Furthermore, if T is ergodic then (8) yields an extension of the Hill-type relation:

$$\int_{\Omega} \mathbf{u} \cdot \mathbf{v} d\mu = \int_{\Omega} \mathbf{u} d\mu \cdot \int_{\Omega} \mathbf{v} d\mu. \quad (9)$$

Now we are in a position to introduce the fundamental notion.

Definition 1. A sequence $\{u^\varepsilon\}_{\varepsilon>0}$ in $L(Q \times \Omega)$ is said to *stochastically two-scale converge in the mean* to $u \in L^2(Q \times \Omega)$ if for all $\psi \in L(Q \times \Omega)$

$$\lim_{\varepsilon \rightarrow 0} \int_{Q \times \Omega} u^\varepsilon(\mathbf{x}, \omega) \psi(\mathbf{x}, T(\varepsilon^{-1}\mathbf{x})\omega) d\mathbf{x} d\mu = \int_{Q \times \Omega} u(\mathbf{x}, \omega) \psi(\mathbf{x}, \omega) d\mathbf{x} d\mu. \quad (10)$$

The properties of stochastically two-scale convergent sequences like $\{u^\varepsilon\}_{\varepsilon>0}$ and $\{\varepsilon \nabla u^\varepsilon\}$ are studied in [4], cf. also [11]. These properties will be exploited in Sect. 4 of the present paper. We also need to extend the mapping E in order to cope with the so-called *stochastic nonuniform homogenisation*. To this end for each $\mathbf{y} \in \mathbb{R}^n$ we define the mapping $\tilde{T}(\mathbf{y}) : Q \times \Omega \rightarrow Q \times \Omega$ by $\tilde{T}(\mathbf{y})(\mathbf{x}, \omega) = (\mathbf{x}, T(\mathbf{y})\omega)$. We observe that $\{\tilde{T}(\mathbf{y}) | \mathbf{y} \in \mathbb{R}^n\}$ is an n -dimensional dynamical system on $Q \times \Omega$. Replacing Ω, T by $(Q \times \Omega, \tilde{T})$ we extend (7) as follows

$$\tilde{T}g(\mathbf{x}, \omega) = E[g(\mathbf{x}, \cdot)](\omega)$$

or

$$\tilde{E}g(\mathbf{x}, \omega) = \lim_{\lambda \rightarrow \infty} \frac{1}{(2\lambda)^n} \int_{[-\lambda, \lambda]^n} g(\mathbf{x}, T(\mathbf{y})\omega) d\mathbf{y} \quad (11)$$

$E\tilde{g}$ does not depend on $\omega \in \Omega$ (μ - a.e.) provided that μ is ergodic for T .

Equations of Flow of Electrolyte Through Piezoelectric Random Porous Medium

Let $Q_\varepsilon^s(\omega) = Q \setminus \overline{Q_\varepsilon}(\omega)$ and $Q_\varepsilon^\ell(\omega) = Q \setminus \overline{Q_\varepsilon^s}(\omega)$, where $\varepsilon > 0$ is a small parameter characterizing microstructure. We assume that the sets $Q_\varepsilon^\ell(\omega)$ are connected. By $\mathbf{u}^\varepsilon(t, \mathbf{x}, \omega)$ and $\mathbf{v}^\varepsilon(t, \mathbf{x}, \omega)$ we denote fields of displacement in the piezoelectric phase $Q_\varepsilon^s(\omega)$ and velocity in the fluid-ionic phase $Q_\varepsilon^\ell(\omega)$, respectively. The pressure field, volume density of positive (negative) ions, and the corresponding current vectors are denoted by $p^\varepsilon(t, \mathbf{x}, \omega)$, $q^{(+)\varepsilon}(t, \mathbf{x}, \omega)$, $q^{(-)\varepsilon}(t, \mathbf{x}, \omega)$, and $\mathbf{J}^{(\pm)\varepsilon}(t, \mathbf{x}, \omega)$, respectively. Obviously, t stands for the time variable, $t \in [0, \tau]$. By $\Phi^\varepsilon(t, \mathbf{x}, \omega)$ we denote the electric potential field.

The set of equations for the fields \mathbf{u}^ε , \mathbf{v}^ε , p^ε , Φ^ε , $q^{(\pm)\varepsilon}$, and $\mathbf{J}^{(\pm)\varepsilon}$ assume the following form:

- in the solid piezoelectric phase $Q_\varepsilon^s(\omega)$

$$\begin{aligned} \rho^s \ddot{\mathbf{u}}^\varepsilon &= \operatorname{div}_{\mathbf{x}} [\mathbf{a}^\varepsilon \mathbf{e}(\mathbf{u}^\varepsilon) - \boldsymbol{\pi}^{\varepsilon(*)} \mathbf{E}(\Phi^\varepsilon)], \\ \operatorname{div}_{\mathbf{x}} [\boldsymbol{\pi}^\varepsilon \mathbf{e}(\mathbf{u}^\varepsilon) + [\boldsymbol{\epsilon}^{s\varepsilon} \mathbf{E}(\Phi^\varepsilon)]] &= 0 \end{aligned} \quad (12)$$

where $\mathbf{a}^\varepsilon(\mathbf{x}, \omega) = \mathbf{a}(\mathbf{x}, T(\varepsilon^{-1}\mathbf{x})\omega)$, $\boldsymbol{\pi}^\varepsilon(\mathbf{x}, \omega) = \boldsymbol{\pi}(\mathbf{x}, T(\varepsilon^{-1}\mathbf{x})\omega)$,
 $\boldsymbol{\epsilon}^{s\varepsilon}(\mathbf{x}, \omega) = \boldsymbol{\epsilon}(\mathbf{x}, T(\varepsilon^{-1}\mathbf{x})\omega)$, $\mathbf{E}_\mathbf{x}(\Phi^\varepsilon) = -\nabla_\mathbf{x}\Phi^\varepsilon$,

$$\left(\boldsymbol{\pi}^{\varepsilon(*)}\mathbf{E}_\mathbf{x}(\Phi^\varepsilon)\right)_{ij} = -\pi_{kij}^\varepsilon \frac{\partial \Phi^\varepsilon}{\partial x_k}.$$

Here $\left(\boldsymbol{\epsilon}_{ij}^{s\varepsilon}\right) = \left(\boldsymbol{\epsilon}_{ij}^{s\varepsilon}(\mathbf{x}, \omega)\right)$ is the matrix of dielectric moduli in the solid phase, $\mathbf{e}(\mathbf{u})$ stands for the small strain tensor, and

$$\dot{\mathbf{u}} = \frac{\partial \mathbf{u}}{\partial t};$$

- in the fluid-ionic phase $Q_\varepsilon^\ell(\omega)$

$$\begin{aligned} \rho^\ell \dot{\mathbf{v}}^\varepsilon &= \varepsilon^2 \eta \Delta_\mathbf{x}(\mathbf{v}^\varepsilon) - \nabla_\mathbf{x} p^\varepsilon + \mathbf{f}^g + q^\varepsilon \mathbf{E}_\mathbf{x}(\Phi^\varepsilon) - \kappa \nabla_\mathbf{x} q^\varepsilon, \\ \operatorname{div}_\mathbf{x} \mathbf{v}^\varepsilon &= 0, \\ \operatorname{div}_\mathbf{x} (\boldsymbol{\epsilon}^{\ell\varepsilon} \mathbf{E}_\mathbf{x}(\Phi^\varepsilon)) &= q^\varepsilon, \\ \frac{\partial q^\pm}{\partial t} + \operatorname{div}_\mathbf{x} \mathbf{J}^{(\pm)\varepsilon} &= 0, \quad q^\varepsilon = q^{(+)\varepsilon} + q^{(-)\varepsilon}. \end{aligned} \tag{13}$$

More precisely, (12) holds in $(0, \tau) \times Q_\varepsilon^s(\omega)$ whilst (13) in $(0, \tau) \times Q_\varepsilon^\ell(\omega)$. The scaling of the viscosity is typical for the flow of Stokesian fluid through porous media, cf.[12],[14]. The assumptions on the moduli \mathbf{a}^ε , $\boldsymbol{\pi}^\varepsilon$ and $\boldsymbol{\epsilon}^{s\varepsilon}$ are similar to those specified in [10] for microperiodic piezocomposites. In our case it suffices to extend conditions (A₁) and (A₂) given in [12] for elastic solid phase.

The conditions on the interface solid-fluid $\Gamma^\varepsilon(\omega)$ are specified by the following relations and hold for $t \in (0, \tau)$:

$$\begin{aligned} \llbracket \boldsymbol{\sigma}^\varepsilon \mathbf{n} \rrbracket &= \mathbf{0}, \quad \llbracket \Phi^\varepsilon \rrbracket = 0, \quad \llbracket \mathbf{D}^\varepsilon \mathbf{n} \rrbracket = \zeta^\varepsilon, \\ \mathbf{v}^\varepsilon &= \dot{\mathbf{u}}^\varepsilon, \quad \mathbf{J}^{(+)\varepsilon} \cdot \mathbf{n} = 0, \quad \mathbf{J}^{(-)\varepsilon} \cdot \mathbf{n} = 0, \end{aligned} \tag{14}$$

where

$$\boldsymbol{\sigma}^\varepsilon = \begin{cases} \mathbf{a}^\varepsilon \mathbf{e}(\mathbf{u}^\varepsilon(t, \mathbf{x}, \omega)) - \boldsymbol{\pi}^{\varepsilon(*)} \mathbf{E}_\mathbf{x}(\Phi^\varepsilon(t, \mathbf{x}, \omega)) & \text{in } (0, \tau) \times Q_\varepsilon^s(\omega), \\ -p^\varepsilon(t, \mathbf{x}, \omega) \mathbf{I} + \varepsilon^2 \eta \mathbf{e}(\mathbf{v}^\varepsilon(t, \mathbf{x}, \omega)) & \text{in } (0, \tau) \times Q_\varepsilon^\ell(\omega); \end{cases} \tag{15}$$

$$\mathbf{D}^\varepsilon = \begin{cases} \boldsymbol{\pi}^\varepsilon \mathbf{e}(\mathbf{u}^\varepsilon(t, \mathbf{x}, \omega)) + \boldsymbol{\epsilon}^{s\varepsilon} \mathbf{E}_\mathbf{x}(\Phi^\varepsilon(t, \mathbf{x}, \omega)) & \text{in } (0, \tau) \times Q_\varepsilon^s(\omega), \\ \boldsymbol{\epsilon}^{\ell\varepsilon} \mathbf{E}_\mathbf{x}(\Phi^\varepsilon(t, \mathbf{x}, \omega)) & \text{in } (0, \tau) \times Q_\varepsilon^\ell(\omega); \end{cases} \tag{16}$$

$$\mathbf{J}^{(\pm)\varepsilon} = \mathbf{b}^{(\pm)\varepsilon} q^{(\pm)\varepsilon} \mathbf{E}_{\mathbf{x}}(\Phi^\varepsilon) + q^{(\pm)\varepsilon} \mathbf{v}^\varepsilon - \mathbf{d}^{(\pm)} \nabla_{\mathbf{x}} q^{(\pm)\varepsilon} \quad \text{in } (0, \tau) \times Q_\varepsilon^\ell(\omega). \quad (17)$$

Here $\mathbf{I} = (\delta_{ij})$ denotes the identity matrix. The interface potential (ζ -potential) ζ^ε may be assumed to be constant. We consider a more general case where $\zeta^\varepsilon = \zeta(\mathbf{x}, T(\varepsilon^{-1}\mathbf{x})\omega)$. Since we are interested in the macroscopic equations, we do not consider boundary conditions on $\partial Q_\varepsilon(\omega)$. For the sake of simplicity we assume homogeneous initial conditions for $\mathbf{u}^\varepsilon, \mathbf{v}^\varepsilon, \Phi^\varepsilon$ and $q^{(\pm)\varepsilon}$.

Stochastic Homogenisation and Macroscopic Relations

Letting ε tend to zero in the sense of stochastic two-scale convergence in the mean we arrive at the homogenized equations. Without the assumptions of ergodicity the fields involved still depend on $\omega \in \Omega$.

Let $F \subset \Omega$ and $G = \Omega \setminus F$; F is assumed to be T -open and T -connected, cf. [11, 13]. We observe that F plays the role of voids in local problems in the case of periodic microstructure. We set $\Psi = \mu(F)$, $Q_\tau = (0, \tau) \times Q$.

Selected results

(i) T is not necessarily ergodic:

- Under physically plausible assumptions $\{\mathbf{u}^\varepsilon, \nabla_{\mathbf{x}} \mathbf{u}^\varepsilon, \Phi^\varepsilon, \nabla_{\mathbf{x}} \Phi^\varepsilon, \mathbf{v}^\varepsilon\}$ stochastically two-scale converges in the mean to

$$\left(\chi_{\Omega \setminus F} \mathbf{u}, \chi_{\Omega \setminus F} (\boldsymbol{\xi} + \nabla_{\mathbf{x}} \mathbf{u}), \Phi, (\boldsymbol{\theta} + \nabla_{\mathbf{x}} \Phi), \chi_F \mathbf{v} \right)$$

and, for instance $\mathbf{u} \in H^1(Q, I^2(\Omega))^n$, $\boldsymbol{\xi} \in L^2(Q, M^2(\Omega))^{n^2}$. Here χ_A denotes the characteristic function of set A .

- The Darcy-Wiedemann law is nonlocal in time:

$$\begin{aligned} \tilde{E}[\chi_F(\omega)(\mathbf{v} - \dot{\mathbf{u}})(t, \mathbf{x}, \omega)] = \\ \frac{1}{\rho^\ell} \int_0^t \mathbf{A}(t-s, \omega) (\mathbf{f}^g - \nabla_{\mathbf{x}} p - q \nabla_{\mathbf{x}} \Phi - \kappa \nabla_{\mathbf{x}} q)(s, \mathbf{x}) ds \end{aligned}$$

where \mathbf{f}^g depends on (s, \mathbf{x}) whilst q and Φ on (s, \mathbf{x}, ω) ; $q = q^{(+)} + q^{(-)}$.

The permeability matrix $\mathbf{A} = (A_{ij})$ is defined by

$$A_{ij} = E[\chi_F(\omega)\dot{\mathbf{w}}^{(i)}(t, \omega) \cdot \mathbf{e}_j], \quad i, j = 1, 2, 3.$$

Here \mathbf{e}_j stands for the j^{th} standard basis vector of \mathbb{R}^3 . The matrix \mathbf{A} is symmetric and positive definite, cf. [11, 12]. The function $\dot{\mathbf{w}}^{(i)}$ is a solution to the *flow cell problem*, given by Eqs. (4.14) in [11], cf. also [12].

(ii) T is ergodic on Ω :

- The macroscopic fields \mathbf{u} , p , Φ and q do not depend on ω .
- The Darcy-Wiedemann law takes the form

$$\langle \chi_F(\omega)(\mathbf{v}(t, \mathbf{x}, \omega) - \dot{\mathbf{u}}(t, \mathbf{x})) \rangle = \frac{1}{\rho^\ell} \int_0^t \mathbf{A}(t-s)(\mathbf{f}^g - \nabla_{\mathbf{x}} p - q \nabla_{\mathbf{x}} \Phi - \kappa \nabla_{\mathbf{x}} q)(s, \mathbf{x}) ds$$

where $A_{ij} = \langle \chi_F(\omega)\dot{\mathbf{w}}^{(i)}(t, \omega) \cdot \mathbf{e}_j \rangle$.

- The macroscopic moduli $\mathbf{a}^h(\mathbf{x})$, etc., can be found by solving cell local problems, being stochastic counterpart of the local problems formulated in [14] for the periodic case. For instance, we have

$$a_{ijpq}^h(\mathbf{x}) = \langle \chi_{\Omega \setminus F}(\omega)[a_{ijpq} + a_{ijmn} e_{mn}^\omega(\mathbf{B}^{(pq)}) - \pi_{kij} E_k^\omega(R^{(pq)})](\mathbf{x}, \omega) \rangle$$

- The macroscopic stress tensor $\langle \boldsymbol{\sigma}^{(0)} \rangle(t, \mathbf{x})$, $\mathbf{x} \in Q$ is expressed by

$$\langle \boldsymbol{\sigma}^{(0)} \rangle(t, \mathbf{x}) = \langle \chi_{\Omega \setminus F}(\omega) \boldsymbol{\sigma}^{s(0)}(t, \mathbf{x}, \omega) \rangle + \langle \chi_F(\omega) \boldsymbol{\sigma}^{\ell(0)}(t, \mathbf{x}, \omega) \rangle.$$

Explicit formula for $\langle \boldsymbol{\sigma}^{(0)} \rangle(t, \mathbf{x})$ generalizes that given by Eqs.(4.19)-(4.21) in [14].

- The stationary Darcy-Wiedemann law is obtained by letting t tend to infinity, cf. [3].

Final Remarks

For other models of flow of electrolytes through porous media the reader is referred to [2], [5], [6]. To take into account FCD (fixed charge density) one has to impose additional condition on the interface $\Gamma^\varepsilon(\omega)$ and the electroneutrality condition. A challenging problem is to use homogenisation methods for the case of finitely deformable skeleton, even hyperelastic. The permeability would then necessarily depend on strains. Such a dependence (nonlinear) is important even for small strain, cf. [7]. It is also important to include ion channels [8].

References

- [1] Adler, P.M. and Thovert, J.-F. (1998) Real Porous Media: Local Geometry and Macroscopic Properties. *Appl. Mech. Rev.* **51(9)**, 537-585
- [2] Adler, P.M., Thovert, J.-F. and Békri, S. (2000) Local Geometry and Macroscopic Properties. *Interfacial Electrokinetics and Electrophoresis*, 35-51, Springer-Verlag, Symbolic Computation, Tokyo
- [3] Bielski, W., Telega, J.J. and Wojnar, R. (1999) Macroscopic Equations for Nonstationary Flow of Stokesian Fluid through Porous Elastic Medium. *Arch. Mech.* **51**, 243-274
- [4] Bourgeat, A., Mikelić, A. and Wright, S. (1994) Stochastic Two-scale Convergence in the Mean. *J. reine angew. Math.* **456**, 19-51
- [5] Gu, W.Y., W. M. Lai, and V. C. Mow. (1998) A Mixture Theory for Charged-hydrated Soft Tissues Containing Multi-electrolytes: Passive Transport and Swelling Behaviors. *J. Biomech. Eng.* **120**, 169-180
- [6] Huyghe, J.M. and Janssen J.D. Quadriphasic Mechanics of Swelling Incompressible Porous Media, *in press*
- [7] Lai, L.M., Mow, V.C. and Roth, V. (1981) Effects of Nonlinear Strain-dependent Permeability and the Rate of Compression on the Stress Behavior of Articular Cartilage. *J. Biomech. Eng.* **103**, 61-66
- [8] Levitt, D.G. (2002) The use of Streaming Potential Measurements to Characterize Biological Ion Channels. *Membrane Transport and Renal Physiology*, 53-63, Springer, New York.
- [9] Reinish, G.B. and Nowick, A.S. (1975) Piezoelectric Properties of Bone as Functions of Moisture Content. *Nature* **253**, 626-627
- [10] Telega J.J. (1991) Piezoelectricity and Homogenization. Application to Biomechanics. *Continuum Models and Discrete Systems*, 220-229, Longman, Essex.
- [11] Telega, J.J. and Bielski, W. (2002) Stochastic Homogenization and Macroscopic Modelling of Composites and the Flow through Porous Media. *Theor. Appl. Mech.* **28-29**, 337-377
- [12] Telega, J.J. and Bielski, W. (2002) Nonstationary Flow of Stokesian Fluid through Random Porous Medium with Elastic Skeleton. *Poromechanics II*, 569-574, Lisse Abbingdon Exton (PA) Tokyo
- [13] Telega, J.J. and Bielski, w. (2003) Flow in Random Porous Media: Effective Models. *Comp. Geotech.* **30**, 271-288
- [14] Telega, J.J. and Wojnar, R. (2000) Flow of Electrolyte through Porous Piezoelectric Medium: Macroscopic Equations. *C. R. Acad. Sci. Paris Série IIb* **328**, 225-230
- [15] Telega, J.J. and Wojnar, R. (2002) Piezoelectric Effects in Biological Tissues. *J. Theor. Appl. Mech.* **40**, 723-759

CHEMOPOROELASTIC PARAMETER IDENTIFICATION OF A REACTIVE SHALE

Emmanuel Detournay

University of Minnesota, USA & CSIRO, Australia

Joel Sarout

University of Minnesota, USA

Chee Tan

CSIRO, Australia

Jean Caurel

Total, France

Abstract This paper is concerned with the experimental identification of some chemoporoelastic parameters of a reactive shale from data obtained in pore pressure transmission - chemical potential tests. The parameter identification is done by matching the observed pressure response with a theoretical solution of the experiment. This solution is obtained within the framework of Biot theory of poroelasticity, extended to include physico-chemical interactions. Results of an experiment on a Pierre II shale performed in a pressure cell are reported and analyzed.

Introduction

The so-called pore pressure transmission-chemical potential test is used in the petroleum industry to assess the osmotic membrane efficiency of a shale in contact with a drilling fluid ([6, 7, 12–1]). It is motivated by the need to assess the capacity of improving the stability of a borehole in a chemically active shale by increasing the salt concentration of the drilling fluid. In this test, a saturated cylindrical sample of shale is subjected sequentially to a hydraulic

Jacques M. Huyghe et al. (eds), IUTAM Proceedings on Physicochemical and Electromechanical Interactions in Porous Media, 125–132.

© 2005 Springer. Printed in the Netherlands.

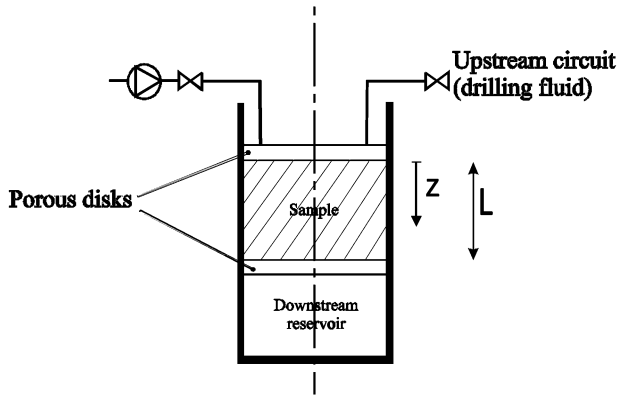


Figure 1. Principle of the pressure transmission-chemical potential test

and a chemical loading on the upstream end of the sample ($z = 0$), with the downstream end ($z = L$) connected to a closed reservoir, see Figure 1. The fluid pressure in the reservoir is monitored during the test. The hydraulic loading consists of applying a pressure p_m at $z = 0$ with the solution used during the saturation phase. In the chemical loading the end $z = 0$ is placed in contact with a solution of a different salt concentration but at the same hydraulic pressure p_m . During both loading phases water and salt ions move through the shale sample, driven by differences in pressure and salt concentration between the upstream and downstream reservoir solutions. The main outcome of the experiment is the determination of the membrane efficiency coefficient, a parameter which quantifies the departure of the shale from an ideal osmotic membrane (for which movement of the salt ions is completely impeded). This parameter is determined from the maximum pressure drop (with respect to p_m) in the downstream reservoir during the chemical loading phase.

In this paper, we analyze this experiment within the framework of Biot theory of poroelasticity, extended to include physico-chemical interactions, and study the parameters that are influencing the fluid pressure response in the downstream reservoir due to hydraulic and chemical loadings.

Chemoporoelasticity

The Biot theory of poroelasticity ([4, 2]) can be extended to account for the physico-chemical interactions taking place between the dissolved salt, pore fluid, and a chemically active shale ([8, 9]). For example, a sample of reactive shale surrounded by a fluid initially in thermodynamic equilibrium with the saturating fluid experiences a contraction ($\varepsilon < 0$) accompanied by a decrease

of fluid content ($\zeta < 0$) if the salt concentration of the surrounding fluid increases ($\Delta x > 0$). These mechanical and hydraulic effects are a consequence of the electrical interaction between the electrolyte and the negatively charged clay platelets at the microscale ([3]).

The volumetric constitutive equations for a chemoporoelastic material can be formulated in terms of the “stress” $\mathcal{S} = \{\sigma, p, \pi\}$ and the “strain” $\mathcal{E} = \{\varepsilon, \zeta, \theta\}$, i.e., in terms of the mean Cauchy stress σ , pore pressure p , osmotic pressure π , volumetric strain ε , variation of fluid content ζ , and relative increment of salt content θ . Note that the stress and strain are measured from a reference initial state where all the “stress” fields are equilibrated. The osmotic pressure π is related to the change in the solute molar fraction x according to $\pi = N\Delta x$ where $N = RT/v$ is a parameter with dimension of a stress, which is typically of $O(10^2)$ MPa (with $R = 8.31$ J/K·mol denoting the gas constant, T the absolute temperature, and v the molar volume of the fluid). The solute molar fraction x is defined as m_s/m with $m = m_s + m_w$ and m_s (m_w) denoting the moles of solute (solvent) per unit volume of the porous solid. The quantities ζ and θ are defined in terms of the increment Δm_s and Δm_w according to

$$\zeta = v_w \Delta m_w + v_s \Delta m_s, \quad \theta = \frac{v}{x_o} \Delta m_s - \frac{v}{1 - x_o} \Delta m_w \quad (1)$$

where v_w and v_s denote the molar volume of the solvent and the solute, respectively and where x_o is the reference salt molar fraction (e.g. at the initial state). For an ideal solution, $v = (1 - x)v_w + xv_s$.

The volumetric constitutive relationships can be written as

$$\begin{Bmatrix} \sigma \\ p \\ \pi \end{Bmatrix} = \begin{bmatrix} C & bC & -\alpha bC \\ bC & S_\sigma & -\beta S_\sigma \\ -\alpha bC & -\beta S_\sigma & \gamma \end{bmatrix} \begin{Bmatrix} \varepsilon \\ \zeta \\ \theta \end{Bmatrix} \quad (2)$$

The set of constitutive parameters contains the (drained) elastic volumetric compliance C and two poroelastic constants: the Biot stress coefficient b , and the unconstrained storage coefficient $S_\sigma = \partial\zeta/\partial p|_\sigma$ which can be expressed as $S_\sigma = bB^{-1}C$ ([13]), where B is the Skempton pore pressure coefficient. The other three parameters, α , β , and γ quantify the physico-chemical interactions. Both α and β are constrained to vary from 0 when there is no chemical interaction to 1 when the salt ions are trapped in the pore network (this limiting case is referred to as the “perfect ion exclusion membrane model”). The coefficient γ can simply be approximated by $\gamma \simeq x_o/n$, where n is the porosity of the shale.

Next, we introduce the specific discharge \mathbf{q} and the relative solute flux \mathbf{r} as

$$\mathbf{q} = v_w \mathbf{I}_w + v_s \mathbf{I}_s, \quad \mathbf{r} = \frac{v}{x} \mathbf{I}_s - \frac{v}{1 - x} \mathbf{I}_w \quad (3)$$

where \mathbf{I}_w and \mathbf{I}_s are mass fluxes of solvent and solution, expressed in number of moles crossing a unit surface of porous rock per unit time. Hence, the transport equations can be rewritten as

$$\mathbf{q} = -\kappa \nabla p + \mathcal{R} \kappa \nabla \pi, \quad \mathbf{r} = \mathcal{R} \kappa \nabla p - \frac{D_c}{N} \nabla \pi \quad (4)$$

where κ is the mobility coefficient defined as the ratio of the intrinsic permeability k over the dynamic viscosity μ , and \mathcal{R} is a so-called reflection coefficient. The ion diffusion coefficient D_c is of similar nature than the classical coefficient that appears in Fick's law ([5]). However, D_c is smaller than the Fick's coefficient, as it must account for the extra "resistance" associated with the tortuous path to be taken by the salt ions as they diffuse in the shale pore network ([10]). Note that $0 \leq \mathcal{R} \leq 1$, with the lower bound corresponding to the limiting case of no chemical interaction and the upper bound corresponding to the ideal ion exclusion membrane model. In terms of \mathbf{q} and \mathbf{r} , the mass balance laws take the simple form

$$\nabla \cdot \mathbf{q} = -\dot{\zeta}, \quad \nabla \cdot \mathbf{r} = -\dot{\theta} \quad (5)$$

Equations (2), (4), and (5) can be combined with the deviatoric elasticity equation and the equilibrium equations to form a set of field equations consisting of a Navier-type equation and two coupled diffusion equations. For the class of problems characterized by an irrotational displacement field with chemical and hydraulic loadings only, the two coupled diffusion equations simplify to

$$A_{hh} D_h \nabla^2 p + A_{hc} D_h \nabla^2 \pi = \frac{\partial p}{\partial t}, \quad A_{ch} D_h \nabla^2 p + A_{cc} D_h \nabla^2 \pi = \frac{\partial \pi}{\partial t} \quad (6)$$

where

$$A_{hh} = \frac{\varphi - \mathcal{C}\mathcal{R}}{\varphi - \mathcal{C}^2}, \quad A_{hc} = \frac{\mathcal{C}\psi\omega - \mathcal{R}\varphi}{\varphi - \mathcal{C}^2}, \quad A_{ch} = \frac{\mathcal{C} - \mathcal{R}}{\varphi - \mathcal{C}^2}, \quad A_{cc} = \frac{\psi\omega - \mathcal{C}\mathcal{R}}{\varphi - \mathcal{C}^2} \quad (7)$$

Two new numbers \mathcal{C} and φ have been introduced to characterize the chemo-mechanical interactions

$$\mathcal{C} = \alpha - (\alpha - \beta) \chi, \quad \varphi = \gamma\psi - \alpha^2(\chi - 1) \quad (8)$$

In the above, $\omega = D_c/D_h$ is the ratio of the chemical to the hydraulic diffusivity, $\psi = 1/NS$ and $\chi = S_\sigma/S \geq 1$ with $S = b[\eta/G + (1/B - b)C]$ denoting the poroelastic oedometric storage coefficient ([13]), $\eta = b(1 - 2\nu)/2(1 - \nu)$ is a number defined over the interval $[0, 1/2]$, G is the shear modulus, and ν is the Poisson ratio. Generally, $\psi = O(10)$, $\varphi = O(1)$, and $\omega = O(10^{-2})$. If the fluid and solid phases can be assumed to be incompressible compared to

the skeleton, $S \simeq \eta/G$ in which case $\psi \simeq G/\eta N$ and $\varphi \simeq \gamma G/\eta N$. Also since $\alpha = \beta = 0$ for a chemically inert rock and $\alpha = \beta = 1$ in the case of an ideal ion exclusion membrane model, $0 \leq \mathcal{C} \leq 1$ with $\mathcal{C} \simeq \alpha$ near the two bounds. However, there are restrictions on the parameters, namely $(\varphi\omega - \mathcal{R}^2)(\psi - \mathcal{C}^2) > 0$ (which in practice implies that $\mathcal{R}^2 < \varphi\omega$ if $\varphi\omega < 1$) to guarantee that the smallest eigenvalue of the matrix of coefficients A 's is positive, as the diffusion equations would be ill-posed otherwise.

Once p and π have been determined for a hydraulic and/or a chemical loading, then the volumetric strain can be computed according to $\varepsilon = \eta(p - \alpha\pi)/G$.

Mathematical Model of Experiment

In order to facilitate the modeling as well as the physical interpretation of the pressure transmission - chemical potential test, the loading is decomposed into two fundamental modes corresponding to a hydraulic and a chemical perturbation. The upstream boundary conditions at $z = 0$ for each of the loading modes can then be written as

$$\text{hydraulic: } p = \sigma_h H(t), \quad \pi = 0; \quad \text{chemical: } p = 0, \quad \pi = \sigma_c H(t) \quad (9)$$

where $H(\cdot)$ is the Heaviside function and $\sigma_h = p_m - p_o$ and $\sigma_c = \pi_m - \pi_o$ are the characteristic stresses for the hydraulic and the chemical mode, respectively (with subscript o denoting an initial field). The existence of a fluid reservoir of volume V_d at the downstream end of the sample translates into the following boundary conditions at $z = L$

$$B_{hh}\nabla p + B_{hc}\nabla\pi = \frac{L}{D_h}\dot{p}, \quad B_{ch}\nabla p + B_{cc}\nabla\pi = \frac{L}{D_h}\dot{\pi} \quad (10)$$

where the coefficients B_{hh} , B_{hc} , B_{ch} and B_{cc} are linearized with respect to the mean molar concentration \bar{c}_s of the salt and the corresponding value of the osmotic pressure $\bar{\pi}$, i.e.,

$$\begin{aligned} B_{hh} &= -\xi, \quad B_{hc} = \xi\mathcal{R}, \quad B_{ch} = \frac{\xi\bar{\pi}}{K_f} [(1 - \bar{c}_s v_s)\mathcal{R} - 1], \\ B_{cc} &= \frac{\xi\bar{\pi}}{K_f} [\mathcal{R} - (1 - \bar{c}_s v_s)\psi\omega] \end{aligned} \quad (11)$$

The parameter $\xi = VSK_f/V_d$ (with K_f denoting the fluid bulk modulus) encapsulates the influence of the experimental set-up.

The coupled diffusion equations (6) together with the boundary conditions (9) and (10) can be solved in close form in the Laplace transform space, and numerically inverted to the time domain. At early time, the solution behaves according to the solution for a semi-infinite domain. At large time, the solution

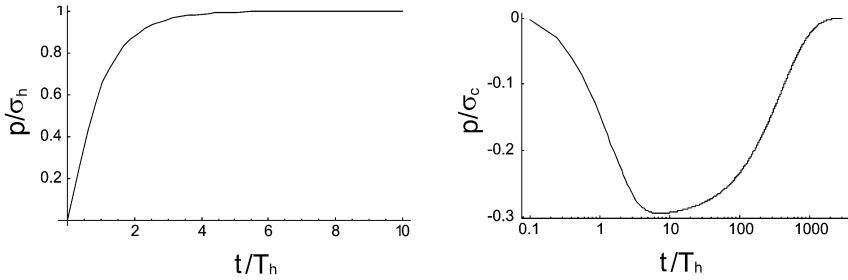


Figure 2. Evolution of the reservoir pressure for a hydraulic and a chemical loading. The pressure is scaled by the corresponding characteristic pressure while time is scaled according to the diffusion characteristic time T_h .

corresponds to the solution of the membrane problem ([10]), where only the jumps of p and π across the sample are of relevance. In the membrane mode, the two fields p and π vary linearly along the sample as they are equilibrated. The large time solution evolves according to a time scaled by the reservoir characteristic time $T_r = L^2 V_d / \kappa V K_f$, which is a function of the hydraulic storage of the reservoir.

The parameter ξ , which enters into the downstream boundary conditions, can actually be interpreted as $\xi = T_h / T_r$, where $T_h = L^2 / D_h$ is the hydraulic diffusion time scale. When $\xi \gg 1$, there exists an intermediate asymptotic behavior corresponding to the zero-flux solution at $z = L$. When $\xi \ll 1$, the solution is essentially the membrane solution.

Figure 2 illustrates the evolution of the downstream reservoir pressure in response to a hydraulic and a chemical loading. The chemical response is characterized by a pressure drop taking place over a time scale similar to the hydraulic response and a return to equilibrium over a time scale that reflects ionic diffusion throughout the sample. Interestingly, the downstream pressure response is hardly affected by the constitutive parameters α , β , and γ and depends essentially on D_h , D_c , ξ , and \mathcal{R} . In fact, the minimum reservoir pressure p_{\min} reached during chemical loading is approximately given by $p_m - p_{\min} \simeq (\pi_m - \pi_o) \mathcal{R}$ (with a strict equality if the solution behaves according to the membrane solution). Note that p_{\min} (and thus the interpreted \mathcal{R}) is virtually independent of the experimental set-up (as embodied in the parameter ξ) and of the sample length.

Results and Parameter Identification

A series of experiments on Pierre II shale (a shale from the Rocky Mountains in Colorado) has been carried out with the Membrane Efficiency Screening Equipment (MESE) in the laboratory of CSIRO Petroleum, Australia. The

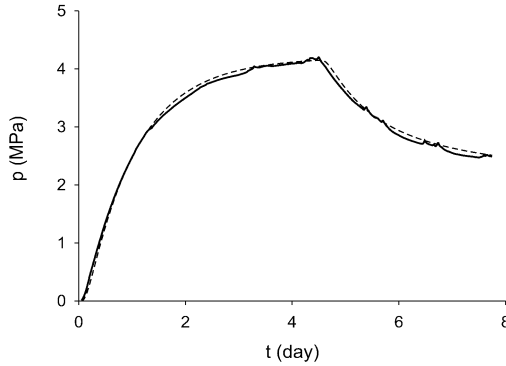


Figure 3. Downstream fluid pressure response for a pore pressure transmission test with a Pierre II Shale, for successive hydraulic and chemical loading (experimental data and matched theoretical response).

samples had a diameter of 25.4 mm and a length of either 13 mm or 25 mm. The saturation stage was conducted with a pressure p_o of about 10 MPa applied on the upstream end of the sample with Pierre II shale simulated pore fluid.

The results of one of the experiments is shown in Figure 3. This particular experiment was conducted on a sample with a length $L = 13$ mm, for a hydraulic load $\sigma_h \simeq 4.2$ MPa applied for about 4 days and a chemical load $\sigma_c \simeq 7.1$ MPa applied for about 3 days (and stopped once the minimum downstream pressure was reached). The chemical loading resulted from increasing the NaCl concentration of the solution from 3.9 wt % to 16.7 wt %. The experimental set-up is characterized by $\xi \simeq 5.1$, corresponding to $V_d \simeq 4$ mm³.

Identification of the parameters by matching the theoretical and experimental downstream pressure gives $\mathcal{R} \simeq 0.27$, $D_h \simeq 7.2 \cdot 10^{-9}$ m²/s, and $D_c \simeq 4.3 \cdot 10^{-10}$ m²/s. A comparison between the theoretical and experimental downstream pressure response is shown in Figure 3.

Concluding Remarks

A mathematical model of the pressure transmission - chemical potential experiment indicates that the two diffusivities D_h and D_c and the reflection coefficient \mathcal{R} can robustly be identified from the downstream pressure response. The analysis also confirms the experimental practice of identifying \mathcal{R} with the membrane efficiency coefficient deduced from the minimum of the downstream pressure ([7, 11]) whose justification is based on simplified considerations.

Acknowledgments

Support for this research has been provided by Total, France and CSIRO, Australia. This support is gratefully acknowledged.

References

- [1] Charlez, P. A., Pradet, V., Onaisi, A., and Gregoire, M. (1999). How to manage well-bore stability in the viking graben tertiary shales by using mud systems environmentally friendly? (SPE/IADC 52865). In *SPE/IADC Drilling Conf.*, pp 317–325.
- [2] Coussy, O. (1995). *Mechanics of Porous Continua*. John Wiley & Sons., New York.
- [3] Coussy, O., Dangla, P., Dormieux, L., and Lemarchand, E. (1999). A two-scale modeling of a swelling clay. *Journal de Physique*, 9:Pr9.21–Pr9.31.
- [4] Detournay, E. and Cheng, A.-D. (1993). *Comprehensive Rock Engineering*, volume 2, chapter 5: Fundamentals of Poroelasticity, pages 113–171. Pergamon, New York.
- [5] Kondepudi, D. and Prigogine, I. (1998). *Modern Thermodynamics : From Heat Engines to Dissipative Structures*. Wiley.
- [6] Mody, F. K. and Hale, A. H. (1993). A borehole stability model to couple the mechanics and chemistry of drilling fluid interaction. In *Proc. SPE/IADC Drilling Conf.*, pages 473–490.
- [7] Oort, E. V., Hale, A. H., Mody, F. K., and Roy, S. (1996). Transport in shales and the design of improved water-based shale drilling fluids (SPE 28309). *SPE Drilling & Completion*, pages 137–146.
- [8] Sherwood, J. D. (1993). Biot poroelasticity of a chemically active shale. *Proc. Roy. Soc. London, Ser. A*, 440:365–377.
- [9] Sherwood, J. D. (1994). A model of hindered solute transport in a poroelastic shale. *Proc. Roy. Soc. London, Ser. A*, pages 679–692.
- [10] Sherwood, J. D. and Craster, B. (2000). Transport of water and ions through a clay membrane. *J. Coll. Interf. Sci*, 230:349–358.
- [11] Tan, C. P., Drummond, C. J., Mody, F. K., and Tare, U. A. (2002). High membrane efficiency water-based drilling fluids: Alternatives to invert emulsion fluids for drilling troublesome shale formations. In *SPE Asia Pacific Oil and Gas Conference and Exhibition, Melbourne, Australia*.
- [12] Tan, C. P., Rahman, S. S., Richards, B. G., and Mody, F. K. (1998). Integrated rock mechanics and drilling fluid design approach to manage shale instability, SPE 47259. In *Proc. SPE/ISRM Eurock '98*.
- [13] Wang, H. F. (2000). *Theory of Linear Poroelasticity*. Princeton University Press.

MEASUREMENTS OF DEFORMATIONS AND ELECTRICAL POTENTIALS IN A CHARGED POROUS MEDIUM

Arjan J.H. Frijns

Eindhoven University of Technology

Department of Mechanical Engineering

P.O. Box 513, 5600 MB Eindhoven, the Netherlands

a.j.h.frijns@tue.nl

Jacques M. Huyghe and Marcel W. Wijlaars

Eindhoven University of Technology

Department of Biomedical Engineering

P.O. Box 513, 5600 MB Eindhoven, the Netherlands

j.m.r.huyghe@tue.nl and m.w.wijlaars@tue.nl

Abstract

When a biological tissue is subjected to a mechanical load, an electrical potential gradient is generated. Such potential gradient is associated with the flow of charged particles through a matrix with fixed charges. A deformation of the matrix causes a fluid flow relatively to the solid matrix. This fluid flow tends to separate the freely moving ions in the fluid from the oppositely charged particles, that are attached to the matrix. In this way, an electrical field is created collinear to the fluid flow. This results in an electrical potential. A similar effect appears when charged particles start moving because of a chemical load.

In this study, uniaxial confined swelling and compression experiments were performed on a hydrogel that mimics the behaviour of biological tissues. The deformation of the sample and the electrical potential difference over the sample, caused by varying mechanical and chemical loads, were measured successfully.

Introduction

When a biological tissue is subjected to a chemical or mechanical load, an electrical potential gradient is generated [1, 2, 7, 8, 13]. Such potential gradient is associated with the flow of charged particles through a matrix with fixed charges. This is caused by a concentration gradient or by a flow induced by a deformation as predicted by, for example, [6, 10–13]. The deformation of the

matrix causes a fluid flow relatively to the solid matrix. This fluid flow tends to separate the freely moving ions in the fluid from the oppositely charged particles, that are attached to the matrix. In this way, an electrical field is created collinear to the fluid flow. This results in an electrical potential.

In articular cartilage, streaming potentials have been demonstrated by permeation experiments and confined compression experiments [2, 4, 7, 9, 14, 15]. In the permeation experiments, a hydrostatic pressure gradient is applied across the sample. The pressure generates a fluid flow and a streaming potential that can be measured [9, 15].

Streaming potentials are also generated by deformation of the tissue. Lee et al. [14] and Frank et al. [4] measured streaming potentials generated by oscillatory compression experiments. Chen et al. [2] measured streaming potentials in confined compression experiments. In these experiments, bovine cartilage discs were subjected to step changes of the compressive stress.

The goal of this study is the measurement of the electrical potential gradient caused by mechanical and chemical loads in a confined swelling and compression experiment.

Material and Methods

We choose to do the experiments with a tissue that mimics the behaviour of biological tissues: a hydrogel. A hydrogel is a synthetic material that consists of large charged polymers that are linked to each other.

Sample preparation

The sample material was a hydrogel, that was made out of 11 g acrylic acid monomer (AA), 11 g acrylamide monomer (AAm), 100 g water (H₂O), 0.5 g cross linker MBAAm (N,N'-methylenebisacrylamide) and 0.1 g of the initialisators (NH₄)₂S₂O₈ and K₂S₂O₅. The solution was neutralised by 6.2 g NaOH. The constituents were put in a test tube where they react with each other as described by de Heus [3]. After the reactions between the components stopped, the material was submerged in a 0.15 molar NaCl-solution for one or two days. Then, the hydrogel was put in a cup filled with a 0.15 molar NaCl solution and was stored at room temperature.

After taking the hydrogel out of the test tube, it was cut by a scalpel in slices with a thickness of about 1 mm. The diameter of these samples was 4.0 mm.

Experimental set-up

The samples were put in an uniaxial swelling and compression testing device (figure 1). In a uniaxial confined swelling and compression experiment, a cylindrical sample was enclosed in an impermeable confining ring made out of Athlon[®] (Trespa International B.V., The Netherlands). This was done in

order to have an electrical insulating ring around the sample. Athlon[®] was used because it was an insulator and it did not swell due to water absorption (water absorption < 1 weight%, according to the manufacturer). A mechanical load was applied on top of the sample via a loading piston, made out of glass. Inside the piston was a chamber filled with a 0.15 M NaCl solution (figure 1). This chamber was closed at the bottom with a dense glass filter. Inside the chamber, a Ag/AgCl electrode was placed (MI-402 Micro-Reference Electrode, Microelectrodes Inc., USA). At the bottom of the sample was a glass filter through which a NaCl solution flowed. The permeability of the glass filter (pore size 16 – 40 μm , permeability $10^{-12} \text{ m}^4\text{N}^{-1}\text{s}^{-1}$) was much larger than the permeability of the sample. Thus, the boundary conditions were well defined for the fluid flow and for the ion concentrations along the filter-sample interface. A chemical load was applied by altering the salt concentration of the bathing solution. A similar electrode as in the piston was mounted in the fluid channel.

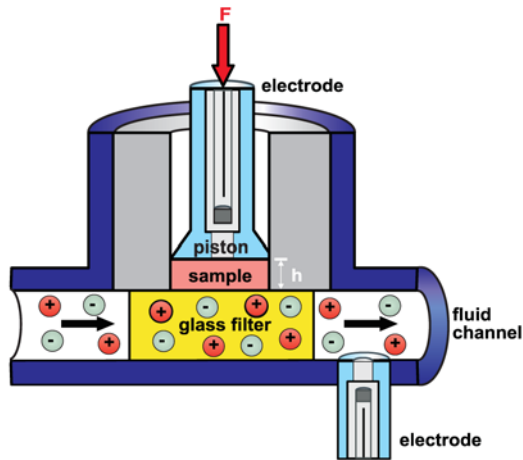


Figure 1. Schematic representation of the experimental set-up.

The deformation of the sample and the electrical potential difference over the sample were measured. The electrical potential difference between both electrodes were amplified by a Unicam 9460 amplifier (Unicam, USA). During the experiments, the displacement of the piston was recorded via a linear variable displacement transducer (LVDT, Schaevitz, USA). The data acquisition sampling was 0.5 Hz. A vibrator was attached to the set-up in order to overcome the sticking of the piston to the wall. This device vibrated intermittently at 50 Hz during 1 second. The vibration started 0.5 second after the data-acquisition. Lateral forces on the piston were minimised by allowing free lateral motion of the measuring chamber floating on a silicon oil film. Further-

more, the piston was greased with vaseline to prevent leakage between the wall and the piston.

Before the experiment started, the electrodes were filled with an electrolyte solution from Microelectrodes Inc., USA (3.0 M KCl solution saturated with AgCl).

Experimental protocol

The experimental protocol is shown in figure 2 (top). In the first three stages an equilibrium was reached. Thereafter, a faster change in the external salt concentration was applied. In these stages no equilibrium was reached for both the sample height and the electrical potential difference. The values for the ion concentration were chosen such that the shrinking of the sample due to the mechanical load was about the same as the swelling due to the chemical load.

Results

The results of 2 representative experiments out of 11 are shown in figure 2 [5].

After 4.5 hours, the sample started swelling due to a change in the chemical load: the concentration of the bathing solution was decreased from 0.45 M to 0.15 M. The tissue swelling was in the range of 30% – 36%.

After 12.5 hours, the sample shrank due to an extra mechanical load. The load was increased from 0.078 MPa to 0.195 MPa. The tissue shrinking was in the range of 33% – 36%. An equilibrium was reached after about 1 to 3 hours, depending on the sample thickness.

In the last part ($t > 20$ hours), the sample started swelling and shrinking because of changes of the chemical loads. These changes were prescribed before a new equilibrium was reached. The change of the salt concentration in the bathing solution was also responsible for the forming of an electrical potential difference over the sample. This is shown in the lower graphs of figure 2.

Discussion

In our experiment, we measured an electrical potential difference between both electrodes. Since the salt concentrations inside the sample can alter, the electrical potential is the sum of a streaming potential and a diffusion potential [13]. We assume that there is a thin layer of fluid on top of the sample, that is in equilibrium with the inner salt concentration. As long as we only alter the mechanical load, we measure a streaming potential. In the other cases, the measured electrical potential difference is a combination of a streaming

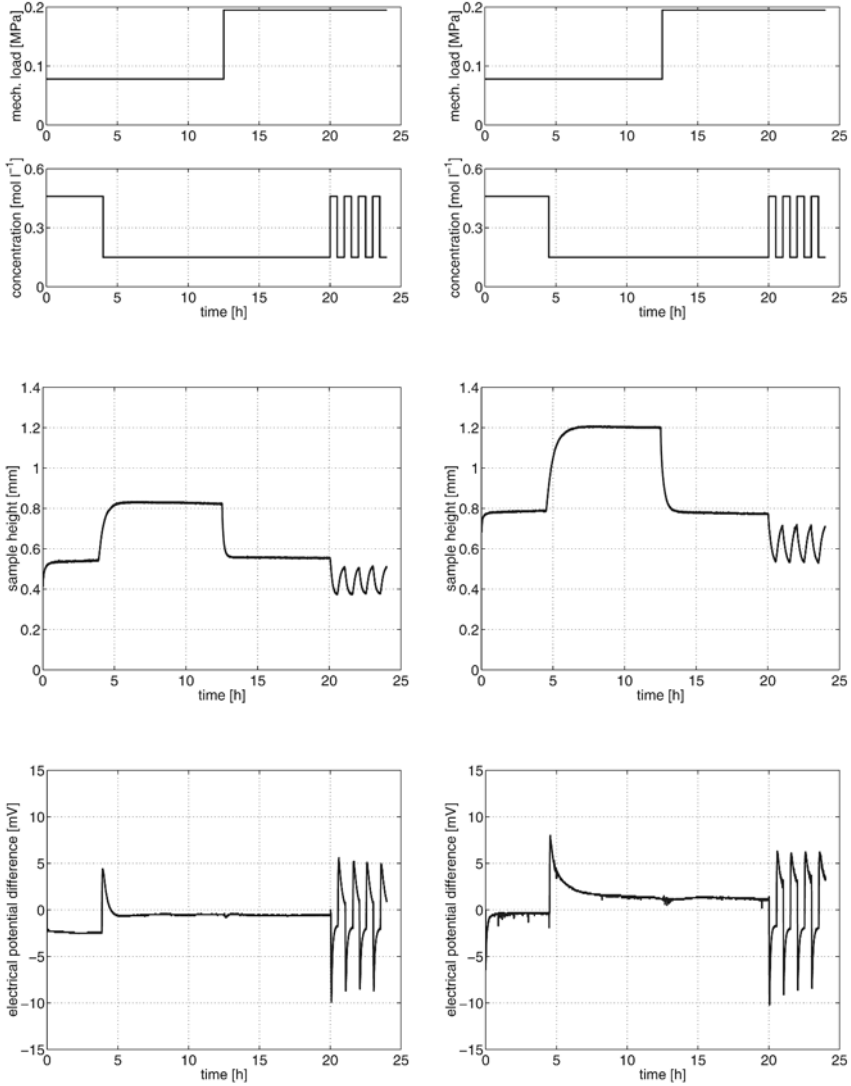


Figure 2. Experimental results for 2 confined swelling and compression experiments performed on hydrogel. The boundary conditions are given in the corresponding top figures.

potential, a diffusion potential and an electrical potential jump over the sample boundaries.

Also in other confined compression experiments, a streaming potential was measured when a mechanical load was applied [2]. This streaming potential is characterised by an electrokinetic coefficient k_e :

$$k_e := \frac{\Delta\xi}{\Delta\sigma}. \quad (1)$$

Here, ξ is the electrical potential and σ is the mechanical load. The value for the electrokinetic coefficient k_e for bovine cartilage was found to be in the range from -2 to -12 mV MPa⁻¹ [2].

In our confined swelling and compression experiment, we also applied a mechanical load to the sample ($t = 12.5$ h). We measured a streaming potential $\Delta\xi = 0.85 \pm 0.65$ mV. The change in the mechanical load $\Delta\sigma$ equals -0.117 MPa. Thus, the value for the electrokinetic coefficient is -7.3 ± 5.6 mV MPa⁻¹. This was in the same range as measured for bovine cartilage.

In the experiments, it is seen that the equilibrium values for the electrical potential difference were different for different concentrations of the bathing solution. The difference between the equilibrium values of the first and the second stage is -0.93 ± 2.96 mV. This may indicate that there was a small leakage over the electrode filters.

Conclusions

We were able to measure the electrical potential difference over a sample, that was caused by a change in the mechanical load or by a change in the chemical load. When altering only the mechanical load, the measured electrical potential difference was in the same range as reported for bovine cartilage.

References

- [1] Bassett, C.A.L. and Pawluk, R.J. (1972) Electrical behavior of cartilage during loading. *Science* **178**, 982–983
- [2] Chen, A.C., Nguyen, T.T. and Sah, R.L. (1999) Streaming potentials during the confined compression creep test of normal and proteoglycan-depleted cartilage. *Annals of Biomechanical Engineering* **25**, 269–277
- [3] de Heus, H.J. (1994) *Verification of Mathematical Models Describing Soft Charged Hydrated Tissue Behaviour*. PhD thesis, Eindhoven University of Technology, Eindhoven
- [4] Frank, E.H. and Grodzinsky, A.J. (1987) Cartilage electromechanics–II. A continuum model of cartilage electrokinetics and correlation with experiments. *Journal of Biomechanics* **20**, 629–639
- [5] Frijns, A.J.H. (2000) *A Four-Component Mixture Theory Applied to Cartilaginous Tissue: Numerical Modelling and Experiments*. PhD thesis, Eindhoven University of Technology, Eindhoven

- [6] Frijns, A.J.H., Huyghe, J.M., Kaasschieter, E.F. and Wijlaars, M.W. (2003) Numerical simulation of deformations and electrical potentials in a cartilage substitute. *Biorheology* **40**, 123–131
- [7] Grodzinsky, A.J., Lipshitz, H. and Glimcher, M.J. (1978) Electromechanical properties of articular cartilage during compression and stress-relaxation. *Nature* **275**, 448–450
- [8] Gross, D. and Williams, W.S. (1982) Streaming potential and the electromechanical response of physiologically-moist bone. *Journal of Biomechanics* **15**, 277–295
- [9] Gu, W.Y., Lai, W.M. and Mow, V.C. (1993) Transport of fluid and ions through a porous-permeable charged-hydrated tissue, and streaming potential data on normal bovine articular cartilage. *Journal of Biomechanics* **26**, 709–723
- [10] Huyghe, J.M. and Janssen, J.D. (1997) Quadriphasic mechanics of swelling incompressible porous media. *International Journal of Engineering Science* **35**, 793–802
- [11] Kaasschieter, E.F., Frijns, A.J.H. and Huyghe, J.M. (2003) Mixed finite element modeling of cartilaginous tissues. *Mathematics and Computers in Simulation* **61**, 549–560
- [12] Lai, W.M., Hou, J.S. and Mow, V.C. (1991) A triphasic theory for the swelling and deformation behaviors of articular cartilage. *ASME Journal of Biomechanical Engineering* **113**, 245–258
- [13] Lai, W.M., Mow, V.C., Sun, D.D. and Ateshian, G.A. (2000) On the electric potentials inside a charged soft hydrated biological tissue: streaming potential versus diffusion potential. *Journal of Biomechanical Engineering* **122**, 336–346
- [14] Lee, R.C., Frank, E.H., Grodzinsky, A.J. and Roylance, D.K. (1981) Oscillatory compressional behavior of articular cartilage and its associated electromechanical properties. *ASME Journal of Biomechanical Engineering* **103**, 280–292
- [15] Maroudas, A. (1968) Physicochemical properties of cartilage in the light of ion exchange theory. *Biophysical Journal* **8**, 575–595

INCORPORATING CHEMICAL EFFECTS IN A POROTHERMOELASTIC FORMULATION AND APPLICATION TO INCLINED BOREHOLES

Shailesh Ekbote¹ and Younane Abousleiman²

¹*Shell International Exploration and Production Inc., Houston, Texas*

²*PoroMechanics Institute, The University of Oklahoma, Norman, Oklahoma 73019*

Abstract A poromechanics formulation for transversely isotropic chemically active poroelastic media under non-isothermal conditions is presented. The formation pore fluid is modeled as a two-species constituent comprising of the solute and the solvent. The model is applied to study the thermo-chemical effects on the stress and pore pressure distributions in the vicinity of an inclined borehole drilled in a chemically active transversely isotropic formation under non-isothermal conditions.

Keywords: porochemothermoelasticity, poromechanics, anisotropy, borehole

Introduction

The coupling effects of various poromechanical processes on the response of a porous medium have been successfully addressed by Biot's theory of poroelasticity and its extensions [3,4,5,8,2]. The chemical effects have also been addressed by considering interaction between the porous matrix and a pore fluid comprising of a solute and solvent [10, 7, 6]. Comprehensive anisotropic poromechanics formulations and corresponding solutions for the inclined borehole problem have been presented [4–2]. However, the coupled chemo-thermo-hydro-mechanical response of an anisotropic porous medium has not been addressed to date.

In this paper, the focus is on the development of a poromechanics model which addresses the chemical effects within the framework of the anisotropic porothermoelastic model [2]. The resulting model, termed as porochemothermoelastic, accounts for fully coupled chemo-thermo-hydro-mechanical response of a chemically active formation saturated with a pore fluid comprising of two species under non-isothermal conditions. The numerical example presented demonstrates the thermo-chemical effect on the stress and pore pres-

sure distributions in the vicinity of an inclined borehole drilled through a transversely isotropic formation.

Transversely Isotropic Porochemothermoelasticity

We consider a porous system comprising of the solid matrix completely saturated with a pore fluid containing two chemical species; a solute and a solvent with mole fractions \bar{m}^s and \bar{m}^w , respectively, and chemical potentials given by [9]

$$\mu^s = pV_s + RT \ln(\varrho^s \bar{m}^s) \quad (1)$$

$$\mu^w = pV_w + RT \ln(\varrho^w \bar{m}^w) \quad (2)$$

where μ^s and μ^w are the chemical potentials for the solute and solvent, V_s and V_w are the partial molar volumes of the solute and solvent, p is the thermodynamic pore pressure, R is the universal gas constant, T is the temperature, ϱ^s and ϱ^w are the activity coefficients of the solute and the solvent, and $\bar{m}^w = 1 - \bar{m}^s$. The solution is assumed to be ideal with $\varrho^s = \varrho^w = 1$. It is assumed that the transversely isotropic material bears an isotropic plane ($x-y$) and a transverse direction (z -axis) along which the material properties are different. The constitutive relations for a chemically active transversely isotropic medium are given as follows

$$\sigma_{xx} = M_{11}\epsilon_{xx} + M_{12}\epsilon_{yy} + M_{13}\epsilon_{zz} - \alpha p - \beta^s T + \gamma^s m^s \quad (3)$$

$$\sigma_{yy} = M_{12}\epsilon_{xx} + M_{11}\epsilon_{yy} + M_{13}\epsilon_{zz} - \alpha p - \beta^s T + \gamma^s m^s \quad (4)$$

$$\sigma_{zz} = M_{13}\epsilon_{xx} + M_{13}\epsilon_{yy} + M_{33}\epsilon_{zz} - \alpha' p - \beta^{s'} T + \gamma^{s'} m^s \quad (5)$$

$$\tau_{xy} = G\gamma_{xy}; \quad \tau_{yz} = G'\gamma_{yz}; \quad \tau_{zx} = G'\gamma_{zx} \quad (6)$$

$$\zeta^s = \bar{m}^s \frac{V_s}{V_{sol}} \left[\frac{p}{M} + \alpha(\epsilon_{xx} + \epsilon_{yy}) + \alpha'(\epsilon_{zz}) - \beta^{sf} T \right] + \bar{\beta}^c m^s \quad (7)$$

$$\zeta^w = (1 - \bar{m}^s) \frac{V_w}{V_{sol}} \left[\frac{p}{M} + \alpha(\epsilon_{xx} + \epsilon_{yy}) + \alpha'(\epsilon_{zz}) - \beta^{sf} T \right] - \bar{\beta}^c m^s \quad (8)$$

where σ_{ij} is the total stress tensor, ϵ_{ij} is the solid strain tensor, ζ^s is the variation of solute content, ζ^w is the variation of the solvent content, p is the pore pressure, T is the temperature, m^s is the variation of the solute mole fraction, M_{11} , M_{12} , M_{13} are components of the drained elastic modulus tensor, M is Biot's modulus, α and α' are the Biot's effective stress coefficients, γ^s and $\gamma^{s'}$ are the chemo-mechanical coupling coefficients, β^c is the hydro-chemical coupling coefficient, β^s and $\beta^{s'}$ are the thermic coefficients related to the solid skeleton, β^{sf} is the thermic coefficient related to the fluid constituent. β^s , $\beta^{s'}$ and β^{sf} are related to the expansion coefficients of the solid matrix and fluid [2,6]. The transport equations for the solute and solvent flux are given by

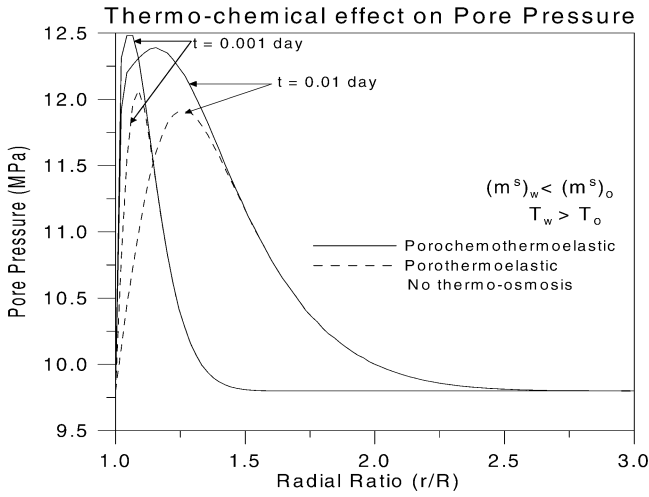


Figure 1. The thermo-chemical effect on the pore pressure distribution for $m_w^s < m_o^s$ with $T_w > T_o$ at $t = 0.001, 0.01$ day

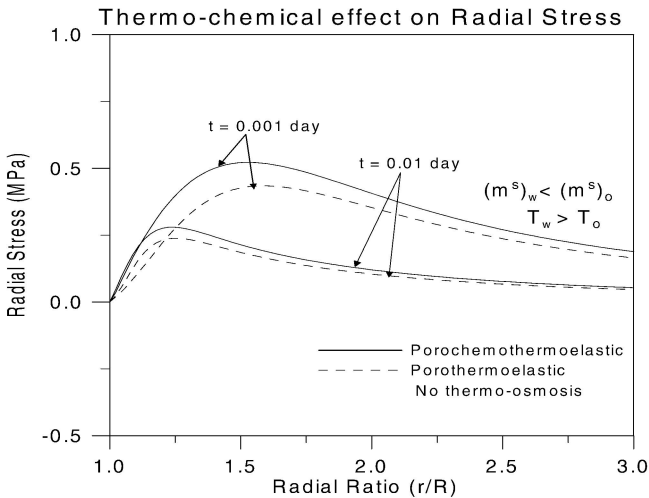


Figure 2. The thermo-chemical effect on the radial stress distribution for $m_w^s < m_o^s$ with $T_w > T_o$ at $t = 0.001, 0.01$ day

$$q_i^s = -(1 - \chi) [\bar{m}^s \kappa_{ij} p_{,j} + D_{ij} m_{,j}^s] \quad (9)$$

$$q_i^w = -(1 - \bar{m}^s) \kappa_{ij} p_{,j} + \frac{1}{V_w} [\chi RT \kappa_{ij} + (1 - \chi) V_s D_{ij}] m_{,j}^s + D_{ij}^T T_{,j} \quad (10)$$

where q_i^s is the solute flux, q_i^w is the solvent flux, κ_{ij} is the mobility coefficient tensor, D_{ij} is the solute diffusivity tensor, D_{ij}^T is a phenomenological coefficient tensor associated with thermo-osmosis and χ is the reflection coefficient.

The constitutive relations are combined with the equilibrium equations to give the Navier-type equations which are expressed as

$$\frac{1}{2}(M_{11} - M_{12})u_{i,jj} + \frac{1}{2}(M_{11} + M_{12})u_{j,ji} = \alpha p_{,i} + \beta^s T_{,i} - \gamma^s m_{,i}^s \quad (i, j = 1, 2) \quad (11)$$

Energy conservation yields the heat diffusion equation given as follows

$$\frac{\partial T}{\partial t} - c_h \nabla^2 T = 0; \quad c_h = \frac{\lambda}{\rho C_v} \quad (12)$$

Also, following the steps outlined in [7], the coupled diffusion equations can be expressed as

$$\frac{\partial}{\partial t} (\Pi_i) - c_i \nabla^2 (\Pi_i) = l_i \frac{\partial T}{\partial t}; \quad i = 1, 2 \quad (13)$$

where Π_1 , Π_2 , c_1 , c_2 , l_1 and l_2 are as given by [7].

Application to the Inclined Bore Hole Problem

The borehole is assumed to be infinitely long and inclined with respect to the in-situ three-dimensional state of stress. The axis of the borehole is assumed to be perpendicular to the plane of isotropy of the transversely isotropic formation. Details of the problem geometry, boundary conditions and solutions for the stresses, pore pressure and temperature are available in [7]. The solution is applied to assess the thermo-chemical effects on stresses and pore pressures. Both the formation pore fluid and the wellbore fluid are assumed to comprise of two chemical species, i.e., a solute fraction and solvent fraction. The formation material properties are those of a Gulf of Mexico shale [7] given as $E = 1853.0$ MPa; $\nu = 0.22$; $B = 0.92$; $k = 10^{-4}$ md; $\mu = 10^{-9}$ MPa.s; $c_h = 8.64 \times 10^{-5}$ m²/day; $\chi = 0.9$; $\phi = 0.14$; $c_h = 0.13824$ m²/day; $\alpha^{sm} = 6.0 \times 10^{-6}$ /°C; $\alpha^{sf} = 3.0 \times 10^{-4}$ /°C. A simplified example is considered wherein the in-situ stress gradients are assumed to be trivial and pore pressure gradients of the formation fluid and wellbore fluid are assumed to be = 9.8 kPa/m. The difference between the formation temperature and the wellbore fluid temperature is assumed to be 50°C. The solute concentration in the pore fluid is assumed to be more than that in the wellbore fluid such that $m_w^s - m_o^s = -1.8 \times 10^{-2}$.

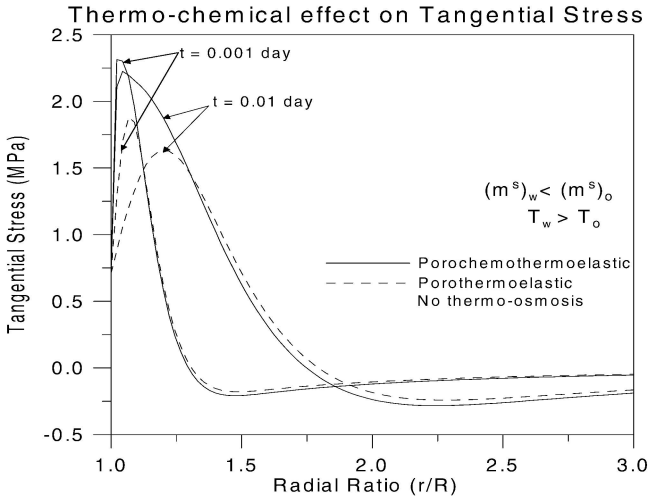


Figure 3. The thermo-chemical effect on the tangential stress distribution for $m_w^s < m_o^s$ with $T_w > T_o$ at $t = 0.001, 0.01$ day

Figure 1 shows the pore pressure variation along the radial distance. Results are shown for the poro thermoelastic and the porochemo thermoelastic analysis for $t = 0.001, 0.01$ day. A higher wellbore fluid temperature results in a temperature-induced pore pressure which is seen in the poro thermoelastic curves. In the porochemo thermoelastic case, the higher chemical potential of the water in the wellbore fluid induces an even higher pore pressure which is the thermo-chemical effect. As seen in figure 1, the magnitude of the pore pressure is higher for small time intervals and reduces as time increases. Figures 2 and 3 show the total radial and tangential stresses respectively generated by the thermo-chemical effect. These stresses are compressive in nature and higher for the porochemo thermoelastic case.

Conclusions

A transversely isotropic porochemo thermoelastic model has been presented in this paper. The model has been applied to the problem of an inclined borehole and the thermo-chemical effects on stress and pore pressure distributions have been isolated in a simplified example. Results from the simplified example show that a higher temperature along with a lower solute concentration of the wellbore fluid results in increased magnitudes of the pore pressure near

the wellbore. For the same case, incorporating thermo-osmotic effects results in even higher near wellbore pore pressures.

Acknowledgments

The authors would like to thank Dr. Rajesh Nair and Dr. Mazen Kanj for the discussion pertaining to the results and constructive suggestions in preparing this manuscript.

References

- [1] Abousleiman, Y. and Cui, L. (1998) Poroelastic solutions in transversely isotropic media for wellbore and cylinder. *Int. J. Solids Structures* **35**, 4905-4929
- [2] Abousleiman, Y. and Ekbote, S. (2005) Porothermoelastic solution for an inclined borehole in transversely isotropic media. *J. Appl. Mech.* **72**, 102-114
- [3] Biot, M.A. (1941) General theory of three-dimensional consolidation. *J. Appl. Phys.* **12**, 155-164
- [4] Biot, M.A. (1955) Theory of Elasticity and consolidation of a porous anisotropic solid. *J. Appl. Phys.* **26**, 182-185
- [5] Coussy, O. (1995) *Mechanics of Porous Continua*, John Wiley & Sons, New York
- [6] Ekbote, S. and Abousleiman, Y. (2005) Porochemoelasticity: Application to the inclined borehole. *J. Engrg. Mech., ASCE*, in press
- [7] Ekbote, S. (2002) Anisotropic Poromechanics of the wellbore coupled with Thermal and Chemical Gradients. *Ph.D. Dissertation*, The University of Oklahoma
- [8] Mody, F.K. and Hale, A.H. (1993) A borehole model to couple the mechanics and chemistry of drilling fluid shale interaction. *Proc. SPE/IADC Drilling Conf.*, **Paper 25728**, Richardson, Texas, Society of Petroleum Engineers
- [9] Sherwood, J.D. (1993) Biot poroelasticity of a chemically active shale. *Proc. R. Soc. Lond. A* **440**, 365-377
- [10] Sherwood, J.D. (1994) A model of hindered solute transport in a poroelastic shale. *Proc. R. Soc. Lond. A* **445**, 679-692

V

MAGNETIC RESONANCE.

Chairman: J. Carmeliet

ION TRANSPORT AND CRYSTALLIZATION IN POROUS MATERIALS AS STUDIED BY MAGNETIC RESONANCE IMAGING

Leo Pel*, Henk P. Huinink and Klaas Kopinga

Department of Applied Physics

Eindhoven University of Technology

P.O. Box 513

5600 MB Eindhoven

The Netherlands

Abstract Salt weathering is one of the major causes of deterioration of buildings and monuments. We have determined the underlying moisture and ion transport within a representative building material by measuring the time evolution of NaCl saturated samples during one-sided drying with Magnetic Resonance Imaging. The obtained NaCl concentration profiles reflect the competition between advection to the surface and redistribution by diffusion. By representing the measured moisture and NaCl profiles in a so-called efflorescence pathway diagram (EPD) also information about the crystallization process is obtained. The pathways followed in the EPDs indicate that for historical objects in general crystallization at the surface cannot be avoided, when evaporation cannot be prevented.

Introduction

Although salt damage has been studied for many years ([2]; [3]; [11]; [7]), the mechanisms that control salt crystallization in porous building materials and the resulting damage by crystal growth are poorly understood. A better knowledge of the transport of water and ions during drying and salt crystallization in porous materials is needed to explain salt damage in different materials and under various conditions. The development of realistic models for combined moisture and ion transport is hampered by the lack of adequate and reliable experimental data. However, using NMR imaging techniques non-

*To whom correspondence should be addressed (email: l.pel@tue.nl).

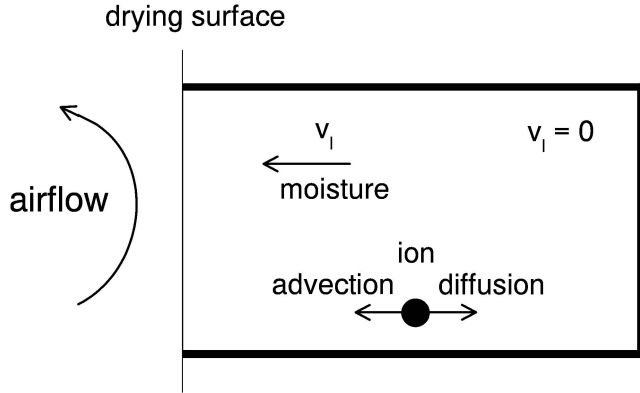


Figure 1. A schematic diagram of the one-sided drying of a sample saturated with a salt solution. v_l is the moisture fluid velocity

destructive measurements of the moisture and ion profiles in these materials are possible ([4]; [8]). This offers new possibilities to approach the problem.

In this paper we focus on the one-dimensional drying of a fired-clay brick initially saturated with a NaCl solution. First we discuss the moisture and ion transport during evaporation. The NMR method and setup for measuring the moisture and Na distribution during drying is discussed in section 3. Finally, we discuss results for fired-clay brick and a new representation of these results in a so-called efflorescence pathway diagram (EPD) in section 4.

Moisture and Ion Transport

In figure 1 a schematic representation is given of the drying process in a sample saturated with a salt solution. During this process moisture is transported to the drying surface. Given that the influence of gravity is negligible, the moisture transport for a one-dimensional problem, considered in this paper, can be described with a nonlinear diffusion equation ([1]):

$$\frac{\partial \theta}{\partial t} = \frac{\partial}{\partial x} D_w(\theta) \frac{\partial \theta}{\partial x}, \quad (1)$$

where θ [m^3m^{-3}] and $D_w(\theta)$ [m^2s^{-1}] are the volumetric liquid moisture content and the so-called isothermal moisture diffusivity, respectively. In this 'lumped' model all mechanisms for moisture transport, i.e., liquid flow, surface flow and vapour diffusion, are combined into a single moisture diffusivity which depends on the actual moisture content. Note that the transport of water due to a salt gradient has been neglected, although salts might have a direct influence on the capillary action, viscosity, and permeability and therefore on the moisture diffusivity. During drying the ions are transported by advection

with the moisture and diffusion within the moisture. If the interactions between the ions and the walls are neglected, which is justified for fired-clay brick, the transport of ions can be described by ([1]):

$$\frac{\partial c\theta}{\partial t} = \frac{\partial}{\partial x} \left[\theta c v_l - \theta D_s(\theta) \frac{\partial c}{\partial x} \right] - R. \quad (2)$$

In this equation c [mol l⁻¹], $D_s(\theta)$ [m²s⁻¹], v_l [ms⁻¹] and R [mol l⁻¹s⁻¹] respectively are the ion concentration in the water, the diffusion coefficient of the ions in the moisture, velocity of the moisture flow and and the crystallization rate. Expression 2 makes clear that during a drying experiment there is a competition between advection, which forces ions to move to the top of the sample and thereby causes accumulation, and diffusion, which levels off any accumulation. It has been shown that the following Peclet number determines the behaviour of the system ([6]):

$$Pe \equiv \frac{hL}{\theta_m D_s(\theta_m)},$$

where h [m³m⁻²s⁻¹], L [m] and θ_m [m³m⁻³] are the drying rate, the sample length and the maximum fluid content by capillary saturation, respectively. For $Pe \ll 1$ diffusion dominates and the distribution of ions will be uniform, whereas for $Pe \gg 1$ advection dominates and ions will accumulate at the drying surface. Note that h/θ_m is in fact the initial the velocity of water at the drying surface.

Nuclear Magnetic Resonance Technique

In a nuclear magnetic resonance (NMR) experiment the magnetic moments of the nuclei are manipulated by suitably chosen radio frequency fields, resulting in a so-called spin-echo signal. The amplitude of this signal is proportional to the number of nuclei excited by the radio frequency field. NMR is a magnetic resonance technique, where the resonance condition for the nuclei is given by:

$$f = \gamma B_0 \quad (3)$$

In this equation f is the frequency of the radio frequency field, γ is the gyromagnetic ratio ($\gamma = 42.6$ MHz/T for ¹H, 11.3 MHz/T for ²³Na and 4.2 MHz/T for ³⁵Cl) and B_0 is the externally applied static magnetic field. Because of this condition the method can be made sensitive to one type of nuclei and therefore to hydrogen (and thus to water), sodium or chloride. Because the sensitivity of chloride is very low this ion was not considered in the present study.

For the experiments described here a home-built NMR scanner is used, which incorporates an iron-cored electromagnet operating at a field of 0.78 T. In order to perform quantitative measurements a Faraday shield was placed

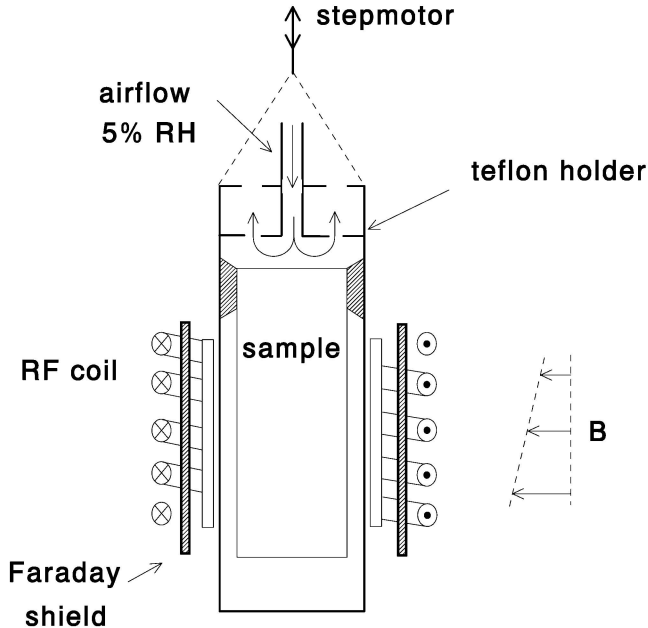


Figure 2. A schematic diagram of the NMR set-up for measuring the moisture and Na distribution during drying.

between the tuned circuit of the probe head and the sample ([8]). In addition the quality factor of the LC circuit was chosen rather low ($Q \approx 40$), to suppress the effects of the (electrically conducting) NaCl solution.

The sample, a fired-clay brick cylinder with a length of 45 mm and a diameter of 20 mm, was placed inside a closed tefflon holder to prevent evaporation. A constant magnetic field gradient of up to 0.3 T/m was applied using Anderson coils, giving a one-dimensional resolution of the order of 2 mm for both water and Na. The spin-echo experiments were performed at a fixed frequency, corresponding to the centre of the RF coil (fig. 2). The sample, which has a cylindrical shape with a diameter of 20 mm and a length of 45 mm, is moved vertically through the magnet with the help of a step motor. It is sealed at all sides, except for the top over which air with a relative humidity of 5% is blown. In this way a one-dimensional drying process is created.

While the sample is drying, first the moisture content in the small region of the sample near the centre of the RF coil is measured. Next, the frequency is changed from 33 MHz (^1H) to 9 MHz (^{23}Na) and the Na concentration in that region is measured. After these two measurements the sample is moved in the vertical direction by the step motor and the moisture and Na concentration are measured again. The measurement time for the moisture content was 1 minute

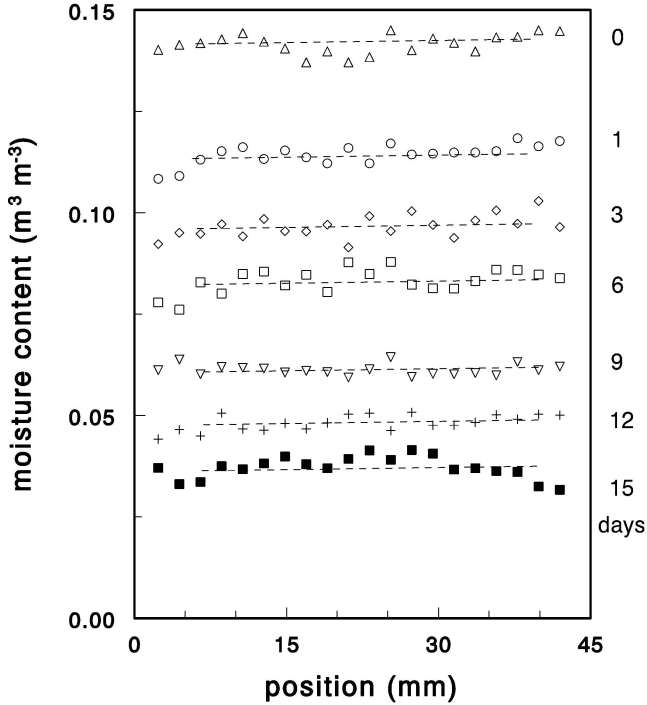


Figure 3. Moisture profiles measured during drying of a fired-clay brick sample of 45 mm length after 0, 1, 3, 6, 9, 12, and 15 days. The drying surface is at 0 mm.

whereas it took 4 minutes to measure the Na content with a similar signal to noise ratio. This procedure is repeated until a complete moisture and Na profile have been measured. A time stamp is given to each measurement point. Measuring an entire Na concentration profile takes about 3 hours. Since the typical time of a drying experiment is several days, the variation of the moisture and ion profiles during a single scan can be neglected. With NMR settings used in these experiments only the Na nuclei in the solution are measured, i.e., no signal is obtained from NaCl crystals.

Efflorescence Pathway Diagram

We have performed experiments on fired-clay bricks, because they show almost no adsorption of ions at the pore wall. As an example of a typical experiment, we first discuss the results for a 3 M NaCl solution. A few representative moisture profiles are shown in figure 3. This figure shows that the moisture profiles are nearly flat, which indicates that the moisture distribution within the sample remains homogeneous during this evaporation experiment, i.e., up

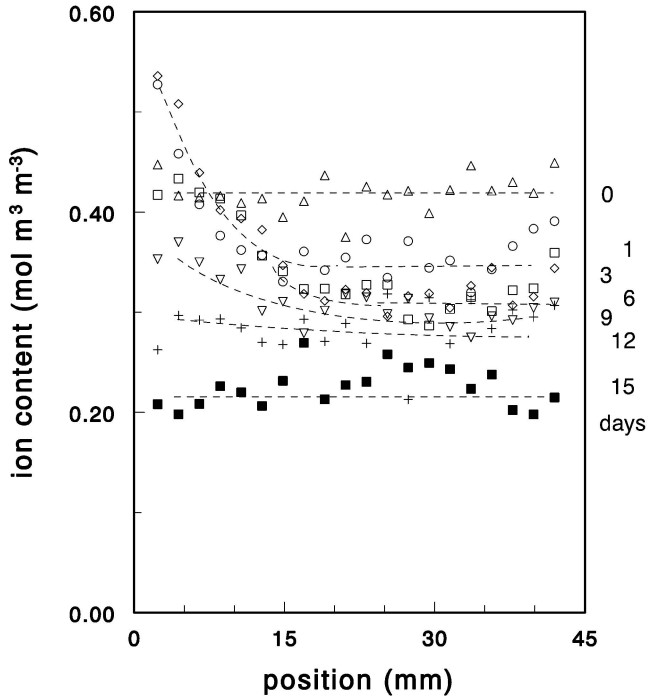


Figure 4. Absolute content of dissolved Na ion profiles measured during drying of a fired-clay brick sample of 45 mm length after 0, 1, 3, 6, 9, 12, and 15 days. The drying surface is at 0 mm.

to 14 days we did not observe a receding drying front. This was observed in all experiments performed within this study. We attribute this to the wetting properties of the NaCl solution and the low drying rates used in these experiments. The Na ion profiles are shown in figure 4. This figure makes clear that within 1 day after the start the Na profiles develops a peak just below the drying surface. At 12-15 days after the start of the drying process the Na profiles are flat again. This behaviour is more clearly visible in the Na concentration profiles, that are obtained via point by point division of the corresponding Na and H profiles. We have plotted these concentration profiles in figure 5. During the initial drying, Na ions are advected to the surface (position 0 mm) and the NaCl concentration increases to 6 M, which is the saturation concentration of a NaCl solution. From this point on any additional advection will lead to crystallization at the top of the sample, which is indeed observed as a white efflorescence. From this point on the NaCl concentration profile starts to level off until the salt concentration is everywhere at 6 M. The total moisture content of the sample can be obtained directly by integrating the moisture profiles. Its

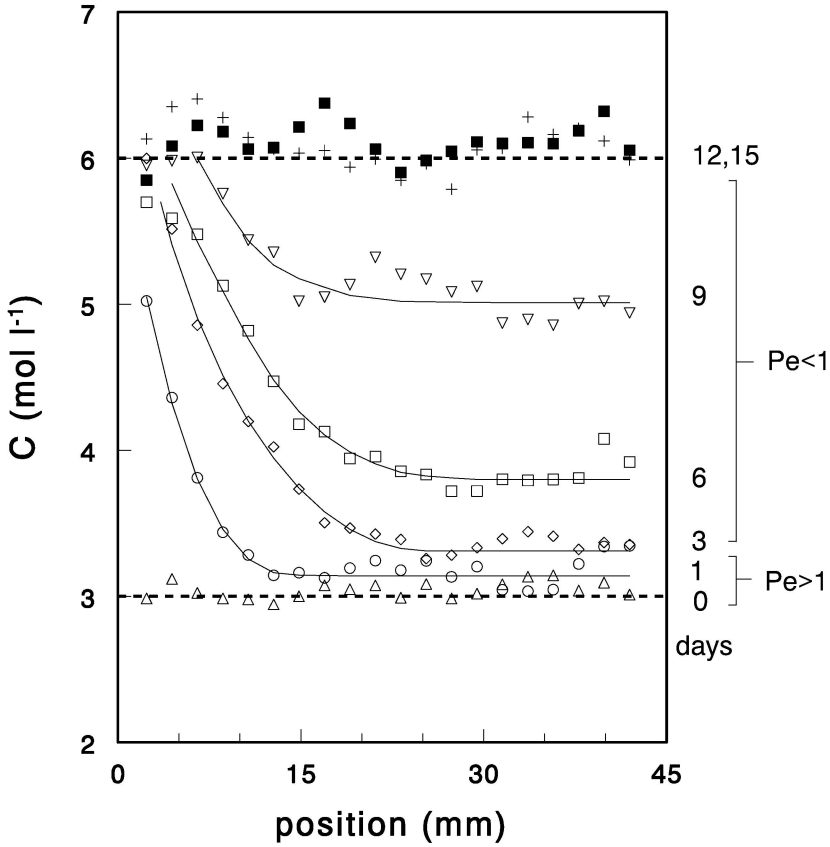


Figure 5. NaCl concentration profiles measured during drying of a fired-clay brick sample of 45 mm length after 0, 1, 3, 6, 9, 12, and 15 days. The drying surface is at 0 mm.

time derivative, together with the sample dimensions, yields the drying rate, h . We have used a value of D_s of the order of $10^{-9} \text{ m}^2\text{s}^{-1}$ to estimate the Peclet number ([5]). Initially the evaporation rate gives rise to $Pe \approx 3$, corresponding to situation in which salts accumulate at the surface, whereas after a few days Pe decreases to 0.7, corresponding to the levelling off of the ion profile. To quantify the crystallization occurring at the surface, the data resulting from the drying experiment, shown in the figures 3-5, have been plotted in a so-called efflorescence pathway diagram, EPD ([10]), figure 6. In an EPD the product of the average salt concentration and the average moisture saturation, $C_{avg}S_{avg}$, is plotted against the average moisture saturation, S_{avg} . Note that $C_{avg}S_{avg}$ is proportional to the total amount of dissolved NaCl present in the solution (with the NMR no signal is obtained from NaCl crystals). Two limiting situations can be distinguished. In the first case the system dries very slow drying,

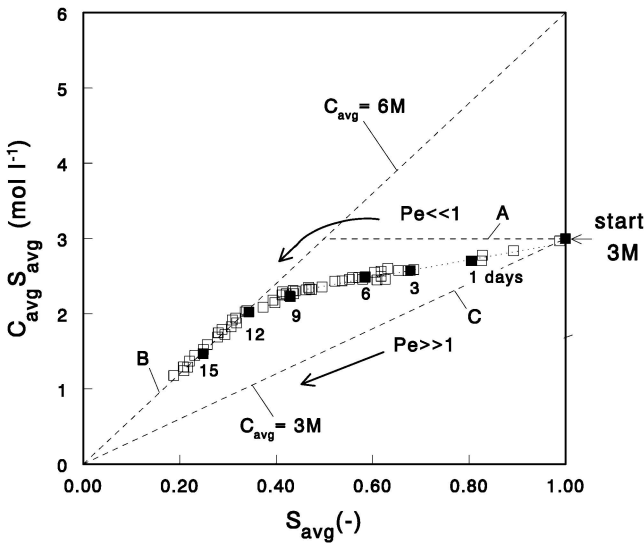


Figure 6. Efflorescence pathway diagram: $C_{avg} S_{avg}$, which represents the total amount of NaCl present in the solution, as a function of the average saturation S_{avg} . The data correspond to the drying experiment plotted in the figures 3-5.

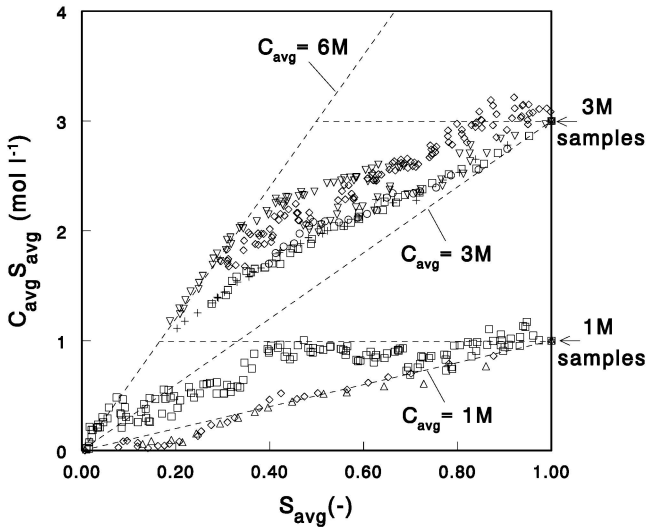


Figure 7. Efflorescence pathway diagram: $C_{avg} S_{avg}$, which represents the total amount of NaCl present in the solution, as a function of the average saturation S_{avg} for all experiments performed on fired-clay brick with initial concentrations of 1M and 3M.

$Pe \ll 1$. The ion profiles will remain homogeneous and for some time no crystallization will occur. The average NaCl concentration slowly increases (line A) until the saturation concentration, 6 M, is reached. From this point on any additional drying results in crystallization (line B). The second case corresponds with a fast drying system, $Pe \gg 1$. Ions are strongly advected with the moisture to the top of the sample and a 6 M peak will build up with a very small width. If the rate of crystallization is high enough, i.e., given that there are enough nucleation sites close to the surface, the average NaCl concentration in the solution in the sample itself will remain constant at nearly the initial concentration (line C).

In any point within the region bounded by the lines A, B and C moisture removal results in an increase of the NaCl concentration. A decrease of $C_{avg}S_{avg}$ can only be caused by crystallization. This requires that salt is transported to a region with a local concentration of 6 M, that is, the drying surface in our experiments. Because the transport is driven by evaporation, crystallization always happens via a (small) change of S_{avg} . The total amount of NaCl ions in the solution, $C_{avg}S_{avg}$, and the average saturation, S_{avg} , have been obtained by integrating the Na profiles and the H profiles measured by NMR, respectively. The resulting pathway for the experiment, shown in the figures 3-5, indicates that a peak in the NaCl concentration is present during the first 9 - 12 days and salt crystallizes at the top, i.e., salt efflorescence occurs. After this period the concentration is at 6 M in the entire sample.

Various additional experiments have been done with different air-flow rates over the samples and different salt concentrations. In figure 7. we have plotted all pathways for the experiments performed with the various samples starting at initial concentrations of 1 and 3 M. In a few experiments indeed the boundary line of $Pe \gg 1$ is followed. This indicates that the salt crystallization is indeed fast enough and is not a limiting factor; that is, there are enough nucleation sites in this type of material and no supersaturation occurs. In contrast to the experiments for 3 M, it is possible to follow the $Pe \ll 1$ boundary line for 1 M.

Conclusion

The NMR measurements on combined moisture and ion transport during drying in combination with the efflorescence pathway diagrams, EPD, prove to be a powerful tool for studying salt weathering. The EPDs reflect the competition between advection to the surface and redistribution by diffusion, but also visualize the crystallization. The EPDs indicate that in general, crystallization at the surface cannot be avoided. However, it is evident that the evaporation rate is the key parameter in the process. Therefore, the solution for salt damage problems strongly depends on the environmental conditions. When

historical objects are preserved indoors, where climatological conditions can be controlled easily, the relative humidity has to be kept as constant as possible and airflow around the object should be prevented, in order to avoid wetting/drying cycles. Outdoor monuments and buildings are exposed to wind and fluctuations of the relative humidity. High drying rates (and thus high Pe numbers) cannot be avoided and hence one should limit the sources of salts, e.g., preventing flooding and hindering rising damp.

Acknowledgments

A part of this project was supported by the Dutch Technology Foundation (STW).

References

- [1] Bear, J. and Bachmat, Y. (1990) Introduction to modelling of transport phenomena in porous media, Vol. 4. Kluwer, Dordrecht
- [2] Evans, I.S. (1970) Salt crystallisation and rock weathering: a review. *Rev. Geomorph. Dynam.* **19**, 153
- [3] Goudie, A.S. and Viles, H. (1997) Salt Weathering Hazards. John Wiley & Sons, Chichester
- [4] Gummerson, R.J., Hall, C., Hoff, W.D., Hawkes, R., Holland, G.N. and Moore, W.S. (1979) Unsaturated water flow within porous materials observed by NMR imaging. *Nature* **281**, 56
- [5] Lide, D.R. (1998) Handbook of Chemistry and Physics, 1998. 79th edn. CRC Press, Boca Raton, Florida
- [6] Huinink, H.P., Pel, L. and Michels, M.A.J. (2002) How ions distribute in a drying porous medium - a simple model. *Phys. Fluids* **14**, 1389
- [7] Lewin, S.Z. (1980) The mechanism of masonry decay through crystallization, Conservation of historic stone buildings and monuments. National Acad. Press, Washington D.C.
- [8] Pel, L. (1995) Moisture transport in porous building materials, PhD thesis. Eindhoven University of Technology, Eindhoven
- [9] Pel, L., Kopinga, K. and Kaasschieter, E.F. (2000) Saline absorption in calcium silicate brick observed by NMR scanning. *J. Phys. D: Appl. Phys.* **33**, 1380
- [10] Pel, L., Huinink, H.P. and Kopinga, K. (2002) Ion transport and crystallization in organic building materials as studied by nuclear magnetic resonance. *Appl. Phys. Lett.* **81**, 2893
- [11] Wellman, H.W. and Wilson, A.T. (1965) Salt weathering, a neglected geological erosive agent in coastal and arid environments, *Nature* **205**, 1097

NUMERICAL AND EXPERIMENTAL STUDIES OF THE WATER AND IONIC MOBILITIES WITHIN SUSPENSIONS OF CHARGED ANISOTROPIC COLLOIDS

Alfred Delville and Patrice Porion

CRMD, CNRS, 1B rue de la Férollerie, 45071 Orléans cedex 2, France

delville@cnrs-orleans.fr or porion@cnrs-orleans.fr

Abstract We use Nuclear Magnetic Resonance relaxometry (*i.e.* the frequency variation of the NMR relaxation rates) of quadrupolar nucleus (^{23}Na) and ^1H Pulsed Gradient Spin Echo NMR to determine the mobility of the counterions and the water molecules within aqueous dispersions of clays. The local ordering of isotropic dilute clay dispersions is investigated by NMR relaxometry. In contrast, the NMR spectra of the quadrupolar nucleus and the anisotropy of the water self-diffusion tensor clearly exhibit the occurrence of nematic ordering in dense aqueous dispersions. Multi-scale numerical models exploiting molecular orbital quantum calculations, Grand Canonical Monte Carlo simulations, Molecular and Brownian Dynamics are used to interpret the measured water mobility and the ionic quadrupolar relaxation measurements.

Keywords: Colloids, Nuclear Magnetic Resonance, Relaxation, Diffusion.

Introduction

Clays are ubiquitous materials used for many industrial applications whose optimisation requires an accurate knowledge of the structure of the clay dispersions [1–5] and the mobility of their labile components (solvent molecules, neutralizing counterions, salt molecules). Nuclear Magnetic Resonance is a powerful tool for deriving structural and dynamical information [6]. We chose to use relaxation measurements of monovalent counterions [7–9] (sodium) because of the high sensitivity of the corresponding nuclear magnetic probes (^{23}Na) and because these counterions interact strongly with the ionised clay surfaces, leading to structural and dynamical information on the colloid itself. Supplementary information on the structure of the clay dispersions is also obtained by measuring the water self-diffusion tensor by means of ^1H Pulsed Gradient Spin Echo NMR measurements [10, 11]. The analysis of these PGSE-

NMR measurements is performed by numerical simulations with a multi-scale modelling [11] of the structure of the clay dispersions and the diffusion of the water molecules or the sodium counterions, by using Brownian Dynamics in order to bridge the gap between the time scale accessible by Molecular Dynamics (typically a few ps) and that explored by the NMR measurements (from ns to ms).

Materials and Methods

Sodium Laponite RD from Laporte was used without purification. Dilute dispersions (maximum concentration 10% w/w) were prepared by stirring during one hour in 10^{-2} M (NaCl) aqueous solution at pH 10. Concentrated clay samples (23-66% w/w) were obtained by oedometric uniaxial compression of dilute dispersions using external pressures between 0.5 and 2 MPa. ^{23}Na NMR spectra were recorded [7–9] on DSX360, MSL200 and DSX100 Bruker spectrometers at fields of 8.465, 4.702 and 2.351 T, respectively obtained with superconducting magnets. ^1H PGSE-NMR was used to determine the macroscopic mobility [10, 11] of the water molecules along the three principal directors of the diffusion tensor within the Laponite dispersions.

Results and Discussion

Isotropic dilute suspensions

^{23}Na spectra recorded in dilute Laponite dispersions (less than 10% w/w) display no residual coupling and so these dilute suspensions, at least as far as NMR is concerned, appear macroscopically isotropic. Despite the lack of residual quadrupolar coupling, structural and dynamical information may be extracted from the frequency variation of the relaxation measurements [7, 8] (see Figure 1). The cross-over frequency displayed in Figure 1 corresponds to the diffusion time required by the sodium counterions to escape from locally ordered micro-domains whose size corresponds to the clay diameter. Increasing this clay size by one order of magnitude reduces this cross-over frequency by two orders of magnitude because of the simultaneous increase of the ordered micro-domains (Figure 1). In addition to ^{23}Na measurements the self-diffusion tensor describing the water mobility in dilute Laponite dispersions is perfectly isotropic (see Table 1).

Concentrated nematic dispersions

Typical ^{23}Na NMR spectra recorded within dense Laponite dispersion are shown in Figure 2, clearly exhibiting a large residual quadrupolar splitting [9] fingerprint of the macroscopic nematic ordering of these dense Laponite dispersions (more than 23% w/w). The cancellation of this residual quadrupolar

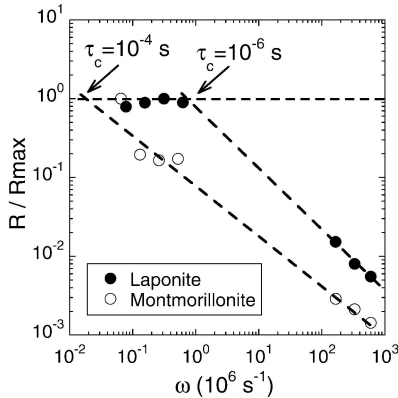


Figure 1. Frequency variation of the ^{23}Na relaxation rates in dilute aqueous dispersions of two different clays.

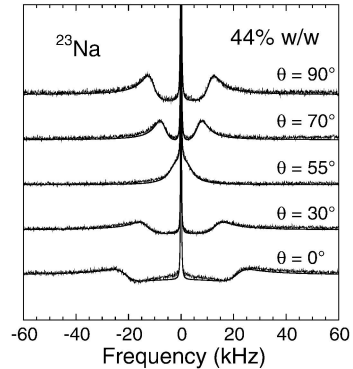


Figure 2. Splitting of the ^{23}Na resonance lines in the presence of dense Laponite dispersion (44% w/w).

splitting at the magic angle ($\theta_M = 54.7^\circ$) results from the existence of a single macroscopic director in these dense dispersions. The water mobility measured by ^1H PGSE-NMR experiments confirms [10, 11] this macroscopic ordering of the dense Laponite suspensions because of the anisotropy of the tensor describing the water self-diffusion (see Table 1).

A multi-scale modelling [11] of the water self-diffusion is necessary to interpret these data by extrapolating the dynamical information accessible by Molecular Dynamics simulations to the time scale investigated by the NMR measurements. We first performed MD simulations of the trajectories of the water molecules and sodium. The density of the solvent molecules and the initial configurations of the water molecules and the sodium counterions was determined by preliminary GCMC simulations. For these GCMC and MD numerical simulations we used an empirical model of bulk water (TIP4P) compatible with an inter-atomic force field extracted from quantum calculations of the water/clay short-range interactions. The self-diffusion coefficient D_α quantifying the water mobility along any direction (denoted \vec{e}_α) is evaluated by integrating the velocity autocorrelation function (see Figure 3):

$$D_\alpha = \lim_{t \rightarrow +\infty} \int_0^t \langle \vec{v}_\alpha(0) \vec{v}_\alpha(\tau) \rangle d\tau \quad (1)$$

Brownian Dynamics is then used to simulate the macroscopic mobility of the water molecules. The water mobility near to the clay surface is identified to the water mobility calculated by MD simulations. The ordering of the simulated dispersions was selected to be compatible with the information obtained

from the line-shape analysis of the ^{23}Na NMR spectra. Two different ordered phases were generated corresponding either to a simple orientational ordering (in nematic phase) or including also some positional ordering of the Laponite disks within a columnar phase. In order to check the influence of the size of the clay particles, the BD simulations were performed for two disk diameters: 200 and 300 Å.

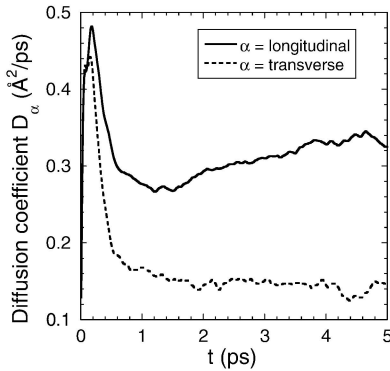


Figure 3. Anisotropy of the water mobility near the clay surface for longitudinal and transverse directions.

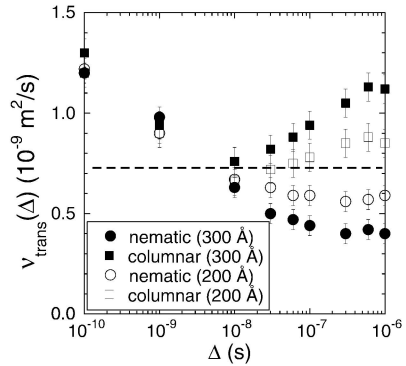


Figure 4. Water transverse mobilities $\nu(\Delta)$ as a function of the diffusion time Δ . The horizontal line corresponds to the water macroscopic mobility measured by ^1H PGSE-NMR.

The correlation between the structure of the clay dispersions and the water mobility is investigated by the use of the self-diffusion propagator $P_s(\vec{r}', \Delta | \vec{r}, 0)$, *i.e.* the probability density of finding at time Δ and position \vec{r}' a diffusing probe initially located at a position \vec{r} :

$$\Psi(\vec{r}', \Delta) = \int \Psi(\vec{r}, 0) P_s(\vec{r}', \Delta | \vec{r}, 0) d\vec{r} \quad (2)$$

where $\Psi(\vec{r}, 0)$ is the bulk density at equilibrium. The Fourier Transform of the self-diffusion propagator along a single direction (\vec{e}_α) is directly comparable with the PGSE-NMR measurements; it is Gaussian for unrestricted motions. However, in the case of diffusion restricted by the collisions of the water molecules at the solid/liquid interfaces, the self-diffusion propagator along a selected director is no longer Gaussian except in two limiting dynamical regimes:

- at very short diffusion times ($\Delta=10^{-10}$ s), when the fraction of colliding water molecules remains negligible;
- at long diffusion times ($\Delta > 3 \times 10^{-7}$ s), when the mobility of the water molecules has been averaged over the whole structure of the solid/liquid interfaces, leading to an effective macroscopic mobility.

Table 1. The tortuosity is defined by the ratio $\tau_\alpha = D_0/D_{\alpha\alpha}$ where D_0 is the self-coefficient of the bulk water ($1.92 \times 10^{-9} \text{ m}^2 \text{ s}^{-1}$). $\Delta\nu_Q^{max}$ is the maximum quadrupolar splitting detected by ^{23}Na NMR. The Laponite samples noted by an asterisk were prepared by oedometric compression.

Sample	τ_\perp	τ_\parallel	$\Delta\nu_Q^{max}$ (kHz)
H ₂ O	1.00	1.00	0
3% w/w	1.07	1.05	0
6% w/w*	1.18	1.13	0
23% w/w*	1.75	1.24	14 ± 2
29% w/w*	1.90	1.33	16 ± 2
32% w/w*	2.20	1.55	16 ± 2
44% w/w*	2.71	1.33	22 ± 2
45% w/w*	2.69	1.32	28 ± 2
66% w/w*	4.31	1.49	30 ± 2

The transverse mobility of the water molecules in the intermediate dynamical regime is displayed in Figure 4 as a function of the diffusion time. A continuous decrease of the apparent water mobility is detected within the pure nematic phases (with only orientational order) significantly underestimating the transverse mobility measured by ^1H PGSE-NMR ($D_{trans} = (0.73 \pm 0.02) \times 10^{-9} \text{ m}^2/\text{s}$). Decreasing the diameter of the disks at constant density of the Laponite particles was shown to enhance the apparent water mobility. By contrast, the apparent transverse mobility of the water molecules evaluated within the columnar phases is a non-monotonic function of the diffusion time, leading to a macroscopic mobility significantly larger than the experimental value. Nevertheless, the agreement between simulated and experimental data is satisfactory since no fitted parameters were used for these simulations. Our numerical simulations clearly exhibit the great sensitivity of the measurements of the solvent mobility by PGSE-NMR as a structural probe of the porous media.

Conclusion

By detecting the residual splitting of the resonance line of quadrupolar cations (^{23}Na) and the anisotropy of the water self-diffusion tensor measured by ^1H PGSE-NMR, we have demonstrated the occurrence of nematic ordering within dense ($>23\%$ w/w) aqueous dispersions of Laponite clays. In contrast, our analysis of the ^{23}Na relaxometry is compatible with only local ordering of the Laponite particles within dilute ($<10\%$ w/w) isotropic suspensions. A multi-scale modelling of the dilute and concentrated clay dispersions was ne-

cessary to fully interpret these measured water mobility and ionic relaxation on the basis of the structure of the clay dispersions. The same structural information could be extracted from the measurements of the solvent or ionic diffusion performed in other porous media also limited by ionised solid/liquid interfaces.

Acknowledgments

We cordially thank Mrs A.M. Faugère and Drs J.R.C. van der Maarel (Leiden University, The Netherlands), P. Levitz, M. Al-Mukhtar, S. Rodts, B. Gherardi and E. Lécolier for their collaboration.

References

- [1] Murchid, A., Delville, A., Lambard, J., Lécolier, E. and Levitz, P. (1995) Phase Diagram of Colloidal Dispersions of Anisotropic Charged Particles: Equilibrium Properties, Structure, and Rheology of Laponite Suspensions. *Langmuir* **11**, 1942-1950
- [2] Bakk, A., Fossum, J.O., Silva, G.J.D., Adland, H.M., Mikkelsen, A. and Elgsaeter, A. (2002) Colloidal dispersions suspensions and aggregates Viscosity and transient electric birefringence study of clay colloidal aggregation. *Physical Review E* **65**, 21407-21500
- [3] Bonn, D., Tanaka, H., Wegdam, G., Kellay, H. and Meunier, J. (1999) Aging of a colloidal "Wigner" glass. *Europhysics Letters* **45**, 52-57
- [4] Gabriel, J.C.P., Sanchez, C. and Davidson, P. (1996) Observation of Nematic Liquid-Crystal Textures in Aqueous Gels of Smectite Clays. *The Journal of Physical Chemistry* **100**, 11139-11143
- [5] Lemaire, B.J., Panine, P., Gabriel, J.C.P. and Davidson, P. (2002) The measurement by SAXS of the nematic order parameter of laponite gels. *Europhysics Letters* **59**, 55-61
- [6] Callaghan, P.T., (1991) *Principles of Nuclear Magnetic Resonance Microscopy*. Clarendon Press, Oxford, Great Britain
- [7] Porion, P., Faugère, M.P., Lécolier, E., Gherardi, B. and Delville, A. (1998) ²³Na Nuclear Quadrupolar Relaxation as a Probe of the Microstructure and Dynamics of Aqueous Clay Dispersions: An Application to Laponite Gels. *The Journal of Physical Chemistry B* **102**, 3477-3485
- [8] Delville, A., Porion, P. and Faugère, A.M. (2000) Ion Diffusion within Charged Porous Network as Probed by Nuclear Quadrupolar Relaxation. *Journal Physical Chemistry B* **104**, 1546-1551
- [9] Porion, P., Al-Mukhtar, M., Meyer, S., Faugère, A.M., van der Maarel, J.R.C. and Delville, A. (2001) Nematic Ordering of Suspensions of Charged Anisotropic Colloids Detected by ²³Na Nuclear Magnetic Resonance. *The Journal of Physical Chemistry B* **105**, 10505-10514
- [10] Porion, P., Rodts, S., Al-Mukhtar, M., Faugère, A.M. and Delville, A. (2001) Anisotropy of the Solvent Self-Diffusion Tensor as a Probe of Nematic Ordering within Dispersions of Nanocomposites. *Physical Review Letters* **87**, 208302-208700
- [11] Porion, P., Al-Mukhtar, M., Faugère, A.M., Pellenq, R.J.M., Meyer, S. and Delville, A. (2003) A Multiscale Analysis of ¹H Pulsed Gradient Spin-Echo NMR Measurements. *The Journal of Physical Chemistry B* **107**, 4012-4023

VI

TWO POROSITIES.

Chairman: Y. Lanir

A CHEMO-MECHANICAL MODEL FOR ARTICULAR CARTILAGE

The Role of Intra- and Extrafibrillar Waters

Fernando M.F. Simões

*Instituto Superior Técnico, Departamento de Engenharia Civil and ICIST,
Avenida Rovisco Pais, 1049-001 Lisboa, Portugal*

fsimoes@civil.ist.utl.pt

Benjamin Loret

*Laboratoire Sols, Solides, Structures
B.P. 53X, 38041 Grenoble Cedex, France*

Benjamin.Loret@hmg.inpg.fr

Abstract A three-phase multi-species electro-chemo-mechanical model of articular cartilage is developed that accounts for the effect of two water compartments, namely intrafibrillar water stored in between collagen fibrils and extrafibrillar water covering proteoglycans. The collagen fibers constitute the solid phase while intrafibrillar water and dissolved NaCl on one hand and extrafibrillar water, ions Na^+ and Cl^- and proteoglycans on the other hand form the two fluid phases. Chemical equilibrium between the fluid phases is assumed and only the mechanical aspects of the behaviour are considered.

Keywords: Articular cartilage; chemo-mechanical couplings; swelling.

Introduction

Articular cartilage is a porous medium bathed in an electrolyte and in which electro-chemo-mechanical couplings play a key role. Appropriate hydration is an essential ingredient that allows articular cartilage to support compressive stresses. Hydration is mainly due to the presence of negatively charged proteoglycans. The gel formed by hydrated proteoglycans is reinforced by collagen fibers. Collagen fibers form fibrillar structures that trap their own water.

Articular cartilage has to sustain changes of chemical composition of the electrolyte and mechanical loads. Its overall bearing capacity is believed to

Jacques M. Huyghe et al. (eds), IUTAM Proceedings on Physicochemical and Electromechanical Interactions in Porous Media, 167–172.

© 2005 Springer. Printed in the Netherlands.

be due to the water pressure generated by proteoglycans that is equilibrated by tension of collagen fibers and external loads. Moreover, in order to sustain external loads, articular cartilage adapts and modifies its internal configuration, through exchanges between intra- and extrafibrillar waters and ions.

In line with the idea of [4], collagen fibrils behave as a semipermeable membrane, impermeable to macromolecules of molecular mass larger than 4000 gm, and permeable to dissolved ions Na^+ and Cl^- and water. They are viewed as separating the two fluid phases.

The presence of proteoglycans in the extrafibrillar compartment would result in water depletion in the intrafibrillar compartment when the salinity of the synovial joint, or of the bath in laboratory experiments, is decreased. Therefore there should be mechanisms that retain intrafibrillar water within fibrils. Here, hydration forces that act at short distances, a few angströms, are postulated to be the main factor that limit the exchangeability of intrafibrillar water.

The constitutive equations use a thermodynamic framework, that in fact embodies not only purely mechanical aspects, but also transfers of masses between the phases and diffusion of matter through the extrafibrillar phase. Since focus is on the chemo-mechanical couplings, we use experimental data that display different salinities. The structure of the constitutive functions and the state variables on which they depend are briefly motivated. Calibration of material parameters is defined and simulations of confined compression tests and of free swelling tests with a varying chemistry are described and compared with available data in [3]. The evolution of internal entities entering the model, e.g. the masses and molar fractions of water and ions, during some of these tests is also documented to highlight the main microstructural features of the model.

Definition of the Phases

Our definition of the phases is mechanically motivated. A kinematical criterion on the other hand would sort species according to their velocities. Cartilage is viewed as a three-phase, multi-species, porous medium:

- the *solid phase S* contains the collagen fibers;
- the *intrafibrillar fluid phase I* contains three species, intrafibrillar water w , sodium ions Na^+ and chloride ions Cl^- ;
- the *extrafibrillar fluid phase E* contains four species, proteoglycans PG, extrafibrillar water, sodium and chloride ions.

A certain minimal concentration of sodium cations is required to ensure electroneutrality of the extrafibrillar phase.

Exchanges of water and ions occur between the fluid phases, but only the extrafibrillar phase communicates with the exterior, Figure 1.

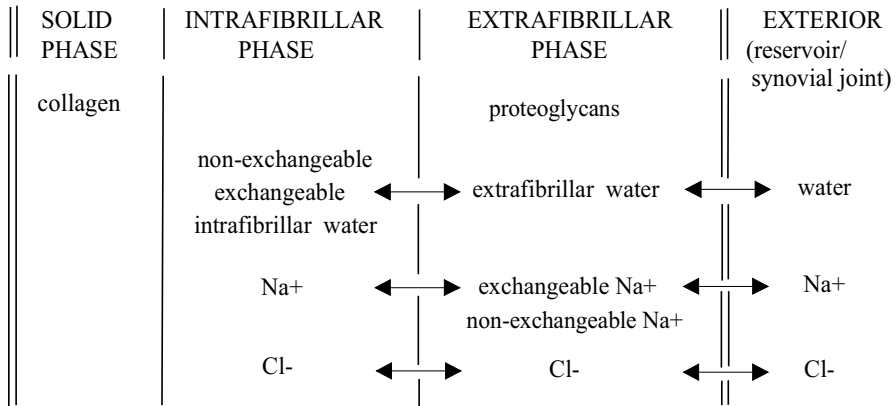


Figure 1. Articular cartilage is partitioned in three phases, one solid phase and two fluid phases. Each fluid phase contains several species. Some of these species are exchangeable, at least partially: water and ions can enter and leave the intrafibrillar space defined by collagen fibrils. Proteoglycans which are macromolecules are too large to be admitted into that space, at least in absence of osteo-arthritis. Water and ions can also be exchanged between the extrafibrillar phase and the exterior.

The three-phase multi-species framework follows the *strongly interacting* model of [1], namely:

- (H1) The mass balance is required for each species. Mass balance for each phase is obtained via mass balances of the species it contains.
- (H2) Momentum balance is required for the mixture as a whole. Water and ions in the extrafibrillar phase are endowed with their own velocities so as to allow the latter to diffuse in their phase (possibly involving electrical effects) and satisfy their own balance of momentum.
- (H3) The velocity of any species in the intrafibrillar phase is that of the solid phase, i.e. of collagen, $\mathbf{v}_{kI} = \mathbf{v}_S, \forall k \in I$. The velocity of the proteoglycans which do not diffuse through the cartilage is also equal to \mathbf{v}_S . Therefore, the balance of momentum of the above species is not required explicitly, but accounted for by the balance of momentum of the mixture. Note that this assumption does not hinder exchange of water and ions between the two fluid phases, this exchange being viewed as a *mass transfer* and not as a diffusion process.
- (H4) In the intrafibrillar phase, the pressure p_I is uniform, while, in the extrafibrillar phase, water and ions are endowed, through constitutive equations, with their own intrinsic pressure.
- (H5) Electroneutrality is required for the extrafibrillar phase alone, and for the solid and intrafibrillar fluid phases together.

As already mentioned, the definition of phases in articular cartilage is not unambiguous, because the mechanical, chemical and electrical roles of proteoglycans (PG's) may dictate contradictory choices. In fact, if the phase criterion was kinematically based (that is on velocity), PG's would be classified as part of the solid phase. However, its osmotic effect is important, not so much because of its concentration or molar fraction itself, but because of its effective charge and the latter should be involved in the electroneutrality condition of the extrafibrillar phase.

The Chemo-Mechanical Model

It is crucial to define a reference configuration, or state, to which all tests can be reckoned. Such a reference state, referred to as *hypertonic state*, is defined as the state of maximum salinity of the extrafibrillar compartment: then as the salt content overweights the presence of proteoglycans, the latter have a very small mechanical effect: the hypertonic configuration is such that the stress is equal to the bath pressure. Therefore, stresses and pressures can be reckoned to their values at the hypertonic state from which all tests start and at which by convention the strain vanishes as well.

As a consequence of electroneutrality in the two fluid phases, the mass content of chloride anions is no longer an independent variable and it can be eliminated in favor of the mass content of the cations sodium. A direct consequence is that the electrical field does not enter the elastic constitutive equations, that can be phrased in terms of chemical, rather than electro-chemical, potentials.

All species are assumed to be incompressible so that the total volume change of the cartilage is equal to the sum of the volume changes of the two fluid phases, $\delta \text{tr } \epsilon = \delta v_I + \delta v_E$. The constitutive equations will thus be phrased in terms of *shifted* generalized stresses, and the intrafibrillar pressure has to be obtained by boundary conditions. The chemical energy of the intrafibrillar phase does not contribute to the chemo-mechanical elastic potential that serves to formulate the constitutive equations. This potential is due to three contributions: a purely chemical contribution to recover the classical logarithmic term in the chemical potentials, a chemo-mechanical coupled contribution, and a configurational part that represents the history of formation of the cartilage, and accounts for the initial equilibrium between phases.

Having obtained the elastic equations in terms of shifted entities, and reverting to total entities, the constitutive equations express the total stress σ , the chemical potentials of the extrafibrillar water μ_{wE} and of the salt μ_{sE} , and the hydration potential of the intrafibrillar water μ^{hydr} , in terms of the generalized strains, namely the strain of the porous medium ϵ , the mass-contents of the extrafibrillar water m_{wE} and of the cations sodium $m_{\text{Na}E}$, and the mass-content of intrafibrillar water m_{wI} . The interested reader is directed to [3].

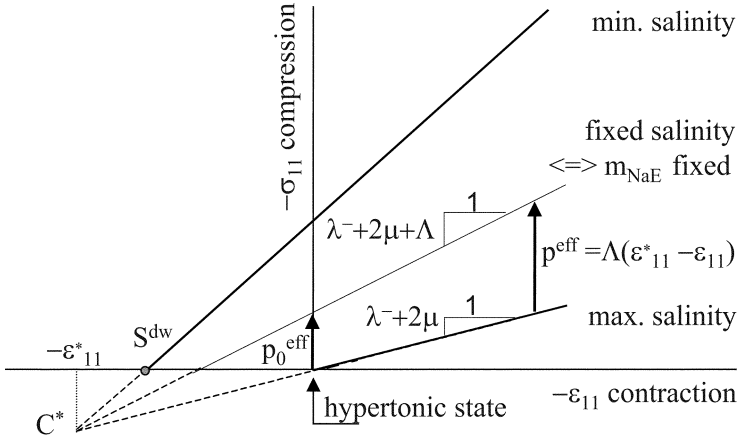


Figure 2. Confined compression tests at given bath salinity correspond to a linear in-axis stress-strain relation. The maximal salinity is associated to the minimal elastic moduli, that is to $\Lambda = 0$, or to a zero intercept with the stress axis $p_0^{eff} = 0$ (reckoning stresses and pressures from the hypertonic state). A given bath salinity is also assumed to correspond to a given mass-content of sodium in the extrafibrillar phase m_{NaE} . The function $p_0^{eff}(m_{NaE})$ embodies the monotonous increase of the slopes of the confined compression tests, as bath salinity decreases.

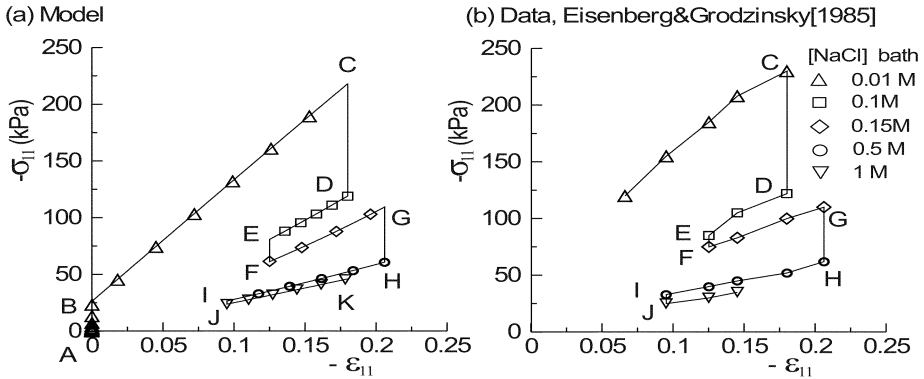


Figure 3. Complex loading path involving successive confined compression, at fixed bath salinity, and increase in bath salinity at fixed strain. Shielding of negative charges of proteoglycans by salt reduces the repulsive forces and the overall compressive stress. (a) Model simulations; (b) Experimental data.

As a partial illustration of the model, Figure 3 shows simulations of experimental data by [2] performed sufficiently slowly so that they represent a

sequence of equilibria. The model provides indications on the internal partition of water during loading tests with controlled mechanical or chemical conditions. Experimental data are crucially needed to a better quantitative understanding of the effects on its overall properties of the mechanisms internal to cartilage.

References

- [1] Bataille, J. and Kestin, J. (1977) Thermodynamics of mixtures. *Journal of Non-Equilibrium Thermodynamics* **2**, 49-65
- [2] Eisenberg, S.R. and Grodzinsky, A.J. (1985) Swelling of articular cartilage and other connective tissues electromechanical forces. *Journal of Orthopaedic Research* **3**, 148-159
- [3] Loret, B. and Simões, F.S. (2003) Articular cartilage with intra- and extrafibrillar waters. A chemo-mechanical model. *Mechanics of Materials*, to appear
- [4] Maroudas, A. (1976) Balance between swelling pressure and collagen tension in normal and degenerate cartilage. *Nature* **260**, 808-809

A DUAL POROSITY MODEL FOR CONTAMINANT TRANSPORT IN EXPANSIVE CLAYS

Márcio A. Murad

Laboratório Nacional de Computação Científica LNCC/MCT

Av Getúlio Vargas 333, 25651-070 Petrópolis, RJ, Brazil

murad@lncc.br

Christian Moyne

LEMTA-INPL-UHP-CNRS (UMR 7563)

2, avenue de la Forêt de Haye, 54504 Vandoeuvre les Nancy Cedex, France

cmoyne@ensem.inpl-nancy.fr

Abstract A three-scale model based on a modified convection-diffusion-reaction equation wherein the partition coefficient governing the instantaneous adsorption/desorption of the species in the micro-pores appears coupled with the local electric potential satisfying a Poisson-Boltzmann equation, is proposed to describe contaminant transport in swelling clays characterized by two levels of porosity (micro and macro-pores). At the microscale the medium is composed of charged clay particles saturated by a binary monovalent aqueous electrolyte solution. At the intermediate (meso) scale the two-phase system is represented in a homogenized fashion with movement of the ionic charges governed by the Nernst-Planck relations. At the macroscale, the mesoscale mixture of clay clusters is homogenized with the bulk solution in the macro-pore system. A notable consequence of the approach proposed herein is the microscopic representation for the partition coefficient which can be exploited to derive the constitutive behavior for this quantity.

Keywords: clay, homogenization, partition coefficient, Poisson-Boltzmann, dual porosity

Introduction

In this article we propose a homogenized form of the modified convection-diffusion equations to describe contaminant transport in expansive clays characterized by three disparate length scales and two levels of porosity. The microscale consists of macromolecular structures saturated by an electrolyte

Jacques M. Huyghe et al. (eds), IUTAM Proceedings on Physicochemical and Electromechanical Interactions in Porous Media, 173–179.

© 2005 Springer. Printed in the Netherlands.

solution whose local electric potential is governed by the Poisson-Boltzmann equation. At the meso (intermediate scale) these continua are homogenized leading a two-scale model wherein flow, ion transport and electric current are governed by Onsager's reciprocity relations. Further, a three-scale form of the convection-diffusion-reaction equation is obtained by homogenizing the two-scale model : the clay clusters with the bulk water (solvent not within but next to the swelling particles). In the macroscopic picture of a dual porosity model, an interconnected network of macro-pores (or fissures) provides most of the global permeability for the macroscopic transport of species in the bulk water whereas most of the storage takes place in the clay clusters. Assuming instantaneous local thermodynamic equilibrium between the clay and macro-pores we show that the constitutive law for the distributed mass transfer function of the species is equivalent to the appearance of a partition coefficient which governs the instantaneous adsorption/desorption of the species by the micro-pores. The notable feature of the three-scale approach relies in its capability in providing a double averaging macro/meso/micro representation for the partition coefficient in terms of the local electric potential satisfying the Poisson-Boltzmann problem.

Mesoscale Model for Ion Transport

We begin by presenting the overall mass conservation equation which governs the movement of the ions in the clay clusters at the mesoscale. The clusters are regarded biphasic aggregates composed of clay particles (solid phase) saturated by an aqueous electrolyte solution consisting of water and an entirely dissociated salt with strong electrolytes Na^+ and Cl^- . For simplicity we neglect steric and hydration effects assuming the liquid phase a structureless dielectric solution with ions treated as point charges. The overall mass conservation of the species reads

$$\frac{\partial}{\partial t}(\phi(C^+ + C^-) + \nabla \cdot \mathbf{J}_c = 0, \quad (1)$$

where C_+ and C_- are the averaged concentration of cations (Na^+) and anions (Cl^-); $\mathbf{J}_c = \mathbf{J}_+ + \mathbf{J}_-$ the corresponding overall flux and ϕ is the intra-cluster porosity. The constitutive equations for the fluxes of each species \mathbf{J}_\pm are given by the Nernst-Planck relations. The diffusion coefficients admit microscopic representations [1]. Since c_\pm are discontinuous across the interface with an outer saline bath, the above equation is usually rewritten in terms of the corresponding bulk concentration c_b . Following Moyne and Murad [1] denoting T , F and R the temperature, Faraday's constant and the ideal gas constant), define the dimensionless electric potential $\bar{\varphi} = F\varphi/RT$ relative to the streaming potential $\bar{\psi}$ as $\bar{\varphi} = \bar{\Phi} - \bar{\psi}$ where $\bar{\Phi}$ is the total electric potential. This leads to a

local characterization of c_b based on the generalized Boltzmann distributions

$$c^\pm = c_b \exp(\mp \bar{\Phi} \pm \bar{\psi}) = c_b \exp(\mp \bar{\varphi}). \quad (2)$$

An important consequence of (2) is the extension of the Boltzmann distributions to the non-equilibrium case provided $\bar{\Phi}$ is replaced by the relative potential $\bar{\varphi} = \bar{\Phi} - \bar{\psi}$. Thus, unlike the streaming potential $\bar{\psi}$ which only appears at non-equilibrium conditions, the excess $\bar{\varphi}$ plays the role of a potential purely related to electrical double layer effects. Using the above change of variables one can rephrase (1) in terms of c_b and $\bar{\varphi}$ as follows

$$\frac{\partial}{\partial t} (\phi \langle \cosh \bar{\varphi} \rangle_z c_b) = -\nabla \cdot \mathbf{J}_c. \quad (3)$$

Coupling Between Clay Clusters and Bulk Water

We now establish the coupled clay cluster/macro-pore model at the meso-scale. For the sake of simplicity we adopt a particular form of mesostructure wherein the clay clusters are isolated from each other by the fissure (macro-pore) system.. Denote $\{\mathbf{V}_f, C_f^\pm, \mathbf{D}_f^\pm, \mathbf{J}_f\}$ the velocity, concentration and diffusion coefficient and the overall flux of species (*NaCl*), the governing equations in Ω_f reduce to

$$\begin{aligned} \frac{\partial C_f}{\partial t} + \nabla \cdot \mathbf{J}_f &= 0, & \nabla \cdot \mathbf{I}_f &= 0, \\ \mathbf{J}_f &= C_f \mathbf{V}_f - \mathbf{D}_f \nabla C_f - \Delta_f C_f \nabla \bar{\psi}_f \end{aligned}$$

with $\mathbf{D}_f = (\mathbf{D}_f^+ + \mathbf{D}_f^-)/2$ and $\Delta_f \equiv (\mathbf{D}_f^+ - \mathbf{D}_f^-)/2$.

The above governing equations are supplemented by initial conditions and boundary conditions on the cluster-macrovoid interface Γ_{fs} . Denote \mathbf{N} the unit normal exterior to Ω_s . continuity of mass, concentrations, streaming potentials, total flux of the species and the normal component of the stress tensor give (where $\psi_f = (RT\bar{\psi}_f/F)$)

$$c_b = C_f, \quad \psi = \psi_f, \quad 2 \mathbf{J}_f \cdot \mathbf{N} = \mathbf{J}_c \cdot \mathbf{N} \quad \text{on } \Gamma_{fs}.$$

Homogenization

To up-scale the previous model to the macroscale we make use of a formal homogenization procedure based on asymptotic expansions in terms of a perturbation parameter ϵ which quantify the ratio between the meso and macroscales. To describe the physics properly, the coefficients must be scaled. Further, denoting v_{ref} and \mathcal{D}_{ref} reference velocity and diffusion coefficient, and

defining $Pe = v_{ref}L/D_{ref}$ the macroscopic Peclet number which quantifies the ratio between convective and diffusive effects we assume that these are of the same order of magnitude such that $Pe = \mathcal{O}(1)$. Further, to control the cluster-macropore mass transfer within a fixed volume as $\epsilon \rightarrow 0$, it is also necessary to scale J_c . Following Douglas and Arbogast [2], within the context of rigid fractured media, this is done by the scaling law $\{K_P^\epsilon = K_P\epsilon^2, \dots\}$. This scaling has the effect of making the aggregates progressively less permeable and diffusive as $\epsilon \rightarrow 0$ and consequently prevents the degeneration of the cluster-macropore mass transfer (see [2] for details).

The formal homogenization process is accomplished by considering every property depending on both global and meso-length scales in the form $f = f(\mathbf{x}, \mathbf{y})$, where \mathbf{x} and \mathbf{y} are the macroscopic and mesoscopic coordinates respectively. The relation between the length scales is $\mathbf{y} = \epsilon^{-1}\mathbf{x}$. This shows that quantities vary ϵ^{-1} faster on the meso level than those the macro one. We then postulate two-scale asymptotic expansions for the unknowns in terms of the perturbation parameter ϵ

$$\mathbf{u}^\epsilon = \mathbf{u}^0 + \epsilon\mathbf{u}^1 + \epsilon^2\mathbf{u}^2 + \dots \quad (4)$$

with the coefficients \mathbf{u}^i , Y -periodic in \mathbf{y} .

Insert the expansions (4) into the set of mesoscopic governing equations with the differential operator ∂/∂_x replaced by $\partial/\partial_x + \epsilon^{-1}\partial/\partial_y$. After a formal matching of the powers of ϵ , we obtain a recursive system of cell problems parametrized by \mathbf{x} . For the fluid in the macropore system the orders of perturbation read as

$$\nabla_y \cdot (D_f \nabla_y C_f^0) = 0, \quad (5)$$

$$\nabla_y \cdot [-D_f (\nabla_x C_f^0 + \nabla_y C_f^1) + C_f^0 \mathbf{V}_f^0] = 0, \quad (6)$$

$$\frac{\partial C_f^0}{\partial t} + \nabla_x \cdot \mathbf{J}_f^0 + \nabla_y \cdot \mathbf{J}_f^1 = 0, \quad (7)$$

$$\mathbf{J}_f^0 = C_f^0 \mathbf{V}_f^0 - D_f (\nabla_x C_f^0 + \nabla_y C_f^1), \quad (8)$$

whereas in the clay clusters the perturbed equations are

$$\frac{\partial}{\partial t} (\phi^0 G_c c_b^0) + \nabla_y \cdot \mathbf{J}_c^1 = 0, \quad (9)$$

$$\mathbf{J}_c^1 = \mathbf{J}^1 + 2\mathbf{v}_D^1 c_b^0, \quad (10)$$

$$\mathbf{J}^1 = -K_C \nabla_y p_b^0 - D_C \nabla_y c_b^0 - \Delta_E \nabla_y \psi^0, \quad (11)$$

along with boundary conditions

$$c_b^0 = C_f^0; \quad \mathbf{J}_f^0 \cdot \mathbf{N} = (C_f^0 \mathbf{V}_f^0 - D_f (\nabla_x C_f^0 + \nabla_y C_f^1)) \cdot \mathbf{N} = 0. \quad (12)$$

Begin by noting that C_f^0 satisfy the Neumann problem given by (5) and boundary conditions whose solution is $C_f^0(\mathbf{x}, \mathbf{y}, t) = C_f^0(\mathbf{x}, t)$. We now derive the overall macroscopic mass balance for the species. To this end we begin by deriving the closure problem for C_f^1 . Given $C_f(\mathbf{x}, t)$, combine (6) with boundary conditions and neglect the advection induced by $\partial \mathbf{u} / \partial t$, to obtain the local Neumann problem

$$\begin{aligned} \nabla_{\mathbf{y}} \cdot (\mathbf{D}_f \nabla_{\mathbf{y}} C_f^1) &= 0 & \text{in } Y_f, \\ -\mathbf{D}_f \left(\nabla_{\mathbf{y}} C_f^1 + \nabla_{\mathbf{x}} C_f^0 \right) \cdot \mathbf{N} &= 0 & \text{on } \partial Y_{fs}. \end{aligned}$$

By linearity the solution can be represented as

$$C_f^1 = \mathbf{f}(\mathbf{y}) \cdot \nabla_{\mathbf{x}} C_f^0(\mathbf{x}, t) + \widehat{c}(\mathbf{x}, t), \tag{13}$$

where \mathbf{f} are auxiliary Y -periodical vectorial parameters satisfying the cell problems with $C_f^0 = \mathbf{I}$. Using (13) in (8) the averaged flux of species is given by

$$\langle \mathbf{J}_f^0 \rangle_y = C_f^0 \langle \mathbf{V}_f^0 \rangle_y - \mathbf{D}_f^{eff} \nabla_{\mathbf{x}} C_f^0, \quad \text{where} \quad \mathbf{D}_f^{eff} \equiv \langle \mathbf{D}_f (\mathbf{I} + \nabla_{\mathbf{y}} \mathbf{f}) \rangle_y \tag{14}$$

is the effective macroscopic diffusion coefficient of the species in the bulk solution. By averaging (7) using the boundary conditions along with the divergence theorem and the periodicity assumption we get

$$\begin{aligned} 2 \frac{\partial}{\partial t} (n_f C_f^0) + 2 \nabla_{\mathbf{x}} \cdot \langle \mathbf{J}_f^0 \rangle_y &= -2 \langle \nabla_{\mathbf{y}} \cdot \mathbf{J}_f^1 \rangle_y \\ &= \frac{2}{|Y|} \int_{\partial Y_{fs}} \mathbf{J}_f^1 \cdot \mathbf{N} d\Gamma \\ &= \frac{1}{|Y|} \int_{\partial Y_{fs}} \mathbf{J}_c^1 \cdot \mathbf{N} d\Gamma \\ &= \frac{1}{|Y|} \int_{Y_s} \nabla_{\mathbf{y}} \cdot \mathbf{J}_c^1 dY \\ &= -\frac{1}{|Y|} \int_{Y_s} \frac{\partial}{\partial t} (\phi^0 G_c c_b^0) dY \end{aligned}$$

in which when combined with (14) and neglecting the movement induced by the velocity of the solid phase leads to

$$\frac{\partial}{\partial t} (n_f C_f^0) + \nabla_{\mathbf{x}} \cdot (C_f^0 \mathbf{V}_{Df}^0) - \nabla_{\mathbf{x}} \cdot (\mathbf{D}_f^{eff} \nabla_{\mathbf{x}} C_f^0) = -\frac{1}{2} \frac{\partial}{\partial t} (\langle \phi^0 G_c c_b^0 \rangle_y).$$

The above result shows a macroscopic convection-diffusion equation governing the concentration of the species in the bulk solution with an additional

source/sink transfer function which governs the mass exchange of the components between the macro-pores and clay aggregates. One may clearly observe that the influence of electrical effects on the mass transfer is manifested through the additional capacity G_c which acts to enhance the adsorption/desorption phenomena.

Within the proposed context the quasi-steady assumption is imposed by neglecting the local spatial variability of the concentration c_b^0 , bulk phase pressure p_b^0 , and streaming potential ψ^0 in the clusters by assuming these quantities equal to their corresponding counterparts in the macro-pore system. Therefore at local equilibrium we postulate $c_b^0(\mathbf{x}, \mathbf{y}, t) = C_f^0(\mathbf{x}, t)$; $\psi^0(\mathbf{x}, \mathbf{y}, t) = \psi^*$. Using the above assumption, the last equation reduces to the form

$$\frac{\partial}{\partial t}(n_f C_f^0) + \nabla_x \cdot (C_f^0 \mathbf{V}_{Df}^0) - \nabla_x \cdot (D_f^{eff} \nabla_x C_f^0) = -\frac{1}{2} \frac{\partial}{\partial t} \left(\langle \phi^0 G_c \rangle_y C_f^0 \right).$$

Hence, given the pair $\{n_f, \mathbf{V}_{Df}^0\}$, we define the sorbed concentration in the clay pedes $C_S^0 \equiv 0.5 C_f^0 \langle \phi^0 G_c \rangle_y$ and obtain the following system in terms of $\{C_f^0, C_S^0\}$

$$\begin{cases} \frac{\partial}{\partial t}(n_f C_f^0) + \nabla_x \cdot (C_f^0 \mathbf{V}_{Df}^0) - \nabla_x \cdot (D_f^{eff} \nabla_x C_f^0) = -\frac{\partial C_S^0}{\partial t} \\ C_S^0 = \frac{1}{2} C_f^0 \langle \phi^0 G_c \rangle_y, \end{cases}$$

Hence, under the quasi-steady approximation, the movement of the species is dictated by a macroscopic convection-diffusion-reaction equation with an instantaneous adsorption/desorption source term. A notable consequence of the three-scale approach is the double-averaging representation for the partition coefficient K_* which is defined as

$$K_* \equiv \frac{1}{2} \langle \phi^0 G_c \rangle_y = \langle \phi^0 \langle \cosh \bar{\varphi}^0 \rangle_z^l \rangle_y = \langle \langle \cosh \bar{\varphi}^0 \rangle_z \rangle_y, \quad (15)$$

where the microscopic representation for the electric capacity G_c has been used. The above representation provides new insight in the physics of adsorption/desorption phenomena in charged clays. The microscopic representation for K_* in (15) allows to establish a direct correlation between K_* and the microscopic behavior of the electrolyte solution whose electric potential distribution is ruled by the Poisson-Boltzmann problem. It should be noted that the quasi-steady model for transport of non-ionic species can easily be recovered from the present formulation by setting $\bar{\varphi} = 0$. In this case the capacity of the medium for adsorption of the contaminant by the micro-pore system is dictated by the micro-porosity ϕ .

References

- [1] Moyne, C. and Murad, M. (2002) Electro-chemo-mechanical couplings in swelling clays derived from a micro/macro homogenization procedure, *International J. Solids and Structures* **25**(1), 11-112
- [2] Douglas, J. and Arbogast, T. (1990) Dual porosity models for flow in naturally fractured reservoirs, in *Dynamics of Fluid in Hierarchical Porous Media*, editor J.H. Cushman, Academic Press, New York, pp. 177-222
- [3] Lai, W.M., Hou, J.S. and Mow, V.C. (1991) A triphasic theory for the swelling and deformation behaviors of articular cartilage, *J. Biomech. Engrg.* **113**, 245-258
- [4] Huyghe, J.M. and Janssen, J.D. (1997) Quadriphasic mechanics of swelling incompressible porous media, *Int. J. Engrg. Sci.* **25**(8), 793-802

VII

DIFFUSION, DISPERSION AND ADSORPTION.

Chairmen: M.A. Murad, D. Smeulders

ON ADSORPTION AND DIFFUSION IN MICROSTRUCTURED POROUS MEDIA

Pasquale Giovine*

*Dipartimento di Meccanica e Materiali, Università "Mediterranea" di Reggio Calabria
Via Graziella, 1 - Località Feo di Vito, I-89060 Reggio Calabria, Italy*

giovine@unirc.it

Abstract We formulate the balance principles for an immiscible mixture of continua with microstructure in the broadest sense for include, *e.g.*, phenomena of diffusion, adsorption and chemical reactions. After we consider the flow of a fluid/adsorbate mixture through big pores of an elastic solid skeleton and propose suitable constitutive equations to study the coupling of adsorption and diffusion under isothermal conditions.

Keywords: Immiscible mixtures, continua with microstructure, diffusion in porous and granular materials, adsorption.

Introduction

In [9] Passman, Nunziato and Walsh presented a multiphase mixture in which each constituent had a simple geometrical structure characterized by a scalar kinematic parameter, its volume fraction. But when the kinematical descriptor is more complex and takes value on a manifold, it is necessary to consider the more general microstructure introduced, *e.g.*, by Capriz in the essay [3], where materials as liquid crystals, granular and porous media, Cosserat and micromorphic continua are studied.

Therefore this work concerns the formulation of a proposal for the thermochemistry of an immiscible mixture of reacting materials with microstructure in presence of diffusion; a new form of the integral balance of moment of momentum appears in the theory, in which the presence of the microstructure is taken into account. Moreover, the density fields can no longer be regarded as determined by the deformation fields because chemical reactions are present,

*This research was partially supported by the Italian M.U.R.S.T. through the project "Cofin2002 - Mathematical Models for the Material Science".

thus the constitutive assumptions must allow for a dependence on a larger number of variables.

After, the essential features of a mechanical model of adsorption and diffusion to characterize, e.g., the transport of a contaminant with rainwater through the soil will be outlined; in particular, the model consists of a fluid carrier of an adsorbate, the adsorbate in the liquid state and an elastic skeleton with ellipsoidal microstructure: it means that each pore has different microdeformation along principal axes, namely a pure strain, but rotates locally with the matrix of the material (see [5, 6]).

Balance Laws

In our development and notation we mainly follow Truesdell [10] and use a subscript to indicate a constituent and a prime to denote material time derivative following the motion of that constituent; thus, $v_i := x'_i$ and $a_i := x''_i$ are the i^{th} peculiar velocity and acceleration, respectively. $F_i, L_i := \text{grad } v_i$ and $D_i := \frac{1}{2}(L_i - L_i^T)$ are the peculiar gradient of deformation, velocity gradient and rate of deformation, respectively.

We consider a mixture of n reacting constituents \mathcal{B}_i which are endowed with a microstructure and assume that every place x in the body is simultaneously occupied by a material particle of each constituent which is present at time τ . Each constituent has its own bulk mass density ρ_i .

The hypothesis that the constituents of the mixture have a Lagrangian microstructure (in the sense of Capriz [3]) means that each material element of a single body reveals a microscopic geometric order at a closer look; then it is there assigned a measure $\nu_i(x)$ of the peculiar microstructure, read on a manifold \mathcal{M}_i of finite dimension m_i : e.g., the space of symmetric tensor in the theory of solids with large pores or the interval $[0, \bar{\nu})$ of real number, with $\bar{\nu} \ll 1$, for fluids in an immiscible mixture (see [5, 9]). We do not fix the rank of the tensor order parameter ν_i .

We suppose that exists a non-negative kinetic energy $\kappa_i(\nu_i, \nu'_i)$, associated with each time-rate of change ν'_i , such that $\kappa_i(\nu_i, 0) = 0$ and $\frac{\partial^2 \kappa_i}{\partial \nu_i'^2} \neq 0$. In the absence of κ_i , the measure ν_i is sooner termed internal (state) variable and ruled by a first order evolution equation instead of a balance equation.

Each constituent suffers actions of three kinds: the prescribed actions at a distance, represented by the densities of body force b_i , microforce γ_i and heating λ_i ; the contact actions, represented by the stress T_i , the microstress \mathcal{S}_i and the heating flux q_i ; the internal microactions ζ_i .

For a region \mathcal{V} of space, we may consider the actions on the part of the constituent body \mathcal{B}_i presently occupying \mathcal{V} and calculate the rates of growth per unit volume of mass α_i^+ , linear momentum m_i^+ , micromomentum ϕ_i^+ ,

rotational momentum w_i^+ , energy ϵ_i^+ and entropy η_i^+ within it. The equations of balance for the constituent i are:

$$\begin{aligned}
 \int \alpha_i^+ dv &\equiv \left(\int \rho_i dv \right)', \\
 \int m_i^+ dv &\equiv \left(\int \rho_i v_i dv \right)' - \int \rho_i b_i dv - \oint T_i n da, \\
 \int \phi_i^+ dv &\equiv \left(\int \rho_i \frac{\partial \chi_i}{\partial \nu_i'} dv \right)' - \int \left[\rho_i \left(\frac{\partial \chi_i}{\partial \nu_i} + \gamma_i \right) - \zeta_i \right] dv - \oint \mathcal{S}_i n da, \\
 \int \left(w_i^+ + p \times m_i^+ + \mathcal{A}_i^T \phi_i^+ \right) dv &\equiv \left[\int \rho_i \left(p \times v_i + \mathcal{A}_i^T \frac{\partial \chi_i}{\partial \nu_i'} \right) dv \right]' \\
 &\quad - \int \rho_i \left(p \times b_i + \mathcal{A}_i^T \gamma_i \right) dv - \oint \left[p \times T_i n + \mathcal{A}_i^T (\mathcal{S}_i n) \right] da, \\
 \int \epsilon_i^+ dv &\equiv \left[\int \rho_i \left(\epsilon_i + \frac{1}{2} v_i^2 + \kappa_i \right) dv \right]' \\
 &\quad - \int \rho_i (\lambda_i + b_i \cdot v_i + \gamma_i \cdot \nu_i') dv + \oint (q_i - T_i^T v_i - \mathcal{S}_i^T \nu_i') \cdot n da, \\
 \int \eta_i^+ dv &\equiv \left(\int \rho_i \eta_i dv \right)' - \int \rho_i \lambda_i \theta_i^{-1} dv + \oint \theta_i^{-1} q_i \cdot n da.
 \end{aligned} \tag{1}$$

In the equations (1), \int denotes integration over the volume \mathcal{V} ; \oint denotes integration over its boundary $\partial\mathcal{V}$; $\chi_i(\nu_i, \nu_i')$ is the density of kinetic co-energy related to κ_i by the Legendre transform: $\kappa_i = \frac{\partial \chi_i}{\partial \nu_i'} \cdot \nu_i' - \chi_i$; $\mathcal{A}_i(\nu_i)$ is the infinitesimal generator of the local action on \mathcal{M}_i of the group of the rotations of characteristic vector r , i.e., $\mathcal{A}_i := \left(\frac{\partial \nu_i}{\partial r} \Big|_{r=0} \right)$ (see [3]); the transpose of the $(m_i + 1)^{\text{th}}$ order tensors \mathcal{A}_i (or \mathcal{S}_i) has the following components $(\mathcal{A}_i^T)_{\alpha \dots \beta i} = (\mathcal{A}_i)_{i \alpha \dots \beta}$; ϵ_i , η_i and θ_i are peculiar internal energy, entropy and temperature, respectively.

The formulation of the balance of rotational momentum (1)₄ appears to be a novelty in the theories of microstructures, even if the deduction of its local form will be in agreement, e.g., with [3]. Equations (1)_{4,5} take into account the presence of the microstructure.

The local forms of the equations of balance are

$$\alpha_i^+ = \rho_i' + \rho_i \operatorname{div} v_i, \tag{2}$$

$$m_i^+ = \alpha_i^+ v_i + \rho_i \nu_i' - \rho_i b_i - \operatorname{div} T_i, \tag{3}$$

$$\phi_i^+ = \alpha_i^+ \frac{\partial \chi_i}{\partial \nu_i'} + \rho_i \left(\frac{\partial \chi_i}{\partial \nu_i'} \right)' - \rho_i \left(\frac{\partial \chi_i}{\partial \nu_i} + \gamma_i \right) - \operatorname{div} \mathcal{S}_i + \zeta_i, \tag{4}$$

$$w_i^+ = \mathcal{E} T_i - \mathcal{A}_i^T \zeta_i - (\operatorname{grad} \mathcal{A}_i^T) \mathcal{S}_i, \tag{5}$$

$$\epsilon_i^+ = m_i^+ \cdot v_i + \phi_i^+ \cdot \nu_i' + \alpha_i^+ (\epsilon_i - 2^{-1} v_i^2 - \kappa_i) \quad (6)$$

$$+ \rho_i \epsilon_i' - \rho_i \lambda_i + \operatorname{div} q_i - T_i \cdot L_i - \zeta_i \cdot \nu_i' - \mathcal{S}_i \cdot \operatorname{grad} \nu_i'$$

$$\eta_i^+ = \alpha_i^+ \eta_i + \rho_i \eta_i' - \rho_i \lambda_i \theta_i^{-1} + \operatorname{div} (\theta_i^{-1} q_i), \quad (7)$$

where \mathcal{E} is the third-order Ricci's tensor; to obtain equation (5) we used the invariance of χ_i under the galilean group, *i.e.*, $(\mathcal{A}_i^T)' \frac{\partial \chi_i}{\partial \nu_i'} = -\mathcal{A}_i^T \frac{\partial \chi_i}{\partial \nu_i}$.

By using the concept of Helmholtz's free energy per unit volume $\Psi_i := \rho_i (\epsilon_i - \theta_i \eta_i)$ and the balances of mass (2) and energy (6), we can recast the entropy equation (7) in the following form:

$$\eta_i^+ = \theta_i^{-1} [\epsilon_i^+ - m_i^+ \cdot v_i - \phi_i^+ \cdot \nu_i' + \alpha_i^+ (2^{-1} v_i^2 + \kappa_i) - \Psi_i' - \rho_i \theta_i' \eta_i$$

$$+ (T_i - \Psi_i I) \cdot L_i + \zeta_i \cdot \nu_i' + \mathcal{S}_i \cdot \operatorname{grad} \nu_i' - \theta_i^{-1} q_i \cdot \operatorname{grad} \theta_i]. \quad (8)$$

In a mixture we assume that chemical reactions and physical transfers are exchanges rather than true processes of creation or destruction, thus we require that the mass, linear and rotational momentum and energy are conserved for the whole mixture, *i.e.*, we have from balances (1) that

$$\sum \alpha_i^+ = 0, \quad \sum m_i^+ = 0, \quad \sum w_i^+ = 0, \quad \sum \epsilon_i^+ = 0; \quad (9)$$

here and henceforth, \sum stands for summation from $i = 1$ to $i = n$.

Following [10], we do not restrict η_i^+ except for the requirement that the total growth of entropy for the mixture remain non-negative, *i.e.*, our axiom of dissipation is

$$\sum \eta_i^+ \geq 0. \quad (10)$$

Finally, we require that the growth of micromomentum ϕ_i^+ should assure the consistency of the axiom of dissipation with constitutive equations; thus, for the subsequent chapters, we must impose the following balance:

$$\sum \theta_i^{-1} (\alpha_i^+ \kappa_i - \phi_i^+ \cdot \nu_i') = 0. \quad (11)$$

Adsorption in Porous Materials

Now, we specialize the theory to an isothermal flow of a fluid component through the channels of a solid skeleton, namely a part of soil. It serves as carrier for an adsorbate whose mass balance contains a source term $\alpha_a^+ = \alpha$, so that we admit mass exchanges between the solid and the adsorbate phase due to adsorption/desorption processes only.

We assume that the fluid component and the adsorbate in the fluid phase, present in a very low concentration, have the same kinematics given by the common velocity field v_f , so that there is no flux of molecular diffusion in the fluids. Thus we can reduce to consider an atypical two-phase immiscible mixture of a solid with big pores, of subscript s , and a particular bi-component fluid, of subscript f (see §8.4 of [11]).

The microstructural kinematic variable ν_s for the skeleton is a 2nd order symmetric tensor with positive determinant $U_s (\in \text{Sym}^+)$, that is the left microstretch, which takes into account for contractions or expansions of the large pores in the material (see [5, 6]). Instead the fluid variable ν_f is the volume fraction β_f , *i.e.*, the proportion of space occupied by the fluid constituent of the body (see [9]). Therefore we have that $\mathcal{A}_f = 0$, because a proportion does not change for a rotation, while $\nu_s (\equiv U_s)$ changes as a 2nd order tensor, thus \mathcal{A}_s has the following components $(\mathcal{A}_s)_{\alpha\beta\iota} = (U_s)_{\alpha\gamma} \mathcal{E}_{\gamma\beta\iota} - \mathcal{E}_{\alpha\gamma\iota} (U_s)_{\gamma\beta}$ (see, also, §3 of [3]).

We observe that the solid volume fraction β_s is closely related to the determinant of the microstretch U_s and that the sum of volume fractions is equal or less to one depending on whether the pores are completely filled by the fluid inclusion or not: $\beta_f + \beta_s = 1 - \beta_v \leq 1$, where β_v is the volume fraction of the bare sites of matter in pores. Here, we suppose that the solid matrix is unsaturated, so $\beta_v > 0$.

The kinetic co-energy χ_i is assumed to be a quadratic form in ν'_i , as is customary for immiscible fluid mixtures or for materials with affine microstructure (see, *e.g.*, [4, 5]); then χ_i coincides with the kinetic energy κ_i and it is

$$\kappa_f = \chi_f := 2^{-1} \mu_f (\beta_f) \beta_f'^2 \quad \text{and} \quad \kappa_s = \chi_s := 2^{-1} \mu_s U_s' \cdot U_s'; \quad (12)$$

here the solid microinertia tensor field is taken spherical with a constant and non-negative coefficient μ_s . The kinetic energies express the inertia due to the local microvariations of the volume of inclusions, as well as that related to the admissible expansional motion of pores' boundaries.

With these hypotheses, the mechanical balance equations reduce to the following ones:

$$\alpha = \rho'_f + \rho_f \text{div } v_f, \quad -\alpha = \rho'_s + \rho_s \text{div } v_s, \quad (1-c)\alpha = \rho_f c'^f, \quad (13)$$

$$m = \alpha v_f + \rho_f v'_f - \rho_f b_f - \text{div } T_f, \quad -m = -\alpha v_s + \rho_s v'_s - \rho_s b_s - \text{div } T_s, \quad (14)$$

$$\phi_f^+ = \alpha \mu_f \beta'_f + \rho_f \left(\mu_f \beta''_f + \frac{1}{2} \frac{d\mu_f}{d\beta_f} (\beta'_f)^2 - \gamma_f \right) - \text{div } \mathcal{S}_f + \zeta_f,$$

$$\phi_s^+ = -\alpha \mu_s U'_s + \rho_s \mu_s U''_s - \rho_s \gamma_s - \text{div } \mathcal{S}_s + \zeta_s, \quad (15)$$

$$M = \text{skw } T_f, \quad -M = \text{skw } (T_s - U_s \zeta_s - \text{grad } U_s \odot \mathcal{S}_s). \quad (16)$$

In these equations we used the balances for the whole mixture (9) and introduced the following notations: the concentration of adsorbate $c := \rho_a/\rho_f$; the fluid growth of linear and angular momentum, $m := m_f^+$ and $M := \frac{1}{2}\mathcal{E}w_f^+$, respectively; the script ‘skw’ to indicate the skew part of a tensor and the tensor product ‘ \odot ’ of components $(\text{grad } U_s \odot \mathcal{S}_s)_{ij} := (U_s)_{ih,k}(\mathcal{S}_s)_{jhk}$.

We notice that stress tensors are not ‘a priori’ symmetric for (16) and that ϕ_s^+ , γ_s , $(\text{div } \mathcal{S}_s)$ and ζ_s are all 2nd order symmetric tensors. Further, the 3rd order microstress tensor \mathcal{S}_s is normally related to boundary microtractions, even if, in some cases, it could express weakly non-local internal effects; γ_s is interpreted as an externally controlled pore pressure; ζ_s includes interactive forces between the gross and fine structures.

From equation (14)₁ we could obtain the Darcy’s law, if we neglect the inertial terms and the mass exchange and make suitable constitutive hypotheses on fields m , b_f and T_f . The equation of balance (15)₁ for the volume fraction β_f generalize the classical Langmuir’s evolution equation, while the balance (15)₂ for the microstretch U_s includes the Wilmanski’s porosity balance as well as the equation which rules the changes of internal surfaces area of the pores (see [8, 11, 1], respectively). The energy balance equations do not appear at all because the process is assumed to be isothermal.

Finally, by means of relation (8) and (11) with $\theta_i = \bar{\theta} = \text{const.}$, the axiom of dissipation (10) is transformed into the following reduced dissipation inequality for our mixture of continua with microstructure:

$$\begin{aligned} & \sum \left(\rho_i K_i^T \cdot L_i + \Psi_i' \right) - \zeta_f \beta_f' - \zeta_s \cdot U_s' \\ & - S_f \cdot \text{grad } \beta_f - S_s \cdot \text{grad } U_s' + u \cdot (m + 2^{-1} \alpha u - \alpha v_s) \leq 0, \end{aligned} \quad (17)$$

where $\rho_i K_i := \Psi_i I - T_i^T$ is the i^{th} chemical potential tensor and $u := v_f - v_s$ the relative velocity, a measures of the diffusion of the fluid in the porous solid.

Constitutive Principles

As with any theory of material behavior, we have to make constitutive assumptions in order to define the peculiar mixture of a poroelastic material and a compressible bi-component fluid. Among other quantities, we must state constitutive relations for the mass supply α and the momentum supply m , which give rise to adsorption/desorption and to diffusion, respectively.

Let $\mathcal{E} := \{ \rho_f, c, p := \text{grad } c, F_s, \beta_f, d := \text{grad } \beta_f, U_s, \Upsilon := \text{grad } U_s \}$ be the array of fields describing the elastic state of our isothermal process and, in addition, let us enclose the relative velocity u and the solid one v_s ; by imposing the principle of equipresence, we postulate that constitutive quantities $\Psi_i, K_i, \zeta_i, S_i, m, M$ and α are all twice continuously differentiable functions with respect to all constitutive fields and require the consistency with the in-

equality (17). Therefore, by introducing the inner part of the free energy of the mixture $\Psi := \sum \Psi_i$, we obtain from the requested consistency that:

$$\begin{aligned}
 \Psi &= \tilde{\Psi}(\mathcal{E}), \quad \zeta_f = \Psi_{,\beta_f}, \quad \zeta_s = \Psi_{,U_s}, \quad \mathcal{S}_f = \Psi_{,d}, \quad \mathcal{S}_s = \Psi_{,\Upsilon}, \\
 \rho_f K_f &= \rho_f \Psi_{,\rho_f} I + \Psi_{,d} \otimes d + \Psi_{,p} \otimes \left(p - \frac{1-c}{\rho_f} \alpha_{,u} \right) - u \otimes \Psi_{f,u}, \\
 \rho_s K_s &= -F_s \Psi_{,F_s}^T + \Upsilon \odot \Psi_{,\Upsilon} + u \otimes (\Psi_{s,v_s} - \Psi_{s,u}) \\
 &\quad + \frac{1-c}{\rho_f} \Psi_{,p} \otimes (\alpha_{,u} - \alpha_{,v_s}), \quad \text{sym} \left(\Psi_{s,p} \otimes u - \frac{1-c}{\rho_f} \Psi_{,p} \otimes \alpha_{,p} \right) = 0, \\
 (\Psi_s u)_{,\rho_f} &= (1-c) \Psi_{,p} \frac{\partial}{\partial \rho_f} \left(\frac{\alpha}{\rho_f} \right), \quad \text{sym} \left(\Psi_{s,d} \otimes u - \frac{1-c}{\rho_f} \Psi_{,p} \otimes \alpha_{,d} \right) = 0, \\
 \left(\Psi_{f,\Upsilon} \otimes u + \frac{1-c}{\rho_f} \alpha_{,\Upsilon} \otimes \Psi_{,p} \right) A &= 0, \quad \forall A \in \text{Sym}, \\
 \left(\Psi_{f,F_s} \otimes u + \frac{1-c}{\rho_f} \alpha_{,F_s} \otimes \Psi_{,p} \right) (AF_s^{-1}) &= 0, \quad \forall A \in \text{Sym}, \quad \text{and} \\
 0 \leq \mathcal{D} &:= \alpha \left(u \cdot v_s - \frac{1}{2} u^2 - \Psi_{,\rho_f} - \frac{1-c}{\rho_f} \Psi_{,c} + \rho_f^{-1} \Psi_{,p} \cdot p \right) \\
 &\quad - \frac{1-c}{\rho_f} \Psi_{,p} \cdot \left(\alpha_{,\beta_f} d + \Upsilon^T \alpha_{,U_s} + \alpha_{,c} p \right) - u \cdot \left(m - \Psi_{s,\beta_f} d + \Upsilon^T \Psi_{f,U_s} - \Psi_{s,c} p \right),
 \end{aligned} \tag{18}$$

where we indicate with a comma after a function the partial derivation with respect to the specified variable and we used the mass balances (13) and the relation $F_s' F_s^{-1} = L_s$. The residual inequality (19), defining the dissipation \mathcal{D} , is clearly due to the adsorption, through the intensity of the mass source of adsorbate α and to the diffusion u between components, while from equations (18)₁₋₅ we have that the Helmholtz free energy Ψ , as well as the microstructural fields ζ_i and \mathcal{S}_i , depend upon the elastic state of the material only. Moreover, equations (18)₈₋₁₂ place restrictions on Ψ_i and α and do imply certain results that will be examined in a forthcoming work, e.g., if we set the velocities equal to zero or if we differenziate the relations and evaluate it at $v_i = 0$, we have informations on the partial derivatives of Ψ_i and α , when $v_i = 0$.

From equations (16) and (18)_{1,3,5,6,7}, we obtain the expression for the growth M and another restriction on the free energies and the source α :

$$\begin{aligned}
 M &= \text{skw} \left[\Psi_{,d} \otimes d + \Psi_{,p} \otimes \left(p - \frac{1-c}{\rho_f} \alpha_{,u} \right) - u \otimes \Psi_{f,u} \right], \\
 0 &= \text{skw} \left[F_s \Psi_{,F_s}^T + U_s \Psi_{,U_s} + d \otimes \Psi_{,d} + p \otimes \Psi_{,p} + \left(\frac{1-c}{\rho_f} \alpha \Psi_{,p} - u \Psi_s \right)_{,v_s} \right].
 \end{aligned} \tag{20}$$

Finally, we observe that, when microstructures are absent, our results are in agreement with those of Bowen [2] for classical mixtures in the isothermal

case. In particular, from equation (20)₂ we obtain the classical condition of symmetry of the Cauchy stress tensor for the whole mixture, while results (18)_{1,6,7,8} reduce to (6.12), (6.15) and (6.17) of [2]; besides, we recover the accordance with his entropy inequality (6.16) if we include the gradients of ρ_f and F_s in our constitutive variables.

Summary

We propose the balance principles for an immiscible mixture of continua with microstructure in presence of phenomena of chemical reactions, adsorption and diffusion by generalizing previous multiphase mixture [9] and use a new formulation for the balance of rotational momentum. New terms are also included in the energy equations corresponding to work done by respective terms in the micromomentum balances.

As an example we consider the flow of a fluid/adsorbate mixture through the big pores of a skeleton, thought like an elastic solid with an ellipsoidal microstructure, and propose suitable constitutive equations to study the coupling of adsorption and diffusion under isothermal conditions; in particular, we insert the concentration of adsorbate and its gradient in the usual variables, other than microstructural ones. Finally, the expression of the dissipation shows clearly its dependence on the adsorption and the diffusion, other than on the microstructural interactions. The model was already applied by G. and Palumbo [7] to describe the transport of pollutants with rainwater in soil.

References

- [1] Albers, B. (2000) Coupling of Adsorption and Diffusion in Porous and Granular Materials. A 1-D Example of the Boundary Value Problem. *Arch. Appl. Mech.* **70**, 519-531
- [2] Bowen, R.M. (1969) The Thermochemistry of a Reacting Mixture of Elastic Materials with Diffusion. *Arch. Rat. Mech. Anal.* **34**, 97-127
- [3] Capriz, G. (1989) *Continua with Microstructure*. Springer Tracts in Natural Philosophy 35. New York: Springer-Verlag
- [4] Giovine, P. (1990) Sulla Dinamica di una Miscela di Due Fluidi Comprimibili e Non Miscibili. *Rend. Mat. Acc. Lincei* **1**(9), 377-385
- [5] Giovine, P. (1996) Porous Solids as Materials with Ellipsoidal Structure. In Batra, R.C. and Beatty, M.F. (eds.): *Contemporary Research in the Mechanics and Mathematics of Materials*. Barcelona: CIMNE, pp. 335-342
- [6] Giovine, P. (2003) A Continuum Theory of Soils: Viewed as Peculiar Immiscible Mixtures. *Mathematical and computer modelling* **37**, 525-532
- [7] Giovine, P., and Palumbo, A. (2003) Modeling Contaminant Transport in Soils. *Proc. Medit. Conf. on Modelling and Simulation '03*, Reggio Calabria, June 2003, Session on Modeling, Tech. Note No. 178 on CD Rom: NeuroLab
- [8] Langmuir, I. (1918) The Adsorption of Gases on Plane Surfaces of Glass, Mica and Platinum. *Journal of American Chemical Society* **40**, 1361-1403

- [9] Passman, S.L., Nunziato, J.W., and Walsh, E.K. (1984). A Theory of Multiphase Mixtures. In Truesdell, C.: *Rational Thermodynamics*, 2nd edition. New York: Springer-Verlag, pp. 218-236
- [10] Truesdell, C. (1969). Thermodynamics of Diffusion. *Rational Thermodynamics*, Lecture 5. New York: McGraw-Hill
- [11] Wilmanski, K. (2002) Mass Exchange, Diffusion and Large Deformations of Poroelastic Materials. Capriz, G., Ghionna, V.N., and Giovine, P. (eds): *Modeling and Mechanics of Granular and Porous Materials*. Series on Modeling and Simul. in Sc., Engineering and Technology, Boston: Birkhauser, pp. 211-242

EFFECT OF WATER VOLUME FRACTION ON ELECTRICAL CONDUCTIVITY AND ION DIFFUSIVITY IN AGAROSE GELS

Wei Yong Gu

Tissue Biomechanics Laboratory

University of Miami

Coral Gables, FL 33146 USA

wgu@miami.edu

Hai Yao

Tissue Biomechanics Laboratory

University of Miami

Coral Gables, FL 33146 USA

Adriana L. Vega

Tissue Biomechanics Laboratory

University of Miami

Coral Gables, FL 33146 USA

Abstract Electrical conductivity of agarose gels in 0.15 M KCl was measured. From the experimental data, a functional relation of solute diffusivity to tissue permeability and solute size was derived. This relationship agreed with the experimental results on macromolecule diffusivity in agarose gel published in the literature.

Keywords: electrical conductivity, ion diffusivity, agarose gel, tissue porosity

Introduction

The long-term objective of this study is to understand the mechanism of nutritional transport in normal and degenerated human intervertebral discs and other cartilaginous tissues under mechanical loading. The intervertebral disc (IVD) is the largest avascular structure in the human body and subjected to mechanical loading in vivo. Poor nutritional supply is suggested to be one of the mechanisms involved in IVD degeneration [1, 6, 7, 18, 21]. With disc de-

Jacques M. Huyghe et al. (eds), IUTAM Proceedings on Physicochemical and Electromechanical Interactions in Porous Media, 193–199.

© 2005 Springer. Printed in the Netherlands.

generation, there are changes in its hydration and fixed charge density (FCD). The mechanical loading also causes the variation of tissue hydration and FCD, leading to an alteration in solute transport in the IVD.

The transport of solute is driven by the gradients of chemical potentials of solute and solvent. The rate of solute transport in tissue is in general governed by hydraulic permeability and solute diffusivities. The hydraulic permeability is a measure of the mechanical interaction between fluid and solid matrix of the tissue. The solute diffusivity is related to the drag coefficients between solute and solvent and between solute and solid matrix [4, 8, 12]. It has been reported that diffusion is the major mechanism for the transport of small solutes in IVD [10, 22, 23]. Many studies have been done on the solute diffusion in cartilage and IVD tissues, e.g., [16, 20, 22, 24], however, little information is available in literature on the regulation of mechanical deformation on solute diffusivity in cartilaginous tissues. The functional relationship between solute diffusivity and mechanical deformation is important to understanding the effect of mechanical loading on the nutrient transport in IVD tissues.

The major factors governing the diffusion coefficients are the solute size and the pore size of the tissue which is related to the tissue hydration. The FCD seems to have little effect on ion (charged solute) diffusivity in tissue with normal saline (0.15 M NaCl) [13, 15, 16]. When a hydrated soft tissue is subjected to mechanical loading, its porosity (or hydration) will change, leading to an increase or decrease in diffusion coefficient of solute within the tissue. In spite of the fact that numerous studies have been conducted on investigating solute diffusion in gels and soft tissues, to date, there is no universal, theoretical model capable of describing the diffusion behavior of solute in gels or biological soft tissues with satisfaction, e.g., [17].

In this paper, we studied ion diffusivity in uncharged gels in order to gain an insight into solute diffusion in charged cartilaginous tissues, because the FCD of the tissues under physiological conditions is not an important factor for regulating solute diffusivity. The major purposes of this study are to investigate the effect of gel porosity on ion (K^+ and Cl^-) diffusion. The other objective of this study is to explore a conductivity method for investigating solute diffusion in gels.

Theoretical Background

Considering a charged porous medium containing monovalent electrolyte, the electrical current (I_e) carried by ions (per unit area) is related to the ion fluxes and given by [4, 8, 12]

$$I_e = F_c (c^+ - c^-) J^w - F_c \phi^w D^+ \nabla c^+ + F_c \phi^w D^- \nabla c^- - \chi \nabla \Psi, \quad (1)$$

where J^w is the solvent flux relative to the solid, c^+ and c^- are cation and anion concentrations (per unit volume of solvent) respectively, ϕ^w is the volume

fraction of water (or porosity), D^+ and D^- are ion diffusivities within the tissue respectively, F_c is the Faraday constant, R is the gas constant, T is absolute temperature, Ψ is the electrical potential, and χ is the electrical conductivity of tissue measured in the absence of convection and diffusion effects:

$$\chi = F_c^2 \phi^w (c^+ D^+ + c^- D^-) / RT. \quad (2)$$

For uncharged agarose gels ($c^F = 0$), Equation (2) reduces to

$$\chi = F_c^2 \phi^w c^* (D^+ + D^-) / RT, \quad (3)$$

where c^* is the bathing solution concentration. If the diffusivity of cation is equal to that of anions, i.e., $D^+ = D^- = D$, one can obtain the following equation

$$\frac{\chi}{\chi_0} = \frac{\phi^w D}{D_0}, \quad (4)$$

where χ_0 is the conductivity of such electrolyte solution, and D_0 is the solute diffusivity in free solution.

Experimental Methods

Specimen preparation

Agarose gel, an uncharged fibrous medium, was used in this study. Low-melting temperature SeaPlaque[®] agarose powder (Cambrex Bio Science, Rockland, ME) was dissolved in 0.15 M KCl solution. The nominal gel concentration was varied from 2% to 24%. The agarose powder was mixed in the KCl solution and heated in covered beakers for 5 - 24 hours. After gelling at room temperature (22 °C), cylindrical specimens (d = 5 mm, h~3 mm) were prepared. The specimens were equilibrated in 0.15 M KCl solution and stored at 4 °C. Before testing, the exact height of each specimen was measured using a current-sensing digital micrometer at room temperature [3].

Porosity measurement

After height measurement, the weight of the specimens in air, W_{wet} , and in the KCl solution in which it was prepared, W_{KCl} , was measured using the density-determination kit of a Sartorius analytical balance (Model LA120S, Goettingen, Germany). The difference between W_{wet} and W_{KCl} , which is due to the buoyancy force, was related to the specimen volume and the mass density of solution (ρ_{KCl}). After the conductivity testing, the specimens were lyophilized and the dry weights, W_{dry} , were recorded. The volume fraction of water (ϕ^w) of the specimens was calculated by [3, 5]

$$\phi^w = \frac{W_{wet} - W_{dry} \rho_{KCl}}{W_{wet} - W_{KCl} \rho_w}, \quad (5)$$

where ρ_{KCl} is the mass density of the KCl solution and ρ_w is the mass density of water. The volume fraction of gel (ϕ^s) can be calculated by $\phi^s = 1 - \phi^w$.

Conductivity measurement

An apparatus and technique for measuring conductivity of hydrated soft tissues under the condition of zero fluid flow (no convection) were recently developed for this investigation [3]. Briefly, the apparatus consisted of two (stainless steel) current electrodes ($d = 5$ mm), two (Ag/AgCl) voltage sensing electrodes made from Teflon coated silver wire ($d = 0.38$ mm), a specimen chamber, a Keithley Sourcemeter, and a current-sensing digital micrometer (for height measurement). The apparatus was calibrated using a conductivity standard (0.1 M KCl) in the range of 2 - 4 mm. Using the four-wire method, the conductivity of specimens was measured with constant direct current of 3 μ A (density: 0.015 mA/cm²) at room temperature (22 ± 1 °C). The electrical conductivity (χ) of gel was calculated according to the following formula:

$$\chi = h/rA \quad (6)$$

where r is the resistance measured by the instrument, h is the sample thickness, and A is the cross-sectional area of the sample.

Results

The electrical conductivity of agarose gel increased with increasing water volume fraction, Figure 1. This is attributed primarily to the dependence of ion diffusivity on water volume fraction [14]. An empirical model for relative ion diffusivity (D/D_0) is proposed to be a function of the hydrodynamic radius (r_s) of solute and intrinsic Darcy permeability (κ) of gel:

$$\frac{D}{D_0} = e^{-\alpha \left(\frac{r_s}{\sqrt{\kappa}} \right)^\beta}, \quad (7)$$

where α and β are parameters. For agarose gels, the Darcy permeability is related to the water volume fraction by [5]

$$\kappa = 0.00339 \left(\frac{\phi^w}{\phi^s} \right)^{3.236} (nm^2). \quad (8)$$

For KCl the hydrodynamic radii for cation and anion are very close [11], so the average radius $r_s = 0.14$ nm could be used in Equation (7) for this study. Curve-fitting of conductivity data using Equations (4, 7, 8) yielded $\alpha = 1.274$ and $\beta = 0.693$ with $R^2 = 0.964$ ($n=72$).

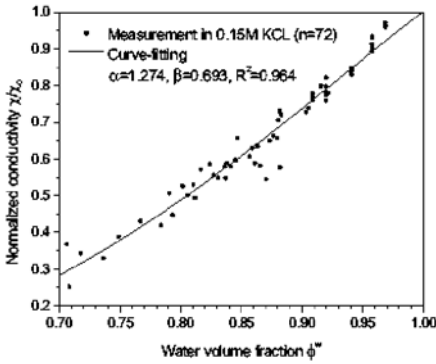


Figure 1. Dependence of normalized conductivity on gel porosity

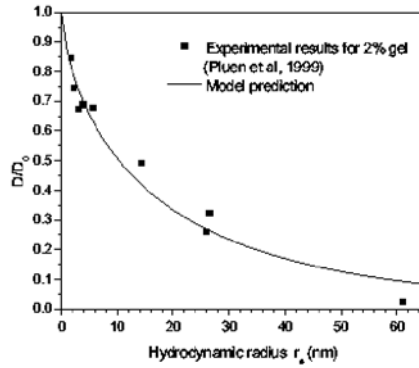


Figure 2. Comparison of model prediction to data from the literature

Discussion

The major objective of this study is to investigate ion diffusivity in uncharged gels using the electrical conductivity method. The dependence of the electrical conductivity for agarose gels measured in this study is similar to that for biological soft tissues in the literature e.g., [2]. From the conductivity data, the functional dependence of the relative solute diffusivity on the ratio of solute radius to the square root of Darcy permeability is obtained. The relative diffusion coefficients of proteins, dextrans, and polymer beads (with radii in the range of 2 - 61 nm) in 2% agarose gel with 0.1M PBS has been reported in the literature [19]. Using $\kappa = 616 \text{ nm}^2$ for 2% agarose gel [9], Equation (7) with ($\alpha = 1.274$ and $\beta = 0.693$) can predict the relative diffusion coefficients of macromolecules up to $r_s \approx 27 \text{ nm}$ (Figure 2). For the solute with $r_s = 61 \text{ nm}$, Equation (7) overestimates the value of relative diffusivity considerably (Figure 2). This is because Equation (7) is not valid for solute with radius much larger than the pore size of the gel [19].

In summary, the effect of porosity on electrical conductivity and ion diffusivity in agarose gels is studied. Both electrical conductivity and ion diffusivity increase with porosity. The model obtained from the electrical conductivity data, i.e., Equation (7), can predict the diffusivity of macromolecules in 2% agarose gel for solutes with hydrodynamic radius less than the pore size of the gel. This study suggests that electrical conductivity method used in this study can be applied to investigating diffusion behavior of macromolecules in uncharged porous media.

Acknowledgments

This work is supported by a grant from the NIH (AR46860) and by the General Research Support Award from the University of Miami.

References

- [1] Bibby, S.R., Fairbank, J.C., Urban, M.R. and Urban, J.P. (2002) Cell viability in scoliotic discs in relation to disc deformity and nutrient levels. *Spine* **27**, 2220-2228
- [2] Gu, W.Y., Justiz, M.A. and Yao, H. (2002) Electrical conductivity of lumbar annulus fibrosis: Effects of porosity and fixed charge density. *Spine* **27**, 2390-2395
- [3] Gu, W.Y. and Justiz, M.A. (2002) Apparatus for measuring the swelling dependent electrical conductivity of charged hydrated soft tissues. *J Biomech Engng* **124**, 790-793
- [4] Gu, W.Y., Lai, W.M. and Mow, V.C. (1998) A mixture theory for charged-hydrated soft tissues containing multi- electrolytes: passive transport and swelling behaviors. *J Biomech Engng* **120**, 169-180.
- [5] Gu, W.Y., Yao, H., Huang, C.Y. and Cheung, H.S. (2003) New insight into deformation-dependent hydraulic permeability of gels and cartilage, and dynamic behavior of agarose gels in confined compression. *J Biomech* **36**, 593-598
- [6] Holm, S. and Nachemson, A. (1982) Nutritional changes in the canine intervertebral disc after spinal fusion. *Clin Orthop*, 243-258
- [7] Horner, H.A. and Urban, J.P. (2001) Volvo Award Winner in Basic Science Studies: Effect of nutrient supply on the viability of cells from the nucleus pulposus of the intervertebral disc. *Spine* **26** 2543-2549
- [8] Huyghe, J.M. and Janssen, J.D. (1997) Quadriphasic mechanics of swelling incompressible porous media. *Int J Engng Sci* **35**, 793-802
- [9] Johnson, E.M. and Deen, W.M. (1996) Hydraulic permeability of agarose gels. *AIChE Journal* **42**, 1220-1224
- [10] Katz, M.M., Hargens, A.R. and Garfin, S.R. (1986) Intervertebral disc nutrition: Diffusion versus convection. *Clin Orthop*, 243-245
- [11] Koneshan, S., Rasaiah, J.C., Lynden-Bell, R.M. and Lee, S.H. (1998) Solvent structure, dynamics, and ion mobility in aqueous solution at 25C. *J Phys Chem* **102**, 4193-4204
- [12] Lai, W.M., Hou, J.S. and Mow, V.C. (1991) A triphasic theory for the swelling and deformation behaviors of articular cartilage. *J Biomech Eng* **113**, 245-258
- [13] Lanir, Y., Seybold, J., Schneiderman, R. and Huyghe, J.M. (1998) Partition and diffusion of sodium and chloride ions in soft charged foam: the effect of external salt concentration and mechanical deformation. *Tissue Engineering* **4**, 365-378
- [14] Mackie, J.S. and Meares, P. (1955) The diffusion of electrolytes in a cation-exchange resin: I. Theoretical. *Proc Roy Soc London* **A232**, 498-509
- [15] Maroudas, A. (1975) Biophysical chemistry of cartilaginous tissues with special reference to solute and fluid transport. *Biorheology* **12**, 233-248
- [16] Maroudas, A. (1979) Physicochemical properties of articular cartilage. In M.A.R. Freeman (ed), *Adult Articular Cartilage*, 2nd edn., pp. 215-290, Pitman Medical
- [17] Masaro, L. and Zhu, X.X. (1999) Physical models of diffusion for polymer solutions, gels and solids. *Progress in Polymer Science* **24**, 731-775

- [18] Nachemson, A., Lewin, T., Maroudas, A. and Freeman, M.A. (1970) In vitro diffusion of dye through the end-plates and the annulus fibrosus of human lumbar inter-vertebral discs. *Acta Orthop Scand* **41**, 589-607
- [19] Pluen, A., Netti, P.A., Jain, R.K. and Berk, D.A. (1999) Diffusion of macromolecules in agarose gels: comparison of linear and globular configuration. *Biophysical Journal* **77**, 542-552
- [20] Torzilli, P.A., Adams, T.C. and Mis, R.J. (1987) Transient solute diffusion in articular cartilage. *J Biomech* **20**, 203-214
- [21] Urban, J.P. (2001) The role of the physicochemical environment in determining disc cell behavior. *Biochem Soc Trans* **30**, 858-864
- [22] Urban, J.P., Holm, S. and Maroudas, A. (1978) Diffusion of small solutes into the intervertebral disc: as in vivo study. *Biorheology* **15**, 203-221
- [23] Urban, J.P., Holm, S., Maroudas, A. and Nachemson, A. (1982) Nutrition of the intervertebral disc: Effect of fluid flow on solute transport. *Clin Orthop* **170**, 296-302
- [24] Urban, J.P.G., Holms, S., Maroudas, A. and Nachemson, A. (1977) Nutrition of the intervertebral disc: An in vivo study of solute transport. *Clin Orthop* **129**, 101-114

HYDRODYNAMIC DISPERSION AND CHEMICAL REACTION IN POROUS MEDIA: THE USE OF SPACE LIKE COORDINATES

David E. Smiles

CSIRO Land and Water, PO Box 1666, Canberra ACT 2601 Australia

david.smiles@csiro.au

Abstract Unsteady liquid flow and chemical reaction characterize hydrodynamic dispersion in soils and other porous materials and flow equations are complicated by the need to account for advection of the solute with the water, and competitive adsorption of solute components. Advection of the water and adsorbed species with the solid phase in swelling systems is an additional complication. Computers facilitate solution of these equations but it is often physically more revealing when we discriminate between flow of the solute with and relative to, the water and the flow of solution with and relative to, the solid phase. Space-like coordinates that satisfy material balance of the water, or of the solid, achieve this separation. Advection terms are implicit in the space-like coordinate and the flow equations are focused on solute movement relative to the water and water relative to soil solid. This paper illustrates some of these issues.

Introduction

Transfer of solute with and relative to the moving water and competitive adsorption of solutes are central to amelioration of saline and alkali soils, agricultural chemical location in soils and management of wastes in soils. This paper illustrates how space-like coordinates based on the distribution of the solid and the water help analyse these problems. We focus on the macroscopic or Darcy scale of discourse [6], which permits unambiguous measurement of the key elements of the flow equations, and we restrict ourselves to 1-dimensional flow, because that seems to limit analysable experiments.

Jacques M. Huyghe et al. (eds), IUTAM Proceedings on Physicochemical and Electromechanical Interactions in Porous Media, 201–206.

© 2005 Springer. Printed in the Netherlands.

Theory

Water movement

One-dimensional material balance for water in soil may be written [8]

$$\left(\frac{\partial \vartheta}{\partial t}\right)_m = -\left(\frac{\partial F}{\partial m}\right)_t. \quad (1)$$

In this equation ϑ is the volume of water per unit volume of solid, t is time, F is the Darcy flux of water relative to the solid, and m is a space like coordinate defined in terms of the distribution of the solid phase. Substitution of Darcy's law in this equation results in equations similar to the Richards equation and, at least in 1-dimension, these can be solved like their non-swelling analogues. This equation implicitly deals with volume change that might accompany change in water content.

Solute movement

In this material convention, the one-dimensional balance equation for a solute is

$$\left(\frac{\partial (C_w \vartheta + \rho_c C_c)}{\partial t}\right)_m = -\left(\frac{\partial (f + C_w F)}{\partial m}\right)_t, \quad (2)$$

with C_w the solute concentration in the water, C_c that associated with the soil solid, and ρ_c the soil solid density. The solute flux, F_s , has components advected with the water $C_w F$, and relative to it f . Thus

$$f = F_s - C_w F = -D_s \frac{\partial C_w}{\partial m}. \quad (3)$$

Equation 3 is Fick's law of diffusion. The diffusion coefficient D_s is characteristic of the porous material and its water content. Dispersion theory and experiments deal with Eqns 1-3 [1, 8]. Early analysis resulted in breakthrough experiments such as those of Day [4], where perturbation, at the outflow end, of a step change or pulse in concentration at the inflow end of a column of porous material, is used to infer detail of the hydraulic and chemical consequences of passage through the column. Day [4] explicitly identified a material coordinate that reduces the solute flow equation to a diffusion equation in such an experiment. Reiniger and Bolt [1] explored competitive reaction during steady saturated flow and related characteristic exchange isotherms to the shapes of reaction fronts and their displacement relative to the notional 'piston front' that separates the invading water from that originally present. Smiles et al. [10] extended experiments and analysis to unsteady unsaturated flow. They showed

that, for initial and boundary conditions of the form

$$\begin{cases} t = 0 & m \geq 0 & \theta_w = \theta_i & C_w = C_i \\ t \geq 0 & m = 0 & \theta_w = \theta_0 & C_w = C_0 \end{cases} \quad (4)$$

the substitution $\lambda = mt^{-1/2}$ eliminates m and t from Eqns (1) and (2) as well as Eqns (4) so that, if Eqns (1) and (2) are valid, then $\vartheta(\lambda)$ and $C_w(\lambda)$ profiles observed in experiments performed over different elapsed times, are similar. Smiles et al. [11] extended these analyses to constant flux absorption and used a water-based coordinate, $g(m, t)$, to better describe the solute flow in their experiments. Cation exchange is complex, however [2], and for modelling purposes simple relations between C_w and C_c are desirable. The most simple is written [3]

$$\beta C_w = C_c, \quad (5)$$

whence

$$dg(m, t) = (\vartheta + \beta) dm - F dt. \quad (6)$$

and the constant β term displaces the solute profile in the water profile relative to piston front and also changes the effective diffusion coefficient that describes the shape of the solute front. In principle, Eqn (5) is the exception rather than the rule and adsorption isotherms for each competing cation pair must be established in the presence of all others. [2, 5], for example, discuss such isotherms and the latter tabulate 350 selectivity coefficients for reversible exchange reactions in soils and clays. The consequences of this theory are complicated but experimental data involving cation exchange during non-steady water flow in non-swelling as well as swelling materials appears to permit, to at least a first approximation, simple data presentation and semi-quantitative explanation.

Experimental Observations and Comments

Two experimental sets where the flow equations apply and conditions (4) were imposed illustrate some uses of material coordinates.

Clay filtration experiments

[9] measured the distribution of Na^+ , K^+ , Ca^{2+} and Mg^{2+} during filtration of a sodic bentonite in contact with a gypsum 'membrane' at its outflow surface. Calcium from the gypsum entered the consolidating clay against the flow of the filtrate where it displaced exchangeable Na^+ and other cations. These were flushed from the clay in the filtrate. At the outflow surface, the clay water content decreased to 2 from about 12kg/kg and the length of the filter cake decreased by more than 40%.

The water content profiles of the clay expressed in physical space, and as $\vartheta_w(M = mt^{-1/2})$ in material space preserved similarity as is consistent with

the flow equations and Eqn (4) [9]. m is the cumulative amount of clay per unit area of cross section measured from $z = 0$, and water content profiles are easy to measure using coordinates defined by the distribution of the solid mass because we extrude the column from its cylindrical container and measure the water and solid contents by oven-drying sequential slices.

Cation exchange occurred but we have yet to measure equilibrium sets of water-soluble and exchangeable cations in these systems so total (soluble plus exchangeable) Na^+ and Ca^{2+} profiles in the clay were graphed in physical and M -based spaces and, also, in terms of the water-based coordinate, $G(M)$, defined by integrating Eqn (6) after dividing by $t^{1/2}$. These profiles also maintained similarity even though a) the volume change is great and non-uniform; b) exchange among four competing cations occurs; c) the solution content and fluxes in the region of reaction change greatly; and d) the physical structure changes in response to the chemistry. Although the theoretical implications of each of these effects are significant, they culminate in relatively simple systematic behaviour.

Absorption of solution by dry soil with varying clay content

These experiments [8] explored the absorption of a tritiated solution containing Co-60 by dry soil and sought to define the fate of these nuclides in soils at potential radioactive waste repositories. The soil clay content varied from about 8% to 14% and a subset of experiments tested the Boltzmann substitution by termination at different times. Variation in clay content resulted in an almost 10-fold change in sorptivity S as well as affecting the cation exchange capacity and hence the retardation of the Co-60. The non-reactive tritium profiles were consolidated using a water based coordinate. The use of a space-like coordinate based on the distribution of clay, normalised according to S virtually eliminated variation in the Co-60 profiles and, with care, appears to be a useful way to generalize results across soils of different clay content and structure when clay-based chemical reaction occurs. Extension of this type of approach according to clay mineralogy and cation exchanges capacity may be profitable. These experiments are consistent with conjectures by [7] who suggested that a coordinate based on the spatial distribution of an 'irreducible' solid component in the soil should be useful when describing chemical reaction accompanied by volume change in organic soils and potential acid-sulfate soils that oxidise as they are drained.

Concluding Remarks

Material coordinates simplify flow equations with advective terms so transfer of the component of concern is more simply described relative to the 'natural' matrix.

Water movement

Water flow in 1- dimension is described relative to the soil solid by Darcy's law and a material coordinate based on the distribution of soil solid matrix and well tested flow equations analogous to the Richards equation result, which are indifferent to volume change accompanying water content change. Matrix mass distributions are generally measured and often used as a critical outcome of an experiment or process so the coordinate definition is a primary measurement and, frequently, more accurate than a space measure. The solid based coordinate is central to description of flow in swelling systems and a general base for describing solute transfer. Equations (1) and (2) thus provide a general and natural point of departure for study of hydrodynamic dispersion, at least in 1-dimensional flow and solutions of [1] for steady flow, and Bond and co-workers [2], for transient flow, immediately apply to these equations.

Solute movement

In the absence of chemical reaction, a water based space-like coordinate can be defined and derived in exactly the same way as the solid-based coordinate used to deal with swelling. The resulting diffusion equation has well-established solutions. This water based coordinate is not a primary measurement, however, and is derived from the water flow equation. It nevertheless provides a framework against which flow and the consequences of reaction can be judged and it is also helps overcome some hydrological consequences of soil heterogeneity [8]. In the presence of chemical reaction, such as cation exchange, a coordinate based on the distribution of exchange sites would seem to be a useful way to generalise cation data across materials with different cation exchange capacities and, perhaps, clay mineralogies. In our examples, we were unable to measure water-soluble salts separately from adsorbed species so the isotherms that describe competitive exchange among the solute components could not be assessed. Nevertheless, recent experiments intended to set limits to behaviour of soils irrigated with pig effluent using the methods of [10] show that simple models such as those identified here provide robust matching of cation distributions under an 'envelope' defined by the distribution of the non-adsorbed anions. These studies await extension to water-soluble and exchangeable cations during transient flow in stiff clays.

References

- [1] Bolt, G.H. (1982) Transport and accumulation of soluble soil components. In G. H. Bolt, editor, *Soil chemistry. B. Physico-chemical models* **143**, Elsevier, Amsterdam, pp. 285–346
- [2] Bond, W.J. and Verburg, K. (1997) Comparison of methods for predicting ternary 3exchange from binary isotherms. *Soil Sci. Soc. Amer. J.* **61**, 444–454

- [3] Crank, J. (1956). *The Mathematics of Diffusion*. Oxford, London, 1st edition
- [4] Day, P.R. (1956) Dispersion of a moving salt-water boundary advancing through saturated sand. *Trans Amer. Geophys. Union* **37**, 595–601
- [5] Bruggenwert, M.G.M and Kamphorst, A. (1982) Survey of experimental information on cation exchange in soil systems. In G.H. Bolt, editor, *Soil chemistry. B. Physico-chemical models* **143**, Elsevier, Amsterdam, pp. 141–203
- [6] Philip, J.R. (1972) Flow in porous media, In *Proc. 13th International Congress of Theoretical and Applied Mechanics*, Moscow, 1972, pp. 279–294 pp. 279–294
- [7] Raats, P.A.C. (1998) Kinematics of subsidence of soils with a non-conservative phase. In Proceedings on CD-Rom of a Symposium on “New Concepts and Theories in Soil Physics”, at the 16th World Congress of Soil Science, Cirad, Montpellier, France, 20–26 August 1998
- [8] Smiles, D.E. (2001) Chemical reaction and Co-60 retardation in unsteady, unsaturated soil water flow: the effect of clay content. *Aust. J. Soil Res.* **39**, 1059–1075
- [9] Smiles, D.E., Kirby, J.M., and Little, I.P. (1996) Hydrodynamic dispersion and chemical reaction in sodium bentonite during filtration in the presence of calcium sulphate. *Chem. Engng Sci.* **51**, 3647–3655
- [10] Smiles, D.E., Philip, J.R., Knight, J.H., and Elrick, D.E. (1978) Hydrodynamic dispersion during absorption of water by soil. *Soil Sci. Soc. Amer. J.* **42**, 229–234
- [11] Smiles, D.E., Perroux, K.M., Zegelin, S.J., and Raats, P.A.C. (1981) Hydrodynamic dispersion during constant rate absorption of water by soil. *Soil Sci. Soc. Amer. J.* **45**, 453–458

DEVELOPMENT OF A FINITE ELEMENT APPROACH TO MECHANICS, TRANSPORT AND BIOSYNTHESIS IN TISSUE ENGINEERING

Bram G. Sengers, Rolf A.A. Pullens, Cees W.J. Oomens and Frank P.T. Baaijens

*Eindhoven University of Technology, Department of Biomedical Engineering
P.O. Box 513, 5600 MB Eindhoven, The Netherlands*

Introduction

In order to reach the stage of clinical applicability a definite need arises for improved control over the functional properties and composition of tissue engineered constructs; [3]. Tissue function is determined by extracellular matrix components such as GAG's and collagen which are produced by cells in response to their local biochemical and mechanical environment which can be partially influenced via global bioreactor input parameters, like nutrient supply and mechanical stimulation; [6]. Many tissue engineering experiments yield only qualitative histological data or quantitative data on a volume averaged basis. This provides valuable clues and indicates research directions, but is open to much speculation on possible mechanisms that govern tissue development. Mathematical models enable a further rationalization of experimental results and will be a key asset in controlling the development and thus the functionality of tissue engineered constructs; [16]. Since only a combination of a suitable biochemical and mechanical environment is likely to provide functional tissue engineered constructs, both aspects should be integrated in a numerical model. This requires a description of highly coupled phenomena such as solute transport, cell growth, matrix biosynthesis and mechanical adaptation. The objective of this study is to develop an integrated numerical framework for tissue engineering that is able to relate the evolution of local functional tissue components to both mechanical and biochemical global bioreactor input parameters. The modeling approach can eventually serve as an aid in tissue bioreactor design and the development of control strategies. To illustrate the approach two cases will be considered. First, dynamic compression combined with supplemented growth factors has been shown to produce synergistic effects on protein and proteoglycan synthesis; [1]. Therefore, apart from direct mechanical stimulation, we will investigate the conditions under which com-

pression induced convection can contribute to increased biosynthesis as well as increased release of newly synthesized matrix molecules; [17, 19, 5]. Secondly the focus will be on cell behavior. We will investigate if viability data can be related to glucose availability in an experimental model of the intervertebral disk by [8].

Methods

The proposed model consists of a biphasic mechanical description of the tissue engineered construct. The resulting fluid velocity and displacement fields are used for evaluating solute transport. Solute concentrations determine biosynthetic behavior. A finite deformation biphasic displacement-velocity-pressure (u-v-p) formulation is implemented; [12, 7]. Compared to the more standard u-p element the mixed treatment of the Darcy problem enables an increased accuracy for the fluid velocity field which is of primary interest here. The system to be solved increases however considerably and for multidimensional flow the use of either stabilized methods or Raviart-Thomas type elements is required; [15, 10]. To model solute transport the input features of a standard convection-diffusion element for compressible flows are employed; [20]. For flexibility (non-linear) solute uptake is included using Strang operator splitting, decoupling the transport equations; [9].

Model Application

Solute transport by mechanically induced convection

The first case considered is solute desorption during unconfined compression. We consider a two dimensional plane strain problem, see Fig. 1. A sinusoidal strain between 0 and 15 % is applied at 0.001 Hz, 0.01 Hz, 0.1 Hz and 1 Hz. To account for microscopic solute spreading due to fluid flow a dispersion parameter is introduced. Against the background of the release of newly synthesized matrix molecules the diffusion parameter is set to the value for chondroitin sulfate in dilute solution: $D_{CS} = 4 \times 10^{-7} \text{ cm}^2 \text{ s}^{-1}$; [4] The dispersion parameter D^d is varied in the range from 0 mm to $1 \times 10^{-1} \text{ mm}$. The fluid volume fraction is set to $n^f = 0.9$, the bulk modulus $\kappa = 8.1 \text{ kPa}$, the shear modulus $G = 8.9 \text{ kPa}$ and the permeability $K = 1 \times 10^{-13} \text{ m}^4 \text{ N}^{-1} \text{ s}^{-1}$; [14]. The initial concentration is normalized to 1 and the evolution of the concentration is followed for a total time period of 4000 s. for the displacement and linear discontinuous. For displacement and fluid velocity a 9 noded quadrilateral is used, the pressure is taken linear discontinuous.

Next the effect of cyclic loading on the distribution of a limited solute is investigated. Small and large solutes are considered (glucose, albumin). Both solutes are assumed limited a priori by diffusion and uptake, resulting in equal

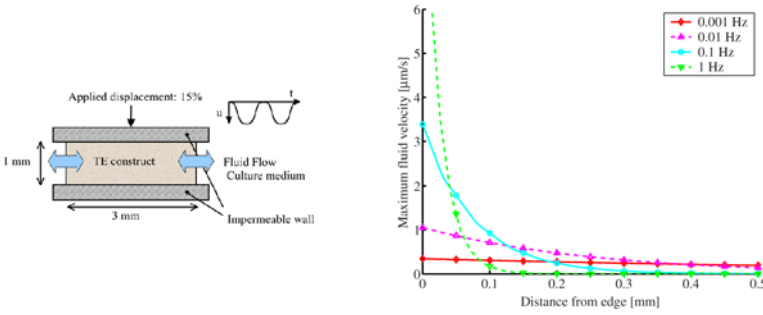


Figure 1. (a) Unconfined compression setup. (b) Maximum fluid velocity induced by dynamic loading in the last cycle before $t = 4000$ s, plotted in the undeformed geometry.

initial concentration profiles. The diffusion coefficient D^m for the small and large solute is set to $1 \times 10^{-5} \text{ cm}^2 \text{ s}^{-1}$ and $1 \times 10^{-7} \text{ cm}^2 \text{ s}^{-1}$ respectively; [13, 18]. Michaelis Menten kinetics are used for solute uptake, the maximum rate for the small and large solute $k_{max} = 4 \times 10^{-3} \text{ mol cell}^{-1} \text{ s}^{-1}$ and $k_{max} = 4 \times 10^{-5} \text{ mol cell}^{-1} \text{ s}^{-1}$ respectively, the half max rate concentration C_m is set to 0.1 mol mm^{-3} . Unconfined compression is applied at frequencies of 0.001 Hz and 0.1 Hz for 87000 s, dispersion parameters D^d of 0 mm, 0.01 mm and 0.1 mm are evaluated.

Results

The maximum fluid velocities for the different frequencies are shown in Fig. 1b. For the case without cell activity Fig. 2 shows the effect of dispersion on solute content. For the case of a large limited solute Fig. 3b indicates that in correspondence with the fluid velocity profiles in Fig. 1b, the solute penetration depth is largest for 0.001 Hz, while for 0.1 Hz solute concentrations are higher in the periphery. Concentration profiles for the small limiting solute are hardly affected by different dispersion parameters and loading conditions.

Glucose availability and viability

To investigate a relation between glucose and cell viability an one dimensional experimental model of the intervertebral disk consisting of cells embedded in agarose was modeled numerically; [8]. The glucose diffusion constant was set to $D^m = 7.4 \times 10^{-6} \text{ cm}^2 \text{ s}^{-1}$; [13]. The glucose consumption rate was a rough estimate from data for cartilage; [11] $3.6 \times 10^{-12} \mu\text{mol cell}^{-1} \text{ s}^{-1}$. The Michaelis Menten constant was set at $2.5 \times 10^{-3} \mu\text{mol mm}^{-1}$ taken from C2C12 cells; [2]. Once a critical glucose level is reached it is assumed that cells start to die at a rate estimated from the experimental case without glucose

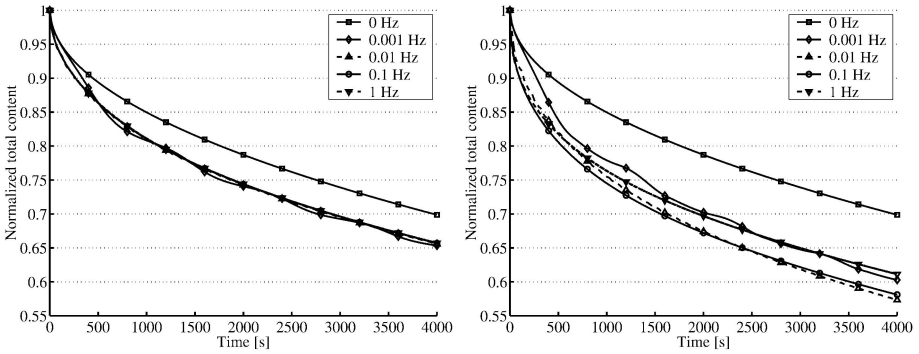


Figure 2. Desorption of an initially homogeneous concentration for different loading conditions and dispersion parameters. Evolution of total content in time (a) $D^d = 0$ mm, (b) $D^d = 0.1$ mm.

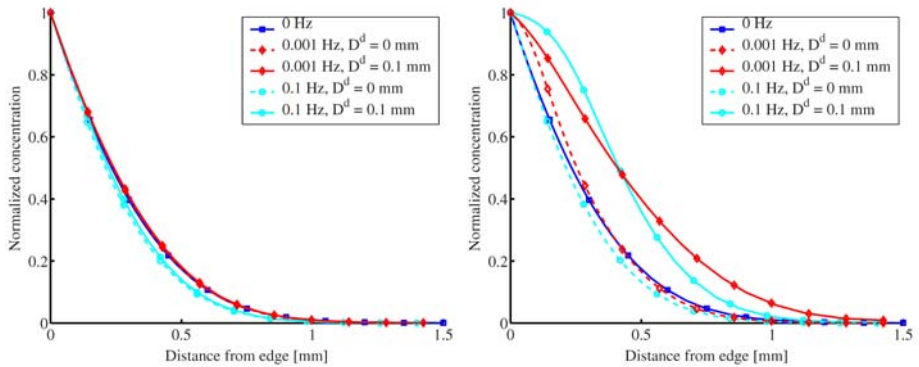


Figure 3. Solute concentration profiles at $t = 87000$ for different loading frequencies and dispersion parameters (a) small solute, (b) large solute.

$6.5 \times 10^{-6} \text{ s}^{-1}$; [8]. The critical glucose level is adjusted to match the data for $2 \times 10^3 \text{ cells mm}^{-3}$.

Results

In Fig. 4 it can be observed that the numerical simulations result in viability profiles qualitatively similar to the experiment. However in contrast to the experiment, in the simulations a considerable fraction of the cells in the center remains viable. In addition the critical glucose level fitted is very high, $4.5 \times 10^{-3} \mu\text{mol mm}^{-3}$ compared to the initial glucose concentration of $5 \times 10^{-3} \mu\text{mol mm}^{-3}$.

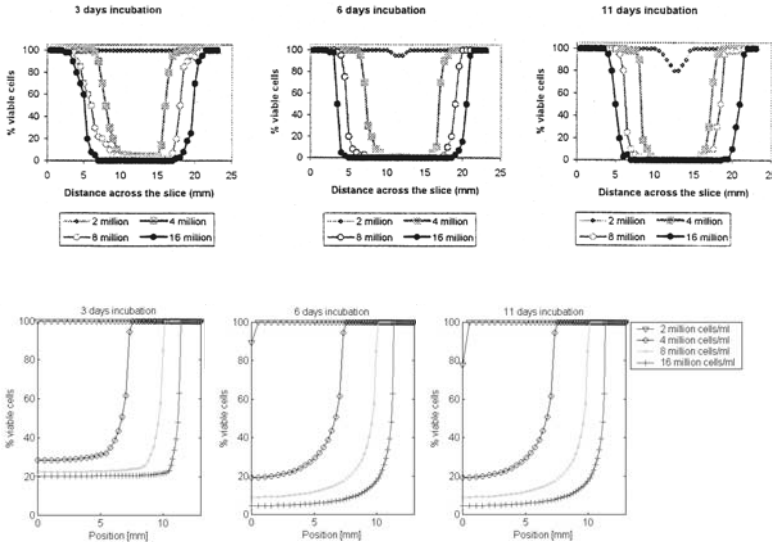


Figure 4. (a) Experimental viability data; [8]. (b) Numerical results.

Discussion

The high level of coupling between mechanical and biochemical factors in functional tissue engineering requires an integrated modeling approach. Compression induced convection can contribute to enhanced biosynthesis in case of a large limited solute and high dispersion. Higher frequencies lead to a higher solute concentration in the periphery, low frequencies provide a large solute penetration depth. As a first approximation friction between solutes and the solid matrix as well as osmotic and electric effects have not been taken into account. Without further assumptions glucose alone cannot fully account for the experimental viability data, particularly the role of lactate accumulation should be investigated further. Comparison with experimental data is required for model validation and for establishing better quantified relations for cell behavior.

Acknowledgments

The research was funded by the European Commission project IMBIOTOR (GRD1-2000-25394).

References

- [1] Bonassar, L.J., Grodzinsky, A.J., Frank, E.H., Davila, S.G., Bhaktav, N.R., and Trippel, S.B. (2001) The effect of dynamic compression on the response of articular cartilage to insulin-like growth factor-I. *J. Orth. Res.* **19**, 11–17

- [2] Breese, T.W. and Admassu, W. (1999) Feasibility of culturing c2c12 mouse myoblasts on glass microcarriers in a continuous stirred tank bioreactor. *Bioprocess Eng.* **20**, 463–468
- [3] Butler, D.L., Goldstein, S.A., and Guilak, F. (2000) Functional tissue engineering: The role of biomechanics. *J. Biomech. Eng.* **122**, 570–575
- [4] Comper, W.D. and Williams, R.P.W. (1987) Hydrodynamics of concentrated proteoglycan solutions. *J. Biol. Chem.* **262**(28), 13464–13471
- [5] Davisson, T., Kunig, S., Chen, A., Sah, R., and Ratcliffe, A. (2002) Static and dynamic compression modulate matrix metabolism in tissue engineered cartilage. *J. Orth. Res.* **20**, 842–848
- [6] Freed, L.E., Martin, I., and Vunjak-Novakovic, G. (1999) Frontiers in tissue engineering: In vitro modulation of chondrogenesis. *Clin. Orthop. Relat. Res.* **367S**, S46–S58
- [7] Frijns, A.J.H. (2000) A four-component mixture theory applied to cartilaginous tissues. *Ph.D. thesis, Eindhoven University of Technology, Eindhoven, The Netherlands*
- [8] Horner, H.A. and Urban, J.P.G. (2001) Effect of nutrient supply on the viability of cells from the nucleus pulposus of the intervertebral disk. *Spine* **26**(23), 2543–2549
- [9] Hundsdorfer, W. and Verwer, J.G. (1995) A note on splitting errors for advection-reaction equations. *Appl. Numer. Math.* **18**, 191–199
- [10] Kaasschieter, E.F., Frijns, A.J.H., and Huyghe, J.M. (2003) Mixed finite element modeling of cartilaginous tissues. *Math. Comput. Simulation* **61**, 549–560
- [11] Lee, R.B. and Urban, J.P.G. (1997) Evidence for a negative pasteur effect in articular cartilage. *Biochem. J.* **321**, 95–102
- [12] Levenston, M.E., Frank, E.H., and Grodzinsky, A.J. (1998) Variationally derived 3-field finite element formulations for quasistatic poroelastic analysis of hydrated biological tissues. *Comput. Methods Appl. Mech. Eng.* **156**, 231–246
- [13] Lundberg, P. and Kuchel, P.W. (1997) Diffusion of solutes in agarose and alginate gels: ¹H and ²³Na PFGSE and ²³Na TQF NMR studies. *Magn. Res. Med.* **37**(1), 44–52
- [14] Martin, I., Obradovic, B., Freed, L.E., and Vunjak-Novakovic, G. (1999) Method for quantitative analysis of glycosaminoglycan distribution in cultured natural and engineered cartilage. *Ann. Biomed. Eng.* **27**, 656–662
- [15] Masud, A. and Hughes, T.J.R. (2002) A stabilized finite element method for darcy flow. *Comput. Methods Appl. Mech. Eng.* **191**, 4341–4370
- [16] Obradovic, B., Meldon, J.H., Freed, L.E., and Vunjak-Novakovic, G. (2000) Glycosaminoglycan deposition in engineered cartilage: Experiments and mathematical model. *AIChE J.* **46**(9), 1860–1871
- [17] O'Hara, B.P., Urban, J.P.G., and Maroudas, A. (1990) Influence of cyclic loading on the nutrition of articular cartilage. *Ann. Rheum. Dis.* **49**, 536–539
- [18] Pluen, A., Netti, P.A., Jain, R.K., and Berk, D.A. (1999) Diffusion of macromolecules in agarose gels: Comparison of linear and globular configurations. *Biophys. J.* **77**, 542–552
- [19] Quinn, T.M., Studer, C., Grodzinsky, A.J., and Meister, J.J. (2002) Preservation and analysis of nonequilibrium solute concentration distributions within mechanically compressed cartilage explants. *J. Biochem. Biophys. Meth.* **52**, 83–95
- [20] Segal, G. (2000) *SEPRAN User's Manual*. Ingenieursbureau SEPRA, Leidschendam, The Netherlands

TRANSPORT ACROSS SINGLE AND SERIES ARRAYS OF MEMBRANES

Peter Raats

Wageningen University and Research Centre

pac.raats@home.nl

Abstract The fluxes of water and solutes across membranes are expressed as functions of differences of the hydraulic and osmotic pressures at both sides. Such difference equations are deduced from more fundamental differential equations. The distributions of concentration and pressure in a series array of membranes are derived. The order in which the individual membranes are placed exerts a strong influence upon the effects of the applied differences of hydraulic and osmotic pressures. The effect of the interchange of two membranes in a series array of an arbitrary number of membranes can be summarized in four simple rules. The special case of reversal of the flow is also discussed.

Keywords: membranes, series arrays, differential description, incremental description, polarity

Introduction

The purpose of this paper is to describe steady flow of water and transport of solutes across single and series arrays of arbitrary numbers of membranes. Differential forms of the flow and transport equations are used as the point of departure and from these the incremental forms are derived. This theory allows one to state concisely some general properties of series arrays of membranes, with regard to nonlinearity, polarity, and changes of the ordering of individual membranes. This study is motivated by the problems of flow of water and transport of solutes in clay soils [1] and of simultaneous uptake of water and solutes by plant roots [2]. Some of the conclusions are generalizations of results obtained earlier for special cases: see [3] for a detailed evaluation of the literature.

Jacques M. Huyghe et al. (eds), IUTAM Proceedings on Physicochemical and Electromechanical Interactions in Porous Media, 213–218.

© 2005 Springer. Printed in the Netherlands.

Transport Across a Single Membrane

Preliminaries

Consider N membranes i arranged in series from left to right. For any variable ϕ , let ϕ_{i-1} and ϕ_i , respectively, denote its values at the left and right hand sides of membrane i . In particular, let x be the spatial coordinate taken perpendicular to the series array, and x_{i-1} and x_i , respectively, the locations of the left and right hand sides of membrane i . Other variables of interest are the hydraulic pressure p , the ion concentration c , and the osmotic pressure $\pi = RTc$, where R is the gas constant and T is the absolute temperature. Parameters describing properties of membrane i are given a subscript (i): $l_{(i)}$, $\sigma_{(i)}$, $\omega_{(i)}$, and $k_{(i)}$ denote, respectively, the hydraulic conductivity, the reflection coefficient, the osmotic permeability, and the active transport of membrane i . Let $\Delta\phi_{(i)}$ denote the change of the variable ϕ across membrane i . The thickness $\Delta x_{(i)}$ of membrane i is given by $\Delta x_{(i)} = x_i - x_{i-1}$.

The volume flux and the distribution of the pressure in a single membrane

The differential expression for the volume flux J_v in membrane i is:

$$J_v = -l_{(i)} \frac{dp}{dx} + \sigma_{(i)} l_{(i)} \frac{d\pi}{dx} . \quad (1)$$

Integration of (1) gives the distribution of the pressure in membrane i :

$$p = p_{i-1} - (J_v/l_{(i)})(x - x_{i-1}) + \sigma_{(i)}(\pi - \pi_{i-1}) . \quad (2)$$

From (2) it follows that the incremental expression for the volume flux across membrane i is given by

$$J_v = -L_{(i)} \Delta p_{(i)} + \sigma_{(i)} L_{(i)} \Delta \pi_{(i)} . \quad (3)$$

where $L_{(i)} = l_{(i)}/\Delta x_{(i)}$ is the hydraulic conductance of membrane i .

The solute flux and the distribution of the concentration in a single membrane

The differential expression for the solute flux in membrane i is:

$$J_s = (1 - \sigma_{(i)}) J_v c - \omega_{(i)} RT \frac{dc}{dx} + k_{(i)} . \quad (4)$$

If J_v and J_s are regarded as given, then this equation is a linear ordinary differential equation for c . It can be written in the form

$$P e_{(i)}^{-1} \frac{dc}{dx/\Delta x_{(i)}} - c = -c_{(i)} , \quad (5)$$

where the Peclet number $Pe_{(i)}$ and the characteristic concentration $c_{(i)}$ of membrane i are given by:

$$Pe_{(i)} = \frac{(1 - \sigma_{(i)})J_v}{\Omega_{(i)}RT}, \quad c_{(i)} = \frac{J_s - k_{(i)}}{(1 - \sigma_{(i)})J_v}, \quad (6)$$

where $\Omega_{(i)} = \omega_{(i)}/\Delta x_{(i)}$ is the osmotic permeance of membrane i . Integration of (5) gives the distribution of the concentration in membrane i :

$$c = c_{(i)} + (c_{i-1} - c_{(i)})\exp(Pe_{(i)}(x - x_{i-1})/\Delta x_{(i)}) . \quad (7)$$

Evaluation of (7) at the downstream side of the membrane gives:

$$c_i = c_{(i)} + (c_{i-1} - c_{(i)})a_{(i)} , \quad (8)$$

where $a_{(i)} = \exp Pe_{(i)}$ is the adjustment factor of membrane i . The concentration difference $\Delta c_{(i)}$ across membrane i is given by:

$$\Delta c_{(i)} = (c_{i-1} - c_{(i)})(a_{(i)} - 1) . \quad (9)$$

To write an incremental expression for J_s , a choice has to be made for the effective concentration in the convective component of this flux. This choice in turn implies a certain choice for the effective osmotic permeance. Three choices for the partitioning of the non-active component of the flux $J_s - k_{(i)}$ in a convective and a diffusive component are:

1. The convective drive $(1 - \sigma_{(i)})J_v$ acts upon the characteristic concentration $c_{(i)}$, rendering the non-active solute transport seemingly purely convective:

$$J_s = (1 - \sigma_{(i)})J_v c_{(i)} + k_{(i)} . \quad (10)$$

2. The convective drive $(1 - \sigma_{(i)})J_v$ acts upon the upstream concentration c_{i-1} :

$$J_s = (1 - \sigma_{(i)})J_v c_{i-1} - F_{(i)}\Omega_{(i)}RT\Delta c_{(i)} + k_{(i)} , \quad (11)$$

where

$$F_{(i)} = \frac{Pe_{(i)}}{a_{(i)} - 1} = \frac{Pe_{(i)}}{\exp Pe_{(i)} - 1} = \sum_{n=0}^{\infty} \frac{B_n Pe_{(i)}^n}{n!} , \quad (12)$$

where the series expansion applies if $|Pe_{(i)}| < 2\pi$. The first twelve Bernoullian numbers B_n have the values 1, -1/2, 1/6, 0, -1/30, 0, -1/42, 0, -1/30, 0, 5/66, 0.

3. The convective drive $(1 - \sigma_{(i)})J_v$ acts upon the average concentration $\bar{c}_{(i)}$:

$$J_s = (1 - \sigma_{(i)})J_v \bar{c}_{(i)} - \Omega_{(i)}RT\Delta c_{(i)} + k_{(i)} , \quad (13)$$

where

$$\bar{c}_{(i)} = (\Delta x_{(i)})^{-1} \int_{x_{i-1}}^{x_i} c dx . \quad (14)$$

Introducing (7) in (14) and using (12) gives:

$$\bar{c}_{(i)} = c_{(i-1)} + \frac{F_{(i)} - 1}{Pe_{(i)}} \Delta c_{(i)} = 1/2(c_{i-1} - c_i) + \sum_{n=2}^{\infty} \frac{B_n Pe_{(i)}^{n-1}}{n!} . \quad (15)$$

This third choice is the most natural one.

Reversing the flow direction, i.e. changing the directions of J_v , J_s , and k_i , will produce hydraulic pressure and concentration profiles that are the mirror images of the former ones. Later it will be shown that for membranes arranged in series such apolarity generally does not hold, except in some special cases.

For a steady flow through a single membrane, the solute flux J_s is by continuity also given by:

$$J_s = c_i J_v . \quad (16)$$

Substituting the second choice (11) for J_s in (16) gives:

$$c_i = (1 - S_{(i)})c_{i-1} \quad \text{or} \quad \Delta c_{(i)} = S_{(i)}c_{i-1} , \quad (17)$$

with the selectivity $S_{(i)}$ of membrane i given by [2]

$$S_{(i)} = \frac{\sigma_{(i)} - k_{(i)}/(c_{i-1}J_v)}{1 + F_{(i)}\Omega_{(i)}RT/J_v} . \quad (18)$$

Introducing $(17)_2$ in (3) and $(17)_1$ in (16) gives:

$$J_v = L_{(i)}(\Delta p_{(i)} - \sigma_{(i)}S_{(i)}RTc_{i-1}) , \quad (19)$$

$$J_s = (1 - S_{(i)})c_{i-1}J_v . \quad (20)$$

Transport Across Series Arrays of Membranes

The pressure increment for a series array

Solving (3) for $\Delta p_{(i)}$ and summing over i gives:

$$\Delta p = L^{-1}J_v + \sum_{i=1}^N \sigma_{(i)}\Delta\pi_{(i)} , \quad (21)$$

where $\Delta p = \sum_{i=1}^N \Delta p_{(i)} = p_0 - p_N$ is the total pressure increment and $L^{-1} = \sum_{i=1}^N (\Delta x_{(i)}/l_{(i)}) = \sum_{i=1}^N \Delta L_{(i)}^{-1}$ is the total hydraulic resistance of the series array. The second term on the right hand side of (21) represents the contributions to Δp from the differences of osmotic pressure across the individual membranes weighted according to the reflection coefficients $\sigma_{(i)}$. Increases in concentration in membranes with low $\sigma_{(i)}$ and in unstirred layers or in compartments between membranes will generally give a contribution to

Δp in successive membranes with larger reflection coefficients. If and only if all $\sigma_{(i)}$'s are equal to each other, and, say, have the value σ , will equation (21) reduce to

$$\Delta p = L^{-1} J_v + \sigma \Delta \pi, \quad (22)$$

where $\Delta \pi = \sum_{i=1}^N \Delta \pi_{(i)} = \pi_0 - \pi_N$. In all other cases Δp depends linearly on the individual $\Delta \pi_{(i)}$'s. According to equation (22), if all the $\sigma_{(i)}$'s are equal to each other, then the volume flow properties of the array are the same as those for single membranes, regardless of the values of the $\omega_{(i)}$'s and the individual $L_{(i)}$'s.

The concentration increment for a series array

Successive application of the downstream expression for c_i , equation (8), gives for, respectively, the first, the second, and the n -th membrane:

$$c_1 = a_{(1)} c_0 - (a_{(1)} - 1) c_{(1)}, \quad (23)$$

$$c_2 = a_{(2)} a_{(1)} c_0 - a_{(2)} (a_{(1)} - 1) c_{(1)} - (a_{(2)} - 1) c_{(2)}, \quad (24)$$

$$c_n = \prod_{j=1}^n a_{(j)} c_0 - \sum_{i=1}^n \prod_{j=i+1}^n a_{(j)} (a_{(i)} - 1) c_{(i)}. \quad (25)$$

The last expression gives the concentration profile in the entire array of membranes. In particular, at the end of the array:

$$c_N = \prod_{j=1}^N a_{(j)} c_0 - \sum_{i=1}^N \prod_{j=i+1}^N a_{(j)} (a_{(i)} - 1) c_{(i)}. \quad (26)$$

According to equation (26), the concentration c_N is a linear combination of c_0 and all the $(a_{(i)} - 1) c_{(i)}$'s, with the coefficient of c_0 being the product of the adjustment factors of all the membranes in the array and the coefficient of $(a_{(i)} - 1) c_{(i)}$ being the product of the adjustment factors of the membranes to the right (downstream) of membrane i .

The effects upon the distribution of the concentration from reversing the flow and from interchanging any two members can be read at once from equations (23) through (26).

Reversing the flow does not affect the coefficient of c_0 , so that any change of c_0 will continue to have the same effect upon c_N . However, the coefficients of the $(a_{(i)} - 1) c_{(i)}$ -terms will in general all be affected by a reversal of the flow. The class of symmetric arrays of membranes, for which the properties of the i -th and the $(N + 1 - i)$ -th membranes are the same, are an important exception. Of course, the single membrane also belongs to this class. When

the flow is reversed the coefficient of $(a_{(i)} - 1)c_{(i)}$ changes from $\prod_{j=i+1}^N a_j$ to $\prod_{j=1}^{i-1} a_j$ and the net effect upon c_N is

$$\Delta c_N = \sum_{i=1}^N \left(\prod_{j=i+1}^N a_{(j)} - \prod_{j=1}^{i-1} a_{(j)} \right) (a_{(i)} - 1) c_{(i)} , \quad (27)$$

In particular for two membranes placed in series equation (27) reduces to:

$$\Delta c_N = (a_1 a_2 - a_2 - 1) c_{(1)} - (a_1 a_2 - a_1 - 1) c_{(2)} . \quad (28)$$

Interchanging two membranes also does not affect the coefficient of c_0 , so that any change of c_0 will continue to have the same effect upon c_N . However it does affect the coefficients of the $(a_{(i)} - 1)c_{(i)}$ -terms of the two membranes that are interchanged and of all the membranes situated between these two membranes. More precisely, the results of interchanging the membranes i and j when $i < j$ are: the coefficients of the $(a_{(n)} - 1)c_{(n)}$ with $n < i$ and $n > j$ are not affected; the new coefficient of $(a_{(i)} - 1)c_{(i)}$ is the old coefficient of $(a_{(j)} - 1)c_{(j)}$; the new coefficient of $(a_{(j)} - 1)c_{(j)}$ is the old coefficient of $(a_{(i)} - 1)c_{(i)}$, with the factor a_j replaced by a_i ; the coefficients of $(a_{(n)} - 1)c_{(n)}$ with $i < n < j$ will be a_i/a_j times the old ones. For two membranes placed in series, reversing the flow and interchanging the two membranes are equivalent. The two membrane case is covered entirely by the second and third rules above. If $a_i = a_j$, then only the second rule will cause a change. Existing theories do not cover all complexity.

References

- [1] Bolt, G.H., and Groenevelt, P.H. (1969) Coupling phenomena as a possible cause of "Non-Darcian" behavior of water in soil, *Bull. Int. Assoc. Sci. Hydrology* **14**, 17–26
- [2] Dalton, F.N., Raats, P.A.C., and Gardner, W.R. (1975) Simultaneous uptake of water and solutes by plant roots, *Agronomy J.* **67**, 334–339
- [3] Raats, P.A.C. (2003) Transport across plane, cylindrical and spherical single and series arrays of membranes, (in preparation)

VIII

MICROSTRUCTURE.

Chairman: P. Giovine

A SECOND GRADIENT MODEL FOR DEFORMABLE POROUS MATRICES FILLED WITH AN INVISCID FLUID

Francesco dell'Isola¹ and Giulio Sciarra²

¹*Dip. Ingegneria Strutturale e Geotecnica,*

²*Dip. Ingegneria Chimica, dei Materiali, delle Materie Prime e Metallurgia,*

Università degli Studi di Roma "La Sapienza", Via Eudossiana 18, 00184 Roma, Italy

Romesh C. Batra

Dept. Engineering Sciences and Mechanics, Virginia Polytechnic Institute and State University, Blacksburg, VA 24060, USA

Abstract In this paper we deal with an enlarged theory of binary mixtures: a second gradient solid constituent and a perfect fluid are considered. On the basis of this assumptions we obtain, for a linear elastic hollow cylinder, a set of density profiles of the solid matrix, parameterized by a suitable energetic coupling coefficient and characterized by the presence of boundary layers arising at the external surfaces of the body. A structural stability analysis of the partial differential equations, governing the motion of the mixture, is also developed, in a case which may be of interest in applications to underground structural engineering.

Introduction

A simplified model for mechanical systems constituted by a solid deformable porous matrix filled by a compressible fluid has been developed by [6], [2] and [10]. The main idea in their works stays in the "homogenization" assumption which leads us to accept the possibility of simultaneous placement of a solid and a fluid material particle at the same current place. In the literature when this assumption is accepted one talks about homogeneous mixtures. Observations of the behavior of fluid saturated solids have shown a not negligible increase of fluid percolation, through the pores of the solid matrix, with respect to the prediction provided by classical models of homogeneous mixtures (see e.g. [9]). In other words experimental evidence (see e.g. [3]) makes clear that the model of homogeneous mixture is not predictive in describing several phenomena occurring in fluid-saturated solids. A possible explanation for the

Jacques M. Huyghe et al. (eds), IUTAM Proceedings on Physicochemical and Electromechanical Interactions in Porous Media, 221–229.

© 2005 Springer. Printed in the Netherlands.

previously described phenomena stays in the circumstances that the increase of percolation is not simply due to the increase of externally applied pressure but also to the pore-opening occurring in the vicinity of the boundary (see [3]). In this paper we do not directly deal with a micro-structured model, but consider a binary mixture model involving a second gradient solid and a perfect fluid; for the relationship between micro-structured and second gradient theories we refer to [7] and [8]. This kind of approach is very close to that based on the volume fraction concept, as this last reduces to the first one once a suitable constraint, among the enlarged set of state parameters, is assumed. On the basis of this approach and considering a linear elastic model, we study the equilibrium static configurations assumed by a porous hollow cylinder filled with a liquid. In particular assuming the energy functional to be split into a first gradient and a second gradient energy contribution, we address the parametric analysis of the equilibrium density profiles of the solid matrix with respect to a suitable energetic coupling coefficient between the solid and the fluid. Since we have chosen to deal with static deformations of the hollow cylinder we require the external tractions applied on both constituents to be conservative. Last but not least we discuss the structural stability properties of the governing equations, with respect to perturbations of the aforementioned coupling coefficient.

Formulation of the Problem

Material particles of the fluid and the solid are identified respectively by their position vectors X_f and X_s in fixed reference configurations Ω_0^f and Ω_0^s . As is usually done in the theory of mixtures we presume that, at any time t , particles of both constituents may occupy the same position \mathbf{x} in the present configuration Ω . The velocity \mathbf{v}_α ($\alpha = f, s$) of the material particle X_α is defined by

$$\mathbf{v}_\alpha = \frac{d_\alpha \mathbf{u}_\alpha(X_\alpha, t)}{dt} \quad (1)$$

i.e. the material time derivative of the displacement of the α -th constituent \mathbf{u}_α from its reference configuration.

Let ρ_f and ρ_s denote the apparent mass densities of the fluid and the solid then the mean velocity \mathbf{v} of the mixture is defined by

$$\rho \mathbf{v} = \rho_f \mathbf{v}_f + \rho_s \mathbf{v}_s. \quad (2)$$

Details of the theory of mixtures are given in [10], [9].

Balance laws

We use the principle of virtual power to derive the balance of linear momentum and the boundary conditions for each constituent. That is,

$$\begin{aligned} & \int_{\Omega} (\mathbf{m}_s \cdot \mathbf{v}_s + \mathbf{m}_f \cdot \mathbf{v}_f + \mathbf{T}_s \cdot \nabla \mathbf{v}_s - p_f \operatorname{div} \mathbf{v}_f + \mathbf{\Pi}_s \cdot \nabla \nabla \mathbf{v}_s) dV = \\ & = \int_{\Omega} (\mathbf{b}_s \cdot \mathbf{v}_s + \mathbf{b}_f \cdot \mathbf{v}_f) dV + \int_{\partial\Omega} \left(\mathbf{t}_s \cdot \mathbf{v}_s + \mathbf{t}_f \cdot \mathbf{v}_f + \boldsymbol{\tau}_s \cdot \frac{\partial \mathbf{v}_s}{\partial n} \right) dA. \end{aligned} \tag{3}$$

Here \mathbf{m}_α is the bulk solid-fluid interaction force, \mathbf{T}_s the partial Cauchy stress in the solid, p_f the hydrostatic pressure in the perfect fluid, $\mathbf{\Pi}_s$ the second-order stress in the solid, \mathbf{b}_α the density of partial body forces, \mathbf{t}_α the partial surface tractions, $\boldsymbol{\tau}_s$ the traction corresponding to the second-order stress tensor in the solid and $\partial \mathbf{v}_s / \partial n$ the directional derivative of \mathbf{v}_s along the outward unit normal \mathbf{n} to the boundary $\partial\Omega$ of Ω .

The physical meaning of $\mathbf{\Pi}_s$ and $\boldsymbol{\tau}_s$ can be grasped in a way similar to that done in different contexts in [7] and [4]. We remark that the external action $\boldsymbol{\tau}_s$ can be regarded as the sum of two different contributions, the first one is a doubly normal double force, i.e. an external areal action which works on the rate of opening, $\nabla \mathbf{v}_s \cdot \mathbf{n} \otimes \mathbf{n}$, of boundary pores along the outward unit normal \mathbf{n} , the other one a tangential couple working on the vorticity of the apparent velocity of the solid. This last areal action is considered in the Cosserat model for granular materials (see e.g. [5]) and in the present approach vanishes. The objectivity of the left hand side of (3) implies that the sum of the two internal supplies \mathbf{m}_f and \mathbf{m}_s of linear momentum equals zero and \mathbf{T}_s is symmetric.

By using the divergence theorem and exploiting the fact that eqn.(3) must hold for all virtual velocities we obtain:

$$\operatorname{div}(\mathbf{T}_s - \operatorname{div} \mathbf{\Pi}_s) - \mathbf{m}_s + \mathbf{b}_s = \mathbf{0}, \text{ in } \Omega, \tag{4}$$

$$-\nabla p_f - \mathbf{m}_f + \mathbf{b}_f = \mathbf{0}, \text{ in } \Omega, \tag{5}$$

$$\mathbf{m}_s + \mathbf{m}_f = \mathbf{0}, \text{ in } \Omega, \tag{6}$$

$$(\mathbf{T}_s - \operatorname{div} \mathbf{\Pi}_s) \mathbf{n} - \operatorname{div}_s(\mathbf{\Pi}_s \mathbf{n}) = \mathbf{t}_s, \text{ on } \partial\Omega, \tag{7}$$

$$(\mathbf{\Pi}_s \mathbf{n}) \mathbf{n} = \boldsymbol{\tau}_s, \text{ on } \partial\Omega, \tag{8}$$

$$-p_f \mathbf{n} = \mathbf{t}_f, \text{ on } \partial\Omega, \tag{9}$$

where div_s is the surface divergence on $\partial\Omega$.

Constitutive relations

The balance laws (4)-(5) are to be supplemented by constitutive relations; we express these in terms of the internal energy. We presume that the mixture is

at a uniform temperature, the constituents are deforming quasi-statically so that their kinetic energy can be neglected, and no energy is dissipated. The internal energy density is split into two parts; a part that depends upon the “local” deformation of the solid and fluid particles and another part that depends upon a “nonlocal” measure of deformation of the solid particles: the latter is taken to be proportional to $|\nabla\rho_s|^2$. Thus we write the balance of internal energy as

$$\begin{aligned} \frac{d_v}{dt} \int_{\Omega} \rho \left[\epsilon(\rho_f, \mathbf{F}_s, X_s) + \frac{\lambda_s}{2\rho} |\nabla\rho_s|^2 \right] dV = \\ \int_{\Omega} (\mathbf{b}_s \cdot \mathbf{v}_s + \mathbf{b}_f \cdot \mathbf{v}_f) dV + \int_{\partial\Omega} \left(\mathbf{t}_s \cdot \mathbf{v}_s + \mathbf{t}_f \cdot \mathbf{v}_f + \boldsymbol{\tau}_s \cdot \frac{\partial \mathbf{v}_s}{\partial n} \right) dA \end{aligned} \quad (10)$$

where \mathbf{F}_s is the deformation gradient for the solid, $\lambda_s > 0$ is a material parameter with units of Newton (meter)⁶/ Kg², and d_v/dt signifies the material time derivative following the mean motion of the mixture. According to the Reynolds transport theorem the following constitutive equations must hold

$$\mathbf{T}_s = \rho \frac{\partial \epsilon}{\partial \mathbf{F}_s} \mathbf{F}_s^{\top} - \lambda_s \left[\frac{f_{ss}}{2} (1 + \xi_f) \mathbf{I} + \nabla\rho_s \otimes \nabla\rho_s \right], \quad (11)$$

$$p_f = \rho\rho_f \frac{\partial \epsilon}{\partial \rho_f} - \frac{\lambda_s}{2} f_{ss} \xi_f, \quad (12)$$

$$\boldsymbol{\Pi}_s = -\lambda_s \rho_s \mathbf{I} \otimes \nabla\rho_s, \quad (13)$$

$$\begin{aligned} \mathbf{m}_s = -\rho \left[\xi_f (\nabla \mathbf{F}_s)^{\top} \frac{\partial \epsilon}{\partial \mathbf{F}_s} + \xi_f \mathbf{F}_s^{-\top} \frac{\partial \epsilon}{\partial X_s} - \xi_s \frac{\partial \epsilon}{\partial \rho_f} \nabla\rho_f \right. \\ \left. + \frac{\lambda_s}{2\rho} \nabla(\xi_f f_{ss}) \right], \end{aligned} \quad (14)$$

where $f_{ss} = \nabla\rho_s \cdot \nabla\rho_s$, and ξ_f is the mass fraction of the fluid phase.

In this paper we limit our attention to external actions for which $\mathbf{b}_s = \mathbf{0}$ and $\mathbf{b}_f = \mathbf{0}$, i.e. only to external surface tractions. In order to find the partial tractions we assume the existence of a potential function such that the working, \dot{W}^{ext} , of external surface tractions is given by

$$\dot{W}^{\text{ext}} = \frac{d}{dt} \int_{\Omega} \psi^{\text{ext}}(\mathbf{x}, \rho_s, \rho_f, \nabla\rho_s) dV, \quad (15)$$

where \dot{W}^{ext} equals the surface integral on the right-hand side of eqn.(10). The external surface tractions for which eqn.(15) holds are conservative. Requiring

that eqn.(15) hold for all choices of the velocity field, we obtain

$$\frac{\partial \psi^{\text{ext}}}{\partial \rho_s} - \text{div} \left(\frac{\partial \psi^{\text{ext}}}{\partial \nabla \rho_s} \right) = C_s, \quad \frac{\partial \psi^{\text{ext}}}{\partial \rho_f} = C_f, \quad \text{in } \Omega, \quad (16)$$

$$\begin{aligned} \mathbf{t}_s = & \left[-\frac{\partial \psi^{\text{ext}}}{\partial \rho_s} \rho_s + \xi_s \psi^{\text{ext}} - \frac{\partial \psi^{\text{ext}}}{\partial \nabla \rho_s} \cdot \nabla \rho_s + \text{div} \left(\rho_s \frac{\partial \psi^{\text{ext}}}{\partial \nabla \rho_s} \right) \right. \\ & \left. + \rho_s \left(\frac{\partial \psi^{\text{ext}}}{\partial \nabla \rho_s} \cdot \mathbf{n} \right) \text{tr} (\nabla^s \mathbf{n}) - \left(\frac{\partial \psi^{\text{ext}}}{\partial \nabla \rho_s} \cdot \mathbf{n} \right) \frac{\partial \rho_s}{\partial \mathbf{n}} \right] \mathbf{n} \\ & + \rho_s \nabla^s \left(\frac{\partial \psi^{\text{ext}}}{\partial \nabla \rho_s} \cdot \mathbf{n} \right), \quad \text{on } \partial \Omega, \end{aligned} \quad (17)$$

$$\mathbf{t}_f = \left(-\frac{\partial \psi^{\text{ext}}}{\partial \rho_f} \rho_f + \xi_f \psi^{\text{ext}} \right) \mathbf{n}, \quad \text{on } \partial \Omega, \quad (18)$$

$$\boldsymbol{\tau}_s = - \left(\rho_s \frac{\partial \psi^{\text{ext}}}{\partial \nabla \rho_s} \cdot \mathbf{n} \right) \mathbf{n}, \quad \text{on } \partial \Omega. \quad (19)$$

Equations (16) with C_s and C_f as constants are necessary conditions for the existence of a ψ^{ext} for which $\mathbf{b}_s = \mathbf{0}$ and $\mathbf{b}_f = \mathbf{0}$.

Solution of a Boundary-Value Problem

We analyze, within a linearized second gradient theory, the static infinitesimal deformations of an annular porous cylinder filled with an inviscid fluid and with the inner and the outer surfaces subjected to uniform external pressures p_1^{ext} and p_2^{ext} respectively. We assume that surface tractions on the inner and the outer surfaces of the cylinder, in the reference configuration, equal $-p_0$ and postulate that

$$\begin{aligned} \epsilon = \frac{1}{\rho_0} & \left[-p_0 \mathbf{I} \cdot \mathbf{H}_s + \gamma_f^0 \Delta \rho_f + \frac{1}{2} \mathcal{C}[\mathbf{H}_s] \cdot \mathbf{H}_s - \frac{1}{4} p_0 \mathbf{H}_s \cdot (\mathbf{H}_s - \mathbf{H}_s^\top) \right. \\ & \left. + \frac{1}{2} \gamma_{ff} (\Delta \rho_f)^2 + \Delta \rho_f K_{sf} \mathbf{I} \cdot \mathbf{H}_s \right], \end{aligned} \quad (20)$$

where $\mathbf{H}_s := \nabla \mathbf{u}_s$ and $\Delta \rho_\alpha = \rho_\alpha - \rho_\alpha^0$, $\alpha = s, f$; ρ_α^0 is the mass density of the α -th constituent in the reference configuration, \mathcal{C} is the elasticity tensor, for the solid constituent, γ_f^0 , γ_{ff} and K_{sf} are material parameters. The spherical tensor $K_{sf} \mathbf{I}$ accounts for the interaction between the solid and the fluid phases because of the deformations of the pores. The following form for the elasticity tensor is prescribed: $\mathcal{C}[\mathbf{E}_s] = \lambda \text{tr}(\mathbf{E}_s) \mathbf{I} + 2\mu \mathbf{E}_s$, where λ and μ are the Lamé.

We assume that deformations of the mixture are axi-symmetric, i.e., in cylindrical coordinates the two in-plane components of the displacement, u_r and u_θ , are functions of the radial coordinate r only. In order to find boundary

conditions on the solid and the fluid phases, we consider only those external tractions for which the following expression for ψ^{ext} holds:

$$\psi^{\text{ext}} = C_s \rho_s + C_f \rho_f + \mathbf{C}_{\text{int}}(r, \theta) \cdot \nabla \rho_s \Delta \rho_s + \hat{\psi}(r), \quad (21)$$

$\hat{\psi}(r) = p_0 + p_1 r$ so that different tractions applied on the inner and the outer surface can be considered. Because of our interest in studying infinitesimal deformations, we retain terms bilinear in $\Delta \rho_s$ and $\nabla \rho_s$.

Influence of coupling coefficient K^{sf} on density profiles

Through these assumptions the governing equations can be reduced to the following two uncoupled ordinary differential equations ($' = \partial/\partial r$):

$$-\lambda_s \rho_s^0 \left[U_r'' + \frac{1}{r} U_r' \right] + q(K_{sf}) \quad U_r = \Gamma_s, \quad U_\theta' + \frac{2}{r} U_\theta = 0 \quad (22)$$

$$q(K_{sf}) = 2\mu + \lambda - 2\xi_f^0 p_0 - \frac{(\xi_s^0 \gamma_f^0 + p_0/\rho_0 - K_{sf})^2}{2\gamma_f^0/\rho_0 + \gamma_{ff}}, \quad (23)$$

where Γ_s is an integration constant to be determined by boundary conditions, $U_r = (u_r' + 1/r u_r) = \text{tr } \mathbf{H}_s$ and $U_\theta = (u_\theta' - 1/r u_\theta)$ are dimensionless quantities; in particular U_r is related to the increment of the solid apparent density by $\Delta \rho_s = -\rho_s^0 U_r$. We specify boundary conditions coming from eqns.(7)-(9) and eqns.(17)-(19). Equation (22)₁, for $\Gamma_s = 0$, (homogeneous equation) belongs to the family of Classical or Modified Bessel equations, according to the sign of the coefficient q . Therefore two different solutions for the increment of the solid apparent density are obtained in dependence of K_{sf} : if $q > 0$ then the solution of eqn.(22)₁ is given by a linear combination of Modified Bessel functions $I_0(\xi)$ and $K_0(\xi)$, conversely if $q < 0$ it is given by a linear combination of Classical Bessel functions $J_0(\xi)$ and $Y_0(\xi)$. In particular we notice that when $K_{sf} \in (K_{sf}^{(1)}, K_{sf}^{(2)})$ the solution of the homogeneous equation is given by a linear combination of the Modified Bessel functions, as $\text{sign}(q) = 1$; conversely when $K_{sf} \in (-\infty, K_{sf}^{(1)}) \cup (K_{sf}^{(2)}, \infty)$ the solution of the homogeneous equation is a linear combination of the Classical Bessel functions, as $\text{sign}(q) = -1$; $K_{sf}^{(1)}$ and $K_{sf}^{(2)}$ being the values of the coupling coefficient for which q vanishes. The solution of eqn.(22)₁ is obtained by simply adding a suitable constant to solution of the homogeneous equation. In the following figures we draw plots of the $\Delta \rho_s$ -profiles, for a damaged salt matrix filled with brine; values of constitutive and geometric parameters and surface tractions are listed in Table 1.

Note that values for the constitutive coefficients λ_s and C_{int} are introduced without any experimental validation of the model. However, this choice of

Table 1. In the first column E and ν are the Young modulus and the Poisson ratio of the solid matrix; in the second one $\hat{\rho}_s^0$ and $\hat{\rho}_f^0$ are the densities of the solid and the fluid constituent in the reference configuration, ν_s^0 and ν_f^0 their volume fractions (in the reference configuration the mixture is saturated).

Constitutive parameters	Referential state parameters	Tensions
$E = 200 \text{ MPa}$	$\hat{\rho}_s^0 = 1850 \text{ Kg/m}^3$	$p_{01}^{\text{ext}} = 20 \text{ MPa}$
$\nu = 0.33$	$\hat{\rho}_f^0 = 1300 \text{ Kg/m}^3$	$p_{02}^{\text{ext}} = 20 \text{ MPa}$
$\lambda_s = 200 \text{ N m}^4/\text{Kg}^2$	$\nu_s^0 = 0.97$	$\tilde{p}_0 = -2.21 \text{ MPa}$
$\gamma_{ff} = 1.64 \cdot 10^6 \text{ N m}^4/\text{Kg}^2$	$\nu_f^0 = 1 - \nu_s^0 = 0.03$	$p_1 = 10^5 \text{ N/m}^3$
$C_s = C_f$	$\rho_s^0 = \hat{\rho}_s^0 \nu_s^0 = 1794.5 \text{ Kg/m}^3$	
$C_{\text{int}} = 1 \text{ N m}^3/\text{Kg}^2$	$\rho_f^0 = \hat{\rho}_f^0 \nu_f^0 = 39 \text{ Kg/m}^3$	
	$R_1 = 2 \text{ m}, \quad R_2 = 20 \text{ m}$	

values is based on the expectation that these values can describe the pore-opening effect close to the boundary of the mixture.

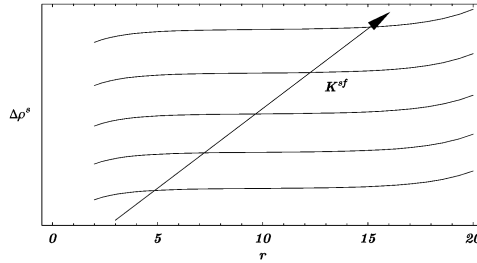


Figure 1. Qualitative $\Delta\rho_s$ -profiles for $K_{sf} \in (K_{sf}^{(1)}, K_{sf}^{(2)})$.

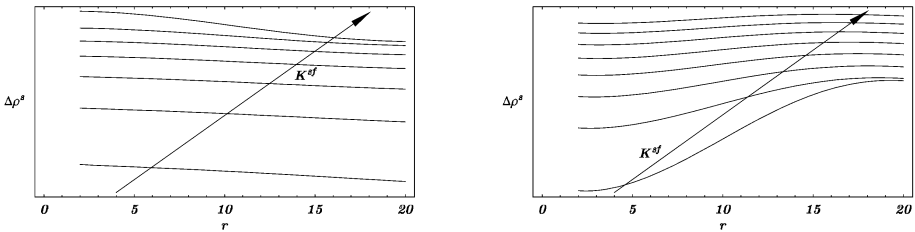


Figure 2. Qualitative $\Delta\rho_s$ -profiles for $K_{sf} \in (-\infty, K_{sf}^{(1)}) \cup (K_{sf}^{(2)}, \infty)$. Figure 2a corresponds to $1.75 < K < 1.81$, and Figure 2b to $1.83 < K < 1.9$.

In Figure 1 the typical behavior of fields exhibiting boundary layers is shown, in Figure 2 the solution apparently shows wide oscillations due to the

change of type occurring in the Bessel equation; this is usually an indication of instability.

On the basis of the previous remarks on admissible values of the coupling coefficient K_{sf} we wish to establish which conditions assure the uniqueness of the solutions of the elastic problem. In doing this our aim is therefore the characterization of those coupling parameters which guarantee the so-called structural stability of the PDEs (defined on the space of the considered state parameters u_s and $\Delta\rho_f$) which describe the governing equations of the mixture. According to the criterion stated by [1], we discuss the possibility that for two different representative elements of this family, corresponding to sufficiently close values of K_{sf} , an homeomorphism on the space of state parameters exists transforming one solution into the other (topological equivalence). In order for the aforementioned PDEs to fulfill this requirement it is assumed that the trajectories of a representative element of the vector field family prescribed by eqns.(22) describes available transformations of a given reference configuration. Indeed we adopt a physically meaningful energetic criterion: the reference configuration is stable if the total energy

$$\mathcal{E}_{tot}(\rho_f, \mathbf{F}_s) = \int_{\Omega} \left[\rho\epsilon(\rho_f, \mathbf{F}_s) + \frac{\lambda_s}{2} |\nabla\rho_s|^2 - \psi^{\text{ext}}(\mathbf{x}, \rho_s, \rho_f, \nabla\rho_s) \right] dV; \quad (24)$$

attains its minimum in the reference configuration. In particular we prove structural stability when the coupling coefficient lies in a suitable subset of the open interval $(K_{sf}^{(1)}, K_{sf}^{(2)})$. The second functional derivative of eqn.(24), evaluated in the reference configuration, is in this case positive definite.

In order to prove this statement we assume the second functional derivative of \mathcal{E}_{tot} evaluated in the reference configuration to equal the integral over Ω of a suitable quadratic form multiplied by a scalar quantity α and determine under which conditions the corresponding spectral problem admits positive eigenvalues. In particular the following quadratic form is assumed for the second functional derivative of \mathcal{E}_{tot}

$$\left. \frac{d^2\mathcal{E}_{tot}}{dt^2} \right|_{(\rho_f^0, \rho_s^0)} = \int_{\Omega} \alpha \left[(\text{div } \mathbf{v}_s)^2 + \text{skw}(\nabla\mathbf{v}_s) \cdot \text{skw}(\nabla\mathbf{v}_s) + (\text{div } \mathbf{v}_f)^2 \right] dV. \quad (25)$$

Numerical simulations show that structural stability is guaranteed in this case for values of the coupling coefficient which belong to a suitable open subset $(K_{sf}^{1s}, K_{sf}^{2s})$ of $(K_{sf}^{(1)}, K_{sf}^{(2)})$. This means that the meaningful solutions of eqns.(22) are those for coupling coefficients belonging to this open interval only.

Concluding Remarks

In this paper a static linear elastic deformation problem for a fluid saturated solid is formulated in which the behavior of the solid matrix is described by a second gradient model. The non-deformed configuration, chosen as a reference configuration, for the considered mixture can not be stress-free: indeed the saturating fluid must exhibit internal stresses acting both on the solid constituent and on its sub-bodies.

When limiting our attention to purely spherical pre-stress we find analytical forms for the solutions of Bessel or Modified Bessel equations in dependence on the coupling coefficient K_{sf} . The obtained density profiles may show an oscillating behavior; we prove the conjecture that oscillating profiles are unstable as well as the non-oscillating ones which correspond to sufficiently high absolute values of K_{sf} .

References

- [1] Arnold, V.I. (1983) *Geometrical methods in the theory of ordinary differential equations*; translated by Joseph Szucs; English translation edited by Mark Levi. Springer, New York
- [2] Biot, M.A. (1941) General theory of three-dimensional consolidation, *J. Applied Physics* **12**, 155-164
- [3] Cosenza, P., Ghoreychi, M., Bazargan-Sabet, B. and de Marsily, G. (1999) In situ rock salt permeability measurement for long term safety assessment of storage, *Int. J. Rock Mech. Min.* **36**, 509-526
- [4] dell'Isola, F. and Seppecher, P. (1997) Edge contact forces and quasi balanced power, *Meccanica* **32**, 33-52
- [5] Elhers, W. (1991) Toward finite theories of liquid-saturated elasto-plastic porous media, *Int. J. of Plasticity* **7**, 433-475
- [6] Fillunger, P. (1936) *Erdbaumechanik?*, Selbstverlag des Verfassers, Wien
- [7] Germain, P. (1973) La méthode des puissances virtuelles en mécanique des milieux continus, *Journal de Mécanique* **12**(2), 235-274
- [8] Germain, P. (1973) The method of virtual power in continuum mechanics. Part 2: microstructure, *SIAM J. Appl. Mech.* **25**(3), 556-575
- [9] Rajagopal, K.R. and Tao, L. (1995) *Mechanics of Mixtures*, World Scientific
- [10] Truesdell, C. (1957) Sulle basi della termomeccanica, *Lincci - Rend. Sc. fis. mat. e nat.* Vol. XXII

RELATIONSHIP BETWEEN PORE STRUCTURE AND FLUID TRANSPORT IN ARGILLACEOUS ROCKS

Alexander Hildenbrand*, Bernhard M. Krooss

Lehrstuhl für Geologie, Geochemie und Lagerstätten des Erdöls und der Kohle, RWTH Aachen, Germany.

**present address: VITO, Belgium,*

alexandra.hildenbrand@vito.be

Janos L. Urai

Endogene Dynamik, RWTH Aachen, Germany.

Introduction

Mudrocks represent the major constituents of sedimentary basins. They form aquitards, chemical barriers and seals for hydrocarbon accumulations. Their low permeabilities and high capillary entry pressures [1, 2] are controlled by rock microstructure and chemical interactions between minerals and the pore fluid. For a pore system containing two immiscible fluids the sealing efficiency is characterised by the capillary displacement pressure [2–7]. This is usually quantified based on Mercury Porosimetry data because other, more direct measurements are difficult and time-consuming. However, for mudstones the conversion of Mercury-air Injection data to other fluids has been questioned in recent papers [8, 9]. The following two sections summarize the findings from two studies which were performed (a) in order to get a better understanding of the processes that occur during invasion of mercury in very fine-grained sediments [10] and (b) to compare the pore volume distribution determined by Mercury Injection and gas breakthrough experiments which were performed under subsurface conditions.

Pore Space Analysis – Results from Mercury and Wood’s Metal Porosimetry

In order to visualize the process of non-wetting fluid injection Wood’s metal Porosimetry was used [11–16]. Wood’s metal Impregnation technique is based on the same principles as Mercury Porosimetry, i.e., an immiscible,

non-wetting fluid is injected at very high pressures into the pore space [14, 17–19]. In our experiments molten Wood’s metal (temperature $> 70\text{ }^{\circ}\text{C}$) is injected at pressure up to 100 MPa which corresponds to an equivalent pore radius of about

8 nm. Images of broken or polished surfaces were subsequently compared with data from Mercury Injection. For this study nineteen less consolidated Tertiary mudstone samples were collected from active quarries in the Lower Rhine Embayment and the Westerwald region. The mineralogy of the samples, determined by whole rock XRD, varies considerably. Beside quartz most of the samples contain major amounts of kaolinite and illite with minor smectite and calcite. Some samples have a well-developed preferred orientation of clay minerals, while others contain clay minerals arranged in card house structures (Fig. 1). Water content porosities are in the range of 25 to 45 %. Samples were dried, by first slow air-drying over a period of two weeks and subsequent oven-drying at $105\text{ }^{\circ}\text{C}$ until weight constancy. Even though the samples had been slowly dried some samples developed microcracks during drying. Data from Mercury Injection were corrected for this by discarding intrusion pressures be-

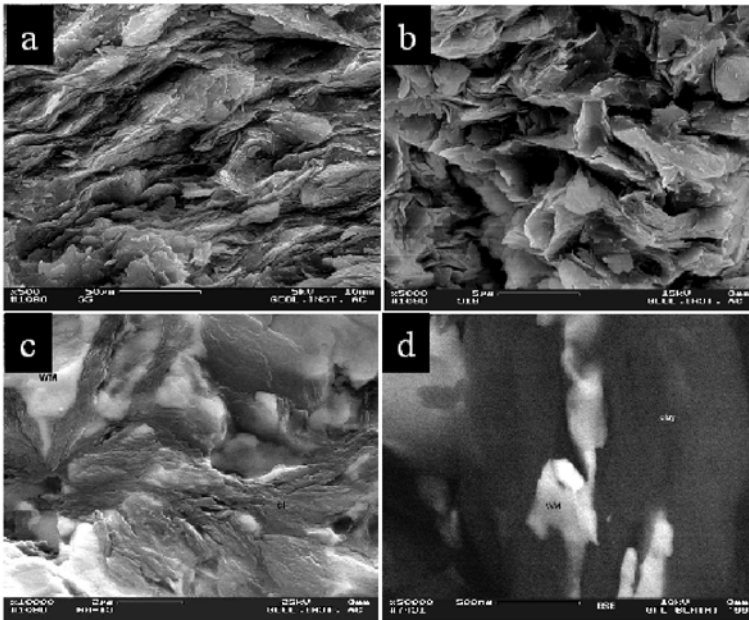


Figure 1. (a, b) Conventional SEM images of broken surfaces illustrating the variation in microstructure of our samples. (c,d) SEM images of WM-impregnated samples, illustrating the fine morphology of pore space in mudstones. Light grey: WM, Dark grey: clay.

low 0.1 MPa. The Mercury Injection pressure which results in a saturation of 10 % is defined as the capillary displacement pressure $P_d(\text{Hg})$. Porosity values range from 19 to 33 %. Bulk densities vary between 1.8 and 2.2 g/cm³, the average grain density is 2.7 g/cm³. Wood's Metal pore casts could be visualized down to 40 nm in diameter (Fig. 1). The largest pores which were observed in this study are larger than 5 μm in diameter and are of irregular, round shape and are interconnected through small pore necks. Fig. 2 is a microstructural model, summarizing the key features observed in this study. Major findings from this study are:

- (i) Because pore size ranges determined from Mercury Injection only refer to pore necks, which indeed is important when trying to find characteristic parameters for fluid flow phenomena, the pore size distribution determined by this method will underestimate the large pore size mode [13].
- (ii) One very fine-grained sample could not be impregnated with the molten alloy. It is suggested that the sample has been compressed during the experiments. In this case also Mercury Injection will yield underestimated capillary displacement pressures and is therefore not applicable to such rocks.
- (iii) Excluding three outliers, two samples with clay contents above 80% and a strongly cemented sample, a regression was found for C [%] the clay content and ϕ [%] the porosity:

$$P_d(\text{Hg}) = -10.24 + 0.47 \cdot C - 0.15 \cdot \phi \quad R^2 = 0.88 \quad (n = 16)$$

Comparison of Pore Size Distributions Determined by Mercury Injection and Gas Breakthrough Experiments

In a study on the gas sealing efficiency of mudrocks, gas (N_2) breakthrough experiments were performed on two initially water-saturated sample plugs from the Norwegian Shelf. These experiments were complemented by Wood's metal Injection and Mercury Porosimetry on the dry samples for qualitative and semi-quantitative pore space analysis. The sample showed a lamination in the sub-mm-range, consisting of alternating siltier and clay-rich layers. Quartz grains were up to 0.2 mm in diameter and were surrounded by a fine-grained clay matrix. Microscopic examination of the samples indicated that the main pathways for Wood's metal Injection were fissures parallel to bedding having a width of 10 to 2 μm. Individual pores within were up to 50 μm in diameter. Some pore casts were found to be less than 100 nm in size and squeezed between clay plates (Fig. 3).

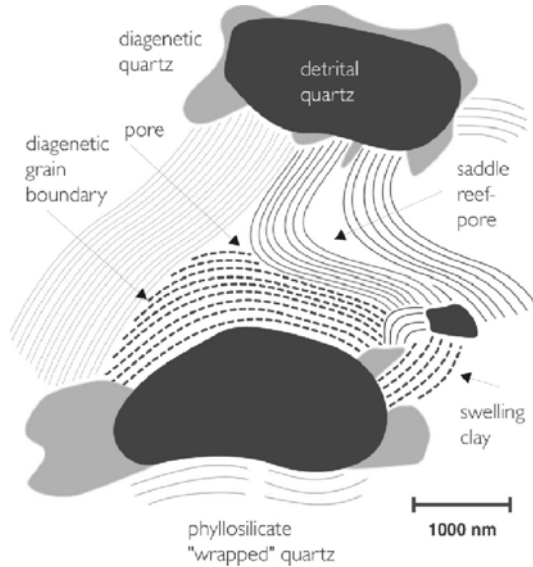


Figure 2. Microstructural model for cemented mudstones.

Mercury Injection data revealed a porosity of 30 % and a bimodal pore size distribution with pore size maxima at 20 and 110 nm. The capillary displacement pressure (P_d) for mercury was 2.7 MPa corresponding to an equivalent $P_d(N_2)$ -value of 0.5 MPa. For the conversion from the mercury-air to the gas-water system the following parameters were used: interfacial tension values of $\rho(\text{Hg-air}) = 480 \text{ mN/m}$, and $\rho(\text{N}_2\text{-water}) = 70 \text{ mN/m}$; contact angles $\theta(\text{Hg-air}) = 141^\circ$, and $\theta(\text{N}_2\text{-water}) = 0^\circ$.

Gas breakthrough experiments were performed by imposing an instantaneous, high gas-pressure gradient across the sample. The resulting gas flux was monitored as a function of time and pressure gradient by means of pressure changes in a closed downstream reservoir of known volume. The experimental procedure and its interpretation are described in detail in reference [7]. Transport parameters derived from these experiments are (a) minimum capillary displacement pressure (P_d) (b) effective permeability to the gas phase (k_{eff}) after gas breakthrough (c) pore size distribution of the conducting pore system (d) transport porosity occupied by gas during maximum gas flow. Prior to the gas breakthrough experiments single-phase flow experiments were conducted to assess the absolute permeability coefficients (k_{abs}) and at the same time establish the full water saturation of the samples. The results of the measurements on two sample plugs perpendicular to the bedding plane are summarized in Tables 1 and 2. Comparison of the resulting pore size distribution and porosity data with those established by Mercury Injection shows:

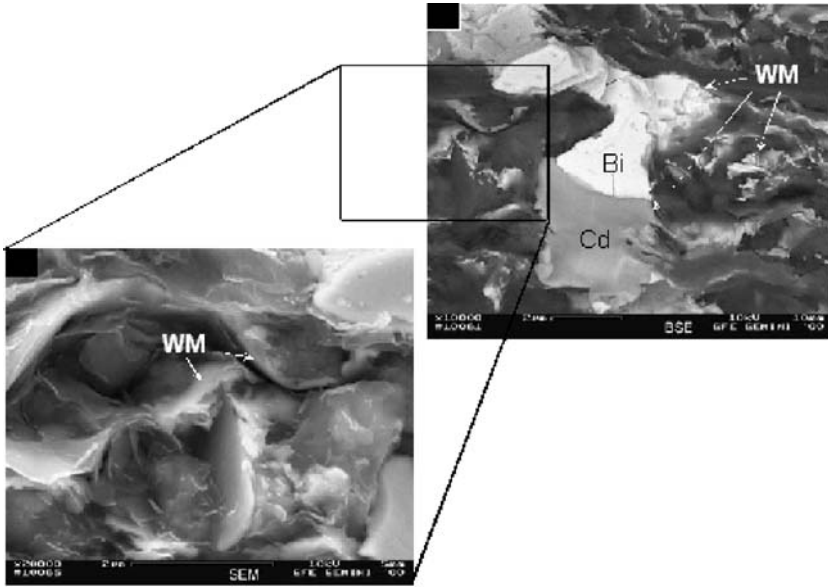


Figure 3. Sample from Norwegian Self which was injected with Wood’s metal at a pressure of 100 MPa; (A) backscatter (BSE) micrograph: differentiation of the alloy into its compounds (here Bismuth and Cadmium), (B) SEM (secondary electron microscopy) micrograph: WM pore casts are smaller than 100 nm in diameter.

Table 1. Petrophysical and fluid flow properties.

Sample plug	Burial depth [m]	clay content (%)	sand content (%)	specif. surf. area (BET) [m ² /g]	k_{abs} [m ²]	$k_{eff(max)}$ [m ²]
1	1515	48.2	10.5	26.2	$2 * 10^{-20}$	$4 * 10^{-22}$
2	1515	48.2	10.5	26.2	$3 * 10^{-20}$	$2 * 10^{-21}$

- (i) The first pore size mode of ~ 20 nm, as revealed by Mercury Injection and by gas breakthrough experiments, represents the major transport pathway for N₂ after gas breakthrough.
- (ii) The transport porosity required for gas transport is several orders of magnitude lower than the total porosity determined from Mercury Injection.
- (iii) The gas displacement pressure determined from Mercury Injection does not show a good agreement with the corresponding data from gas breakthrough experiments.

Table 2. Comparison between data from Mercury Injection (Hg) and gas breakthrough experiments (N_2); " N_2 " denotes the N_2 displacement pressure converted from mercury data to the system N_2 -water.

Sample plug	Porosity			Max. of pore size distribution		Min. cap. displ. pressure (P_d)		
	ϕ_{Hg} (%)	ϕ_{water} (%)	ϕ_{N_2} (%)	$r(Hg)$ [nm]	$r(N_2)$ [nm]	Hg [MPa]	" N_2 " [MPa]	N_2 [MPa]
1	29.9	42.8	10^{-5}	20 & 110	22	2.7	0.5	2.5
2	29.9	42.8	10^{-5}	20 & 110	24	2.7	0.5	1.2

References

- [1] Neuzil, C.E. (1994) How permeable are clays and shales? *Water Resources Research* **30**(2), 145-150
- [2] Harrington, J.F. and Horseman, S.T. (1999) Gas transport properties of clays and mudrocks. In: *Geological Society, Special Publications*, London, pp. 107-124
- [3] Ibrahim, M.A., Tek, M.R. and Katz, D.L. (1970) *Threshold pressure in gas storage*. Pipeline Research Committee American Gas Association at the University of Michigan, Michigan, 309 pp.
- [4] Schowalter, T.T. (1979) Mechanics of secondary hydrocarbon migration and entrapment. *AAPG Bulletin* **63**, 723-760
- [5] Thomas, L.K., Katz, D.L. and Tek, M.R. (1968) Threshold pressure phenomena in porous media. *Society of Petroleum Engineers Journal* **243**, 174-184
- [6] Gallé, C. (2000) Gas breakthrough pressure in compacted Fo-Ca clay and interfacial gas overpressure in waste disposal context. *Applied Clay Science* **17**, 85-97
- [7] Hildenbrand, A., Schlömer, S. and Krooss, B.M. (2002) Gas breakthrough experiments on fine-grained sedimentary rocks. *Geofluids* **2**, 3-23
- [8] Horseman, S.T., Higgo, J.J.W., Alexander, J. and Harrington, J.F. (1996) *Water, gas and solute movement through argillaceous media*, Report 96/1 OECD, Paris, 290 pp.
- [9] Schlömer, S. and Krooss, B.M. (1997) Experimental characterisation of the hydrocarbon sealing efficiency of cap rocks. *Marine and Petroleum Geology* **14**, 565-580
- [10] Hildenbrand, A. and Urai, J.L. (2003) Investigation of the morphology of pore space in mudstones - first results. *Marine and Petroleum Geology* **20**, 1185-1200
- [11] Wardlaw, N.C. and McKellar, M. (1981) Mercury Porosimetry and the Interpretation of Pore Geometry in Sedimentary Rocks and Artificial Models. *Powder Technology* **29**, 127-143
- [12] Swanson, B.F. (1979) Visualizing pores and nonwetting phase in porous rock. *J. Petro. Tech.* **31**, 10-18
- [13] Dullien, F.A.L. (1981) Wood's metal Porosimetry and its relation to Mercury Porosimetry. *Powder Technology* **29**, 109-116.

- [14] Pyrak-Nolte, L.J. and Haley, G.M. (1993) Effective cleat porosity and cleat geometry from Wood's metal Porosimetry. *Proceedings of the 1993 International Coalbed Methane Symposium*, University of Alabama/Tuscaloosa, May 17-21, 639-647
- [15] Kamran, M., Nemati, Paulo, J.M. and Monteiro (1997) A New Method to Observe Three-Dimensional Fractures in Concrete Using Liquid Metal Porosimetry Technique. *Cement and Concrete Research* **27**, 1333-1341
- [16] Nemati, K.M. (2000) Preserving microstructure of concrete under load using the Wood's metal Technique. *International Journal of Rock Mechanics and Mining Science* **37**, 133-142
- [17] Agrawal, D.L., Cook, N.G.W. and Myer, L.R. (1991) The effect of percolating structures on the petrophysical properties of Berea sandstone. In: *Rock Mechanics as a Multi-disciplinary Science*, Balkema, pp. 345-354
- [18] Montemagno, C.D. and Pyrak-Nolte, L.J. (1995) Porosity of natural fracture networks. *Geophysical Research Letters* **22**, 1397-1400
- [19] Darot, M. and Reuschlé, T. (1999) Direct assessment of Wood's metal wettability on quartz. *Pure and Applied Geophysics* **155**, 119-129

IX

ELECTROMAGNETIC WAVES.

Chairman: C. Santamarina

TOWARDS A BETTER UNDERSTANDING OF THE ELECTRO-MAGNETIC PROPERTIES OF SOILS

Katherine Klein

University of Toronto, Toronto, Ontario, Canada

Yu-Hsing Wang

Hong Kong University of Science and Technology, Clear Water Bay, Kowloon, Hong Kong

Abstract Given the sensitivity of soils to disturbance, the use of low perturbation (i.e., non-destructive) electromagnetic waves provides a viable option for studying soil properties. The measured parameters during the excitation of a material by an electromagnetic wave are electrical conductivity, dielectric permittivity, and magnetic permeability. Electrical conductivity is a measure of charge mobility in response to an electrical field. Dielectric permittivity represents the polarizability of a material. Magnetic permeability indicates the degree of magnetic dipole alignment within a material under the excitation of the magnetic field. Factors that affect electromagnetic wave parameters include water content/degree of saturation, porosity, spatial distribution of the phases (e.g., anisotropy), particle properties (e.g., specific surface), pore fluid characteristics, and temperature. This paper presents a review of electromagnetic parameters, provides experimental data showing the impact of the various factors on the electromagnetic response, and gives a physical explanation of why these factors affect electromagnetic properties. Finally, various applications of electromagnetic wave-based techniques are presented, including monitoring the diffusion of salt through a soft kaolinite sediment and the hydration process in cemented paste backfill.

Introduction

The macroscale behaviour of high specific surface particulate minerals is directly related to microscale interparticle electrical forces, thus, the physical interpretation of electromagnetic wave parameters allows inferring important properties about these materials. Furthermore, the properties of high specific surface particulate materials are environmentally dependent, hence, they are difficult to determine without altering them in the measurement process. In

Jacques M. Huyghe et al. (eds), IUTAM Proceedings on Physicochemical and Electromechanical Interactions in Porous Media, 241–250.

© 2005 Springer. Printed in the Netherlands.

such a medium, small perturbation electromagnetic waves offer the advantage of having no permanent effect on the medium or the internal processes being monitored. Given sufficient skin depth, the propagation of electromagnetic waves permits conducting non-destructive measurements on the boundaries of the specimen and inference of the spatial distribution of electromagnetic parameters within the body. This paper presents a review of electromagnetic parameters, summarizes the impact of soil characteristics, including pore fluids, on the electromagnetic parameters, and gives a physical explanation of why these factors affect the electromagnetic properties. Selected examples of process monitoring using electromagnetic waves are presented.

Electromagnetic Properties

It follows from Maxwell's equations that three material parameters are needed to describe interactions between electromagnetic waves and the medium: complex dielectric permittivity $\varepsilon^* = \varepsilon' + j\varepsilon''$, electrical conductivity σ , and complex magnetic permeability $\mu^* = \mu' + j\mu''$ ($j = \sqrt{-1}$ denotes an imaginary number). Since most particulate materials are non-ferromagnetic, the magnetic properties of the materials are often assumed to be the same as air. Electrical conductivity s is a measure of charge mobility in response to an electric field. In the case of particle-electrolyte mixtures, the conductivity depends on the characteristics of the pore fluid and particles, and the mixture fabric. Surface conduction λ (ionic movement in the diffuse double layer) gains relevance in mixtures of low conductivity fluids and high specific surface minerals [14]. The permittivity of a material is often expressed as the relative permittivity $\kappa^* = \varepsilon^*/\varepsilon_0$ where $\varepsilon_0 = 8.85 \times 10^{-12} F/m$ is the permittivity of vacuum. The real relative dielectric permittivity κ' represents the polarizability of the material, while the imaginary relative permittivity κ'' captures polarization losses. Since charge migration is also an energy loss, the imaginary permittivity and conductivity are often reported as a single parameter, either as effective imaginary permittivity $\kappa''_{eff} = \kappa'' + \sigma/(\omega\varepsilon_0)$ or as effective conductivity $\sigma_{eff} = \kappa''_{eff}\omega\varepsilon_0$, where ω is angular frequency [rad/s]. Note that conduction losses may overwhelm the polarization losses at low frequencies in high conductivity specimens.

Polarization mechanisms: microscale view

The mechanisms that cause polarization depend on the frequency of the applied electric field and the composition of the material. Real permittivity increases as frequency decreases since polarizations accumulate (see Figures 1 and 2). Single-phase materials may experience three types of polarization: electronic ($\tau \approx 10^{-16} s$), ionic ($\tau \approx 10^{-13} s$), and orientational ($\tau = \text{variable}$). Non-polar materials do not experience orientational polarization and have very

low real relative permittivity values ($\kappa' < \approx 10$). Polar molecules, such as water, have much high permittivity values. Polarization mechanisms that reflect interactions between phases in particle-fluid mixtures include Stern layer polarization, bound water polarization, double layer polarization, and interfacial (Maxwell-Wagner) polarization. Stern layer polarization arises due to the movement of ions tightly bound to the particle surface. Only local movement of these ions is permitted due to the presence of large energy barriers coming from the interactions with surfaces (i.e., high frequency polarization). Water molecules adsorbed onto the surface of a soil particle experience bound water polarization due to the application of an electric field parallel to the particle. In addition, double layer polarization arises due to the relative displacement of the double layer counterion cloud with respect to the charged particle in response to an electric field. Interfacial (Maxwell-Wagner) polarization develops when charges in solution and in double layers accumulate at interfaces normal to the applied field. A detailed review of polarization mechanisms can be found in [18].

Water The orientational polarization of water molecules depends on its state, as evidenced by the data shown in Figure 1. For each state, the relaxation frequency is a function of the structural arrangement: GHz for liquid water, MHz for bound or adsorbed water, and kHz for ice and hydrate. Some materials may show a distribution of relaxation times indicating the presence of multiple polarizations owing to specimen heterogeneity. Pure water and ice tend to show one relaxation time, while studies have shown that water adsorbed onto surfaces may have a distribution of relaxation times [3, 4, 16, 21, 11]. Temperature affects both the static permittivity and the relaxation time. The enhanced thermal agitation due to an increase in temperature shifts the relaxation to a higher frequency (i.e., shorter relaxation time), but disrupts the alignment of polarized molecules thereby decreasing the static permittivity [23, 11]. The static permittivity of ice is slightly greater than liquid water because the distance between water molecules is less in ice; thus, the enhancing effect of the neighbouring molecules on the induced dipole moment is greater [8]. Hydrates have a similar relaxation time and activation energy to ice at 273 K. However, hydrates have a lower permittivity than ice, most likely due to the lower density of water molecules in hydrates [5].

Soil-Water Mixtures Figure 2 presents the dielectric spectra of clay-water mixtures (kaolinite and montmorillonite) after the influence of dc conductivity is removed. In addition to the orientational polarization of bulk water at ≈ 20 GHz and adsorbed water at ≈ 10 MHz, a low frequency polarization is observed at kHz to MHz frequencies. It should be noted that this low-frequency relaxation process cannot be generalized for all mineral-water

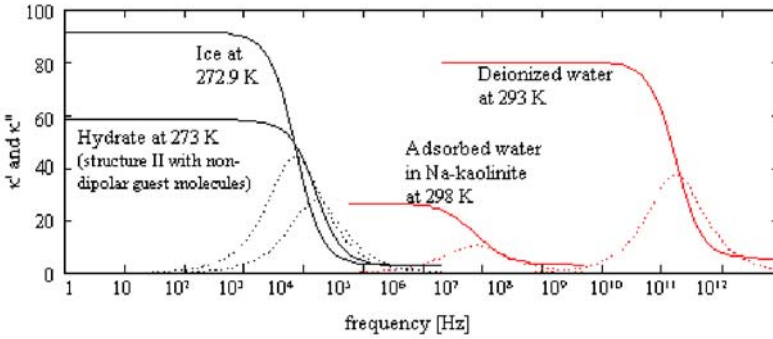


Figure 1. Debye-type relaxation spectra for liquid water, adsorbed water, ice, and hydrate. Solid lines correspond to real relative permittivity κ' and dotted lines represent imaginary permittivity κ'' [3, 5, 11, 10].

systems [9, 10]. The causes of the low frequency polarization may be interfacial polarization and/or double layer polarization.

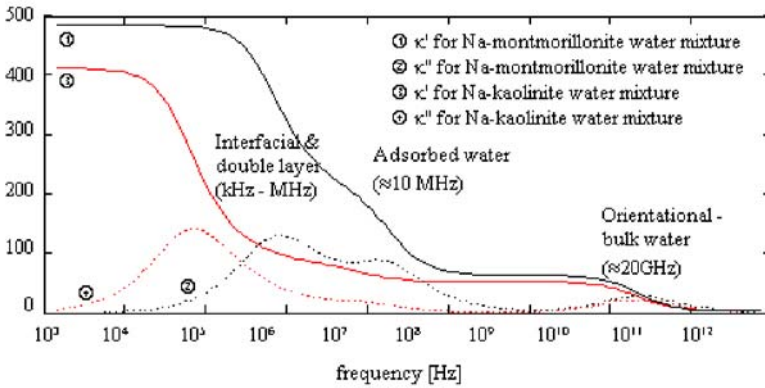


Figure 2. Dielectric spectral responses of clay-water mixtures at 298 K. Parameters used in the Debye-type relaxation spectral functions are compiled from Ishida et al. (2000).

The nonconformity of electromagnetic properties between soil particles and the surrounding pore fluid gives rise to interfacial polarization at radio frequencies. For soils with low specific surface, the Maxwell-Wagner model is used to explain the relaxation. However, for high specific surface soils, the counterion atmosphere around the soil particle can move tangentially due to an applied field, resulting in double layer polarization. This polarization mechanism may explain the high permittivity measurements for colloidal suspensions [20]. Double layer polarization may be impeded by surface conduction at high

particle contents or due to the exchange of the counterions in the diffuse double layer with the surrounding electrolyte [18]. In addition, fabric arrangement may favour interfacial polarization over double layer polarization, as depicted in Figure 3. These observations imply the difficulties associated with experimentally distinguishing the individual polarization contributions and with choosing appropriate mechanisms for interpretation. Additionally, the measurement of dielectric responses at frequencies less than approximately 100 MHz may be biased by electrode polarization in high conductivity clay-water mixtures [13, 12]. Further studies of the mechanisms affecting interfacial and double layer polarization in clay-water mixtures are needed.

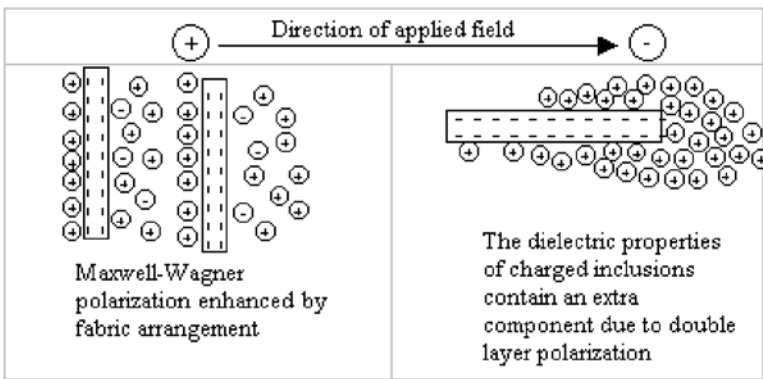


Figure 3. Interfacial and double layer polarization [18].

Relationships Between Electromagnetic Parameters and Soil Properties

Electromagnetic parameters are sensitive to the properties of soils, including volumetric water content/porosity, specific surface, ionic concentration, anisotropy, and temperature. The general trends are summarized in Table 1. Table 2 presents selected models relating the electromagnetic parameters to mixture properties.

Conductivity

Since most conduction takes place in the pore space of soils, pore fluid conductivity is an important parameter. Many models relating fluid conductivity and pore fluid concentration are applicable only for low ionic concentrations, since at higher concentrations, ion-ion interactions reduce ionic mobility [15]. Additionally, ionic mobility is sensitive to temperature, increasing as temperat-

ure increases. In 1942, Archie developed a relationship between conductivity, porosity, and the connectivity of the pore spaces in soils. This model is only applicable for low specific surface soils (i.e., surface conduction is negligible). As the tortuosity of the pore spaces increases, the conductivity decreases due to the fact that the ions must follow a more complex path in order to respond to the electric field, and some ions may become trapped at interfaces perpendicular to the field direction. The accumulation of ions at interfaces has implications on the real relative permittivity (e.g., interfacial polarization). The impact of tortuosity on conductivity measurements depends on the frequency of the applied field. At high frequencies, there is local ion movement, which is minimally affected by particle orientation and tortuosity. Measuring the electrical conductivity of soil-fluid mixtures in different directions gives a good idea of the fabric anisotropy in the mixture, which also impacts engineering properties such as hydraulic conductivity. Klein and Santamarina (2003) developed a model to show the importance of surface conduction in a system of saturated infinitely long particles oriented parallel to the applied electric field. This model demonstrates that the contribution of surface conduction to the mixture conductivity increases as pore fluid concentration and porosity decrease, and as specific surface increases. The mixture conductivity can be greater than the fluid conductivity in the case of high surface conduction. The impact of surface conduction on polarization mechanisms has been briefly addressed in Section “Soil-Water Mixtures”.

Real relative permittivity

The real relative permittivity is sensitive to changes in volumetric water content and to the presence of less polar fluids [19] due to water’s high polarizability. Topp et al. (1980) developed an empirical relationship between the real relative permittivity and the volumetric water content at 1 GHz. Dirksen and Dasberg (1993) found that this equation is applicable for soils with specific surface less than approximately $100 \text{ m}^2/\text{g}$ and bulk densities between 1.35 and $1.50 \text{ g}/\text{cm}^3$. The real permittivity of high specific soils is less than low specific surface soils for a given water content at GHz frequencies, since the amount of free water decreases as specific surface increases. In water, the real relative permittivity κ' decreases as ionic concentration increases due to a hindrance of free water polarization as the water molecules hydrate the ions in the bulk fluid [8]. In soil-fluid mixtures at frequencies less than about 1 GHz, the interplay between phases strongly affects the polarization mechanisms and the effects of volumetric water content, ionic concentration, fabric, specific surface, and surface conduction are not obvious. Wraith and Or (1999) found that the effect of temperature on κ' at ≈ 1 GHz depends on the water content and the specific surface of the soil. For soils with low specific surface and/or high water con-

Table 1. Relationships between EM Parameters and Soil Properties

EM	Soil Properties	Engineering Applications	General Trend
λ	ionic concentration c specific surface S_a	detect the presence of clay	$\lambda \uparrow$ in importance as $c \downarrow$ $\lambda \uparrow$ in importance as $S_a \uparrow$
σ, κ'	ionic concentration c	process monitoring (diffusion)	$\sigma \uparrow$ as $c \uparrow$ $\kappa' \downarrow$ as $c \uparrow$ ($f \gg \approx \text{GHz}$)
σ	porosity n volumetric water content θ_v	hydraulic conductivity	saturated (low λ): $\sigma \uparrow$ as $n \uparrow$ saturated (high λ): $\sigma \uparrow$ as $n \downarrow$
σ	anisotropy	hydraulic conductivity	$\sigma_{ } > \sigma_{\perp}$
κ''_{eff} κ'	temperature T	quality control	$\kappa''_{\text{eff}} \uparrow$ as $T \uparrow$ ($f \approx 1 \text{ GHz}$) low S_a : $\kappa' \downarrow$ as $T \uparrow$ high S_a , high w : $\kappa' \downarrow$ as $T \uparrow$ high S_a , low w : $\kappa' \uparrow$ as $T \uparrow$
κ'	volumetric water content θ_v	process monitoring (cement hydration)	$\kappa' \downarrow$ as $\theta_v \downarrow$ ($f \approx 1 \text{ GHz}$)
κ'	polar or non-polar fluid	monitor contaminant diffusion	$\kappa' \downarrow$ as fluid polarity \downarrow (e.g., $\kappa'_{\text{contaminant}} < \kappa'_{\text{water}}$)
κ'	specific surface	clay classification	$\kappa' \downarrow$ as $S_a \uparrow$ (given $w, f > \text{GHz}$)

Notation: σ =electrical conductivity, κ' =real relative permittivity, κ'' =imaginary relative permittivity, λ =surface conduction, subscript "eff" denotes an effective quantity, f =frequency, w =water content

tent, κ' decreases as temperature increases because the behaviour of the bulk water governs. For soils with high specific surface and low water content, κ' increases as temperature increases because the thickness of the adsorbed water layer decreases as temperature increases [6], thereby increasing the quantity of free water, which is reflected as an increase in κ' [17]. Note that adsorbed water is not polarized at 1 GHz as indicated in Figure 1.

Examples

Examples of process monitoring using conductivity measurements are presented in Figure 4a for diffusion and cement hydration. The data indicate that conductivity measurements are very sensitive to changes in pore fluid composition. Figure 4b shows that changes in water content are reflected as changes in the real relative permittivity during the curing of a cemented mixture.

Table 2. Selected Models

Model	References
$\sigma_f = z c u F$	Lyklema (1991)
$\sigma_f = 0.15 \text{ TDS [mS/m]}$	Annan (1992)
$\sigma_{\text{mix}} = a \sigma_f n^m$	Archie (1942)
$\sigma_{\text{mix}} = (1 - n) \sigma_p + n \sigma_f + (1 - n) \lambda \rho_p S_a$	Klein & Santamarina (2003)
$\kappa' = 3.03 + 9.3 \theta_v + 146 \theta_v^2 - 76.7 \theta_v^3$	Topp et al. (1980)

Notation: σ =electrical conductivity, κ' =real relative permittivity, subscripts mix, f and p denote soil-fluid mixture, fluid, and particle, respectively, z =ionic valence, c =ionic concentration, u =ionic mobility is, $F=96485.3 \text{ C/mol}$ is Faraday's constant, TDS=total dissolved salts in [mg/L], n =porosity, ρ =density, λ =surface conduction, S_a =specific surface, a =degree of saturation, m =cementation factor, θ_v =volumetric water content

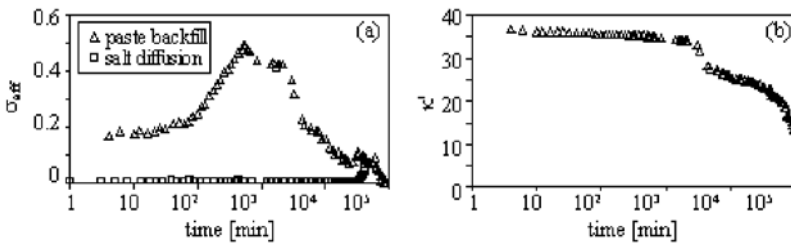


Figure 4. Examples of process monitoring. (a) Change in effective conductivity at 200 MHz during the diffusion of salt through a soft kaolinite sediment and the hydration of a cemented paste backfill. (b) Change in the real relative permittivity at 1.3 GHz during the hydration of a cemented paste backfill (paste data from D. Simon).

Final Comments

Electromagnetic measurements of high conductivity soil-fluid mixtures at low frequencies are difficult to obtain due to electrode polarization. Caution must be used when interpreting data in the literature, as electrode effects may be viewed as being material behaviour. In addition, difficulties with data interpretation arise at kHz and MHz frequencies for clay-fluid mixtures due to the possible manifestation of both double layer polarization and interfacial polarization phenomena.

References

- [1] Annan, A.P. (1992) Ground Penetrating Radar, *Workshop Notes, Sensors and Software, Mississauga*
- [2] Archie, G.E. (1942) The electrical resistivity log as an aid in determining some reservoir characteristics, *Transactions of the American Institute of Mining, Metallurgical, and Petroleum Engineers* **146**, 54-62
- [3] Auty, R.P. and Cole, R.H. (1952) Dielectric properties of ice and solid D₂O, *The Journal of Chemical Physics* **20 Suppl. 8**, 1309-1314
- [4] Calvet, R. (1975) Dielectric properties of montmorillonites saturated by bivalent cations, *Clays and Clay Minerals* **23**, 257-265
- [5] Davidson, D.W. (1983) Gas hydrates as clathrate ices, in *Natural Gas Hydrates - Properties, Occurrence and Recovery*, J.L. Cox (ed.), Butterworths, Boston, pp. 1-16
- [6] Derjaguin, B.V., Churaev, N.V. and Muller, V.M. (1987) *Surface Forces*, Consultants Bureau, New York, 440
- [7] Dirksen, C. and Dasberg, S. (1993) Improved calibration of time domain reflectometry soil water content measurements, *Soil Science Society of America Journal* **57**, 660-667
- [8] Hasted, J.B. (1973) *Aqueous Dielectrics*, Chapman and Hall, London, 302
- [9] Ishida, T. and Makino, T. (1999) Effects of pH on dielectric relaxation of montmorillonite, allophone, and imogolite suspensions, *Journal of Colloid and Interface Science* **212**, 152-161
- [10] Ishida, T., Makino, T. and Wang, C. (2000) Dielectric-relaxation spectroscopy of kaolinite, montmorillonite, allophone, and imogolite under moist conditions, *Clays and Clay Minerals* **48 Suppl. 1**, 75-84
- [11] Kaatzte, U. (1997) The dielectric properties of water in its different states of interaction, *Journal of Solution Chemistry* **26 Suppl. 11**, 1049-1112
- [12] Klein, K. (2004) Permittivity measurements of high conductivity specimens using an open-ended coaxial probe-measurement limitations, *Journal of Environmental & Engineering Geophysics* **9**, 191-200
- [13] Klein, K. and Santamarina, J.C. (1997) Methods for broad-band dielectric permittivity measurements (soil-water mixtures, 5 Hz to 1.3 GHz), *ASTM Geotechnical Testing Journal* **20**, 168-178
- [14] Klein, K. and Santamarina, J.C. (2003) Electrical conductivity in soils: Underlying phenomena, *Journal of Environmental and Engineering Geophysics* **8**, 263-273
- [15] Lyklema, J. (1991) Fundamentals of Interface and Colloid Science, *Volume I: Fundamentals*, Academic Press, London
- [16] Mamy, J. (1968) Recherches sur l'hydratation de la montmorillonite: propriétés diélectriques et structure du film d'eau, *Annales Agronomiques* **19**, 175-246
- [17] Or, D. and Wraith, J.M. (1999) Temperature effects on soil bulk dielectric permittivity measured by time domain reflectometry: A physical model, *Water Resources Research* **35 Suppl. 2**, 371-383
- [18] Santamarina, J.C., Klein, K.A. and Fam, M.A. (2001) *Soils and Waves*, John Wiley & Sons, New York, 488
- [19] Santamarina, J.C. and Fam, M.A. (1996) Dielectric permittivity of soils mixed with organic and inorganic fluids (0.02 GHz to 1.30 GHz), *Journal of Environmental and Engineering Geophysics* **2**, 37-51

- [20] Schwarz, G. (1962) A theory of the low-frequency dielectric dispersion of spherical colloidal particles in electrolyte solution, *Journal of Physical Chemistry* **66**, 2636-2642
- [21] Sposito, G. and Prost, R. (1982) Structure of water adsorbed on smectites, *Chemical Reviews* **82 Suppl. 6**, 553-572
- [22] Topp, G.C., Davis, J.L. and Annan, A.P. (1980) Electromagnetic determination of soil water content: Measurement in coaxial transmission lines, *Water Resources Research* **16 Suppl. 3**, 574-582
- [23] von Hippel, A. (1988) The dielectric relaxation spectra of water, ice, and aqueous solution, and their interpretation, II. tentative interpretation of the relaxation spectrum of water in the time and frequency domain, *IEEE Transactions on Electrical Insulation* **23 Suppl. 5**, 801-816
- [24] Wraith, J.M. and Or, D. (1999) Temperature effects on soil bulk dielectric permittivity measured by time domain reflectometry: Experimental evidence and hypothesis development, *Water Resources Research* **35 Suppl. 2**, 361-369

POROUS MEDIA EVALUATION USING FREQUENCY-DEPENDENT ELECTROKINETICS

Philip M. Reppert and Taufiqar R. Khan
Clemson University, Clemson, SC 29634, USA

Abstract Frequency-dependent electrokinetics offers a different approach to obtaining information about porous media. In this work, we examine the possibility of using frequency-dependent streaming potential (FDSP) and frequency-dependent electro-osmosis (FDE) to obtain information concerning porous media. The theoretical basis for this work is done using the simple geometry of a capillary because it allows for an easier interpretation of the underlying physics. Pride [1994] formulated a more generalized porous media case which has been shown to give equivalent results to the capillary case for streaming potentials [Reppert et al., 2001].

Keywords: Porous Media, Electrokinetics, Permeability

Introduction

The underlying physics that governs FDSP and FDE relies on coupled flow between a fluid and the ions within the fluid. As the frequency of the driving force is increased, inertial effects in the fluid start to retard the motion of the fluid in the center of the capillary. Consequently, the ratio of responding phenomenon to the driving force is reduced. FDSP and FDE are closely related phenomena, in FDSP an applied pressure causes fluid to move which in turn cause ions to move setting up convection and conduction currents. On the other hand, FDE has as its driving force an electric field which moves ions in the electrical double layer (EDL) that pull the fluid along with them. In both cases, the coupled flow problem is controlled by the surface/fluid properties that affect the EDL as well as the geometry of the pore/capillary space. A schematic representation of the fluid velocity profiles for FDSP and FDE are shown in Figure 1.

Background

These phenomena arise because at the surface/fluid interface a charge distribution often exists where there is an abundance of one species of ions close

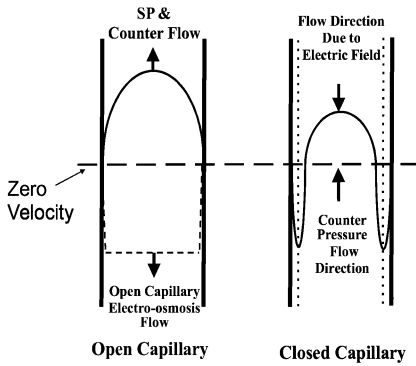


Figure 1. Fluid Velocity Profiles

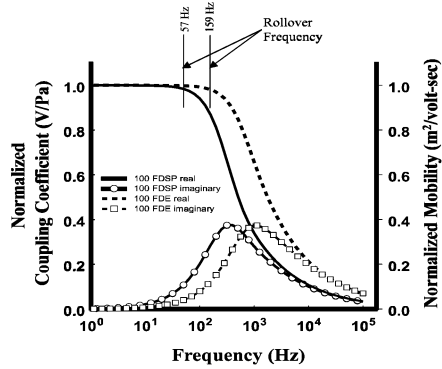


Figure 2. FDE & FDSP

to the pore wall. The Stern model can be used to describe the charge distribution which divides the EDL into two parts, the Helmholtz layer and the diffuse layer. For this work we are primarily interested in the diffuse layer which includes the slipping plane which is where the fluid velocity goes to zero when the fluid motion is parallel to the surface.

Frequency dependent streaming potential

There are different ways of describing the coupled flow problem in streaming potentials, one is by at Onsager's reciprocity relations and the other is by

$$\mathbf{I}_{\text{conv}}(\mathbf{r}) = \int 2\pi r \mathbf{v}_z(\mathbf{r}) \rho_c(\mathbf{r}) d\mathbf{r}, \quad (1)$$

where \mathbf{I}_{conv} is the convection current caused by the fluid pulling the ions along in the EDL, \mathbf{v}_z is the fluid velocity profile, and ρ_c is the charge distribution in the EDL. Once the convection current is determined, the streaming potential (ΔV) can be determined by calculating the resulting conduction current which is caused by ions trying to return to their original position to maintain equilibrium condition. The conduction current is then set equal to the convection current to give the ratio $(\Delta V / \Delta P) = (\epsilon \zeta / \eta \sigma)$, which is referred to as the Helmholtz-Smoluchowski equation where ϵ is the permittivity of the fluid, ΔP is the pressure across the sample, η is the viscosity of the fluid, and ζ is the zeta potential. In the case of FDSP we have oscillating fluid flow in a capillary whose fluid motion is governed by

$$i\rho\omega \mathbf{v}_c(\mathbf{r}, \omega) = \eta \nabla^2 \mathbf{v}_c(\mathbf{r}, \omega) - \nabla P(\omega). \quad (2)$$

The inertial terms on the left side of the equation are balanced by the viscous forces minus the driving force on the right side of the equation. The solution

to this equation has been previously presented [Crandall, 1926; Reppert et al., 2001], and is

$$\mathbf{v}_c(\mathbf{r}, \omega) = \frac{\Delta \mathbf{P}(\omega)}{\eta l k^2} \left[\frac{\mathbf{J}_0(k\mathbf{r})}{\mathbf{J}_0(k\mathbf{a})} - \mathbf{1} \right]. \quad (3)$$

Where l is the length of the capillary, \mathbf{a} is the radius of the capillary, \mathbf{J}_0 , is a Bessel function of the first kind and $\mathbf{k} = \sqrt{(-i\omega\rho)/\eta}$. $\sqrt{(\eta/\rho\omega)} = \delta$, is the viscous skin depth, which is the distance at which the amplitude of the vorticity (transverse) wave has attenuated by a factor of the natural logarithm “e”. Inserting (3) into (1) and using Poisson’s equation for the charges distribution we can solve for the FDSP Helmholtz-Smoluchowski equation [Reppert et al., 2001],

$$\mathbf{C}(\omega) = \frac{\Delta \mathbf{V}_{SP}(\omega)}{\Delta \mathbf{P}_{SP}(\omega)} = - \left[\frac{\epsilon \zeta}{\sigma \eta} \right] \frac{2 \mathbf{J}_1(k\mathbf{a})}{k\mathbf{a} \mathbf{J}_0(k\mathbf{a})} = -\text{SP}_{DC} \frac{2 \mathbf{J}_1(k\mathbf{a})}{k\mathbf{a} \mathbf{J}_0(k\mathbf{a})}, \quad (4)$$

whose response (Figure 2) is dependent on the capillary/pore radius. It has been shown [Reppert et al., 2001], by using Bessel function approximations and the appropriate permeability model, that (4) goes to the same form as Pride’s [1994] porous media formulation.

Frequency-dependent electro-osmosis

In the case of FDE the driving force is an electric field, which moves the ions of the EDL pulling the fluid along with them due to viscous forces in the fluid. This case can also be described by

$$i\rho\omega\mathbf{v}(\mathbf{r}, \omega) = \eta\nabla^2\mathbf{v}(\mathbf{r}, \omega) - \epsilon\nabla^2\psi(\mathbf{r})\mathbf{E}(\omega), \quad (5)$$

where $\psi(\mathbf{r})$ is the potential distribution. Equation (5) does not have a closed form solution unless certain restrictions are place on the solution and it is solved for the near wall and bulk fluid regions which are then combined into a final solution [Reppert and Morgan, 2002].

For the near wall solution, from the slipping plane to 3 Debye lengths from the wall, the solution is restricted to cases where there are no inertial effects within this region. In other words the left hand side of (5) goes to zero and we are left with an equation of the same form as the DC electro-osmosis equation but now with an AC electric field. The solution to this equation is

$$\mathbf{v}_{ew}(\mathbf{x}, \omega) = \frac{\epsilon\zeta}{\eta} [\exp(-\kappa\mathbf{x}) - \mathbf{1}] \mathbf{E}(\omega) \quad (6)$$

where κ is the Debye Hückel parameter and the potential distribution is assumed to be the Debye-Hückel approximation, $\psi(\mathbf{x}) = \zeta\exp(-\kappa\mathbf{x})$. The boundary conditions that exist in the bulk fluid are different than those for the

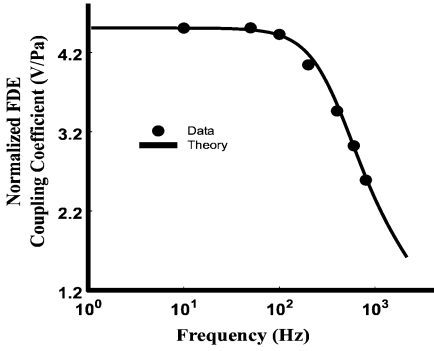


Figure 3. FDE Theory & Data

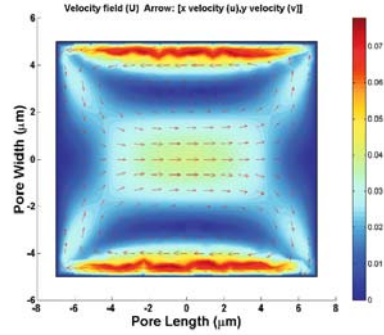


Figure 4. FDE FEM Simulation

near wall solution. In the bulk fluid the potential distribution $\psi(\mathbf{r})$ drops to essentially zero, it can also be concluded that in the bulk fluid of the capillary $\nabla^2\psi(\mathbf{x}) \rightarrow 0$. Equation (5) now becomes,

$$i\rho\omega\mathbf{v}_{eB}(\mathbf{r}, \omega) = \eta\nabla^2\mathbf{v}_{eB}(\mathbf{r}, \omega), \quad (7)$$

which has a solution

$$\mathbf{v}_{eB}(\mathbf{r}, \omega) = -\frac{\epsilon\zeta\mathbf{E}(\omega)}{\eta} \frac{\mathbf{J}_0(\mathbf{kr})}{\mathbf{J}_0(\mathbf{kb})}, \quad (8)$$

and when combined with the near wall solution gives a velocity profile defined by

$$\mathbf{v}(\mathbf{r}, \omega) = \frac{\epsilon\zeta\mathbf{E}(\omega)}{\eta} \left[\exp(-\kappa\mathbf{r}) - \frac{\mathbf{J}_0(\mathbf{kr})}{\mathbf{J}_0(\mathbf{kb})} \right], \quad (9)$$

where $\mathbf{b} = (\mathbf{a} - \mathbf{3}/\kappa)$. For electro-osmosis in an open capillary we are concerned about the volume flow in the capillary. Therefore, calculating the mean fluid velocity and taking the ratio of $\mathbf{v}_{eB}/\mathbf{E}(\omega)$ gives,

$$\mathbf{u}(\omega) = \frac{\mathbf{v}(\omega)}{\mathbf{E}(\omega)} = -\frac{\epsilon\zeta}{\eta} \frac{2}{\mathbf{ka}} \frac{\mathbf{J}_1(\mathbf{ka})}{\mathbf{J}_0(\mathbf{kb})} = \frac{2\mathbf{u}_{dc}}{\mathbf{ka}} \frac{\mathbf{J}_1(\mathbf{ka})}{\mathbf{J}_0(\mathbf{kb})}. \quad (10)$$

It can be seen when comparing (10) to (4) that the equations are of the same form with identical transfer functions multiplied by different constants. However, we want to compare the FDSP case to the electro-osmosis closed capillary case where the same ratio of $\Delta\mathbf{V}/\Delta\mathbf{P}$ can be compared. To get this ratio for the closed capillary the electro-osmosis volume flow must be balance by counter flow which is caused by a pressure build-up at the ends of the capillary. The counter flow is Poiseuille flow in a capillary and whose solution is

the same as (4). The volume flows can then be calculated for both the electro-osmosis flow and the counter flow by integrating the flows across the cross-sectional area of the capillaries. Setting these volume flows equal to each other and solving for the ratio $\Delta V/\Delta P$ [Reppert and Morgan. 2002] gives,

$$\frac{\Delta V(\omega)}{\Delta P(\omega)} = \frac{a}{2\epsilon\zeta k} \left(\frac{2 J_1(ka)}{ka J_0(ka)} - 1 \right) / \left(\frac{J_1(ka)}{J_0(kb)} \right). \quad (11)$$

It can be seen that (11) has a different form than (4) as well as a different frequency response (Figure 2). The response has the same general shape but a higher rollover frequency.

These differences in response are due to the differences in vorticity waves associated with the phenomena. In the FDSP case there is one wave that emanates from the surface while in the FDE case there are two vorticity waves, one the emanates from the surface and another the emanates from the second velocity zero (Figure 1) [Reppert & Morgan, 2001].

We have now demonstrated that both the FDSP and FDE responses are dependent on the capillary/pore dimension. Once the pore dimension is known this can applied to an appropriate permeability model to obtain more information about the porous media. Using an appropriate permeability model along with formation factor measurements we can estimate the permeability of porous samples. Alternatively, if we measure the permeability of a sample we can then use the permeability model to determine the formation factor and tortuosity of the sample using measurements that are base on the hydraulic properties and not the electrical properties. This is currently a work in progress to compare formation factor measurements made using the two methods.

Data

The first data presented is for FDE in a closed 0.127 mm diameter capillary (Figure 3). It can be seen that the theory has a good fit to the data which demonstrates that FDE can be used to determine capillary diameters. Figure 4 shows a finite element (FEM) simulation of FDE in a closed capillary where it can be seen that a circulation/mixing of fluid occurs within the capillary. The last data is for a porous glass filter with pore radii ranging from 35-50 mm (Figure 5). The theory has a good fit to the data and provides a pore size for the glass filter of 40 μm . Using this pore diameter a permeability of 9.8 Darcies is calculated which compares favorably to the measured permeability of 8.2 Darcies.

Conclusion

It has been demonstrated that FDSP has the potential to provide information on the pore microstructure that can be used to estimate permeability. It

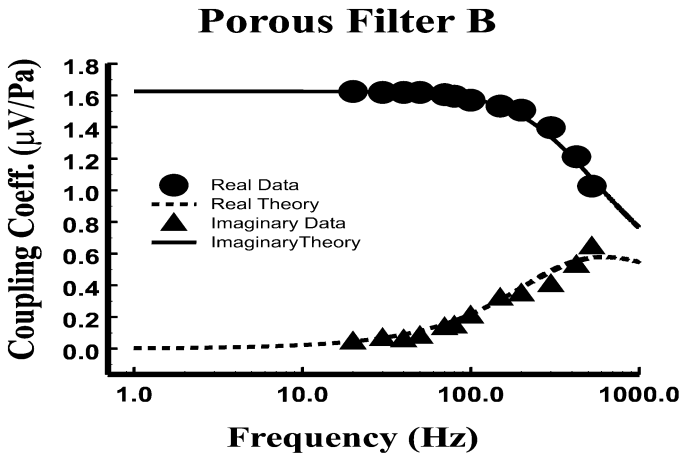


Figure 5. FDSP, Porous Glass Filter

has been demonstrated that FDE may have the same possibility to provide information on the pore structure. Additionally, FDE may be used as a mixing mechanism within pore spaces.

References

- [1] Crandall, I.B. (1926) *Theory of Vibrating Systems and Sound*, New York: D. Van Norstrand Co.
- [2] Pride, S.R. (1994) Governing equations for the coupled electromagnetics and acoustic porous-media, *Physical Rev. B*, 50 **15**, 678
- [3] Reppert, P.M., Morgan, F.D., Lesmes, D. and Jouniaux, L. (2001) Frequency-dependent streaming potentials, *Journal of Colloid Interface Sci* **234**, 194-203, 93-1
- [4] Reppert, P.M. and Morgan, F.D. (2002) Frequency-dependent electroosmosis, *Journal of Colloid Interface Sci* **254**, 372-383

X

CHEMO- AND ELECTRO-OSMOSIS.

Chairmen: S.C. Cowin, C. Moyne

CHARGE NEUTRALITY – DOES IT EXIST?

Lynn S. Bennethum

Department of Mathematics, University of Colorado at Denver

Lynn.Bennethum@cudenver.edu

Abstract In a thermodynamic framework which exploits the entropy inequality to obtain constitutive equations, it is common practice to assume charge neutrality and enforce this restriction using Lagrange multipliers. In this paper we show that the Lagrange multiplier used to enforce charge neutrality does not correspond to any known physical parameter, raising the question of whether charge neutrality can really be enforced.

Introduction

One method for developing a model for complex porous materials with multiple phases, constituents, and charges, is to use first principles and build it based on conservation laws and the second law of thermodynamics. Within this formulation it has been frequently assumed (including by this author) that charge neutrality holds [14, 13, 15, 5], with this condition being forced via a Lagrange multiplier. The interpretation of the Lagrange multiplier is that it is associated with the electrical potential. In this paper, a Hybrid Mixture Theory (HMT) formulation is used to show that the Lagrange multiplier does not appear to be associated with anything physical.

As a reference to something more familiar, consider the case of a fluid where incompressibility is enforced via a Lagrange multiplier. For a stokesian fluid, it is assumed that the constitutive variables (stress, energy, heat flux) are a function of density, ρ , temperature, T , rate of deformation tensor, \mathbf{d} , and possibly other variables (such as the gradients of density and temperature). Exploiting the entropy inequality in this framework produces the following constitutive restriction for the Cauchy stress tensor [10]

$$\mathbf{t} = -p\mathbf{I} + \mathbf{f}_D(\mathbf{d}, \rho, T)$$

where p is the pressure defined thermodynamically in terms of the Helmholtz potential, A , as $p = -\frac{\partial A}{\partial \rho^{-1}}$. The tensor \mathbf{f} is a possibly nonlinear function of \mathbf{d} , ρ , and T , and must be zero at equilibrium. Compare this with the result of assuming incompressibility. In this case, ρ is not considered an independent variable, and the incompressibility is enforced with the Lagrange multiplier, λ . The resulting constitutive restriction for the Cauchy stress tensor is [10]

$$\mathbf{t} = -\lambda \mathbf{I} + \mathbf{f}_D(\mathbf{d}, \rho, T).$$

Similarly, in results for more complex media such as swelling porous media, it can be shown that the Lagrange multiplier appears exactly where the thermodynamic pressure appears in *every* relation derived from exploiting the entropy inequality [2, 3]. Thus we come to the conclusion that the Lagrange multiplier has the physical interpretation of pressure. It is this sort of relation which is sought when enforcing charge neutrality. We do this in the hybrid mixture theory setting.

Macroscale Field Equations

Hybrid mixture theory is a hybridization of classical volume averaging of field equations (conservation of mass, momenta, energy) and classical theory of mixtures [8] whose theory of constitution results from the exploitation of the entropy inequality in the sense of Coleman and Noll [9]. In [4] the microscale field equations for each species of each phase, modified appropriately to include charges, polarization, and an electric field, are averaged to the macroscale, defined to be the scale where the phases are indistinguishable. Thus at the macroscale the porous media is viewed a mixture, with each thermodynamic property for each constituent of each phase defined at each point in space.

To simplify the presentation, we limit this discussion to two phases, liquid and solid, with N constituents per phase, and restrict our discussion to results pertaining to the continuity equations and momenta balance. Interfacial effects are assumed negligible, although these effects have been incorporated into HMT [1, 12]. In [4] the following macroscale equations are derived.

Conservation of mass

The macroscopic mass balance for constituent j in phase α is

$$\frac{D^{\alpha_j}(\varepsilon^\alpha \rho^{\alpha_j})}{Dt} + \varepsilon^\alpha \rho^{\alpha_j} (\nabla \cdot \mathbf{v}^{\alpha_j}) = \sum_{\beta \neq \alpha} \varepsilon^\alpha \rho^{\alpha_j} \widehat{e}_\beta^{\alpha_j} + \varepsilon^\alpha \rho^{\alpha_j} \widehat{r}^{\alpha_j} \quad (1)$$

where $\frac{D^{\alpha_j}}{Dt}$ is the material time derivative given by

$$\frac{D^{\alpha_j}}{Dt} = \frac{\partial}{\partial t} + \mathbf{v}^{\alpha_j} \cdot \nabla, \quad (2)$$

\mathbf{v}^{α_j} is the mass averaged velocity of species α_j , ε^α is the volume fraction of phase α , \hat{r}^{α_j} is the rate of mass transfer to species j from other species due to chemical reactions, and $\hat{e}_\beta^{\alpha_j}$ represents the net rate of mass gained by constituent j in phase α from phase β . The bulk phase counterpart is obtained by summing over all constituents. The relationship between these macroscale variables and their microscale counterparts are given in [4].

Conservation of electric charge

The conservation of charge equation at the macroscale is

$$\begin{aligned} \nabla \cdot (\varepsilon^\alpha \mathcal{J}^{\alpha_j} + \varepsilon^\alpha q_e^{\alpha_j} \mathbf{v}^{\alpha_j}) + \frac{\partial}{\partial t} (\varepsilon^\alpha q_e^{\alpha_j}) = \varepsilon^\alpha \hat{q}^{\alpha_j} + \varepsilon^\alpha \rho^{\alpha_j} z^{\alpha_j} \hat{r}^{\alpha_j} \\ + \sum_{\beta \neq \alpha} \varepsilon^\alpha \rho^{\alpha_j} (\hat{Z}_\beta^{\alpha_j} + z^{\alpha_j} \hat{e}_\beta^{\alpha_j}) \end{aligned} \quad (3)$$

where z^{α_j} is the charge per unit mass, \mathcal{J}^{α_j} is the free current density in the material frame of reference, $q_e^{\alpha_j}$ is the charge density (per volume), and \hat{q}^{α_j} is the rate of gain of charge density due to the presence of other constituents but not due to chemical reactions. $\hat{Z}_\beta^{\alpha_j}$ represents the rate of exchange of charge of constituent j from phase β to phase α not due to mass exchange. Using the continuity equation, (1), equation (3) may be re-written as:

$$\varepsilon^\alpha \rho^{\alpha_j} \frac{D^{\alpha_j} z^{\alpha_j}}{Dt} + \nabla \cdot (\varepsilon^\alpha \mathcal{J}^{\alpha_j}) = \varepsilon^\alpha \hat{q}^{\alpha_j} + \sum_{\beta \neq \alpha} \varepsilon^\alpha \rho^{\alpha_j} \hat{Z}_\beta^{\alpha_j}. \quad (4)$$

Linear momentum balance

The macroscale linear momentum equation is given by

$$\begin{aligned} \varepsilon^\alpha \rho^{\alpha_j} \frac{D^{\alpha_j} \mathbf{v}^{\alpha_j}}{Dt} - \nabla \cdot (\varepsilon^\alpha \mathbf{t}^{\alpha_j}) - \varepsilon^\alpha \rho^{\alpha_j} \mathbf{g} - \varepsilon^\alpha q_e^{\alpha_j} \mathbf{E}_T \\ - \varepsilon^\alpha \mathbf{P}^{\alpha_j} \cdot \nabla \mathbf{E}_T = \varepsilon^\alpha \rho^{\alpha_j} \hat{\mathbf{i}}^{\alpha_j} + \sum_{\beta \neq \alpha} \varepsilon^\alpha \rho^{\alpha_j} \hat{\mathbf{T}}_\beta^{\alpha_j} \end{aligned} \quad (5)$$

where \mathbf{E}_T is the upscaled (total) electric field, \mathbf{P}^{α_j} is polarization density of species α_j , \mathbf{t}^{α_j} is the partial Cauchy stress tensor, \mathbf{g} is gravity, and $\hat{\mathbf{T}}_\beta^{\alpha_j}$ represents the effect constituent j of phase β has on the rate of change of mechanical momentum of the same constituent in phase α . The exchange

term, $\widehat{\mathbf{i}}^{\alpha_j}$, takes into account all gain of momenta due to the presence of other species but not due to chemical reactions. Note that unlike [11, 16] we assume it is the *total* electric field which contributes to the Lorentz and Kelvin forces.

Constitutive Equations and Comparison

The constitutive restrictions are obtained by assuming a set of independent variables (variables upon which the constitutive variables depend) and then exploiting the entropy inequality. We compare the results of not assuming charge neutrality (where the charge of each constituent is included in the list of independent variables) and enforcing charge neutrality using a Lagrange multiplier where the list of independent variables does not include the charge of each constituent, z^{α_j} . For a charged porous media we assume the independent variables (variables upon which the constitutive variables depend) include [4]

$$\begin{aligned} \varepsilon^l, \rho^{\alpha_j}, \mathbf{v}^{l,s}, \mathbf{v}^{\alpha_j,\alpha}, \mathbf{E}_T, z^{\alpha_j}, \\ \nabla \varepsilon^l, \nabla \rho^{\alpha_j}, \mathbf{d}^l, \nabla \mathbf{v}^{l_j,l}, \nabla \mathbf{E}_T, \quad j = 1, \dots, N, \quad \alpha = l, s, \end{aligned} \quad (6)$$

where $\mathbf{v}^{l,s} = \mathbf{v}^l - \mathbf{v}^s$ is the velocity of the liquid phase relative to the solid, $\mathbf{v}^{\alpha_j,\alpha} = \mathbf{v}^{\alpha_j} - \mathbf{v}^\alpha$ is the diffusive velocity of species α_j , and $\mathbf{d}^l = \frac{1}{2}(\nabla \mathbf{v}^l + (\nabla \mathbf{v}^l)^T)$ is the rate of deformation tensor.

Next we present the results of exploiting the entropy inequality which involve the Lagrange multiplier Λ , and/or the charge of a constituent, z^{α_j} . In each case, the first form is the result from enforcing charge neutrality:

$$\frac{D^s}{Dt} \left(\varepsilon^l q_e^l + \varepsilon^s q_e^s \right) = 0,$$

and the second form is the result of incorporating charge densities.

The constitutive form of the Cauchy stress tensors for the solid and liquid phases are [5]

$$\mathbf{t}^s = -(p^s - q_e^s \Lambda) \mathbf{I} + \mathbf{t}_e^s + \frac{\varepsilon^l}{\varepsilon^s} \mathbf{t}_s^l \quad \mathbf{t}^l = -(p^l - q_e^l \Lambda) \mathbf{I} + \mu \mathbf{d}^l \quad (7)$$

$$\mathbf{t}^s = -p^s \mathbf{I} + \mathbf{t}_e^s + \frac{\varepsilon^l}{\varepsilon^s} \mathbf{t}_s^l \quad \mathbf{t}^l = -p^l \mathbf{I} + \mu \mathbf{d}^l \quad (8)$$

where \mathbf{t}_e^s and \mathbf{t}_s^l are the effective stress and hydration stress tensors, respectively [7]. Note that in this case the Lagrange multiplier, Λ , has nothing which corresponds with it.

The electrochemical potential is defined as

$$\widetilde{\mu}^{\alpha_j} = \mu^{\alpha_j} - z^{\alpha_j} \Lambda \quad \widetilde{\mu}^{\alpha_j} = \mu^{\alpha_j} - z^{\alpha_j} \frac{\rho^\alpha}{\rho^{\alpha_j}} \frac{\partial A^\alpha}{\partial z^{\alpha_j}} \quad (9)$$

where $\mu^{\alpha_j} = \frac{\partial(\varepsilon^\alpha \rho^\alpha \widetilde{A}^\alpha)}{\partial(\varepsilon^\alpha \rho^{\alpha_j})}$ is the chemical potential and $\widetilde{A}^\alpha = A^\alpha - \frac{1}{\rho^\alpha} \mathbf{E}_T \cdot \mathbf{P}^\alpha$ is a modified Helmholtz free energy (per unit mass). This definition is chosen

so that (1) it is a scalar quantity representing change in energy due to change in quantity of species α_j , (2) the chemical potential of one species in two phases are equal at equilibrium, and (3) as much as possible it is the potential for diffusion [6]. In this definition we see that Λ corresponds to the change in energy with respect to charge density of a species. Note that if the charge density does not change (as in most processes not involving plasma), then this term is constant up to mass concentration.

With this definition of chemical potential, Fick’s law of diffusion (neglecting gravitational effects) becomes [4]

$$r^{l_{jj}} \mathbf{v}^{l_{j,l}} = -\varepsilon^l \rho^{l_j} \nabla \tilde{\mu}^{l_j} - \varepsilon^l \rho^{l_j} \Lambda \nabla z^{l_j} - \varepsilon^l \frac{\rho^{l_j}}{\rho^l} q_e^l \mathbf{E}_T - \sum_{i \neq j} r^{l_{ij}} \mathbf{v}^{l_{i,l}} - r^{l_j} \mathbf{v}^{l,s}$$

$$r^{l_{jj}} \mathbf{v}^{l_{j,l}} = -\varepsilon^l \rho^{l_j} \nabla \tilde{\mu}^{l_j} - z^{l_j} \nabla \left(\frac{\rho^l}{\rho^{l_j}} \frac{\partial \tilde{A}^l}{\partial z^{l_j}} \right) - \varepsilon^l \frac{\rho^{l_j}}{\rho^l} q_e^l \mathbf{E}_T$$

$$- \sum_{i \neq j} r^{l_{ij}} \mathbf{v}^{l_{i,l}} - r^{l_j} \mathbf{v}^{l,s}$$

where $r^{l_{ij}}$ and r^{l_j} are material coefficients which satisfy the Onsager relationship. The terms involving $r^{l_{ij}}$ account for coupling due to hydration of charged particles. Thus the principal driving force is the electrochemical potential as defined in (9).

Another place the Lagrange multiplier appears is in Darcy’s Law, the equation which governs the rate of flow through porous media. In this formulation we get

$$R \mathbf{v}^{l,s} = -\varepsilon^l \nabla p^l - \pi^l \nabla \varepsilon^l + \varepsilon^l \rho^l \mathbf{g} + \varepsilon^l q_e^l \nabla \Lambda + \varepsilon^l q_e^l \mathbf{E}_T \quad (10)$$

$$R \mathbf{v}^{l,s} = -\varepsilon^l \nabla p^l - \pi^l \nabla \varepsilon^l + \varepsilon^l \rho^l \mathbf{g} + \varepsilon^l q_e^l \mathbf{E}_T \quad (11)$$

where $\pi^l = \varepsilon^l \rho^l \frac{\partial \tilde{A}^l}{\partial \varepsilon^l}$ is a swelling potential which measures the affinity the solid and liquid have for each other [7]. So in both Fick’s and Darcy’s law, there is nothing which clearly correspondence to the Lagrange multiplier.

Conclusion

Unlike the case of an incompressible fluid where the Lagrange multiplier used to enforce incompressibility weakly can be associated with the pressure, there is no such correlation for the Lagrange multiplier enforcing charge neutrality. The resulting Lagrange multiplier at times appears to be associated with the electric potential part of the chemoelectric potential, and at other times has no clear correlation at all.

As a side remark, the most consistent form of the thermodynamic definition of the electrochemical potential is

$$\tilde{\mu}^{\alpha_j} = \mu^{\alpha_j} - z^{\alpha_j} \frac{\rho^\alpha}{\rho^{\alpha_j}} \frac{\partial A^\alpha}{\partial z^{\alpha_j}}$$

so that unless a species changes charge in the process, the electrochemical potential is simply

$$\tilde{\mu}^{\alpha_j} = \mu^{\alpha_j} = \frac{(\varepsilon^\alpha \rho^\alpha \tilde{A}^\alpha)}{\partial(\varepsilon^\alpha \rho^{\alpha_j})},$$

i.e. the energy required to insert a particle into the system accounting for density *and* charge. The particular constitutive equation for the electrochemical potential can then include both the chemical part and the part due to charge.

References

- [1] Achanta, S., Cushman, J.H. and Okos, M.R. (1994) On multicomponent, multiphase thermomechanics with interfaces, *International Journal of Engineering Science* **32**(11), 1717-1738
- [2] Bennethum, L.S. (1994) Multiscale, hybrid mixture theory for swelling systems with interfaces, PhD thesis, Purdue University, West Lafayette, 47907.
- [3] Bennethum, L.S. and Cushman, J.H. (1996) Multiscale, hybrid mixture theory for swelling systems - II: Constitutive theory, *International Journal of Engineering Science* **34**(2), 147-169
- [4] Bennethum, L.S. and Cushman, J.H. (2002) Multicomponent, multiphase thermodynamics of swelling porous media with electroquasistatics: I. Macroscale field equations, *Transport in Porous Media*, **47**(3), 309-336
- [5] Bennethum, L.S. and Cushman, J.H. (2002) Multicomponent, multiphase thermodynamics of swelling porous media with electroquasistatics: II. Constitutive theory, *Transport in Porous Media* **47**(3), 337-362
- [6] Bennethum, L.S., Murad, M.A., and Cushman, J.H. (2000) Macroscale thermodynamics and the chemical potential for swelling porous media *Transport in Porous Media* **39**(2), 187-225
- [7] Bennethum, L.S. and Weinstein, T. (2002) Three pressures in porous media *Transport in Porous Media*, To Appear.
- [8] Bowen, R.M. (1971) *Theory of Mixtures*, in: Continuum physics Vol. 3, ed. Eringen, A.C. Academic Press, New York
- [9] Coleman, B.D. and Noll, W. (1963) The thermodynamics of elastic materials with heat conduction and viscosity, *Archive for Rational Mechanics and Analysis* **13**, 167-178
- [10] Eringen, A.C. (1967) *Mechanics of Continua*, John Wiley and Sons, New York
- [11] Eringen, A.C. (1998) A mixture theory of electromagnetism and superconductivity, *International Journal of Engineering Science* **36**(5,6), 525-543
- [12] Gray, W.G. (1999) Thermodynamics and constitutive theory for multiphase porous-media flow considering internal geometric constraints, *Advances in Water Resources* **22**(5), 521-547

- [13] Gu, W.Y., Lai, W.M., and Mow, V.C. (1999) Transport of multi-electrolytes in charged hydrated biological soft tissues, *Transport in Porous Media* **34**, 143-157
- [14] Gu, W.Y., Lai, W.M., and Mow, V.C. (1998) A mixture theory for charged-hydrated soft tissues containing multi-electrolytes: Passive transport and swelling behaviors, *Journal of Biomechanical Engineering* **120**, 169-180
- [15] Huyghe, J.M. and Janssen, J.D. (1999) Thermo-chemo-electro-mechanical formulation of saturated charged porous solids, *Transport in Porous Media* **34**, 129-141
- [16] Kelly, P.D. (1964) A reacting continuum, *International Journal of Engineering Science* **2**, 129-153

SHRINKING AND CRACKING OF SWELLING POROUS MEDIA

Pieter H. Groenevelt
University of Guelph
Guelph, Ontario, Canada
pgroenev@lrs.uoguelph.ca

Abstract Volume reduction of wet non-rigid porous media is at first “normal”, i.e. the void ratio reduction is equal to the moisture ratio reduction. Upon air entry, with or without cracking, and further drying, several stages of shrinkage can usually be observed, such as “structural”, “proportional”, and “zero” shrinkage. The complete shrinkage phenomenon, from the saturated to the oven-dry state, can be accurately modelled using the Groenevelt-Bolt constitutive shrinkage equation [2]. The first derivative of this equation (slope) provides the tool to predict how the water potential will change upon loading the porous body. The second derivative (curvature) provides the tool to separate the different stages of shrinkage. The location of these separation points reveals important structural properties of the porous body. Experimental data for swelling soils will be used to demonstrate several principles and practical implications.

Keywords: shrinkage curves, loading, bimodal shrinkage

Introduction

The shrinking and cracking of porous and colloidal materials, such as clays, tooth paste, cheese, shoe polish, and clay-rich soils has important physical and economical consequences. First we present a general schematic diagram of the shrinking and cracking process of such a medium under atmospheric pressure (zero load pressure). The model follows the shrinkage process from the state where the medium is fully swollen, along the drying range where the medium stays saturated (normal shrinkage), to the cracking (air-entry) point. Upon further drying the model describes the ranges of “structural”, “proportional”, “residual” and “zero” shrinkage. Subsequently we model the bundle of shrinkage curves for which the lines are for different load (overburden) pressures. Finally we present a procedure to model the behaviour of media that exhibit bi-modal shrinkage.

General Shrinkage Diagram for Unloaded Porous Media

The theoretical development by Groenevelt and Bolt [2] provides the following equation for the bundle of shrinkage curves for which the lines are for different load (overburden) pressures, P

$$\zeta(e) = [k_2(e^n P - k_1)[k_2 P + \ln[(e - \epsilon)k_3^{-1} + \exp(-k_1 k_2 \epsilon^{-n})]]^{-1}]^{\frac{1}{n}}, \quad (1)$$

where ζ is the moisture ratio (volume water / volume solids), e is the void ratio (volume voids / volume solids), P is the load pressure, ϵ is the void ratio at air entry, and k_1 , k_2 , k_3 , and n are fitting parameters. For unloaded (“unburdened”) soil the load pressure $P = 0$ and (1) can be inverted, such that the void ratio e appears explicitly:

$$e(\zeta) = \epsilon + k_3 \left(\exp - \left(\frac{k_0}{\zeta^n} \right) - \exp - \left(\frac{k_0}{\epsilon^n} \right) \right), \quad (2)$$

where n , $k_0 = k_1 k_2$, and k_3 are dimensionless fitting parameters. Differentiation of eqn. (2) produces the slope, $\sigma(\zeta)$, of the shrinkage curve:

$$\sigma(\zeta) = k_3 \frac{k_0}{\zeta^n} \frac{n}{\zeta} \exp \frac{-k_0}{\zeta^n} \quad (3)$$

Differentiation of eqn. (3) produces the curvature, $\kappa(\zeta)$, of the shrinkage curve:

$$\kappa(\zeta) = k_3 \frac{k_0}{\zeta^n} \frac{n}{\zeta} \left(\frac{n \frac{k_0}{\zeta^n} - n - 1}{\zeta} \right) \exp \frac{-k_0}{\zeta^n} \quad (4)$$

For the wet part of the shrinkage curve the curvature is negative. In order to show this part of the curvature line in the diagram, we reverse the sign, i.e. in effect we plot the absolute value of κ . By differentiating eqn. (4) and setting the result equal to zero, one finds the locations where the absolute values of the curvature are maximal:

$$\zeta_{\text{wet}}^{\text{dry}} = [(2nk_0)[3(n+1)]^{\frac{+}{-}} [9(n+1)^2 - 4(n+1)(n+2)]^{0.5}]^{-1}]^{\frac{1}{n}} \quad (5)$$

The location of the absolute value of the maximum curvature at the wet end can be used to separate the regions of “structural” and “proportional” shrinkage [3]. The location of the maximum curvature at the dry end can be used to separate the regions of “proportional” and “zero” shrinkage [4]. A general diagram of the shrinkage curve with its derivatives is presented in Fig. 1.

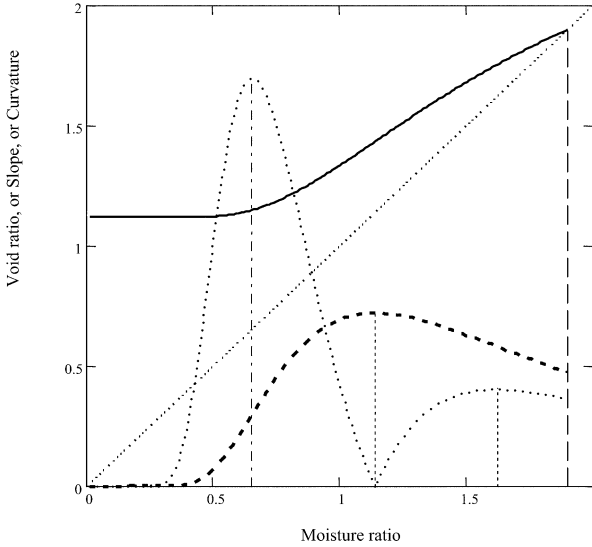


Figure 1. General diagram of the shrinkage curve and its derivatives. On the horizontal axis is the moisture ratio (volume of water per unit volume of solids, dimensionless). On the vertical axis is, for the solid line (the shrinkage curve), the void ratio (volume of voids per unit volume of solids, dimensionless), and, for the broken line, the value of the slope of the shrinkage curve (dimensionless), and, for the dotted line, the absolute value of the curvature of the shrinkage curve (dimensionless). The following values were used for the parameters: $k_0 = 2$, $k_3 = 1.6$, $n = 1.6$, and $\epsilon = 1.9$.

Examples of unloaded shrinkage curves

We analyse here the sets for two of the six British clay-rich cracking subsoils presented by [7], which they removed from under their overburdens, such that $P = 0$. The results are shown in Figs. 2 and 3. The magnitude of the structural shrinkage that occurs upon drying just after air entry is a clear indicator of the structural quality of a clay soil. The extent of the structural shrinkage can easily be seen from the distance between the shrinkage curve to the 1:1 line. The larger this distance, the larger the amount of air that is present in the soil during water extraction by plant roots, and thus, the higher the structural quality of the soil. From the above two graphs it can be seen that the structural quality of Wyre Bw soil is far superior to that of Fladbury soil. The slope of the shrinkage curve, $\sigma(\zeta)$, can be used to calculate the overburden potential, Ω [1], which is defined as:

$$\Omega = p - p_{\text{unloaded}} \tag{6}$$

where p is the actual matric potential, while the medium is under a load (overburden) pressure P , and p_{unloaded} is the matric potential that would be observed if the load were removed. The overburden potential $\Omega(\zeta)$ can be calcu-

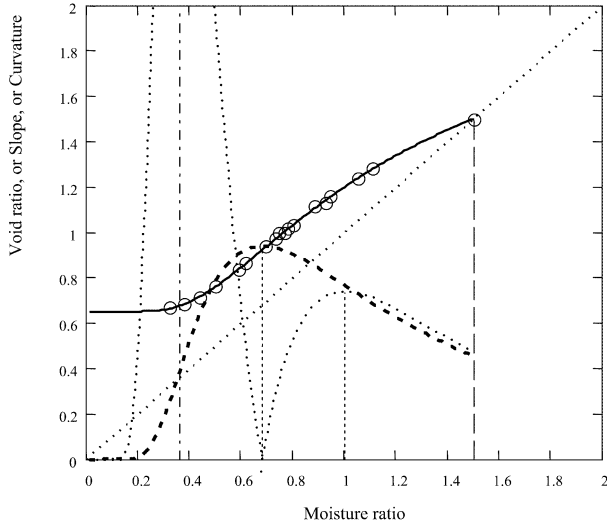


Figure 2. Shrinkage diagram for Wyre Bw soil (data points from [7], showing the shrinkage curve (solid line), with its first derivative (broken line) and its second derivative (dotted line). The following values were used for the parameters: $k_0 = 1.025$, $k_3 = 1.531$, $n = 1.361$, and $\epsilon = 1.500$.

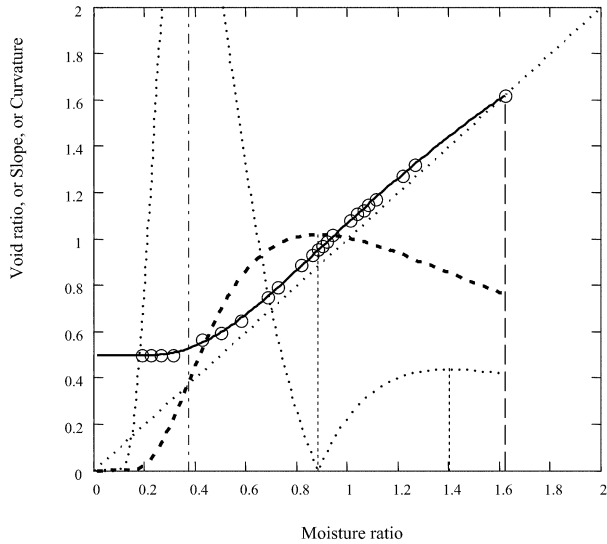


Figure 3. Shrinkage diagram for Fladbury soil (data points from [7], showing the shrinkage curve (solid line), with its first derivative (broken line) and its second derivative (dotted line). The following values were used for the parameters: $k_0 = 1.790$, $k_3 = 3.436$, $n = 0.977$, and $\epsilon = 1.620$.

lated from:

$$\Omega(\zeta) = P\sigma(\zeta) \tag{7}$$

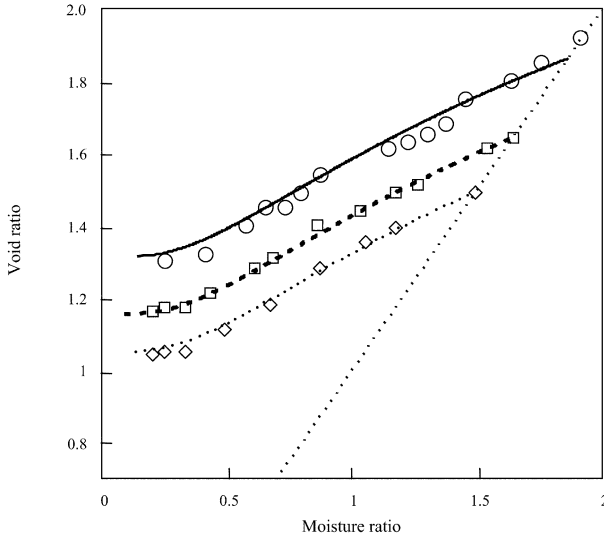


Figure 4. Shrinkage curves for a remolded clay soil under different load (overburden) pressures (data points from [8]: The following values were used for the parameters: $k_1 = 1\text{MPa}$, $k_2 = 2\text{MPa}_{-1}$, $k_3 = 2$ and $n = 0.7$. The circles and the solid line are the shrinkage data and the shrinkage curve for the unloaded soil ($P = 0$) with $\epsilon = 1.860$. The boxes and the broken line are the shrinkage data and the shrinkage curve for the soil under a load pressure of 63 mbar ($P = 0.0063\text{MPa}$) with $\epsilon = 1.640$. The diamonds and the dotted line are the shrinkage data and the shrinkage curve for the soil under a load pressure of 112 mbar ($P = 0.0112\text{MPa}$) with $\epsilon = 1.490$.

A complete bundle of shrinkage curves under different loads

A data set provided by [8] was analysed using the general Groenevelt-Bolt [2] shrinkage equation (1) [6]. The results are shown in Fig. 4.

Submodels

The general model was built up from the following sub-models, [2] 1. The load pressure in saturated porous media is the sum of the matric pressure p and the swelling pressure Π :

$$P = p + \Pi \tag{8}$$

2. The swelling pressure Π is, under saturated conditions, a function of the void ratio e according to

$$\Pi = k_1 e^{-n} \tag{9}$$

3. The void ratio at air entry e_{ae} is a function of the load pressure P and the void ratio e_{ae0} at air entry for $P = 0$, according to

$$e_{ae} = e_{ae0} \exp(-k_2 P) \tag{10}$$

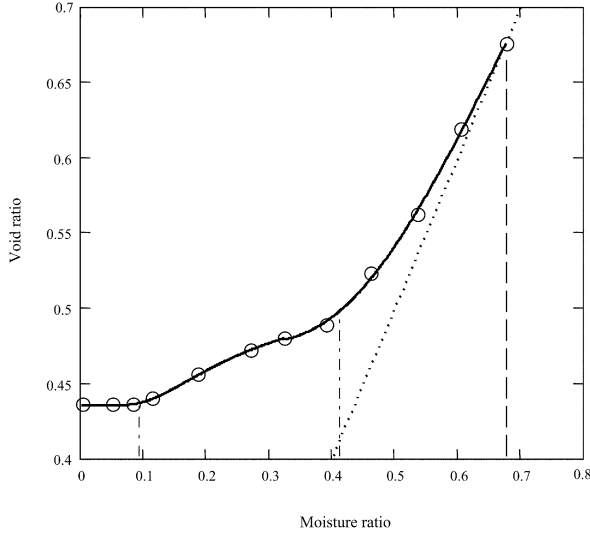


Figure 5. Shrinkage curve for Nunn clay loam mixed with 10 percent sand (data points from [9] with bimodal curve fitting: For the wet part of the curve the following values were used for the parameters: $k_0 = 0.859$, $k_3 = 1.061$, $n = 1.695$ and $\epsilon = 0.676$. For the dry part of the curve the following values were used for the parameters: $k_0 = 0.111$, $k_3 = 0.082$, $n = 1.513$ and $\epsilon = 0.495$.

4. The extent of the residual shrinkage, $e_{ae} - e_{\zeta=0}$, is related to the swelling pressure at air entry according to

$$e_{ae} - e_{\zeta=0} = k_3 \exp(-k_2 \Pi_{ae}) \tag{11}$$

5. The shape of the residual shrinkage curve behaves according to

$$(e - e_0) = k_3 \exp[-k_2 \left[1 + \frac{e_{ae}^n - e^n}{\zeta^n} \right] P - \frac{\zeta_{ae}^n}{\zeta^n} p_{ae}] \tag{12}$$

These sub-models deserve closer inspection and refinement.

Bi-modal Shrinkage Processes

Experimental data [9, 10] sometimes clearly show the onset of a secondary shrinkage process while the primary shrinkage process is underway. By using equation (2) for the wet end and the dry end separately one obtains an excellent fit (Fig. 5) for the complete data set [5] and can use the fitting parameters and the curvature maxima for the identification of the two shrinkage phenomena.

Discussion and Conclusions

The analysis of shrinkage data reveals important characteristics of the porous medium of concern [1]. These characteristics include the onset of cracking

(air entry), which is of interest to the ceramics and the food industry, and the volumetric air content during the stage of proportional shrinkage of swelling soils, where water consumption by crops is of utmost importance.

Acknowledgments

The author wishes to thank the International Union of Theoretical and Applied Mechanics for financial support to attend the Symposium in Kerkrade.

References

- [1] Grant, C.D., Groenevelt, P.H. and Bolt, G.H. (2002) On hydrostatics and matristatics of swelling soils. In: Raats, P.A.C., Smiles, D. and Warrick, A.W. (eds.). *Environmental Mechanics. Water, Mass and Energy Transfer in the Biosphere (The Philip Volume)*, Geophysical Monograph **129**, pp 95-105, American Geophysical Union, Wasinghton, DC
- [2] Groenevelt, P.H. and Bolt, G.H. (1972) Water retention in soil. *Soil Sci.* **113**, 238-245
- [3] Groenevelt, P.H. and Grant, C.D. (2001) Re-evaluation of the structural properties of some British swelling soils. *European J. Soil Sci.* **52**, 469-477
- [4] Groenevelt, P.H. and Grant, C.D. (2002) Curvature of shrinkage lines in relation to the consistency and structure of a Norwegian clay soil. *Geoderma* **106**, 235-245
- [5] Groenevelt, P.H. and Grant, C.D. (2004) Analysis of shrinkage data. *Soil and Tillage Research* (In Print)
- [6] Groenevelt, P.H., Grant, C.D. and Semetsa, S. (2001) A new procedure to determine soil water availability. *Austr. J. Soil Res.* **39**, 577-598
- [7] Reeve, M.J. and Hall, D.G.M. (1978) Shrinkage in clayey subsoils of contrasting structure. *J. Soil Sci.* **29**, 315-323
- [8] Talsma, T. (1977) A note on the shrinkage behaviour of a clay paste under various loads. *Aust. J. Soil Res.* **15**, 275-277
- [9] Tariq, A.U.R. and Durnford, D.S. (1993) Soil volume shrinkage measurements: A simple method. *Soil Sci.* **155**, 325-330
- [10] Tariq, A.U.R. and Durnford, D.S. (1993) Analytical volume change model for swelling clay soils. *Soil Sci. Soc. Am. J.* **57**, 1183-1187

MODELLING OF CHEMICAL OSMOSIS IN CLAY

Sam Bader and Ruud J. Schotting

TU Delft, Faculty of Civil Engineering and Technical Geosciences,

Section for Hydrology

s.bader@citg.tudelft.nl, r.j.schotting@citg.tudelft.nl

Abstract An alternative formulation of the model for chemical osmosis in clay membranes is presented. It is shown that it exhibits the correct behaviour for limiting values of the reflection coefficient. The model results compare reasonably well with experimental data and a method is developed to obtain analytical solutions that agree in most cases with results derived from numerical simulations.

Keywords: chemical osmosis, reflection coefficient, analytical modelling

Introduction

When a compacted clayey soil is subjected to a considerable salt concentration gradient, groundwater flowing through the soil is not only driven by hydraulic gradients, but by chemical and electrical gradients as well. These processes are called chemical- and electro-osmosis, respectively. They may be of importance in, for instance, the evaluation of contaminant leakage of waste of high salt concentration from disposal sites with clay as an impermeable liner.

In 2001, the Netherlands Organization for Scientific Research (NWO) started a project called ‘Chemically and electrically coupled transport in clayey soils and sediments’ to quantify the role of chemically and electrically coupled transport in clayey soils and to assess its relevance for the distribution and emission of contaminants and water. The project involves three Ph.D. students working on field and laboratory experiments and modelling of chemical- and electro-osmosis.

In this paper, a continuum model for chemical osmosis in clay membranes is presented and its novel features, as compared to previous formulations are shown. A simplified version of the model, that allows for analytical solutions, is presented, and an application of this method is shown.

Theory

In general, the flow of water due to a chemical potential gradient is called chemical osmosis. When compacted, clay can act as a semi-permeable membrane due to overlapping diffuse double layers. This means that the movement of solute particles is restricted across the membrane, while solvent is free to flow. To attain chemical equilibrium in case of an initial concentration gradient across the clay, water flows from low to high salt concentration. The degree of semi-permeability is described by the reflection coefficient σ , which ranges from 0 (no osmosis) to 1 (no solute transport).

The description of coupled flow and transport phenomena is usually based on non-equilibrium thermodynamics [2]. Application of this theory leads to a set of linear equations, relating all thermodynamical fluxes \mathbf{J}_i to all thermodynamical forces \mathbf{X}_j in a system:

$$\mathbf{J}_i = \sum_j L_{ij} \mathbf{X}_j. \quad (1)$$

The coefficients L_{ij} are called the coupling coefficients and are assumed to obey the so-called Onsager reciprocity relations $L_{ij} = L_{ji}$.

In a soil system, the relevant coupled processes that influence groundwater flow and solute transport arise from hydraulic, chemical, electrical and thermal driving forces, see Table 1.

Table 1. Direct and coupled flow phenomena

	<i>gradient $\mathbf{X} \rightarrow$</i>			
<i>flow $\mathbf{J} \downarrow$</i>	hydraulic	chemical	electrical	temperature
fluid	hydraulic flow	chemical osmosis	electro-osmosis	thermo-osmosis
ion	streaming current	diffusion	electrophoresis	Soret effect
current	Rouss effect	diffusion pot.	electrical cond.	Seebeck effect
heat	conv. heat flow	Dufour effect	Peltier effect	thermal cond.

If we consider only chemical and hydraulic processes, the equations (1) for specific discharge \mathbf{q} and solute mass flux relative to the solution \mathbf{J}_m^d in terms of gradients of pressure p and salt mass fraction ω_s reduce to [1]

$$\mathbf{q} = -(k/\mu)\nabla p + \lambda\rho_f\nabla\omega_s, \quad (2)$$

$$\mathbf{J}_m^d = -\sigma\rho_f\omega_s\mathbf{q} - D\rho_f\nabla\omega_s. \quad (3)$$

Here, k is the permeability of the porous medium and μ is the dynamic viscosity; ρ_f is the fluid density, and $\lambda = (k/\mu)\sigma\frac{RTd_s}{M_s}$, where R is the universal gas

constant, T is temperature, d_s is a salt dissociation factor, and M_s the molar mass of the solute. The diffusion coefficient D should vanish for $\sigma = 1$, so we assume $D = D_0(1 - \sigma)$, with D_0 a Fickian diffusion coefficient; this is called implicit coupling [5]. The expressions for \mathbf{q} and \mathbf{J}_m^d reduce to Darcy's law and Fick's law, respectively, for $\sigma = 0$.

The difference with other formulations [5, 7] resides mainly in the expression for solute flux relative to the solution. If we consider the solute mass flux \mathbf{J}_m relative to the porous medium:

$$\mathbf{J}_m = \mathbf{J}_m^d + \rho_f \omega_s \mathbf{q} = (1 - \sigma) \rho_f \omega_s \mathbf{q} - D_0(1 - \sigma) \rho_f \nabla \omega_s, \quad (4)$$

we see that for $\sigma = 1$, \mathbf{J}_m vanishes, as it should. This is not the case in other formulations.

The mass balances for the fluid and the salt are:

$$\frac{\partial n \rho_f}{\partial t} + \nabla \cdot (\rho_f \mathbf{q}) = 0, \quad (5)$$

$$\frac{\partial n \rho_f \omega_s}{\partial t} + \nabla \cdot \mathbf{J}_m = 0, \quad (6)$$

where n is the porosity.

In combination with the flux equations and appropriate equations of state, (5) and (6) constitute the full set of model equations accounting for chemical osmosis in groundwater flow and solute transport.

Analysis

Substitution of the flux equations and the equations of state in the equations for the mass balance leads to set of non-linear differential equations. Dimensional analysis [1] shows that these equations, expressed in terms of pressure and concentration, can be reduced to a simple form when the storage parameters, i.e. soil compressibility α and liquid compressibility β , are relatively small:

$$n S_s \frac{\partial p}{\partial t} = \frac{k}{\mu} \frac{\partial^2 p}{\partial x^2} - \lambda M_s \frac{\partial^2 c}{\partial x^2}, \quad (7)$$

$$n \frac{\partial c}{\partial t} = D \frac{\partial^2 c}{\partial x^2}, \quad (8)$$

where $S_s = \beta + \alpha/n$ is an effective storage parameter.

Introduction of a new variable $\phi = \frac{k}{\mu} p - \frac{\lambda}{1-\epsilon} c$ allows one to rewrite (7) and (8) into

$$\frac{\partial \phi}{\partial t} = \delta \frac{\partial^2 \phi}{\partial x^2} \quad (9)$$

with $\delta = \frac{k/\mu}{nS_s}$. Using the equations (8) and (9), exact solutions can be obtained for various experimental situations. The analytical results can be exploited to investigate model behaviour and to examine results of numerical simulations. As an application, it can be shown that the model yields the expected pressure profile for limiting values of σ as depicted in Katchalsky and Curran (1965). Consider an infinite domain that consists of a clay ($x \leq 0$, with initial concentration c_i ; the subscript 1 refers to this region) and a porous medium without membrane behaviour ($x > 0$, with initial concentration 0). Due to chemical osmosis, water will be drawn into the clay. When the clay is ideal ($\sigma = 1$), pressure will build up in the clay up to an asymptotic value. However, when the clay is not entirely restrictive ($0 < \sigma < 1$), pressure will build up, reach a maximum value, and decline. This is shown with an (intuitive) picture in e.g. Katchalsky and Curran (1965), but using our model the exact solution of the pressure p_1 in the clay leads to a similar graph; this solution reads

$$p_1 = A_1 \operatorname{erfc} \left(\frac{-x}{2\sqrt{\delta_1 t}} \right) - A_2 \operatorname{erfc} \left(\frac{-x}{2\sqrt{D_1 t}} \right), \quad (10)$$

where

$$A_1 = \frac{\lambda c_i \mu}{k_1} \left(1 + \frac{\sqrt{S_{s1} \mu D_1 k_1}}{k_2} \right), \quad A_2 = \frac{\lambda c_i}{\left(\frac{k_1}{\mu} - S_{s1} D_1 \right) \left(1 + \frac{k_1}{k_2} \right)} \quad (11)$$

Figure 1 shows this solution for $0 < \sigma < 1$ and $\sigma = 1$ ($D_1 = 0$). The parameters used were the same as in the analysis in the next paragraph, see Table 2, except for the concentration and storage coefficient in the porous medium: $c_{i2} = 0$, $S_{s2} = 4.6 \cdot 10^{-10}$ and the storage coefficient in the clay, i.e. $S_{s1} = 10^{-6}$. Figure 1 shows that the model supports the limiting behaviour for σ .

Comparison with Experiments

The full set of equations was used to model experiments from the literature using numerical methods. In one of these experiments [3], a clay sample in a flexible wall permeameter was subjected to a salt concentration gradient and salinity and pressure profiles were measured. In [4], a scripted finite element solver was used to provide numerical simulations. Using a least mean squares fit, the storage parameter and the reflection coefficient were inferred from the experimental data. Relevant parameters for this experiment are shown in Table 2.

The numerical results were compared with analytical expressions, derived from the simplified set of equations. In Figure 2, it is shown that modelling

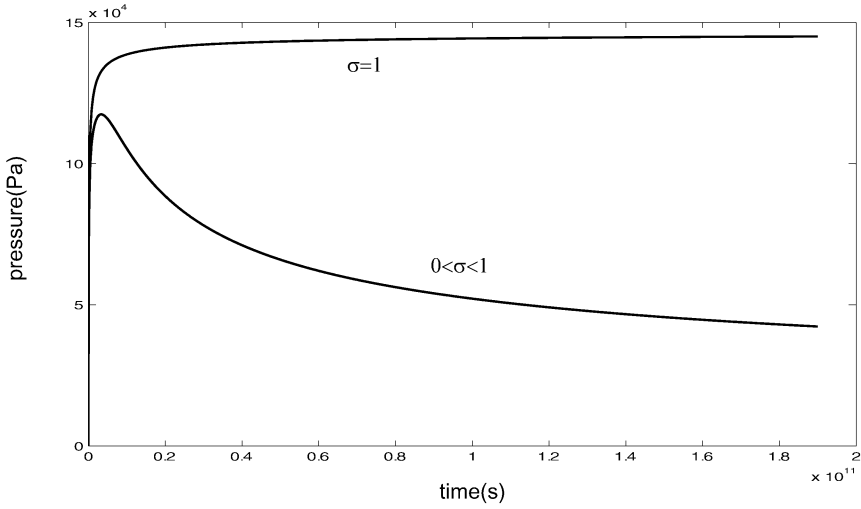


Figure 1. Pressure evolution in clay for an infinite composite domain

Table 2. Parameters Keijzer model

parameter	value in clay
c_i (mol/l)	0.1
n	0.56
$k(m^2)$	$1.2 \cdot 10^{-19}$
$D(m^2/s)$	$2.6 \cdot 10^{-13}$
$T(^{\circ}C)$	25
$S_s(1/Pa)$	$1 \cdot 10^{-8}$
ϵ	$1.0 \cdot 10^{-6}$
σ	0.019
λ	$1.85 \cdot 10^{-13}$

parameter	value in porous stone
c_i (mol/l)	0.1 (left) 0.01 (right)
n	0.5
$k(m^2)$	$1 \cdot 10^{-13}$
$D(m^2/s)$	$1.2 \cdot 10^{-10}$
$S_s(1/Pa)$	$3.4 \cdot 10^{-6}$

results coincide reasonably well with experimental data and that numerical and analytical graphs show excellent mutual agreement.

Because the storage parameters were small, the approximation that led to the simplified model, was valid.

In another experiment [6] that was modelled, salinity and pressure profiles were measured in a field situation. Results of this modelling exercise showed indeed that when the storage parameters are significant, the approximation does not hold.

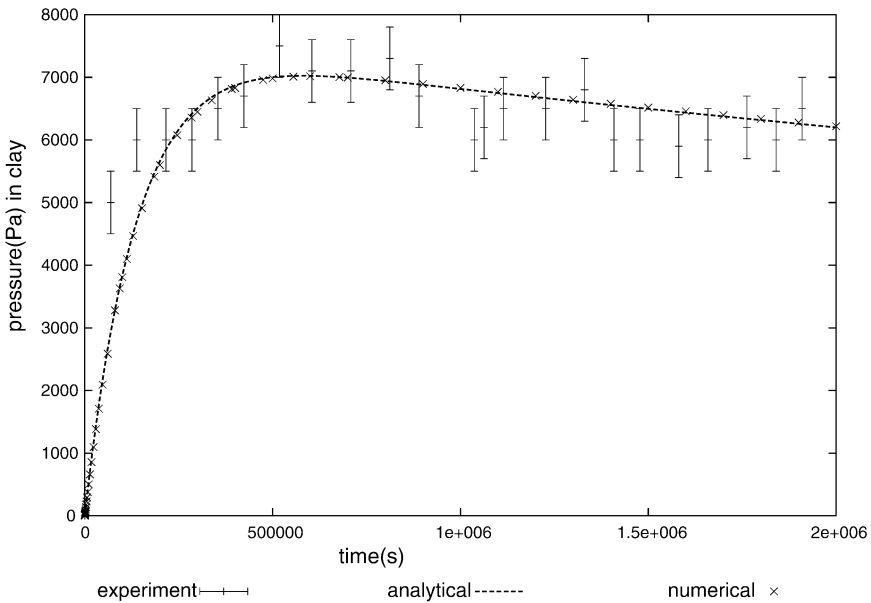


Figure 2. Pressure evolution: Keijzer experiment

Discussion

The results of the model that was presented compare rather well with experimental data; moreover, they were shown to be consistent with the expected behaviour for limiting values of the reflection coefficient σ . The analytical approximation that was used to obtain exact solutions holds solely for situations where the storage behaviour is minimal.

Aside from chemical osmosis, we have also been studying electro-osmosis and streaming potential, i.e. electrical current due to an hydraulic gradient. Within the research project, experimental results have been obtained for these phenomena that will be compared with modelling data to eventually acquire a combined model for chemico-electro-osmotic phenomena in groundwater.

References

- [1] Bader, S. (2003) Modelling of chemical osmosis across clay membranes: comparison with experiments, submitted to *Advances in Water Resources*
- [2] Katchalsky, A. and Curran. P.F. (1965) *Nonequilibrium thermodynamics in biophysics*, Harvard University Press, Cambridge, MA
- [3] Keijzer, T.J.S. (2000) *Chemical osmosis in natural clayey materials*, Ph.D. thesis, University of Utrecht

- [4] Kooi, H., Garavito, A.M. and Bader, S. (2003) Numerical modelling of chemical osmosis and ultrafiltration across clay formations, *Journal of Geochemical Exploration* **78-79**, 333-336
- [5] Malusis, M.A. and Shackelford, C.D. (2002) Theory for reactive solute transport through clay membrane barriers, *Journal of Contaminant Hydrology* **59**(3,4), 291-316
- [6] Neuzil, C.E. (2000) Osmotic generation of 'anomalous' fluid pressures in geological environments, *Nature* **403**, 182-184
- [7] Yeung, A.T. and Mitchell, K.J. (1993) Coupled fluid, electrical and chemical flows in soil, *Geotechnique* **43**, 121-134

COUPLING BETWEEN CHEMICAL AND ELECTRICAL OSMOSIS IN CLAYS

J.P. Gustav Loch, Katja Richter and Thomas J.S. Keijzer

*Department of Geochemistry, Faculty of Earth Sciences, Utrecht University
P.O. Box 80021, 3508TA Utrecht, The Netherlands*

e-mail: jvgl@geo.uu.nl

Abstract A permeameter was developed for measurement of coupled flow phenomena in clayey materials. Results are presented on streaming potentials in a Na-bentonite induced by hydraulic flow of electrolyte solutions. Transport coefficients are derived from the experiments, assuming the theory of irreversible thermodynamics to be applicable. Hydraulic and electro-osmotic conductivities are consistent with data reported elsewhere. However the electrical conductivity of the clay is substantially lower. This is ascribed to the high compaction of the clay resulting in overlap of double layers

Keywords: coupled flow, irreversible thermodynamics, bentonite, clay, streaming potential

Introduction

Clays are generally considered to be effective barriers for flow of water and solutes due to their low permeability and high ion adsorption capacity. However, as environmental criteria for the emission of contaminants and water from clay barriers become increasingly stringent, it is crucial to be aware of all relevant driving forces and fluxes and to take them into account in model assessments. In this respect the processes of chemical and electro-osmosis may not be neglected in clayey materials of hydraulic conductivity $< 10^{-9}$ m/s [7]. At these low conductivities the surface charge of the clay particles and the counter-ion accumulation in diffuse double layers enable explanation and quantification of osmotic processes and semi-permeability in clays [1].

During flow of water in clays, be it driven by hydraulic or chemical osmotic gradients, streaming potentials are being induced due to the accumulation of cations near the particle surfaces. Depending on the thickness of these diffuse double layers, part of the excess countercharge is mobile, causing an electric potential gradient in the clay, provided electrical shorting is absent. Thus downstream movement of cations becomes hampered, which counteracts

the movement of water molecules [3, 7]. In laboratory experiments on both bentonite clay and clayey dredging sludge, [6] applied a gradient of salt concentration across a thin slab of material and observed the resulting osmotic water flow. Since the end faces of their samples were electrically shorted, induction of a streaming potential gradient was prevented. Thus counterflow of water was excluded. However in the field, and in most laboratory permeameters, clays are not electrically shorted and electro-osmotic counterflow of water may become relevant.

The present study is aimed at assessing the magnitude of the counterflow of water in bentonite clay, using a permeameter without short-circuiting the clay. In the experiments presented here water flow is initiated by a hydraulic gradient. By using the theory of irreversible thermodynamics, the counterflow by induced electro-osmosis, quantified in this paper, will provide an indication of the effect of active application of electro-osmosis in the clay.

Theory and Literature

In the absence of gradients of salt concentration and temperature, flows of water and electric current in bentonite clay are coupled through a set of linear phenomenological equations, derived from the theory of irreversible thermodynamics (Katchalsky and Curran, 1967), making use of Onsager's Reciprocal Relations (Groenevelt, 1971):

$$J_v = k_h^* \nabla(-h) + k_e \nabla(-E), \quad (1)$$

$$I = k_e \gamma \nabla(-h) + \kappa \nabla(-E), \quad (2)$$

where J_v is fluid flux per unit area [m/s], I is electric current density [A/m²], h is hydraulic head [m], E is electric potential [V], k_h^* is hydraulic conductivity at shorted condition [m/s], k_e is the coefficient of electro-osmotic hydraulic conductivity [m²/Vs], γ is the unit weight of water (9810 N/m³), and κ is the electrical conductivity [S/m].

During water flow in clays driven by a hydraulic pressure gradient in absence of electrical shorting, a streaming potential gradient, $\nabla(-E)$, tends to be induced. In this condition the streaming current I will be zero. From (2) it then follows that *under non-shortcd conditions*

$$\nabla(-E) = -\frac{k_e \gamma}{\kappa} \nabla(-h). \quad (3)$$

On the other hand, under *electrically shortcd conditions* (1) becomes

$$J_v = k_h^* \nabla(-h). \quad (4)$$

Equations (1), (2) and (3) will be used in the analysis of our experimental data. Numerical values of the three soil parameters in equations (1) and (2) have

been reported elsewhere in the literature. However, since they strongly depend on clay type, salt concentration, cation occupation of the exchange complex, bulk density and overburden load, they are of limited value for reference. [7] concludes that the value of the electrical conductivity (κ) for saturated soils is usually in the range of 0.01 to 1.0 S/m. For saturated Na-montmorillonite at water contents of 170% and 2000%, with fresh water as equilibrium solution, [2] reports k_e -values of $2 \cdot 10^{-9}$ and $12 \cdot 10^{-9} \text{ m}^2/\text{Vs}$ respectively. The corresponding hydraulic conductivities calculated by Mitchell are 10^{-11} and 10^{-10} m/s respectively. For a silty clay of bulk density 1.55 kg/dm^3 , [9] finds $k_h^* = 7.05 \cdot 10^{-11} \text{ m/s}$; $k_e = 3.08 \cdot 10^{-9} \text{ m}^2/\text{Vs}$; $\kappa = 0.115 \text{ S/m}$.

Materials and Methods

Experiments were conducted with a flexible wall permeameter in which the clay sample is connected with two reservoirs. Within a Plexiglas cell (ID 70 mm, OD 90 mm) the sample is mounted between two 0.45 mm Millipore filters and two porous stones. The porous stones are pasted marginally on a pedestal on the bottom plate of the cell and on the top cap, respectively, which are both of hard rubber. On the surface of each porous stone an annular gold wire is imprinted. In-between the Millipore-filters and the porous stones a nylon filter is situated. The nylon filter has a vapour deposited gold grid that makes contact with the gold wire. Thus, the nylon filters act as electrodes by which electrical potentials can be measured or applied. All tubing and electrical connections are led through the pedestal and the top cap, and out of the cell in an insulated and pressure-tight way. From pedestal to top cap the sample is wrapped in two neoprene membranes, each with a thickness of 0.2 mm, fitted with o-rings. The cell around the sample is filled with silicone oil in which a pressure can be created by argon gas. To ensure electrical insulation, the reservoirs consist of plastics.

In these experiments a commercially available bentonite, marketed under the name Colclay A90TM (Ankerpoort, Geertruidenberg, The Netherlands) was used. It is a sodium-montmorillonite with a third of the exchange complex occupied by calcium. 5.0 g of the air-dried powdered bentonite was weighed into a stainless steel mould with an ID of 50 mm between two porous stones of the same diameter. Then the clay was subjected to a compaction pressure of 20.3 MPa for 30 minutes. After compaction, the mould was placed in a bowl of NaCl-solution for five days in which the clay became saturated and swollen. Thus samples were obtained with thickness of 3.8 and 2.8 mm respectively and a diameter of 50 mm.

The sample was placed in the permeameter and the cell was partly filled with silicone oil. Thereafter a pressure of 1 bar was applied by use of argon gas. Both reservoirs were filled with the same NaCl-solution used for sat-

urating the clay, in two experiments at respectively 0.01 M and 0.36 M. So chemical gradients at the start of the experiments were avoided. In the reservoir at the bottom-end of the sample a constant head of 5 m was maintained by nitrogen gas. In the other reservoir a tube for gravimetric measurement of the outflow was installed. A water lock prevented evaporation. The electrodes at the interface of the sample were connected to a Consort multi-channel controller R305 (Consort, Turnhout, Belgium) to read the induced potential across the sample in millivolts. The whole set-up is situated in a temperature controlled room at $25^{\circ}\text{C} \pm 0.4^{\circ}\text{C}$.

Results and Discussion

The specifications of the samples in the two experiments are presented in table 1. During the experiments the volume of the samples increased 15 to 20 % by volume due to additional swelling.

Table 1. Sample parameters in the two experiments

	0.01 M NaCl		0.36 M NaCl	
	initial	final	initial	final
volume [cm^3]	7.499	8.516	5.435	6.503
cross section [cm^2]	19.555	22.147	19.720	21.029
thickness [cm]	0.3835	0.3845	0.2756	0.3092
moisture content [% vol]	79.31	76.30	74.97	64.28

The development of the streaming potential in the first experiment is shown in Figure 1. The effect of short-circuiting and of closing the reservoirs under non-short-circuited conditions are clearly visible. A graph of similar shape is obtained for the second experiment. Figure 1 clearly shows the disappearance of the streaming potential upon short-circuiting the clay layer and the reversibility of the effects of shorting. The streaming potential is well reproducible upon re-opening the electrical circuit. Upon closure of the reservoirs in the first experiment, J_v is set equal to zero. Figure 1 indicates that in response this leads to a small increase of the streaming potential. For at least the first 16 hrs no dissipation of the induced streaming potential is observed, which implies slow dissipation of the residual hydraulic pressure gradient.

Table 2 presents the measured water fluxes and driving forces at the two salt concentrations. The water flux components J_h and J_e are defined from (1): $J_v = J_h + J_e$, with $J_h = k_h^* \nabla(-h)$ the water flux in short-circuited situation and $J_e = k_e \nabla(-E)$ the water flux driven by the streaming potential.

As expressed by equation (3) the induced streaming potentials counteract the hydraulic driven water flow. From the fluxes and forces in table 2 the flow

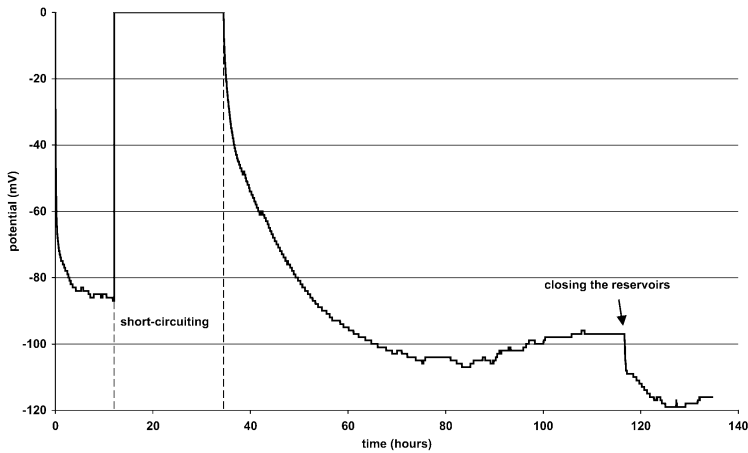


Figure 1. Development of a streaming potential during flow of a 0.01 M NaCl-solution in bentonite clay

Table 2. Water fluxes and driving forces derived from permeameter experiments with water of two different salt concentrations

	0.01 M NaCl	0.36 M NaCl
J_v [m/s]	$2.8 \cdot 10^{-8}$	$3.7 \cdot 10^{-8}$
J_h [m/s]	$3.2 \cdot 10^{-8}$	$6.3 \cdot 10^{-8}$
J_e [m/s]	$-0.4 \cdot 10^{-8}$	$-2.6 \cdot 10^{-8}$
$\nabla(-h)$ [-]	1300	1810
$\nabla(-E)$ [$\frac{V}{m}$]	-24	-19

Table 3. Flow parameters derived from the fluxes and forces in table 2

	0.01 M NaCl	0.36 M NaCl
k_h^* [m/s]	$2.4 \cdot 10^{-11}$	$3.5 \cdot 10^{-11}$
k_e [$\frac{m^2}{Vs}$]	$1.7 \cdot 10^{-10}$	$1.37 \cdot 10^{-9}$
κ [S/m]	$9.0 \cdot 10^{-5}$	$1.28 \cdot 10^{-3}$

parameters listed in Table 3 are derived, using equation (3) and the equations for J_h and J_e .

The effect of increased salt concentration on the flow parameters is remarkable. k_h^* is hardly influenced, consistent with the observations by Heister et al (submitted) that under an overburden load as applied here, increased salt concentration will not result in flocculation and therefore will not have effect on hydraulic conductivity. However the effect on k_e was expected to be opposite, as explained by [1], using the Gouy Chapman double layer theory. As expected the electric conductivity increases with salt concentration of the permeating solution. But both values of κ in table 3 are some orders of magnitude smaller than κ -values reported in literature. The ratio $\nabla(-E)/\nabla(-h)$ is respectively 18.5 and 10.5 mV/m in the two experiments, and is higher than reported in literature (Bolt, 1982). These higher values are explained by the very low electric conductivity. The high degree of compaction and the monovalent ions in the permeating solution will have caused a strong overlap of diffuse double layers.

The contribution of free salt ions to the electric conductivity may therefore be negligible and only the adsorbed countercharge of cations will then contribute to electric conduction. The derived values of k_e enable the prediction of the electro-osmotic water flux by *active* application of an electric potential gradient. Thus, at 0.01 M NaCl in the compacted bentonite, a gradient of 1 V/m will, in the absence of a hydraulic pressure gradient, cause a water flux of the order of 10^{-10} m/s.

Conclusions

The experiments demonstrate the development of a streaming potential in consolidated bentonite clay when flushed by a NaCl-solution of either low or high concentration. The streaming potential measured in our experiments is at least 5 to 10 times larger than values reported for bentonite in the literature. Apparently this is caused by a very low electric conductivity of the bentonite samples studied. This low conductivity might be ascribed to overlapping diffuse double layers on the clay particles, caused by the high compaction and the presence of monovalent ions in the equilibrium solution. The bentonite, thus compacted, will be a very effective medium for active application of electro-osmosis. Compared with electrically shorted conditions, chemical osmosis will be reduced when the clay is not short-circuited.

References

- [1] Bolt, G.H. (1982) Electrochemical phenomena in soil and clay systems. In: *Soil Chemistry. B. Physico-Chemical Models* (G.H. Bolt, ed). Elsevier, Amsterdam, pp. 387-432
- [2] Casagrande, L. (1952) Electro-osmotic stabilization of soils, *Journal of the Boston Society of Civil Engineers*, Vol. XXXIX, no. 1; reprinted in: *Contributions to Soil Mechanics, 1941-1953*
- [3] Elrick, D.E., Smiles, D.E., Baumgartner, N. and Groenevelt, P.H. (1976) Coupling phenomena in saturated homo-ionic montmorillonite: I. Experimental, *Soil Sci. Soc. Am. J.* **40**, 490-491
- [4] Groenevelt, P.H. (1971) Onsager's reciprocal relations, *Search* **2**, 264-267
- [5] Katchalsky, A. and Curran, P.F. (1967) *Non-equilibrium Thermodynamics in Biophysics*, Harvard University Press, Cambridge, Mass.
- [6] Keijzer, Th.J.S. and Loch, J.P.G. (2001) Chemical osmosis in compacted dredging sludge, *Soil Sci. Soc. Am. J.* **65**, 1045-1055
- [7] Mitchell, J.K. (1993) *Fundamentals of Soil Behavior*, 2nd edn. Wiley, New York
- [8] Heister, K., Keijzer, Th.J.S. and Loch, J.P.G. (2004) Stability of clay membranes in chemical osmotic processes. Submitted to: *Soil Science*
- [9] Yeung, A.T. (1994) Effects of electro-kinetic coupling on the measurement of hydraulic conductivity. In: *Hydraulic Conductivity and Waste Contaminant Transport in Soils*, ASTM STP 1142 (D.E. Daniel and S.J. Trautwein, eds.). Am. Soc. for Testing Materials, Philadelphia

THEORETICAL ANALYSIS OF THE INFLUENCE OF A DIFFUSE DOUBLE-LAYER ON DARCY'S LAW

David Smith

School of Engineering

The University of Newcastle

David.Smith@newcastle.edu.au

Peter Pivonka

School of Engineering

The University of Newcastle

Peter.Pivonka@newcastle.edu.au

Abstract It is known that when the concentration of background electrolyte in a charged porous medium increases, the permeability of the porous medium also increases. In this paper, a set of coupled governing equations is derived that describe Navier-Stokes flow of a pore fluid through a charged porous medium (i.e. flow in the presence of a diffuse double-layer). The set of coupled partial differential equations describe the transport of the individual ions along their electrochemical potential gradient, the transport of the pore fluid together with the ions in solution, and the voltage distribution through the porous medium, while simultaneously maintaining electro-neutrality of the system. The governing equations are solved for an example problem. By using this approach, new insight is gained into the origin of permeability changes arising from changes in the background electrolyte concentration.

Keywords: Navier-Stokes equation, diffuse double-layer, Darcy's law

Introduction

It is well known that the permeability of a clay soil is not only a function of its porosity, but also of the concentration of ions in the pore fluid, and the permittivity of the pore fluid. While this may be well known, an explanation for the behaviour is not well known. In fact, in a recent paper Hueckel identified the explanation for this behaviour as one of the outstanding problems in soil mechanics ([4]): 'The controversy over these two inconsistent data sets (i.e., increased

Jacques M. Huyghe et al. (eds), IUTAM Proceedings on Physicochemical and Electromechanical Interactions in Porous Media, 289–298.

© 2005 Springer. Printed in the Netherlands.

permeability but no change in pore size distribution as measured by mercury porosimetry) remains unsolved and awaits a breakthrough in experimental techniques and/or in the way we understand flow through porous media.'

In this paper, we seek to explain this experimentally observed behaviour theoretically by calculating the dissipation of power in a flowing fluid caused by friction in the pore fluid, and by friction between the pore fluid and ions in a diffuse double-layer. We will do this by formulating a set of governing equations for fluid flow (using the Navier-Stokes equation) and the transport of the individual ions in solution (using a generalised Nernst-Planck equation), while at the same time maintaining electroneutrality of the system (using Gauss's electrostatic theorem). The diffuse double-layer will be coupled to the fluid transport by a body force term in the Navier-Stokes equation. The resulting system of governing partial differential equations will be fully coupled. This system of equations will be solved for some simple problems and the results interpreted in terms of Darcy's law.

Governing Equations

The key constitutive equation describing microscale multi-ion transport in the presence of electrochemical forces is the generalised Nernst-Planck (N-P) equation ([1]):

$$\mathbf{f}^i = -D^i(\nabla c^i + \frac{F}{RT}c^i z^i \nabla \Psi) + \mathbf{v}^f c^i, \quad (1)$$

where \mathbf{f}^i , c^i , and ∇c^i is the mass flux density, the concentration of the i -th ion, and the concentration gradient of the i -th ion, respectively. D^i is the free-solution diffusion coefficient of the i -th ion¹. The quantities z^i and $\nabla \Psi$ are the valence of the i -th ion and the voltage gradient. \mathbf{v}^f is the fluid velocity and F , R , and T are the Faraday constant, gas constant, and absolute temperature, respectively.

The first term inside the brackets results in transport of the i -th ion species along minus of the chemical potential gradient (assuming an ideal solution). The second term inside the brackets results in transport along the voltage gradient². The generalized N-P Equation (1) is a generalisation of Fick's law, taking into account electrical effects on charged solutes, and taking into account the movement of the fluid. The voltage Ψ appearing in Equation (1) is made up of two distinct parts. The first part of the voltage arises from any external potential applied to the system (for example, the external voltage may result from the accumulation of excess ions on one side of a clay barrier membrane). The second part of the voltage arises from the potential generated by the diffusion coefficients of the individual ions being different, leading to the formation of ion-pair dipoles. This second potential is known as the diffusion potential. However, the ions in solution are influenced by the electric potential

irrespective of its origin, so the two voltages arising from either process may be summed and represented by a single Ψ .

The transport Equations (1) are supplemented by mass conservation equations. Mass conservation for each conservative ion species is expressed by,

$$\frac{\partial c^i}{\partial t} = -\nabla \cdot \mathbf{f}^i, \quad (2)$$

where $\nabla \cdot \mathbf{f}^i$ is the divergence of the flux vector of the i -th ion and t is the time. Substitution of the flux Equation (1) into the mass conservation Equation (2) leads the governing partial differential equation for mass transport. However, charge conservation of ions in solution exerts an important constraint on the behaviour of a multi-ion system by enforcing electroneutrality of the system at all times. This constrained can be expressed by means of Gauss's electrostatic theorem for a system consisting of N ions:

$$\nabla(\varepsilon \nabla \Psi) = F \sum_{i=1}^N z^i c^i, \quad (3)$$

where the permittivity ε is the product of the permittivity of free space, ε_0 , and the permittivity of water, ε_w , relative to the permittivity of free space, i.e., $\varepsilon = \varepsilon_0 \varepsilon_w$.

Equation (1), (2) and (3) can be employed in order to gain information on the structure of the diffuse double-layer for any ion composition of the pore fluid and solid geometry. Further, these equations are suitable for the analysis of ion diffusion through a charged porous medium containing a stationary fluid, i.e., $\mathbf{v}^f = \mathbf{0}$. For these reasons, it is clear that the equations constitute a very powerful model, and can solve many problems dealing with colloidal domain processes and the chemomechanical behaviour of clays³. However, for systems characterized by movement of the pore fluid (i.e., $\mathbf{v}^f \neq \mathbf{0}$), an additional equation describing the fluid flow is required. In this case, there are couplings between the flow of fluid in the pore spaces and the movement of ions in the pore fluid (e.g. as occurs in a clay soils or a charged biological tissues).

When pore fluid motion occurs relative to the counterions⁴ in the pore fluid, there is initially a drift of counterions in the direction of fluid flow. However soon after this drift begins, large electrical and chemical forces comes into play, effectively 'pinning' the counterions in solution⁵. The counterions pinned in pore fluid can contribute significantly to the dissipation of energy in the fluid (the counterions can be imagined to be small spheres suspended in the fluid, interrupting the flow). In clay soils with a high cation exchange capacity, calculations made here show this may be the principal means for energy dissipation during fluid flow. Assuming no source or sink is present, the governing equations required for the analysis of this system are the continuity equation

([5]),

$$\nabla \cdot \mathbf{v}^f = 0 \quad (4)$$

and the generalized Navier-Stokes (N-S) equation describing electrohydrodynamic flow ([3], pp 553)⁶,

$$\rho_f \left(\frac{\partial \mathbf{v}^f}{\partial t} + \mathbf{v}^f \cdot \nabla \mathbf{v}^f \right) = \mathbf{F}^m + \mathbf{F}^e + \mathbf{F}^\mu + \mathbf{F}^g, \quad (5)$$

where ρ^f is the fluid density. \mathbf{F}^m , \mathbf{F}^e , \mathbf{F}^μ , and \mathbf{F}^g are force vectors of mechanical, electrical, viscous, and gravitational origin. These forces can be expressed for an incompressible homogeneous fluid as,

$$\mathbf{F}^m = -\nabla p, \quad (6)$$

$$\mathbf{F}^e = qE + \nabla \left(\rho^f \frac{E^2}{2} \left(\frac{\partial \varepsilon}{\partial \rho^f} \right)_\theta \right) - \frac{E^2}{2} \nabla \varepsilon, \quad (7)$$

$$\mathbf{F}^\mu = \mu^f \nabla^2 \mathbf{v}^f, \quad (8)$$

$$\mathbf{F}^g = \rho^f g. \quad (9)$$

p denotes the fluid pressure in the pore fluid within the porous medium, μ^f is the fluid viscosity. θ is the temperature. $q = F \sum z^i c^i$ is the net charge and $E = -\nabla \Psi$ is the electric field strength. Ignoring electrostriction and the gradient of permittivity the electrical force (7), for a strong ionic salt the equation becomes:

$$\mathbf{F}^e = qE = -F \sum_{i=1}^N z^i c^i \nabla \Psi. \quad (10)$$

Considering the N-S Equation (5), in the case of zero fluid velocity, identifies 'hydrostatic pressures' arising from 'electrical body forces' ([2]). However, this 'hydrostatic pressure' is misleading terminology, as it is in fact a thermodynamic pressure arising from the entropic contribution to the free energy of the water due to the presence of the solute in the solvent. The 'electrical body forces' can be transformed (using Gauss's electrostatic equation) to Maxwell stresses. But once again the terminology is misleading. The Maxwell stresses do not contribute to a change in pressure in the fluid, but represents stored electrical energy (that changes the free energy of the solvent). We would like to remove this thermodynamic pressure from the N-S Equation (5).

In the case of hydrostatic pressure arising from gravitational forces, this may be removed by simply neglecting the gravitational body force in the N-S Equation (5). For the thermodynamic pressure, it is less obvious what can be done. However it may be noticed that at equilibrium, the N-P Equation (1) is satisfied and the ion fluxes are zero. It can now be seen that the thermodynamic

pressure may be removed (for $\mathbf{v}^f = \mathbf{0}$) by introducing a 'diffusive body force' that is equal and opposite to the electrical body force (10), that is,

$$\mathbf{F}^e = - \sum_{i=1}^N (RT\nabla c^i + z^i F c^i \nabla \Psi) = - \sum_{i=1}^N \frac{z^i c^i (\mathbf{v}^f - \mathbf{v}^i)}{u^i}, \quad (11)$$

where \mathbf{v}^i is the velocity of the i -th ion and u^i denotes the ion mobility.

It is noted that the modified Equation (11) is rather fortuitous, in that it accounts for both electrical and chemical forces, and so is a generalization of equation (10). It will be shown that this generalized equation is necessary for the investigation of coupled fluid flow and diffusion through uncharged and charged porous media (see for example problem 1 in Section 3).

The total power (energy/time) dissipated per unit volume of fluid in this system is the sum of the power dissipated due to fluid viscosity and the power dissipated by friction between the pore fluid the counterions 'pinned' in the fluid⁷. For two-dimensional flow the power dissipated due to fluid viscosity is given by ([5]),

$$\mathcal{P}^\mu = \mu^f \left(2 \left(\frac{\partial v_1}{\partial x} \right)^2 + 2 \left(\frac{\partial v_2}{\partial y} \right)^2 + \left(\frac{\partial v_1}{\partial y} + \frac{\partial v_2}{\partial x} \right)^2 \right), \quad (12)$$

while the power dissipated due to the counterions pinned in the pore fluid under steady-state conditions is given by (ions fixed in position):

$$\mathcal{P}^e = \frac{c^i (\mathbf{v}^f)^2}{u^i}. \quad (13)$$

Finally the power dissipated under transient conditions by counterions pinned in the pore fluid is given by (ions moving):

$$\mathcal{P}^e = \sum_{i=1}^N \frac{u^i}{c^i} (RT\nabla c^i + z^i F c^i \nabla \Psi)^2 = - \sum_{i=1}^N \frac{z^i c^i (\mathbf{v}^f - \mathbf{v}^i)^2}{u^i}. \quad (14)$$

Numerical Analysis

In the following, the consequences of the proposed theory will be demonstrated by two example problems. The first problem deals with N-S flow of an uncharged species through a semipermeable membrane. This example demonstrates how concentration gradients accounted for in the generalized force term (Equation (11)) influence fluid flow. The second problem investigates the influence on fluid flow of a charged slit opening containing an electrolyte. Parameters used for the coupled Navier-Stokes–Nernst-Planck equation are given in Table 1.

Table 1. Model parameters used for the numerical analyses.

symbol	value	dimension
ε_0	8.85×10^{-12}	$C^2/(J\ m)$
ε_w	78	–
D^+	1.5×10^{-9}	m^2/s
D^-	1.5×10^{-9}	m^2/s
F	96500	C/mol
T	293	K
R	8.31	J/(K mol)
μ^f	0.001	kg/(m s)
ρ^f	1000	kg/m ³

Semipermeable membrane

The first example deals with 2D transient fluid flow through a region bounded by two semipermeable membranes, permeable to the water flow but impermeable for solutes. The employed geometry together with the boundary conditions and the finite element mesh (consisting of 386 triangular elements) are shown in Figure 1. Initially the (uncharged) solute is uniformly distributed over the region ($c = 10\ \text{mol/m}^3$) and the fluid pressure equals zero. At t_0 a pressure gradient ($p_1 = 1 \cdot 10^4\ \text{N/m}^2$ and $p_2 = 0\ \text{N/m}^2$) is applied leading to fluid flow. Investigation of the pressure profiles (crosssection ($x, y = 0$)) at t_1

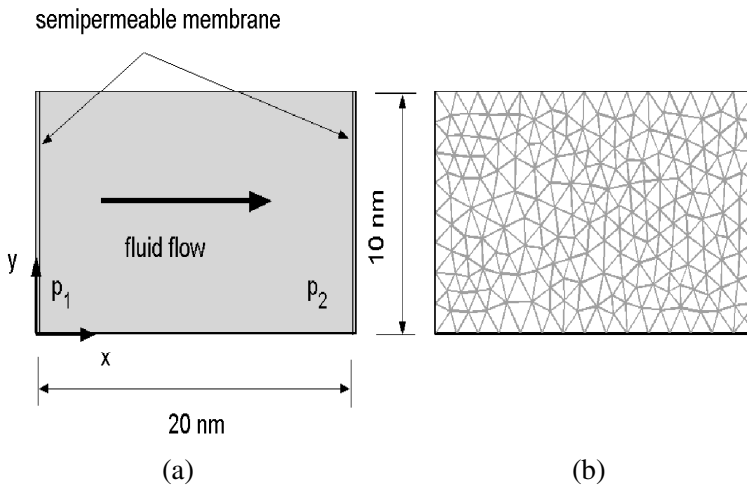


Figure 1. Navier-Stokes flow through a semipermeable membrane: (a) geometry and (b) finite element mesh.

and t_2 indicate a redistribution of pressure with time (see Figure 2).

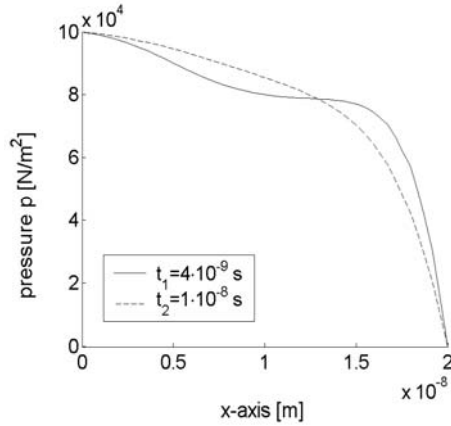


Figure 2. Navier-Stokes flow through a semipermeable membrane: plots of the fluid pressure p (N/m^2).

Navier-Stokes flow through a charged slit

The second example deals with 2D stationary fluid flow ($\partial \mathbf{v}^f / \partial t = 0$) of an electrolyte through a charged slit opening. The geometrical dimensions of the slit together with a zoom of the employed FE-mesh (consisting of 1344 triangular elements) are shown in Figure 3. The boundary conditions are chosen such that a pressure p_1 of 10 N/m^2 is applied at the upper end of the slit whereas zero pressure p_2 is applied to the lower end. At the side walls no slip boundary conditions were used. Two cases are investigated: (i) an idealized problem where solutes are pinned in the pore fluid (i.e., setting $F = 0$) demonstrates the importance of solutes dissipating energy and (ii) fluid flow through charged pore walls containing an ionic 1:1 background electrolyte. A parameter study is performed in order to investigate the model predictions under various electrolyte concentrations and charge densities ρ (applied on the side walls of the slit).

Investigation of the velocity profiles obtained for the first case (cross-section $(x, y = 70 \text{ nm})$) indicates a strong decrease of the maximum fluid velocity with increasing electrolyte concentration (see Figure 4). Furthermore, a transition of the velocity curves from a parabolic curve classically obtained from the Navier-Stokes problem (i.e., $c = 0 \text{ mol/m}^3$) to a very flattened curve for high electrolyte concentration ($c = 1000 \text{ mol/m}^3$) can be seen.

The fluid flux through the slit for Problem 1 (uniformly distributed solute) and Problem 2 (for a diffuse double-layer in the slit) are shown in Figure 5. Again

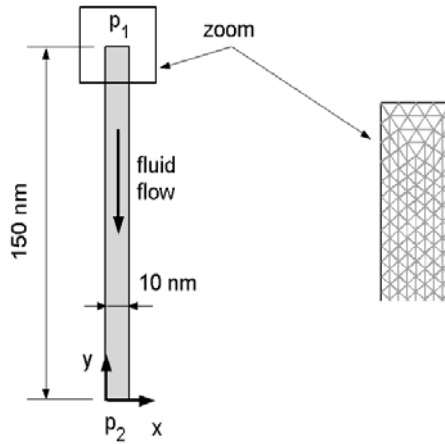


Figure 3. Navier-Stokes flow through a slit: geometrical dimensions and zoom of finite element mesh.

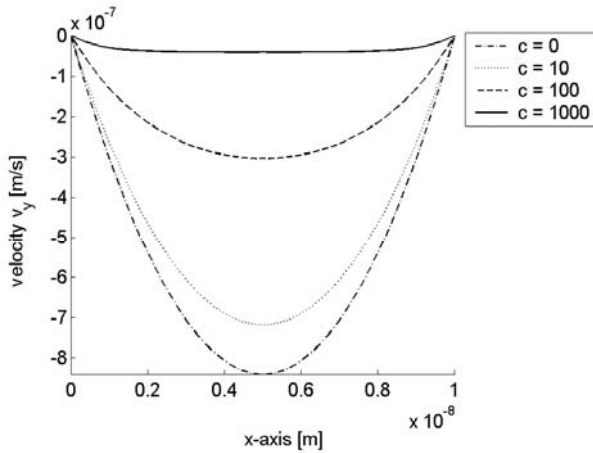


Figure 4. Navier-Stokes flow through a slit: velocity profiles for various uniform concentrations c in mol/m^3 .

it is seen that increasing the concentration of uncharged solutes pinned in the pore solution strongly decreases the fluid flux (Figure 5(a)). Most importantly though, it is apparent that increasing the concentration of the ionic background electrolyte leads to an increase of the fluid flux (Figure 5(b)). This is the crucial finding. The increased permeability of a slit with a diffuse double-layer is due to the compression of the double layer upon increasing the background electrolyte concentration c .

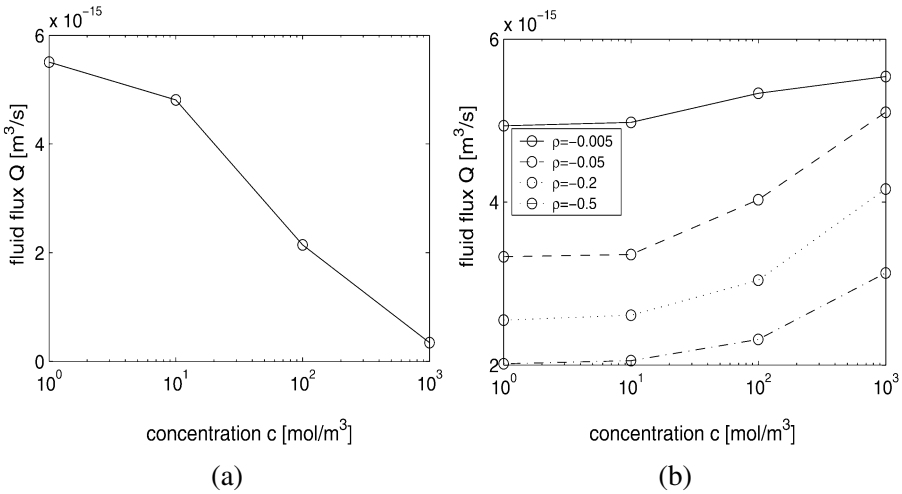


Figure 5. Navier-Stokes flow through a slit: solvent flux for: (a) uncharged species and (b) charged species.

Summary and Conclusions

Based on the numerical results obtained for the electrohydrodynamics equations the following conclusions can be drawn:

For the example ‘charged slit problem’, a four fold reduction of the fluid flux through the slit was obtained (Figure 5). This reduction of fluid flux strongly depends on the surface charge on the slit wall, and on the ionic concentration of background electrolyte. Increasing the surface charge while keeping the electrolyte concentration constant leads to a decrease of permeability, as more counterions are pinned in the solution. On the other hand, increasing the electrolyte concentration (while keeping the surface charge constant) leads to a compression of the diffuse double-layer and so to an increase of fluid flow through the slit as counterions move closer to the slit wall. Consideration of finite size of the hydrated ions (rather than modelling them as point charges) may lead to an even more pronounced dependence of the permeability on the diffuse double-layer. While these early findings are very promising, clearly, further pore geometries warrant careful investigation.

Acknowledgments

The second author gratefully acknowledge the financial support of this study by the Austrian Foundation for the Promotion of Scientific Research (FWF) in the course of an Erwin Schrödinger scholarship.

Notes

1. There are several refinements that may be incorporated in the estimated diffusion coefficient, for example, taking into account the activity of the ions in solution (arising from correlated spatial movements/arrangements of ions, see ([1]) for details).
2. Note that the direction of transport depends on the charge z^i of the ion.
3. It is noted that the finite size of ions may be taken into account using a modified Gouy-Chapman model of the diffuse double-layer. The finite size of ions limits the maximum concentrations of ions close to the particle surface.
4. Counterions are the ions required to maintain electroneutrality of the charged clay particles.
5. The counterions are pinned in a spatial location in a time-averaged sense (there are thermally induced fluctuations about the mean position).
6. Use of the N-S equation assumes $\rho^f = \text{const}$ and $\mu^f = \text{const}$, though these restrictions may be relaxed.
7. The energy dissipated in the fluid must be equal to the rate of work done on the system by pressure-volume work on the system boundaries.

References

- [1] Cussler, E. (1997) *Diffusion mass transfer in fluid systems*. Cambridge University Press, New York, USA, 2nd edition
- [2] Derjaguin, B. (1989) *Theory of stability of colloids and thin films*. Consultants Bureau, New York, USA
- [3] Eringen, A. and Maugin, G. (1990) *Electrohydrodynamics of continua II: fluids and complex media*. Springer-Verlag, New York, USA
- [4] Hueckel, T. (2002) Coupled constitutive models in environmental geomechanics. In Vulliet, Z., Laloui, F., and Schrefler, P., editors, *Workshop on GeoEnvironmental Engineering*, pages 27–44, Ascona, Switzerland. Environmental Geomechanics Publications EPFL Press
- [5] Slattery, J. (1999) *Advanced transport phenomena*. Cambridge University Press, Cambridge, USA

FLUID FLOW IN THE SELF-OPTIMISED STRUCTURE OF COMPACT BONE

Theo H. Smit

Department of Physics and Medical Technology, Vrije Universiteit medical center, Amsterdam, The Netherlands

Jacques M. Huyghe

Department of Mechanical Engineering, Eindhoven University of Technology, Eindhoven, The Netherlands

Abstract Compact bone is a well-organised, multi-level porous structure. Strain-derived fluid flow likely steers the activity of cells within the bone matrix, which in turn orchestrate the concerted activity of bone resorbing and bone forming cells at the surface. We present a model of the strain-driven bone remodelling process, which could explain the mechanically optimised structure of compact bone.

Introduction

Bone is a natural composite with a rich hierarchical structure and at least three levels of porosity. At the highest level, porous trabecular bone consisting of struts and plates (thickness $200\ \mu\text{m}$, porosity 60-95 %, pore size $>500\ \mu\text{m}$) is distinguished from dense, compact bone with a porosity of less than 10 %. Compact bone essentially consists of thick-walled cylindrical structures (*osteons* - $200\ \mu\text{m}$) around the vascular canals ($40\ \mu\text{m}$). The smallest porosity both in trabecular and compact bone is a system of lacunae ($10\ \mu\text{m}$) and canals ($200\ \text{nm}$), which contain mutually connected bone cells (*osteocytes*) and extracellular fluid. In humans after one year of age, bone is renewed bit-by-bit and replaced by units of secondary bone. This process is called *remodelling* and involves groups of different cells, which collaborate in basic multi-cellular units (*BMUs*). BMUs proceed by tunnelling, during which *osteoclasts* excavate a canal in the main loading direction, which is partly refilled by *osteoblasts*, thus forming an osteon (Figure 1). It is unclear, however, how the concerted activity of osteoclasts and osteoblasts (*BMU-coupling*) is orchestrated. There also is no satisfying explanation for the load-alignment of the remodelling process. A necessary condition for load-directed bone remodel-

Jacques M. Huyghe et al. (eds), IUTAM Proceedings on Physicochemical and Electromechanical Interactions in Porous Media, 299–305.

© 2005 Springer. Printed in the Netherlands.

ling would be, that sensors exist to detect mechanical strains. Good candidates for this are osteocytes, which reside inside the bone matrix and thus have a good position for mechanosensing. With their long slender protrusions they form a three-dimensional network that reaches to the bone surface, which also allows them to signal the effector cells, osteoclasts and osteoblasts, respectively. Another signalling pathway is possible through the extra-cellular fluid that flows through the lacuno-canalicular porosity upon mechanical loading. Fluid flow may give rise to at least three biophysical effects: first, an enhanced

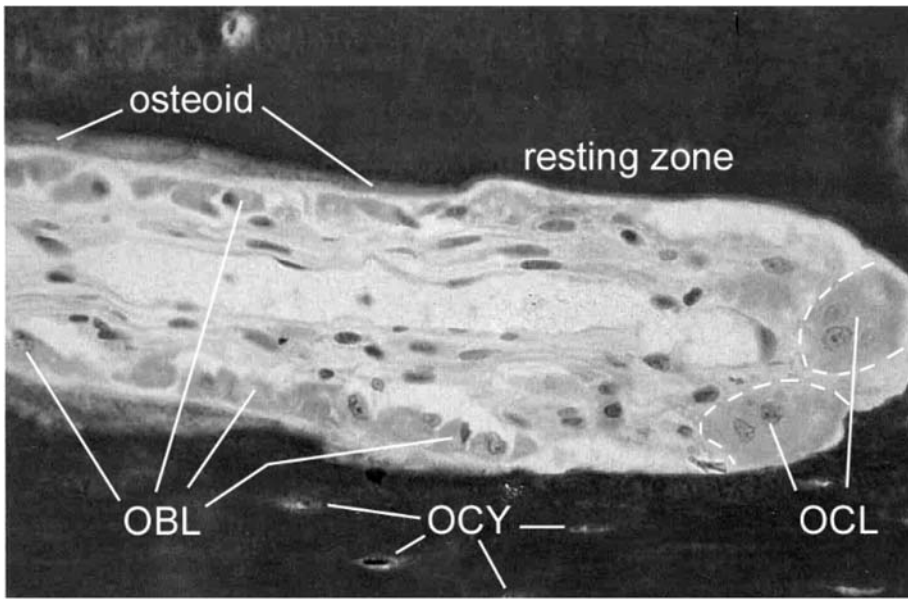


Figure 1. The cellular activity during bone remodelling. At the tip (cutting cone) multi-nucleated osteoclasts (OCLs) excavate the mineralised bone tissue. At some distance, after the resting zone, osteoblasts (OBLs) refill the tunnel with (osteoid) that is subsequently mineralised. Osteocytes (OCYs) are former osteoblasts that were entombed within the bone matrix, but remained connected to the bone surface by numerous long slender protrusions (not visible). Courtesy R. Schenk.

mass transport that ensures osteocytes to receive sufficient nutrients for survival within the bone matrix, and their waste products to be washed away to the bone surface. Second, due to the charged bone matrix and the ionic composition of the extra cellular fluid, an electro-kinetic effect occurs in the form of streaming potentials. Streaming potentials might modulate the movement of ions such as calcium across the cell membrane, and subsequently cell behaviour. Thirdly, a fluid shear stress is generated on the cell membrane, which is a well-known stimulus for cells [2]. It is difficult to estimate the actual role

of each of the three biophysical effects, because in the *in vivo* situation they occur simultaneously. Nevertheless, all three are potentially powerful modulators of cell behaviour, and strain-induced fluid flow thus appears to be a good mediator of mechanical information. In order to challenge this theory of strain-driven bone remodelling and to obtain further understanding of the biophysical process of bone adaptation, quantitative models and experiments are required. Here, we aim to determine the local pattern of fluid flow at a remodelling site. In particular, we tested the hypothesis that physiological loading of cortical bone produces specific patterns of fluid flow along the osteocytes around a tunnelling osteon.

Model

An axisymmetric finite-element mesh was built representing a typical cortical resorption space (Figure 2,3). The cylindrical tunnel and the spherical cutting cone have a diameter of $200\ \mu\text{m}$. The outer diameter was made $700\ \mu\text{m}$, large enough to allow local strain effects to dampen out. The pressure within the tunnel itself can be neglected as compared to the pressure within the lacuno-canalicular porosity of the bone tissue. Bone was modelled as a saturated interconnected porous medium, essentially described by six parameters [5]. The mineralised matrix was considered an isotropic solid, characterised by a drained Young's modulus of 15.8 GPa and a Poisson's ratio of 0.33. The porosity at this level of organisation consists of canaliculi and osteocyte lacunae, assumed to occupy some 5 % of the total bone volume. The bulk modulus of the bone matrix was determined at 17.7 GPa; that of the cells and extracellular fluid was equalled to water: 2.3 GPa [5]. The resistance against fluid flow through the porosity was quantified by the *hydraulic permeability*, which relates to the fluid viscosity and the geometry of the porosity (for details, see [5]). As canaliculi mainly run in the transverse plane towards the bone surface and osteons, we introduced an anisotropy of the permeability, conservatively estimated at a factor ten. The value used for the hydraulic permeability in the transverse plane was $2.2 \cdot 10^7\ \text{m}^4/(\text{Ns})$ [5]. The model was loaded in the longitudinal direction by a typical loading pattern recorded *in vivo* in a person walking at 4 km/h [1]. The maximum deformation of the bone matrix was set at 1500 microstrain (0.15 %), which is in the physiological range of the activities of daily life. The walking cycle was divided in 40 time increments of 0.025 s. The analyses were performed with the finite-element code DIANA (DIANA Analysis BV, Delft, The Netherlands) on a Silicon Graphics workstation (Silicon Graphics Inc., Mountain View, CA, USA).

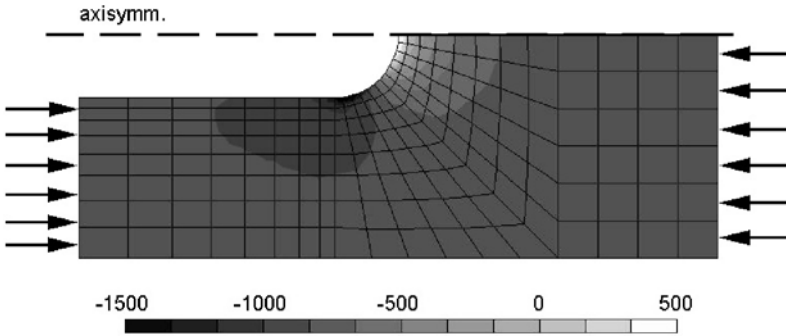


Figure 2. Volumetric deformation of the bone matrix under maximum load. Values are in microstrain.

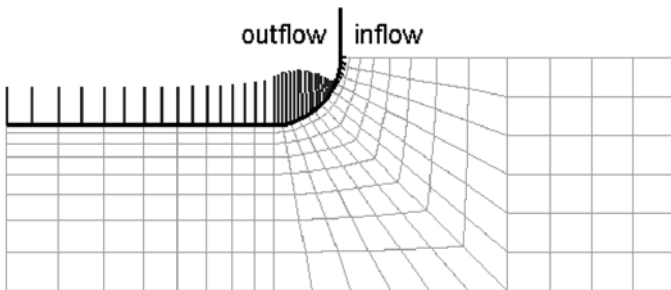


Figure 3. Fluid flow pattern at the bone surface at maximum compression during the walking cycle.

Results

At maximal loading during the heel strike of the walking cycle, a typical volumetric strain pattern appears in the wall of the tunnel around the BMU (Figure 2). The volumetric strain results in a flow of canalicular fluid that is different at the tip of the cutting cone and at its base (Figure 3). At the base of the cutting cone and along the reversal zone, fluid is pressed out of the canaliculi into the resorption tunnel. At the tip of the cutting cone however, fluid is sucked into the canaliculi as a result of local volumetric expansion. Influx occurs only in a shallow layer some 10 micrometer deep, after which the flow changes into an efflux (Figure 4). So, just below the surface of the cutting cone, where influx and efflux meet, the net canalicular fluid flow is about zero, even at maximal loading of the bone. At unloading of the specimen, during the swing phase of the walking cycle, the fluid pattern is more or less reversed, resulting in fluid outflow at the tip of the cutting cone and inflow along its base and the reversal zone. Flow magnitude is now about 5 times lower than during heel strike loading (data not shown). At both sites, reversal zone and cutting cone tip, the canalicular flow damps out at a depth of some 100 micrometer around the tunnel, even at maximal loading during heel strike (Figure 3).

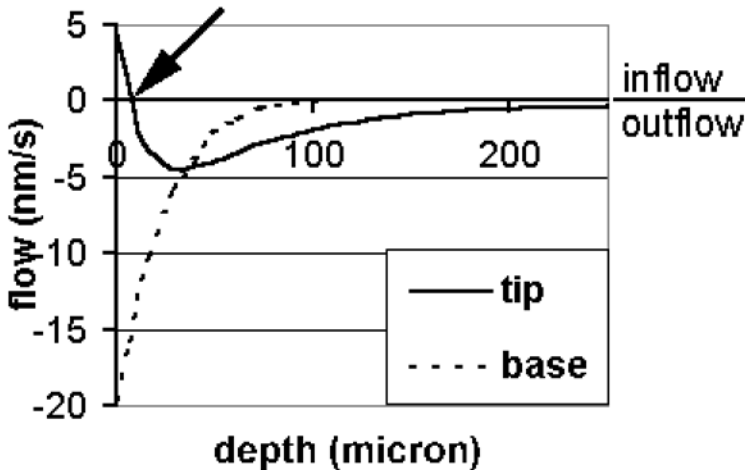


Figure 4. Canalicular fluid flow pattern within the bone tissue at maximum load during the walking cycle. At the tip of the cutting cone (continuous line), the inflow (resulting from volumetric expansion of the superficial bone layer) changes into an outflow because of volumetric compression of the deeper bone layer. The reversal (indicated by arrow) occurs at a depth of about 10 micrometer. At this depth, canalicular fluid flow will be zero. At the base of the cutting cone (dashed line), high volumetric compression leads to high fluid flow in the canaliculi, which runs towards the resorption tunnel and is maximal near the bone surface.

Discussion

The different canalicular flow patterns around the tip and the base of a cutting cone during loading, indicate that the osteocytes in these two locations receive different mechanical information. Both at maximal loading and unloading, the flow in the bony wall of the tip was opposite to the flow in the wall of the base. More important however is the difference in magnitude of flow at these two locations. At the tip of the cutting cone, a small superficial zone, some 10 micrometer deep, of volumetric expansion was followed by volumetric compression which reached its maximum at 30 micrometer depth (Figure 4). As a result, the net fluid flow is close to zero at a depth of some 10 micrometer in the wall of the cutting cone tip. At the base of the cutting cone, the flow pattern was unidirectional under both loading and unloading. At loading, fluid was pressed out of the bone, reaching maximal canalicular flow at the bone surface. At unloading this strain pattern was reversed, but because strain rate was slower, flow magnitude was considerably lower as well. What will be the effect of these wholly different stress conditions on the osteocytes? Obviously, the osteocytes behind the tip of the cutting cone hardly experience any fluid flow during the whole loading cycle and will be deprived of nutrients and mechanical stimulation. Also, they will stop producing nitric oxide (NO), which is necessary to inhibit osteoclasts from resorbing the matrix. Osteoclasts thus will proceed their resorptive activity in the direction of loading, as determined by the absence of strain driven fluid flow. By contrast, the fluid flow at the closing cone is increased due to the void in the bone matrix. Here the osteocytes are more strongly stimulated, which results in an increased production of -among others- NO and prostaglandin E2 (PGE2) [3]. NO not only inhibits the activity of osteoclasts, but also induces -like PGE2- bone formation by activating osteoblasts. These two antagonistic activities together explain the concerted action of osteoclasts and osteoblasts in a BMU (BMU-coupling). The concept of a group of osteoclasts that digs a tunnel in response to strain-dependent osteocyte signals is attractive, because it not only explains the alignment of secondary osteons to the dominant loading direction, but also why the diameter of osteons remains within certain limits. In healthy bone, the size of osteons is fairly constant, meaning that osteoclasts stop resorbing when a certain gap size has been reached. Our proposal links this observation to the magnitude of local strain, as strain induces osteocytes to inhibit further osteoclastic resorption. If bone is not strained sufficiently, our model predicts that osteocytes are not sufficiently activated to inhibit further osteoclastic attack, which leads to a larger osteon diameter. Also, the inner diameter of the osteon will be larger, as the stimulation of the osteocytes at the closing zone will be reduced as well, thereby reducing the production of NO and PGE2, and consequently the activity of osteoblasts. Ultimately, this leads to trabecularisation

of cortical bone, as observed in situations of disuse. Summarising, we conclude that bone remodelling is a local, self-organising process of mechanical adaptation, and may be regulated by strain-induced flow of extra-cellular fluid along the osteocytes. As it involves the activity and mutual communication of all three types of bone cells within well-defined spatial and temporal boundaries, the remodelling osteon is a valuable model for the study of the mechanical adaptation of bone.

References

- [1] Bergmann, G., Graichen, F. and Rohlmann, A.
www.ukbf.fu-berlin.de/biomechanik/Homeframe.htm - <results> - <measurements of hip joint forces> - <walking on a treadmill> - <EBR120B>.
- [2] Burger, E.H. and Klein-Nulend, J. (1999) Mechanotransduction in bone - role of the lacuno-canalicular network, *FASEB Journal* **13**, S101-S112
- [3] Klein-Nulend, J., Van der Plas, A., Semeins, C.M., Ajubi, N.E., Frangos, J.A., Nijweide, P.J. and Burger, E.H. (1995) Sensitivity of osteocytes to biomechanical stress in vitro, *FASEB Journal* **9**, 441-445
- [4] MacIntyre, I., Zaidi, M., Alam, A.S.M.T., Datta, H.K., Moonga, B.S. Lidbury, P.S., Hecker, M. and Vane, J.R. (1991) Osteoclast inhibition : An action of nitric oxide not mediated by cyclic GMP, *Proc. Nat. Ac. Sc.* **88**, 2936-2940
- [5] Smit T.H., Huyghe J.M. and Cowin S.C. (2002) A two-level poroelastic model of cortical bone: estimation of the linear isotropic parameters, *J. Biomech.* **35**, 829-836

INTERACTION BETWEEN AQUEOUS SOLUTION TRANSPORT AND STRESS/STRAIN IN A DEFORMABLE POROUS MEDIUM

Jean-Claude Béné, Jérôme Boscus and Vincent Richefeu

Laboratoire de Mécanique et Génie Civil, UMR CNRS 5508

Université Montpellier 2, CC 48, Place E. Bataillon, 34095 Montpellier Cedex 5, France

benet@lmgc.univ-montp2.fr, boscus@lmgc.univ-montp2.fr, richefeu@lmgc.univ-montp2.fr

Abstract Liquid phase transport in heterogeneous media such as gels and biopolymers may induce very large strains. These produces internal mechanical stresses that interact with water transport mechanisms. We analyze transfers in porous media saturated with an ionic solution using the linear thermodynamics of irreversible processes. The interaction between mass transfer and stress/strain is analyzed using free energy. A large number of coefficients appears and we proposed theoretical and experimental method for their determination. A validation of the model is given in the simplified case of osmotic dehydration of Agar gel.

Keywords: aqueous solution, ions, coupling, Darcy coefficient, free energy, stress, strain, dehydration, Agar gel.

Introduction

When a sphere of Agar gel is placed in an aqueous solution of polyethylene glycol (PEG), a variation of its diameter can be observed during time, which reveals mass exchanges between the sphere and the solution [8]. This phenomenon depends on the PEG concentration and on the molecule size. It is possible to add to this transport mechanism, related to the presence of concentration gradients, the effect of an electric field [3]. These exchanges come along with stresses and strains that can induce cracks in the gel (fig. 1 and 2). We propose to establish a model coupling the transfer of an ionic solution and the stress/strain in an elastic, isotropic, and two-phase (solid-liquid) porous medium under isothermal conditions. Experiments will validate the model in the case of Agar gel saturated by pure water.

Jacques M. Huyghe et al. (eds), IUTAM Proceedings on Physicochemical and Electromechanical Interactions in Porous Media, 307–312.

© 2005 Springer. Printed in the Netherlands.

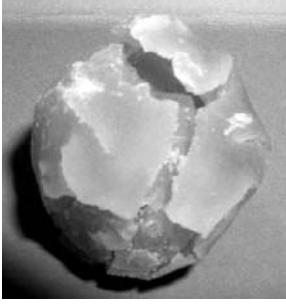


Figure 1. View of a sphere of Agar gel after fast dehydration.



Figure 2. Appearance of a gel crack during electro-osmosis tests.

Electro-Osmotic Mass Fluxes

We consider a system made of a solid phase (denoted by s) containing a liquid phase (denoted by L). The latter is composed by water (denoted by e) and by two kinds of ions (denoted by $+$ and $-$). An electric field is applied. The methods of the linear thermodynamics of irreversible processes permits the description of transport phenomena by linear relations. For the liquid phase [9] (in this paper, the indices or exponents k and m refer to cartesian coordinates):

$$v_L^k - v_s^k = -\frac{L}{T} (\rho_e \mu_{e,k} + \rho_+ \mu_{+,k} + \rho_- \mu_{-,k} + \rho_L g z_{,k} + Z_L \phi_{,k}) \quad (1)$$

where v_L^k and v_s^k are the velocities of the liquid and solid phases, respectively, L is a phenomenological coefficient, T is the temperature, ρ_i are the apparent mass densities ($i = e, +, -, L$), μ_e , μ_+ and μ_- are the chemical potentials of water, cation and anion, g is the gravity acceleration, z is the height, Z_L is the electric charge of the liquid phase per unit mass, and ϕ is the electric potential.

With the expression of the chemical potentials, equation (1) gives the Darcy's law [9]:

$$v_L^k - v_s^k = -K_w \left(\frac{P_{L,k}^*}{\rho_e^* g} + z_{,k} + \frac{Z_L \phi_{,k}}{g} \right) \quad (2)$$

where K_w is the Darcy coefficient defined by: $K_w = Lg/\rho_L T$, P_L^* is the pressure of the liquid phase at the pores scale and ρ_e^* is the real mass density of water.

Coupling with the Solid Phase Mechanics

The method used here [2, 10, 4, 6] consists of assuming the existence of a free energy function Φ that depends on state variables of the medium. With the

above assumptions, the chosen state variables are w , the water content of the medium, ε^{km} , the strain of the skeleton, n_+ and n_- , the numbers of cations and anions per unit mass of the solid:

$$\Phi = \Phi \left(w, \varepsilon^{km}, n_+, n_- \right) \quad (3)$$

The second order development near a reference state (referred to by exponent 0) leads to the following state relations:

$$\mu_e = \mu_e^0 + \frac{1}{\rho_s} \left(d_e \Delta w - 3K\beta \delta^{km} \Delta \varepsilon^{km} - d_+^e \Delta n_+ - d_-^e \Delta n_- \right) \quad (4)$$

$$\mu_+ = \mu_+^0 + \frac{1}{\rho_s M_+} \left(-d_+^e \Delta w + d_+^e \delta^{km} \Delta \varepsilon^{km} + d_+ \Delta n_+ - d_+^+ \Delta n_- \right) \quad (5)$$

$$\mu_- = \mu_-^0 + \frac{1}{\rho_s M_-} \left(-d_-^e \Delta w + d_-^e \delta^{km} \Delta \varepsilon^{km} - d_-^+ \Delta n_+ + d_- \Delta n_- \right) \quad (6)$$

$$\begin{aligned} \sigma^{km} = & \sigma^{km0} - 3K\beta \Delta w \delta^{km} + \lambda \Delta \varepsilon^{jj} \delta^{km} + 2\mu \Delta \varepsilon^{km} + d_+^e \Delta n_+ \delta^{km} \\ & + d_-^e \Delta n_- \delta^{km} \end{aligned} \quad (7)$$

in which appear the molar mass of the cation M_+ and anion M_- , the unit tensor δ^{km} , the coefficient of compressibility K , the Lamé coefficients λ and μ , and nine partial derivatives of free energy (d_e , β , d_+^e , d_-^e , d_+ , d_- , d_+^+ , d_-^+ and d_-^+). Introducing (4), (5) and (6) in (1) gives an new expression of the liquid phase transport:

$$v_L^k - v_s^k = -D_w w_{,k} + D_\varepsilon (tr \varepsilon)_{,k} - D_+ n_{+,k} - D_- n_{-,k} - \frac{L \rho_L g}{T} z_{,k} - \frac{L \rho_L Z_L}{T} \phi_{,k} \quad (8)$$

where D_w , D_ε , D_+ and D_- can be expressed using K_w and coefficients appearing in (4), (5), (6) and (7). This equation provides the coupling between the transport phenomena and the mechanics of the medium.

Although the equation (7) restricts the consideration to small strains, it is possible to consider large strains by moving the state reference (w^0 , ε^{km0} , n_+^0 , n_-^0) and by updating the coefficients, which depend all on state variables.

In the general case, the model depends on two mechanical coefficients (the Young's modulus E and the Poisson's ratio ν), one transport coefficient (L or K_w) and the nine coefficients defined in the equations (4) to (7). Coefficients d_+ , d_- , d_+^e , d_-^e , d_+^+ , and d_-^+ were determined in the case of an ideal solution [8].

Experimental Determination of Some Coefficients – Case of Pure Water in Agar Gel

In order to analyze coefficients D_w , D_ε , d_e , and β , the liquid phase is assumed to be pure water. In this case, the chemical potential of water is given

by: $\mu_e = \mu_e^0 + P_L^*/\rho_e^*$. The relation (4) takes the shape proposed by Biot [1]:

$$\Delta P_L^* = \frac{\rho_e^*}{\rho_s} \left(d_e \Delta w - 3K\beta \delta^{km} \Delta \varepsilon^{km} \right) \tag{9}$$

The two coefficients d_e and β , which can be related to the two physical coefficients introduced by Biot in the theory of consolidation [1], are defined by:

$$d_e = \rho_s \left(\frac{\partial \mu_e}{\partial w} \right) \quad ; \quad 3K\beta = - \frac{\partial (tr\sigma)}{\partial w} \tag{10}$$

For Agar gel, experimental study of these coefficients were performed [7]. The coefficient E was determined by compressive tests. Ultrasonic measurements of the Poisson's ratio ν showed that it is almost equal to 0.5. Compressibility K (fig. 3) is deduced from $K = E/(3(1 - 2\nu))$.

Agar gel is a hygroscopic medium for $w < 60\%$ [7]. In this range, the equation (10) allows the determination of d_e from the chemical potential of water given by the desorption isotherm. Assuming that the two-phase structure of the medium is conserved, the coefficient β can be expressed by: $\beta = 1/3 (\alpha + w)$, where α is the ratio between the specific mass of the water and the specific mass of the solid. This expression is confirmed by experimental tests (fig. 4). The coefficient K_w (fig. 5) was measured for a plate of gel placed in a PEG solution [6]. D_w and D_ε (fig. 6) are deduced from:

$$D_w = \frac{K_w d_e w}{g} \quad ; \quad D_\varepsilon = \frac{K_w 3K\beta w}{g} \tag{11}$$

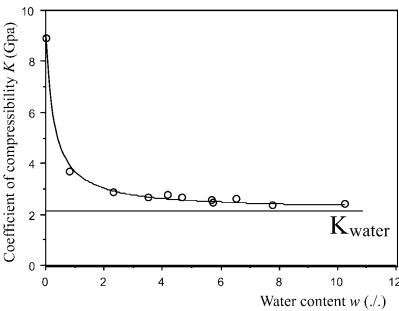


Figure 3. Variation of the coefficient K with water content.

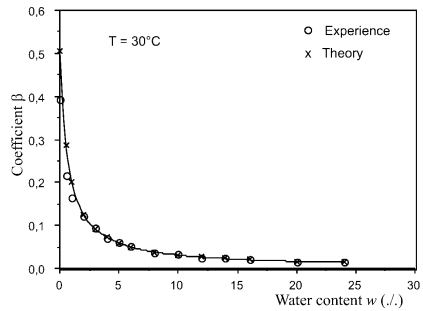


Figure 4. Variation of the coefficient β with water content.

Experimental Validation

Associated with the mass balance of water and the mechanical equilibrium equation, relations (7) and (8) give a model of solution transport in a deformable porous medium. The result of an incremental numerical method was

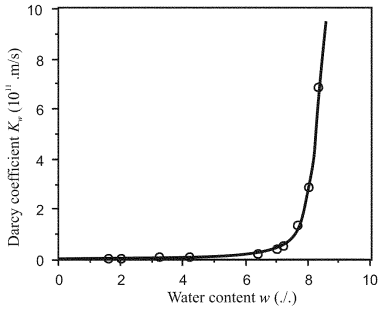


Figure 5. Variation of Darcy coefficient K_w with water content.

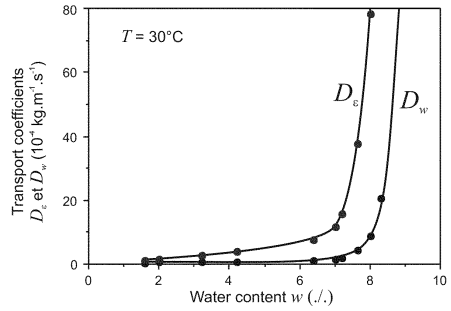


Figure 6. Variation of transport coefficients D_w and D_ε with water content.

compared to experiments accomplished for the case of a sphere with an initial radius of 2 cm placed in a PEG solution. Figure 7 gives an example of the comparison between experimental and numerical water content profiles. The model permits the analysis of the evolution of stress profiles. Figure 8 shows the evolution of the circumferential stress at different times in the case of the sphere. Figure 9 represents the final experimental and theoretical deformations of a cylinder. There is a good agreement between experience and theory.

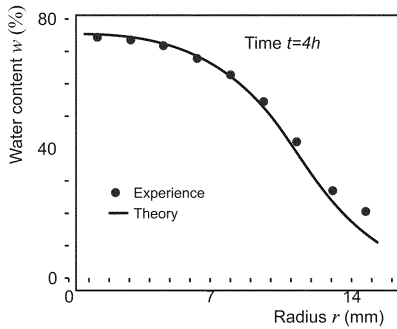


Figure 7. Experimental and theoretical water content profiles in the sphere.

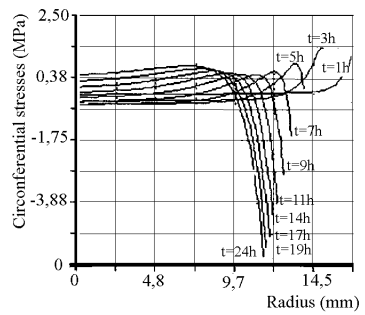


Figure 8. Circumferential stresses in the sphere at different times.

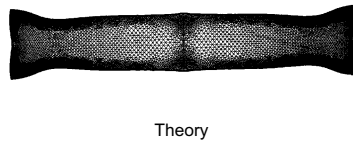
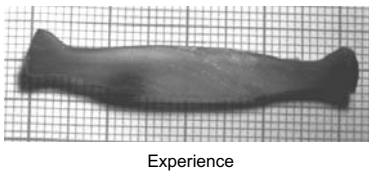


Figure 9. Experimental and theoretical deformations of a cylinder after dehydration.

Conclusion

In this paper, we give a model coupling mass transfer and stress/strain in an elastic porous medium whose pores are filled by an ionic solution. In this model, the chemical potential and mechanical behaviour laws are developed from a free energy potential. A large number of coefficients appears and we proposed theoretical and experimental method for their determination. In the simple case of pure water, we have shown that it is possible to analyze the coefficients of the model in Agar gel. A good agreement between the experiments and the numerical model was found in the case of dehydration of a sphere. This suggests to extend the analysis on the effect of ionic species on the coefficients of the model and the simulation of electro-osmosis in deformable media.

References

- [1] Biot, M.A. (1941) General theory of three-dimensional consolidation. *Journal of Applied Physics* **12**, 155-164
- [2] Biot, M.A. (1972) Theory of finite deformations of porous solids. *Indiana University Mathematics Journal* **21**, 597-620
- [3] Boscus, J. (2001) *Phénomènes électrocinétiques en milieux poreux*, Master's thesis, USTL Montpellier 2
- [4] Coussy, O. (1991) *Mécanique des milieux poreux*, Technip Ed., Paris
- [5] Guggenheim, E. A. (1965) *Thermodynamique*, Dunod, Paris
- [6] Mrani, I., Bénet, J.-C., and Fras, G. (1995) Transport of water in a biconstituent elastic medium. *Appl. Mech. Rev.* **48**, 717-721
- [7] Mrani, I., Fras, G., and Bénet, J.-C. (1995) Microstructure et propriétés hygromécaniques du gel d'agar. *J. Physique III France* **5**, 985-998
- [8] Richefeu, V., El Youssoufi, M. S. and, Bénet, J.-C. (2002) Saturated porous medium strain under osmotic actions. *Poromechanics II*, Auriault et al. (ed.), Balkema, Rotterdam, 533-537
- [9] Ruiz, T., and Bénet, J.-C. (1998) Potentiels de transport d'une solution diluée en milieux poreux. *C.R. Acad. Sci. Paris* **326**, 415-421
- [10] Sih, G. C., and Michopoulos, J. C. (1986) *Hygrothermoelasticity*, Martinus Nijhoff Publishers

XI

PHASE TRANSITION AND CAPILLARITY.

Chairmen: C.C. van Donkelaar, P. Raats

ABOUT THE PROPER CHOICE OF VARIABLES TO DESCRIBE FLOW-INDUCED CRYSTALLIZATION IN POLYMER MELTS

Jan van Meerveld

Institute of Polymers, Department of Materials, ETH Zurich, Switzerland

meerveld@mat.ethz.ch

Markus Hütter

Department of Chemical Engineering, Massachusetts Institute of Technology, Cambridge, U.S.A.

mhuetter@mit.edu

Abstract The influence of flow on the crystallization of polymers is divided into four different regimes, using a molecular description of polymer rheology: (1) close-to equilibrium configurations, (2) orientated chains, (3) weak chain stretching, and (4) strong chain stretching where the chain conformation can be affected. It can be shown that these regimes correlate well with the different morphologies observed in flow induced crystallization experiments. An explanation for the change in nucleation dynamics can be given based on kinetic and/or thermodynamic processes depending on the orientation and stretch of the polymer chains. The different morphologies are characterized by Minkowski functionals, and their development in time are described by the so-called Schneider rate equations.

Keywords: Flow induced crystallization, polymers melts, molecular based rheology, classification

Introduction

The application of a flow field has pronounced effects on the crystallization dynamics and semi-crystalline morphology of polymeric systems. Under quiescent, no-flow conditions the crystallization dynamics is governed by the temperature, T , and spherulites are formed. In the presence of flow, increasing the flow rate can result in an increase of the nuclei density up to factors of 10^6 , but the morphology remains spherulitic [18]. At even higher flow rates the so-called ‘shish-kebab’ morphology is observed. This results from the de-

Jacques M. Huyghe et al. (eds), IUTAM Proceedings on Physicochemical and Electromechanical Interactions in Porous Media, 315–320.

© 2005 Springer. Printed in the Netherlands.

velopment of a bundle like structure, the ‘shish’, in the flow direction from which the lamellae, the ‘kebab’, are growing in the direction perpendicular to the flow. For further details the reader is referred to complete reviews [4, 10].

With respect to the change in crystallization dynamics and the development of the different morphologies two questions will be addressed. Firstly; which physical processes govern the influence of flow on the nucleation dynamics and the development of the different morphologies? Secondly; what are appropriate model parameters to describe the crystallization dynamics? In order to address and discuss these questions a good understanding of how the flow affects the orientation and ordering of the polymer chains is important. Hence the main features of molecular based rheological models are briefly reviewed in Section 2, before addressing the two questions in Sections 3 and 4, respectively.

Molecular Based Rheological Modeling

In molecular based mean field rheological models a flexible polymer chain is represented by the contour path [3]. This contour path is a smoothed curve through the actual configuration of the backbone of a chain and disregards the atomistic, chemical details of the particular polymer. In general evolution equations are formulated for the dynamic behavior of the average orientation and the extension of the contour path. The latter is described by the chain stretch parameter λ , $\lambda = L/L_0$, with L the current length and L_0 the equilibrium length of the contour path.

The relaxation mechanisms for the orientation and chain stretch are different and two different time scales need to be considered [3]. The relaxation time for orientation relaxation is denoted by the reptation time, τ_{rep} , and that for the chain retraction is the stretching time, τ_s . These two time scales are connected to each other via the relationship $\tau_{\text{rep}}/\tau_s = 3Z$, with Z the number of entanglements, valid for well entangled chains ($Z > 100$) [3]. For typical polymer melts $Z > 60$ and the magnitudes of τ_{rep} and τ_s are thus separated by at least two orders of magnitude. This observation directly implies that the contour path can be orientated at much lower flow rates compared to those required to stretch it. This is conveniently expressed by the Deborah numbers, De , based on τ_{rep} and τ_s , defined as $De_{\text{rep}} = \tau_{\text{rep}}\dot{\gamma}$, $\tau_{\text{rep}}\dot{\epsilon}$ and $De_s = \tau_s\dot{\gamma}$, $\tau_s\dot{\epsilon}$ with $\dot{\gamma}$ the shear rate and $\dot{\epsilon}$ the extension rate, respectively.

If the chain is stretched, two different regimes can be identified based on the global configuration of the chain and the rotational isomerization, RI, (the change in the distribution of the conformation of the monomers, or sequence of monomers, due to chain stretching) at temperature well above the melting temperature T_m [1, 20]. For small stretching, $\lambda < \lambda^*$, the chain maintains a Gaussian configuration and the amount of RI is small. For large stretching, $\lambda > \lambda^*$,

the influence of the finite extensibility of the chain sets in, and the chain configuration becomes non-Gaussian and the amount of RI is large. The transition between the two different regimes is denoted by λ^* . Hence the orientation and conformation can be affected on an atomistic level for $De_s > 1$, $\lambda > \lambda^*$. For $T > T_m$ the magnitude of λ_{\max} , and hence λ^* , can be estimated for a particular melt [3, 20]. However, for $T < T_m$ the conformations of the monomers are not homogeneously distributed along the chain. This affects the stiffness, or Kuhn length, of the chain which increases with decreasing T [8]. Accordingly, the magnitude of λ^* is temperature dependent, $\lambda^* = \lambda^*(T)$, and decreases with decreasing T . The regime $De_s > 1$, $\lambda < \lambda^*$ thus decreases with decreasing T . Thus the chain conformation becomes similar to that in the crystalline state by decreasing T or increasing λ .

Summarizing the above, four regimes are identified. For $De_{\text{rep}} < 1$, $De_s < 1$ the chains are randomly oriented and not stretched. Subsequently three transitions can be identified corresponding to increasing orientational order of the chains, $De_{\text{rep}} > 1$, the onset of chain stretching, $De_s > 1$, and finally strong chain stretching conditions where the chain conformation can be influenced, $\lambda > \lambda^*(T)$. In polydisperse melts the enhanced crystallization dynamics is ascribed to the high molecular weight tail of the system [15]. In the next Section the magnitude of De_{rep} , De_s and λ refers to this part of the melt only.

Phase Change Dynamics

The change in order between the amorphous melt at $T > T_m$ and the crystalline phase can be specified according to different order parameters associated to (1) the density, (2) the periodic (crystallographic) ordering of the monomers, (3) the orientational order of the chains and (4) the change in conformational order of the chain. It should be noted that the ordering of the material in the nucleus is not necessarily identical to that of the crystalline phase [16]. The application of the flow field is observed to primarily affect the number density of spherulites and ‘shish’ as well as the length of the ‘shish’ [4]. The thickness and growth rate of a lamellae, and hence of a spherulite, are not or only weakly affected [15]. We focus on the nucleation dynamics only in the discussion below.

From the previous Section it is expected that the application of the flow field will primarily affect the last two order parameters, i.e. the orientation and conformation of the chain. In the discussion of the nucleation dynamics, it is helpful to separate the contributions from the ‘kinetic’ and ‘thermodynamic’ processes. The first represents the fundamental timescale to form a nucleus, the prefactor, and the second describes the driving force for the phase transition based on the position of the system in the phase diagram.

First, the kinetic contribution is discussed. Under quiescent conditions,

$De_{\text{rep}} < 1$, $De_s < 1$, the nucleation dynamics is stochastic in nature as a critical fluctuation in one, or more, order parameters is required for the development of a nucleus. For $De_{\text{rep}} > 1$, $De_s < 1$ the chains become more uniformly oriented in the flow direction but the conformation remains unaffected. Hence a thermally activated fluctuation in the conformation can be sufficient for the development of a nucleus. For a number of polymers, for example PET and PEEK, the Kuhn length is larger than the distance between two entanglements. For this class of polymers, the nucleation dynamics is very similar to the phase transition observed in liquid crystalline polymers under quiescent [8], and flow conditions [21]. In fast flows, $De_{\text{rep}} > 1$, $De_s > 1$, $\lambda > \lambda^*(T)$, one reaches the condition where the chains are fully oriented and the chain conformation becomes similar to that of the crystalline state. Critical fluctuations in the orientation and conformation of the chain are therefore no longer needed, as these requirements are fulfilled, in a more deterministic manner, by the applied flow field. Hence, an increase of the parameters De_{rep} , De_s and λ results into a shift of the nucleation dynamics from a stochastic to a more deterministic process, resulting into an increase of the nucleation rate.

Besides the kinetic contribution, the applied flow field also modifies the thermodynamic driving force. Following the pioneering work of [6] the influence of the flow field can again be separated into four different regimes. The increase in orientational ordering and chain stretching results into an increase of the equilibrium melting temperature and associated increase of the thermodynamic driving force at given T . The detailed information of conformational ordering cannot be described by the stretch parameter λ . This can be approximated by means of rubber theory of finite extensible chains [20].

The transition from spherulitic to the shish-kebab morphology is generally ascribed to 'strong' chain stretching conditions [10]. Analysis of experimental investigations reported in literature [4, 12, 19], in terms of De_{rep} and De_s , indicates that the nuclei density of spherulites is enhanced under the conditions $De_{\text{rep}} > 1$, $De_s < 1$ and the shish-kebab morphology develops for $De_s \gg 1$, suggesting $\lambda > \lambda^*(T)$. These findings are discussed in detail for a more extensive set of experiments in [13]. It is noted that the regime $De_{\text{rep}} > 1$, $De_s > 1$, $\lambda < \lambda^*(T)$ is in general small, especially in uniaxial flows, and not always observed experimentally. These findings indicate that the conformational order of the chain is important for the transition in the nucleation kinetics. It is however difficult to identify whether this results from a significant change in (1) the kinetic process, (2) the thermodynamic driving force, or (3) a cooperative effect of both, as the kinetic and thermodynamic processes change at approximately identical flow conditions. It is noted that the influence of an applied electrical field on the crystallization dynamics of glycine can only be explained from both kinetic and thermodynamic arguments [7].

Morphological Description

The requirements on how to describe the morphology of the solid-liquid system are twofold. Firstly, the separation of nucleation and growth prominent in polymer crystallization must be reflected in the model. Secondly, the model must be capable to distinguish properly spherulites from the shish-kebab structure. These requirements are met by the integral model of Kolmogoroff [11], Avrami [2], Johnson & Mehl [9] and Evans [5] (but not by most of its simplified versions), which can be reformulated into a set of coupled differential equations, the so-called Schneider rate equations [4, 17]. For a spherulitic morphology this results in dynamic equations for four structural variables connected to: (1) the real volume fraction of the crystalline phase, (2) the average grain surface, (3) the average grain radius and (4) the number density of spherulites. These four structural variables are in direct relation to the Minkowski functionals as used in integral geometry [14]. Also the dynamic behavior for the formation of the shish-kebab structure can be formulated into a similar set of equations, which have been successfully applied to describe experiments [4, 22].

Conclusion

A realistic rheological model describing both orientation and stretch of the chain is essential to understand, and describe, the influence of the flow field on the kinetic and thermodynamic contributions to the crystallization dynamics. Characterizing an experiment according to De_{rep} , De_s and λ gives good agreement with the transitions in the morphologies found experimentally. The individual contributions from the nucleation and growth dynamics on the development of the spherulitic or shish-kebab morphology can be conveniently described by the Schneider rate equations.

References

- [1] Abe, Y. and Flory, P.J. (1970) Rotational isomerization of polymer chains by stretching, *J. Chem. Phys.* **52**(6), 2814–2820
- [2] Avrami, M. (1939) Kinetics of phase change. I. General theory, *J. Chem. Phys.* **7**, 1103–1112; Kinetics of phase change. II. Transformation-time relations for random distribution of nuclei, *J. Chem. Phys.* **8**, 212–224; Kinetics of phase change. III. Granulation, phase change, and microstructure, *J. Chem. Phys.* **9**, 177–184
- [3] Doi, M. and Edwards, S.F. (1986) *The theory of polymer dynamics*, Oxford, United Kingdom, Clarendon Press
- [4] Eder, G. and Janeschitz-Kriegl, H. (1997) Crystallization, *Materials Science and Technology*, Vol. 18, H. Meijer (ed.), Wiley-VCH, Weinheim, pp. 269–342
- [5] Evans, U.R. (1945) The laws of expanding circles and spheres in relation to the lateral growth of surface films and grain-size of metals, *Trans. Faraday. Soc.* **41**(7), 365–374

- [6] Flory, P.J. (1947) Thermodynamics of crystallization in high polymers. I. Crystallization induced by stretching, *J. Chem. Phys.* **15**(6), 397–408
- [7] Garetz, B.A., Matic, J. and Myerson, A.S. (2002) Polarization switching of crystal structure in the nonphotochemical light-induced nucleation of supersaturated aqueous glycine solutions, *Phys. Rev. Lett.* **89**(17), 175501
- [8] Imai, M., Kaji, K. and Kanaya, T. (1993) Orientation fluctuations of poly(ethylene terephthalate) during the induction period of crystallization, *Phys. Rev. Lett.* **71**(25), 4162–4165
- [9] Johnson, W.A. and Mehl, R.F. (1939) Reaction kinetics in processes of nucleation and growth, *Trans. Am. Inst. Min. Engrs.* **135**, 416–458
- [10] Keller, A. and Kolnaar, H.W.H. (1997) Flow induced orientation and structure formation *Materials Science and Technology*, Vol. 18, H. Meijer (ed.), Wiley-VCH, Weinheim, pp. 269–342
- [11] Kolmogoroff, A.N. (1937) On the statistical theory of the crystallization of metals, *Bull. Acad. Sci. USSR Mat. Ser* **1**, 355–359
- [12] Koscher, E. and Fulchiron, R. (2002) Influence of shear on polypropylene crystallization: morphology development and kinetics, *Polymer* **42**(25), 6931–6942
- [13] van Meerveld, J., Hütter, M. and Peters, G.W.M. (2003) In preparation
- [14] Mecke, K.R. (2000) Additivity, convexity, and beyond: Applications of Minkowski functionals in statistical physics, in *Statistical Physics and Spatial Statistics: The Art of Analyzing and Modeling Spatial Structures and Pattern Formation*, K.R. Mecke and D. Stoyan (eds.), Springer, Berlin, pp. 111–184
- [15] Nogales, A., Hsiao, B.S., Somani, R.H., Srinivas, S., Tsou, A.H., Balta-Callja, F.J. and Ezquerro, T.A. (2001) Shear-induced crystallization of isotactic polypropylene with different molecular weight distributions: in situ small- and wide-angle X-ray scattering studies, *Polymer* **42**(12), 5247–5256
- [16] Oxtoby, D.W. (2002) Density functional methods in the statistical mechanics of materials, *Annu. Rev. Mater. Res.* **32**, 39–52
- [17] Schneider, W., Köppel, A. and Berger, J. (1988) Non-isothermal crystallization of polymers, *Int. Polym. Proc.* **2**, 151–154
- [18] Stadlbauer, M. (2001) Rheo-kinetics of polymers in extension: Rheometry, rheology, and structure development, Ph.D. thesis, University of Linz, Austria
- [19] Swartjes, F.H.M. (2001) Stress induced crystallization in elongational flow, Ph.D. thesis, University of Technology Eindhoven, the Netherlands
- [20] Treloar, L.R.G. (1975) *The Physics of Rubber Elasticity*, Oxford, United Kingdom, Clarendon Press
- [21] Welsh, G.E., Blundell, D.J. and Windle, A.H. (1998) A transient liquid crystalline phase as a precursor for crystallization in random co-polyester fibers, *Macromol.* **31**(5), 7562–7565
- [22] Zuidema, H., Peters, G.W.M. and Meijer, H.E.H. (2002) Development and validation of a recoverable strain based model for flow-induced crystallization of polymers, *Macromol. Theory Simul.* **10**(5), 447–460

A MICROMECHANICS APPROACH TO THE MECHANICALLY-INDUCED DISSOLUTION IN POROUS MEDIA

Eric Lemarchand

LML, CNRS UMR 8107, Villeneuve d'Ascq, France

eric.lemarchand@univ-lille1.fr

Luc Dormieux

Institut Navier, LMSGC-ENPC, Marne-la-Vallée, France

dormieux@lmsgc.enpc.fr

Franz-Josef Ulm

CEE-MIT, Cambridge, United States of America

ulm@mit.edu

Abstract When subjected to a mechanical loading, the solid phase of a saturated porous medium undergoes a dissolution due to strain-stress concentration effects along the fluid-solid interface. Through a micromechanical analysis, the mechanical affinity is shown to be the driving force of the local dissolution. For cracked porous media, the elastic free energy is a dominant component of this driving force. This allows to predict dissolution-induced creep in such materials.

Keywords: creep, dissolution, micromechanics, damage, chemoporoelasticity

Introduction

Let us consider an elementary volume V of saturated porous material. At the microscopic scale, the porous material appears as a heterogeneous material in which the solid and fluid phases occupy two distinct domains. V_s^t and V_f^t are the volume of the solid phase and of the fluid phase respectively, and the solid-fluid interface is denoted by \mathcal{I}_{fs}^t . The unit outward normal to the solid phase is denoted by \underline{n}_s . We denote by \underline{x} , \underline{v} , $\underline{\epsilon}$ and $\underline{\sigma}$, the position vector, the velocity, the strain and the stress at the microscopic scale, respectively.

Dissolution processes are superficial phenomena taking place along the fluid-

solid interface \mathcal{I}_{fs}^t . The volume of the reactive solid which is dissolved between times t and $t + dt$ is represented by a rate of reactive mass per unit of surface \dot{m} . The celerity of the solid-fluid interface along the dissolution process is $\underline{c} = \underline{v}_s - \dot{m}/\rho_s \underline{n}_s$, where ρ_s is the mass density of the solid matrix phase. \underline{v}_s is the velocity associated with the strain field in the solid matrix, while the second term accounts for the dissolution process. The rate of the total porosity as follows:

$$\dot{\phi} = \dot{\phi}^m + \dot{\phi}^c ; \quad \dot{\phi}^m = -\frac{1}{|V|} \int_{\mathcal{I}_{fs}^t} \underline{v}_s \cdot \underline{n}_s d\Gamma ; \quad \dot{\phi}^c = \frac{1}{|V|} \int_{\mathcal{I}_{fs}^t} \frac{\dot{m}}{\rho_s} d\Gamma \quad (1)$$

$\dot{\phi}^m$ represents the rate of porosity induced by the mechanical strain of the solid matrix. $\dot{\phi}^c$ denotes the change of porosity due to the chemical dissolution of the solid matrix. Then, integration of (1) with respect to time yields the total porosity at time t as a function of the strain-induced porosity ϕ^m and of the chemical porosity ϕ^c :

$$\phi(t) = \phi_o + \phi^m + \phi^c \quad \text{with} \quad \phi^\beta = \int_{t_o}^t \dot{\phi}^\beta d\tau \quad (\beta = m, c) \quad (2)$$

In the present study, we assume infinitesimal strains, so that $\phi^m \ll 1$. The free energy of the solid matrix at time t is denoted by $\Psi_S(t)$. It involves at least two components: the elastic potential ψ^{el} and the chemical potential ψ^c of the crystals bound in the solid phase. At any time t , the elastic energy stored in the solid phase is denoted by $\Psi^{\text{el}}(t)$:

$$\Psi^{\text{el}}(t) = \int_{V_s^t} \rho_s \psi^{\text{el}} dV ; \quad \Psi_S(t) = \Psi^{\text{el}}(t) + \int_{V_s^t} \rho_s \psi^c dV \quad (3)$$

Dissipation in a Chemomechanical Loading

We aim in the present section at determining the dissipation occurring during chemomechanical processes in a porous material, in which the solid matrix phase is submitted to dissolution in addition to the purely mechanical loading. We are going to investigate the thermodynamic evolutions of the system \mathcal{M} constituted by the material located in the solid domain V_s^t at a given time t . At time $t + dt$, \mathcal{M} is made up of V_s^{t+dt} and of the solute which has dissolved into the fluid in the interval $[t, t + dt]$. Only isothermal quasistatic evolutions are considered. Let $\Psi_{\mathcal{M}}$ and \mathcal{D} respectively denote the free energy of \mathcal{M} and the dissipation. The latter is subjected to Clausius-Duhem inequality:

$$\mathcal{D} = -\mathcal{P}^{\text{int}} - \frac{d\Psi_{\mathcal{M}}}{dt} = \mathcal{P}^{\text{ext}} - \frac{d\Psi_{\mathcal{M}}}{dt} \geq 0 \quad (4)$$

\mathcal{P}^{int} (resp. \mathcal{P}^{ext}) denoting the work of internal (resp. external) forces. The uniform pore pressure p and the macroscopic strain \mathbf{E} are the two inde-

pendent mechanical loading parameters. The macroscopic strain rate $\mathbf{D} \approx \dot{\mathbf{E}}$ is introduced through Hashin boundary conditions on the velocity at the edge ∂V of the r.e.v. of the form $\underline{v}_s = \dot{\mathbf{E}} \cdot \underline{x}$. Accordingly, $\dot{\mathbf{E}}$ is related to the rate of the microscopic strain field through the average rule $\dot{\mathbf{E}} = \langle \dot{\mathbf{e}} \rangle$ and the macroscopic stress Σ is defined as the volume average $\langle \sigma \rangle$ of the local stress σ over the r.e.v. The rate of external work \mathcal{P}^{ext} can be divided into a mechanical part and a chemical one. The “mechanical” part comprises the work of the macroscopic stress ($\Sigma : \dot{\mathbf{E}}$) and that of the pore pressure ($p \dot{\phi}^m$). The “chemical” part is the external energy supplied to the matrix along the dissolution process:

$$\mathcal{P}_c^{ext} = \int_{\mathcal{I}_{fs}^t} p \frac{\dot{m}}{\rho_s} d\Gamma - \int_{\mathcal{I}_{fs}^t} \frac{p_i}{\rho_i} \dot{m} d\Gamma \quad (5)$$

The last term in (5) is associated to the introduction of the dissolved solid into the fluid: p_i and ρ_i are respectively the partial pressure and the mass density of these reacting ions in solution. The total external work thus reads:

$$\mathcal{P}^{ext} = |V| \left(\Sigma : \dot{\mathbf{E}} + p \dot{\phi}^m - \frac{1}{|V|} \int_{\mathcal{I}_{fs}^t} \left(\frac{p_i}{\rho_i} - \frac{p}{\rho_s} \right) \dot{m} d\Gamma \right) \quad (6)$$

At time t , the free energy $\Psi_{\mathcal{M}}(t)$ of the system \mathcal{M} is equal to $\Psi_S(t)$ given in (3). Still, at time $t + dt$, one part of the system is dissolved in the fluid. The free energy of \mathcal{M} at $t + dt$ thus differs from $\Psi_S(t + dt)$ which only represents the contribution of the solid phase. At time t , the free energy of the solid matrix system can be expressed as follows:

$$\Psi_{\mathcal{M}}(t) = \Psi^{el}(t) + \int_{V_s^{t+dt}} \rho_s \psi_c dV + dt \int_{\mathcal{I}_{fs}^t} \psi_c \dot{m} d\Gamma \quad (7)$$

At time $t + dt$, the free energy of the same system is the sum of the contribution of the remaining solid matrix (domain V_s^{t+dt}) and of the dissolved material. φ_i denoting the mass density of the free energy of the ions in solution, the free energy of the whole system at $t + dt$ reads:

$$\Psi_{\mathcal{M}}(t + dt) = \Psi^{el}(t + dt) + \int_{V_s^{t+dt}} \rho_s \psi_c dV + dt \int_{\mathcal{I}_{fs}^t} \varphi_i \dot{m} d\Gamma \quad (8)$$

Comparing (8) and (7), and assuming that ψ_c is constant in time, yields the rate of the free energy of the system:

$$\dot{\Psi}_{\mathcal{M}} = \dot{\Psi}^{el} + \int_{\mathcal{I}_{fs}^t} (\varphi_i - \psi_c) \dot{m} d\Gamma \quad (9)$$

The rate of dissipation \mathcal{D} between t and $t + dt$ in (4) is obtained from (6) and (9). Introducing $\Psi_*^{\text{el}} = \Psi^{\text{el}} - |V| p \phi^m$, that is the potential energy of the solid matrix (Deude et al., 2002), Clausius-Duhem inequality becomes:

$$\mathcal{D} = |V| (\boldsymbol{\Sigma} : \dot{\mathbf{E}} - \dot{p} \phi^m) - \dot{\Psi}_*^{\text{el}} + \int_{\mathcal{T}_{fs}} \left(\frac{p}{\rho_s} + \psi_c - \psi_i \right) \dot{m} d\Gamma \geq 0 \quad (10)$$

where $\psi_i = \varphi_i + p_i/\rho_i$ is the chemical potential of the dissolving ions.

Chemoporoelastic Theory

For an elastic behavior of the solid phase, Ψ_*^{el} only depends on the loading parameters, that is the macroscopic strain \mathbf{E} and the fluid pressure p , and on the evolving morphology of the r.e.v.. We formally account for this evolution of the morphology through a parameter ζ , which micromechanical interpretation will be obtained in particular cases.

State equations

In an incremental evolution without dissolution ($\dot{m} = 0$), the intrinsic dissipation of the material is equal to 0, i.e. $\dot{\Psi}_*^{\text{el}} = |V| (\boldsymbol{\Sigma} : \dot{\mathbf{E}} - \dot{p} \phi^m)$. The macroscopic state equations thus read:

$$\boldsymbol{\Sigma} = \frac{1}{|V|} \frac{\partial \Psi_*^{\text{el}}}{\partial \mathbf{E}}(\mathbf{E}, p, \zeta) \quad ; \quad \phi^m = -\frac{1}{|V|} \frac{\partial \Psi_*^{\text{el}}}{\partial p}(\mathbf{E}, p, \zeta) \quad (11)$$

If the solid is linear elastic (stiffness tensor $\mathbb{C}^s = \mathbb{S}^{s^{-1}}$), the potential energy Ψ_*^{el} takes the form (Deude et al., 2002):

$$\frac{1}{|V|} \Psi_*^{\text{el}}(\mathbf{E}, p, \zeta) = \frac{1}{2} \mathbf{E} : \mathbb{C}^{\text{hom}}(\zeta) : \mathbf{E} - \frac{p^2}{2M(\zeta)} - p \mathbf{B}(\zeta) : \mathbf{E} \quad (12)$$

Then, application of (12) in (11) gives:

$$\boldsymbol{\Sigma} = \mathbb{C}^{\text{hom}}(\zeta) : \mathbf{E} - p \mathbf{B}(\zeta) \quad ; \quad \phi^m = \frac{p}{M(\zeta)} + \mathbf{B}(\zeta) : \mathbf{E} \quad (13)$$

The macroscopic behavior of a saturated porous material undergoing a dissolution of its linear elastic solid matrix is therefore described by the classical Biot's theory, where the poroelastic properties now depend on the morphological parameter ζ . Formally, ζ plays the role of a "damage" parameter accounting for the dissolution.

Estimates for the macroscopic drained stiffness tensor $\mathbb{C}^{\text{hom}}(\zeta)$ as a function of the morphological parameter ζ can be derived from various micromechanical techniques. The micromechanical approach classically refers to the concept of strain concentration tensor, denoted here by \mathbb{A} . By definition, in an evolution

of the r.e.v. defined by $\dot{p} = 0$, $\dot{m} = 0$ and by a given macroscopic strain rate $\dot{\mathbf{E}}$, \mathbb{A} linearly relates the local strain rate $\dot{\mathbf{e}}$ to $\dot{\mathbf{E}}$:

$$\dot{\mathbf{e}}(\mathbf{x}) = \mathbb{A}(\mathbf{x}) : \dot{\mathbf{E}} \quad (14)$$

The macroscopic drained stiffness tensor $\mathbb{C}^{\text{hom}}(\zeta)$ and Biot's coefficient $\mathbf{B}(\zeta)$ can then be expressed as a function of the average of \mathbb{A} over the fluid saturated pore space (\mathbb{I} =fourth identity tensor):

$$\mathbb{C}^{\text{hom}} = \mathbb{C}^s : (\mathbb{I} - \phi \langle \mathbb{A} \rangle_f) \quad ; \quad \mathbf{B} = \phi_o \boldsymbol{\delta} : \langle \mathbb{A} \rangle_f = \boldsymbol{\delta} : (\mathbb{I} - \mathbb{S}^s : \mathbb{C}^{\text{hom}}) \quad (15)$$

Dissolution law at the microscopic scale

Introducing the state equations (13) into (10) yields:

$$\mathcal{D} = -\frac{\partial \Psi_*^{\text{el}}}{\partial \zeta} \dot{\zeta} + \int_{\mathcal{I}_{fs}^t} \left(\frac{p}{\rho_s} + \psi_c - \psi_i \right) \dot{m} d\Gamma \geq 0 \quad (16)$$

with

$$-\frac{\partial \Psi_*^{\text{el}}}{\partial \zeta} = |V| \left(\frac{p^2}{2} \frac{\partial}{\partial \zeta} \left(\frac{1}{M} \right) + p \frac{\partial \mathbf{B}}{\partial \zeta} : \mathbf{E} - \frac{1}{2} \mathbf{E} : \frac{\partial \mathbb{C}^{\text{hom}}}{\partial \zeta} : \mathbf{E} \right) \quad (17)$$

In particular, when $p + \rho^s(\psi_c - \psi_i)$ is uniform along the solid-fluid interface, the dissipation can be formulated in terms of the macroscopic variables \mathbf{E} , p , ϕ^c and ζ :

$$\mathcal{D} = -\frac{\partial \Psi_*^{\text{el}}}{\partial \zeta}(\mathbf{E}, p, \zeta) \dot{\zeta} + |V| [p + \rho_s(\psi_c - \psi_i)] \dot{\phi}^c \geq 0 \quad (18)$$

(18) could therefore be used in a standard macroscopic modelling of chemoporoelasticity. Still, the understanding of the driving forces of dissolution requires to analyze dissipation at the scale it takes place, namely along the fluid-solid interface. For this purpose, a micromechanical interpretation of the macroscopic thermodynamic force associated with ζ is due. Starting from the definition (3) of Ψ^{el} , its time derivative yields:

$$\frac{d\Psi^{\text{el}}}{dt} = \int_{V_s^t} \rho_s \dot{\psi}^{\text{el}} dV - \int_{\mathcal{I}_{fs}^t} \psi^{\text{el}} \dot{m} d\Gamma = \int_{V_s^t} \boldsymbol{\sigma} : \dot{\mathbf{e}} dV - \int_{\mathcal{I}_{fs}^t} \psi^{\text{el}} \dot{m} d\Gamma \quad (19)$$

Recalling that the stress state in the fluid is the uniform pressure p and using Hill's lemma in the form $\langle \boldsymbol{\sigma} : \dot{\mathbf{e}} \rangle = \boldsymbol{\Sigma} : \dot{\mathbf{E}}$, (19) then yields the rate of total potential energy and allows to relate the convective term of free energy to the thermodynamic force associated with ζ :

$$\dot{\Psi}_*^{\text{el}} = |V| (\boldsymbol{\Sigma} : \dot{\mathbf{E}} - \dot{p} \phi^m) - \int_{\mathcal{I}_{fs}^t} \psi^{\text{el}} \dot{m} d\Gamma \Rightarrow \int_{\mathcal{I}_{fs}^t} \psi^{\text{el}} \dot{m} d\Gamma = -\dot{\zeta} \frac{\partial \Psi_*^{\text{el}}}{\partial \zeta} \quad (20)$$

Introducing (20) into (16), the dissipation rate reduces to:

$$\mathcal{D} = \int_{\mathcal{I}_{fs}^t} \left(\psi^{\text{el}} + \frac{p}{\rho_s} + \psi_c - \psi_i \right) \dot{m} d\Gamma = - \int_{\mathcal{I}_{fs}^t} A_m \frac{\dot{m}}{\rho_s} d\Gamma \geq 0 \quad (21)$$

where $A_m = \rho_s(\psi_i - \psi_s)$ with $\psi_s = \psi_c + \psi^{\text{el}} + p/\rho_s$. The driving force of the chemical process thus proves to be the difference between the chemical potential ψ_i of the fluid phase and the chemical potential ψ_s of the solid phase. A_m is generally referred to as the "mechanical" affinity. In order to ensure the positivity of the local dissipation, the simplest form of the dissolution law reads (Ghoussoub and Leroy, 2001):

$$\dot{m}(\underline{x}) / \rho_s = -\kappa A_m(\underline{x}) \quad (22)$$

where κ is a positive, assumed constant, kinetic coefficient. It can be determined from a purely chemical dissolution process, for which the driving force reduces itself to the Gibbs energy.

Application: dissolution-induced creep in a cracked medium

Let us consider the case where the pore space is a network of saturated cracks. In order to implement the classical micromechanical estimates of the strain concentration tensor \mathbb{A} introduced in (14), the cracks are modelled as flat oblate spheroids. For simplicity, a uniform crack radius a is considered. N denotes the crack density. For an isotropic distribution of crack orientations, the macroscopic behavior derived from (15) is isotropic as well (Deude et al., 2002):

$$\mathbb{C}^{\text{hom}} = \mathbb{C}^s : (\mathbb{I} - \zeta \mathbb{Q}) \quad ; \quad \mathbb{Q} = \frac{16}{9} \frac{1 - \nu_s^2}{1 - 2\nu_s} \mathbb{J} + \frac{32}{45} \frac{(1 - \nu_s)(5 - \nu_s)}{2 - \nu_s} \mathbb{K} \quad (23)$$

where $\zeta = Na^3$, $J_{ijkl} = \delta_{ij}\delta_{kl}/3$ and $\mathbb{K} = \mathbb{I} - \mathbb{J}$. In particular, the macroscopic bulk modulus and Biot coefficient are derived from (15):

$$b = \beta\zeta \quad \text{with} \quad \beta = \frac{16}{9} \frac{1 - \nu_s^2}{1 - 2\nu_s} \quad ; \quad K^{\text{hom}} = K^s(1 - b) \quad (24)$$

The morphological parameter ζ which controls the damaging effect of cracks appears to depend only on the crack density and the crack radius. In the case of cracks, the macroscopic mechanical loading defined by \mathbf{E} or p is expected to induce a strong heterogeneity of the mechanical affinity, due to the stress/strain concentration in the vicinity of the crack tips.

For simplicity, let us consider perfectly drained conditions ($p = 0$) and start from an equilibrium between solid and solute ($\psi_c - \psi_i$). The equilibrium is disturbed by application of a constant macroscopic stress $\boldsymbol{\Sigma} = \Sigma \boldsymbol{\delta}$ ($\Sigma > 0$).

The macroscopic strain is $E(t)\delta$ and reads:

$$E(t) = \frac{\Sigma}{3K^s(1 - \zeta(t)\beta)} \quad (25)$$

The increase of ζ thus induces a macroscopic creep under constant stress. Assuming an instantaneous diffusion of the solute within the pore space, the mechanical affinity is $A_m \approx -\rho_s \psi^{\text{el}}$. The strain concentration effect at the crack tip then implies that the dissolution process concentrates at this place and is negligible elsewhere. The rate of crack radius increase \dot{a} is derived from (22) and gives the evolution $\zeta(t)$ of the damage parameter:

$$\dot{a} \approx \frac{\kappa E_s}{2(1 - \nu_s^2)} \left(\text{Log}\left(\frac{\omega(t)}{\omega_o(t)}\right) \right)^2 ; \quad \omega(t) - \omega_o(t) = \frac{3\beta}{4\pi} \frac{\Sigma}{K^s} \quad (26)$$

where E_s is the Young modulus of the solid and ω is the crack aspect ratio (initial value ω_o), and $\omega_o(t) = \omega_o a_o / a(t)$.

Conclusion

Based on a local dissolution law, the micromechanical approach is able to discuss the effects of the local heterogeneity of the mechanical affinity on the dissolution process and to predict the evolution of the pore space morphology. Whenever it is possible to describe the latter by a scalar parameter ζ , (22) yields its evolution $\zeta(t)$ which captures the chemomechanical coupling in so far as it controls the evolution of the poroelastic coefficients in (13). Nevertheless, the implementation of this modelling requires to be able to determine the microscopic strain state along the fluid-solid interface by appropriate micromechanical techniques.

References

- [1] Deudé, V., Dormieux, L., Kondo, D. and Maghous, S. (2002) Micromechanical approach to non linear poroelasticity: application to cracked rocks, *Journal of Engineering Mechanics* **128**(8), 848–855
- [2] Ghousoub, J. and Leroy, Y. (2001) Solid-fluid phase transformation within grain boundaries during compaction by pressure solution, *J. Mech. Phys. Solids* **49**, 2385-2430

MODELING OF ICE FORMATION IN POROUS MEDIA

Joachim Bluhm

Institute of Mechanics

University of Duisburg-Essen, 45117 Essen, Germany

Joachim.Bluhm@uni-essen.de

Max J. Setzer and Jens Kruschwitz

Institute of Building Physics and Materials Science

University of Duisburg-Essen, 45117 Essen, Germany

MJ.Setzer@uni-essen.de, Jens.Kruschwitz@uni-essen.de

Abstract A simplified quintuple model for the description of freezing and thawing processes in gas and liquid saturated porous materials is investigated by using a continuum mechanical approach based on the Theory of Porous Media (TPM). The porous solid consists of two phases, namely a granular or structured porous matrix and an ice phase. The liquid phase is divided in bulk water in the macro pores and gel water in the micro pores. In contrast to the bulk water the gel water is substantially affected by the surface of the solid. This phenomenon is already apparent by the fact that this water is frozen by homogeneous nucleation.

Keywords: Porous materials, bulk water and pore solution, micro and macro pores, micro-ice-lenses, frost shrinkage

Introduction

Freezing and thawing are important processes in civil engineering. On the one hand frost damage of porous building materials like road pavements and concrete in regions with periodical freezing is well known. On the other hand, artificial freezing techniques are widely used, e.g., for tunneling in non-cohesive soils and other underground constructions as well as for the protection of excavation and compartmentalization of contaminated tracts.

Bulk or free water and gas are in the macroscopic pores with a hydraulic diameter greater than $0.1 \mu\text{m}$. The gel pores are filled with pore solution (gel water). Their diameter is much smaller (1 - 30 nm). During cooling below the freezing point of bulk water ice is formed in the larger pores with sufficient su-

Jacques M. Huyghe et al. (eds), IUTAM Proceedings on Physicochemical and Electromechanical Interactions in Porous Media, 329–334.

© 2005 Springer. Printed in the Netherlands.

percooling by heterogeneous nucleation. The gel water is still liquid because of its strong surface interactions with the pore walls. Thermodynamics shows that the unfrozen water is under increasing negative pressure with decreasing temperature. The pressure reduction is 1.22 MPa/K, see SETZER [1]. The pressure is balanced by the matrix. The pore walls are under tension which is macroscopically comparable to a compressive force. The primary mode of transport of the complete unfrozen water is viscous flow. The unfrozen water is squeezed out of the gel matrix and is trapped at the existing ice crystals in capillaries, leading to the growth of micro-ice-lenses. This is called frost shrinkage. During melting the pressure difference between unfrozen pore water and ice decreases and transport from ice to water takes place. The matrix expands. If liquid water is available from external sources it will be sucked into the expanding matrix during the movement of the melting front. The degree of saturation of the system increases and becomes much higher than that by normal capillary suction.

Taking into account the aforementioned effects of ice formation in porous materials, a macroscopic quintuple model within the framework of the Theory of Porous Media (TPM) for the numerical simulation of initial and boundary value problems of freezing and thawing processes in saturated porous materials will be investigated. The porous solid is made up of a granular or structured porous matrix ($\alpha = S$) and ice ($\alpha = I$), where it will be assumed that both phases have the same motion. Due to the different freezing points of water in the macro and micro pores, the liquid will be distinguished into bulk water ($\alpha = L$) in the macro pores and gel water ($\alpha = P$, pore solution) in the micro pores. With exception of the gas phase ($\alpha = G$), all constituents will be considered as incompressible.

Basics

Within the framework of the TPM, the thermo-mechanical behavior of a saturated porous solid consisting of κ constituents is described by using the local statements of the balance equation of mass,

$$(\rho^\alpha)'_\alpha + \rho^\alpha \operatorname{div} \mathbf{x}'_\alpha = \hat{\rho}^\alpha, \quad (1)$$

the balance equations of momentum and moment of momentum,

$$\operatorname{div} \mathbf{T}^\alpha + \rho^\alpha (\mathbf{b}^\alpha - \mathbf{x}''_\alpha) = \hat{\rho}^\alpha \mathbf{x}'_\alpha - \hat{\mathbf{p}}^\alpha, \quad \mathbf{T}^\alpha = (\mathbf{T}^\alpha)^T, \quad (2)$$

and the balance equation of energy,

$$\begin{aligned} & \rho^\alpha [(\Psi^\alpha)'_\alpha + \Theta^\alpha (\eta^\alpha)'_\alpha + (\Theta^\alpha)'_\alpha \eta^\alpha] - \mathbf{T}^\alpha \cdot \mathbf{D}^\alpha - \rho^\alpha r^\alpha + \operatorname{div} \mathbf{q}^\alpha = \\ & = \hat{e}^\alpha - \hat{\mathbf{p}}^\alpha \cdot \mathbf{x}'_\alpha - \hat{\rho}^\alpha (\Psi^\alpha + \Theta^\alpha \eta^\alpha - \frac{1}{2} \mathbf{x}'_\alpha \cdot \mathbf{x}'_\alpha), \end{aligned} \quad (3)$$

for each individual constituent as well as the saturation condition:

$$\sum_{\alpha=1}^{\kappa} n^{\alpha} = \sum_{\alpha=1}^{\kappa} \rho^{\alpha} / \rho^{\alpha R} = 1 . \quad (4)$$

In these equations, \mathbf{T}^{α} is the partial Cauchy stress tensor, \mathbf{x}'_{α} the velocity, \mathbf{x}''_{α} the acceleration and \mathbf{b}^{α} the external acceleration of the constituent φ^{α} . The free Helmholtz energy function, the specific entropy, the absolute temperature, the external heat supply and the influx of energy are denoted by Ψ^{α} , η^{α} , Θ^{α} , r^{α} and \mathbf{q}^{α} . The quantities $\hat{\rho}^{\alpha}$, $\hat{\mathbf{p}}^{\alpha}$ and \hat{e}^{α} represent the local supply terms of mass, momentum and energy of φ^{α} arising out of all other constituents $\kappa - 1$ that occupy the same position as φ^{α} at time t . The second representation form of the saturation condition implies that each of the individual constituents φ^{α} has a real density $\rho^{\alpha R}$, which is defined as the mass of φ^{α} per unit of the partial volume v^{α} . With the aid of volume fractions n^{α} , these properties can be “smeared” over the control space and one obtains the partial density $\rho^{\alpha} = n^{\alpha} \rho^{\alpha R}$. The tensor \mathbf{D}_{α} is the symmetric part of the velocity gradient $\mathbf{L}_{\alpha} = \text{grad } \mathbf{x}'_{\alpha}$. In addition, “div” is the divergence operator and the symbol $(\dots)'_{\alpha}$ defines the material time derivative with respect to the trajectory of φ^{α} . With respect to the supply terms of mass, momentum and energy the following conservation relationships apply:

$$\sum_{\alpha=1}^{\kappa} \rho^{\alpha} = 0 , \quad \sum_{\alpha=1}^{\kappa} \hat{\mathbf{p}}^{\alpha} = \mathbf{o} , \quad \sum_{\alpha=1}^{\kappa} \hat{e}^{\alpha} = 0 . \quad (5)$$

Readers interested in the foundation of the governing equations of the TPM are referred to DE BOER [2].

Field Equations and Constitutive Relations

In view of the numerical simulation of ice formation in porous solids, in this section the field equations for a simplified 5-phase model will be derived.

In saturated porous media viscous fluid flow is slow. This can be observed in reality as well as in standard experiments. Therefore, dynamic effects will be neglected in the model ($\mathbf{x}''_{\alpha} = \mathbf{o}$). Furthermore, it will be postulated that the local temperatures of all constituents are equal and that the motions of solid χ_S , ice χ_I , and gel water χ_P are the same, i.e., $\Theta^{\alpha} = \Theta$ and $\chi_S = \chi_I = \chi_P$. The distance and response time for movement from gel to ice are negligible. Experiments have shown that the motion occurs in situ, compare STOCKHAUSEN & SETZER [3].

Concerning the mass supply terms it will be assumed that the mass exchange is restricted to the ice, gel water and liquid phase and the mass exchanges of solid and gas phases are negligible.

Considering the aforementioned assumptions and provided that solid, ice, gel water and liquid are incompressible, i.e., $\rho^{\beta R} = \rho_0^{\beta R} = \text{const.}$ for $\beta \in$

$\{S, I, P, L\}$, one obtains a set of coupled field equations for the determination of the following set of unknown field quantities:

$$\mathcal{U} = \{\chi_S, \chi_L, \chi_G, \Theta, n^{\text{SIP}}, n^S, n^P, n^L, \rho^{\text{GR}}\}, \quad (6)$$

where $n^{\text{SIP}} = n^S + n^I + n^P$. The field equations are a combination of the balance equations of mass,

$$\begin{aligned} (n^{\text{SIP}})'_S + n^{\text{SIP}} \operatorname{div} \mathbf{x}'_S &= \hat{\rho}^P (1/\rho_0^{\text{PR}} - 1/\rho_0^{\text{IR}}) - \hat{\rho}^L / \rho_0^{\text{IR}}, \\ (n^S)'_S + n^S \operatorname{div} \mathbf{x}'_S &= 0, \quad (n^P)'_S + n^P \operatorname{div} \mathbf{x}'_S = \hat{\rho}^P / \rho_0^{\text{PR}}, \\ (n^L)'_L + n^L \operatorname{div} \mathbf{x}'_L &= \hat{\rho}^L / \rho_0^{\text{LR}}, \\ -[(n^{\text{SIP}})'_S + (n^L)'_L] \rho^{\text{GR}} - (n^{\text{SIP}} + n^L) (\rho^{\text{GR}})'_G \operatorname{div} \mathbf{x}'_G - \\ - \operatorname{grad} n^{\text{SIP}} \cdot \mathbf{w}_{\text{GS}} + \operatorname{grad} n^L \cdot (\mathbf{w}_{\text{LS}} - \mathbf{w}_{\text{GS}}) &= 0, \end{aligned} \quad (7)$$

and the balance equations of momentum,

$$\begin{aligned} \operatorname{div}(-n^{\text{SIP}} \lambda \mathbf{I} + \mathbf{T}_{\text{E}}^{\text{SIP}}) + \rho^{\text{SIP}} \mathbf{b} &= -\hat{\rho}^L \mathbf{x}'_S + \hat{\mathbf{p}}^L + \hat{\mathbf{p}}^G, \\ \operatorname{div}(-n^L \lambda \mathbf{I} + \mathbf{T}_{\text{E}}^L) + n^L \rho_0^{\text{LR}} \mathbf{b} &= \hat{\rho}^L \mathbf{x}'_L - \hat{\mathbf{p}}^L, \\ \operatorname{div}[-(1 - n^{\text{SIP}} - n^L) \lambda \mathbf{I} + \mathbf{T}_{\text{E}}^G] + (1 - n^{\text{SIP}} - n^L) \rho^{\text{GR}} \mathbf{b} &= -\hat{\mathbf{p}}^G, \end{aligned} \quad (8)$$

as well as the balance equation of energy for the mixture,

$$\begin{aligned} n^S \rho_0^{\text{SR}} (\eta^S)'_S + (n^{\text{SIP}} - n^S - n^P) \rho_0^{\text{IR}} (\eta^I)'_S + n^P \rho_0^{\text{PR}} (\eta^P)'_S + \\ + n^L \rho_0^{\text{LR}} (\eta^L)'_L + (1 - n^{\text{SIP}} - n^L) \rho^{\text{GR}} (\eta^G)'_G + \operatorname{div} \mathbf{q}^{\text{SIPLG}} + \\ + \lambda [n^{\text{SIP}} (\mathbf{D}_S - \mathbf{D}_G) + n^L (\mathbf{D}_L - \mathbf{D}_G) + \mathbf{D}_G] \cdot \mathbf{I} = \\ = -\hat{\mathbf{p}}^L \cdot \mathbf{w}_{\text{LS}} - \hat{\mathbf{p}}^G \cdot \mathbf{w}_{\text{GS}} - \hat{\rho}^P [\Psi^P - \Psi^I + \Theta (\eta^P - \eta^I)] - \\ - \hat{\rho}^L [\Psi^L - \Psi^I + \Theta (\eta^L - \eta^I)] - \frac{1}{2} (\mathbf{x}'_L \cdot \mathbf{x}'_L - \mathbf{x}'_S \cdot \mathbf{x}'_S), \end{aligned} \quad (9)$$

in which the external heat supply terms of the constituents φ^α have been neglected. Furthermore, in (7) – (9) the saturation condition, the relations for partial densities and the restrictions for the supply terms have been used. The quantities $\mathbf{w}_{\text{LS}} = \mathbf{x}'_L - \mathbf{x}'_S$ and $\mathbf{w}_{\text{GS}} = \mathbf{x}'_G - \mathbf{x}'_S$ are the velocities of liquid and gas relative to the solid. The remaining quantities in the set of field equations require constitutive assumptions.

With the constitutive assumptions

$$\begin{aligned}\Psi^S &= \Psi^S(\Theta, \mathbf{C}_S), \quad \Psi^{I,P} = \Psi^{I,P}(\Theta, \mathbf{C}_S, \rho^{I,P}), \\ \Psi^L &= \Psi^L(\Theta, J_L, \rho^L), \quad \Psi^G = \Psi^G(\Theta, \rho^G, \rho^{GR})\end{aligned}\quad (10)$$

for the free Helmholtz energy functions of the constituents, from the second law of thermodynamics for the mixture, extended by the material time derivative of the saturation condition following the solid motion, one obtains the following constitutive equations for the stress tensors $\mathbf{T}_E^{\text{SIP}} = \mathbf{T}^S + \mathbf{T}^I + \mathbf{T}^P$, \mathbf{T}_E^L , \mathbf{T}_E^G and the interaction pressure λ :

$$\begin{aligned}\mathbf{T}_E^{\text{SIP}} &= -[(\rho^I)^2 \frac{\partial \Psi^I}{\partial \rho^I} + (\rho^P)^2 \frac{\partial \Psi^P}{\partial \rho^P} - \rho^P J_P \frac{\partial \Psi^P}{\partial J_P}] \mathbf{I} + \\ &\quad + \mathbf{F}_S [2\rho^S \frac{\partial \Psi^S}{\partial \mathbf{C}_S} + 2\rho^I \frac{\partial \Psi^I}{\partial \mathbf{C}_S}] \mathbf{F}_S^T, \quad \lambda = (\rho^{GR})^2 \frac{\partial \Psi^G}{\partial \rho^{GR}} \mathbf{I}, \\ \mathbf{T}_E^{L,G} &= -[(\rho^{L,G})^2 \frac{\partial \Psi^{L,G}}{\partial \rho^{L,G}} - \rho^{L,G} J_{L,G} \frac{\partial \Psi^{L,G}}{\partial J_{L,G}}] \mathbf{I}.\end{aligned}\quad (11)$$

Therein, $\mathbf{C}_S = \mathbf{F}_S \mathbf{F}_S^T$ and $J_{L,G} = \det \mathbf{F}_{L,G}$ are the right Cauchy-Green deformation tensor of the solid and the Jacobian of the gas and liquid phases respectively, where \mathbf{F}_α denotes the deformation gradient of φ^α . The interrelations between the free energies and the specific entropies of the constituents φ^α are given as $\eta^\alpha = -(\partial \Psi^\alpha)/(\partial \Theta)$.

It should be noted, that the constitutive assumptions (10) and the corresponding rates, respectively, as well as the relations (5) and (11) have already been included in the balance equation of energy. Furthermore, for the phases which are involved with mass exchange processes (φ^I , φ^P and φ^G), the partial density and the Jacobian of the corresponding phase have been considered as process variables. Due to the mass exchange, the partial density of φ^α can not be expressed by the Jacobian of the phase.

In connection with the dissipation mechanism of the entropy inequality, the relations for the heat flux vector

$$\mathbf{q}^{\text{SIPLG}} = \sum_{\alpha=1}^{\kappa} \mathbf{q}^\alpha = -\alpha_{\partial\Theta} \text{grad } \Theta - \alpha_{\mathbf{w}_{LS}} \mathbf{w}_{LS} - \alpha_{\mathbf{w}_{GS}} \mathbf{w}_{GS}, \quad (12)$$

as well as the supply terms of mass and the supply term of momentum

$$\begin{aligned}\hat{\rho}^{L,P} &= -\beta_{\Psi^P}^{L,P} (\Psi^P - \Psi^I) - \beta_{\Psi^L}^{L,P} (\Psi^L - \Psi^I), \\ \hat{\mathbf{p}}^{L,G} &= \lambda \text{grad } n^{L,G} - \gamma_{\partial\Theta}^{L,G} \text{grad } \Theta - \gamma_{\mathbf{w}_{LS}}^{L,G} \mathbf{w}_{LS} - \gamma_{\mathbf{w}_{GS}}^{L,G} \mathbf{w}_{GS}\end{aligned}\quad (13)$$

can be derived. In (13)₁, Ψ^α is the chemical potential of each involved phase which is given by

$$\Psi^\alpha = \Psi^\alpha + n^\alpha \lambda / \rho^\alpha + (\rho^\alpha)^2 \frac{\partial \Psi^\alpha}{\partial \rho^\alpha} - \frac{1}{2} \mathbf{x}'_\alpha \cdot \mathbf{x}'_\alpha. \quad (14)$$

The parameters in (12) and (13) are restricted by

$$\begin{aligned} \alpha_{\partial\Theta} \geq 0, \quad \beta_{\Psi^{L,P}I}^{L,P} \geq 0, \quad \gamma_{\mathbf{w}^{L,G}S}^{L,G} \geq 0, \\ \alpha_{\mathbf{w}^{L,G}S} + \gamma_{\partial\Theta}^{L,G} = 0, \quad \beta_{\Psi^{LI}}^P + \beta_{\Psi^{PI}}^L = 0, \quad \gamma_{\mathbf{w}^{GS}}^L + \gamma_{\mathbf{w}^{LS}}^G = 0. \end{aligned} \quad (15)$$

As a first approximation, the stresses for the solid, ice and gel water can be formulated with the help of a linearized Hookean type law, where the depression of the gel water below the macroscopic freezing point of water must be considered. This can be done by including the micro-ice-lens model of SETZER [1] in the constitutive relations for the aforementioned stress tensor. The gas phase can be described as an ideal gas. Concerning the constitutive assumptions for the liquid stresses, the heat flux and the interactions, the reader is referred to DE BOER *et al.* [4]. There a ternary model for the numerical simulation of freezing and thawing processes is discussed.

Conclusions

During cooling, frost-shrinkage described by the micro-ice-lens model takes place. The volume fraction of the gel phase reduces while the volume fraction of coarse macroscopic ice filled pores increases. Water transport at a macroscopic scale is retarded by the formed ice. During melting the pressure difference decreases and external water might be sucked in. This is the only possible significant water transport. By using TPM, it is possible to describe the quintuple phase porous media macroscopically. The nano-structure of the matrix has been homogenized and put in the concept of thermodynamics.

References

- [1] Setzer, M.J. (2001) Micro-ice-lens formation in porous solid, *Journal of Colloid and Interface Science* **243**, 193–201
- [2] de Boer, R. (2000) *Theory of Porous Media – Highlights in the Historical Development and Current State*, Springer-Verlag, Berlin/Heidelberg/New York
- [3] Stockhausen, N. and Setzer, M.J. (1980) Anomalien der thermischen Ausdehnung und der Gefriervorgänge in Zementstein, *Tonindustrie Zeitung* **104/2**, 83–88
- [4] de Boer, R., Bluhm, J., Wähling, M. and Ricken, T. (2003) Phasenübergänge in porösen Medien. Forschungsbericht aus dem Fachbereich Bauwesen, Universität Duisburg-Essen

THERMOMECHANICAL MODELLING FOR FREEZING OF SOLUTE SATURATED SOIL

Juha Hartikainen

Laboratory of Structural Mechanics

Helsinki University of Technology, P.O. Box 2100, FIN-02015 HUT, Finland

juha.hartikainen@csc.fi

Martti Mikkola

Institute of Mathematics

Helsinki University of Technology, P.O. Box 1100, FIN-02015 HUT, Finland

martti.mikkola@hut.fi

Abstract An approach based on the theory of mixtures with the concept of molar volume fractions and on the basic principles of continuum mechanics and macroscopic thermodynamics is introduced to model soil freezing of solute saturated soil.

Keywords: Soil, salinity, frost phenomenon, molar volume fractions

Introduction

A thermomechanical theory for a porous medium with chemically reacting components is introduced. The porous medium is considered as a multi-component mixture by means of the concept of molar volume fractions, which makes it possible to deal with immiscible and miscible components equally at macroscopic level. The basis are the conservation laws and the entropy inequality which is exploited to derive the constitutive relations through the specific free energy functions and the dissipation potential in the terms of the variables of state and of dissipation. The approach is applied to model freezing of saline water saturated frost-susceptible soil involving the relevant features of the frost phenomenon, i.e. gradual freezing of adsorbed water at sub-zero temperatures, creation of cryogenic suction, driving of water from unfrozen soil to the freezing zone, consolidation of unfrozen soil and heaving of frozen soil (Williams, 1989), with the implications of pore water salinity, i.e. lowering of freezing point, concentration of salinity during the freezing process and transportation of solutes (Hivon and Sego, 1995 and Mahar et al, 1983).

Jacques M. Huyghe et al. (eds), IUTAM Proceedings on Physicochemical and Electromechanical Interactions in Porous Media, 335–341.

© 2005 Springer. Printed in the Netherlands.

Kinematics

Let a multi-component mixture be a collection of immiscible phases \mathcal{P}^κ , $\kappa = 1, \dots, m$, with the volume fractions $\beta^\kappa = dv^\kappa / \sum_{\pi=1}^m dv^\pi$, where dv^κ is the volume element of \mathcal{P}^κ , and let each \mathcal{P}^κ be a composition of miscible substances $\mathcal{S}_\lambda^\kappa$, $\lambda = 1, \dots, N_\kappa$ with the molar fractions $\zeta_\lambda^\kappa = n_\lambda^\kappa / \sum_{\pi=1}^{N_\kappa} n_\pi^\kappa$, where n_λ^κ is the mole number of $\mathcal{S}_\lambda^\kappa$. Hence, the mixture consists of $N = \sum_{\kappa=1}^m N_\kappa$ constituents \mathcal{K}_α , $\alpha = 1, \dots, N$ coexisting in the molar volume fractions

$$\xi_\alpha := \zeta_\lambda^\kappa \beta^\kappa, \quad (1)$$

such that for each $\kappa \in [1, m]$ and $\lambda \in [1, N_\kappa]$ $\alpha = \sum_{i=1}^{\kappa-1} N_i + \lambda$ and that

$$\sum_{\alpha=1}^N \xi_\alpha = 1, \quad \xi_\alpha \geq 0, \quad \alpha = 1, \dots, N. \quad (2)$$

The intrinsic density of each \mathcal{K}_α is denoted by $\bar{\rho}_\alpha$ while the apparent one is given by $\rho_\alpha = \xi_\alpha \bar{\rho}_\alpha$.

The motion of the body of \mathcal{K}_α between its reference configuration, Ω_α^0 , and the current configuration, Ω , is defined by the mappings

$$\begin{aligned} \chi_\alpha : \Omega_\alpha^0 &\rightarrow \Omega & \chi_\alpha^{-1} : \Omega &\rightarrow \Omega_\alpha^0 \\ \mathbf{x}_\alpha^0 &\mapsto \mathbf{x} & \mathbf{x} &\mapsto \mathbf{x}_\alpha^0. \end{aligned} \quad (3)$$

In general, $\Omega_\alpha^0 \neq \Omega_\gamma^0$ holds for $\alpha \neq \gamma$, while it is required that all constituents coincide with the same current configuration.

The Green strain tensor, \mathbf{e}_α^0 , and the Almansi strain tensor, \mathbf{e}_α , are given by

$$\mathbf{e}_\alpha^0 = \frac{1}{2} (\mathbf{F}_\alpha^T \cdot \mathbf{F}_\alpha - \mathbf{I}^0) \quad \mathbf{e}_\alpha = \frac{1}{2} (\mathbf{I} - \mathbf{F}_\alpha^{-T} \cdot \mathbf{F}_\alpha^{-1}), \quad (4)$$

where the deformation gradient $\mathbf{F}_\alpha = \text{grad}^0 \chi_\alpha$ and its inverse $\mathbf{F}_\alpha^{-1} = \text{grad} \chi_\alpha^{-1}$ have been introduced.

The material time derivatives of the physical quantities $Q^0(\mathbf{x}^0, t)$ and $Q(\mathbf{x}, t)$ following the motion of \mathcal{K}_α are defined as

$$\begin{aligned} (Q^0)_\alpha^\cdot &= \frac{\partial}{\partial t} Q^0 & (Q)_\alpha^\cdot &= \frac{\partial}{\partial t} Q + \text{grad} Q \cdot \mathbf{v}_\alpha \\ & & &= (Q)_*^\cdot + \text{grad} Q \cdot \mathbf{v}_{\alpha*}, \end{aligned} \quad (5)$$

where \mathbf{v}_α is the spatial velocity of \mathcal{K}_α and $\mathbf{v}_{\alpha*} = \mathbf{v}_\alpha - \mathbf{v}_*$ gives the objective relative velocity of \mathcal{K}_α with respect to an arbitrary reference motion.

The generalized Darcian flux $\mathbf{J}_{\beta^\kappa} = \beta^\kappa (\mathbf{V}^\kappa - \mathbf{v}_*)$ and the generalized Fickian flux $\mathbf{J}_{\zeta_\lambda^\kappa} = \zeta_\lambda^\kappa (\mathbf{v}_\lambda - \mathbf{V}^\kappa)$ are introduced with the phase velocity $\mathbf{V}^\kappa = \sum_\lambda \zeta_\lambda^\kappa \mathbf{v}_\lambda$ to define the molar volume flux as

$$\mathbf{J}_{\xi_\alpha} := \xi_\alpha \mathbf{v}_{\alpha*} = \zeta_\lambda^\kappa \mathbf{J}_{\beta^\kappa} + \beta^\kappa \mathbf{J}_{\zeta_\lambda^\kappa}. \quad (6)$$

The spatial velocity gradient $\mathbf{l}_\alpha = \text{grad} \mathbf{v}_\alpha$ can be decomposed into symmetric and skew-symmetric parts as $\mathbf{l}_\alpha = \text{sym} \mathbf{l}_\alpha + \text{skw} \mathbf{l}_\alpha = \mathbf{d}_\alpha + \mathbf{w}_\alpha$, where \mathbf{d}_α and \mathbf{w}_α are the deformation rate and the spin tensors, respectively.

Balance Laws and Entropy Inequality

In consideration of the principle of material frame indifference the fundamental laws for the multi-component mixture in the Eulerian description are formulated in the following local forms.

The balance of mass:

$$\sum_{\alpha} \theta_{\alpha} = 0, \quad \theta_{\alpha} = (\rho_{\alpha})_{\alpha}^{\cdot} + \rho_{\alpha} \operatorname{div} \mathbf{v}_{\alpha}, \quad (7)$$

where θ_{α} is the rate of mass production.

The balance of momentum:

$$\sum_{\alpha} \dot{\mathbf{m}}_{\alpha} = \mathbf{0}, \quad \dot{\mathbf{m}}_{\alpha} = \rho_{\alpha} (\mathbf{v}_{\alpha})_{\alpha}^{\cdot} - \operatorname{div} \boldsymbol{\sigma}_{\alpha} - \rho_{\alpha} \mathbf{g} + \theta_{\alpha} \mathbf{v}_{\alpha*}, \quad (8)$$

where $\dot{\mathbf{m}}_{\alpha}$, $\boldsymbol{\sigma}_{\alpha}$ and \mathbf{g} are the objective rate of momentum production, the Cauchy stress tensor and the acceleration of gravity, respectively.

The balance of moment of momentum:

$$\sum_{\alpha} \dot{\mathbf{M}}_{\alpha} = \mathbf{O}, \quad \dot{\mathbf{M}}_{\alpha} = \operatorname{skw} \boldsymbol{\sigma}_{\alpha}, \quad (9)$$

where $\dot{\mathbf{M}}_{\alpha}$ is the objective rate of moment of momentum production tensor.

The balance of energy:

$$\sum_{\alpha} \dot{i}_{\alpha} = 0, \quad \dot{i}_{\alpha} = \rho_{\alpha} (e_{\alpha})_{\alpha}^{\cdot} - \operatorname{sym} \boldsymbol{\sigma}_{\alpha} : \mathbf{d}_{\alpha} + \operatorname{div} \mathbf{q}_{\alpha} - r_{\alpha} + (e_{\alpha} + \frac{1}{2} \mathbf{v}_{\alpha*} \cdot \mathbf{v}_{\alpha*}) \theta_{\alpha} + \dot{\mathbf{m}}_{\alpha} \cdot \mathbf{v}_{\alpha*} - \mathbf{M}_{\alpha} : \mathbf{w}_{\alpha*}, \quad (10)$$

where \dot{i}_{α} , e_{α} , \mathbf{q}_{α} and r_{α} denote the objective rate of energy production, the specific internal energy, the heat flux vector and the external energy supply, respectively, and $\mathbf{w}_{\alpha*} = \mathbf{w}_{\alpha} - \mathbf{w}_{*}$ is the objective relative spin tensor.

The entropy inequality:

$$\sum_{\alpha} \gamma_{\alpha} \geq 0, \quad \gamma_{\alpha} = \rho_{\alpha} (s_{\alpha})_{\alpha}^{\cdot} + s_{\alpha} \theta_{\alpha} + \operatorname{div} (\mathbf{q}_{\alpha} / T_{\alpha}) - r_{\alpha} / T_{\alpha}, \quad (11)$$

where γ_{α} , s_{α} and T_{α} are the rate of entropy production, the specific entropy and the absolute temperature, respectively.

Constitutive Theory

Let $\mathcal{S} = \{\vec{a} = (T_{\alpha}, \mathbf{e}_{\alpha}, \xi_{\alpha}, \bar{\rho}_{\alpha}), \alpha = 1, \dots, N\}$ and $\mathcal{D} = \{\vec{d} = ((T_{\alpha})_{\alpha}^{\cdot}, \mathbf{d}_{\alpha}, (\bar{\rho}_{\alpha})_{\alpha}^{\cdot}, \mathbf{q}_{\alpha}, \theta_{\alpha}, \mathbf{v}_{\alpha*}, \mathbf{w}_{\alpha*}, \dot{i}_{\alpha}), \alpha = 1, \dots, N\}$ be convex sets of variables of state and dissipation, respectively, defined by physical properties and the constraining equations (2), (7₁) and (10₁). Further, let the specific free energies $\Psi_{\alpha}(\vec{a}_{\alpha}) = e_{\alpha} - T_{\alpha} s_{\alpha}$ be subdifferentiable functions of $\mathcal{S}_{\alpha} = \{\vec{a}_{\alpha} = (T_{\alpha}, \mathbf{e}_{\alpha}, \xi_1, \dots, \xi_N, \bar{\rho}_{\alpha})\}$, $\mathcal{S}_{\alpha} \subset \mathcal{S}$ and let the dissipation potential $\varphi(\vec{d}; \mathcal{S})$ be a subdifferentiable function of \mathcal{D} such that $(\vec{d}, \vec{d}') \geq 0$

for all $\vec{d} \in \mathcal{D}$ and all $\vec{d}' \in \partial\varphi(\vec{d})$, where \vec{d}' is the subgradient of φ at \vec{d} , $\partial\varphi(\vec{d}) = \{\vec{d}' = ((T'_\alpha)_\alpha, \mathbf{d}'_\alpha, (\bar{\rho}'_\alpha)_\alpha, \mathbf{q}'_\alpha, \theta'_\alpha, \mathbf{v}'_{\alpha*}, \mathbf{w}'_{\alpha*}, i'_\alpha), \alpha = 1, \dots, N\}$ denotes the subdifferential of φ and (\bullet, \bullet) symbolizes the standard Euclidean inner product. Moreover, let Ψ_α and φ be decomposed into $\Psi_\alpha = \tilde{\Psi}_\alpha + (T_\alpha/T_0)I_{S_\alpha}$ and $\varphi = \tilde{\varphi} + I_D$, respectively, such that the indicator functions (Frémond and Nicolas, 1990)

$$I_{S_\alpha} = \begin{cases} 0 & \text{if } \vec{a}_\alpha \in \mathcal{S}_\alpha \\ +\infty & \text{if } \vec{a}_\alpha \notin \mathcal{S}_\alpha \end{cases}, \quad I_D = \begin{cases} 0 & \text{if } \vec{d} \in \mathcal{D} \\ +\infty & \text{if } \vec{d} \notin \mathcal{D} \end{cases} \quad (12)$$

take over the restrictions on \mathcal{S}_α and \mathcal{D} while $\tilde{\Psi}_\alpha$ and $\tilde{\varphi}$ involve the remaining characteristics. Then, from the postulate: $\sum_\alpha \gamma_\alpha - (\vec{d}, \vec{d}') = 0$ for all $\vec{d} \in \mathcal{D}$ and all $\vec{d}' \in \partial\varphi(\vec{d})$ by making use of (11₂), (10₂), (5₂) and (7₂) with the relations $(\Psi_\alpha(\mathbf{e}_\alpha))'_\alpha = (\Psi_\alpha^0(\mathbf{e}_\alpha^0))'_\alpha$ and $(\mathbf{e}_\alpha^0)'_\alpha = \mathbf{F}_\alpha^T \cdot \mathbf{d}_\alpha \cdot \mathbf{F}_\alpha$ the following conditions are obtained

$$\begin{aligned} \mathcal{C} = & \left\{ -\frac{\rho_\alpha}{T_\alpha} [s_\alpha + \partial\Psi_\alpha(T_\alpha)] - \partial\varphi((T_\alpha)_\alpha) \ni 0, \right. \\ & \frac{1}{T_\alpha} [\text{sym } \boldsymbol{\sigma}_\alpha - \rho_\alpha \mathbf{F}_\alpha \cdot \partial\Psi_\alpha^0(\mathbf{e}_\alpha^0) \cdot \mathbf{F}_\alpha^T + p_\alpha^{\text{th}} \mathbf{I}] - \partial\varphi(\mathbf{d}_\alpha) \ni \mathbf{O}, \\ & -\frac{1}{T_\alpha} \left[\rho_\alpha \partial\Psi_\alpha(\bar{\rho}_\alpha) - \frac{1}{\bar{\rho}_\alpha} p_\alpha^{\text{th}} \right] - \partial\varphi((\bar{\rho}_\alpha)_\alpha) \ni 0, \\ & -\frac{1}{T_\alpha} \frac{\text{grad } T_\alpha}{T_\alpha} - \partial\varphi(\mathbf{q}_\alpha) \ni \mathbf{O}, \quad -\frac{1}{T_\alpha} g_\alpha - \partial\varphi(\theta_\alpha) \ni 0, \\ & -\frac{1}{T_\alpha} \dot{\mathbf{m}}_\alpha - \sum_\lambda \left(\frac{\rho_\alpha}{T_\alpha} \nabla\Psi_\alpha(\xi_\lambda) - \frac{\rho_\lambda}{T_\lambda} \nabla\Psi_\lambda(\xi_\alpha) \right) - \partial\varphi(\mathbf{v}_{\alpha*}) \ni \mathbf{O}, \\ & \left. \frac{1}{T_\alpha} \dot{\mathbf{M}}_\alpha - \partial\varphi(\mathbf{w}_{\alpha*}) \ni \mathbf{O}, \quad \frac{1}{T_\alpha} - \partial\varphi(i_\alpha) \ni 0, \alpha = 1, \dots, N \right\}, \end{aligned} \quad (13)$$

which hold for any thermodynamic process satisfying the field equations (7)–(10). Above, the denotations $\partial\Psi_\alpha(T_\alpha) = \{T'_\alpha\}$, $\partial\varphi((T_\alpha)_\alpha) = \{(T'_\alpha)_\alpha\}$, etc. and the terms $p_\alpha^{\text{th}} = \xi_\alpha \sum_\lambda (T_\alpha/T_\lambda) \rho_\lambda \partial\Psi_\lambda(\xi_\alpha)$ and $g_\alpha = \Psi_\alpha + p_\alpha^{\text{th}}/\rho_\alpha - \frac{1}{2} \mathbf{v}_{\alpha*} \cdot \mathbf{v}_{\alpha*}$ representing the thermodynamic pressure and the Gibbs free energy, respectively, have been introduced. Further, $\nabla\Psi_\alpha(\xi_\lambda)$ stands for $\partial\Psi_\alpha(\xi_\lambda) \text{grad } \xi_\lambda$.

Mathematical Model

Freezing soil is considered as porous medium of skeleton (*s*) of soil grains filled up with pore fluid (*f*) and ice (*i*). It is assumed that skeleton and ice are elastic solids and have equal displacements and velocities, pore fluid is an ideal solution of water (*w*) and dissolved salts (*c*) and governed by adsorption

and that all constituents are intrinsically incompressible. The reference motion is the one of skeleton and dissipation is generated by heat conduction, pore fluid flow and diffusion of solutes. Further, inertia forces and kinetic energy are negligibly small in the evolution of soil freezing.

The governing field equations deduced from (7), (8) and (10) are given by

$$\begin{aligned} \theta_s = 0, \quad \theta_c = 0, \quad \theta_w + \theta_i = 0, \\ \theta_\alpha = (\bar{\rho}_\alpha \xi_\alpha)_s + \bar{\rho}_\alpha \xi_\alpha \operatorname{div} \mathbf{v}_s + \operatorname{div} (\bar{\rho}_\alpha \mathbf{J}_{\xi_\alpha}) \end{aligned} \quad (14)$$

$$\sum_\alpha (\operatorname{div} \boldsymbol{\sigma}_\alpha + \rho_\alpha \mathbf{g}) = \mathbf{0}, \quad (15)$$

$$\sum_\alpha \left[\rho_\alpha (e_\alpha)_s + \bar{\rho}_\alpha \operatorname{grad} e_\alpha \cdot \mathbf{J}_{\xi_\alpha} + e_\alpha \theta_\alpha + \operatorname{div} \mathbf{q}_\alpha - r_\alpha \right] = 0 \quad (16)$$

and the relevant constitutive relations are derived as follows.

The sets of state variables are defined as

$$\begin{aligned} \mathcal{S}_\alpha = \{ \bar{a}_\alpha = (T_\alpha, \mathbf{e}_{\alpha \notin \{w,c\}}, \xi_s, \xi_w, \xi_c, \xi_i, \bar{\rho}_\alpha) \mid \sum_\lambda \xi_\lambda = 1, \xi_\lambda \geq 1, \\ \lambda \in \{s, w, c, i\}; \bar{\rho}_\alpha = \bar{\rho}_{\alpha 0} \}, \quad \alpha \in \{s, w, c, i\}, \end{aligned} \quad (17)$$

where the molar volume fractions $\xi_s = \beta^s$, $\xi_w = \zeta_w^f \beta^f$, $\xi_c = \zeta_c^f \beta^f$ and $\xi_i = \beta^i$ comply with (1), and the variables of dissipation are given by

$$\begin{aligned} \mathcal{D} = \{ \vec{d} = (\mathbf{q}_\alpha, \theta_\alpha, \mathbf{v}_{\alpha s}, \mathbf{w}_{ss}, \overset{\circ}{l}_\alpha), \alpha \in \{s, w, c, i\} \mid \theta_s = 0, \theta_c = 0, \\ \theta_w + \theta_i = 0; \mathbf{v}_{ss} = \mathbf{0}, \mathbf{v}_{is} = \mathbf{0}; \mathbf{w}_{ss} = \mathbf{0}; \sum_\lambda \overset{\circ}{l}_\lambda = 0 \}. \end{aligned} \quad (18)$$

The expressions for the specific free energies $\tilde{\Psi}_\alpha$ are given by

$$\begin{aligned} \tilde{\Psi}_s &= -c_s T_s \ln(T_s/T_0) + 1/\bar{\rho}_s W_s(\mathbf{e}_s), \\ \tilde{\Psi}_w &= -c_w [T_w \ln(T_w/T_0) - (T_w - T_0)] - \ell(T_w - T_0)/T_0 \\ &\quad + RT_w/M_w \ln(\xi_w/(\xi_w + \xi_c)) + RT_w/M_w f(\xi_s, \xi_w, \xi_c), \\ \tilde{\Psi}_c &= -c_c T_c \ln(T_c/T_0) + RT_c/M_c \ln(\xi_c/(\xi_w + \xi_c)) + \\ &\quad + RT_c/M_c f(\xi_s, \xi_w, \xi_c), \\ \tilde{\Psi}_i &= -c_i [T_i \ln(T_i/T_0) - (T_i - T_0)] + 1/\bar{\rho}_i W_i(\mathbf{e}_i), \end{aligned} \quad (19)$$

where c_α , M_α , R and ℓ denote the specific heat capacity, the molecular weight, the universal gas constant and the latent heat of fusion at $T_0 = 273.15$ K, respectively. Furthermore, $W_\alpha(\mathbf{e}_\alpha)$, $\alpha \in \{s, i\}$ are strain energy functions and the function

$$f(\xi_s, \xi_w, \xi_c) = \begin{cases} a [\xi_s/(\xi_w + \xi_c) - b]^2 & \text{if } \xi_s/(\xi_w + \xi_c) \geq b \\ 0 & \text{if } \xi_s/(\xi_w + \xi_c) < b \end{cases} \quad (20)$$

characterizes adsorption. a and b are material parameters.

The expression for $\tilde{\varphi}$ to characterize dissipation properties is given by

$$\tilde{\varphi} = \sum_\alpha \frac{1}{2} K_{q_\alpha} \mathbf{q}_\alpha \cdot \mathbf{q}_\alpha + \frac{1}{2} K_{\zeta_c^f} \mathbf{J}_{\zeta_c^f} \cdot \mathbf{J}_{\zeta_c^f} + \frac{1}{2} K_{\beta^f} \mathbf{J}_{\beta^f} \cdot \mathbf{J}_{\beta^f}, \quad (21)$$

where the dissipation coefficients $K_{q_\alpha} = 1/(T_\alpha^2 \xi_\alpha \lambda_\alpha)$, $K_{\zeta_c^f} = (\xi_w + \xi_c)^3 / (\xi_w \xi_c) (\bar{\rho}_c RT_c / M_c) / D$ and $K_{\beta^f} = (\xi_w / T_w + \xi_c / T_c) / (\xi_w + \xi_c) \mu / \kappa$ are functions of the thermal conductivity λ_α , the diffusion coefficient D , the dynamic viscosity μ and the permeability κ , which is assumed to be a function of the unfrozen fluid content $\chi = (\xi_w + \xi_c) / (\xi_w + \xi_c + \xi_i)$ of the form $\kappa = \kappa_0 \chi^c$, $c \geq 0$.

Using (13) choices (19) and (21) yield the following constitutive equations

$$\begin{aligned}
 e_s &= c_s T, \quad e_w = c_w (T - T_0) + \ell, \quad e_c = c_c T, \quad e_i = c_i (T - T_0), \\
 \boldsymbol{\sigma}_s &= \boldsymbol{\sigma}_s^{\text{ef}} - \hat{p}_s^{\text{th}} \mathbf{I}, \quad \boldsymbol{\sigma}_w = -\hat{p}_w^{\text{th}} \mathbf{I}, \quad \boldsymbol{\sigma}_c = -\hat{p}_c^{\text{th}} \mathbf{I}, \quad \boldsymbol{\sigma}_i = \boldsymbol{\sigma}_i^{\text{ef}} - \hat{p}_i^{\text{th}} \mathbf{I}, \\
 \boldsymbol{\sigma}_\alpha^{\text{ef}} &= \xi_\alpha \mathbf{F}_\alpha \cdot \frac{\partial W_\alpha^0}{\partial \mathbf{e}_\alpha^0} \cdot \mathbf{F}_\alpha^T, \quad \hat{p}_\alpha^{\text{th}} = \xi_\alpha \left[(\xi_w + \xi_c) \bar{\rho}_w \frac{RT}{M_w} \frac{\partial f}{\partial \xi_\alpha} + \hat{B}_\alpha \right], \\
 \mathbf{q}_\alpha &= -\xi_\alpha \lambda_\alpha \text{grad } T, \quad \alpha \in \{s, w, c, i\}, \\
 \mathbf{J}_{\beta^f} &= -\frac{\kappa}{\mu} \left[\text{grad} \left(\frac{\hat{p}_w^{\text{th}} + \hat{p}_c^{\text{th}}}{\xi_w + \xi_c} \right) - \frac{\rho_w + \rho_c}{\xi_w + \xi_c} \mathbf{g} + \bar{\rho}_w \frac{RT}{M_w} \text{grad } f \right], \\
 \mathbf{J}_{\zeta_c^f} &= -D \left[\text{grad} \left(\frac{\xi_c}{\xi_w + \xi_c} \right) - \frac{M_c - M_w}{RT} \frac{\xi_w \xi_c}{(\xi_w + \xi_c)^2} \mathbf{g} \right], \\
 0 &= -(c_w - c_i) \left[T \ln \left(\frac{T}{T_0} \right) - (T - T_0) \right] - \ell \frac{T - T_0}{T_0} + \\
 &\quad + \left(\frac{\hat{p}_w^{\text{th}}}{\rho_w} - \frac{\hat{p}_i^{\text{th}}}{\rho_i} \right) + \frac{RT}{M_w} \ln \left(\frac{\xi_w}{\xi_w + \xi_c} \right) + \frac{RT}{M_w} f,
 \end{aligned} \tag{22}$$

where the relation $e_\alpha = \Psi_\alpha - T_\alpha \partial \Psi_\alpha / \partial T_\alpha$, the feature $\bar{\rho}_w / M_w = \bar{\rho}_c / M_c$ for ideal solution, the equalities $\hat{g}_w = \hat{g}_i$ and $T_s = T_w = T_c = T_i = T$ resulting from the constraints $\theta_w + \theta_i = 0$ and $\dot{i}_s + \dot{i}_w + \dot{i}_c + \dot{i}_i = 0$ through the subdifferentials $\partial I_D(\theta_w, \theta_i)$ and $\partial I_D(\dot{i}_s, \dot{i}_w, \dot{i}_c, \dot{i}_i)$, respectively, and the pressure components $(\hat{B}_s, \hat{B}_w, \hat{B}_c, \hat{B}_i) \in T/T_0 \sum_\lambda \rho_\lambda \partial I_{S_\lambda}(\xi_s, \xi_w, \xi_c, \xi_i)$ with the property $\hat{B}_s = \hat{B}_w = \hat{B}_c = \hat{B}_i$ due to the constraint $\xi_s + \xi_w + \xi_c + \xi_i = 1$ have been introduced.

Acknowledgments

The research was supported by STUK – Radiation and Nuclear Safety Authority of Finland.

References

- [1] Frémond, M. and Nicolas P. (1990) Macroscopic thermodynamics of porous media, *Continuum Mech. Thermodyn.* **2**, 119–139
- [2] Hivon, E.G. and Sego, D.C. (1995) Strength of frozen saline soils., *Can. Geotech. J.* **32**, 336–354
- [3] Mahar, L.J., Wilson, R.J. and Vinson, T.S. (1983) Physical and numerical modeling of uniaxial freezing in a saline gravel, *PERMAFROST, Proceedings of the Fourth International*

Conference on Permafrost, Fairbanks, Alaska. Washington, D.C.: National Academy Press, 773–778

[4] Williams, P.J. (1989) *The Frozen Earth*, Cambridge University Press

A MICROSCOPIC DESCRIPTION OF CRYSTAL DISSOLUTION AND PRECIPITATION

C.J. van Duijn and I. Sorin Pop
*Department of Mathematics and Computer Science
Eindhoven University of Technology
P.O. Box 513, 5600 MB Eindhoven, The Netherlands
{C.J.v.Duijn, I.Pop}@tue.nl*

Abstract In this paper we discuss a pore scale model for crystal precipitation and dissolution in porous media. We consider weak solutions in general domains and dissolution/precipitation fronts in thin strips. The latter yields an upscaled transport–reaction model.

Keywords: Porous media, precipitation, dissolution, fronts, upscaling

Introduction and Mathematical Formulation

In this paper we consider a pore scale model for crystal dissolution and precipitation processes. We follow the ideas in [3], where the corresponding macroscopic model was introduced. Let $\Omega \subset \mathbb{R}^d$ ($d > 1$) denote the void region. This region is occupied by a fluid in which cations (M_1) and anions (M_2) are dissolved. The boundary of Ω has an internal part (Γ_G), which is the surface between the fluid and the porous matrix (grains), and an external part, which is the outer boundary of the domain. In a precipitation reaction,

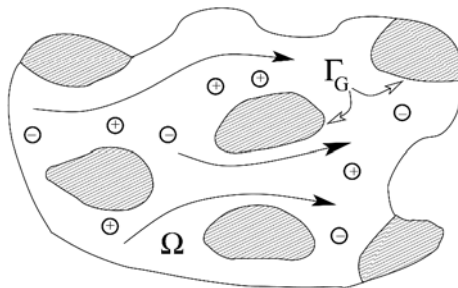


Figure 1. Flow domain with grains.

n particles of M_1 , and m particles of M_2 can precipitate in the form of one particle of a crystalline solid M_{12} , which is attached to the surface of the grains and thus immobile. The reverse reaction of dissolution is also possible.

We assume that the flow geometry, as well as the fluid density and viscosity ($\mu > 0$, given) are not affected by the reactions and that the flow is described by the Stokes equations relating the fluid velocity \vec{q} and fluid pressure p :

$$\left. \begin{aligned} \mu \Delta \vec{q} &= \nabla p, \\ \nabla \cdot \vec{q} &= 0, \end{aligned} \right\} \text{ in } \Omega. \quad (1)$$

Along the internal grain boundary we assume a no-slip condition, implying

$$\vec{q} = \vec{0} \quad \text{along } \Gamma_G. \quad (2)$$

Let c_i be the volumetric molar concentration of M_i in Ω and c_{12} the surface molar concentration of M_{12} on Γ_G . Assuming that both types of ions have the same diffusion coefficient $D > 0$ and since crystalline is immobile, mass conservation for M_i gives

$$\partial_t c_i + \nabla \cdot (\vec{q} c_i - D \nabla c_i) = 0, \quad \text{in } \Omega. \quad (3)$$

On the interior boundary Γ_G the flux of c_i is directly related to changes in crystalline concentration c_{12} . Using (2) we have

$$\partial_t c_{12} = -\frac{1}{n} D \vec{\nu} \cdot \nabla c_1 = -\frac{1}{m} D \vec{\nu} \cdot \nabla c_2 \quad \text{on } \Gamma_G, \quad (4)$$

where $\vec{\nu}$ denotes the normal unit vector pointing into the grains.

A second equation for c_{12} results from a description of the precipitation and dissolution processes. Following the detailed discussion in Knabner et al. [3] we have

$$\partial_t c_{12} = r_p - r_d \quad \text{on } \Gamma_G.$$

Here r_p denotes the precipitation rate expressed by

$$r_p = k_p r(c_1, c_2),$$

where k_p is a positive rate constant and r a rate function depending on c_1 and c_2 . A typical example is mass action kinetics leading to

$$r(c_1, c_2) = c_1^n c_2^m. \quad (5)$$

The dissolution rate r_d is constant ($k_d > 0$) in the presence of crystal, i. e. for $c_{12} > 0$ somewhere on Γ_G , and has to be such that in the absence of crystal the overall rate is zero (for a fluid that is not oversaturated, i. e. $r(c_1, c_2) \leq k_d/k_p$). To achieve this we introduce the set-valued expression

$$r_d(c_{12}) \in k_d H(c_{12}),$$

where H denotes the Heaviside graph,

$$H(u) = \begin{cases} 0, & \text{if } u < 0, \\ [0, 1], & \text{if } u = 0, \\ 1, & \text{if } u > 0. \end{cases}$$

If c_1 and c_2 are such that

$$r(c_1, c_2) > \frac{k_d}{k_p} \quad \text{somewhere on } \Gamma_G,$$

we have oversaturation and precipitation ($\partial_t c_{12} > 0$) will occur at such points. If the concentrations c_1 and c_2 are below the *solubility product*, i. e.

$$r(c_1, c_2) < \frac{k_d}{k_p} \quad \text{somewhere on } \Gamma_G,$$

while crystal is present, we have $\partial_t c_{12} < 0$ at such points and dissolution occurs. If it also happen that $c_{12} = 0$, we set

$$r_d = \frac{k_p}{k_d} r(c_1, c_2) < 1,$$

implying $\partial_t c_{12} = 0$. Summarizing this discussion we have for the crystalline solid the equation

$$\partial_t c_{12} \in k_d \left(\frac{k_p}{k_d} r(c_1, c_2) - H(c_{12}) \right) \quad \text{on } \Gamma_G. \tag{6}$$

Dimensionless form

The unknowns in the model are the fluid velocity \vec{q} and fluid pressure p , which can be determined without a-priori knowledge of dissolution/precipitation, and the concentrations c_1 , c_2 and c_{12} . We note that the total negative charge

$$c = mc_1 - nc_2, \tag{7}$$

is a conserved quantity with respect to the reactions. Indeed, (3) and (4) imply

$$\partial_t c + \nabla \cdot (\vec{q}c - D\nabla c) = 0 \quad \text{in } \Omega,$$

and

$$D\vec{\nu} \cdot \nabla c = 0 \quad \text{on } \Gamma_G.$$

Putting appropriate conditions on c_1 and c_2 along the outer boundary of Ω , and thus on c , the total charge in (7) can be determined a-priori as well. With respect to the reactions, the essential variables therefore are

$$c_1 \text{ (say)} \quad \text{and} \quad c_{12}.$$

The other concentration (c_2) follows directly from (7).

Let \hat{c}_1 and \hat{c}_{12} be characteristic values for the concentrations of cation c_1 and precipitate c_{12} . Further, let Q , P and L be characteristic values for flow, pressure and distance. Rescaling length with L and time with L/Q , and setting

$$\begin{aligned} u &:= \frac{c_1}{\hat{c}_1}, & v &:= \frac{c_{12}}{\hat{c}_{12}}, & c &:= \frac{c}{\hat{c}_1}, & \vec{q} &:= \frac{\vec{q}}{Q}, & p &:= \frac{p}{P}, \\ \mu &:= \frac{\mu Q}{PL}, & D &:= \frac{D}{LQ}, & k &:= \frac{k_d L}{Q \hat{c}_{12}}, & \varepsilon &:= \frac{\hat{c}_{12}}{L \hat{c}_1}, \\ r(u, c) &:= \frac{k_p}{k_d} r(\hat{c}_1 u, \hat{c}_1 \frac{mu-c}{n}), \end{aligned}$$

gives in the scaled domain Ω the set of equations

$$\left\{ \begin{array}{l} \mu \Delta \vec{q} = \nabla p, \\ \nabla \cdot \vec{q} = 0, \\ \partial_t c + \nabla \cdot (\vec{q}c - D \nabla c) = 0, \\ \partial_t u + \nabla \cdot (\vec{q}u - D \nabla u) = 0. \end{array} \right. \quad (8)$$

On the scaled interior boundary Γ_G we have

$$\left\{ \begin{array}{l} \vec{q} = \bar{0}, \\ \vec{v} \cdot \nabla c = 0, \\ -D \vec{v} \cdot \nabla u = \varepsilon n \partial_t v, \\ \partial_t v = k(r(u, c) - w), \\ w \in H(v). \end{array} \right. \quad (9)$$

REMARK 1 *The auxiliary function w plays the role of the scaled dissolution rate r_d/k_d . At boundary points where $v > 0$, w attains its maximal value ($w = 1$). At points where $v = 0$ and $\partial_t v = 0$ we have $w = r(u, c)$.*

REMARK 2 *It seems natural to choose the characteristic values \hat{c}_1 and \hat{c}_{12} such that the system contains about the same number of moles for both crystals and solutes. Mathematically this is expressed by*

$$\hat{c}_{12} \cdot \text{meas}(\Gamma_G) \approx \hat{c}_1 \cdot \text{meas}(\Omega). \quad (10)$$

Using the above definition of ε we find

$$\varepsilon L \text{meas}(\Gamma_G) \approx \text{meas}(\Omega).$$

Hence, on the pore level, ε can be seen as the ratio of two length scales: the characteristic pore scale length $\text{meas}(\Omega)/\text{meas}(\Gamma_G)$ and the problem related scale L . The balance (10) is quite natural for a porous medium, where $\text{meas}(\Gamma_G)$ denotes the total surface of the porous skeleton and $\text{meas}(\Omega)$ the total void volume. Assuming the medium being periodic with periodicity ε it

is easy to see that $\text{meas}(\Omega)/\text{meas}(\Gamma_G)$ is of order $1/\varepsilon$. When upscaling to a macroscopic model, the total internal surface goes to infinity as $\varepsilon \searrow 0$. The appearance of ε in the boundary flux in (9_3) allows us to control this growth, see, e. g., [2].

Results

Two situations are considered. Existence of solutions is obtained for general geometries, while for strips we study the occurrence of dissolution/precipitation fronts.

General domains

Under quite general conditions on the geometry of the flow domain and the data we show that the model has a solution that satisfies the equations and boundary conditions in an integrated or weak sense. Clearly, the fluid velocity \vec{q} , as well as the electrical charge c are solved independent of the chemistry. This part of the model ((8_{1-3}) and $(9_{1,2})$) is standard and its solution is straightforward. The challenging non-standard issue is the description of the chemistry ((8_4) and (9_{3-5})), in particular the multi-valued dissolution rate in (9_5) . Existence is demonstrated by regularization, where $(9_{4,5})$ are replaced by

$$\partial_t v = k(r(u, c) - H_\delta(v)). \tag{11}$$

Here $\delta > 0$ is a small parameter and H_δ a smooth approximation of H . For given \vec{q} and c , this yields a solution triple $\{u_\delta, v_\delta, w_\delta = H_\delta(v)\}$, which is shown to converge to $\{u, v, w\}$ as $\delta \searrow 0$. Details are given in [1].

Thin strips

To mimic flow and transport in porous media we consider here the special case where the flow domain is the thin strip $\Omega := \{(x, z)/0 < x < 1, -\varepsilon < z < \varepsilon\}$, with $0 < \varepsilon \ll 1$. Then the flow is given explicitly by the Poiseuille formula. Further, under compatible boundary conditions (see [3]), the charge c is constant in space and time. In this setting the chemical processes given in (9_{3-5}) take place at the side walls $\Gamma_G = \{(x, z)/0 < x < 1, z = \pm\varepsilon\}$. Initially we assume the system to be in chemical equilibrium throughout Ω , i. e.

$$u|_{t=0} = u^*, \quad \text{where} \quad r(u^*, c) = 1. \tag{12}$$

We consider the following two characteristic cases:

Dissolution fronts. Assuming $u < u^*$ at the inlet $x = 0$ and $v|_{t=0} = v_0 > 0$ on the side walls, a dissolution front occurs after a *waiting time* that can be computed explicitly.

Precipitation fronts. Assuming oversaturation ($u > u^*$) at the inlet and $v|_{t=0} = 0$ on the side walls, a precipitation front occurs instantaneously.

In both cases the front position is a *free boundary*, which moves in flow direction and increases continuously with time.

Defining the cross-section average of u as $\bar{u} = \frac{1}{2\varepsilon} \int_{-\varepsilon}^{\varepsilon} u(t, x, z) dz$ and letting $\varepsilon \searrow 0$, the triple $\{\bar{u}, v, w\}$ converges to the unique weak solution triple $\{U, V, W\}$ of the upscaled one-dimensional transport-reaction model introduced in [3],

$$\begin{cases} \partial_t (U + nV) + Q\partial_x U &= D\partial_x^2 U, \\ \partial_t V &= k(r(U) - W), \\ W &\in H(V). \end{cases}$$

Here $Q = \frac{1}{\varepsilon} \int_0^\varepsilon q(z) dz$ is the averaged Poiseuille velocity.

References

- [1] van Duijn, C.J. and Pop, I.S. (2003) Crystal dissolution and precipitation in porous media: pore scale analysis, RANA Preprint, Eindhoven University of Technology
- [2] Hornung, U. (1997) *Homogenization and Porous Media*, Interdisciplinary Applied Mathematics 6, Springer Verlag, Berlin
- [3] Knabner, P., van Duijn, C.J. and Hengst, S. (1995) An analysis of crystal dissolution fronts in flows through porous media. Part 1: Compatible boundary conditions, *Adv. Water Res.* **18**, 171-185

THEORETICAL MODELING AND EXPERIMENTAL MONITORING OF MATERIAL DESTRUCTION DURING DRYING

Stefan Jan Kowalski

Poznań University of Technology

Institute of Technology and Chemical Engineering

pl. Marii Skłodowskiej Curie 2, 60-965 Poznań, Poland

Abstract The objective of this paper is a fluid saturated capillary-porous material under drying process. The aim of this paper is to present the theoretical model enabling numerical calculation of the drying induced stresses, and the acoustic emission method (AE) as an experimental method for monitoring *on line* the material destruction. It is shown that the period of drying in which the drying induced stresses reach their maximum is accompanied by an enhanced emission of acoustic signals. These phenomena are illustrated on the example of a cylindrically shaped kaolin sample exposed to convective drying.

Introduction

The stresses arising in dried materials due to nonuniform shrinkage generate an amount of elastic energy. At the beginning of the drying process, when the strength of the dried material is weak, the stresses give rise to small displacements leading to grain reformulation and as well as small microcracks. Later, when the strength increases significantly and the accumulated elastic energy overcomes some critical value, a fracture of the material may occur, the energy released in this way spreading through the medium in the form of stress waves. A great part of these waves arrive at the boundary of the body. Registration of acoustic signals at the boundary surface for the purpose of inspection and identification of the phenomena occurring in the interior of the material has been termed *the acoustic emission method (AE)*.

One can state that in the case of moistened capillary-porous materials the friction between grains, moisture movement, grain reformulation and micro- and macrocrack formations all create the sources for emission of acoustic signals. The intensity of acoustic signals, their number and energy, may be used

for assessment of the state of stresses generated in moist materials during drying.

The evidence of a correlation between the drying induced stresses and the AE is illustrated on the cylindrical kaolin sample under convective drying. Although the AE method enables us to point out the period in which the stresses reach maximal values, we are not able yet to assess the magnitude of these stresses.

Basic Equations of the Drying Model

The body under drying is a moistened capillary-porous solid. This body is assumed here to be of isotropic structure and obeying the viscoelastic Maxwell model of the form

$$\dot{s}_{ij} + \frac{M}{\eta}s_{ij} = 2M\dot{e}_{ij}, \quad \dot{\sigma} + \frac{K}{\kappa}\sigma = K(\dot{\varepsilon} - \dot{\varepsilon}^{(TX)}) \quad (1)$$

In this equation s_{ij} is the deviator and σ is the spherical part of the stress tensor σ_{ij} , e_{ij} is the strain deviator and ε the volumetric part of the strain tensor ε_{ij} , $K = (2M + 3A)/3$ is bulk modulus with M and A corresponding to the familiar Lamé coefficients in the theory of elasticity, while η and κ can be termed the viscous shear and bulk moduli.

The temperature and moisture content generate the volumetric thermal-humid strain, which is expressed as

$$\varepsilon^{(TX)} = 3\left(\kappa^{(T)}\vartheta + \kappa^{(X)}\theta\right) \quad (2)$$

where $\kappa^{(T)}$ and $\kappa^{(X)}$ are the coefficients of linear thermal and humid expansion, $\vartheta = T - T_0$ and $\theta = X - X_0$ denote the relative temperature and the relative moisture content, with X being the specific moisture content (dry basis).

For the sake of simplicity and clarity of the presentation, we confine further considerations to the so-called constant drying rate period. In this period, the temperature of the dried body is constant and equal to the temperature of the wet bulb thermometer if the drying condition are stable, i.e.,

$$\vartheta_{wb} = \vartheta_a - \frac{l}{\alpha^{(T)}}\mathbf{W} \cdot \mathbf{n} = const \quad (3)$$

where ϑ_a is the temperature of the ambient (drying) medium, l is the latent heat of evaporation, \mathbf{W} is the mass flux of the moisture (proportional to the gradient of moisture potential [1, 2]), and $\alpha^{(T)}$ is the coefficient of the convective heat transfer between the body and the ambient medium.

The moisture content distribution is determined from the diffusion equation. Its very simplified form for the cylindrical sample reads

$$\dot{\theta} = \Lambda_m \left(\frac{\partial^2 \theta}{\partial r^2} + \frac{1}{r} \frac{\partial \theta}{\partial r} \right) \quad (4)$$

where $\Lambda_m \simeq \Lambda^{(\mu)} C^{(X)} / \rho^s$ is the diffusivity, $\Lambda^{(\mu)}$ is the moisture mobility coefficient, $C^{(X)}$ a coefficient expressing the capillary uplift of moisture [2], and ρ^s is the mass density of the dry body.

The boundary conditions for the moisture transfer are as follows

$$\frac{\partial \theta}{\partial r} \Big|_{r=0} = 0, \quad -\frac{\partial \theta}{\partial r} \Big|_{r=R} = \frac{B}{R} (\theta \Big|_{r=R} - \theta_e) \quad (5)$$

where $B = \alpha^{(X)} R / \Lambda^{(\mu)}$ is equivalent of the Biot number for moisture transfer, $\alpha^{(X)}$ is the coefficient of convective moisture exchange between the body and the ambient medium, R is the cylinder radius, and θ_e is the equilibrium (final) moisture content, which is dependent on the external drying conditions, i.e. on the physical parameters of drying air. Of these two conditions, the former is the symmetry condition with respect to the center of the cylinder and the latter presents the convective exchange of the moisture at the cylinder surface.

Assuming a uniform distribution of moisture content in the initial state, i.e. $\theta(r, t) \Big|_{t=0} = \theta_0$, we find the following solution for moisture distribution in the cylinder

$$\frac{\theta(r, \tau) - \theta_e}{\theta_0 - \theta_e} = 2B \sum_{n=1}^{\infty} \frac{J_0(\omega_n \frac{r}{R})}{(\omega_n^2 + B^2) J_0(\omega_n)} \exp(-\Lambda \omega_n^2 \tau) \quad (6)$$

where $\Lambda = \Lambda_m t_R / R^2$ is the dimensionless diffusivity coefficient, $t_R = \eta / M \simeq \kappa / K$ is the relaxation time for stresses, $\tau = t / t_R$ is the dimensionless time, and ω_n denotes the n -th eigenvalue, that is the n -th root of the characteristic equation

$$J_1(\omega_n) = \frac{B}{\omega_n} J_0(\omega_n) \quad (7)$$

and J_0 and J_1 are the Bessel functions of order zero, first and second kind.

The basic statement of this paper is that the magnitude of the drying induced stresses depends on the moisture distribution. The greater the non-uniformity in the distribution, the greater stresses arise in the dried body.

The Biot number B is the most important parameter that influences the drying rate in our model. If the external drying conditions are conducive to drying (high temperature, high speed of the ambient air) and the mobility of the moisture inside the material is low (high moisture viscosity, small surface tension), then the coefficient of convective moisture exchange $\alpha^{(X)}$ is high and the mobility coefficient $\Lambda^{(\mu)}$ is low, which results in the high value of the Biot number. In such a case one can expect a large non-uniformity in moisture distribution.

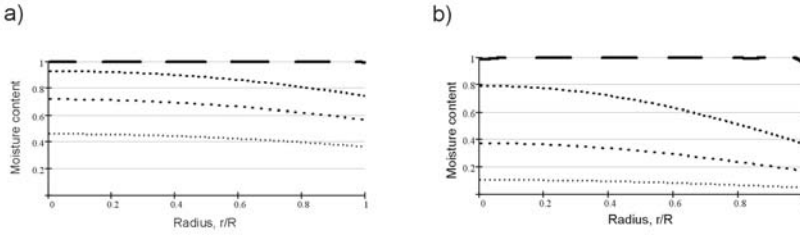


Figure 1. Distribution of moisture content along cylinder radius in different instants of time: a) for $B = 0.5$, b) for $B = 2$ ($\tau = 0$ - solid line, $\tau = 0.2$ - dashed line, $\tau = 0.5$ - dotted line, $\tau = 1$ - dash-dot line).

Indeed, this is shown in the plots constructed on the basis of equation (6). Figure 1 illustrates the moisture distribution in the cylinder for $B = 0.5$ and for $B = 2$ in different instants of time. It is seen from these plots that the difference between the rate of drying of the cylinder surface ($r/R = 1$) and its core ($r = 0$) is greater for $B = 2$ than for $B = 0.5$. Thus, the stresses of a greater value will be generated by drying with $B = 2$. Because of page limitation, we show this statement only for the tangential stresses expressed by the formula

$$\frac{\sigma_{\varphi\varphi}^{(v)}(r, \tau)}{\sigma} = 2B^2 \sum_{n=1}^{\infty} \left[1 + \frac{\omega_n}{J_1(\omega_n)} \left(\frac{J_1(\omega_n \frac{r}{R})}{\omega_n \frac{r}{R}} - J_0(\omega_n \frac{r}{R}) \right) \right] \times (8)$$

$$\times \frac{\exp(-\tau) - \Lambda \omega_n^2 \exp(-\Lambda \omega_n^2 \tau)}{(1 - \Lambda \omega_n^2) \omega_n^2 (\omega_n^2 + B^2)}$$

where σ is a reference stress defined as

$$\sigma = \frac{2M (3K \kappa^{(X)})}{2M + A} (\theta_0 - \theta_e)$$

Figure 2. illustrates the distribution of tangential stresses in the cylinder for $B = 0.5$ and for $B = 2$ in different instants of time. It is seen from these plots that the stresses are much greater for $B = 2$ than for $B = 0.5$. A characteristic feature of the tangential stresses is that they are tensional at the cylinder surface and compressional in the core. If the material was assumed to be elastic, the stresses would rise from zero to a maximum and then tend to zero, when time goes to infinity. Quite a different behavior is presented by the viscoelastic model. Here, the stresses rise from zero to a maximum, then tend to change their sign and finally go to zero, when time goes to infinity. This means that the stress reverse phenomenon may occur when the material reveals viscoelastic properties. Indeed, many materials under drying suffer stress reverse, which can be detected with the use of the acoustic emission method (AE). Namely,

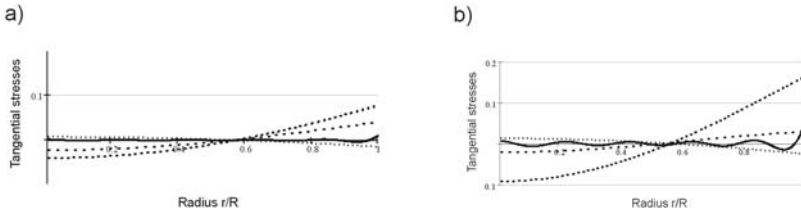


Figure 2. Distribution of tangential stresses along cylinder radius in different instants of time: a) for $B = 0.5$, b) for $B = 2$ ($\tau = 0$ - solid line, $\tau = 0.2$ - dashed line, $\tau = 0.5$ - dadot line, $\tau = 1$ - dot line).

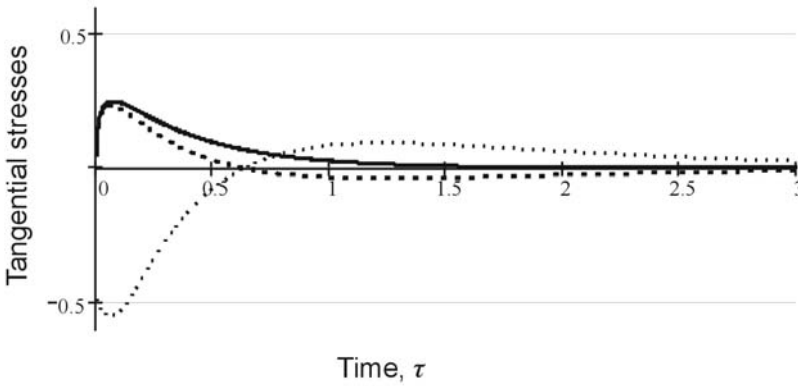


Figure 3. Time evolution of tangential stresses for $B = 2$: elastic at ($r/R = 1$) - solid line, viscoelastic at ($r/R = 1$) - dashed line, viscoelastic at ($r = 0$) - dot line.

one observes an enhanced emission of acoustic signals when the tensional stresses are generated in the material. This can be explained by the fact that a lot of dried materials display smaller strength in tension than in compression. Therefore, the enhanced emission occurs twice during drying: first, when the surface of the body is in tension, and second, when the core of the body is in tension after the stress reverse.

Figure 3 presents the time evolution of tangential stresses at the surface and the core of the cylinder according to the viscoelastic and elastic models. The stress reverse can be explained as follows: when the body dries, the drier surface attempts to shrink but is restrained by the wet core. The surface is stressed in tension and the core in compression and inelastic strain occurs. Later, under a surface with reduced shrinkage, the core dries and attempts to shrink causing the stress state to reverse [4].

Experimental Monitoring of Material Destruction

When the energy accumulated in a stressed body is released, because of e.g. body destruction, the stress waves are generated. The waves propagating through the body create acoustic signals that arrive at the boundary surface where they can be monitored. The intensity of these signals and their energy may supply important information on destructive processes that occur inside the material.

The AE signals are measured *on line* with the help of an acoustic analyzer that transduces the acoustic signals into electric current throughout the piezoelectric sensor [3]. The AE signals are amplified and filtrated in the conversion unit and converted into voltage current proportional to the value of the transmitted signal. Finally, the envelope of high frequency signals from the logarithmic converter is sent to the computer through a GPIB card. The humidity and temperature sensors that register the humidity and the temperature in the drier chamber, and the balance that monitors the loss of moisture in the body complete the measurement system. All incoming data are analyzed *on line* and stored in computer memory.

The commonly used AE activity parameter is called *the AE count rate*. It denotes the number of AE impulses crossing the pre-set level. However, because of different acoustic absorbency of individual materials, instead of count rate it is convenient to use *the AE occurrence* that denotes a package of AE impulses per time increment. Another important indicator of AE is *the energy of acoustic signals*. This indicator may reflect the level of stresses existing in the material. Although we are not able yet to estimate precisely the magnitude of the stresses generated by drying, we can indicate the period at which the stresses reach critical values. The moment at which the plot of total emitted energy suffers a jump denotes a crack of material structure.

Figure 4 presents the AE occurrence rate and the drying curve. Three groups of the AE occurrence rate appear during the process illustrated in figure 4: the first group appears during the heating of the material at the beginning of the constant drying rate period, the second one at the end of the period, and the third one can be sometimes noticed at the final stage of drying. The first group of AE occurrences is of small energy and is caused by insignificant thermal stresses. The second group is of high energy and is evidenced for the kaolin sample when the surface layer shrinks intensively and the tensional stresses arise at the surface. The number of AE occurrences is the highest in this stage of drying. The third maximum of AE occurrences depends on the drying conditions. For high temperature or low humidity of the drying medium the third maximum is quite significant. It is generated by the tensional stresses in the core after the stress reverse.

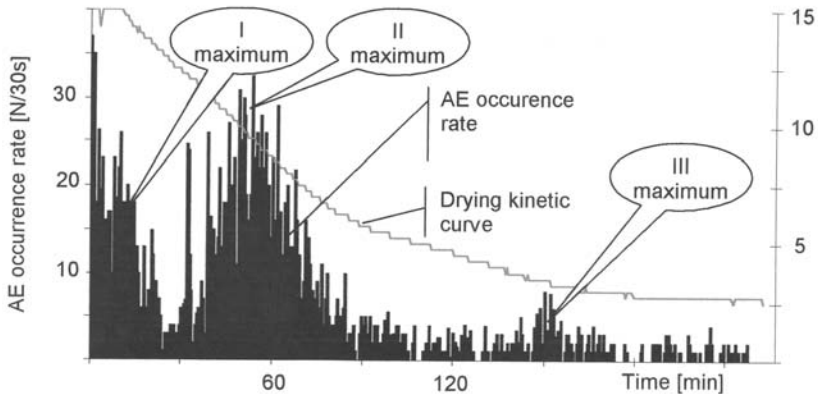


Figure 4. AE occurrence rate (left axis) and the curve of drying (right axis).

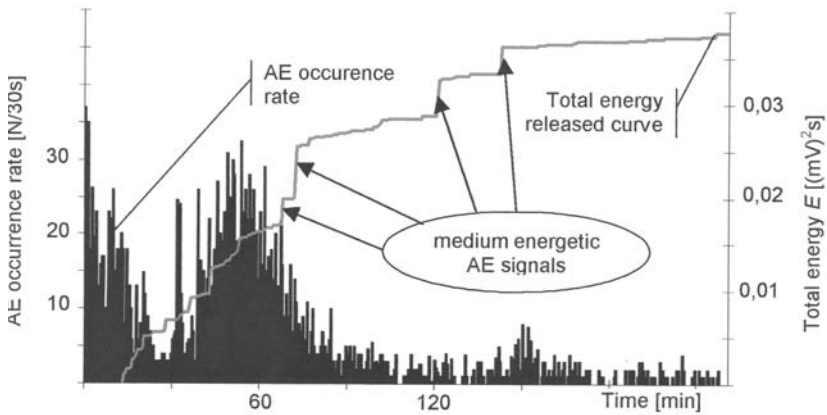


Figure 5. AE occurrence rate and the total energy released during drying.

The plot of total energy emitted during drying shown in figure 5 illustrates the periods at which the stresses reach their maximum, and when the destruction of the material takes place. The descriptor of total energy may serve as an indicator of quality of dried products. The number and magnitude of the straight vertical lines visible in the plot indicate how many cracks arose in the material during drying and how big they are. A good or optimal drying process is one which has a smooth plot of total energy.

Very informative plots are presented in figure 6. The envelope of AE occurrence rates and the theoretically estimated evolution of circumferential stresses based on the viscoelastic model are presented together in this figure. We can

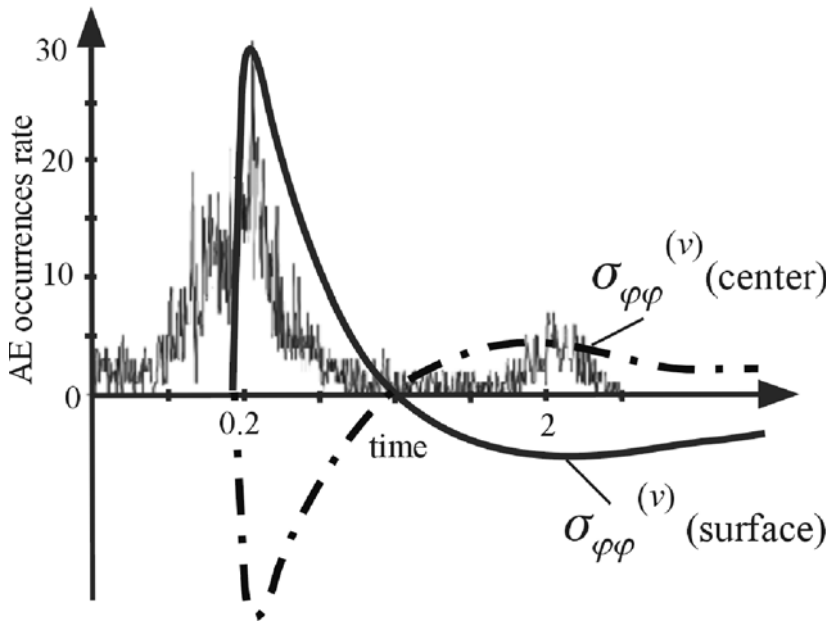


Figure 6. Envelope of AE occurrence rates and the theoretical curve circumferential stresses.

see that the increase of stresses correlates with an increase of the AE occurrences rate. The first maximum of the AE occurrence rate corresponds to the maximal tensional stresses at the cylinder surface, while the second one corresponds to the maximal tensional stresses in the core after the stress reverse.

Final Remarks

The obtained results indicate that the enhanced emission of AE occurrences takes place at the moments when the drying induced tensional stresses reach their maximum. One can state that the plot of total energy released during drying may serve for assessment of the destruction of the material during drying because discontinuities in this plot correspond to cracks occurring in the material.

The following conclusions can be drawn: a) the AE occurrence rate descriptor is useful for determination of the periods at which the state of stress becomes destructive for the material; b) three possible groups of AE occurrence rates may arise during drying: first, during the heating of the material; second, when the tensional stresses at the surface reach their maximum; third, when the tensional stresses in the core reach their maximum after the stress reverse; c) the descriptor of total energy reflects accurately the stress state in the material and indicates whether the material suffers the destruction or not.

Acknowledgement

This work was carried out as a part of the research project DS-32/112/2003 sponsored by the Poznań University of Technology in the year 2003.

References

- [1] Kowalski, S.J. (2000) Towards a thermodynamics and mechanics of drying processes, *Chemical Engineering Science* **55**, 1289-1304
- [2] Kowalski, S.J. (2003) *Thermomechanics of Drying Processes*, Springer, Berlin/Heidelberg
- [3] Kowalski, S.J. and Rajewska, K. (2002) Drying induced stresses in elastic and viscoelastic saturated materials, *Chemical Engineering Science* **57**, 3883-3892
- [4] Milota, M.R. and Qinglin, W. (1994) Resolution of the stress and strain components during drying of a softwood, *Proceedings of 9th Intern. Drying Symp. (IDS'94)*, Australia

TWO PHASE FLOW IN CAPILLARY POROUS THERMO-ELASTIC MATERIALS

Tim Ricken and Reint de Boer

Institut für Mechanik

Universität Duisburg-Essen, Standort Essen, 45117 Essen, Germany

tim.ricken@uni-essen.de, reint.deboer@uni-essen.de

Abstract In this contribution, the coupled flow of liquids and gases in capillary thermo-elastic porous materials is investigated by using a continuum mechanical model based on the Theory of Porous Media. The movement of the phases is influenced by the capillarity forces, the relative permeability, the temperature and the given boundary conditions. In the examined porous body, the capillary effect is caused by the intermolecular forces of cohesion and adhesion of the constituents involved. The treatment of the capillary problem, based on thermomechanical investigations, yields the result that the capillarity force is a volume interaction force. Moreover, the friction interaction forces caused by the motion of the constituents are included in the mechanical model. The relative permeability depends on the saturation of the porous body which is considered in the mechanical model. In order to describe the thermo-elastic behaviour, the balance equation of energy for the mixture must be taken into account. The aim of this investigation is to provide with a numerical simulation of the behavior of liquid and gas phases in a thermo-elastic porous body.

Keywords: Theory of Porous Media (TPM), ternary model, capillarity, thermo-elasticity

Introduction

In the last 20 years, there has been a growing interest in investigations concerning porous multi phase bodies. Due to the fact of the increasing body of acquired knowledge in the physics of multi body system, connecting with the wide range of applications, this interest is not remarkable. However, all these new perceptions have to be embedded in a thermomechanical concept. This can be afforded by the Theory of Porous Media.

In the following investigation, we use this theory allowing a continuum thermomechanical approach to the two-phase flow problem in a porous solid. The transient and stationary motion of liquids in porous solids with small pores is complex and not all related problems have been solved yet. The main internal

forces acting in these systems are the capillary and friction forces which are both influenced by saturation, though unfortunately not in the same way.

The capillary forces have been recognized as intermolecular forces which are created by cohesion and adhesion at interfaces. From the evaluation of the thermomechanical treatment we could clearly make out that these forces depend on the free HELMHOLTZ energy functions of the solid phase and the density gradient of the liquid.

The friction forces are taken into account using the well known VAN GENUCHTEN formulation. Both forces are introduced as interaction forces between the phases involved. Using these constitutive equations, the equations of motion of the liquid and gas phases are developed, forming the framework for the presented ternary calculation concept.

Additionally, the thermo-elastic behaviour will be described. Although, not all constitutive relations can be identified right now, the theoretical treatment of the entropy inequality is finished for the three phase model.

Basics

The Theory of Porous Media is the Mixture Theory, restricted by the concept of the Volume Fractions. Hereby, we have a look at a continuum which consists of several constituents. In this investigation we deal with a solid phase ($\alpha = S$), a Liquid phase ($\alpha = L$) and a Gas phase ($\alpha = G$). The components of the real structure will be statistically distributed over the control space, so that we gain to a smeared model of the real structure.

In order to keep also the physical properties for the smeared body, such as the material compressibility or incompressibility of the constituents involved, the mixture theory is restricted by the concept of volume fractions. Therefore, the volume V of the control space is divided into the partial volume fractions n^α . The sum of the volume fractions has to fill the whole control space. With the concept of volume fractions we obtain the partial density ρ^α for the constituents

$$\rho^\alpha = n^\alpha \rho^{\alpha R} . \quad (1)$$

where n^α and $\rho^{\alpha R}$ are the volume fraction and the real density of φ^α , respectively.

The reader who is interested in a review of the Theory of Porous Media and the kinematics is referred to DE BOER [4].

Field Equations

The system is investigated under the assumption of a material incompressible solid and liquid and a compressible gas. The pores in the solid are restricted to a value in between micro and coarse pores. Moreover, we allow no mass exchange between the phases and we use a quasi static description. Therefore,

the local statements of the balance equations of mass and momentum are given for each individual constituent φ^α by

$$(\rho^\alpha)'_\alpha + \rho^\alpha \operatorname{div} \mathbf{x}'_\alpha = 0, \quad \operatorname{div} \mathbf{T}^\alpha + \rho^\alpha \mathbf{b} + \hat{\mathbf{p}}^\alpha = \mathbf{0}, \quad (2)$$

wherein \mathbf{x}'_α denotes the velocities, \mathbf{T}^α the partial CAUCHY stress tensors, \mathbf{b} the volume forces and $\hat{\mathbf{p}}^\alpha$ the interaction forces between the phases. Additionally, the balance of energy concerning the whole mixture body must be taken into account. In order to keep the numerical complexity in a manageable scope, we assume that all constituents have the same temperature at the same place:

$$\sum_{\alpha}^{\text{S,L,G}} \{ \rho^\alpha (\varepsilon^\alpha)'_\alpha - \mathbf{T}^\alpha \cdot \mathbf{D}_\alpha - \rho^\alpha r^\alpha + \operatorname{div} \mathbf{q}^\alpha \} = \sum_{\alpha}^{\text{S,L,G}} \{ \hat{\varepsilon}^\alpha - \hat{\mathbf{p}}^\alpha \cdot \mathbf{x}'_\alpha \}. \quad (3)$$

Furthermore, the partial rates of the specific internal energy ε , the symmetric part of the velocity gradient \mathbf{D}_α , the external heat supply r^α , the heat flux \mathbf{q}^α and the supply of energy between the phases $\hat{\varepsilon}^\alpha$ are included. Finally, the physical constrain conditions have to be considered as well as the saturation condition and the conditions that the sum of all partial interaction forces and the sum of all partial energy supplies have to be vanished:

$$n^{\text{S}} + n^{\text{L}} + n^{\text{G}} = 1, \quad \hat{\mathbf{p}}^{\text{S}} + \hat{\mathbf{p}}^{\text{L}} + \hat{\mathbf{p}}^{\text{G}} = \mathbf{0}, \quad \hat{\varepsilon}^{\text{S}} + \hat{\varepsilon}^{\text{L}} + \hat{\varepsilon}^{\text{G}} = 0. \quad (4)$$

Constitutive Equations

In the above mentioned field equations the number of unknown quantities does not correspond to the number of equations, thus we have to conclude the problem with the constitutive equations for the partial stress tensors \mathbf{T}^α , the interaction forces $\hat{\mathbf{p}}^\alpha$, the partial internal energies ε^α and the partial heat flows \mathbf{q}^α . From the evaluation of the entropy inequality of the saturated porous body, see DE BOER [4], we obtain for the solid phase and the mobile phases with Index $\beta = \text{L, G}$ the constitutive relations for \mathbf{T}^α and $\hat{\mathbf{p}}^\alpha$:

$$\mathbf{T}^{\text{S}} = -n^{\text{S}} \lambda \mathbf{I} + \mathbf{T}_{\text{E}}^{\text{S}}, \quad (5)$$

$$\mathbf{T}^\beta = -p^\beta \mathbf{I} = (-n^\beta \lambda + p_{\text{E}}^\beta) \mathbf{I} = -n^\beta p^{\beta\text{R}} \mathbf{I},$$

$$\hat{\mathbf{p}}^\beta = p^{\beta\text{R}} \operatorname{grad} n^\beta + \hat{\mathbf{p}}_{\text{E}}^\beta. \quad (6)$$

Therein, λ denotes the interface pressure (whole pore pressure), $p^{\beta\text{R}}$ the realistic pressure, $\mathbf{T}_{\text{E}}^{\text{S}}$ denotes the partial effective CAUCHY stress tensor and \mathbf{I} is the unit tensor. With the expression $\lambda = n^{\text{S}} \lambda + n^{\text{L}} p^{\text{LR}} + n^{\text{G}} p^{\text{GR}}$ (DALTON'S law), the constrain

$$p_{\text{E}}^{\text{L}} = -p_{\text{E}}^{\text{G}} \quad (7)$$

has to be considered. In order to describe the pressure behavior of the mobile phases, for the extra supply terms p_E^α the approach

$$p_E^L = n^L n^G \hat{k}^L \sqrt{-\log(n^L/n^F)}, \quad (8)$$

has been developed, wherein \hat{k}^L characterizes a material parameter and $n^F = 1 - n^S$ describes the whole pore volume (porosity), see RICKEN [7]. Considering (5), (7) and (8), the volume fractions n^β are given by

$$n^L = n^F \exp\left(\frac{(p^{LR} - p^{GR})^2}{-(\hat{k}^L n^F)^2}\right), \quad n^G = (1 - n^F) \exp\left(\frac{(p^{LR} - p^{GR})^2}{-(\hat{k}^L n^F)^2}\right). \quad (9)$$

Moreover, the density of the compressible gas phase can be calculated from the modified Gas law:

$$\rho^{GR} = \rho_0^{GR} \exp\left(\frac{p^{GR}}{\rho_0^{GR} \theta R_G}\right), \quad (10)$$

wherein ρ_0^{GR} is the reference density, θ is the temperature of all phases and R_G is the specific gas constant.

The cause of the capillary motion is indicated in the "extra" supply terms of momentum \hat{p}_E^α in (6), which are postulated for the liquid and gas with

$$\begin{aligned} \hat{p}_E^L &= -c_L \text{grad} \rho^L - \mathbf{S}_L \mathbf{w}_L - \tilde{\mathbf{S}}_G \mathbf{w}_G, \\ \hat{p}_E^G &= -c_G \text{grad} \rho^L - \tilde{\mathbf{S}}_L \mathbf{w}_L - \mathbf{S}_G \mathbf{w}_G. \end{aligned} \quad (11)$$

Herein, c_L and c_G are parameters responding to the capillary forces which has an effect between the solid and gas phase and between the liquid and gas phase, respectively. They depend on the form and nature of the pores and of the surface tensions between the phases. This new approach to the interaction forces allows the description of capillary motion in porous solids, see DE BOER & DIDWANIA [6].

Both last terms on the right side of (11) denotes the friction influence on each of the fluids in relation to their seepage velocities $\mathbf{w}_\beta = \mathbf{x}'_\beta - \mathbf{x}'_S$. The material parameter functions \mathbf{S}_β are postulated in dependence on the saturation $s_e = n^L/(1 - n^S)$ with the well known relation by VAN GENUCHTEN [1], which is expressed in a modified way as:

$$\begin{aligned} \mathbf{S}_L^{-1} &= \frac{k_0^L}{(n^L)^2} s_e^{\frac{1}{2}} \left[1 - \left(1 - s_e^{\frac{1}{m}} \right)^m \right]^2 \mathbf{I}, \\ \mathbf{S}_G^{-1} &= \frac{k_0^G}{(n^G)^2} \left(1 - s_e^{\frac{1}{2}} \right)^{\frac{1}{2}} \left[1 - s_e^{\frac{1}{m}} \right]^{2m} \mathbf{I}. \end{aligned} \quad (12)$$

Therein, $k_0^\beta = k_F/\mu_\beta$ represents a specific friction parameter concerning the Darcy permeability k_F and the effective shear viscosity μ_β . Moreover, m denotes a VAN GENUCHTEN parameter.

In (11), $\tilde{\mathbf{S}}_\beta$ characterizes the influence of the fluid velocities on each other and will be neglected in the following.

For further particulars concerning the thermo-elastic modelling of the solid including the constitutive equations with the heat flux \mathbf{q}^α and the internal energy we refer you to BLUHM [5].

Numerical Treatment

In the calculation concept we gained 14 unknown quantities in the case of a 2 dimensional problem. By using the constitutive equations and the physical constrain conditions we were able to reduce this number to 10. In order to develop an effective calculation concept, we additionally insert the integral statement of the balance of mass concerning the solid phase with $n^S = n_{0S}^S \det \mathbf{F}_S$, wherein n_{0S}^S is the reference volume fraction of the solid and $\det \mathbf{F}_S$ denotes the deformation gradient. Moreover, the velocities of the mobile phases will be calculated using the balance of momentum in the quasi static Darcy formulation:

$$\begin{aligned} n^L \mathbf{w}_L &= n^L (\mathbf{S}_L)^{-1} (-n^L \text{grad } p^{\text{LR}} + \rho^L \mathbf{b} - c_L \text{grad } n^L), \\ n^G \mathbf{w}_G &= n^G (\mathbf{S}_G)^{-1} (-n^G \text{grad } p^{\text{GR}} + \rho^G \mathbf{b} - c_G \text{grad } n^L). \end{aligned} \quad (13)$$

Finally, we receive a system of equations with 5 unknown quantities which are the motion of the solid phase \mathbf{u}_S , the realistic pressure of the Liquid p^{LR} and the Gas phase p^{GR} and the temperature θ . Thus, in order to determinate these quantities we use the weak forms of the balance of momentum and of the balance of energy for the mixture:

$$\int_{B_S} \{\mathbf{T} \cdot \text{grad } \delta \mathbf{u}_S - \rho \mathbf{b} \delta \mathbf{u}_S\} dv = \int_{\partial B_S} \{\mathbf{t} \cdot \delta \mathbf{u}_S\} da, \quad (14)$$

$$\int_{B_S} \sum_{\alpha}^{\text{S,L,G}} \{\rho^\alpha (\varepsilon^\alpha)'_\alpha - \mathbf{T}^\alpha \cdot \mathbf{D}_\alpha - \rho^\alpha r^\alpha + \text{div } \mathbf{q}^\alpha + \hat{\mathbf{p}}^\alpha \cdot \mathbf{x}'_\alpha\} dv = 0, \quad (15)$$

with $\mathbf{T} = \mathbf{T}^S + \mathbf{T}^L + \mathbf{T}^G$, $\rho = \rho^S + \rho^L + \rho^G$ and a NEUMANN boundary condition with the external stress tensor $\mathbf{t} = \mathbf{T} \mathbf{n}$. Additionally, the weak

forms of the balances of mass for the Liquid and Gas phase are used:

$$\int_{B_S} \{ (n^L)'_S \delta p^{LR} - n^L \text{grad} \delta p^{LR} \cdot \mathbf{w}_L + n^L \text{div} \mathbf{x}'_S \delta p^{LR} \} dv = \\ = - \int_{\partial B} \{ n^L \delta p^{LR} \mathbf{w}_L \cdot \mathbf{n} \} da , \quad (16)$$

$$\int_{B_S} \{ (\rho^G)'_S \delta p^{GR} - \rho^G \text{grad} \delta p^{GR} \cdot \mathbf{w}_G + \rho^G \text{div} \mathbf{x}'_S \delta p^{GR} \} dv = \\ = - \int_{\partial B} \{ \rho^G \delta p^{GR} \mathbf{w}_G \cdot \mathbf{n} \} da . \quad (17)$$

For the NEUMANN boundary condition we received a volume stream for the Liquid and a mass stream for the Gas phase.

References

- [1] van Genuchten, M.T. (1980) A closed-form equation for predicting the hydraulic conductivity of unsaturated soils, *Soil Science Society of America Journal* **44**, 892-898
- [2] Kuenzel, H.M. (1994) Verfahren zur ein- und zweidimensionalen Berechnung des gekoppelten Waerme- und Feuchtetransports in Bauteilen mit einfachen Kennwerten, Dissertation, Lehrstuhl Konstruktive Bauphysik, Fakultae Bauingenieur- und Vermessungswesen der Universitaet Stuttgart
- [3] Helmig, R. (1997) *Multiphase Flow and Transport Processes in the Subsurface: A Contribution to the Modeling of Hydrosystems*, Springer-Verlag, Berlin/Heidelberg/New York
- [4] de Boer, R. (2000) *Theory of Porous Media: Highlights in the Historical Development and Current State*, Springer-Verlag, Berlin/Heidelberg/New York
- [5] Bluhm, J. (2002) Modelling of saturated thermo-elastic porous solids with different phase temperatures, in *Porous Media: Theory, Experiments and Numerical Applications*, W. Ehlers, J. Bluhm (eds.), Springer-Verlag, Berlin/Heidelberg/New York
- [6] de Boer, R. and Didwania, A.K. (2002) Capillarity in porous bodies: contribution of the Vienna School and recent findings, *Acta Mechanica* **159**, 173-188
- [7] Ricken, T. (2002) *Kapillaritaet in poroesen Medien - theoretische Untersuchung und numerische Simulation*, Dissertation, Shaker Verlag, Aachen

AUTHOR INDEX

- Abousleiman, Y., 141
Acartuerk, A., 69
Alvarellós, J., 45
Baaijens, F.P.T., 207
Bader, S., 275
Barocas, V.H., 37
Batra, R.C., 221
Bénet, J.C., 307
Bennethum, L.S., 259
Bluhm, J., 329
Boscus, J., 307
Caurel, J., 125
Chandran, P.L., 37
Cortis, A., 53
Cowin, S.C., 3
de Boer, R., 359
dell'Isola, F., 221
Delville, A., 159
Detournay, E., 125
Dormieux, L., 321
Ehlers, W., 69
Ekbote, S., 141
Frijns, A.J.H., 133
Gawin, D., 91
Giovine, P., 183
Groenevelt, P.H., 267
Gu, W.Y., 193
Guermont, J.L., 53
Hartikainen, J., 335
Hildenbrand, A., 231
Huinink, H.P., 149
Hutter, K., 81
Hütter, M., 315
Huyghe, J.M., 133, 299
Jankovic, D., 99
Keijzer, T.J.S., 283
Khan, T.R., 251
Klein, K., 241
Kopinga, K., 149
Kowalski, S.J., 349
Krooss, B.M., 231
Kruschwitz, J., 329
Lafarge, D., 53
Lemarchand, E., 321
Liu, Z.P., 75
Loch, J.P.G., 283
Loret, B., 167
Markert, B., 69
Mikkola, M., 335
Moyné, C., 173
Murad, M.A., 173
Oomens, C.W.J., 207
Ooms, G., 61
Palomino, A.M., 45
Pel, L., 149
Pesavento, F., 91
Pivonka, P., 289
Poesio, P., 61
Pop, I.S., 343
Porion, P., 159
Pudasaini, S.P., 81
Pullens, R.A.A., 207
Raats, P., 213
Radtke, G.A., 75
Reppert, P.M., 251
Richefeu, V., 307
Richter, K., 283
Ricken, T., 349
Rigby, P.H., 75
Risso, F., 111
Santamarina, J.C., 45
Sarout, J., 125
Sciarra, G., 221
Schotting, R.J., 275
Schrefler, B.A., 91
Sengers, B.G., 207
Setzer, M.J., 329
Sherwood, J.D., 111
Simões, F.M.F., 167
Simon, B.R., 75

Smeulders, D., 53
Smiles, D.E., 201
Smit, T.H., 299
Smith, D., 289
Tan, C., 125
Telega, J.J., 117
Ulm, F.-J., 321
Urai, J.L., 231
Valdes, J.R., 45

van Duijn, C.J., 343
van Meerveld, J., 315
Vega, A.L., 193
Wang, Y., 81
Wang, Y.-H., 241
Wijlaars, M.W., 133
Williams, S.K., 75
Wojnar, R., 117
Yao, H., 193

Mechanics

SOLID MECHANICS AND ITS APPLICATIONS

Series Editor: G.M.L. Gladwell

Aims and Scope of the Series

The fundamental questions arising in mechanics are: *Why?*, *How?*, and *How much?* The aim of this series is to provide lucid accounts written by authoritative researchers giving vision and insight in answering these questions on the subject of mechanics as it relates to solids. The scope of the series covers the entire spectrum of solid mechanics. Thus it includes the foundation of mechanics; variational formulations; computational mechanics; statics, kinematics and dynamics of rigid and elastic bodies; vibrations of solids and structures; dynamical systems and chaos; the theories of elasticity, plasticity and viscoelasticity; composite materials; rods, beams, shells and membranes; structural control and stability; soils, rocks and geomechanics; fracture; tribology; experimental mechanics; biomechanics and machine design.

1. R.T. Haftka, Z. Gürdal and M.P. Kamat: *Elements of Structural Optimization*. 2nd rev.ed., 1990
ISBN 0-7923-0608-2
2. J.J. Kalker: *Three-Dimensional Elastic Bodies in Rolling Contact*. 1990 ISBN 0-7923-0712-7
3. P. Karasudhi: *Foundations of Solid Mechanics*. 1991 ISBN 0-7923-0772-0
4. *Not published*
5. *Not published*.
6. J.F. Doyle: *Static and Dynamic Analysis of Structures*. With an Emphasis on Mechanics and Computer Matrix Methods. 1991 ISBN 0-7923-1124-8; Pb 0-7923-1208-2
7. O.O. Ochoa and J.N. Reddy: *Finite Element Analysis of Composite Laminates*.
ISBN 0-7923-1125-6
8. M.H. Aliabadi and D.P. Rooke: *Numerical Fracture Mechanics*. ISBN 0-7923-1175-2
9. J. Angeles and C.S. López-Cajún: *Optimization of Cam Mechanisms*. 1991
ISBN 0-7923-1355-0
10. D.E. Grierson, A. Franchi and P. Riva (eds.): *Progress in Structural Engineering*. 1991
ISBN 0-7923-1396-8
11. R.T. Haftka and Z. Gürdal: *Elements of Structural Optimization*. 3rd rev. and exp. ed. 1992
ISBN 0-7923-1504-9; Pb 0-7923-1505-7
12. J.R. Barber: *Elasticity*. 1992 ISBN 0-7923-1609-6; Pb 0-7923-1610-X
13. H.S. Tzou and G.L. Anderson (eds.): *Intelligent Structural Systems*. 1992
ISBN 0-7923-1920-6
14. E.E. Gdoutos: *Fracture Mechanics*. An Introduction. 1993 ISBN 0-7923-1932-X
15. J.P. Ward: *Solid Mechanics*. An Introduction. 1992 ISBN 0-7923-1949-4
16. M. Farshad: *Design and Analysis of Shell Structures*. 1992 ISBN 0-7923-1950-8
17. H.S. Tzou and T. Fukuda (eds.): *Precision Sensors, Actuators and Systems*. 1992
ISBN 0-7923-2015-8
18. J.R. Vinson: *The Behavior of Shells Composed of Isotropic and Composite Materials*. 1993
ISBN 0-7923-2113-8
19. H.S. Tzou: *Piezoelectric Shells*. Distributed Sensing and Control of Continua. 1993
ISBN 0-7923-2186-3
20. W. Schiehlen (ed.): *Advanced Multibody System Dynamics*. Simulation and Software Tools.
1993 ISBN 0-7923-2192-8
21. C.-W. Lee: *Vibration Analysis of Rotors*. 1993 ISBN 0-7923-2300-9
22. D.R. Smith: *An Introduction to Continuum Mechanics*. 1993 ISBN 0-7923-2454-4
23. G.M.L. Gladwell: *Inverse Problems in Scattering*. An Introduction. 1993 ISBN 0-7923-2478-1

Mechanics

SOLID MECHANICS AND ITS APPLICATIONS

Series Editor: G.M.L. Gladwell

24. G. Prathap: *The Finite Element Method in Structural Mechanics*. 1993 ISBN 0-7923-2492-7
25. J. Herskovits (ed.): *Advances in Structural Optimization*. 1995 ISBN 0-7923-2510-9
26. M.A. González-Palacios and J. Angeles: *Cam Synthesis*. 1993 ISBN 0-7923-2536-2
27. W.S. Hall: *The Boundary Element Method*. 1993 ISBN 0-7923-2580-X
28. J. Angeles, G. Hommel and P. Kovács (eds.): *Computational Kinematics*. 1993
ISBN 0-7923-2585-0
29. A. Curnier: *Computational Methods in Solid Mechanics*. 1994 ISBN 0-7923-2761-6
30. D.A. Hills and D. Nowell: *Mechanics of Fretting Fatigue*. 1994 ISBN 0-7923-2866-3
31. B. Tabarrok and F.P.J. Rimrott: *Variational Methods and Complementary Formulations in Dynamics*. 1994 ISBN 0-7923-2923-6
32. E.H. Dowell (ed.), E.F. Crawley, H.C. Curtiss Jr., D.A. Peters, R. H. Scanlan and F. Sisto: *A Modern Course in Aeroelasticity*. Third Revised and Enlarged Edition. 1995
ISBN 0-7923-2788-8; Pb: 0-7923-2789-6
33. A. Preumont: *Random Vibration and Spectral Analysis*. 1994 ISBN 0-7923-3036-6
34. J.N. Reddy (ed.): *Mechanics of Composite Materials*. Selected works of Nicholas J. Pagano. 1994
ISBN 0-7923-3041-2
35. A.P.S. Selvadurai (ed.): *Mechanics of Poroelastic Media*. 1996 ISBN 0-7923-3329-2
36. Z. Mróz, D. Weichert, S. Dorosz (eds.): *Inelastic Behaviour of Structures under Variable Loads*. 1995
ISBN 0-7923-3397-7
37. R. Pyrz (ed.): *IUTAM Symposium on Microstructure-Property Interactions in Composite Materials*. Proceedings of the IUTAM Symposium held in Aalborg, Denmark. 1995
ISBN 0-7923-3427-2
38. M.I. Friswell and J.E. Mottershead: *Finite Element Model Updating in Structural Dynamics*. 1995
ISBN 0-7923-3431-0
39. D.F. Parker and A.H. England (eds.): *IUTAM Symposium on Anisotropy, Inhomogeneity and Nonlinearity in Solid Mechanics*. Proceedings of the IUTAM Symposium held in Nottingham, U.K. 1995
ISBN 0-7923-3594-5
40. J.-P. Merlet and B. Ravani (eds.): *Computational Kinematics '95*. 1995 ISBN 0-7923-3673-9
41. L.P. Lebedev, I.I. Vorovich and G.M.L. Gladwell: *Functional Analysis*. Applications in Mechanics and Inverse Problems. 1996
ISBN 0-7923-3849-9
42. J. Menčík: *Mechanics of Components with Treated or Coated Surfaces*. 1996
ISBN 0-7923-3700-X
43. D. Bestle and W. Schiehlen (eds.): *IUTAM Symposium on Optimization of Mechanical Systems*. Proceedings of the IUTAM Symposium held in Stuttgart, Germany. 1996
ISBN 0-7923-3830-8
44. D.A. Hills, P.A. Kelly, D.N. Dai and A.M. Korsunsky: *Solution of Crack Problems*. The Distributed Dislocation Technique. 1996
ISBN 0-7923-3848-0
45. V.A. Squire, R.J. Hosking, A.D. Kerr and P.J. Langhorne: *Moving Loads on Ice Plates*. 1996
ISBN 0-7923-3953-3
46. A. Pineau and A. Zaoui (eds.): *IUTAM Symposium on Micromechanics of Plasticity and Damage of Multiphase Materials*. Proceedings of the IUTAM Symposium held in Sèvres, Paris, France. 1996
ISBN 0-7923-4188-0
47. A. Naess and S. Krenk (eds.): *IUTAM Symposium on Advances in Nonlinear Stochastic Mechanics*. Proceedings of the IUTAM Symposium held in Trondheim, Norway. 1996
ISBN 0-7923-4193-7
48. D. Ieşan and A. Scalia: *Thermoelastic Deformations*. 1996
ISBN 0-7923-4230-5

Mechanics

SOLID MECHANICS AND ITS APPLICATIONS

Series Editor: G.M.L. Gladwell

49. J.R. Willis (ed.): *IUTAM Symposium on Nonlinear Analysis of Fracture*. Proceedings of the IUTAM Symposium held in Cambridge, U.K. 1997 ISBN 0-7923-4378-6
50. A. Preumont: *Vibration Control of Active Structures*. An Introduction. 1997 ISBN 0-7923-4392-1
51. G.P. Cherepanov: *Methods of Fracture Mechanics: Solid Matter Physics*. 1997 ISBN 0-7923-4408-1
52. D.H. van Campen (ed.): *IUTAM Symposium on Interaction between Dynamics and Control in Advanced Mechanical Systems*. Proceedings of the IUTAM Symposium held in Eindhoven, The Netherlands. 1997 ISBN 0-7923-4429-4
53. N.A. Fleck and A.C.F. Cocks (eds.): *IUTAM Symposium on Mechanics of Granular and Porous Materials*. Proceedings of the IUTAM Symposium held in Cambridge, U.K. 1997 ISBN 0-7923-4553-3
54. J. Roorda and N.K. Srivastava (eds.): *Trends in Structural Mechanics*. Theory, Practice, Education. 1997 ISBN 0-7923-4603-3
55. Yu.A. Mitropolskii and N. Van Dao: *Applied Asymptotic Methods in Nonlinear Oscillations*. 1997 ISBN 0-7923-4605-X
56. C. Guedes Soares (ed.): *Probabilistic Methods for Structural Design*. 1997 ISBN 0-7923-4670-X
57. D. François, A. Pineau and A. Zaoui: *Mechanical Behaviour of Materials*. Volume I: Elasticity and Plasticity. 1998 ISBN 0-7923-4894-X
58. D. François, A. Pineau and A. Zaoui: *Mechanical Behaviour of Materials*. Volume II: Viscoplasticity, Damage, Fracture and Contact Mechanics. 1998 ISBN 0-7923-4895-8
59. L.T. Tenek and J. Argyris: *Finite Element Analysis for Composite Structures*. 1998 ISBN 0-7923-4899-0
60. Y.A. Bahei-El-Din and G.J. Dvorak (eds.): *IUTAM Symposium on Transformation Problems in Composite and Active Materials*. Proceedings of the IUTAM Symposium held in Cairo, Egypt. 1998 ISBN 0-7923-5122-3
61. I.G. Goryacheva: *Contact Mechanics in Tribology*. 1998 ISBN 0-7923-5257-2
62. O.T. Bruhns and E. Stein (eds.): *IUTAM Symposium on Micro- and Macrostructural Aspects of Thermoplasticity*. Proceedings of the IUTAM Symposium held in Bochum, Germany. 1999 ISBN 0-7923-5265-3
63. F.C. Moon: *IUTAM Symposium on New Applications of Nonlinear and Chaotic Dynamics in Mechanics*. Proceedings of the IUTAM Symposium held in Ithaca, NY, USA. 1998 ISBN 0-7923-5276-9
64. R. Wang: *IUTAM Symposium on Rheology of Bodies with Defects*. Proceedings of the IUTAM Symposium held in Beijing, China. 1999 ISBN 0-7923-5297-1
65. Yu.I. Dimitrienko: *Thermomechanics of Composites under High Temperatures*. 1999 ISBN 0-7923-4899-0
66. P. Argoul, M. Frémond and Q.S. Nguyen (eds.): *IUTAM Symposium on Variations of Domains and Free-Boundary Problems in Solid Mechanics*. Proceedings of the IUTAM Symposium held in Paris, France. 1999 ISBN 0-7923-5450-8
67. F.J. Fahy and W.G. Price (eds.): *IUTAM Symposium on Statistical Energy Analysis*. Proceedings of the IUTAM Symposium held in Southampton, U.K. 1999 ISBN 0-7923-5457-5
68. H.A. Mang and F.G. Rammerstorfer (eds.): *IUTAM Symposium on Discretization Methods in Structural Mechanics*. Proceedings of the IUTAM Symposium held in Vienna, Austria. 1999 ISBN 0-7923-5591-1

Mechanics

SOLID MECHANICS AND ITS APPLICATIONS

Series Editor: G.M.L. Gladwell

69. P. Pedersen and M.P. Bendsøe (eds.): *IUTAM Symposium on Synthesis in Bio Solid Mechanics*. Proceedings of the IUTAM Symposium held in Copenhagen, Denmark. 1999
ISBN 0-7923-5615-2
70. S.K. Agrawal and B.C. Fabien: *Optimization of Dynamic Systems*. 1999
ISBN 0-7923-5681-0
71. A. Carpinteri: *Nonlinear Crack Models for Nonmetallic Materials*. 1999
ISBN 0-7923-5750-7
72. F. Pfeifer (ed.): *IUTAM Symposium on Unilateral Multibody Contacts*. Proceedings of the IUTAM Symposium held in Munich, Germany. 1999
ISBN 0-7923-6030-3
73. E. Lavendelis and M. Zakhrevsky (eds.): *IUTAM/IFTToMM Symposium on Synthesis of Non-linear Dynamical Systems*. Proceedings of the IUTAM/IFTToMM Symposium held in Riga, Latvia. 2000
ISBN 0-7923-6106-7
74. J.-P. Merlet: *Parallel Robots*. 2000
ISBN 0-7923-6308-6
75. J.T. Pindera: *Techniques of Tomographic Isodyne Stress Analysis*. 2000
ISBN 0-7923-6388-4
76. G.A. Maugin, R. Drouot and F. Sidoroff (eds.): *Continuum Thermomechanics*. The Art and Science of Modelling Material Behaviour. 2000
ISBN 0-7923-6407-4
77. N. Van Dao and E.J. Kreuzer (eds.): *IUTAM Symposium on Recent Developments in Non-linear Oscillations of Mechanical Systems*. 2000
ISBN 0-7923-6470-8
78. S.D. Akbarov and A.N. Guz: *Mechanics of Curved Composites*. 2000
ISBN 0-7923-6477-5
79. M.B. Rubin: *Cosserat Theories: Shells, Rods and Points*. 2000
ISBN 0-7923-6489-9
80. S. Pellegrino and S.D. Guest (eds.): *IUTAM-IASS Symposium on Deployable Structures: Theory and Applications*. Proceedings of the IUTAM-IASS Symposium held in Cambridge, U.K., 6–9 September 1998. 2000
ISBN 0-7923-6516-X
81. A.D. Rosato and D.L. Blackmore (eds.): *IUTAM Symposium on Segregation in Granular Flows*. Proceedings of the IUTAM Symposium held in Cape May, NJ, U.S.A., June 5–10, 1999. 2000
ISBN 0-7923-6547-X
82. A. Lagarde (ed.): *IUTAM Symposium on Advanced Optical Methods and Applications in Solid Mechanics*. Proceedings of the IUTAM Symposium held in Futuroscope, Poitiers, France, August 31–September 4, 1998. 2000
ISBN 0-7923-6604-2
83. D. Weichert and G. Maier (eds.): *Inelastic Analysis of Structures under Variable Loads*. Theory and Engineering Applications. 2000
ISBN 0-7923-6645-X
84. T.-J. Chuang and J.W. Rudnicki (eds.): *Multiscale Deformation and Fracture in Materials and Structures*. The James R. Rice 60th Anniversary Volume. 2001
ISBN 0-7923-6718-9
85. S. Narayanan and R.N. Iyengar (eds.): *IUTAM Symposium on Nonlinearity and Stochastic Structural Dynamics*. Proceedings of the IUTAM Symposium held in Madras, Chennai, India, 4–8 January 1999
ISBN 0-7923-6733-2
86. S. Murakami and N. Ohno (eds.): *IUTAM Symposium on Creep in Structures*. Proceedings of the IUTAM Symposium held in Nagoya, Japan, 3–7 April 2000. 2001
ISBN 0-7923-6737-5
87. W. Ehlers (ed.): *IUTAM Symposium on Theoretical and Numerical Methods in Continuum Mechanics of Porous Materials*. Proceedings of the IUTAM Symposium held at the University of Stuttgart, Germany, September 5–10, 1999. 2001
ISBN 0-7923-6766-9
88. D. Durban, D. Givoli and J.G. Simmonds (eds.): *Advances in the Mechanics of Plates and Shells The Avinoam Libai Anniversary Volume*. 2001
ISBN 0-7923-6785-5
89. U. Gabbert and H.-S. Tzou (eds.): *IUTAM Symposium on Smart Structures and Structonic Systems*. Proceedings of the IUTAM Symposium held in Magdeburg, Germany, 26–29 September 2000. 2001
ISBN 0-7923-6968-8

Mechanics

SOLID MECHANICS AND ITS APPLICATIONS

Series Editor: G.M.L. Gladwell

90. Y. Ivanov, V. Cheshkov and M. Natova: *Polymer Composite Materials – Interface Phenomena & Processes*. 2001 ISBN 0-7923-7008-2
91. R.C. McPhedran, L.C. Botten and N.A. Nicorovici (eds.): *IUTAM Symposium on Mechanical and Electromagnetic Waves in Structured Media*. Proceedings of the IUTAM Symposium held in Sydney, NSW, Australia, 18-22 Januari 1999. 2001 ISBN 0-7923-7038-4
92. D.A. Sotiropoulos (ed.): *IUTAM Symposium on Mechanical Waves for Composite Structures Characterization*. Proceedings of the IUTAM Symposium held in Chania, Crete, Greece, June 14-17, 2000. 2001 ISBN 0-7923-7164-X
93. V.M. Alexandrov and D.A. Pozharskii: *Three-Dimensional Contact Problems*. 2001 ISBN 0-7923-7165-8
94. J.P. Dempsey and H.H. Shen (eds.): *IUTAM Symposium on Scaling Laws in Ice Mechanics and Ice Dynamics*. Proceedings of the IUTAM Symposium held in Fairbanks, Alaska, U.S.A., 13-16 June 2000. 2001 ISBN 1-4020-0171-1
95. U. Kirsch: *Design-Oriented Analysis of Structures*. A Unified Approach. 2002 ISBN 1-4020-0443-5
96. A. Preumont: *Vibration Control of Active Structures*. An Introduction (2nd Edition). 2002 ISBN 1-4020-0496-6
97. B.L. Karihaloo (ed.): *IUTAM Symposium on Analytical and Computational Fracture Mechanics of Non-Homogeneous Materials*. Proceedings of the IUTAM Symposium held in Cardiff, U.K., 18-22 June 2001. 2002 ISBN 1-4020-0510-5
98. S.M. Han and H. Benaroya: *Nonlinear and Stochastic Dynamics of Compliant Offshore Structures*. 2002 ISBN 1-4020-0573-3
99. A.M. Linkov: *Boundary Integral Equations in Elasticity Theory*. 2002 ISBN 1-4020-0574-1
100. L.P. Lebedev, I.I. Vorovich and G.M.L. Gladwell: *Functional Analysis*. Applications in Mechanics and Inverse Problems (2nd Edition). 2002 ISBN 1-4020-0667-5; Pb: 1-4020-0756-6
101. Q.P. Sun (ed.): *IUTAM Symposium on Mechanics of Martensitic Phase Transformation in Solids*. Proceedings of the IUTAM Symposium held in Hong Kong, China, 11-15 June 2001. 2002 ISBN 1-4020-0741-8
102. M.L. Munjal (ed.): *IUTAM Symposium on Designing for Quietness*. Proceedings of the IUTAM Symposium held in Bangkok, India, 12-14 December 2000. 2002 ISBN 1-4020-0765-5
103. J.A.C. Martins and M.D.P. Monteiro Marques (eds.): *Contact Mechanics*. Proceedings of the 3rd Contact Mechanics International Symposium, Praia da Consolação, Peniche, Portugal, 17-21 June 2001. 2002 ISBN 1-4020-0811-2
104. H.R. Drew and S. Pellegrino (eds.): *New Approaches to Structural Mechanics, Shells and Biological Structures*. 2002 ISBN 1-4020-0862-7
105. J.R. Vinson and R.L. Sierakowski: *The Behavior of Structures Composed of Composite Materials*. Second Edition. 2002 ISBN 1-4020-0904-6
106. Not yet published.
107. J.R. Barber: *Elasticity*. Second Edition. 2002 ISBN Hb 1-4020-0964-X; Pb 1-4020-0966-6
108. C. Miehe (ed.): *IUTAM Symposium on Computational Mechanics of Solid Materials at Large Strains*. Proceedings of the IUTAM Symposium held in Stuttgart, Germany, 20-24 August 2001. 2003 ISBN 1-4020-1170-9

Mechanics

SOLID MECHANICS AND ITS APPLICATIONS

Series Editor: G.M.L. Gladwell

109. P. Ståhle and K.G. Sundin (eds.): *IUTAM Symposium on Field Analyses for Determination of Material Parameters – Experimental and Numerical Aspects*. Proceedings of the IUTAM Symposium held in Abisko National Park, Kiruna, Sweden, July 31 – August 4, 2000. 2003
ISBN 1-4020-1283-7
110. N. Sri Namachchivaya and Y.K. Lin (eds.): *IUTAM Symposium on Nonlinear Stochastic Dynamics*. Proceedings of the IUTAM Symposium held in Monticello, IL, USA, 26 – 30 August, 2000. 2003
ISBN 1-4020-1471-6
111. H. Sobieckzky (ed.): *IUTAM Symposium Transsonicum IV*. Proceedings of the IUTAM Symposium held in Göttingen, Germany, 2–6 September 2002, 2003
ISBN 1-4020-1608-5
112. J.-C. Samin and P. Fiset: *Symbolic Modeling of Multibody Systems*. 2003
ISBN 1-4020-1629-8
113. A.B. Movchan (ed.): *IUTAM Symposium on Asymptotics, Singularities and Homogenisation in Problems of Mechanics*. Proceedings of the IUTAM Symposium held in Liverpool, United Kingdom, 8-11 July 2002. 2003
ISBN 1-4020-1780-4
114. S. Ahzi, M. Cherkaoui, M.A. Khaleel, H.M. Zbib, M.A. Zikry and B. LaMatina (eds.): *IUTAM Symposium on Multiscale Modeling and Characterization of Elastic-Inelastic Behavior of Engineering Materials*. Proceedings of the IUTAM Symposium held in Marrakech, Morocco, 20-25 October 2002. 2004
ISBN 1-4020-1861-4
115. H. Kitagawa and Y. Shibutani (eds.): *IUTAM Symposium on Mesoscopic Dynamics of Fracture Process and Materials Strength*. Proceedings of the IUTAM Symposium held in Osaka, Japan, 6-11 July 2003. Volume in celebration of Professor Kitagawa's retirement. 2004
ISBN 1-4020-2037-6
116. E.H. Dowell, R.L. Clark, D. Cox, H.C. Curtiss, Jr., K.C. Hall, D.A. Peters, R.H. Scanlan, E. Simiu, F. Sisto and D. Tang: *A Modern Course in Aeroelasticity*. 4th Edition, 2004
ISBN 1-4020-2039-2
117. T. Burczyński and A. Osyczka (eds.): *IUTAM Symposium on Evolutionary Methods in Mechanics*. Proceedings of the IUTAM Symposium held in Cracow, Poland, 24-27 September 2002. 2004
ISBN 1-4020-2266-2
118. D. Ieşan: *Thermoelastic Models of Continua*. 2004
ISBN 1-4020-2309-X
119. G.M.L. Gladwell: *Inverse Problems in Vibration*. Second Edition. 2004
ISBN 1-4020-2670-6
120. J.R. Vinson: *Plate and Panel Structures of Isotropic, Composite and Piezoelectric Materials, Including Sandwich Construction*. 2005
ISBN 1-4020-3110-6
121. *Forthcoming*
122. G. Rega and F. Vestroni (eds.): *IUTAM Symposium on Chaotic Dynamics and Control of Systems and Processes in Mechanics*. Proceedings of the IUTAM Symposium held in Rome, Italy, 8–13 June 2003. 2005
ISBN 1-4020-3267-6
123. E.E. Gdoutos: *Fracture Mechanics. An Introduction*. 2nd edition. 2005
ISBN 1-4020-3267-6
124. M.D. Gilchrist (ed.): *IUTAM Symposium on Impact Biomechanics from Fundamental Insights to Applications*. 2005
ISBN 1-4020-3795-3
125. J.M. Hughe, P.A.C. Raats and S. C. Cowin (eds.): *IUTAM Symposium on Physicochemical and Electromechanical Interactions in Porous Media*. 2005
ISBN 1-4020-3864-X
126. H. Ding and W. Chen: *Elasticity of Transversely Isotropic Materials*. 2005
ISBN 1-4020-4033-4
127. W. Yang (ed): *IUTAM Symposium on Mechanics and Reliability of Actuating Materials*. Proceedings of the IUTAM Symposium held in Beijing, China, 1–3 September 2004. 2005
ISBN 1-4020-4131-6
128. J.P. Merlet: *Parallel Robots*. 2005
ISBN 1-4020-4132-2

Mechanics

SOLID MECHANICS AND ITS APPLICATIONS

Series Editor: G.M.L. Gladwell

129. G.E.A. Meier and K.R. Sreenivasan (eds.): *IUTAM Symposium on One Hundred Years of Boundary Layer Research*. Proceedings of the IUTAM Symposium held at DLR-Göttingen, Germany, August 12–14, 2004. 2005 ISBN 1-4020-4149-7
130. H. Ulbrich and W. Günthner (eds.): *IUTAM Symposium on Vibration Control of Nonlinear Mechanisms and Structures*. 2005 ISBN 1-4020-4160-8
131. L. Librescu and O. Song: *Thin-Walled Composite Beams*. Theory and Application. 2005 ISBN 1-4020-3457-1